The First Caltech-Jodrell Bank VLBI Survey

Thesis

by

Wenge Xu

In Partial Fulfillment of the Requirements

for the Degree of

Doctor of Philosophy

California Institute of Technology

Pasadena, California

1995

(Submitted December 1994)

ACKNOWLEDGEMENTS

I would like to thank all the people who provided help and support over the past 6 years. My first and foremost thanks go to my advisor, Tony Readhead, for his guidance and extreme patience, and also for his enthusiasm, optimism and ceaseless encouragement. To him, I will always be in debt. Many thanks also go to the current and past members of the VLBI group, Marshall Cohen, Tim Pearson, Steve Unwin, Charles Lawrence, Rene Vermeulen, Greg Taylor, Martin Shepherd, Dhiraj Thakkar, Ann Wehrle, John Conway and Tiziana Venturi, for their useful suggestions and fruitful discussions. I would especially like to thank Tim for his critical reading of the manuscript of this thesis. I would also like to thank Martin for developing the DIFMAP package, and Greg for his joint effort with Martin to develop the AUTOMAP procedure. It is these tools which made the re-analysis of the VLBI data possible. It was a pleasure working with Charles Lawrence and Chris Impey (of Univ. of Arizona) from whom I learned to deal with optical data.

I would like to thank Peter Wilkinson and Antonis Polatidis for their hospitality during my visit at Jodrell Bank. It was a great pleasure to work with Antonis. I wish that we will have other chances to work together in the future.

I would also like to thank the VLBI friends of the participating stations of the US and European VLBI network for making the VLBI observations, and to the staff of the JPL/Caltech Block 2 correlator for correlating these observations. Thanks are also due to the staff of the Palomar observatory, Steward observatory, VLA and MERLIN for their help on observations.

I would like to thank all the people who have helped me to adapt to this country. It is not possible to mention all the names here. Nonetheless, I would like to thank my fellow

students and officemates, Tom Herbig, Jose Navarro and Nick Weir. I wish the best for their life and career and I will always treasure their friendship. I would also like to thank the faculty members, staff and other students for their help and making me feel welcome, and the fellow Chinese students at Caltech for providing a familiar voice and a place to ease my nostalgia.

Last but not the least I would like to thank my parents, sister and brothers for their support and understanding. I would especially like to thank Xiuqin for being a loving wife and caring friend whom I can always count on. Soon we will be proud parents. I would like to thank my yet-to-be-born baby for infusing new excitement to my life. I am looking forward to sharing our life together.

致　　秀琴

To　　Xiuqin

ABSTRACT

This thesis presents the author's major contributions to the first Caltech-Jodrell Bank VLBI survey (CJ1). It demonstrates convincingly that the VLBI snapshot technique is a reliable and highly efficient method of making images of large samples of objects.

The CJ1 sample consists of 135 objects with 1.3 Jy $> S_{5\ \mathrm{GHz}} \geq$ 0.7 Jy, $\delta(1950) \geq 35°$ and $|b| > 10°$. The combination of the CJ1 sample with the Pearson–Readhead sample provides a complete, flux density limited sample of 200 objects with $S_{5\ \mathrm{GHz}} \geq$ 0.7 Jy, $\delta(1950) \geq 35°$ and $|b| > 10°$ for which all of the objects accessible to Mark II VLBI have been mapped at both 5 GHz and 1.6 GHz. In this thesis we present the 5 GHz VLBI observations from the CJ1 survey and follow-up observations of 8 compact symmetric objects (CSO) or CSO candidates at 8.4 GHz. In addition, we present 5 GHz MERLIN observations of 20 objects and 1.4 GHz VLA observations of 92 objects in the CJ1+PR sample. The VLA maps, together with L band (1.3–1.7 GHz) maps available in the literature, provide a complete set of VLA maps for the CJ1+PR sample. Furthermore, we present new redshifts, optical counterparts and optical polarimetry measurements of the objects in the CJ1 sample.

Based on morphological attributes on scales < 5 kpc and ≥ 5 kpc, we identify six physically distinct classes in the CJ1+PR sample, one of which is the CSO class. Identification of CSO's may have a profound impact on our understanding of AGN. Detailed study of one archetypal CSO, 2352+495, has demonstrated that the CSO's are likely a class of short-lived powerful galaxies.

We have confirmed the bimodal distribution of the misalignment angle and identified that the peak near 90° is contributed by a group of objects with high optical polarization, high fractional core flux, high radio variability and flat radio spectrum. All of these are

symptoms of relativistic beaming.

The mean angular sizes of the CJ1+PR objects show only slight dependence on redshift, contrary to the finding by Kellermann. However, our results show that the angular size distributions of objects with $z < 0.1$ and those with $z > 0.1$ are significantly different. This may indicate an evolutionary effect.

CONTENTS

Acknowledgements . . . . . **ii**

Abstract . . . . . **v**

List of Tables . . . . . **xii**

List of Figures . . . . . **xiii**

Chapter 1 Introduction **1–1**

1.1 Historical Background 1–1

1.2 Extragalactic Radio Sources 1–4

1.2.1 The Lobe-dominated Sources 1–4

1.2.1.1 FR I Sources 1–5

1.2.1.2 FR II Sources 1–6

1.2.2 The Core-dominated Sources 1–7

1.2.3 The Compact Steep-spectrum Sources 1–8

1.2.4 The Gigahertz-peaked Spectrum Sources 1–9

1.3 The Relativistic Beaming Model and Unification Schemes 1–10

1.4 Motivation for This Thesis 1–13

1.5 A Synopsis of This Thesis 1–13

1.6 Some Definitions 1–14

1.7 Publications Based Totally or In Part on This Thesis 1–15

Chapter 2 The First Caltech–Jodrell Bank Survey **2–1**

2.1 Background 2–1

2.2 The First Caltech–Jodrell Bank Sample 2–4

2.3 Observation Strategy 2–5

2.3.1 VLBI Observations 2–5

2.3.2 VLA Observations 2–7

2.3.3 MERLIN Observations 2–7

2.3.4 Complementary Optical Observations 2–7

Chapter 3 Radio Observations and Data Reduction 3–1

3.1 Introduction 3–1

3.2 VLBI Observations and Data Reduction 3–2

3.2.1 The Snapshot Technique 3–2

3.2.2 VLBI Observations 3–3

3.2.3 Data Reduction 3–4

3.2.3.1 Fringe-fitting and Initial Phase Calibration 3–5

3.2.3.2 Amplitude Calibration 3–6

3.2.3.3 Data Editing 3–7

3.2.3.4 Mapping 3–8

3.2.4 Final Maps 3–11

3.2.5 Modelfitting 3–11

3.3 Text of a Paper Submitted to the ApJ Supplement Series 3–13

Abstract 3–14

1 Introduction 3–15

2 Observations and Data Reduction 3–16

2.1 VLBI Observations and Data Reduction 3–16

2.2 MERLIN Observations and Data Reduction 3–20

2.3 VLA Observations and Data Reduction 3–21

2.4 Radio Spectra 3–21

3 Conclusion 3–22

Acknowledgements 3–23

References 3–24

3.4 Presentation of Maps and Spectra 3–26

Chapter 4 Optical Observations and Data Reduction 4–1

4.1 Introduction 4–1

4.2 New Redshifts 4–2

4.3 Optical Identifications 4–10

4.3.1 Observations 4–10

4.3.2 Identification Procedure 4–10

4.4 Optical Polarimetry Measurements 4–15

4.4.1 Introduction 4–15

4.4.2 Observations 4–16

Chapter 5 The Classification of Powerful Extragalactic Radio Sources 5–1

5.1 Introduction 5–1

5.2 Morphological Attributes 5–2

5.2.1 Morphological Attributes on Scales $\geq$ 5 kpc 5–2

5.2.2 Morphological Attributes on Scales $<$ 5 kpc 5–5

5.3 Physically Distinct Classes 5–10

5.4 Discussion 5–11

Chapter 6 Statistical Studies 6–1

6.1 General Studies 6–1

6.2 Linear Size Distribution of Physical Classes 6–5

6.3 Alignment of Structures on Milliarcsecond and Arcsecond Scales . . . 6–8

6.3.1 Distribution of Misalignment Angles in the PR+CJ1 Sample . . 6–12

6.3.1.1 Position Angle Measurements 6–12

6.3.1.2 ΔPA Distribution 6–14

6.3.2 Correlations of ΔPA with Other Observable Properties 6–21

6.3.2.1 ΔPA and Optical Polarization 6–21

6.3.2.2 ΔPA and Spectral Indices 6–23

6.3.2.3 ΔPA and F_c: the fraction

of the total flux density in the core 6–24

6.3.2.4 ΔPA and Radio Variability 6–25

6.3.2.5 Summary of Observation Status 6–26

6.3.4 Possible Models 6–28

6.4 Angular Size – Redshift Test 6–30

Chapter 7 The Compact Symmetric Objects 7–1

7.1 Introduction 7–1

7.2 Detailed Discussion of CSO's in PR+CJ1 Sample 7–9

0108+388 7–9

0258+350 (NGC 1167) 7–12

0404+768 7–12

0646+600 7–14

0710+439 7–16

1031+567 7–17

1225+368 7–19

1242+410 7–21

1250+568 7–23

1333+459 7–23

1333+589 7–25

1358+624 7–27

1437+624 7–27

1627+626 7–29

1734+508 7–29

1819+396 7–31

1843+356 7–33

1943+546 7–35

2324+435 7–35

2342+821 7–35

7.3 Summary 7–41

Chapter 8 Conclusions 8–1

8.1 The Snapshot Technique 8–1

8.2 Identification of Physically Distinct Classes of Powerful Extragalactic Radio Sources 8–1

8.3 Confirmation of the Bimodal Distribution of the Misalignment Angle . 8–3

8.4 Angular Size – Redshift Relation 8–3

8.5 Identification of Interesting Objects 8–3

References 9–1

LIST OF TABLES

Table 2.1 The First Caltech-Jodrell Bank Sample 2–9

Table 3.1 Telescope Characteristics 3–28

Table 3.2 VLBI Map Parameters 3–30

Table 3.3 Gaussian Models 3–35

Table 3.4 MERLIN Map Parameters 3–44

Table 3.5 VLA Map Parameters 3–45

Table 4.1 Redshifts of Caltech-Jodrell Bank Survey Sources 4–7

Table 4.2 Optical Identification 4–12

Table 4.3 Error Estimation for Optical Coordinates 4–14

Table 4.4 Optical Polarimetry for CJ1 Sources 4–18

Table 5.1 Physical Classification of the CJ1 Sample 5–13

Table 5.2 Physical Classification of the PR Sample 5–22

Table 6.1 Distribution of Morphological Attributes on Scale $\geq$ 5 kpc 6–6

Table 6.2 Distribution of Morphological Attributes on Scale $<$ 5 kpc 6–6

Table 6.3 Distribution amongst Physical Classes 6–6

Table 6.4 ΔPA, F_c, P, α and V 6–15

Table 6.5 Summary of the KS tests 6–26

Table 6.6 Precession Periods of Close Binary Blackholes 6–29

Table 6.7 Angular Sizes of the PR+CJ1 and Kellermann's Samples 6–37

Table 7.1 The CSO's and CSO Candidates in the PR+CJ1 Sample 7–3

Table 7.2 Journal of VLBI Observations 7–5

Table 7.3 Spectral Indices of Individual Emission Regions

LIST OF FIGURES

Fig. 1.1 The "Standard Model" of powerful radio sources 1–12

Fig. 3.1 Sample *uv* coverages for VLBI observations 3–49

Fig. 3.2 Sample *uv* coverages for MERLIN observations 3–50

Fig. 3.3 Sample *uv* coverage for VLA observations 3–51

Fig. 3.4 VLBI, MERLIN, VLA maps and radio spectra of the following sources

0010+405 3–52

0022+390 3–53

0102+480 3–54

0218+357 3–55

0248+430 3–57

0402+379 3–58

0404+768 3–59

0602+673 3–61

0615+820 3–62

0620+389 3–63

0642+449 3–64

0646+600 3–65

0650+371 3–66

0707+476 3–67

0716+714 3–68

0740+828 3–69

0746+483 3–70

0755+379 3–71
0805+410 3–72
0812+367 3–73
0820+560 3–74
0821+394 3–75
0828+493 3–77
0833+585 3–78
0900+428 3–79
0917+449 3–80
0917+624 3–81
0955+476 3–82
1003+830 3–83
1015+359 3–84
1020+400 3–85
1030+415 3–86
1039+811 3–87
1044+719 3–88
1053+704 3–89
1053+815 3–90
1058+726 3–91
1101+384 3–93
1128+385 3–94
1138+594 3–95
1144+402 3–97
1144+542 3–98
1150+497 3–99
1150+812 3–100

1213+350 3–101
1216+487 3–103
1225+368 3–104
1242+410 3–106
1311+678 3–108
1317+520 3–109
1333+459 3–110
1333+589 3–111
1342+663 3–112
1347+539 3–113
1357+769 3–115
1418+546 3–116
1435+638 3–117
1437+624 3–118
1438+385 3–120
1504+377 3–121
1547+507 3–122
1638+398 3–123
1656+477 3–124
1656+482 3–125
1719+357 3–126
1732+389 3–127
1734+508 3–128
1738+476 3–129
1751+441 3–130
1758+388 3–131
1800+440 3–132

1819+396 3–133
1842+681 3–134
1843+356 3–135
1926+611 3–136
1943+546 3–137
2007+777 3–139
2010+723 3–140
2207+374 3–141
2214+350 3–143
2229+695 3–144
2253+417 3–145
2255+416 3–146
2311+469 3–148
Fig. 3.5 Other MERLIN maps 3–150
Fig. 3.6 Other VLA maps 3–152
Fig. 3.7 Radio spectra of other objects 3–158
Fig. 6.1 Redshift distributions of the PR, CJ1 and PR+CJ1 samples 6–2
Fig. 6.2 Optical magnitude distributions of the PR, CJ1 and PR+CJ1 samples . 6–3
Fig. 6.3 Spectral index distributions of the PR, CJ1 and PR+CJ1 samples . . . 6–4
Fig. 6.4 Linear size distribution of physical classes 6–7
Fig. 6.5a An example of aligned object — 1807+698 (3C 371) 6–9
Fig. 6.5b An example of misaligned object — 1823+698 6–10
Fig. 6.6 ΔPA distribution of Pearson & Readhead (1988)
and Conway & Murphy (1993) 6–11
Fig. 6.7 ΔPA distribution of the PR+CJ1 sample 6–14
Fig. 6.8 ΔPA distributions of objects with $P > 5\%$ and $P \leq 5\%$ 6–22
Fig. 6.9 ΔPA distributions of objects with flat and steep spectrum 6–23

Fig. 6.10 ΔPA distributions of objects with $F_c > 0.3$ and $F_c \leq 0.3$ 6–24

Fig. 6.11 ΔPA distributions of objects with $V > 0.15$ and $V \leq 0.15$ 6–25

Fig. 6.12 Summary of observation status 6–27

Fig. 6.13 Angular Size—Redshift relation 6–35

Fig. 6.14 Angular size distribution of objects with $z > 0.1$ and $z < 0.1$ 6–36

Fig. 7.1 VLBI observations and spectra of 0108+388 7–11

Fig. 7.2 VLBI observations and spectra of 0404+768 7–13

Fig. 7.3 VLBI observations and spectra of 0646+600 7–15

Fig. 7.4 VLBI observations and spectra of 0710+439 7–18

Fig. 7.5 VLBI observations and spectra of 1225+368 7–20

Fig. 7.6 VLBI observations and spectra of 1242+410 7–22

Fig. 7.7 VLBI observations and spectra of 1333+459 7–24

Fig. 7.8 VLBI observations and spectra of 1333+589 7–26

Fig. 7.9 VLBI observations and spectra of 1437+624 7–28

Fig. 7.10 VLBI observations and spectra of 1734+508 7–30

Fig. 7.11 VLBI observations and spectra of 1819+396 7–32

Fig. 7.12 VLBI observations and spectra of 1843+356 7–34

Fig. 7.13 VLBI observations and spectra of 1943+546 7–36

Fig. 7.14 VLBI observations and spectra of 2352+495 7–40

Chapter 1

INTRODUCTION

1.1. HISTORICAL BACKGROUND

Discrete radio sources were first distinguished from the general background radio emission by Hey et al. (1946). Soon afterwards two of the strongest radio sources were identified with the nearby galaxies M87 and NGC 5128 (Bolton & Stanley 1949) and later the powerful radio source Cygnus A was identified with a relatively faint (15^m) galaxy at $z = 0.056$ (Baade & Minkowski 1954). The association of discrete radio sources with extragalactic objects was gradually recognized in the years following as more radio sources were identified with various types of galaxies. Follow-up studies revealed that the optical counterparts of the powerful radio galaxies tend to be luminous elliptical galaxies, frequently with peculiarities and with strong emission lines (see, e.g., Woltjer 1990; McCarthy 1993 and references therein). A fraction of the early identified radio sources were apparently associated with stellar objects. Not until the early sixties did Schmidt (1963) identify the emission lines in the spectrum of the 13^m stellar object associated with the radio source 3C 273 at a redshift of 0.158. Enlightened by this major development, Greenstein & Matthews (1963) were able to identify emission lines in 3C 48 with an even larger redshift $z = 0.367$. It suddenly became clear that these stellar objects, which are called quasi-stellar radio sources, i.e., *quasars* (Chiu 1964), are at great distances and have very high luminosities. In the course of identifying quasars, Sandage (1965) realized that there are a large population of blue stellar objects which resemble quasars in many optical properties, but are radio quiet, i.e.,

radio-quiet quasars. Later observations showed that most radio-quiet quasars do have low level radio emission (Kellermann et al. 1989).

It became clear, as the observational data accumulated, that a small fraction of galaxies are different from the majority. The majority of galaxies, i.e., normal galaxies, typically have radio luminosities between 10^{36} and 10^{39} erg s^{-1}, while radio galaxies and quasars have radio luminosities in the range of 10^{41} to 10^{47} erg s^{-1}. The radio emission of normal galaxies is synchrotron radiation from relativistic electrons in magnetic fields in the galactic disc and free-free emission from H II regions. Most of the relativistic electrons in normal galaxies are thought to be accelerated by supernova remnants produced by stars more massive than $M \sim 8\ M_{\odot}$. H II regions are ionized by these massive stars as well (Condon 1992). In contrast, the radio emission of radio galaxies and quasars originates from synchrotron radiation from active regions powered by a central engine in the nucleus of the galaxy. Many of the radio galaxies and quasars have extended structures, with lobes on opposite sides of the central galaxy. The radio lobes have tremendous total energy, as much as 10^{60} erg, in the form of particle and magnetic field energy. Normal galaxies emit mostly starlight at optical wavelengths, consisting of a thermal continuum plus absorption lines, whereas Seyfert nuclei, radio-loud and radio-quiet quasars, and most of the radio galaxies have strong emission lines and a nonthermal continuum. These differences show that this small fraction of galaxies have an energy source not related to ordinary stellar processes. These galaxies are distinguished from other galaxies as active galaxies. The nuclei of such galaxies, where the activities occur, are named active galactic nuclei (henceforth AGN).

AGN with luminosities $\sim 10^{46}$ erg s^{-1} are formed in $\sim 1\%$ of galaxies at redshifts around 2, whereas a few percent of galaxies contain AGN with luminosities $\sim 10^{44}$ erg s^{-1}. It is possible that somewhat weaker AGN are still more common (Krolik 1992). Generally speaking, there are three different types of AGN (Woltjer 1990):

(1) The radio galaxies and quasars associated with elliptical galaxies;

(2) The BL Lac objects and OVV (i.e., optically violent variable) quasars associated with elliptical galaxies and presumably involving relativistic jets seen at small angles;

(3) The Seyferts and radio-quiet quasars associated with spiral galaxies at the lower luminosities and possibly at least in part with ellipticals at higher luminosities.

Since 1950 the advent of interferometric techniques has dramatically improved the imaging of the radio sources, providing high resolution and sensitivity, which make it possible to study the morphology of these radio sources in great detail. Studies of strong radio sources have made great contributions to our understanding of AGN and were a major factor leading to the ***black hole hypothesis*** , namely that all active galaxies contain $\sim 10^6 - 10^9 M_\odot$ black holes in their nuclei and that these objects together with their orbiting accretion disks are the prime energy generator for most of the powerful activities. One of the most successful steps towards understanding these objects was the development of the relativistic beaming model, which consists of a spinning supermassive black hole and two well-collimated relativistic jets in opposite directions (Readhead, Cohen & Blandford 1978; Blandford & Königl 1979; Scheuer & Readhead 1979; Readhead 1980; Orr & Browne 1982; Begelman, Blandford & Rees 1984; *see Section 1.2.4 also*). On this model, the lobe- and core-dominated radio sources can be understood as similar objects viewed from different orientations. Attempts are also made with some success to relate OVV quasars, quasars and radio galaxies (Readhead et al. 1978; Barthel 1989; Hes et al. 1993; Kapahi 1990), and to unify BL Lac objects with favorably oriented radio galaxies with low or moderate luminosities, i.e., FR I sources (Blandford & Rees 1978; Bicknell 1994; Padovani & Urry 1992a; Urry et al. 1991; Urry 1993). The beaming model provides a ready framework for understanding the nonthermal optical continuum, X-ray and γ-ray radiation of AGN.

1.2. EXTRAGALACTIC RADIO SOURCES

Extragalactic radio sources are usually placed in four classes:

Lobe-dominated Sources: having most of their emission in regions far away from their nuclei, and almost exclusively steep radio spectra.

Core-Dominated Sources: having most of their emission in the nuclear regions, and flat radio spectra in general.

Compact Steep-spectrum Sources: having small projected linear sizes ($\leq$ 5 kpc) (*see Section 1.5*) and steep radio spectra.

Gigahertz Peaked Sources: having simple convex radio spectra with steep spectral indices at high frequencies and spectral turnovers near 1 GHz (e.g., O'Dea et al. 1991).

The general properties of these classes are briefly summarized below. Detailed reviews can be found in Miley(1980), Kellermann & Pauliny-Toth (1981), Bridle & Perley (1984), Kellermann & Owen (1988), Saikia & Salter (1988), Muxlow & Garrington (1991), Fanti et al. (1990a) and O'Dea et al. (1991).

1.2.1. THE LOBE-DOMINATED SOURCES

Lobe-dominated sources consist of a central component and extended double structure which straddles the central component. Many of them have well-collimated jets, which connect the central component to at least one of the outlying extended lobes. The lobe-dominated sources typically have steep radio spectra (flux density $S \propto \nu^{\alpha}$; spectral index $\alpha \sim -0.7$). Their projected linear sizes can be up to a few megaparsecs. The lobe-dominated sources show a change in morphology at an absolute luminosity of $P_{178\mathrm{MHz}} \simeq 5 \times 10^{25}$ W/Hz. Fanaroff & Riley (1974) discovered that sources weaker than this appear limb-darkened, whereas brighter sources show limb-brightened outer structure.

The two classes are referred to as Fanaroff-Riley type I and type II (FR I and FR II), respectively. The lobe-dominated sources generally exhibit a high degree of polarization at radio wavelengths. Radio jets with linear polarization up to 40% are common while those with low polarization ($\leq 5\%$) are exceptional at centimeter wavelengths. In outer edges of hotspots the polarization approaches values as high as $\sim 30\%$. Degrees of polarization approaching the theoretical maximum of 75% (for $\alpha = -1$) have also been seen in filamentary structures and on the outer edges of shells embedded in diffuse lobes (e.g., Bridle & Perley 1984; Saikia & Salter 1988). The polarization observations have revealed that apart from their difference in luminosities, FR I and FR II sources also have different magnetic field structures, as described below.

1.2.1.1. FR I SOURCES

FR I sources are almost exclusively associated with galaxies, often found in nearby rich clusters. The most luminous FR I sources are usually associated with bright D or cD galaxies located in the center of their associated clusters. Almost all FR I sources have a prominent central component and smooth two-sided jets running into large-scale lobe structures. Most straight jets are one-sided close to the core but become two-sided after a few kiloparsecs. The jet with the one-sided base tends to be brighter on the large scale. Although jets on opposite sides usually have comparable brightness (within a factor of a few), some FR I sources do show significant side to side asymmetry. For example, in NGC 6251 the jet to counterjet brightness ratio is $\sim$ 50:1 (Willis et al. 1982). The morphologies of FR I sources are often distorted by processes in the clusters. A subclass of FR I sources has two-sided jets which have been bent by $\sim 90°$ on each side and merged into long diffuse tails. They are referred to as narrow-angle tail (NAT) sources. Such objects are found in clusters of galaxies where the parent galaxy has a large proper motion with respect to the cluster. Another subclass of FR I sources has C-shaped structures, which are referred to as wide-angle-tail (WAT) sources. They are associated with the optically dominant galaxies in

rich clusters (Owen & Rudnick 1976). Their outer structure is characterized by disrupted lobes with inner hotspots linked to the central component by jets. VLBI observations of the central components of FR I sources are sparse. However, a trend has begun to emerge: in most cases the jet on parsec-scales is one-sided and points to the brighter kiloparsec jet (Jones et al. 1986; Venturi et al. 1993a). An example of twin jets has also been discovered recently in 3C 338 on scales < 10 mas, i.e., 4 pc (Feretti 1993).

The magnetic fields in the FR I sources are predominantly orthogonal to the jet axes, although they may be parallel at the bases of the jets. Some jets have a configuration with the field perpendicular to the jet axis near the center but becoming parallel to the axis near one or both its edges. This configuration is often found where jets bend with the outer edge being more strongly polarized. In some cases the fields wrap around the edges of the lobes. The magnetic fields in the tails of both NAT and WAT sources are directed largely along their axes.

1.2.1.2. FR II SOURCES

FR II sources are usually identified with giant elliptical galaxies not usually in rich clusters and quasars which are probably associated with elliptical galaxies also (Véron-Cetty & Woltjer 1990). Compared with the host galaxies of FR I sources, the host galaxies of FR II sources are more likely to appear 'disturbed', perhaps due to interaction with companion galaxies (Heckman et al. 1986).

In FR II sources identified with galaxies, there are hot-spots either located at the farthest edges or embedded in diffuse lobe structures. A relatively weak compact core is often seen in the center of the galaxy, but in some cases the core is too faint to be seen in even the best images. There are many examples in which the core has been detected once maps with high dynamic range are made. A weak one-sided continuous jet can be seen connecting the core with the outer hot spots in some cases (Fernini et al. 1993). A counter

jet has been detected in a few sources, namely Cygnus A, 3C 438 and 0319-454 (Saripalli et al. 1994 and reference therein).

In FR II sources identified with quasars, the structure is basically similar to that of FR II galaxies, but the core tends to be stronger and bright one-sided jets are more common than in FR II galaxies with similar luminosities. Moreover, the lobe structures in quasars show a greater degree of bending or distortion than that found in galaxies (Leahy et al. 1989). Candidates for counterjet emission are detected in 7 out of 12 extended quasars selected from the 3CR sample with deep VLA imaging (Bridle et al. 1994). VLBI observations show that the cores of FR II quasars have one-sided jets which always lie on the same side of the source as the kiloparsec jets (Hough 1986; Hough & Readhead 1987; Hough et al. 1993). This indicates that there is a common origin of the one-sidedness.

In FR II sources, the one-sided jets tend to have magnetic fields parallel to their axes which appear to follow bends and wriggles. Some knots have perpendicular fields while fainter emission near them has parallel fields. In the jets that have been resolved transversely, the polarization tends to be higher on outer edges where the jet bends. The magnetic fields in the outer lobes are often circumferential at the outer edges, parallel to the ridge line, and sometimes change to orthogonal to the ridge near the center. Recent studies by Laing (1988) and Garrington et al. (1988) revealed that the lobe on the opposite side of the one-sided jet is always more depolarized, which strongly indicates that orientation and relativistic beaming are the major factors determining the asymmetry of the powerful radio sources.

1.2.2. THE CORE-DOMINATED SOURCES

With the advent of the Very Large Array (VLA), the quality of radio images has improved dramatically. At a dynamic range of a few thousand to one, most core-dominated radio sources have been found to have faint extended emission around them with luminosities

comparable to that of FR II sources (Browne et al. 1982; Perley et al. 1982; Murphy 1988; Murphy et al. 1993; Rusk 1988; *see Chapter 3 also*). On the kilo-parsec scales, the extended structures of the core-dominated sources show diverse morphologies. For simplicity, they could be classified as (1) halo-like; (2) one-sided; and (3) two-sided. Some of the two-sided core-dominated sources resemble FR II sources except that their cores and/or one-sided jets are relatively much stronger. These objects have been the prime targets of VLBI studies, many of which have been imaged with milliarcsecond resolution. These observations demonstrate that the majority of the core-dominated sources have an asymmetric morphology on parsec scales, which consists of an unresolved core at one end and a jet with a spectrum steeper than that of the core. These studies also show that the parsec-scale jet almost always lies on the same side of the core as the kiloparsec-scale jet. In a few cases where the parsec-scale jet apparently points away from the kilo-parsec-scale jet, detailed studies have shown that the VLBI jet bends through a large angle and then connects with the kilo-parsec jet, e.g., 3C 395 (Saikia et al. 1990) and 1347+539 (Xu et al. 1993). Significant bending of the jet, especially near the core, is a common feature in the core-dominated sources. One of the most important achievements of VLBI observations was the discovery of superluminal motion of bright knots in the parsec-scale jet. This is quite common in core-dominated sources (Pearson et al. 1987a; Porcas 1987). Many core-dominated sources show variability on time scales as short as days (Quirrenbach et al. 1992; Witzel et al. 1993).

1.2.3. THE COMPACT STEEP-SPECTRUM SOURCES

The compact steep-spectrum sources have steep spectra typically with $\alpha \leq -0.7$ and small overall linear sizes ($< 10 \sim 15$ pc). Systematic observations with the VLA, MERLIN and VLBI have been undertaken by several groups. These observations reveal a wide variety of morphologies. Some sources resemble the doubles seen in larger sources while others appear to be asymmetric core-jets. Many have complex structure and cannot easily be classified.

There is a clear division between structures of quasars and galaxies in this class: the galaxies are generally doubles while the quasars tend to be triple at moderate resolution ($\sim 0.1''$) with a steep spectrum dominant central component. At higher resolution the central components often turn out to be one-sided jets, which are much brighter than in large radio sources and often exceed 80% of the total flux density (Fanti et al. 1990a,b).

1.2.4. THE GIGAHERTZ-PEAKED SPECTRUM SOURCES

Gigahertz-peaked spectrum radio sources (GPS) have simple convex radio spectra with steep spectra at high frequencies and turnovers near 1 GHz (e.g., O'Dea et al. 1991). These sources tend to be very compact $\sim$ 100–1000 pc (e.g., Mutel & Phillips 1988). Their radio luminosities are comparable to the most powerful quasars. VLBI observations reveal that GPS sources identified with galaxies often have symmetric structure, which consists of two well-separated emission regions with similar flux densities (within a factor of a few) and similar spectra, strongly in contrast with the asymmetric one-sided jets found in core-dominated sources (Phillips & Mutel 1980, 1981, 1982; Hodges et al. 1984; Hodges & Mutel 1987; Mutel et al. 1985; Mutel & Hodges 1986; Pearson & Readhead 1988). GPS sources exhibit less variability and less polarization than core-dominated sources (Rudnick & Jones 1982; Seielstad et al. 1983; Rusk 1988). Recent studies have established a new class of symmetric sources—compact triple (Conway et al. 1990, 1992), which was first noted by Readhead et al. (1984). To avoid confusion we have introduced the term 'compact symmetric object' (CSO) to describe objects with proven symmetric structure on scales $\leq$ 5 kpc (Readhead 1993; Wilkinson et al. 1994; *see Chapter 5 and 7 also*). CCD images of small samples of GPS galaxies suggest that they probably are interacting or merging (O'Dea et al. 1990a; Stanghellini et al. 1993).

1.3. THE RELATIVISTIC BEAMING MODEL AND UNIFICATION SCHEMES

The different morphologies of lobe-dominated and core-dominated sources were a great puzzle in the pre-VLBI era. However, it is well-accepted now that powerful extragalactic radio sources have a common origin, largely due to the VLBI discovery of the common phenomena of one-sided jets and superluminal motions in AGN. The standard model consists of two well-collimated relativistic outflows in opposite directions, as illustrated in Fig. 1.1. The central energy source of the outflow is believed to be a super-massive black-hole (e.g., Begelman, Blandford & Rees 1984; Rees 1984). Although the current observation techniques are not able to detect black holes directly, they have provided much evidence supporting this model besides the one-sided jets and superluminal motions in AGN, such as rapid variability with time scales as short as 1 min., increases in the central velocity dispersion of stars within nearby galaxies, existence of faint broad emission lines in most galactic nuclei, and so on (e.g., Blandford 1990). Another piece of radio astronomical evidence is the persistence of radio source axes fixed in space for times as long as $\sim 10^7$ years in some cases (Readhead, Cohen & Blandford 1978; Bridle & Perley 1984). A spinning supermassive black hole is capable of maintaining the angular momentum on such time scales.

Many attempts have been made to unify active galaxies under this model (Readhead et al. 1978; Blandford & Königl 1979; Scheuer & Readhead 1979; Readhead 1980; Orr & Browne 1982; Barthel 1989), among which unification between lobe-dominated and core-dominated sources has been the most successful. According to this model, when the relativistic outflow is moving close to the line of sight to the observer (i.e., the angle between the direction of the outflow and the line of sight to the observer $\theta < \gamma^{-1}$, where γ is the bulk Lorentz factor of the outflow), the radio source appears core-dominated. When θ is larger than γ^{-1}, the source appears lobe-dominated. The luminosity of the outflow within a cone

of half opening angle $\sim \gamma^{-1}$ is boosted whereas that outside the cone is dimmed by the Doppler effect. It naturally accounts for many radio observational results. Moreover, since the core-dominated sources are lobe-dominated sources seen "pole-on," it is expected that they are surrounded by a low brightness, steep-spectrum halo. This has been confirmed (Browne et al. 1982; Perley et al. 1982; Murphy 1988; Murphy et al. 1993; Rusk 1988; *see Chapter 3 also*). The existence of counterjets in FR II sources expected on this model have also been confirmed recently (Bridle et al. 1994; Saripalli et al. 1994). Other unification schemes, such as radio galaxies with quasars, BL Lac objects with FR I objects, radio-quiet quasar and radio-loud quasars, are also successful at some level (e.g., Antonucci 1993; Urry 1993).

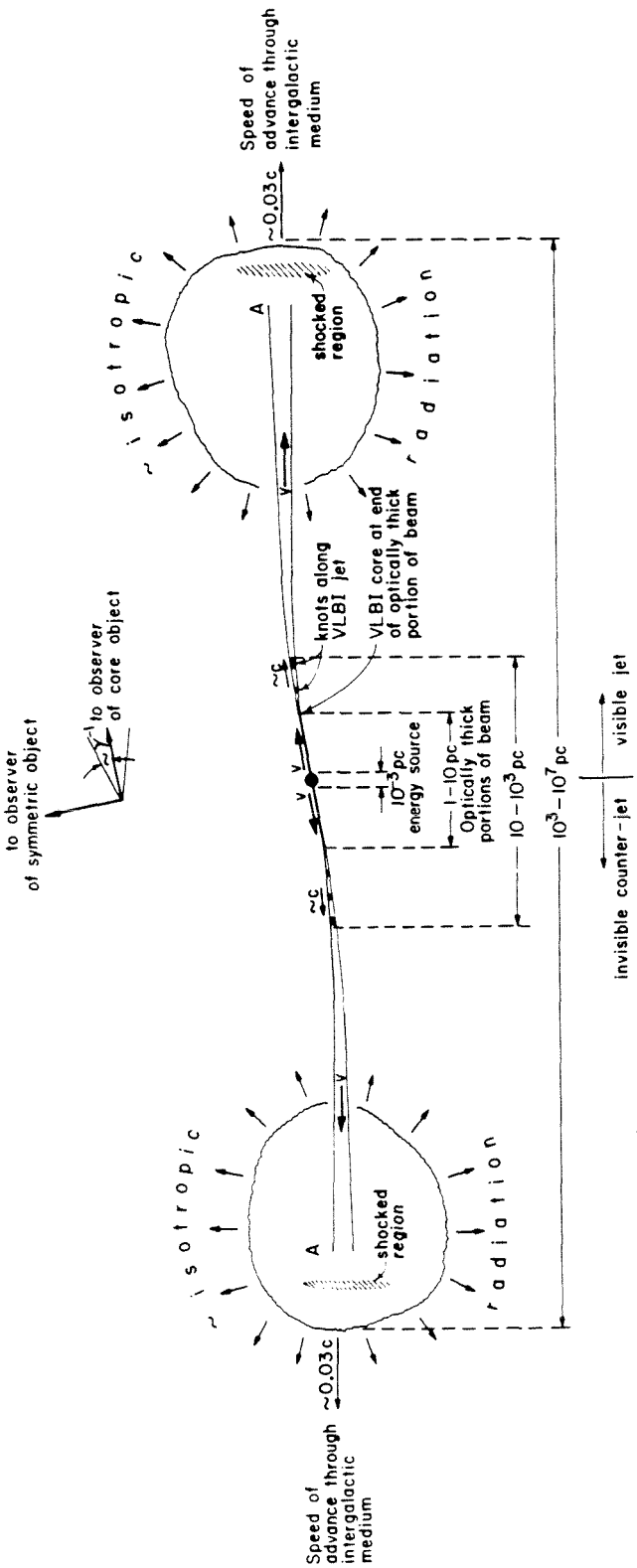

Fig. 1.1. The "Standard Model" of powerful extragalactic radio sources—two-sided strongly beamed emission while radiation from the outer lobes is $\sim$ isotropic. Observers with lines of sight within γ^{-1} of the source axis see strong anisotropic emission from the nuclear regions; observers with lines of sight $> \gamma^{-1}$ see predominantly isotropic emission. Obscuration by thick disks contributes further to orientation dependent effects. Unified theories of active galaxies are all based on these effects. Figure is taken from Readhead (1980).

1.4. MOTIVATION FOR THIS THESIS

Our understanding of extragalactic radio sources has been improved dramatically over the past two decades. However, there are many fundamental questions still to be answered. For example, what is the nature of the central engine? Do the morphological differences reflect a fundamental difference in the central engine or are they caused by environmental differences in their parent galaxies and surrounding medium? What is the evolutionary history of active galaxies? Moreover, unification schemes are often only tested qualitatively, and still require thorough quantitative tests. To address these questions, one must identify physically distinct classes of objects and determine the relative population of each class, which has initiated studies of complete samples of active galaxies (Pearson & Readhead 1981, 1988; Fanti et al. 1985, 1990a,b; Hough 1986; Zensus & Porcas 1986; Eckart et al. 1987; Hough & Readhead 1989; Wehrle et al. 1990, 1992). For this thesis, I have undertaken the First Caltech-Jodrell Bank VLBI Survey (CJ1) at 5 GHz. The CJ1 sample extends the flux density limit of the Pearson-Readhead sample from 1.3 Jy to 0.7 Jy and increases the total number of sources from 65 to 200.

1.5. A SYNOPSIS OF THIS THESIS

In Chapter 2 we define the CJ1 sample, describe the selection of VLBI targets, and observation strategy; Chapter 3 concentrates on radio observations with VLBI, MERLIN and the VLA and the data reduction. VLBI and MERLIN images at 5 GHz, VLA images at 1.4 GHz and radio spectra are presented. Chapter 4 presents complementary optical observations—new redshifts, optical identifications and optical polarimetry for sources in the CJ1 sample are reported. In Chapter 5 we discuss a physical classification scheme based on morphological attributes on both parsec- and kilo-parsec-scales. Examples of five out of eight possible physically distinct classes have been identified, although some classes have only a few members. It is found that $\sim$ 10% of the sources belong to the class of compact

symmetric objects; Chapter 6 reports on the distribution of the position angle differences between parsec scale and kilo-parsec scale radio structures (i.e., misalignment angle) for the combined CJ1+PR sample and also on the angular-size–redshift relation on parsec scales. The bimodal distribution of misalignment angles is confirmed in a subsample of sources with high optical polarization. Further study reveals that the peak near 90° is contributed by a group of objects with high optical polarization, high fractional core flux densities, flat radio spectra and high radio variability. The θ-z diagram of this sample does show only slight dependence of angular size on redshift contrary to the finding by Kellermann (1993). Chapter 7 presents details of the CSO's and CSO candidates in the sample. VLBI observations at 1.6 and 5 GHz and at 8.4 GHz in some cases enable us to estimate spectral indices for individual emission regions, which show that the outer emission regions have similar spectra. We have identified the core in at least 1 case, 0404+768, and possibly another, 1225+368, based on the spectral information. In Chapter 8 we summarize the major findings of this survey. References are given at the end of the thesis.

1.6. SOME DEFINITIONS

Spectrum: Throughout this thesis we adopt $S \propto \nu^{\alpha}$. A spectrum having a spectral index $\alpha \leq -0.5$ is defined as a steep spectrum and that having a spectral index $\alpha > -0.5$ as a flat spectrum.

Compact & Extended Sources: In this thesis we select 5 kpc as the division between extended and compact sources, i.e., sources with projected linear sizes < 5 kpc are compact and others are extended.

Dynamic Range: This term is usually used to indicate the quality of maps. We define the dynamic range as the ratio between peak flux to rms noise measured in a blank area.

H_0 and q_0: $H_0 = 100$ km/s/Mpc and $q_0 = 0.5$ are adopted throughout the thesis.

1.7. PUBLICATIONS BASED TOTALLY OR IN PART ON THIS THESIS

Refereed Journal Articles

Xu, W., Lawrence, C.R., Readhead, A.C.S., & Pearson, T.J. 1994a, "New Redshifts of Radio Sources from the S4 and S5 Surveys," AJ, 108, 395

Xu, W., Readhead, A.C.S., Pearson, T.J., Wilkinson, P.N., & Polatidis, A.G. 1995, "The First Caltech-Hodrell Bank VLBI Survey, III — 5 GHz VLBI Observations of 88 Sources, 5 GHz MERLIN Observations of 20 Sources, and 1.4 GHz VLA Observations of 92 sources," ApJS, submitted

Polatidis, A.G., Wilkinson, P.N., Xu, W., Readhead, A.C.S., & Pearson, T.J. 1995, "The First Caltech–Jodrell Bank VLBI Survey. I: λ18cm Observations of 87 Sources," ApJS, in press

Readhead, A.C.S., Xu, W., Pearson, T.J., Taylor, G.B., Wilkinson, P.N., & Polatidis, A.G. 1995, "Compact Symmetric Objects," in preparation

Thakkar, D.D., Xu, W., Readhead, A.C.S., Pearson, T.J., Polatidis, A.G., & Wilkinson, P.N. 1995, "The First Caltech–Jodrell Bank VLBI Survey. II: λ18cm Observations of 25 Sources," ApJS, in press

Wilkinson, P.N., Polatidis, A.G., Readhead, A.C.S., Xu, W., & Pearson, T.J. 1994, "Two-sided Ejection in Powerful Radio Sources: The Compact Symmetric Objects," ApJ, 432, L87

Published Conference Proceedings

Xu, W., Polatidis, A., Pearson, T.J., Readhead, A.C.S., & Wilkinson, P.N. 1993, "Two Core–Jet Sources with Large Misalignment," in *Sub-arcsecond Radio Astronomy*, ed. R.J. Davis and R.S. Booth, p.216

Xu, W., Readhead, A.C.S., Pearson, T.J., Wilkinson, P.N., & Polatidis, A. 1994b, "The Bimodal Distribution of Misalignment Angle in Powerful Extragalactic Radio Sources," in *Compact Extragalactic Radio Sources*, eds. J.A. Zensus and K.I. Kellermann, p.7

Henstock, D.R., Wilkinson, P.N., Browne, I.W.A., Taylor, G.B., Readhead, A.C.S., Pearson, T.J., Vermeulen, R.C., & Xu, W. 1995, "A Global VLBI Search for Milli-lenses," in *Proceedings of the Second EVN/JIVE VLBI Symposium*, in press

Pearson, T.J., Xu, W., Thakkar, D.D., Readhead, A.C.S., Wilkinson, P.N., & Polatidis, A. 1994, "The First Caltech-Jodrell Bank VLBI Survey," in *Compact Extragalactic Radio Sources*, eds. J.A. Zensus and K.I. Kellermann, p.1

Wilkinson, P.N., Polatidis, A.G., Readhead, A.C.S., Xu, W., & Pearson, T.J. 1993, "The Caltech–Jodrell Bank VLBI Survey," in *Sub-arcsecond Radio Astronomy*, eds. R.J. Davis and R.S. Booth, p.213

Chapter 2

THE FIRST CALTECH-JODRELL BANK SURVEY

2.1. BACKGROUND

The advent of the Very Long Baseline Interferometry (VLBI) technique has brought radio astronomy into a new regime with its high resolution. The global VLBI network, constituted by radio telescopes throughout the world, can provide an angular resolution of ~ 1 milliarcsecond (mas) at 5 GHz, which corresponds to a linear resolution of 0.15 pc at $z = 0.01$ and 4 pc at $z = 2$. Routine observations with VLBI can be made at several wavebands below 23 GHz, and pilot observations at 43 and 100 GHz have been performed successfully, providing angular resolution as high as 0.05 mas, i.e., a linear resolution $\sim 7.5^{-3}$ pc at $z = 0.01$ and 0.2 pc at $z = 2$. To put this in perspective, the black hole's gravity may begin to dominate at ~ 10 pc, the broad line region is on the order of 1 pc, and the central engine is on the order of 10^{-4} pc. So far VLBI is the only routinely available technique which can image active galactic nuclei with parsec and even subparsec resolution. VLBI studies of compact radio sources have greatly improved our understanding of the central engine and will certainly continue to do so, even though they cannot provide direct observations of the central engine itself and the radio emission detected by VLBI is only a small portion of the energy output of the central engine.

VLBI observations have demonstrated that active galactic nuclei have a variety of radio morphologies on mas scales. The majority of compact sources show a one-sided core-jet

morphology which consists of an unresolved flat spectrum core at one end and a jet with steeper spectrum (e.g., Pearson & Readhead 1988; Wehrle et al. 1992). The jets are often comprised of one or several knots. These knots are frequently observed to move away from the core with apparent superluminal speed (e.g., Zensus & Pearson 1987, 1990). Complex structures are observed in some CSS sources (Fanti et al. 1990a) and compact symmetric structures similar to the classical doubles are also known (e.g., Readhead et al. 1984; Conway et al. 1992; Readhead 1993; Wilkinson et al. 1994).

The relationship between the various types of sources and the underlying causes of the different morphologies remains unclear. For instance, the nature of CSS and GPS sources and their relation to other sources are still unclear. It is also not known whether the morphological differences reflect fundamental differences in the central engine, or are caused by environmental differences in the parent galaxies or the surrounding medium. In order to answer these questions, one must identify physically distinct classes of objects and determine the relative population of each class. For the past 15 years a number of groups have been studying complete samples of active galaxies with VLBI. Eckart et al. (1987) and Witzel et al. (1988) have studied 13 flat spectrum sources selected from the S5 survey (Kühr et al. 1981) with δ (B1950.0) $> 70°$ and $S_{5\ \mathrm{GHz}} > 1$ Jy. Weak cores of lobe-dominated sources have been studied in several orientation unbiased samples; results on more than 30 objects have been published so far (e.g., Hough 1986; Zensus & Porcas 1987; Hooimeyer et al. 1992; Giovannini et al. 1992; Hough et al. 1993). About 50 CSS sources selected from the 3CR and Peacock & Wall (1982) catalogues have been mapped at multiple frequencies (e.g., Fanti et al. 1985; Fanti et al. 1990b; Sanghera 1992). A group of astronomers mainly from Brandeis University has been studying the radio polarization of quasars and BL Lac objects on mas scales; results on 24 objects have been published to date (Cawthorne et al. 1993a,b). Wehrle et al. (1992) have been conducting a VLBI survey on 41 sources with flux density exceeding 4.5 Jy at 8.4 GHz at any epoch.

The largest systematic study with VLBI prior to this thesis was that of Pearson & Readhead (1988), who studied a flux-density limited complete sample of 65 objects with $S_{5\ \mathrm{GHz}} \geq 1.3$ Jy, $\delta(1950) \geq 35°$ and $|b| > 10°$, selected from the S4 and S5 surveys (Pauliny-Toth et al. 1978; Kühr et al. 1981). They mapped 45 objects (all those accessible to Mark II VLBI) with VLBI at 5 GHz. Most of these sources have also been observed at 2nd and 3rd epochs. They made a provisional morphological classification with five major classes: very compact and asymmetric sources, compact double sources, compact steep spectrum sources, irregular flat spectrum sources, and lobe-dominated sources, some of which are divided into subclasses. They also found that the distribution of the difference in position angle between milliarcsecond scale and arcsecond scale structures peaks at both 0° and 90°, which may imply that there are different types of central engines. But the result is not overwhelmingly convincing since it is drawn from a small number of sources.

The interpretation of Pearson & Readhead's results has been hampered by the small size of their sample. The large number of different classes of AGN, some of which have only one or two members, raises the question of whether the full range of morphological types has been observed and identified. Moreover, it is impossible to perform statistical tests within these classes due to their small sizes. An increase of the number of sources by a factor of three would constitute a major improvement. Therefore, we decided to treble the size of the sample. This project is a joint effort between California Institute of Technology (Caltech) and Nuffield Radio Astronomical Laboratories at Jodrell Bank, UK (University of Manchester). To distinguish this survey from another survey which followed, we have named it the first Caltech–Jodrell Bank survey or CJ1 survey.

Our main objectives were:

(a) To identify physically distinct classes of AGN based on all information accessible, such as morphological attributes on both milliarcsecond and arcsecond scales, spectral indices, linear sizes, optical identifications, etc.

(b) To provide a sample which is large enough to make interesting statistical tests both as a whole and within and between different classes. In particular, we can investigate the distribution of misalignment angles between structures on the milliarcsecond scale and arcsecond scale (Pearson & Readhead 1988) and study the cosmological evolution of different classes using the luminosity-volume test (e.g., Herbig, Readhead & Xu 1995). Testing the applicability of "Unified Schemes" is another goal of this study. It has been suggested recently that the relation between VLBI angular size and redshift can be used as a probe of universal geometry (Kellermann 1993; Gurvits 1993). This sample can also be used to test such findings.

(c) To identify objects with particularly interesting or unusual structure.

(d) To provide first-epoch observations for a systematic study of superluminal motion in a large complete sample (Vermeulen & Cohen 1994).

2.2. THE FRIST CALTECH–JODRELL BANK SAMPLE

The Caltech–Jodrell sample is selected from the NRAO–MPIfR 5 GHz strong sources survey (S4 & S5) (Pauliny-Toth et al. 1978; Kühr et al. 1981) by the following criteria:

1) total flux density at 5 GHz: $0.7 \leq S_{5GHz} < 1.3$ Jy;

2) declination (B1950.0) $\delta \geq 35°$;

3) Galactic latitude $|b| > 10°$.

The S4 and S5 surveys contain 137 sources satisfying the above criteria. One of them, 1758+666, is identified with a planetary nebula and another, 1038+528, consists of two independent quasars (Owen et al. 1980), neither of which is brighter than 0.7 Jy at 5 GHz. Thus these two sources have been excluded and the final CJ1 sample contains 135 objects, which are listed in Table 2.1. This sample is an extension of the PR sample to

lower flux densities. The combination of the CJ1 and PR samples forms a flux-density limited complete sample of 200 sources, by far the largest sample studied by VLBI.

2.3. OBSERVATION STRATEGY

To identify physically distinct classes of AGN, information as complete as possible on various aspects is required. Through extensive literature searches, we collected information on optical identifications, redshifts and radio spectra and images made with various instruments at different frequencies. We filled the gaps in information wherever necessary with our own observations. Thus this project involved observations with several instruments.

2.3.1. VLBI OBSERVATIONS

The global VLBI network was used to obtain milliarcsecond scale structures, which is the most crucial part of the project. Many VLBI images show two or more knots, and it is often difficult to identify the core, which introduces ambiguity into classification. In light of this, we decided to observe at two frequencies—a high frequency which can provide high resolution and a low frequency which can detect steep-spectrum extended structure. Balancing the availability and reliability of the antennas participating in the global VLBI network, we chose 1.6 and 5 GHz as our working frequencies. Traditionally, VLBI images were made with long track ($\sim$ 8–10 hours) observations. Such an observing scheme is unsuitable for studying large samples. In order to finish the dual-frequency observations of such a large sample within $\sim$ three years, we decided to make a VLBI snapshot survey with three 20 – 30 min. snapshot on each object (*Chapter 3*). We were very successful in persuading both the US and European VLBI networks to allocate the required observing time. The actual observations often yielded maps with dynamic range $\sim$ 200:1 as expected. Our success has proven the reliability and efficiency of the snapshot technique, which has initiated the second Caltech-Jodrell Bank VLBI Survey (CJ2) (Taylor et al. 1994) and the second epoch observations of the CJ1 sample.

The narrow band (1.8 MHz) Mark II recording system can only image sources with a compact component brighter than $\sim$ 100 mJy. For reasons of time and economy, we did not perform a finding survey like PR; instead, we used the radio spectra and images we collected to identify targets for VLBI observations. We sorted the sources into three groups:

1) Sources which had been observed previously with VLBI and for which the maps were of sufficient quality to allow us to make an unambiguous classification. There are seven sources in this group, namely, 0248+430, 0716+714, 1039+811, 1150+812, 1504+377, 1637+826, 2007+777 (Alef 1988; Eckart et al. 1987; Zensus & Porcas 1985). Six of these (except 1637+826) were observed again in the CJ2 survey. The CJ2 team has generously offered the data to us.

2) Sources which are almost certain to have structure that can be mapped with Mark II VLBI. This group consists of sources unresolved by the VLA, preferably at high frequency, sources with overall angular size $< 2''$ if no observations with higher resolution available, extended sources with core flux density at 5 GHz above 300 mJy, and all objects observed with VLBI by Preston et al. (1985) for which at least 20% of the total flux density is detected on intercontinental baselines. There are 81 sources in this group.

3) Sources which do not have a strong enough compact feature to be mapped by Mark II VLBI. These sources are predominantly large, lobe-dominated sources with weak or undetected cores. There are 47 sources in this group.

In our 5 GHz VLBI observations, we observed all sources in group 2, and in addition one object in the PR sample, 0404+768, since it had not been mapped at 5 GHz. In our 1.6 GHz observations, we observed all sources in groups 1 and 2 and 28 sources in the PR sample for which VLBI observations at this frequency have not been made. This thesis deals with the observations at 5 GHz. The 1.6 GHz observations were processed by Polatidis et al. (1995) and Thakkar et al. (1995).

2.3.2. VLA OBSERVATIONS

A complete set of large scale images of the sources in both CJ1 and PR samples is needed for classification and for measurements of misalignment angles and overall angular sizes. These two samples had not been mapped systematically with the VLA. Two previous VLA surveys, conducted by Murphy (1988) and Rusk (1988), have many sources in common with the PR and CJ1 samples. Both surveys were made with the VLA A array at L band, i.e., 1.4 GHz (in fact Murphy's observations were made with the A + C array), which provide images with dynamic range $\geq$ 3000:1. Some other objects have also been mapped with the VLA at L band with similar quality. Following an extensive literature search we found that 92 objects in the PR and CJ1 sample had not been adequately imaged at low frequency. We therefore decided to observe these 92 sources with the VLA at L band so that we could have a nearly uniform set of VLA images of these two samples.

2.3.3. MERLIN OBSERVATIONS

MERLIN observations can provide information on structures on intermediate scales (100 – 500 mas). Structures on intermediate scales are helpful in identifying compact steep-spectrum sources and compact symmetric objects, and are also useful for measurements of misalignment angles in some cases. We planned to observe all 88 sources in groups 1 and 2 with MERLIN, but due to time constraints only 36 of them have been observed thus far. Although it would have been useful to have a complete set of MERLIN maps, we concluded that these were not essential for our purpose since the VLA maps at high frequencies do give information down to a few tenths of an arcsecond. For example, none of these 36 objects was re-classified as a result of the MERLIN observations, but they did provide tighter constraints on the angular sizes for some objects.

2.3.4. COMPLEMENTARY OPTICAL OBSERVATIONS

Optical observations were made with the Double Spectrograph on the Palomar 200 inch

telescope to measure redshifts, which yielded 23 new redshifts out of 32 objects observed. Optical identifications for 14 sources have been found or confirmed with CCD images taken at r-band with the Palomar 60 inch telescope. Optical polarimetry observations for 59 sources in the CJ1 sample were obtained with the 90- and 61-inch telescopes of the Steward Observatory. These data are used to study the misalignment distribution (*Chapter 6*).

Table 2.1. The First Caltech–Jodrell Bank Sample

Source	alias	R.A.	Decl.	Ref	b	S_{5GHz}	ID	V	z	Ref
(1)	(2)	(3)	(4)	(5)	(6)	(7)	(8)	(9)	(10)	(11)
0010+405	4C 40.01	00 10 54.30	40 34 56.7	1	−21.4	1.05	G	17.9	0.255	1
0010+775	—	00 10 22.31	77 32 06.4	1	15.1	0.781	G	18.0	0.326	0,16
0013+790	3C 6.1	00 13 34.36	79 00 11.1	2	16.5	1.044	G	23.0	0.840	2
0022+390	OA 026	00 22 46.67	39 02 59.0	3	−23.3	0.859	Q	18.4	1.946	0,14
0048+509	3C 22.0	00 48 04.71	50 55 45.4	2	−11.7	0.760	G	22.0	0.937	3
0102+480	—	01 02 55.46	48 02 00.5	3	−14.5	0.982	EF	*	*	14
0106+729	3C 33.1	01 06 06.48	72 55 59.2	2	10.4	0.890	G	19.5	0.181	2
0206+355	4C 35.03	02 06 39.11	35 33 43.0	4	−24.4	0.894	G	14.3	0.037	2
0218+357	OD 330	02 18 04.13	35 42 32.0	3	−23.5	1.17	BL	20.0	>0.686	4
0220+397	3C 65.0	02 20 36.57	39 47 19.0	3	−19.5	0.770	G	23.0	1.176	3
0248+430	—	02 48 18.49	43 02 56.9	3	−14.4	1.21	Q	18.6	1.310	5
0258+350	4C 34.09	02 58 35.39	35 00 32.6	11	−20.5	0.926	G	13.5	0.0165	14
0307+444	4C 44.07	03 07 09.15	44 24 27.2	4	−11.6	0.733	Q	18.8	1.165	5
0309+390	4C 39.11	03 09 12.63	39 05 15.9	9	−15.9	0.728	G	14.0	1.161	2
0402+379	4C 37.11	04 02 29.88	37 55 26.9	1	−10.5	1.15	G	18.5	0.055	0,14
0407+747	4C 74.08	04 07 04.6	74 43 29	5	17.0	0.962	G	20.5	0.373	0,17
0602+673	—	06 02 38.89	67 21 18.4	3	20.9	1.07	Q	20.6r	*	14
0615+820	—	06 15 32.77	82 03 56.4	3	26.0	0.999	Q	17.5	0.71	5
0620+389	—	06 20 51.53	38 58 27.3	3	11.8	0.874	Q	20.0	3.470	0,14
0642+449	OH 471	06 42 53.02	44 54 30.8	3	17.9	0.778	Q	18.5	3.406	5

Table 2.1. The First Caltech–Jodrell Bank Sample (*continued*)

Source	alias	R.A.	Decl.	Ref	b	S_{5GHz}	ID	V	z	Ref
(1)	(2)	(3)	(4)	(5)	(6)	(7)	(8)	(9)	(10)	(11)
0646+600	OH 577.1	06 46 04.11	60 05 14.2	3	23.2	0.788	Q	18.9	0.455	6
0650+371	—	06 50 35.28	37 09 27.1	3	16.4	0.971	Q	18.0	1.982	5
0651+542	3C 171.0	06 51 11.01	54 12 49.0	3	22.2	1.16	G	18.8	0.239	2
0702+749	3C 173.1	07 02 47.91	74 54 16.6	2	27.3	0.789	G	18.9	0.292	2
0703+426	4C 42.23	07 03 11.6	42 36 41	4	20.6	0.985	G	15.0	0.06	7
0707+476	—	07 07 02.55	47 37 07.9	3	22.8	0.998	Q	18.2	1.292	14
0707+689	4C 68.08	07 07 55.24	68 57 12.7	9	27.1	0.749	Q	20.5	1.141	0,14
0716+714	—	07 16 13.03	71 26 15.2	3	28.0	1.121	BL	13.2	*	10
0734+805	3C 184.1	07 34 25.05	80 33 24.1	2	28.9	1.134	G	19.7	0.119	2
0740+828	—	07 40 33.20	82 49 24.2	1	28.8	0.931	Q	18.5	1.991	0,16
0746+483	OI 478	07 46 39.93	48 22 30.5	3	29.4	0.796	Q	18.5	1.951	5
0755+379	3C 189	07 55 09.20	37 55 20.9	4	28.8	1.26	G	14.9	0.043	2
0805+410	—	08 05 33.63	41 01 33.1	3	31.4	0.766	Q	19.0	1.420	0,14
0812+367	OJ 320	08 12 10.71	36 44 27.5	3	31.9	1.01	Q	18.0	1.025	5
0816+526	4C 52.18	08 16 01.6	52 41 57	4	34.4	0.776	G	18.0	0.189	14
0818+472	3C 197.1	08 18 01.11	47 12 11.0	3	34.5	0.860	G	16.5	0.130	2
0820+560	OJ 535	08 20 53.20	56 02 27.5	3	35.1	0.917	Q	18.5	1.417	5
0821+394	4C 39.23	08 21 37.31	39 26 28.2	1	34.2	0.993	Q	18.5	1.216	5
0827+378	4C 37.24	08 27 55.15	37 52 17.9	1	35.1	0.930	Q	18.11	0.914	5
0828+493	OJ 448	08 28 47.97	49 23 33.0	3	36.4	1.02	BL	18.5	0.548	10

Table 2.1. The First Caltech–Jodrell Bank Sample (*continued*)

Source	alias	R.A.	Decl.	Ref	b	S_{5GHz}	ID	V	z	Ref
(1)	(2)	(3)	(4)	(5)	(6)	(7)	(8)	(9)	(10)	(11)
0833+585	—	08 33 23.76	58 35 30.3	3	36.6	1.11	Q	18.0	2.101	5
0844+540	4C 54.17	08 44 11.19	54 03 42.0	6	38.6	0.732	G	13.7	0.0453	2
0900+428	4C 42.28	09 00 58.74	42 50 01.2	6	41.9	0.761	Q	19.9	0.328	7
0917+449	—	09 17 41.92	44 54 39.6	3	44.8	0.803	Q	19.0	2.180	5
0917+624	OK 630	09 17 40.31	62 28 38.6	3	41.0	0.996	Q	19.5	1.446	5
0936+361	3C 223.0	09 36 50.87	36 07 35.0	2	48.7	1.29	G	17.0	0.137	2
0938+399	3C 223.1	09 38 18.21	39 58 22.1	9	48.9	0.870	G	16.0	0.108	2
0945+664	4C 66.09	09 45 14.90	66 28 57.7	3	41.9	1.22	G	21.6	*	14
0955+476	OK 492	09 55 08.53	47 39 28.3	3	50.7	0.739	Q	18.0	1.880	5
1003+830	—	10 03 25.84	83 04 56.7	3	32.5	0.716	G	20.5	0.322	0,16
1007+417	4C 41.21	10 07 26.09	41 47 25.5	7	54.2	0.706	Q	16.5	0.613	5
1015+359	OL 326	10 15 16.23	35 57 41.3	3	56.4	0.916	Q	19.0	1.226	5
1020+400	4C 40.25	10 20 14.56	40 03 26.6	3	56.9	0.866	Q	17.5	1.254	0,14
1030+415	—	10 30 07.80	41 31 34.5	3	58.4	1.13	Q	18.2	1.120	5
1030+585	3C 244.1	10 30 19.75	58 30 05.2	2	50.7	1.12	G	19.0	0.428	2
1039+811	—	10 39 27.76	81 10 23.7	3	34.7	1.144	Q	16.5	1.259	8
1044+719	—	10 44 49.74	71 59 26.9	3	42.3	0.707	Q?	—	—	0
1053+704	—	10 53 27.72	70 27 47.9	3	43.9	0.710	Q	18.5	2.492	0,18
1053+815	—	10 53 36.22	81 30 35.6	3	34.7	0.770	G	18.5	0.706	0,17
1056+432	3C 247	10 56 08.38	43 17 30.6	2	62.3	0.949	G	21.5	0.749	3

Table 2.1. The First Caltech–Jodrell Bank Sample (*continued*)

Source	alias	R.A.	Decl.	Ref	b	S_{5GHz}	ID	V	z	Ref
(1)	(2)	(3)	(4)	(5)	(6)	(7)	(8)	(9)	(10)	(11)
1058+726	4C 72.16	10 58 20.10	72 41 44.8	1	42.3	0.778	Q	17.4	1.46	5
1100+772	3C 249.1	11 00 25.00	77 15 11.0	1	38.5	0.772	Q	15.7	0.311	5
1101+384	MKR 421	11 01 40.58	38 28 42.8	3	65.0	0.725	BL	13.8	0.0308	5
1111+408	3C 254	11 11 53.10	40 53 41.0	3	65.9	0.790	Q	18.0	0.734	5
1128+385	OM 346.9	11 28 12.51	38 31 51.6	3	69.8	0.771	Q	16.0	1.733	0,14
1137+660	3C 263.0	11 37 10.83	66 04 23.9	3	49.7	1.04	Q	16.3	0.652	5
1138+594	4C 59.16	11 38 05.73	59 29 02.9	1	55.7	0.767	Q?	—	—	0
1144+402	—	11 44 21.02	40 15 14.2	3	71.5	0.941	Q	18.0	1.088	0,5
1144+542	—	11 44 04.58	54 13 22.8	3	60.7	0.878	Q	20.5	2.201	0,14
1150+497	4C 49.22	11 50 48.01	49 47 50.0	3	65.0	1.11	Q	17.1	0.334	5
1150+812	—	11 50 23.48	81 15 10.3	3	35.8	1.181	Q	18.5	1.25	5
1152+551	4C 55.22	11 52 55.50	55 10 37.0	8	60.4	0.843	G	16.0	0.050	14
1203+645	3C 268.3	12 03 54.09	64 31 22.5	3	52.2	1.16	G	20.0	0.371	2
1213+350	4C 35.28	12 13 24.83	35 04 54.9	3	79.2	1.01	Q	20.0	0.86	9
1213+538	4C 53.24	12 13 01.48	53 52 35.7	7	62.7	0.904	Q	18.0	1.065	5
1216+487	ON 428	12 16 38.57	48 46 35.0	3	67.7	1.08	Q	18.5	1.073	5
1225+368	ON 343	12 25 30.77	36 51 47.0	3	79.3	0.767	Q	21.5	1.974	0,14
1242+410	ON 470.5	12 42 26.40	41 04 30.0	3	76.3	0.744	Q	19.0	0.813	0,14
1250+568	3C 277.1	12 50 15.22	56 50 36.2	3	60.6	1.05	Q	17.9	0.320	5
1311+678	4C 67.22	13 11 45.04	67 51 42.3	3	49.4	0.923	G?	—	—	0

Table 2.1. The First Caltech–Jodrell Bank Sample (*continued*)

Source (1)	alias (2)	R.A. (3)	Decl. (4)	Ref (5)	b (6)	S_{5GHz} (7)	ID (8)	V (9)	z (10)	Ref (11)
1317+520	4C 52.27	13 17 41.15	52 03 49.0	1	64.8	0.716	Q	17.0	1.060	5
1319+428	3C 285	13 19 05.22	42 50 55.7	2	73.4	0.760	G	15.99	0.079	2
1333+459	—	13 33 15.70	45 57 56.4	1	69.5	0.757	Q	18.5	2.449	0,5
1333+589	4C 58.26	13 33 36.47	58 59 18.0	1	57.5	0.826	Q?	—	—	0
1336+391	3C 288	13 36 38.37	39 06 24.0	3	74.7	0.992	G	18.3	0.246	2
1342+663	—	13 42 41.04	66 21 13.2	3	50.2	0.817	Q	19.4	1.351	0,14
1347+539	4C 53.28	13 47 42.57	53 56 08.4	3	61.4	0.962	Q	17.3	0.978	0,5
1349+647	3C 292	13 49 14.3	64 44 33	4	51.4	0.720	G	20.7	0.71	3
1357+769	—	13 57 42.12	76 57 53.4	3	39.8	0.844	Q	19.0	—	19
1418+546	OQ 530	14 18 06.19	54 36 58.1	3	58.3	1.09	BL	14.5	0.152	10
1419+419	3C 299	14 19 06.46	41 58 29.9	3	66.6	0.900	G	19.4	0.367	2
1435+638	—	14 35 37.24	63 49 35.9	3	49.7	1.24	Q	15.0	2.060	5
1437+624	OQ 663	14 37 32.02	62 24 47.0	3	50.7	0.862	Q	19.0	1.090	5
1438+385	OQ 363	14 38 22.53	38 33 02.8	1	64.6	0.770	Q?	—	—	0
1441+522	3C 303	14 41 24.82	52 14 18.4	2	57.5	0.940	G	17.0	0.141	14
1448+634	3C 305	14 48 17.45	63 28 36.5	3	49.1	0.920	G	13.74	0.041	13
1504+377	OR 306	15 04 12.96	37 42 23.3	3	59.9	1.10	G	21.1	0.674	14
1547+507	OR 580	15 47 52.27	50 47 09.3	3	49.1	0.738	Q	18.5	2.169	14
1549+628	3C 325	15 49 13.99	62 50 20.0	2	44.1	0.830	G	21	0.86	3
1557+708	4C 70.19	15 57 37.1	70 49 45	5	39.3	1.02	G	13.3	0.026	0,17

Table 2.1. The First Caltech–Jodrell Bank Sample (*continued*)

Source	alias	R.A.	Decl.	Ref	b	S_{5GHz}	ID	V	z	Ref
(1)	(2)	(3)	(4)	(5)	(6)	(7)	(8)	(9)	(10)	(11)
1627+444	3C 337	16 27 19.07	44 25 38.2	2	43.6	0.910	G	21.0	0.635	3
1637+626	3C 343.1	16 37 55.30	62 40 34.3	3	39.0	1.20	G	22.5	0.750	2
1637+826	NGC 6251	16 37 56.97	82 38 18.5	3	31.2	0.978	G	14.0	0.023	2
1638+398	NRAO 512	16 38 48.17	39 52 30.1	3	41.4	1.16	Q	16.5	1.666	5
1656+477	—	16 56 39.60	47 42 19.6	3	38.4	0.923	Q	18.0	1.622	5
1656+482	4C 48.41	16 56 24.95	48 13 04.5	1	38.5	0.776	Q?	—	—	0
1658+471	3C 349.0	16 58 04.44	47 07 20.3	2	38.2	1.14	G	18.6	0.205	2
1704+608	3C 351.0	17 04 03.49	60 48 30.9	2	36.4	1.21	Q	15.3	0.371	5
1719+357	OT 332	17 19 23.03	35 45 08.8	3	32.9	0.859	Q	17.5	0.263	5
1732+389	OT 355	17 32 40.49	38 59 46.9	3	31.0	1.15	Q	19.0	0.976	5
1734+508	—	17 34 36.74	50 50 59.6	1	32.4	0.803	Q?	—	—	0
1738+476	OT 465	17 38 36.31	47 39 28.8	3	31.4	0.904	BL	19.5	*	5
1751+441	OT 486.4	17 51 53.72	44 10 17.8	3	28.5	1.04	Q	19.5	0.871	14
1758+388	OT 398	17 58 44.70	38 48 32.5	3	26.0	0.916	Q	17.8	2.092	14
1800+440	OU 401	18 00 03.19	44 04 18.3	3	27.1	1.02	Q	16.8	0.663	5
1819+396	4C 39.56	18 19 42.34	39 41 15.0	10	22.4	0.971	G	19.0	*	14
1825+743	3C 379.1	18 25 56.1	74 19 05	5	27.9	0.728	G	18.0	0.256	2
1832+474	3C 381	18 32 24.47	47 24 39.0	2	22.5	1.29	G	18.6	0.161	2
1833+653	3C 383	18 33 33.7	65 19 11	4	26.3	0.799	G	17.0	0.161	1
1842+681	—	18 42 43.40	68 06 19.8	3	25.9	0.810	Q	17.9	0.475	5

Table 2.1. The First Caltech–Jodrell Bank Sample (*continued*)

Source	alias	R.A.	Decl.	Ref	b	S_{5GHz}	ID	V	z	Ref
(1)	(2)	(3)	(4)	(5)	(6)	(7)	(8)	(9)	(10)	(11)
1843+356	OU 373	18 43 48.34	35 38 02.4	3	16.5	0.812	G?	21.9	—	15
1926+611	—	19 26 49.65	61 11 20.7	3	19.4	0.721	BL	17.5	*	1
1940+504	3C 402	19 40 21.4	50 28 49	4	13.3	0.933	G	14.0	0.0239	2
1943+546	OV 573	19 43 22.65	54 40 48.0	1	14.8	0.850	G	17.7	0.263	1
2007+777	—	20 07 20.43	77 43 58.1	3	22.7	1.279	BL	16.7	0.342	10
2010+723	4C 72.28	20 10 16.21	72 20 20.7	3	20.2	0.917	BL	19.0	*	6
2104+763	3C 427.1	21 04 45.80	76 21 09.5	2	19.3	0.997	G	23.3	0.572	3
2207+374	4C 37.65	22 07 11.72	37 27 33.0	1	−14.9	0.791	Q	18.5	1.493	9
2214+350	OY 324	22 14 07.02	35 03 15.2	3	−17.6	0.824	Q	18.5	0.51	5
2229+695	—	22 29 11.66	69 31 02.6	3	10.2	0.812	G	19.6	*	19
2253+417	OY 489	22 53 19.84	41 46 51.3	3	−15.8	0.990	Q	18.8	1.476	5
2255+416	4C 41.45	22 55 04.68	41 38 13.2	1	−16.1	0.993	Q	20.9	1.149	14
2311+469	4C 46.47	23 11 28.87	46 55 54.4	1	−12.5	0.726	Q	17.9	0.742	0,14
2323+435	OZ 438	23 23 18.18	43 30 28.3	3	−16.4	1.01	G	18.0	0.145	12
2324+405	3C 462	23 24 30.71	40 31 38.3	4	−19.3	1.12	G	19.9	0.394	6

Notes to Table 2.1.

Column 1: Source name in the IAU convention;

Column 2: Alternative source name;

Column 3: Right Ascension (1950.0);

Column 4: Declination (1950.0);

Column 5: References for radio position in column (3) and (4): 1 – Patnaik et al. 1992; 2 – Laing et al. 1983; 3 – The VLA Calibration Manual, 1990 edition; 4 – Pauliny-Toth et al. 1978; 5 – Kühr et al. 1981; 6 – Kapahi 1981; 7 – Owen & Puschell 1984; 8 – Polatidis 1993; 9 – Morabito et al. 1982; 10 – Gregorini et al. 1988; 11 – Argyle & Eldridge 1990.

Column 6: Galactic latitude;

Column 7: Flux density at 5 GHz as measured in the S4 and S5 surveys;

Column 8: Optical identification — G: galaxy; Q: quasar; BL: BL Lac object; EF: empty field.

Column 9: Approximate visual magnitude of the optical object;

Column 10: Redshift;

Column 11: References for optical identification and redshift: 0 – this work; 1 – Stickel & Kühr 1993b; 2 – Kühr et al. 1979; 3 – Spinrad et al. 1985; 4 – Browne et al. 1993; 5 – Veron & Veron 1991; 6 – Stickel & Kühr 1993a; 7 – Vigotti et al. 1989; 8 – Burbidge & Hewitt 1989; 9 – Burbidge & Hewitt 1987; 10 – Stickel, Fried & Kühr 1993; 11 – Preston et al. 1985; 12 – Stickel & Kühr 1992; 13 – Spinrad et al. 1985; 14 – Stickel & Kühr 1994. 15 – Stanghellini et al. 1993; 16 – Kühr et al. 1987; 17 – Taken from the NASA/IPAC Extragalactic Database; 18 – Preston et al. 1985; 19 – Perley et al. 1982.

Chapter 3

RADIO OBSERVATIONS AND DATA REDUCTION

3.1. INTRODUCTION

The results of our 5 GHz VLBI observations from the CJ1 survey have been submitted for publication to the *Astrophysical Journal Supplement Series.* This paper also reports MERLIN observations at 5 GHz of 20 objects and VLA observations at 1.4 GHz of 92 objects in the combined CJ1+PR sample, and presents radio spectra of all 135 CJ1 objects. In the interest of brevity, many details of the VLBI observations and data reduction were omitted in the paper, and the maps from each instrument have been collected into three separate sets of figures. In this chapter we give a more extensive account of the observations and analysis, and we group all the observations of each object on a single page so that the reader can see the structure on pc and kpc scales and spectral information at a glance. Section 3.2 gives a detailed description of the VLBI observations and data reduction. Section 3.3 presents the text which we have submitted to the *Astrophysical Journal Supplement Series.* This leads to some repetition, but since the submitted text is very short, we judged that this was not excessive. Section 3.4 describes the format in which the maps and spectra are presented.

3.2. VLBI OBSERVATIONS AND DATA REDUCTION

3.2.1. THE SNAPSHOT TECHNIQUE

In synthesis imaging an interferometer array is used to measure the Fourier components of the source brightness distribution, i.e., the complex visibility. The brightness distribution of the object is derived by Fourier transformation and deconvolution (Högbom 1974; Clark 1980; Schwab 1984). In order to make a good image the visibility measurements should be fairly uniformly distributed on the *uv* plane over the range of the baselines covered. To achieve good *uv* coverage, conventional VLBI observations are made with long tracks ($\sim$ 8–10 hours). However, this method is not suitable for studies of large samples. For example, it took PR nearly five years to complete the first-epoch observations of 40 sources in the PR sample, which were made with $\sim$ 10-hour tracks. Clearly, it is not practical to carry out the CJ1 survey with long track observations. There have been two major improvements in VLBI networks since the first PR survey. First, the number of telescopes routinely participating in the VLBI observations has increased to $\sim$ 15 in contrast to the 4–5 telescopes used by PR; second, the advent of the Caltech/JPL Block 2 correlator has made it possible to correlate up to 16 stations in one pass. In light of these developments, we investigated the possibility of making a VLBI snapshot survey. Simulations showed that observations with three 20-minute snapshots give maps of complicated sources with dynamic range $\geq$ 200:1, which is adequate for our objectives. Thus the snapshot observations provide a good compromise between image quality and observing efficiency. We noted that a larger number of shorter scans would provide more uniform *uv* coverage and better images, but since some of the telescopes have slow slew speeds—especially the 100-m telescope in Effelsberg, Germany, which is one of the most sensitive telescopes—frequent switches between sources would lead to a large loss of observing time. Thus we compromised by accepting a slight reduction in image quality for the sake of much better observing efficiency. It is worth pointing out that the approach with many short scans is viable with the VLBA owing to its fast slew speed.

3.2.2. VLBI OBSERVATIONS

We observed 81 objects in the CJ1 sample at 5 GHz with the global VLBI network, a combination of the European VLBI network (EVN), U.S. VLBI network, and partially completed VLBA. Data were recorded with left circular polarization (IEEE convention) and with a bandwidth of 1.8 MHz using the Mark II VLBI format (Clark 1973) and cross-correlated with the JPL/Caltech Block 2 correlator. One object, 0404+768, in the PR sample was also observed since it had not been mapped previously at 5 GHz. All objects, except 0218+357 and 0404 + 768, were observed with the snapshot technique — generally with three 20-30 min scans, but some objects had 1 or 2 extra-scans to fill gaps in the schedules. 0218+357 were observed for 4.5 hours and 0404+768 for 3 hours. The observations were completed in six sessions between 1990 and 1992 (Table 3.1). Thirteen to seventeen stations participated in each session. The locations and basic parameters of these stations are listed in Table 3.1. In the session of September 1991 MERLIN observed simultaneously. Data from three of the six MERLIN stations (Cambridge, MK II at Jodrell Bank and Knockin) were recorded in Mark II format so that we could cross-correlate them with other non-MERLIN stations. The MERLIN data were combined with VLBI data, hence 21 stations participated in this session. In addition to our observations, six other sources in the CJ1 sample, for which we had planned to use published images, were observed as part of the CJ2 survey. The CJ2 team has generously donated these data to us. Therefore, we have a uniform set of VLBI observations for all sources but one (1637+826) in the CJ1 sample accessible with Mark II VLBI.

The snapshot observations require careful scheduling. The time during which a source can been seen by all the participating stations depends on the declination of the source and varies from $\sim$ 4 hours at $\delta \sim 35°$ to over 10 hours at $\delta > 60°$. To optimize the *uv* coverage, we scheduled the three snapshots in the following fashion. For sources with mutual observing time of 8 hours or longer, the snapshots were separated by about four

hours, which provided very good *uv* coverage. For other sources three snapshots were taken at the beginning, the middle and the end of the mutual observing time. For sources with a declination near 35°, the lower limit of our sample, the mutual time is so short as to leave huge holes in the *uv* coverage, which may lead to uncertainties in the map. One or two station were often given up in order to gain $\sim$ 1.5 hours or more in mutual observing time. Fig. 3.1 shows *uv* coverages for three representative sources, at $\delta \simeq 38°, \delta \simeq 52°$ and $\delta \simeq 77°$.

We adjusted the length of the snapshots as we gained experience during the course of this project. In March 1990, our first session of snapshot observations, each snapshot lasted from 24 minutes to 30 minutes (including slew time). The variations were due to different slew times between sources. Extra time was added for long slews. Our goal was to ensure 20 minutes of useful data for each snapshot. But the variable observing times added tremendously to the difficulties of scheduling. Therefore, we adopted a standard snapshot time of 30 minutes for the following three sessions of observations at 5 GHz in June and September 1991 and in March 1992, and for all of the observations at 1.6 GHz (Polatidis 1993; Polatidis et al. 1994). In the last two sessions, June and September 1992, we shortened the snapshot time to 20 minutes. This reflected our confidence in the snapshot technique, which had proven very successful in the previous observations.

3.2.3. DATA REDUCTION

Maps were made during the course of the observations. However, it was found in March 1994 that FRING, the AIPS task which performs fringe-fitting, gave erroneous results owing to a penalty function which was used when delay windows smaller than the Nyquist window were selected. This caused some errors in the maps. At about the same time we realized that the data in the June 1991 session suffered ionospheric scintillation, which also resulted in errors in the maps. In view of these problems, we decided to reprocess all the data with a correct version of FRING. It should perhaps be pointed out that the FRING problem

was a subtle one which only affected maps at $\leq 2\%$ level and it was used by the world VLBI community for 3 years. The final VLBI data reduction is described in the following sections.

3.2.3.1 FRINGE-FITTING AND INITIAL PHASE SELF-CALIBRATION

For any interferometer, the correlated signal appears at a delay and phase that depend on the geometry of the interferometer, the source position, the atmosphere and ionosphere, and on details of the instrumental hardware. When the data are correlated, the expected delay is calculated and the data streams for each elements are aligned to the calculated delay. The rate of change of the difference between the expected and actual phases is referred as the residual fringe rate. For connected-element interferometers, the *a priori* uncertainties in delay and rate can easily be made insignificant. However, in VLBI the use of separate clocks, uncertainties in the geometry and atmosphere, and long baselines combine to make sufficiently accurate *a priori* determinations of the delay and phase difficult. Thus "fringe-fitting" must be performed to solve for and remove any residual delay and fringe rate offsets (Walker 1988).

For our final maps, fringe-fitting was performed with the AIPS task FRING (July 1994 edition), the global fringe-fitting algorithm developed by Schwab & Cotton (1983), with the penalty term disabled. Nyquist search windows were used. The Effelsberg 100-m antenna was chosen as the reference antenna whenever possible, otherwise the Green Bank telescope was selected. The parameter SOLINT (i.e., solution integration time) in FRING was set to 4–6 minutes in most cases. A value as long as 15-minutes was used for weak sources. A solution interval of 2-minutes was used for 0218+357 due to its large size $\sim$ 330 mas. After fringe-fitting, the 2-second data were converted to MERGE format used by the Caltech VLBI Package (Pearson 1991). The data were phase self-calibrated in DIFMAP (Shepherd et al. 1994) with a 10-second solution time to remove the residual phase errors. A point source model was used for all sources except 0218+356, for which

a model with two Gaussian components, derived from EVN observations (Patnaik, private communication), was used. The data then were averaged coherently for 60 seconds in all but two cases. A 10-second averaging interval was used in 0218+356 to avoid significant time-average smearing. For the same reason, a 30-second averaging interval was adopted for 0404+768.

The error bars of the averaged data were calculated from the internal scatter of individual data points within the averaging period.

3.2.3.2 AMPLITUDE CALIBRATION

Amplitude calibration was performed with the program CAL in the Caltech VLBI package, which calibrates the correlation coefficients using measurements of antenna system temperatures and antenna gain curves (Cohen et al. 1975). Accurate calibration relies on accurate determination of antenna system temperatures and antenna gain curves, which are difficult to obtain. Thus the *a priori* calibration always has errors which can be quite large. For example, HSTK had an offset of $\sim$ 20% in the session of June 1991. Fortunately, most of the errors can be corrected with a station-dependent multiplicative factor. In order to determine this factor and improve the *a priori* calibration, we observed calibrator sources of known structure, 0133+476, 0552+398, 1638+398 and 1739+522. All of these are strong sources ($>$ 1 Jy) known to be barely resolved or highly core-dominated. A calibrator scan was scheduled every 4–6 hours, and 2-3 calibrators were used during each observing session. We used two methods to find the station-dependent calibration offsets. First, we mapped the calibrators and self-calibrated the original data with the final clean component model allowing the gain of each telescope to be scaled by a constant factor. This provided a set of correction factors. Since the calibrators have known structure, we were confident of the final models and hence that the corrections were correct. The correction factors obtained from different calibrators also provided an independent check. They were consistent for most antennas, which enhanced our confidence. Second, we used the program UVCROSS

in the Caltech VLBI package to estimate the corrections. UVCROSS calculates gain correction factors for each station by equating the correlated flux densities at baseline crossing points in the *uv* plane. In practice nearby data points are treated as 'crossing points'. This procedure works well for compact sources, such as the calibrators we used. For our observations we used a 3-Mλ radius within which the correlated flux were averaged (the longest baseline is $\sim$ 155 Mλ). The corrections found with different calibrators were consistent. Moreover, they were in good agreement ($\leq 3\%$) with those found through mapping. Thus a set of averaged correction factors for each telescope was derived, and then were used to calibrate the entire observing session. Closure phases were also examined for obvious baseline dependent errors, but none was found in our observations. In our final-epoch of data processing, the calibrated data were converted back to FITS format for editing and mapping.

We believe that the final calibration was good to $\sim$ 5%. Time dependent calibration errors were later corrected through self-calibration on time scales of 15–30 minutes.

3.2.3.3. DATA EDITING

Our data were continuously recorded even when the telescopes were switching between sources. The corresponding data should be flagged. Since the switching periods are different for each telescope due to different slew speeds, it is difficult to edit data globally without sacrificing good data. Moreover, there are individual corrupted points due to interference and occasional bad readout by the correlator. Thus the data editing was done on a point-by-point basis. At the beginning of our observations, the data were edited with program IED of the Caltech VLBI package. It took $\sim$ 1 hour to edit one source. Later we used DIFMAP (*see below*) to perform this task. DIFMAP provides an excellent graphical interface and a variety of options for data editing. Data can be edited interactively by station or baseline, according to time and/or flux density range on a plot of visibilities. Data can also be edited on the visibility–*uv* distance plot. As a result, the time required to edit one source dropped

to $\sim$ 10 minutes, a factor of 6 improvement.

3.2.3.4 MAPPING

Our mapping methodology went through three generations as the mapping software and computing facility evolved during the course of this survey:

(i) *AMPHI–INVERT–CLEAN*

Maps were made with AMPHI–INVERT–CLEAN (Caltech VLBI Package) loops at the beginning of the survey. Program AMPHI performs self-calibration using the method of Cornwell & Wilkinson (1981). INVERT makes maps from calibrated visibility data by Fourier transformation. And CLEAN deconvolves the dirty maps produced by INVERT using the algorithm invented by Högbom (1974). The general idea was to start with a point source model and clean slowly to build a model close to the real distribution of brightness on the sky. We designed a procedure consisting of seven AMPHI–INVERT–CLEAN loops. Each loop took a starting model used by AMPHI to perform self-calibration and generated a model with delta functions produced by CLEAN. A point source starting model was used in the first loop and the delta-function model from the previous loop was used later. In each of the first five loops, a phase self-calibration was performed with the starting model and 10, 20, 40, 80 and 200 delta-functions were extracted; In the sixth loop a constant amplitude correction for each telescope was allowed in AMPHI and 200 delta-functions were cleaned. In the final loop amplitude correction on a timescale of 30 minutes was allowed and 400 delta-functions were cleaned. The procedure provided maps of good quality in most cases. However, since we started with a point source model, which tends to distribute flux symmetrically, some maps had suspicious counterjets, and there were probably errors at a low level for many sources. We therefore did modelfitting to the original data with Gaussian components based on the main features of the map (*see below for the need of modelfitting*). The agreement factor of the final models to the original data ranged from 1 – 1.3 for closure

phases and 1.3 – 2 for amplitudes. The model was used to start another procedure to make a final map. This procedure usually contained four AMPHI–INVERT–CLEAN loops. First, a phase self-calibration was performed with the model and original data, and 400 – 1000 delta-functions were subtracted, depending on the complexity of the structure; second, a constant correction of amplitude was allowed for each station; third, amplitude correction on a timescale of 30 minutes was allowed; and in the final step the third loop was repeated with natural weighting in INVERT. The weights were usually scaled with the inverse of the amplitude errors. We were satisfied with $\sim$ 90% of the maps obtained with this MAPPING – MODEL-FITTING – MAPPING procedure. The remainder were mapped individually, with carefully chosen windows.

(ii) *DIFMAP*

DIFMAP, written by Dr. M. C. Shepherd at Caltech, is an integration of many useful functions, including data display, data editing, self-calibration, imaging (i.e., Fourier transform), and deconvolution (i.e., clean). It takes advantage of the speed, large internal memory and graphics capability of Sun workstations. A difference mapping clean algorithm is used by DIFMAP. In this the subtraction of model components is performed in the uv plane rather than the image plane (Shepherd et al. 1994). This approach provides faster iterative self-calibration since only the changes to the model have to be computed in each iteration. It also guides users to recognize source structure and hence position clean windows, which is very helpful in identifying faint, extended emission.

The mapping was generally begun with tight windows. The brightest feature on the dirty map was windowed and cleaned first, then the brightest feature on the residual map and so on. This procedure was continued until no dominant bright feature remained in the residual map. We then self-calibrated the phases, followed by more cleaning. When the cleaned flux density reached about 90% of the flux density on the shortest baseline, we performed an amplitude self-calibration with a constant correction factor for each station.

The amplitude was then allowed to change on a time scale from 300 minutes down to 15-30 minutes. A clean step was used after each self-calibration. Maps were made with uniform weighting or natural weighting, with the weights scaled inversely with the amplitude errors. Uniform weighting provided higher resolution, while natural weighting provided higher sensitivity with slightly less resolution, which often revealed more extended structures. Data were tapered with a Gaussian function of a value 0.3 at uv distance 50 Mλ to reveal extended structures. Such a taper provides angular resolution similar to that of our 1.6 GHz VLBI observations, so that maps at two frequencies could easily be compared. For the sake of consistency, the sources mapped previously were remapped with DIFMAP. The quality of the maps is basically the same, but improved slightly in some cases.

(iii) *AUTOMAP*

A script, called AUTOMAP, has recently been developed by M. C. Shepherd and G. B. Taylor at Caltech to run DIFMAP automatically. In AUTOMAP an image is first produced by DIFMAP, assuming a point source starting model. The position of the highest surface brightness feature on the map is then identified and a small rectangular window is centered on this position. The map is then "CLEANed" (Högbom 1974) for a number of iterations, specified by the user, and a loop gain of typically $\sim$ 0.01. In each CLEAN iteration the highest surface brightness feature remaining within the window in the residual or "difference" map is selected for CLEANing. AUTOMAP then performs a phase self-calibration (i.e., it makes a hybrid map), and finds the position of the highest surface brightness feature in the difference map. It then places a window centered on this position and repeats the above process. We made a number of tests of AUTOMAP, and modified it to suit our needs for the mapping of the CJ1 objects. The final version of AUTOMAP which we used consisted of three basic steps:

1) The CLEAN loop had a cutoff at 6σ, where σ is the residual rms noise in the difference

map;

2) a Gaussian taper with a value of 0.3 at a spacing of 50 Mλ in the *uv* plane was applied to the visibility amplitudes—this helped to show up any faint extended structure; and

3) amplitude self-calibration was applied, followed by more CLEAN loops with a cutoff at 4.5σ.

Note that the rms noise on the residual map was changing during the above process, so the CLEAN cutoff was adjusted for each step. After choosing adequate map sizes, $\sim$ 60% of the maps generated by AUTOMAP are equivalent to those made interactively; $\sim$ 35% contain slight errors at low levels and can be corrected interactively with ease. The rest had to be mapped interactively with care. Even for these objects, the structure revealed by AUTOMAP is basically correct. AUTOMAP failed entirely on only one complex object, 1311+678.

Our final procedure generated three images: a uniformly weighted map, a naturally weighted map, and a map made from data which had been tapered with a Gaussian function with a value 0.3 at 50 Mλ. The tapered maps have map sizes four times as large as the other two maps—to search for structure on larger scales.

3.2.4. FINAL MAPS

The final maps are limited by thermal noise in most cases. The typical rms noise of a blank area in the map is $\sim$ 0.5 mJy with natural weighting and $\sim$ 1 mJy with uniform weighting. The dynamic range of the images (i.e., the ratio of the brightest feature in the map to rms noise of a blank area) is larger than 300:1, with exception of a few sources for which the dynamic range is below 300:1. The maps are presented in Figs. 3.4.1–3.4.84. The map layouts are described in Section 3.4. The parameters of the maps are listed in Table 3.2.

3.2.5. MODELFITTING

There is a major difference between VLBI and conventional aperture synthesis. In conventional aperture synthesis with N stations (i.e., $N(N-1)/2$ baselines), there are $N(N-1)/2$ well measured amplitudes and phases. However, VLBI arrays are not phase stable because they are not connected, thus in VLBI there are N arbitrary phase offsets, one for each antenna, instead of $N(N-1)/2$ reliable phases. One of these offsets can be set to zero by throwing away information on absolute position, which leaves $(N-1)$ phases undetermined. Another way of looking at this is that there are $(N-1)(N-2)/2$ measured closure phases, and therefore phases have to be invented on $(N-1)$ baselines before the closure phase relations can be solved to yield a total of $N(N-1)/2$ phases. These $(N-1)$ undetermined phases can *in principle* be set to any value and still yield an image which fits the data. The phases are usually set by phase self-calibration with a starting model. The starting model has to be close to the true brightness distribution on sky in order to achieve a reliable map. Using modelfitting to find such a model without any prior knowledge of the structure except observational data has been described in detail in *Introduction to the Caltech VLBI Programs, Chapter 5 MODELFITTING* (Pearson 1991). This step is often time consuming (Venturi et al. 1993c). With our approach of mapping of either the conventional AMPHI–INVERT–CLEAN loops or DIFMAP, we had a good idea of the source structure before we started modelfitting. It reduced greatly the time which we spent on modelfitting. The output model used in the third step of our AMPHI–INVERT–CLEAN mapping procedure served to improve the quality of the map.

Another reason for doing modelfitting is that it provides a parameterization of the source structure. A model is useful both for comparing structural changes between epochs, and for carrying out physical calculations. Thus we performed modelfitting each source with the final self-calibrated data. The parameters of the final models are listed in Table 3.3.

3.3

The First Caltech–Jodrell Bank VLBI Survey. III
VLBI and MERLIN Observations at 5 GHz
and VLA Observations at 1.4 GHz

W. Xu, A. C. S. Readhead, T. J. Pearson

Owens Valley Radio Observatory

California Institute of Technology

Pasadena, CA 91125

A. G. Polatidis, P. N. Wilkinson

Nuffield Radio Astronomy Laboratories

University of Manchester

Jodrell Bank, Macclesfield, Cheshire, SK11 9DL, U.K.

Submitted to the *Astrophysical Journal Supplement Series*

ABSTRACT

We present the 5 GHz results from the first Caltech–Jodrell Bank (CJ1) VLBI survey. The 1.6 GHz maps were presented in two separate papers (Polatidis et al. 1995, Thakkar et al. 1995). These three papers complete the first stage of this program to map at both 1.6 and 5 GHz all objects accessible to Mark II VLBI in the complete sample of 135 objects with $1.3 > S_{5\ \mathrm{GHz}} \geq 0.7$ Jy, $\delta(1950) \geq 35°$ and $|b| > 10°$. The combination of the CJ1 sample with the Pearson–Readhead sample provides a complete, flux density limited sample of 200 objects with $S_{5\ \mathrm{GHz}} \geq 0.7$ Jy, $\delta(1950) \geq 35°$ and $|b| > 10°$ for which all of the objects accessible to Mark II VLBI have been mapped at both 5 GHz (129 objects) and 1.6 GHz (132 objects).

In addition to the 5 GHz VLBI maps, we present in this paper 5 GHz MERLIN observations of 20 objects and 1.4 GHz VLA observations of 92 objects in the combined CJ1+PR sample. The VLA maps, together with L band (1.3–1.7 GHz) maps available in the literature, provide a complete set of VLA maps for the combined CJ1+PR sample. Finally, we present the radio spectra of the objects in the CJ1 sample.

The combined CJ1+PR VLBI surveys provide a sample which is large enough for a number of important astrophysical and cosmological studies. These will be presented in further papers in this series.

Subject headings: quasars: general — radio continuum: galaxies — surveys

1. INTRODUCTION

This is the third paper in a series presenting results of the first Caltech–Jodrell Bank VLBI survey (the CJ1 Survey). The CJ1 sample comprises the 135 objects from the S4 and S5 surveys (Pauliny-Toth et al. 1978; Kühr et al. 1981a) with 1.3 Jy $> S_{5\ \mathrm{GHz}} \geq 0.7$ Jy, $\delta(1950) \geq 35°$ and $|b| \geq 10°$. Together with the Pearson–Readhead sample (Pearson & Readhead 1988 — hereafter PR) of objects with $S_{5\ \mathrm{GHz}} \geq 1.3$ Jy, the CJ1+PR sample has a combined total of 200 objects with $S_{5\ \mathrm{GHz}} \geq 0.7$ Jy, $\delta(1950) \geq 35°$ and $|b| \geq 10°$.

In two previous papers (Polatidis et al. 1995; Thakkar et al. 1995) we have catalogued the sample and presented the results of 1.6 GHz VLBI observations of 81 objects in the CJ1 sample accessible to Mark II VLBI imaging, and 31 objects from the PR sample that had not previously been imaged with VLBI at 1.6 GHz. In this paper we present the 5 GHz VLBI observations of the 87 objects in the CJ1 sample and 1 remaining object in the PR sample accessible to Mark II VLBI. These three papers, combined with the 5 GHz maps of PR and maps available in the literature, provide a complete set of VLBI maps at 1.6 and 5 GHz of all objects accessible to Mark II VLBI in the CJ1+PR sample.

In addition to the 5 GHz VLBI maps of CJ1 objects, we present radio spectra of all CJ1 objects, 1.4 GHz VLA maps of 92 objects, and 5 GHz MERLIN maps of 20 objects from the combined CJ1+PR sample. The objects mapped with the VLA are those CJ1+PR objects for which no adequate VLA maps exist in the literature. Thus, the VLA maps presented here, plus those available in the literature, provide an almost uniform set of $\sim$ 1.4 GHz maps of the large-scale radio structure of the complete CJ1+PR sample.

The VLBI maps presented in these three papers were made with the "snapshot" technique, which has proved extremely effective in mapping compact structure in radio sources, and increases the efficiency of VLBI arrays by over a factor ~ 20. The technique is described in detail by Polatidis et al. (1995).

The results of the combined CJ1+PR surveys provide a sample which is large enough for a number of important astrophysical and cosmological studies—including determination of physically distinct classes, proper motion–redshift tests, angular diameter–redshift tests, and misalignment between parsec-scale and kiloparsec-scale radio structures. In particular, there were some classes of object in the PR sample with very few members, and these have now been augmented significantly by the addition of the CJ1 objects. The dual-wavelength observations presented in these three papers provide for a much more secure classification of radio-loud active galaxies than do single-frequency observations. The classification of these objects will be discussed in a later paper in this series. In addition, a number of interesting objects—including compact symmetric objects and possible gravitational lenses—have been discovered in the course of the 1.6 and 5 GHz VLBI surveys. These topics will be addressed in a number of papers describing follow-up studies of the CJ1 survey.

2. OBSERVATIONS AND DATA REDUCTION

2.1. VLBI Observations and Data Reduction

We observed 87 objects in the CJ1 sample with the global VLBI network at 5 GHz. Observations were recorded with left circular polarization (IEEE convention) and with a bandwidth of 1.8 MHz, using the Mark II VLBI format (Clark 1973), and cross-correlated with the JPL/Caltech Block 2 correlator. One object, 0404+768, in the PR sample was also observed since it had not been mapped previously at 5 GHz. All objects, except 0218+357 and 0404+768, were observed with the snapshot technique (Polatidis et al. 1995)—generally with three 20–30 min scans, but a few objects had 1 or 2 extra scans; 0218+357 was observed for 4.5 h and 0404+768 for 3 h. The observations were completed in six sessions between 1990 and 1992 (Table 3.1). Thirteen to seventeen stations participated in each session. The locations and parameters of the stations are listed in Table 3.1. In the session of September 1991, we obtained simultaneous MERLIN observations. Data from three of the

six MERLIN stations (Cambridge, Mark II at Jodrell Bank, and Knockin) were recorded in Mark II format for cross-correlation with the non-MERLIN stations. The MERLIN data were combined with VLBI data, giving 21 stations in this session. The length of the snapshots was shortened from 30 min to 20 min during the course of this project as we gained confidence in the technique. To optimize the *uv* coverage, the three snapshots were scheduled as follows: for objects with mutual observing time of 8 h or longer, the snapshots were separated by about 4 h, which provided very good *uv* coverage; for other objects three snapshots were taken at the beginning, the middle and the end of the mutual observing time. For objects with a declination near 35°, the lower limit of our sample, the mutual observing time is only $\sim$ 4 h, which leaves large holes in the *uv* coverage and may lead to uncertainties in the map. In these cases one or two stations were often given up in order to gain $\sim$ 1.5 h or more in mutual observing time. Fig. 3.1 shows the *uv* coverage for three representative objects, at $\delta \simeq 38°$, $\delta \simeq 52°$, and $\delta \simeq 77°$.

After correlation, data were fringe-fitted with the NRAO Astronomical Image Processing System (AIPS) program FRING (July 1994 edition), the global fringe-fitting algorithm developed by Schwab & Cotton (1983). Nyquist search windows, i.e., 2000 ns in delay and 500 mHz in rate centered on zero, were used. The Effelsberg 100-m antenna was chosen as the reference antenna whenever possible, otherwise the Green Bank 140-foot telescope was selected. The solution interval was set to 4–6 min in most cases, but values up to 15 min were used for weak objects. For 0218+357, a 2 min interval was used since this object is a large double of separation $\sim$ 330 mas. After fringe-fitting, the 2 s data were phase self-calibrated in DIFMAP (Shepherd, Pearson, & Taylor 1994) with a 10 s solution time to remove the residual phase errors. A point-source model was used for all objects except 0218+357, for which a model with two gaussian components, derived from EVN observations (Patnaik, private communication), was used. The data were then averaged coherently for 60 s in all but two cases. An averaging interval of 10 s was used for 0218+357 and 30 s

for 0404+768 to avoid significant time-average smearing. The error bars of the averaged data were calculated from the scatter of individual data points within the averaging period.

Amplitude calibration was performed with the program CAL in the Caltech VLBI package, which calibrates the correlation coefficients using measurements of antenna system temperatures and antenna gain curves (Cohen et al. 1975). Station-dependent calibration gain factors were derived from the observations of the strong, barely resolved or highly core-dominated calibrator objects 0133+476, 0552+398, 1638+398, and 1739+522. These gain factors were applied to the entire observing session. We believe that the final calibration is good to $\sim$ 5%. Time-dependent calibration errors were later corrected by self-calibration. After calibration, the data were edited in DIFMAP.

All of the objects were first mapped and self-calibrated non-interactively using an automatic script, called AUTOMAP, to drive DIFMAP. In AUTOMAP the data are first phase-self-calibrated with a point-source model and a "dirty" image is produced by Fourier inversion. The position of the highest surface brightness feature on the dirty map is then identified and a small rectangular window is centered on this position. The map is then "CLEANed" (Högbom 1974) for a number of iterations, with a loop gain of typically $\sim$ 0.01. In each CLEAN iteration the highest surface brightness feature remaining within the window in the residual or "difference" map is subtracted from the data. AUTOMAP then performs another phase self-calibration using the clean-component model and makes a new difference map. It finds the position of the highest surface brightness feature in this map, adds another window centered on this position, and repeats the above process. In later loops amplitude self-calibration is allowed in addition to phase self-calibration. After some experimentation we developed a final version of AUTOMAP in which: (a) the CLEAN loop had a cutoff at 6σ, where σ is the residual rms noise in the difference map; (b) a gaussian taper with a value of 0.3 at a spacing of 50 Mλ in the uv plane was applied to the visibility amplitudes—this helped to show up any faint extended structure; and

(c) amplitude self-calibration was applied, followed by more CLEAN loops with a cutoff at 4.5σ. Note that the rms noise on the residual map was changing during the above process, so the CLEAN cutoff was adjusted for each step. After choosing adequate map sizes, $\sim 60\%$ of the maps generated by AUTOMAP are equivalent to those made interactively, and $\sim$ 35% contain slight errors at low levels and can be corrected interactively with ease. The rest had to be mapped interactively with care. Even for these objects, the structure revealed by AUTOMAP is basically correct. AUTOMAP failed entirely on only one—complex—object, 1311+678.

Our final procedure generated three images: a uniformly weighted map, a naturally weighted map, and a map made from data which had been tapered with a gaussian function with a value 0.3 at 50 Mλ. The tapered maps have map sizes four times as large as the others, to search for structure on larger scales. The final maps are limited by thermal noise in most cases. The typical rms noise in a blank area in the map is $\sim$ 0.5 mJy with natural weighting and $\sim$ 1 mJy with uniform weighting. The dynamic range of the images (i.e., the ratio of the brightest feature in the map to rms noise in a blank area) is larger than 300:1 in most cases. Four objects, 0707+689, 0827+378, 1203+645, and 1637+626, were very heavily resolved and only detected on a few short baselines, and were not mapped. The naturally weighted and tapered maps of the other 84 objects are presented in Figs. 3.4.1 – 3.4.84. The objects 0218+357, 0821+394, 1138+594, and 1437+624 have large angular sizes, and we present maps of individual components so that more detail can be seen. The parameters of the maps are listed in Table 3.2.

The final step in the data analysis was to fit the closure phases and self-calibrated amplitudes with elliptical gaussian models using the program MODELFIT in the Caltech VLBI package (Pearson 1991). Such models provide a parameterization of the object structure, which is useful both for comparing structural changes between epochs and for estimating physical parameters. The models and agreement factors (square root of reduced chi-square)

between the models and observed visibilities are listed in Table 3.3. Separate agreement factors are given for amplitude and closure phase. In addition a "total" agreement factor (a weighted average of the amplitude and closure phase agreement factors) is given; this is the quantity that is minimized in the least-squares model fitting procedure. A detailed description of the agreement factor is given by Henstock et al. (1995).

In addition to the 87 CJ1 objects discussed in this paper, 6 other CJ1 objects have been observed with global VLBI or the EVN at 1.6 GHz (Paper I and references therein). A good quality 5 GHz map of 1637+826 (NGC 6251) has been published by Jones et al. (1986), thus we did not observe it. The objects 0010+775, 0945+664, and 2324+405 were heavily resolved at 1.6 GHz, while 1250+568 and 2323+435 have no bright compact feature in their 1.6 GHz EVN images, and hence are not accessible to Mark II VLBI observations. Therefore, we did not attempt to observe these five objects at 5 GHz.

2.2. MERLIN Observations and Data Reduction

MERLIN observations at 5 GHz of 20 objects in the CJ1 and PR samples were made in February 1992. Parameters for the MERLIN telescopes are summarized in Table 3.1. The object list is given in Table 3.4. Each object was observed with many 20–30-min scans spanning $\sim$ 12 h, with a total integration time from 4 to 6 h. Our observations were made with left circular polarization (IEEE convention) and recorded with a bandwidth of 7 MHz separated into seven 1 MHz channels. The data were calibrated with the OLAF package of the Nuffield Radio Astronomy Laboratories. The objects 3C 286 and OQ 208 were used as the flux density calibrators. Bandpass corrections were made with the AIPS package. The maps were made with DIFMAP. Typical *uv* coverages are shown in Fig. 3.2. Uniformly weighted maps are presented in Figs. 3.4 and 3.5. For four objects with large-scale structure, naturally weighted maps restored with a circular gaussian beam of FWHM 100 mas are also presented. For the object 0812+367 we include a map of the central and southern component to show more detail. Its northern component is slightly resolved. The

parameters of the maps are listed in Table 3.4.

2.3. VLA Observations and Data Reduction

Observations were made with the VLA in the A configuration at L band on November 5, 1992. Two IFs centered on 1464.9 and 1364.9 MHz, with a bandwidth of 50 MHz each, were used. The 92 objects observed are listed in Table 3.5. Each object was observed with three 2-min snapshots, which were separated by 1.5 h to improve the *uv* coverage. A typical *uv* coverage is shown in Fig. 3.3. The data were reduced in the AIPS package. The object 3C 286 was used as the flux density calibrator. The MX program was used to make the maps and the CALIB program was used to perform self-calibration. In most cases the final maps were convolved with a circular gaussian beam of FWHM 1.5 arcsecond. For objects dominated by large-scale structure, the final maps were convolved with a larger beam (3 or 5 arcsecond).

In VLA observations at this frequency there are often other radio sources present in the field. These objects must also be mapped in order to achieve high dynamic range on the target object. Thus we mapped an $11' \times 11'$ field for each object to locate possible confusing sources. All sources brighter than $\sim$ 10 mJy were mapped. The rms noise of a blank area of sky in the maps ranges from 0.1 to 0.5 mJy for most objects (see Table 3.5). Several strong sources have large rms noise, which could not be corrected with self-calibration. Of the 92 objects 28 are unresolved, and for these we do not present maps. The maps of the other 64 objects are presented in Figs. 3.4 and 3.6, and the parameters of the maps are listed in Table 3.5.

2.4. Radio Spectra

We collected flux density measurements at various frequencies from the literature. For the most part, the data were taken from the catalogue of radio objects compiled by Kühr et al. (1979). Part of the catalogue containing objects brighter than 1 Jy has been published

(Kühr et al. 1981b). Other data were taken from the VLA calibrator list (1990 edition), Edelson (1987), Ficarra, Grueff, & Tomassetti (1985), Patnaik et al. (1992), Steppe et al. (1988), and White & Becker (1992). We used the same spline-fit routine as Herbig & Readhead (1992) to draw the overall spectrum. The spectra of all the CJ1 objects are presented in Figs. 3.4 and 3.7.

3. CONCLUSION

In this third paper of the series we have reported 5 GHz VLBI and MERLIN observations and 1.4 GHz VLA observations of objects in the CJ1 and PR samples. We now have a large body of observational data on the majority of objects in the complete sample of 200 objects with $S_{5\ \mathrm{GHz}} \geq 0.7$ Jy, $\delta \geq 35°$, and $|b| \geq 10°$, including VLBI images at 1.6 GHz (Papers I and II), VLBI images at 5 GHz (this paper and Pearson & Readhead 1988), MERLIN and VLA images (this paper and published results), and radio spectra (this paper). Optical observations to measure redshifts are in progress (Xu et al. 1994).

The CJ1+PR sample of 200 objects is large enough to refine the classification of compact radio objects presented by Pearson & Readhead, and to undertake a number of important astrophysical and cosmological studies. These subjects will be addressed in subsequent papers in the series. A number of particularly interesting objects have already been identified, including several compact symmetric objects (e.g., 2352+495, Wilkinson et al. 1994; Readhead et al. 1995), gravitational lenses (e.g., 0218+357, Patnaik et al. 1993), and a high-redshift superluminal object (0642+449, Vermeulen et al. 1995).

While this paper completes the VLBI observations for the CJ1 survey, we are also in the process of enlarging the sample still further with the second Caltech–Jodrell Bank VLBI survey (CJ2) of flat-spectrum radio objects (Taylor et al. 1994; Henstock et al. 1995).

ACKNOWLEDGEMENTS

We thank the staffs of the observatories in the European and the US VLBI networks and the staff of the JPL/Caltech Block 2 correlator for their assistance during the CJ1 survey. We also thank R. C. Vermeulen and G. B. Taylor for their help with fringe-fitting and automatic mapping, and G. B. Taylor and D. R. Henstock for observing six objects for us. AGP acknowledges the receipt of a British Council Fellowship for the year 1991. The work at the California Institute of Technology was supported by the National Science Foundation (grants AST-8814554 and AST-9117100). The VLA and VLBA are instruments of the National Radio Astronomy Observatory, which is operated by Associated Universities, Inc., under cooperative agreement with the National Science Foundation.

REFERENCES

Clark, B. G. 1973, Proc. IEEE, 61, 1242

Cohen, M. H., Moffet, A. T., Romney, J. D., Schilizzi, R. T., Shaffer, D. B., Kellermann, K. I., Purcell, G. H., Grove, G., Swenson, G. W., Yen, J. L., Pauliny-Toth, I. I. K., Preuss, E., Witzel, A., & Graham, D. 1975, ApJ, 201, 249

Edelson, R. A. 1987, AJ, 94, 1150

Ficarra, A., Grueff, G., & Tomassetti, G. 1985, A&AS, 59, 255

Henstock, D. R., Wilkinson, P. N., Browne, I. W. A., Taylor, G. B., Vermeulen, R. C., Pearson, T. J., & Readhead, A. C. S. 1995, ApJS, submitted

Herbig, T., & Readhead, A. C. S. 1992, ApJS, 81, 83

Högbom, J. A. 1974, A&AS, 15, 417

Jones, D. L, Unwin, S. C., Readhead, A. C. S., et al. 1986, ApJ, 305, 684

Kühr, H., Nauber, U., Pauliny-Toth, I. I. K., & Witzel, A. 1979, MPIfR Preprint 55

Kühr, H., Pauliny-Toth, I. I. K., Witzel, A., & Schmidt, J. 1981a, AJ, 86, 854

Kühr, H., Witzel, A., Pauliny-Toth, I. I. K., & Nauber, U. 1981b, A&AS, 45, 367

Patnaik, A. R., Browne, I. W. A., King, L. J., Muxlow, T. W. B., Walsh, D., & Wilkinson, P. N. 1993, MNRAS, 261, 435

Patnaik, A. R., Browne, I. W. A., Wilkinson, P. N., & Wroble, J. M. 1992, MNRAS, 254, 655

Pauliny-Toth, I. I. K., Witzel, A., Preuss, E., Kühr, H., Kellermann, K. I., Fomalont, E. B., & Davis, M. M. 1978, AJ, 83, 451

Pearson, T. J. 1991, BAAS, 23, 991

Pearson, T. J., & Readhead, A. C. S., 1988, ApJ, 328, 114

Polatidis, A. G., Wilkinson, P. N., Xu, W., Readhead, A. C. S., Pearson, T. J., Taylor, G. B., & Vermeulen, R. C. 1995, ApJS, in press

Readhead, A. C. S., Xu, W., Pearson, T. J., Wilkinson, P. N., & Polatidis, A. G. 1995, ApJ, submitted

Schwab, F. R., & Cotton, W. D. 1983, AJ, 88, 688

Shepherd, M. C., Pearson, T. J., & Taylor, G. B. 1994, BAAS, 26, 987

Steppe, H., Salter, C. J., Chini, R., Kreysa, E., Brunswig, W., & Lobato Perez, J. 1988, A&AS, 75, 317

Taylor, G. B., Vermeulen, R. C., Pearson, T. J., Readhead, A. C. S., Henstock, D. R., Browne, I. W. A., & Wilkinson, P. N. 1994, ApJS, in press

Thakkar, D. D., Xu, W., Readhead, A. C. S., Pearson, T. J., Taylor, G. B., Vermeulen, R. C., Polatidis, A. G., & Wilkinson, P. N. 1995, ApJS, in press

Vermeulen, R. C. et al. 1995, in preparation

White, R. L., & Becker, R. H. 1992, ApJS, 79, 331

Wilkinson, P. N., Polatidis, A. G., Readhead, A. C. S., Xu, W., & Pearson, T. J. 1994, ApJ, in press

Xu, W., Lawrence, C. R., Readhead, A. C. S., & Pearson, T. J. 1994, AJ, 108, 395

3.4. PRESENTATION OF MAPS AND SPECTRA

All maps made for the CJ1 survey are presented in this section. For sources observed with VLBI at 5 GHz, we present the VLBI, VLA, and MERLIN maps and radio spectra together on a single page. Each page is divided into six panels. The VLBI maps, uniformly weighted, naturally weighted and tapered, are presented in the three panels on the left column. Radio spectra are presented in the top panel on the right, VLA maps in the middle, and MERLIN maps at the bottom. For VLBI maps, the peak brightness, rms noise and beam size are displayed beneath each map. The observing frequency and weighting method are noted in the top-left and top-right corner, respectively. The contour levels are -2, -1, 1, 2, 4, 8, 16, 32, 64, 128, 256 times of 3σ (rms noise). MERLIN maps are arranged similarly. For VLA maps, observing frequency is labeled above the map frame, while peak brightness and contour levels are printed below the map. The contour levels appear as:

```
Levs = X * (-2.00, -1.00, 1.00, 2.00, 4.00, 8.00, 16.00, 32.00, 64.00,

          128.00, 256.00, 512.00, 1024.00)
```

among which, `X` is the 3σ value.

The VLBI maps shown in this fashion are adequate for sources which do not have much extended structure, but do not work well in presenting sources with extended structure. Thus we also attach full page maps for these sources so that more details can be seen.

Other MERLIN maps are presented together with 6 maps on each page, so are other VLA maps. The radio spectra of sources in the CJ1 sample which we did not observe with VLBI are also presented together. The radio spectra of sources in the PR sample can be found in Herbig & Readhead (1992).

The maps and spectra are presented in the following order:

Fig. 3.4.1 — 3.4.84: maps and spectra of sources observed with VLBI.

Fig. 3.5.: MERLIN maps of other sources.

Fig. 3.6.: VLA maps of other sources.

Fig. 3.7.: Spectra of other sources in the CJ1 sample.

TABLE 3.1. TELESCOPE CHARACTERISTICS

Telescope	Code	Location	Diameter (meter)	Sensitivity (K/Jy)	T_{sys} (K)	Network	1990 Mar	1991 Jun	1991 Sep	1992 Mar	1992 Jun	1992 Sep
Onsala	S	Sweden	26	0.059	150	EVN	√	√	√	√	√	√
Effelsberg	B	Germany	100	2.38	45	EVN	√	√	√		√	√
WSRT	W	Netherlands	14×25	—[a]	110	EVN	√	√	√	√	√	√
JBNK	J2	Jodrell Bank, UK	25	0.12	46	EVN		√	√	√		
						MERLIN						
Medicina	L	Bologna, Italy	32	0.16	45	EVN	√	√	√	√	√	√
Noto	No	Noto, Italy	32	0.146	45	EVN	√	√	√	√	√	√
Cambridge	C	Cambridge, UK	32	0.23	32	MERLIN			√	√		
Knockin	Kn	Knockin, UK	25	0.12	33	MERLIN			√			
Tabley	T	Tabley, UK	25	0.13	34	MERLIN			√			
Defford	De	Defford, UK	25	0.032	55	MERLIN			√			
Darnhall	Da	Darnhall, UK	25	0.12	32	MERLIN			√			
Haystack	K	Westford, MA, USA	36	0.16	74	US	√	√	√	√	√	√
NRAO	G	Green Bank, WV, USA	43	0.27	33	US	√	√	√	√	√	√
FDVS	F	Fort Davis, TX, USA	26	0.095	88	US	√					
VLBA_Nl	Nl	North Liberty, IA, USA	25	0.142	40	VLBA		√	√	√	√	√
VLBA_Fd	Fd	Fort Davis, TX, USA	25	0.131	42	VLBA		√	√	√	√	√
VLBA_La	La	Los Alamos, NM, USA	25	0.139	40	VLBA	√	√	√	√	√	√
VLBA_Pt	Pt	Pie Town, NM, USA	25	0.126	42	VLBA	√	√	√	√	√	√
VLBA_Kp	Kp	Kitt Peak, AZ, USA	25	0.128	43	VLBA	√	√	√	√	√	√
VLBA_Ov	Ov	Owens Valley, CA, USA	25	0.124	36	VLBA				√	√	√
VLBA_Br	Br	Brewster, WA, USA	25	0.130	34	VLBA			√	√	√	√
VLA[b]	Y	Socorro, NM, USA	25	0.119	37	US	√	√	√	√	√	√
OVRO	O	Owens Valley, CA, USA	40	0.201	70	US	√	√	√			

NOTES TO TABLE 1. — [a] WSRT provided T_{sys} in K and Jy, from which the sensitivity could be derived. But the value varied from 0.3 to 1, depending on the number of antenna actually used. [b] The VLA was used in single antenna mode.

EXPALANATION OF COLUMNS — (1, 2) The name and code used of each telescope. Affiliations: **S**—Onsala Space Observatory; **B**—Max-Planck-Institut für Radioastronomie; **W**—Westerbork Synthesis Radio Telescope; **J2**—MK II telescope, Nuffield Radio Astronomy Laboratories; **L, No**—Istituto di Radioastronomia; **C, Kn, T, De, Da**—Nuffield Radio Astronomy Laboratories; **K**— Haystack Observatory; **G**—National Radio Astronomy Observatory; **F**—George A. Agassiz Station of Harvard University; **Nl, Fd, La, Pt, Kp, Ov, Br**—National Radio Astronomy Observatory, VLBA; **Y**—National Radio Astronomy Observatory, VLA; **O**—Owens Valley Radio Observatory. (3) The location of each telescope. (4) The diameter of each telescope (in meters). (5,6) The sensitivity in K/Jy and system temperature in K of each telescope. (7) The network which each telescope is associated with. (8 - 13) A tick indicates whether the telescope participated in that session.

TABLE 3.2. VLBI MAP PARAMETERS

Source	Observation	Naturally Weighted Maps					Tapered Maps				
		Beam[a]			S_{peak}	rms	Beam			S_{peak}	rms
		a (mas)	b (mas)	θ (°)			a (mas)	b (mas)	θ (°)		
0010+405	1990 Mar	2.0	0.9	−14	417.0	0.5	5.8	3.9	10	466.0	0.6
0022+390	1990 Mar	2.7	0.8	−12	395.0	0.8	7.3	3.8	20	518.0	0.8
0102+480	1990 Mar	1.7	0.9	−11	695.0	0.7	5.6	3.9	18	1060.0	0.8
0218+357[c]	1992 Mar	3.7	2.2	−52	221.3	0.7	5.2	4.5	6	380.0	0.7
0248+430	1992 Sep	1.7	1.0	−7	609.0	0.6	4.5	4.0	12	982.0	0.7
0402+379	1990 Mar	2.1	0.9	−17	143.0	1.0	6.0	4.6	22	413.0	0.9
0404+768	1991 Sep	1.9	1.2	70	153.0	1.0	11.4	10.1	84	997.6	1.2
0602+673	1990 Mar	1.2	1.0	−7	560.0	0.4	5.2	4.3	30	649.0	0.9
0615+820	1990 Mar	1.1	1.0	−29	458.0	0.5	3.6	3.1	9	717.0	1.1
0620+389	1991 Jun	2.4	0.9	−9	403.0	0.4	4.8	3.2	12	464.0	0.8
0642+449	1991 Jun	1.9	0.9	−10	1470.0	0.7	5.8	4.2	14	1580.0	1.2
0646+600	1991 Jun	1.3	1.0	−11	430.0	0.4	4.9	4.3	24	813.0	0.7
0650+371	1990 Mar	2.3	0.8	−14	959.0	0.4	6.5	3.8	14	1280.0	0.7
0707+476	1990 Mar	2.0	0.8	−14	645.0	0.5	6.3	3.8	18	770.0	0.8
0707+689[b]	1991 Jun										
0716+714	1992 Sep	1.3	0.9	1	598.0	0.5	5.6	4.4	28	640.0	0.7
0740+828	1990 Mar	1.1	1.0	−82	310.0	0.6	5.0	4.7	−44	573.0	0.9
0746+483	1991 Jun	1.6	1.0	−11	439.0	0.4	5.2	4.3	13	757.0	0.8
0755+379	1991 Jun	3.2	0.8	−24	143.0	0.4	6.8	3.5	−4	175.0	0.6
0805+410	1991 Jun	1.9	0.9	−12	910.0	0.6	5.5	4.1	7	966.0	0.9

TABLE 3.2. VLBI MAP PARAMETERS (*continued*)

Source	Observation	NATURALLY WEIGHTED MAPS					TAPERED MAPS				
		Beam[a]			S_{peak}	rms	Beam			S_{peak}	rms
		a (mas)	b (mas)	θ (°)			a (mas)	b (mas)	θ (°)		
0812+367	1990 Mar	2.6	0.8	−11	701.0	0.5	6.4	3.7	15	782.0	0.9
0820+560	1990 Mar	1.6	0.9	−17	1160.0	0.5	5.9	3.9	10	1320.0	0.6
0821+394[c]	1990 Mar	2.3	0.8	−9	642.0	0.9	5.6	3.5	12	694.0	0.7
0827+378[b]	1991 Jun										
0828+493	1990 Mar	2.0	0.8	−18	192.0	0.6	6.4	4.0	17	265.0	0.7
0833+585	1990 Mar	1.6	0.9	−10	386.0	0.7	5.5	3.9	19	604.0	0.8
0900+428	1991 Jun	1.8	0.9	−12	218.0	0.4	5.8	4.2	14	273.0	0.6
0917+449	1991 Jun	1.8	0.9	−12	973.0	0.6	6.0	4.2	17	1260.0	0.8
0917+624	1991 Jun	1.2	1.1	−8	843.0	0.4	4.9	4.6	28	1020.0	0.7
0955+476	1991 Jun	1.8	1.0	−10	993.0	0.5	5.3	3.5	14	1050.0	0.8
1003+830	1991 Jun	1.9	0.8	−81	258.0	0.3	6.9	4.1	−55	304.0	0.5
1015+359	1991 Sep	3.3	1.0	−7	569.0	0.3	7.3	5.1	15	668.0	0.4
1020+400	1991 Sep	3.0	1.0	−6	698.0	0.4	7.3	4.9	15	762.0	0.5
1030+415	1991 Sep	2.7	1.0	−6	282.0	0.3	6.9	5.1	16	324.0	0.3
1039+811	1992 Sep	1.1	1.1	61	869.0	0.5	4.4	4.3	−85	1090.0	0.7
1044+719	1991 Jun	1.5	0.9	−86	757.0	0.6	6.2	4.1	−65	958.0	0.9
1053+704	1991 Jun	1.6	0.9	−89	480.0	0.4	6.3	4.0	−70	556.0	0.6
1053+815	1991 Jun	1.2	1.0	−80	492.0	0.3	5.5	4.4	−77	554.0	0.6
1058+726	1991 Jun	1.3	1.0	−70	105.0	0.4	5.7	4.4	−54	311.0	0.6
1101+384	1991 Sep	2.9	1.1	−5	374.0	0.3	10.8	8.0	30	421.0	0.4

TABLE 3.2. VLBI MAP PARAMETERS (*continued*)

Source	Observation	Naturally Weighted Maps					Tapered Maps				
		Beam[a]			S_{peak}	rms	Beam			S_{peak}	rms
		a (mas)	b (mas)	θ (°)			a (mas)	b (mas)	θ (°)		
1128+385	1992 Mar	3.1	1.0	−3	823.0	0.4	4.6	4.0	14	936.0	0.6
1138+594[c]	1991 Jun	1.5	0.9	−9	79.2	0.6	6.6	4.2	27	90.0	0.8
1144+402	1992 Mar	3.0	1.0	−1	532.0	0.5	4.6	4.0	17	580.0	0.6
1144+542	1991 Jun	1.4	1.0	−14	230.0	0.4	5.1	4.2	14	349.0	0.6
1150+497	1992 Jun	1.8	0.9	−8	325.0	0.5	4.6	3.8	31	440.0	0.6
1150+812	1992 Sep	1.2	1.0	25	727.0	0.4	4.6	3.9	79	1050.0	0.5
1203+645 [b]	1990 Mar										
1213+350	1992 Mar	3.5	0.9	−3	433.0	0.7	4.9	4.2	18	691.0	0.7
1216+487	1992 Mar	2.9	1.0	−4	312.0	0.5	4.8	4.2	22	498.0	0.5
1225+368	1992 Mar	3.4	1.0	−6	226.0	0.6	4.8	4.1	8	457.0	0.6
1242+410	1992 Mar	3.6	0.9	−6	66.5	0.6	6.0	4.3	25	157.0	0.7
1311+678	1990 Mar	4.8	3.3	−84	148.0	2.0	5.8	5.0	82	184.0	2.2
1317+520	1992 Jun	1.7	1.0	−16	161.0	0.5	4.6	3.9	23	179.0	0.7
1333+459	1992 Jun	1.8	1.0	−21	350.0	0.6	4.6	3.7	4	579.0	0.6
1333+589	1992 Jun	1.6	1.0	−25	219.0	0.8	4.6	3.7	18	307.0	1.9
1342+663	1991 Jun	1.3	1.0	−28	597.0	0.4	5.0	4.5	−14	682.0	0.6
1347+539	1990 Mar	1.3	1.0	15	437.0	0.6	5.1	4.3	49	505.0	0.6
1357+769	1991 Jun	1.4	0.9	14	584.0	0.4	5.4	4.2	40	643.0	0.6
1418+546	1990 Mar	1.3	0.9	−15	1470.0	0.6	5.1	4.3	6	1930.0	1.0
1435+638	1990 Mar	1.4	0.9	79	536.0	0.6	5.9	4.0	−61	733.0	0.6

TABLE 3.2. VLBI MAP PARAMETERS (*continued*)

Source	Observation	NATURALLY WEIGHTED MAPS					TAPERED MAPS				
		Beam[a]			S_{peak}	rms	Beam			S_{peak}	rms
		a (mas)	b (mas)	θ (°)			a (mas)	b (mas)	θ (°)		
1437+624[c]	1991 Jun	1.2	1.0	−29	129.0	0.4	5.2	4.4	−4	267.0	0.6
1438+385	1992 Jun	2.2	0.9	−12	321.0	0.6	4.9	3.8	14	429.0	0.5
1504+377	1992 Jun	2.3	0.9	−13	349.0	0.5	5.0	3.8	13	534.0	0.5
1547+507	1992 Jun	1.7	1.0	−13	438.0	0.5	4.7	4.0	24	557.0	0.6
1637+626[b]	1991 Jun										
1638+398	1990 Mar	2.0	0.9	−19	1570.0	0.7	5.3	3.7	5	1760.0	1.0
1656+477	1990 Mar	1.7	0.9	−16	1230.0	0.8	5.3	3.8	14	1440.0	1.0
1656+482	1991 Sep	2.4	1.0	−18	393.0	0.3	6.5	5.2	15	566.0	0.5
1719+357	1991 Sep	3.1	1.0	−16	288.0	0.3	7.3	5.4	4	387.0	0.3
1732+389	1990 Mar	2.0	0.9	−12	1040.0	0.7	5.8	3.8	8	1230.0	1.0
1734+508	1991 Sep	1.8	1.2	−20	465.0	0.4	6.1	5.7	8	722.0	0.5
1738+476	1990 Mar	1.5	0.9	−11	797.0	0.6	5.1	4.0	14	1030.0	0.8
1751+441	1990 Mar	2.1	0.8	−18	604.0	0.6	6.7	3.8	10	843.0	0.7
1758+388	1990 Mar	2.4	0.8	−13	691.0	0.6	6.2	3.7	9	889.0	0.7
1800+440	1990 Mar	2.1	0.8	−19	389.0	0.6	6.3	3.8	5	501.0	0.7
1819+396	1990 Mar	7.8	3.1	−5	228.0	1.8	10.0	5.5	17	245.0	2.2
1842+681	1990 Mar	1.2	0.9	−50	622.0	0.8	5.0	4.2	−26	801.0	1.0
1843+356	1991 Sep	3.5	1.0	−12	245.0	0.3	7.5	5.3	14	528.0	0.4
1926+611	1990 Mar	1.4	0.9	−38	399.0	0.6	5.6	4.1	−7	551.0	0.7
1943+546	1991 Sep	1.9	1.1	−12	245.0	0.3	6.3	5.4	13	481.0	0.4

TABLE 3.2. VLBI MAP PARAMETERS (*continued*)

Source	Observation	NATURALLY WEIGHTED MAPS					TAPERED MAPS				
		Beam[a]			S_{peak}	rms	Beam			S_{peak}	rms
		a (mas)	b (mas)	θ (°)			a (mas)	b (mas)	θ (°)		
2007+777	1992 Jun	1.2	1.1	−8	1540.0	0.7	4.8	3.8	16	1950.0	0.7
2010+723	1991 Jun	1.1	1.0	−18	519.0	0.4	5.3	4.4	−4	919.0	0.5
2207+374	1991 Sep	2.9	1.0	−10	152.0	0.3	10.5	8.0	27	277.0	0.4
2214+350	1990 Mar	2.7	0.8	−14	527.0	0.5	6.7	3.7	9	586.0	0.6
2229+695	1990 Mar	1.7	0.8	−33	650.0	0.5	6.4	3.8	2	949.0	0.8
2253+417	1990 Mar	2.2	0.8	−19	624.0	0.4	6.3	3.8	9	958.0	0.7
2255+416	1990 Mar	2.0	0.9	−20	236.0	0.7	6.3	3.8	8	304.0	0.8
2311+469	1990 Mar	2.6	0.8	−17	71.8	0.5	3.1	1.2	−25	78.0	0.7

Note:

[a] The restoring beam is an elliptical Gaussian with FWHM major axis a and minor axis b, with major axis at position angle θ.

[b] Heavily resolved. [c] Same contour levels are used for maps of individual components.

EXPLANATION OF COLUMN —

(1) Source name. (2) Observation date. (3, 4, 5) The beam characteristics of the naturally weighted maps. (6) The peak flux density of the naturally weighted maps (mJy/beam). (7) The rms noise in the the naturally weighted maps (mJy/beam). (8, 9, 10) The beam characteristics of the tapered maps. (11) The peak flux density of the tapered maps (mJy/beam). (12) The rms noise in the tapered maps (mJy/beam).

TABLE 3.3. GAUSSIAN MODELS

Source	S (Jy)	r (mas)	θ (°)	a (mas)	b/a	ϕ (°)	Amp. A.F.	Phase A.F.	Total A.F.
0010+405	0.423	0.00	0.0	0.55	0.40	144.8	1.004	1.059	1.029
	0.058	0.97	−30.2	1.41	0.30	−31.2			
0022+390	0.395	0.00	0.0	0.55	0.86	109.8	1.041	1.077	1.057
	0.087	5.28	168.8	9.19	0.11	153.9			
	0.118	1.04	159.6	0.68	0.41	44.8			
0102+480	0.664	0.50	194.1	1.63	0.72	11.2	1.035	1.041	1.038
	0.453	0.00	0.0	0.28	0.34	111.3			
0248+430	0.718	0.00	0.0	0.99	0.41	150.2	1.261	1.127	1.201
	0.353	1.29	145.5	0.51	0.00	61.5			
	0.044	5.43	154.3	4.80	0.00	150.5			
	0.128	11.93	140.8	1.30	0.64	10.9			
0402+379	0.403	0.65	235.0	2.90	0.78	89.6	1.017	1.354	1.172
	0.094	0.24	158.3	0.75	0.00	29.9			
	0.048	2.72	91.3	1.07	0.81	178.4			
	0.162	27.72	35.3	11.68	0.34	23.2			
0602+673	0.642	0.00	0.0	0.53	0.66	−19.7	1.052	1.061	1.056
	0.036	3.46	187.3	6.84	0.21	173.7			
0615+820	0.528	0.00	0.0	0.67	0.64	154.1	1.027	1.105	1.063
	0.254	0.84	238.9	1.12	0.56	−5.6			
0620+389	0.436	0.00	0.0	0.47	0.68	−62.2	0.949	0.997	0.971
	0.049	1.20	149.8	1.98	0.00	27.0			
	0.089	6.68	134.2	2.22	0.67	−32.9			
0642+449	1.566	0.00	0.0	0.34	0.76	82.3	0.998	0.975	0.987
	0.086	3.03	92.1	1.57	0.81	25.4			
0646+600	0.449	0.00	0.0	0.51	0.64	38.1	1.018	1.106	1.059
	0.493	3.03	−144.8	0.53	0.81	12.4			
	0.102	1.35	−139.1	1.59	0.08	12.6			
	0.012	3.39	13.0	0.58	0.33	153.8			
0650+371	1.288	0.00	0.0	0.77	0.57	43.8	1.109	1.214	1.157
	0.022	3.01	87.3	1.23	0.30	99.5			
0707+476	0.434	0.00	0.0	0.29	0.95	−52.4	1.041	1.032	1.037
	0.279	0.62	−16.0	0.44	0.68	48.7			
	0.040	5.16	23.4	2.28	0.38	134.9			
	0.087	1.80	6.1	4.19	0.21	−0.9			
	0.014	15.94	51.7	10.36	0.50	−34.7			
0716+714	0.631	0.00	0.0	0.34	0.22	28.1	1.078	1.035	1.058
	0.018	1.99	6.5	0.00	0.10	0.0			

TABLE 3.3. GAUSSIAN MODELS (*continued*)

Source	S (Jy)	r (mas)	θ (°)	a (mas)	b/a	ϕ (°)	Amp. A.F.	Phase A.F.	Total A.F.
0740+828	0.319	0.00	0.0	0.36	0.74	9.9	1.137	1.148	1.142
	0.119	0.87	10.3	0.00	0.01	105.2			
	0.258	2.76	−5.5	1.18	0.85	101.1			
	0.049	8.63	−4.2	3.10	0.29	19.4			
	0.048	17.67	−5.1	10.29	0.23	−2.7			
0746+483	0.363	0.00	0.0	0.47	0.35	93.4	1.075	1.129	1.100
	0.391	0.82	−85.4	0.74	0.59	−75.0			
	0.087	3.10	−92.4	1.52	0.60	81.3			
0755+379	0.120	0.00	0.0	0.26	0.00	54.6	1.028	1.087	1.055
	0.031	0.72	127.8	0.54	0.00	−93.8			
	0.048	1.52	119.8	2.85	0.26	118.9			
0805+410	0.956	0.00	0.0	0.42	0.60	10.4	1.127	1.002	1.071
	0.025	2.46	27.8	1.51	0.00	13.1			
	0.070	6.54	46.8	5.73	0.37	58.1			
0812+367	0.549	0.00	0.0	0.21	0.51	−91.3	1.089	1.043	1.069
	0.231	1.00	−12.2	0.35	0.96	−27.6			
	0.170	8.61	−9.5	9.22	0.21	−20.1			
0820+560	1.168	0.00	0.0	0.28	0.66	115.2	1.164	1.095	1.134
	0.126	0.73	97.4	0.73	0.00	59.9			
	0.133	2.63	97.6	1.93	0.47	88.7			
	0.159	18.88	75.0	12.98	0.44	90.5			
0821+394	0.597	0.00	0.0	0.29	0.95	34.0	1.305	1.068	1.205
	0.115	0.61	−22.0	0.81	0.66	−36.8			
	0.095	4.28	−44.8	1.58	0.48	133.4			
	0.257	294.64	−49.8	10.91	0.81	35.5			
0828+493	0.202	0.00	0.0	0.37	0.63	88.2	1.008	1.063	1.033
	0.070	0.74	67.6	1.27	0.71	−43.2			
	0.038	9.93	61.4	11.18	0.34	67.5			
0833+585	0.396	0.00	0.0	0.47	0.64	69.8	1.103	1.114	1.108
	0.246	0.94	85.1	0.95	0.61	61.5			
0900+428	0.175	0.00	0.0	0.20	0.86	111.1	1.039	1.064	1.051
	0.106	0.70	−62.1	0.91	0.01	−79.4			
	0.017	4.54	−79.6	0.71	0.67	−25.0			
	0.025	13.29	−76.6	1.51	0.59	−16.9			
	0.047	21.41	−67.1	2.89	0.82	142.6			
	0.098	23.20	−76.2	21.41	0.59	90.8			

TABLE 3.3. GAUSSIAN MODELS (*continued*)

Source	S (Jy)	r (mas)	θ (°)	a (mas)	b/a	ϕ (°)	Amp. A.F.	Phase A.F.	Total A.F.
0917+449	0.705	0.00	0.0	0.50	0.07	−30.5	1.020	1.031	1.025
	0.578	0.91	176.1	1.02	0.50	3.9			
	0.080	5.92	−162.7	7.07	0.44	26.1			
	0.043	19.59	−161.3	8.79	0.26	80.1			
0917+624	0.811	0.00	0.0	0.42	0.43	145.0	1.035	1.030	1.033
	0.213	0.72	−21.0	0.60	0.18	20.6			
	0.236	5.56	−18.6	2.57	0.78	−19.5			
	0.042	20.78	−25.9	10.72	0.64	27.1			
0955+476	1.051	0.00	0.0	0.33	0.80	114.6	0.988	1.008	0.997
	0.022	1.85	132.6	2.08	0.56	144.3			
1003+830	0.278	0.00	0.0	0.51	0.26	71.1	1.056	1.040	1.049
	0.041	2.67	83.1	1.10	0.00	64.5			
	0.111	5.88	85.1	2.20	0.43	114.3			
	0.048	18.98	96.5	14.04	0.63	104.0			
1015+359	0.426	0.00	0.0	0.13	0.00	87.3	1.143	1.028	1.092
	0.176	0.82	187.0	0.55	0.66	39.0			
	0.099	2.75	181.9	1.51	0.46	175.7			
1020+400	0.694	0.00	0.0	0.21	0.01	−69.7	1.150	1.055	1.108
	0.118	2.73	−40.7	3.13	0.23	−41.9			
	0.060	12.14	−33.9	7.11	0.41	−22.8			
1030+415	0.223	0.00	0.0	0.00	1.00	120.6	1.040	1.033	1.036
	0.060	0.69	−4.5	0.41	0.15	−56.9			
	0.073	3.70	3.8	4.50	0.33	9.7			
	0.035	8.95	−15.0	14.76	0.09	−17.4			
1039+811	0.833	0.00	0.0	0.30	0.40	−60.3	1.183	1.010	1.107
	0.244	0.83	−64.8	0.81	0.40	−63.8			
	0.072	2.56	−68.2	1.19	0.55	−89.2			
	0.043	6.10	−78.0	5.70	0.28	−88.1			
1044+719	0.234	0.00	0.0	0.00	1.00	−54.4	1.041	1.019	1.031
	0.737	0.36	113.2	0.69	0.93	−36.3			
1053+704	0.269	0.00	0.0	0.29	0.94	172.2	1.047	1.017	1.033
	0.264	0.25	199.5	0.44	0.57	13.8			
	0.043	1.62	−144.5	1.83	0.40	56.3			
1053+815	0.372	0.00	0.0	0.19	0.98	178.1	1.033	1.030	1.032
	0.175	0.21	−143.0	0.76	0.35	−140.8			
	0.017	1.61	−129.8	1.66	0.62	150.4			

TABLE 3.3. GAUSSIAN MODELS (*continued*)

Source	S (Jy)	r (mas)	θ (°)	a (mas)	b/a	ϕ (°)	Amp. A.F.	Phase A.F.	Total A.F.
1058+726	0.122	0.00	0.0	0.59	0.26	−3.1	1.015	1.172	1.090
	0.034	0.76	−4.7	0.00	1.00	0.0			
	0.101	1.95	3.2	0.59	0.00	−127.3			
	0.148	3.40	9.9	0.95	0.62	23.7			
	0.024	23.74	19.8	4.81	0.44	−1.2			
1101+384	0.366	0.00	0.0	0.32	0.54	142.1	1.126	1.069	1.101
	0.072	1.39	−24.1	3.40	0.26	−21.8			
	0.144	42.16	−52.6	80.97	0.41	−68.9			
1128+385	0.759	0.00	0.0	0.70	0.04	3.4	1.032	1.011	1.023
	0.191	0.73	−136.1	1.03	0.41	−1.9			
	0.055	3.34	−81.0	7.72	0.58	−49.1			
1138+594	0.087	0.00	0.0	0.00	0.07	−97.4	0.928	1.224	1.068
	0.019	15.57	162.0	1.96	0.28	13.0			
	0.147	225.41	171.7	24.02	0.39	61.2			
1144+402	0.457	0.00	0.0	0.06	0.96	153.1	1.036	1.027	1.032
	0.087	2.70	−0.0	4.00	0.56	2.4			
	0.095	0.65	11.0	0.63	0.87	58.5			
1144+542	0.162	0.00	0.0	0.00	1.00	12.2	0.996	1.079	1.035
	0.044	0.60	177.1	0.12	0.00	−3.5			
	0.121	1.10	177.7	0.85	0.70	−2.3			
	0.060	2.63	196.3	1.92	0.37	122.9			
1150+497	0.327	0.00	0.0	0.46	0.22	25.1	1.044	1.068	1.055
	0.149	1.55	−157.5	0.75	0.22	23.4			
	0.037	9.41	−156.0	14.62	0.17	−154.3			
1150+812	0.702	0.00	0.0	0.36	0.43	−4.3	0.987	1.009	0.997
	0.316	0.99	182.1	0.53	0.54	136.7			
	0.188	2.97	168.4	2.74	0.38	150.2			
	0.036	7.60	144.5	8.28	0.26	133.6			
1213+350	0.420	0.00	0.0	0.72	0.00	−70.9	1.064	1.104	1.082
	0.325	1.15	204.3	2.44	0.59	138.4			
	0.233	3.38	117.3	9.51	0.44	46.6			
	0.025	36.84	−125.5	0.97	0.00	36.3			
1216+487	0.265	0.00	0.0	0.13	0.00	30.5	1.000	1.065	1.030
	0.287	1.48	102.1	2.00	0.25	100.1			
	0.066	4.95	103.9	8.12	0.24	116.2			

TABLE 3.3. GAUSSIAN MODELS (*continued*)

Source	S (Jy)	r (mas)	θ (°)	a (mas)	b/a	ϕ (°)	Amp. A.F.	Phase A.F.	Total A.F.
1225+368	0.351	0.00	0.0	1.37	0.73	−153.4	1.154	1.341	1.241
	0.240	2.27	−32.8	1.78	0.45	−16.1			
	0.117	18.48	−78.1	2.41	0.30	−101.8			
	0.050	25.08	−80.0	1.62	0.00	−71.9			
	0.062	31.80	−80.7	2.10	0.00	89.0			
	0.040	54.78	−85.5	4.75	0.69	−29.3			
1242+410	0.116	0.00	0.0	0.78	0.92	152.3	1.005	1.526	1.261
	0.152	7.81	25.7	4.86	0.20	24.6			
	0.160	21.11	29.4	4.79	0.74	37.2			
	0.056	3.37	−140.8	1.64	0.24	131.2			
	0.229	8.66	−154.8	9.33	0.76	−23.8			
1311+678	0.166	0.00	0.0	1.43	0.41	67.4	1.141	1.892	1.504
	0.157	4.66	−67.2	5.07	0.45	−83.8			
	0.410	37.12	−121.0	11.13	0.74	−13.2			
	0.065	41.35	144.6	3.50	0.00	165.5			
	0.035	29.12	175.0	5.26	0.28	34.7			
1317+520	0.181	0.00	0.0	0.47	0.38	116.5	0.985	1.078	1.029
	0.067	4.52	124.4	2.91	0.35	135.5			
	0.007	19.90	129.9	3.46	0.00	6.6			
1333+459	0.345	0.00	0.0	0.82	0.33	113.2	1.058	1.178	1.115
	0.298	1.19	−62.7	1.16	0.26	108.4			
1333+589	0.097	0.00	0.0	0.50	0.71	−44.9	1.140	1.304	1.218
	0.227	0.01	−108.9	1.21	0.64	−35.1			
	0.325	12.73	−161.7	1.69	0.67	117.4			
1342+663	0.685	0.00	0.0	0.48	0.80	110.8	1.058	1.005	1.034
	0.007	2.78	107.6	1.66	0.00	−35.7			
	0.006	4.79	81.1	1.47	0.01	−21.1			
1347+539	0.419	0.00	0.0	0.23	0.00	−53.4	1.111	1.048	1.083
	0.034	0.84	145.0	0.01	0.49	4.7			
	0.063	1.44	141.2	1.76	0.00	132.2			
	0.072	5.41	141.0	3.86	0.20	−41.9			
	0.102	15.98	128.2	13.82	0.34	105.0			
	0.094	58.94	141.3	16.12	0.75	37.4			
1357+769	0.635	0.00	0.0	0.34	0.86	125.3	1.027	1.025	1.026
	0.025	2.87	−111.2	2.84	0.10	−5.5			

TABLE 3.3. GAUSSIAN MODELS (*continued*)

Source	S (Jy)	r (mas)	θ (°)	a (mas)	b/a	ϕ (°)	Amp. A.F.	Phase A.F.	Total A.F.
1418+546	1.470	0.00	0.0	0.34	0.42	−68.8	1.097	1.042	1.073
	0.415	1.07	129.3	0.55	0.56	110.6			
	0.230	2.92	128.2	4.34	0.35	128.5			
	0.083	16.59	121.0	9.25	0.86	72.3			
1435+638	0.418	0.00	0.0	0.75	0.38	63.6	1.166	1.125	1.148
	0.241	0.46	−134.8	0.00	0.00	133.5			
	0.202	2.61	−125.9	1.64	0.25	26.6			
	0.124	9.08	−144.6	0.94	0.70	52.1			
	0.006	22.41	−133.4	1.97	0.05	30.0			
1437+624	0.193	0.00	0.0	1.01	0.65	105.5	1.068	1.286	1.172
	0.093	2.11	−74.5	2.58	0.62	100.4			
	0.183	5.74	−68.3	13.29	0.23	−35.8			
	0.058	104.24	170.4	2.47	0.15	65.1			
	0.198	103.32	169.9	4.53	0.49	63.2			
	0.057	6.64	−93.9	2.72	0.62	−5.4			
1438+385	0.244	0.00	0.0	0.33	0.78	47.2	1.025	1.073	1.048
	0.140	0.72	8.9	1.03	0.69	−5.6			
	0.093	2.24	−13.8	2.01	0.50	−0.4			
	0.106	8.15	−12.0	6.74	0.26	−2.5			
1504+377	0.413	7.07	44.9	0.67	0.15	37.0	0.989	1.066	1.025
	0.116	5.92	45.4	0.00	0.30	42.0			
	0.149	0.57	40.3	11.28	0.16	45.2			
1547+507	0.430	0.00	0.0	0.18	0.85	168.6	1.052	1.044	1.048
	0.088	1.01	−152.1	0.79	0.00	3.8			
	0.159	3.50	−147.2	1.78	0.28	41.0			
	0.106	7.26	−130.5	1.13	0.41	−0.2			
	0.063	5.84	−136.4	1.58	0.21	71.1			
1638+398	1.752	0.00	0.0	0.47	0.85	−41.0	1.103	1.056	1.083
	0.034	1.40	−58.4	2.54	0.00	11.2			
1656+477	1.122	0.00	0.0	0.56	0.49	−1.5	1.138	1.085	1.115
	0.325	0.51	1.9	0.86	0.60	−24.4			
	0.063	4.38	−25.5	3.38	0.28	−46.1			
	0.043	5.86	−18.7	0.99	0.83	28.7			
1656+482	0.392	0.00	0.0	0.37	0.00	84.8	1.084	1.052	1.069
	0.116	0.81	−108.6	0.29	0.00	−16.7			
	0.046	0.94	−108.4	1.40	0.00	−119.9			
	0.036	3.27	−104.5	6.41	0.41	−111.0			
	0.059	7.50	−98.8	9.87	0.56	82.1			

TABLE 3.3. GAUSSIAN MODELS (*continued*)

Source	S (Jy)	r (mas)	θ (°)	a (mas)	b/a	ϕ (°)	Amp. A.F.	Phase A.F.	Total A.F.
1719+357	0.212	0.00	0.0	0.00	1.00	0.0	1.045	1.028	1.037
	0.103	0.93	184.0	0.00	0.50	0.0			
	0.138	4.27	178.3	2.06	0.28	−1.5			
1732+389	0.995	0.00	0.0	0.52	0.52	174.1	1.278	1.062	1.187
	0.234	0.54	105.6	0.00	0.50	100.0			
1734+508	0.416	0.00	0.0	0.41	0.87	−121.7	1.182	1.162	1.173
	0.188	0.88	21.7	0.61	0.72	−174.1			
	0.223	3.36	19.3	1.02	0.67	30.4			
1738+476	0.924	0.00	0.0	0.59	0.47	51.2	0.915	1.113	1.008
	0.139	1.05	−86.4	0.64	0.83	9.0			
	0.017	2.70	−94.2	0.73	0.46	50.8			
1751+441	0.695	0.00	0.0	0.53	0.67	80.3	1.088	1.041	1.067
	0.232	1.48	87.3	1.39	0.53	−82.2			
	0.026	8.30	80.5	8.44	0.63	79.8			
1758+388	0.828	0.00	0.0	0.60	0.53	82.3	1.051	1.082	1.065
	0.091	1.05	−99.1	1.23	0.00	79.1			
1800+440	0.331	0.00	0.0	0.17	0.68	73.4	1.045	1.058	1.051
	0.090	0.52	−160.0	0.33	0.00	44.7			
	0.088	1.36	−156.8	0.65	0.62	−177.0			
	0.047	14.58	−155.7	30.54	0.10	24.3			
1819+396	0.273	0.00	0.0	1.61	0.43	−56.5	1.435	1.414	1.426
1842+681	0.647	0.00	0.0	0.45	0.57	107.0	1.149	1.075	1.117
	0.181	1.32	134.3	1.31	0.53	−28.0			
	0.024	3.64	148.4	6.96	0.09	−35.5			
1843+356	0.173	0.00	0.0	0.49	0.98	51.9	1.075	1.251	1.159
	0.116	0.91	53.5	0.62	0.45	3.1			
	0.313	7.06	43.3	1.29	0.70	157.8			
	0.101	5.15	43.8	1.58	0.50	39.6			
	0.140	8.30	45.6	1.67	0.03	54.2			
1926+611	0.394	0.00	0.0	0.43	0.72	121.2	1.038	1.091	1.062
	0.133	0.94	118.7	0.73	0.22	130.4			
	0.049	1.53	141.0	1.88	0.53	166.0			
	0.024	6.76	179.6	2.64	0.69	102.5			
	0.008	12.83	−145.8	0.69	0.02	3.5			

TABLE 3.3. GAUSSIAN MODELS (*continued*)

Source	S (Jy)	r (mas)	θ (°)	a (mas)	b/a	ϕ (°)	Amp. A.F.	Phase A.F.	Total A.F.
1943+546	0.024	0.00	0.0	6.18	0.06	125.7	1.161	1.170	1.165
	0.234	16.80	−91.8	0.63	0.69	63.1			
	0.248	15.33	−91.0	2.98	0.27	−98.0			
	0.184	13.07	−79.8	7.42	0.85	2.0			
	0.038	19.06	85.9	4.70	0.74	75.1			
	0.122	23.11	85.0	2.00	0.78	161.3			
	0.118	24.13	84.7	0.49	0.00	74.1			
2007+777	1.698	0.00	0.0	0.45	0.49	73.8	1.098	1.040	1.071
	0.268	1.00	−107.5	0.00	0.00	−117.2			
	0.124	3.90	−94.5	5.23	0.25	−99.9			
	0.023	17.68	−97.0	3.18	0.50	−171.8			
2010+723	0.350	0.00	0.0	0.27	0.00	−36.4	1.071	1.088	1.079
	0.142	0.23	−25.1	1.29	0.00	−30.4			
	0.426	0.99	−39.2	0.82	0.47	110.5			
	0.021	2.52	−128.1	1.61	0.00	111.5			
	0.089	3.93	−118.6	7.44	0.47	27.7			
2207+374	0.143	0.00	0.0	0.57	0.34	45.4	1.080	1.169	1.121
	0.048	0.57	−140.6	1.28	0.00	−129.1			
	0.073	5.24	−133.6	1.43	0.52	8.1			
	0.090	14.98	−138.9	2.47	0.57	−40.8			
	0.238	14.92	−134.3	8.36	0.47	−153.5			
	0.048	21.89	−130.2	12.74	0.26	−84.8			
	0.187	57.08	−105.7	48.57	0.55	116.0			
2214+350	0.551	0.00	0.0	0.35	0.82	−22.1	1.015	1.038	1.026
	0.049	1.96	169.4	1.13	0.55	−30.3			
2229+695	0.523	0.00	0.0	0.44	0.97	28.2	1.027	1.053	1.039
	0.456	0.56	−108.3	0.87	0.26	81.5			
	0.003	2.66	79.1	0.01	0.49	20.0			
2253+417	0.507	0.00	0.0	0.81	0.18	28.0	1.075	1.059	1.068
	0.487	1.33	−10.6	1.24	0.42	−25.7			
	0.042	4.63	21.1	1.16	0.33	47.8			
	0.064	6.65	36.3	4.11	0.35	12.3			
2255+416	0.242	0.00	0.0	0.65	0.34	−17.2	1.125	1.152	1.137
	0.054	1.13	170.3	2.15	0.36	−27.2			
	0.050	5.09	167.4	1.70	0.23	−61.2			
	0.180	8.85	165.1	3.23	0.52	−36.9			
	0.276	19.13	172.8	8.70	0.59	16.1			
	0.138	31.96	−151.5	14.69	0.65	70.3			
	0.193	42.24	−136.6	8.28	0.55	152.5			

NOTE —
Parameters of each Gaussian components of the model brightness distribution: S, flux density; r, θ, polar coordinates of the center of the components relative to an arbitrary origin, with polar angle measured from north through east; a, b, major and minor axes of the FWHM contour; ϕ, position angle of the major axis measured from north through east. The sources 0218+357 and 0404+768 are too complicated to model.

TABLE 3.4. MERLIN MAP PARAMETERS

Source	Sample	Beam[a]			S_{peak}	rms
		a (mas)	b (mas)	θ (°)		
0707+476	CJ1	49.7	37.8	37	948	1.52
0812+367	CJ1	100.0	100.0	0	747	0.23
0814+425	PR	56.8	37.7	30	906	0.59
0820+560	CJ1	51.2	37.8	26	1753	0.52
0900+428	CJ1	49.0	41.0	44	376	0.23
		100.0	100.0	0	430	0.15
0917+624	CJ1	48.5	38.2	30	1059	0.46
0945+408	PR	53.4	38.8	33	1232	0.82
		100.0	100.0	0	1317	0.47
0954+556	PR	47.7	38.1	32	967	0.91
1039+811	CJ1	47.0	40.9	7	1000	0.36
1150+812	CJ1	47.3	38.5	26	979	0.32
1347+539	CJ1	44.2	36.3	−48	592	0.33
1418+546	CJ1	44.0	36.0	−48	1429	0.49
1633+382	PR	47.5	38.9	33	2113	0.94
1638+398	CJ1	48.4	38.7	31	1230	0.68
1749+701	PR	47.6	37.7	8	469	0.44
1800+440	CJ1	63.7	43.7	−37	402	0.20
		100.0	100.0	0	412	0.21
1803+784	PR	47.0	38.6	−64	1951	0.56
1819+396	CJ1	56.9	41.1	−39	324	0.53
1943+546	CJ1	50.6	38.9	24	655	0.58
1954+513	PR	50.0	38.1	25	1403	0.51

Note: [a] The restoring beam is an elliptical Gaussian with FWHM major axis a and minor axis b, with major axis at position angle θ.

EXPLANATION OF COLUMN — (1) Source name. (2) Sample. (3, 4, 5) The beam characteristics of the maps. (6, 7) The peak flux density and rms noise of the maps (mJy/beam).

TABLE 3.5. VLA MAP PARAMETERS

Source	Sample	S_{peak} (mJy)	rms (mJy)	Structure
0010+775	CJ1	1979.8	0.36	E
0016+731	PR	969.0	0.21	E?[a]
0022+390	CJ1	738.9	0.18	E
0102+480	CJ1	751.9	0.17	U
0133+476	PR	1172.8	0.41	U
0153+744	PR	1794.3	0.29	U
0212+735	PR	2443.6	0.36	U
0248+430	CJ1	1052.3	0.18	E
0309+390	CJ1	68.5	0.35	E[c]
0402+379	CJ1	1092.3	0.21	E
0404+768	PR	5639.2	0.82	U
0454+844	PR	392.1	0.10	U
0602+673	CJ1	519.1	0.18	U
0620+389	CJ1	834.3	0.27	E?
0642+449	CJ1	475.6	0.15	U
0650+371	CJ1	836.6	0.20	U
0703+426	CJ1	39.8	0.50	E[d]
0707+689	CJ1	1450.5	0.42	E
0710+439	PR	2005.3	0.28	U
0740+828	CJ1	1325.7	0.54	E
0746+483	CJ1	704.1	0.22	U
0755+379	CJ1	149.6	0.60	E[f]
0755+379	CJ1	208.3	0.64	E[e]
0805+410	CJ1	528.4	0.22	E
0818+472	CJ1	101.1	0.53	E
0821+394	CJ1	1257.0	0.56	E
0827+378	CJ1	1755.1	0.29	E
0827+378	CJ1	1920.2	0.37	E[c]
0831+557	PR	8064.7	1.28	E
0844+540	CJ1	22.9	0.36	E[c]

TABLE 5. VLA MAP PARAMETERS (*continued*)

Source	Sample	S_{peak} (mJy)	rms (mJy)	Structure
0900+428	CJ1	811.1	0.43	E
0917+449	CJ1	913.7	0.18	E
0945+664	CJ1	1490.7	0.24	E
0954+658	PR	636.6	0.29	E
0955+476	CJ1	650.3	0.37	U
1003+351	PR	2824.6	0.70	E[g]
1003+830	CJ1	476.3	0.15	E
1015+359	CJ1	622.0	0.31	E
1020+400	CJ1	680.6	0.21	E
1030+415	CJ1	417.8	0.16	E
1031+567	PR	1815.6	0.32	U
1044+719	CJ1	785.9	0.19	E
1053+704	CJ1	441.4	0.11	E
1053+815	CJ1	392.9	0.13	E
1058+726	CJ1	748.4	0.21	E
1101+384	CJ1	626.2	0.17	E
1138+594	CJ1	1982.0	0.43	E
1144+542	CJ1	373.4	0.14	U
1216+487	CJ1	616.9	0.15	E
1225+368	CJ1	2072.2	0.43	U
1242+410	CJ1	1366.1	0.28	U
1254+476	PR	2414.1	0.64	E
1311+678	CJ1	2427.1	0.35	E?
1333+459	CJ1	253.9	0.18	U
1333+589	CJ1	305.3	0.26	U
1336+391	CJ1	97.7	0.37	E
1342+663	CJ1	581.5	0.26	E?
1347+539	CJ1	935.2	0.21	E
1357+769	CJ1	471.0	0.12	U
1358+624	PR	4426.1	0.54	U

TABLE 5. VLA MAP PARAMETERS (*continued*)

Source	Sample	S_{peak} (mJy)	rms (mJy)	Structure
1437+624	CJ1	2322.4	0.32	E?
1438+385	CJ1	580.0	0.17	E
1547+507	CJ1	624.3	0.11	E?
1557+708	CJ1	24.1	0.20	E
1609+660	PR	2813.5	0.93	E
1624+416	PR	1632.4	0.89	E
1634+628	PR	4900.0	0.63	E?[h]
1638+398	CJ1	1118.2	0.31	E
1652+398	PR	1428.2	0.25	E
1656+482	CJ1	788.1	0.16	E
1719+357	CJ1	402.6	0.25	E
1732+389	CJ1	992.4	0.15	U
1734+508	CJ1	485.1	0.28	U
1738+476	CJ1	848.1	0.15	E?[b]
1749+701	PR	725.8	0.15	E
1751+441	CJ1	554.0	0.17	E
1758+388	CJ1	281.7	0.74	E
1800+440	CJ1	450.6	0.39	E
1833+653	CJ1	200.5	0.50	E
1842+681	CJ1	886.0	0.13	E
1843+356	CJ1	947.3	0.22	U
1926+611	CJ1	825.4	0.15	E?
1943+546	CJ1	1710.3	0.24	U
1954+513	PR	1377.3	0.47	E
2010+723	CJ1	1388.3	0.26	E
2021+614	PR	2169.8	0.32	U
2207+374	CJ1	1674.2	0.28	E
2214+350	CJ1	363.6	0.19	E
2229+695	CJ1	757.1	0.12	E
2253+417	CJ1	1333.7	0.29	U

TABLE 5. VLA MAP PARAMETERS (*continued*)

Source	Sample	S_{peak} (mJy)	rms (mJy)	Structure
2255+416	CJ1	2069.3	0.34	U
2342+821	PR	3736.2	0.47	E?[h]
2351+456	PR	1684.5	0.28	E?[h]
2352+495	PR	2515.8	0.34	U

EXPLANATION OF COLUMNS —

(1) Source name. (2) Sample. (3, 4) The peak flux density and rms noise in the map, in mJy/beam. (5) Structure: U – unresolved; E – extended structure detected; E? – hint of extended structure shown (see notes also). (6) Notes.

NOTES —

[a] Faint component $\sim 12''$ to the North.

[b] Faint component $\sim 1'$ to the West.

[c] Logarithmic contour levels in steps of $\sqrt{2}$.

[d] Convolved with $3''$ circular Gaussian beam.

[e] Convolved with $5''$ circular Gaussian beam.

[f] The lowest contour is 2σ .

[g] The lowest contour is 4σ.

[h] Source resolved at long baselines.

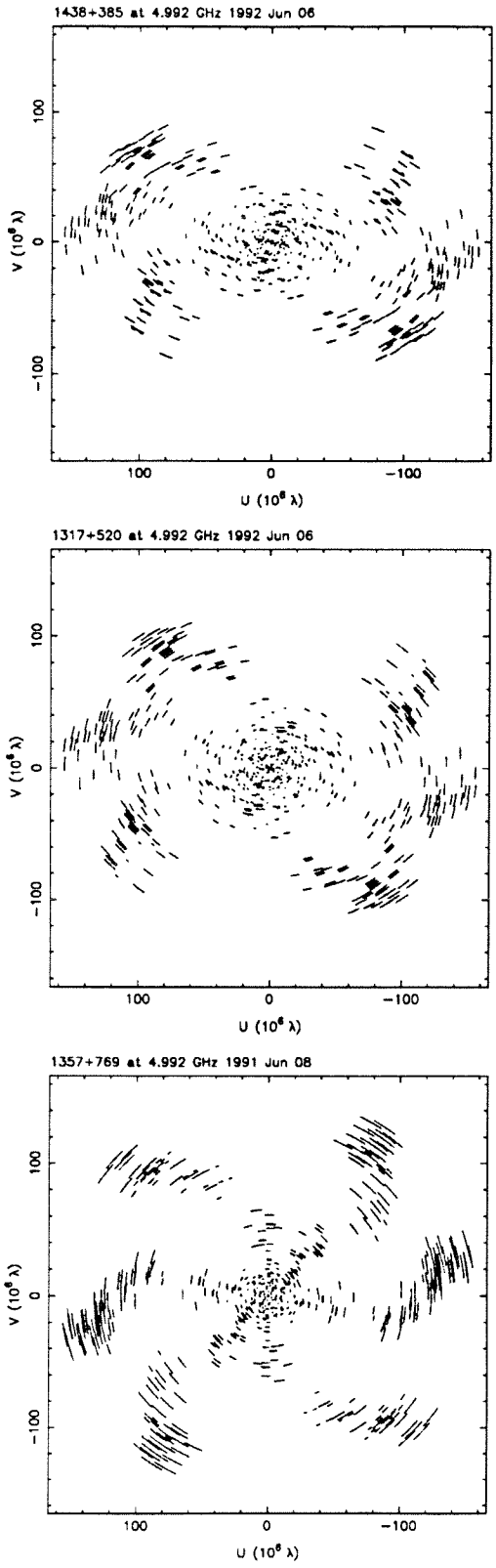

Fig. 3.1. Sample *uv* coverages for VLBI observations: top: $\delta = 38°$; middle: $\delta = 52°$; bottom: $\delta = 77°$

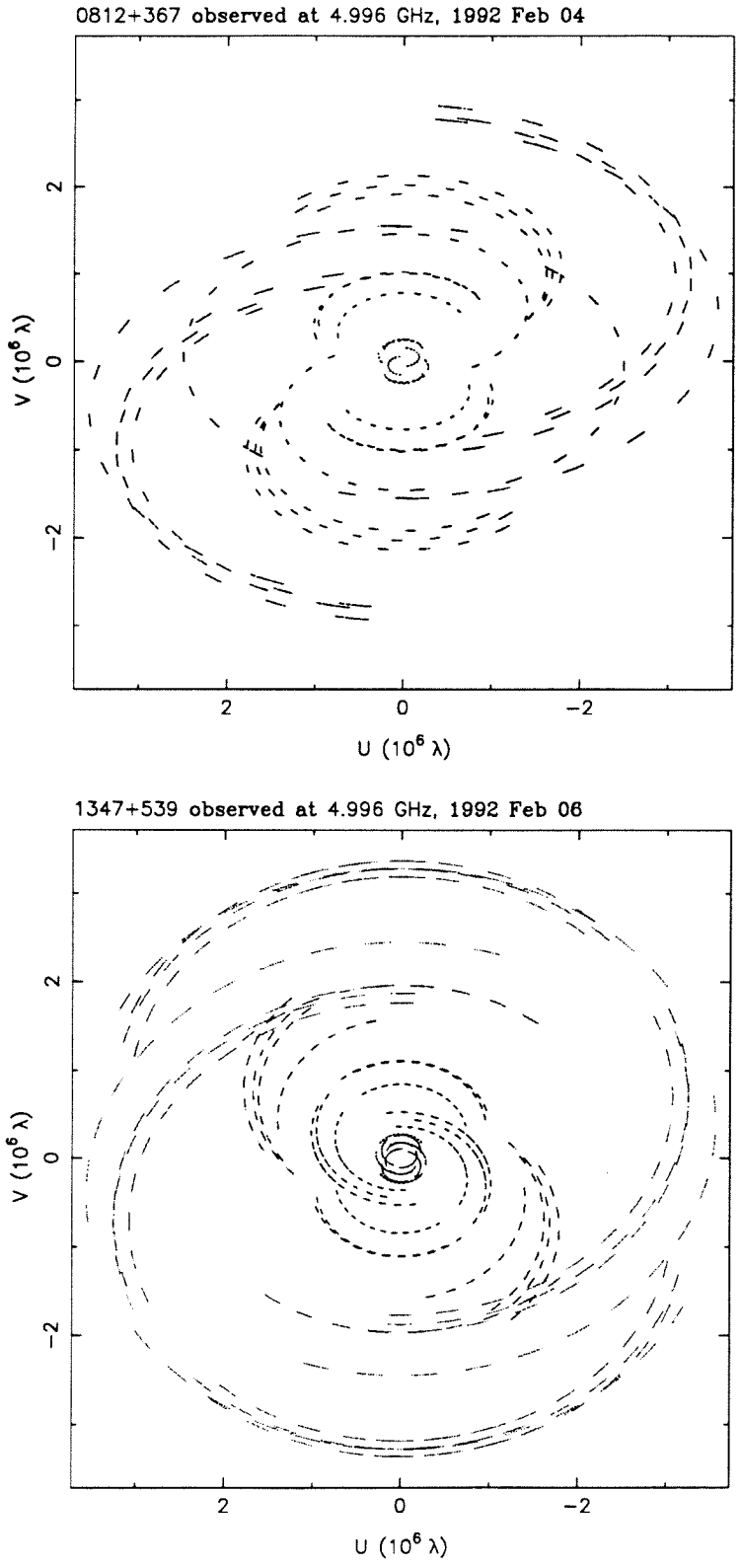

Fig. 3.2. Sample *uv* coverages for MERLIN observations:
top: $\delta = 37°$; bottom: $\delta = 54°$

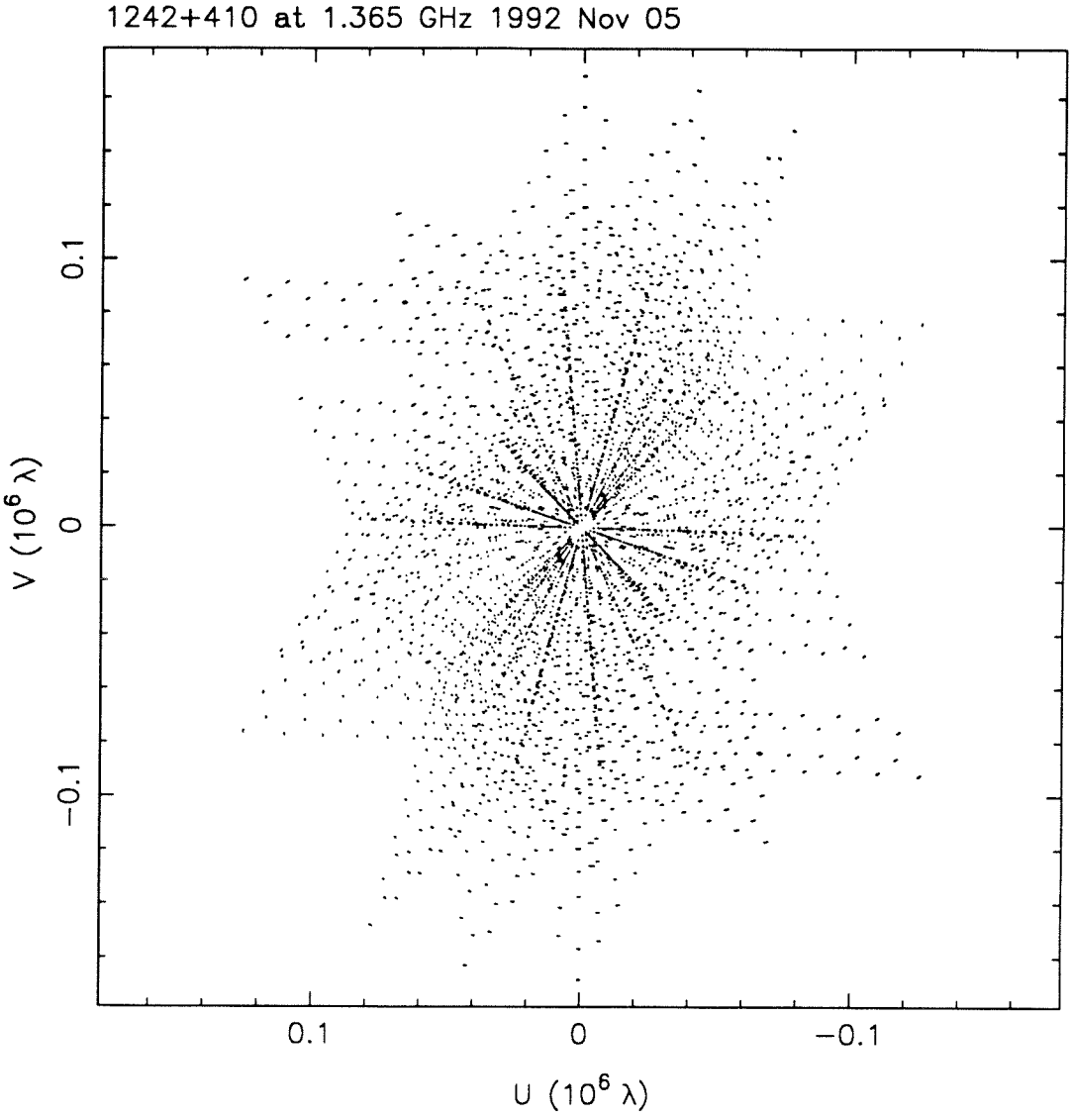

Fig. 3.3. Sample *uv* coverage for VLA observations:
$\delta = 41°$

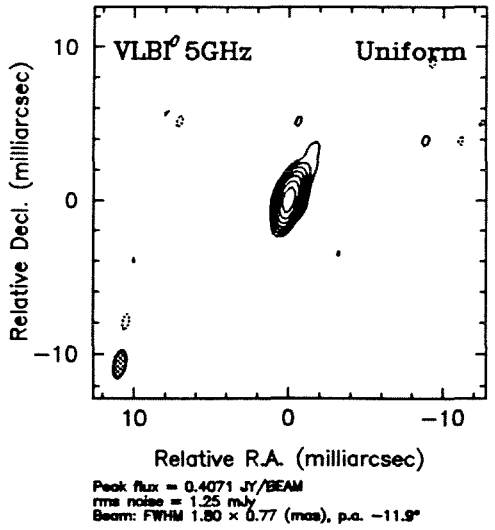

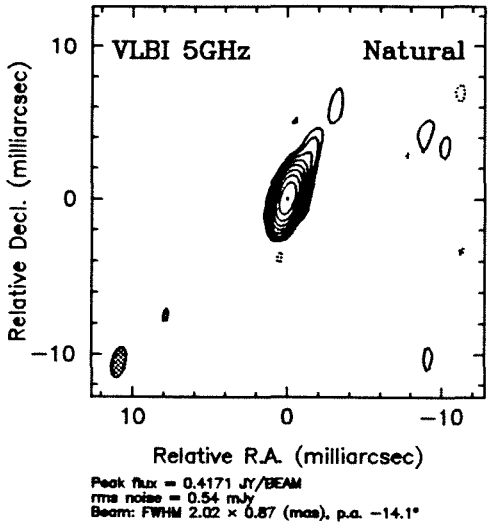

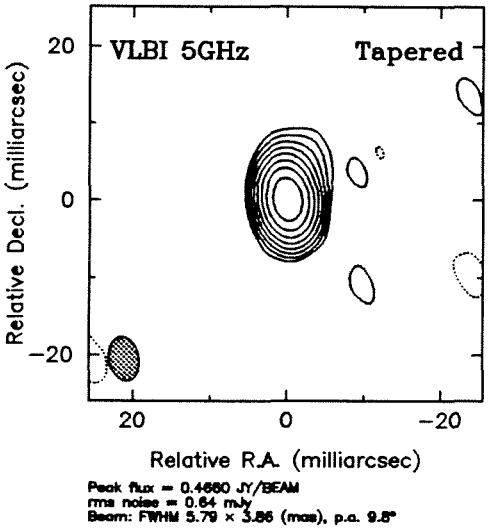

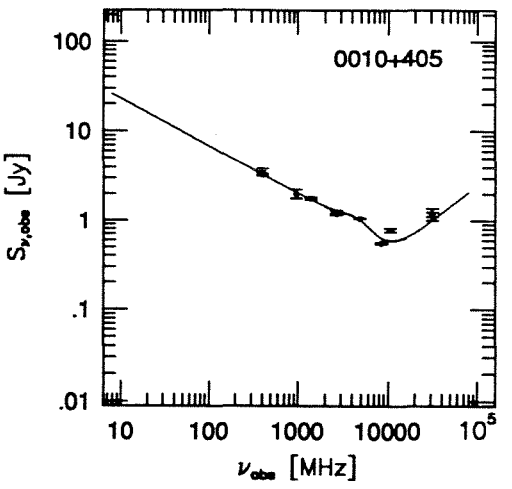

Figure 3.4.1. The maps and spectrum for 0010+405

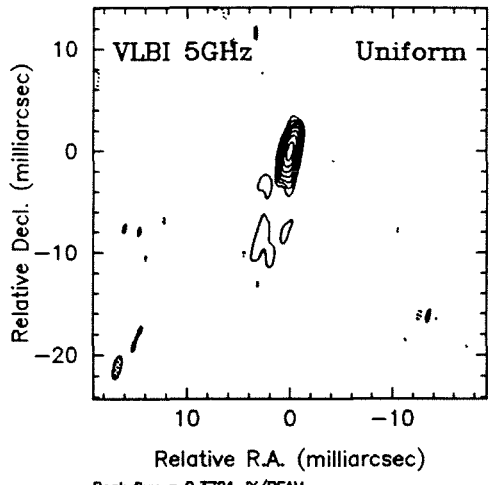

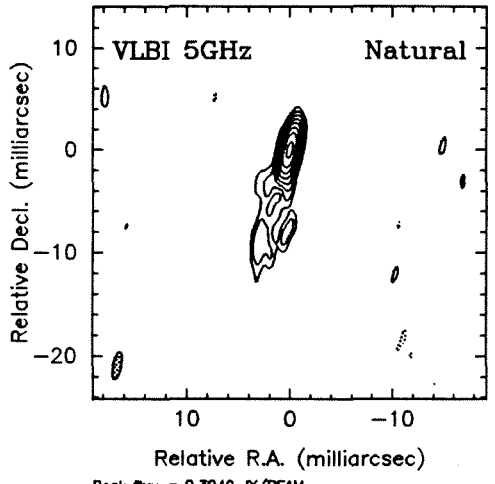

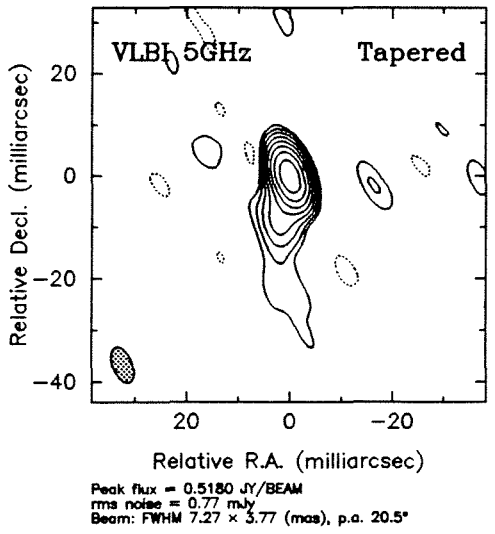

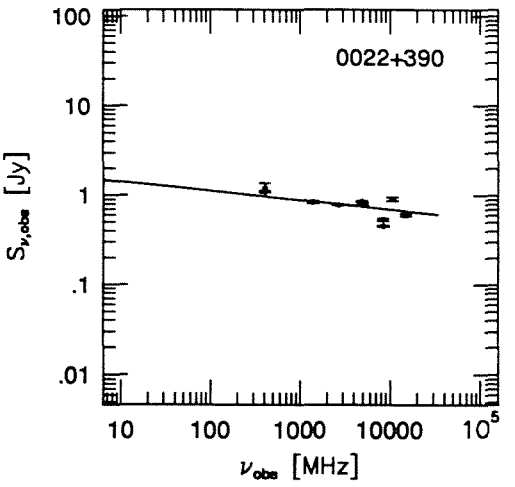

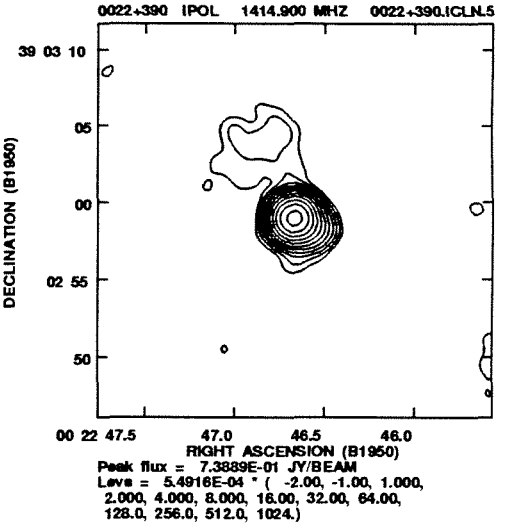

Figure 3.4.2. The maps and spectrum for 0022+390

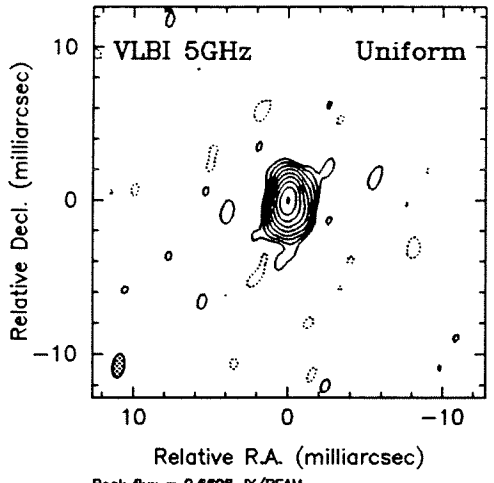

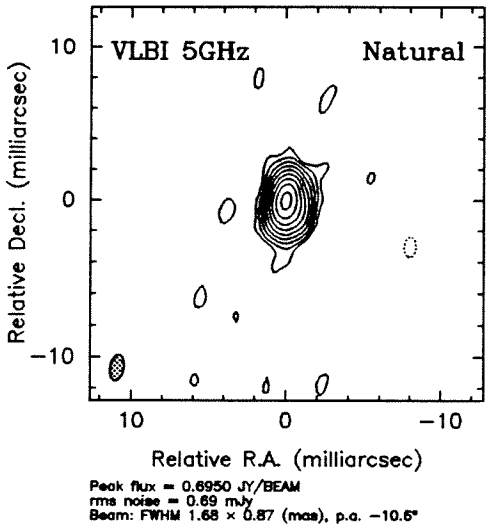

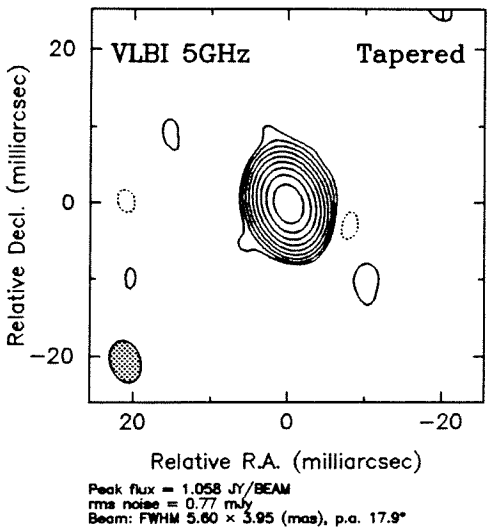

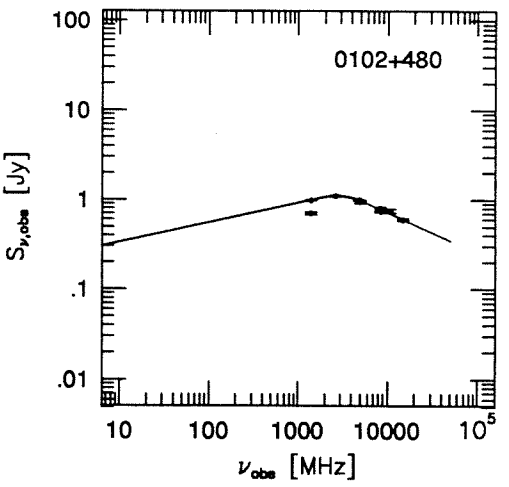

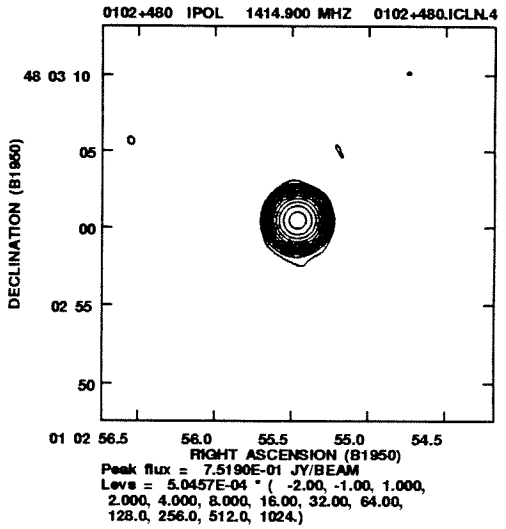

Figure 3.4.3. The maps and spectrum for 0102+480

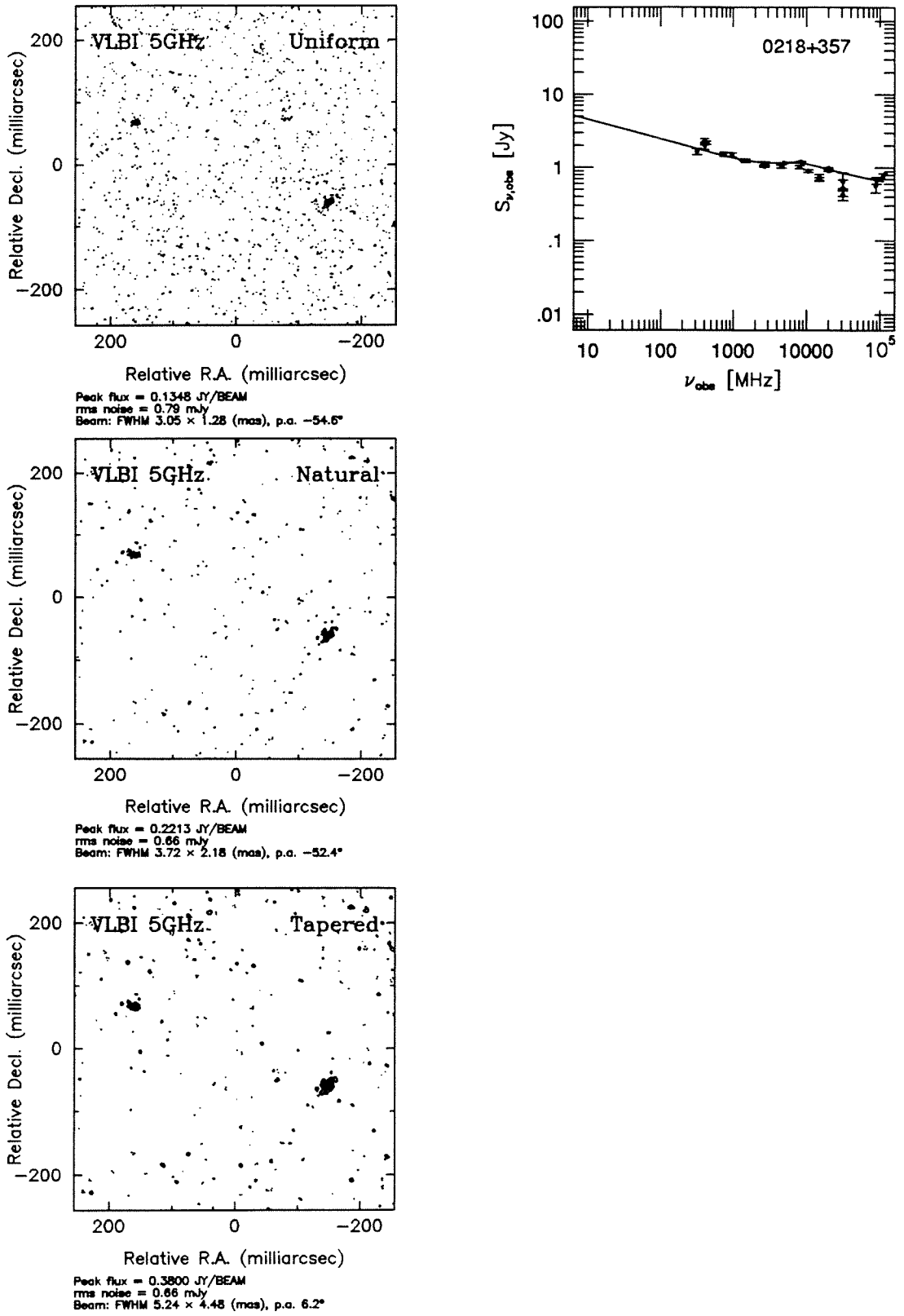

Figure 3.4.4. The maps and spectrum for 0218+357

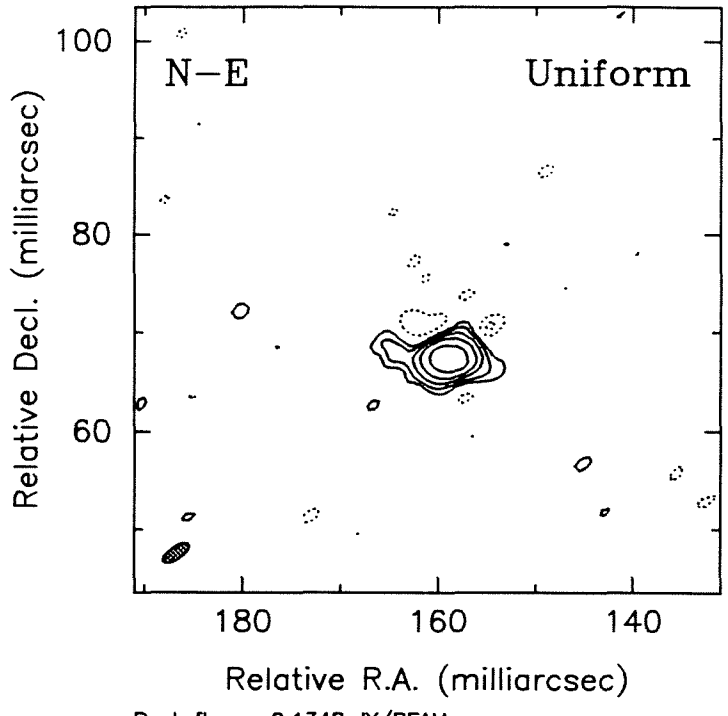

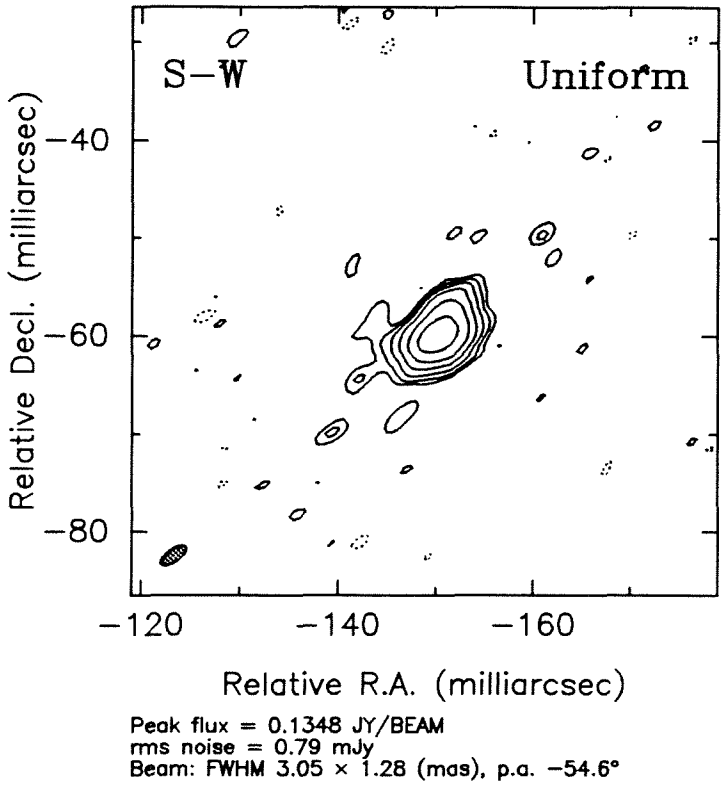

Figure 3.4.4. VLBI observations of 0218+357

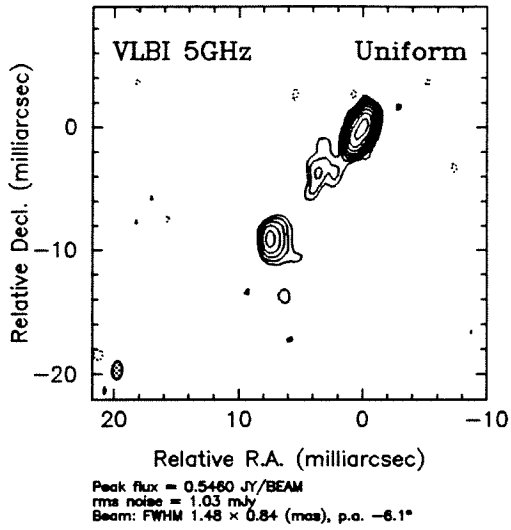

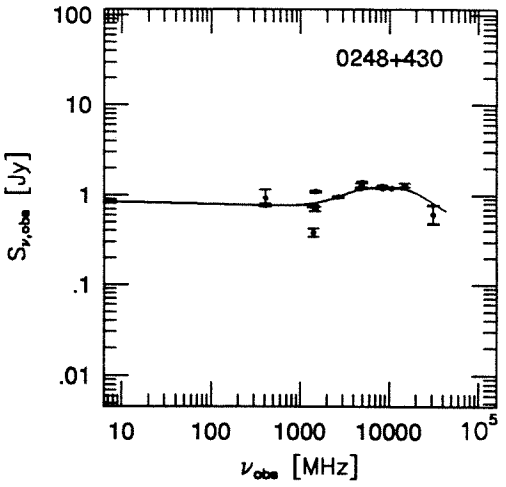

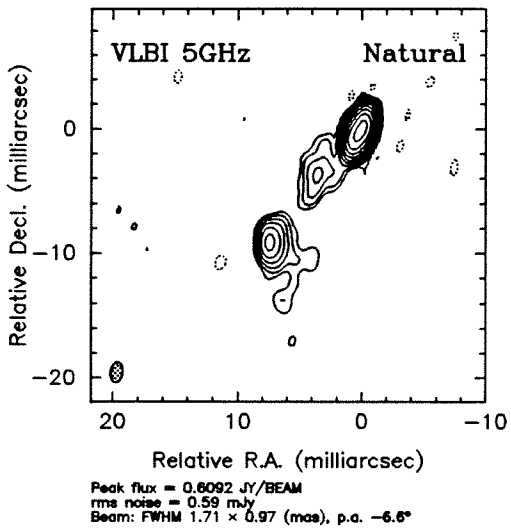

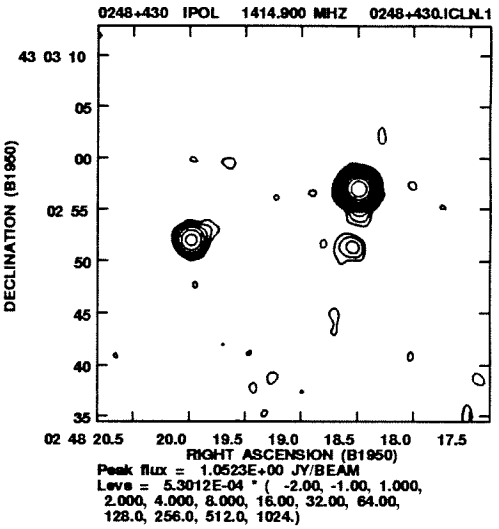

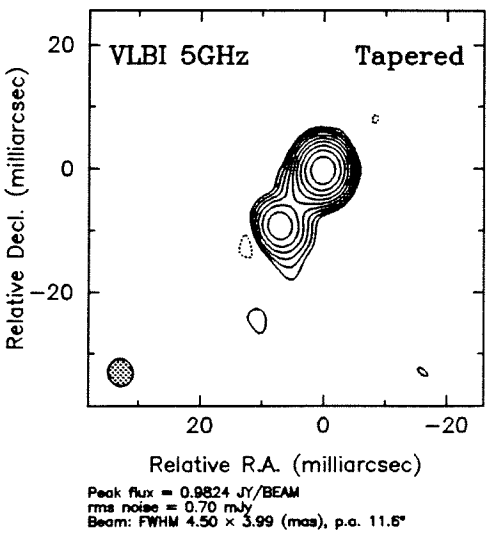

Figure 3.4.4. The maps and spectrum for 0248+430

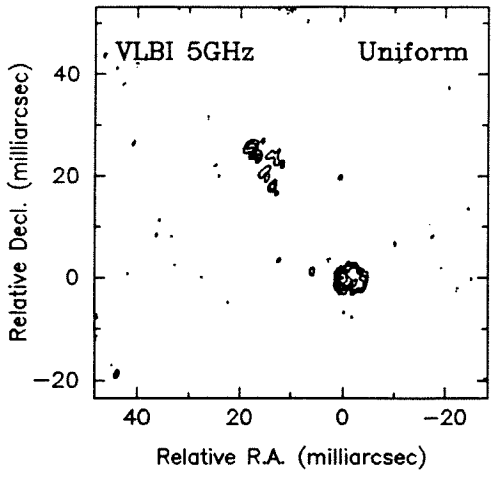

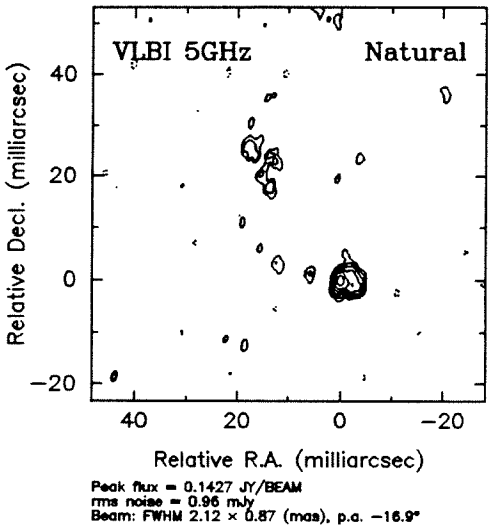

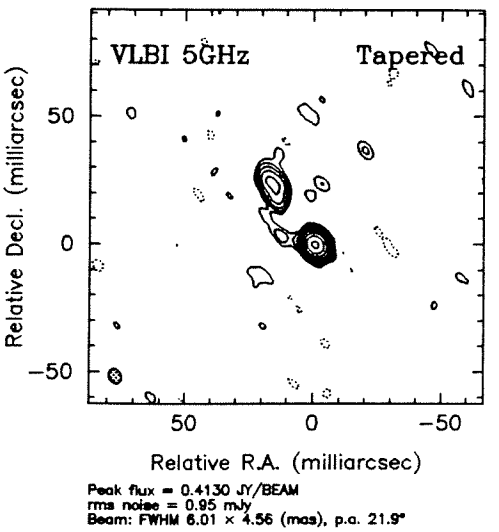

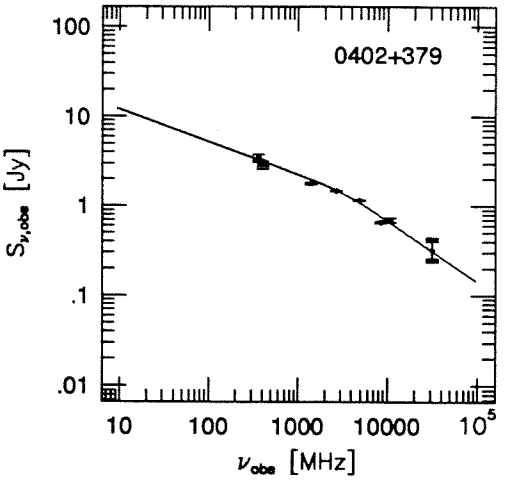

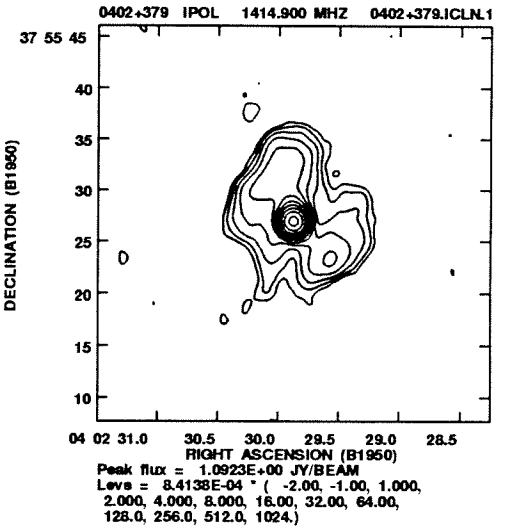

Figure 3.4.5. The maps and spectrum for 0402+379

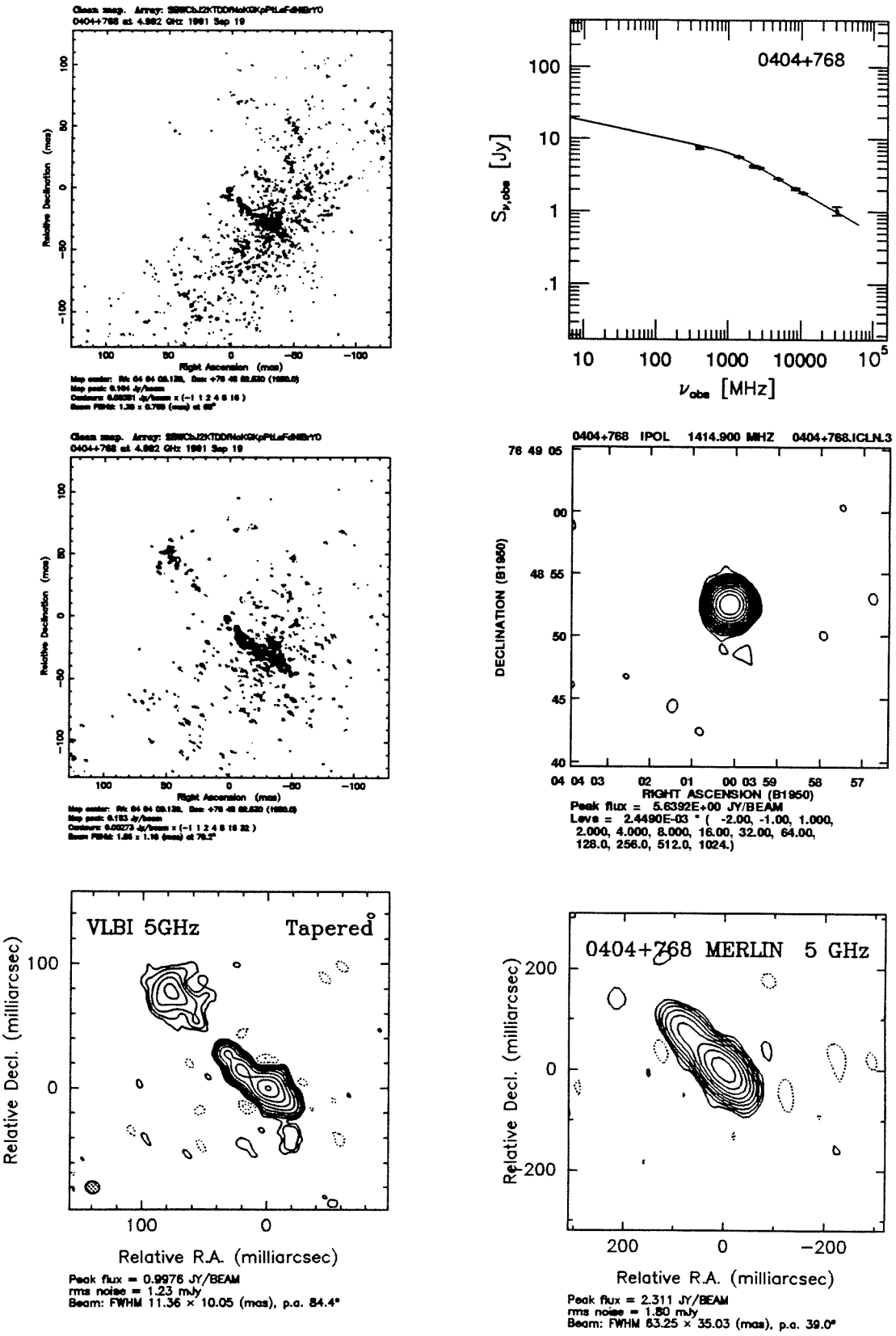

Figure 3.4.6. The maps and spectrum for 0404+768

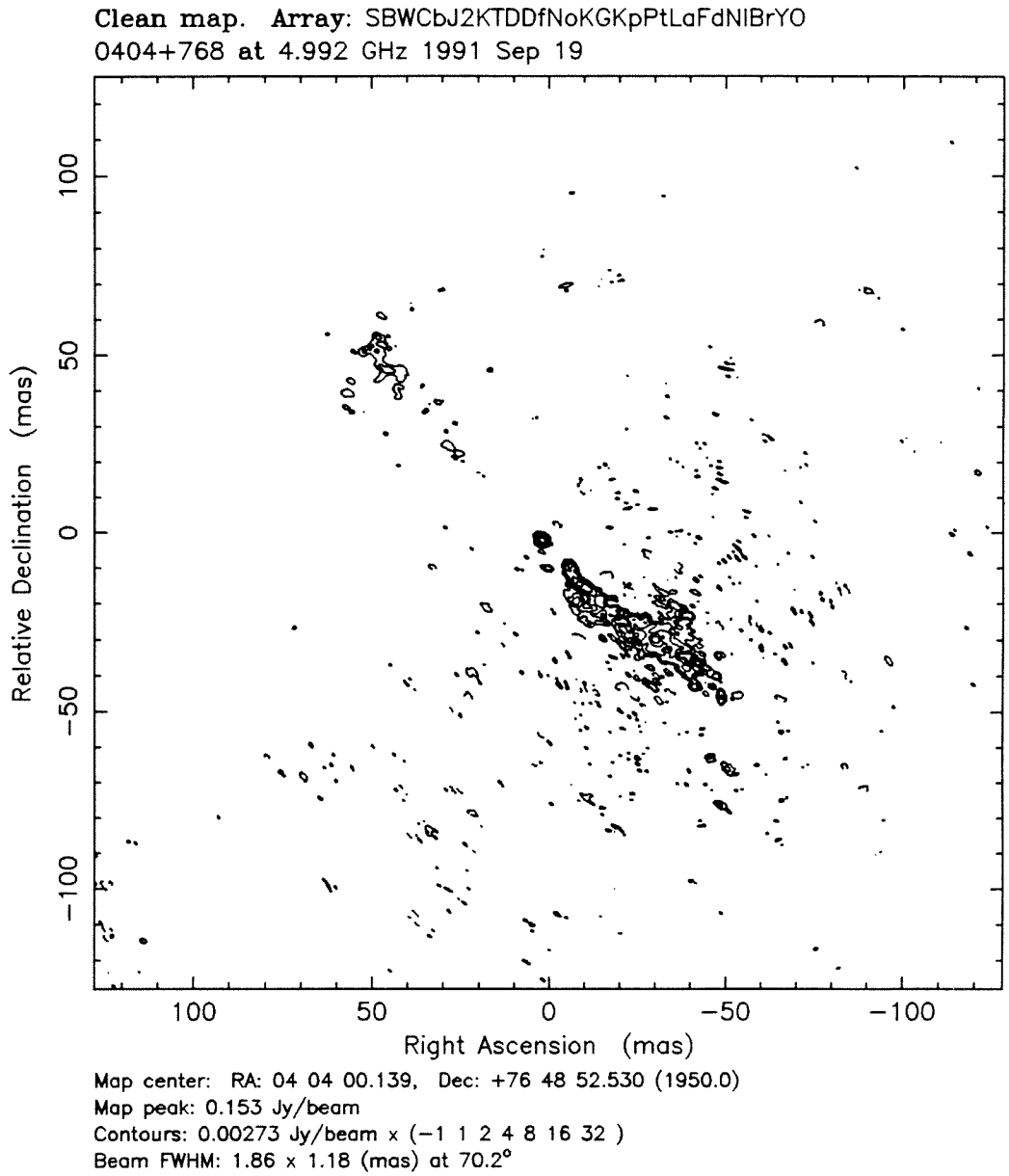

Figure 3.4.6. The VLBI map of 0404+768

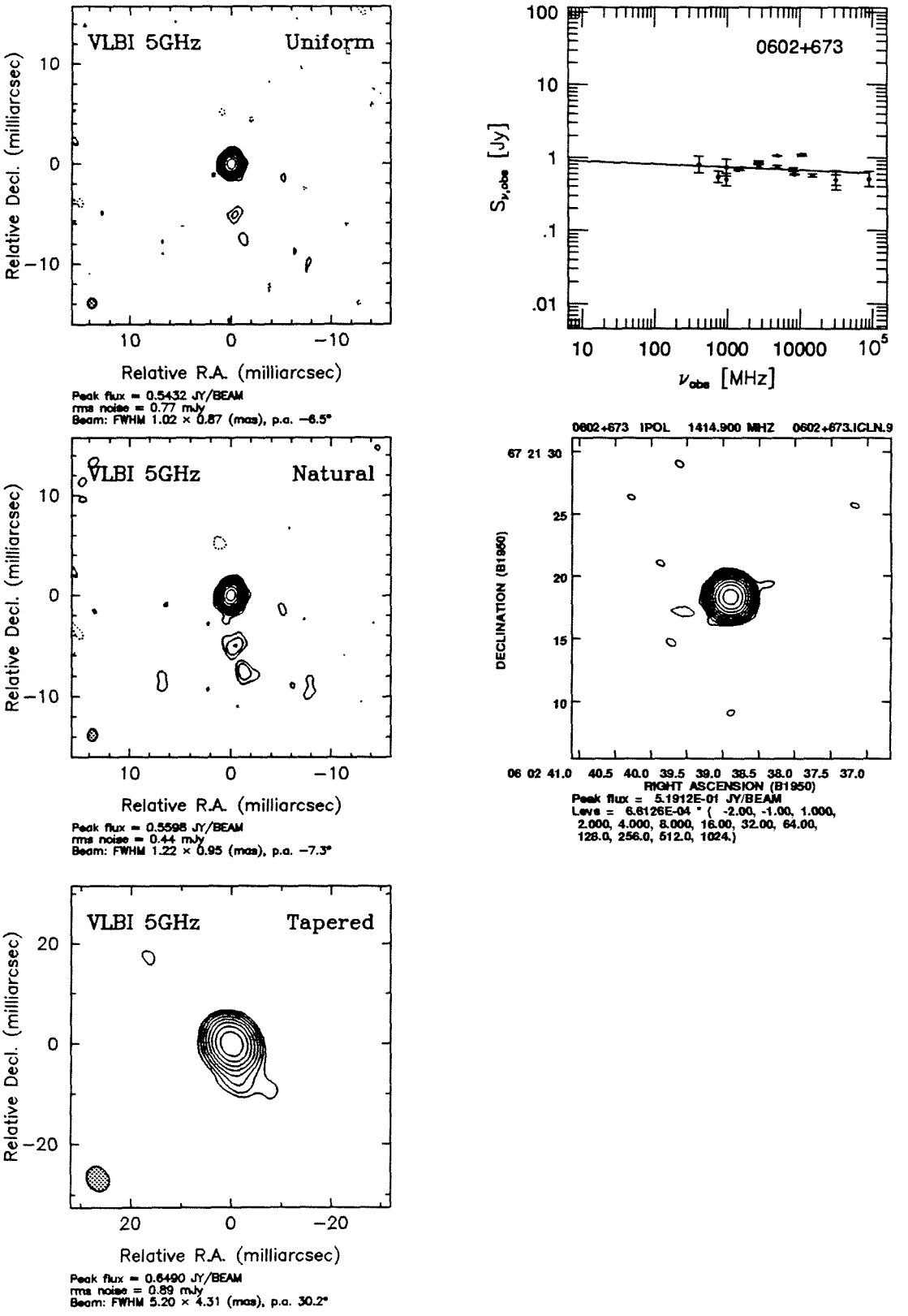

Figure 3.4.6. The maps and spectrum for 0602+673

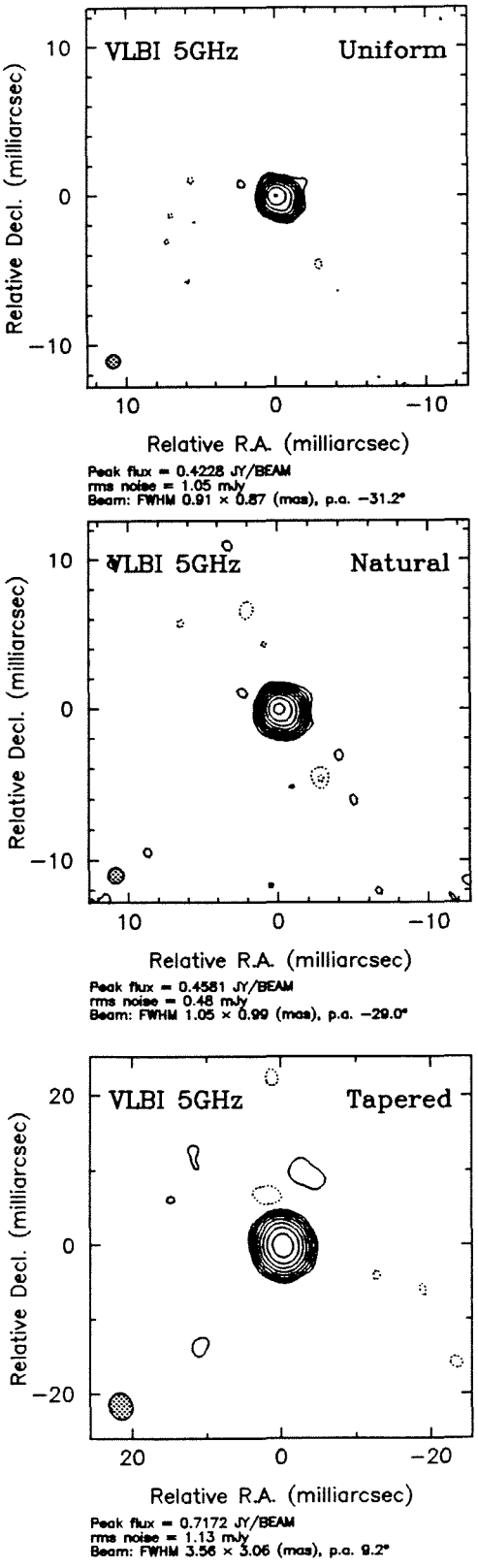

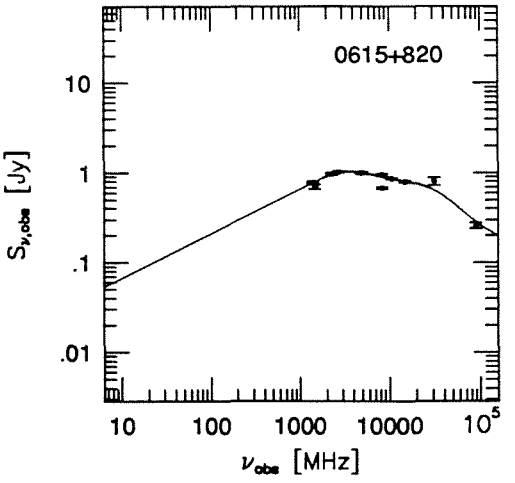

Figure 3.4.7. The maps and spectrum for 0615+820

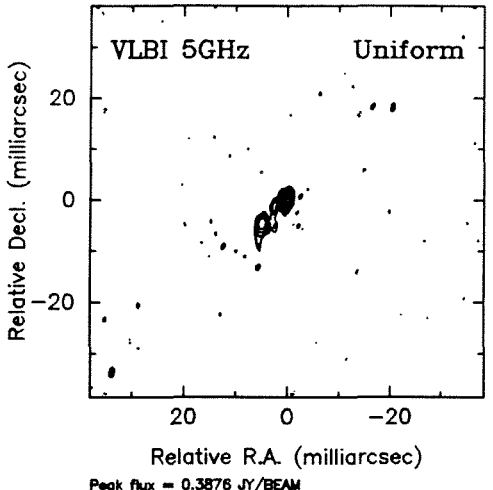

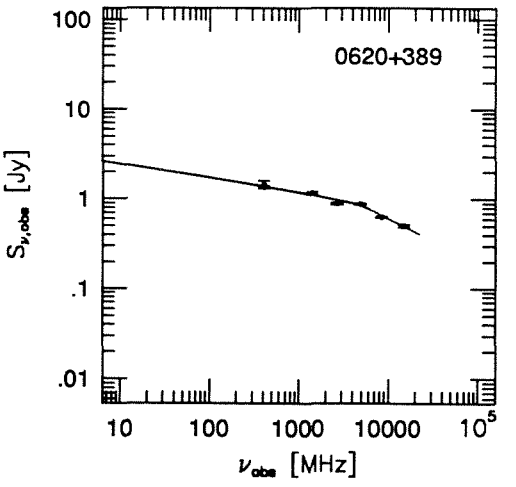

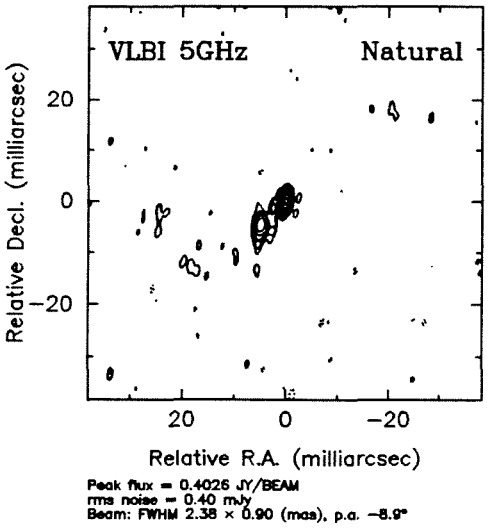

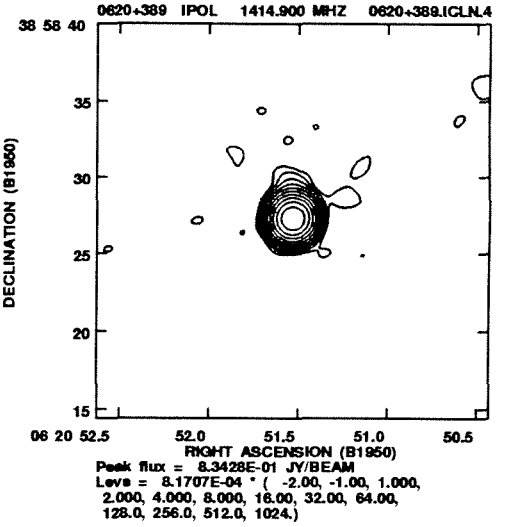

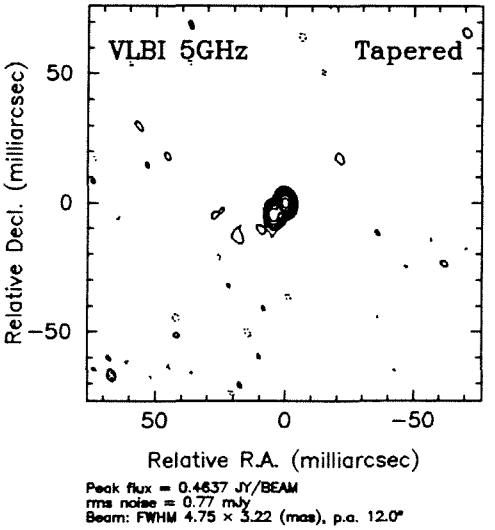

Figure 3.4.8. The maps and spectrum for 0620+389

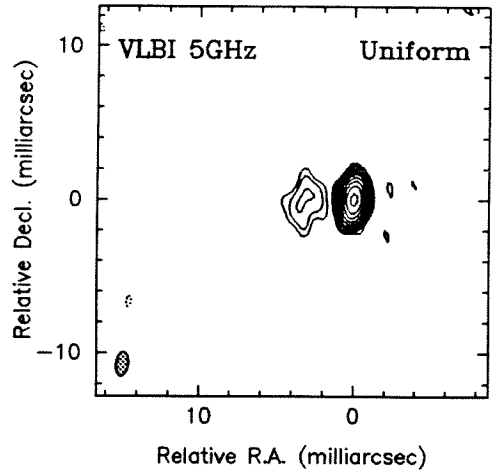

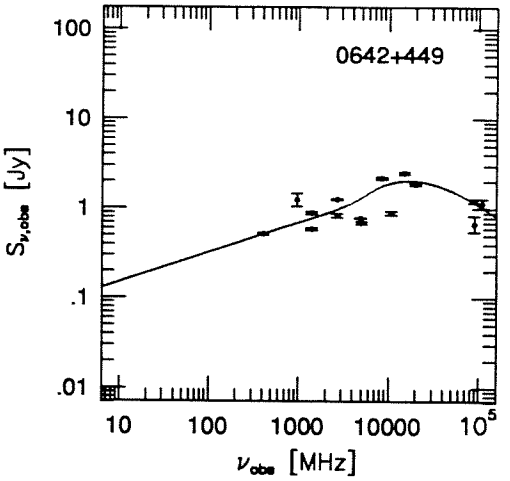

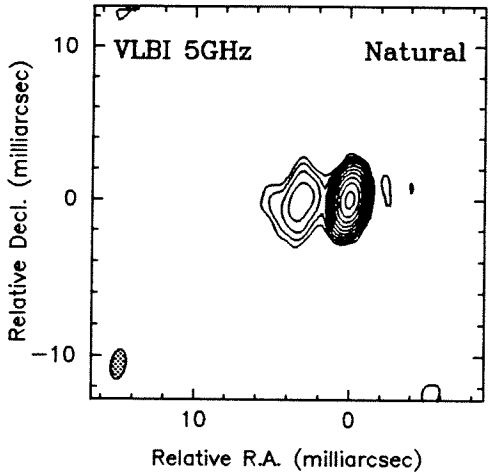

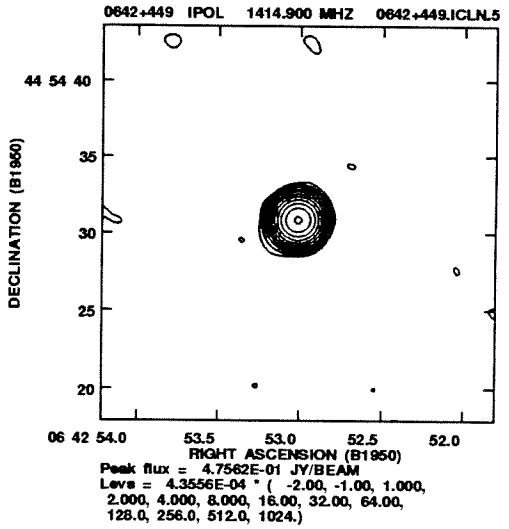

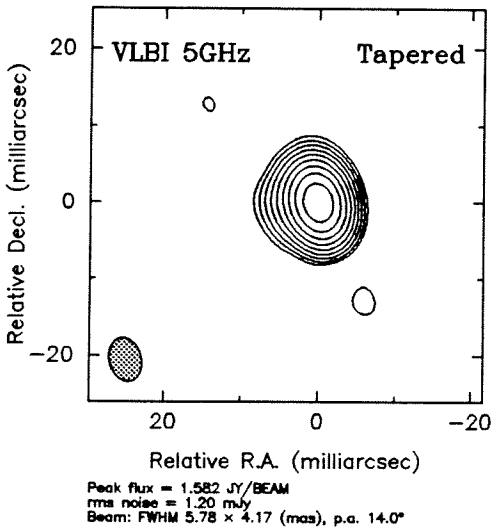

Figure 3.4.9. The maps and spectrum for 0642+449

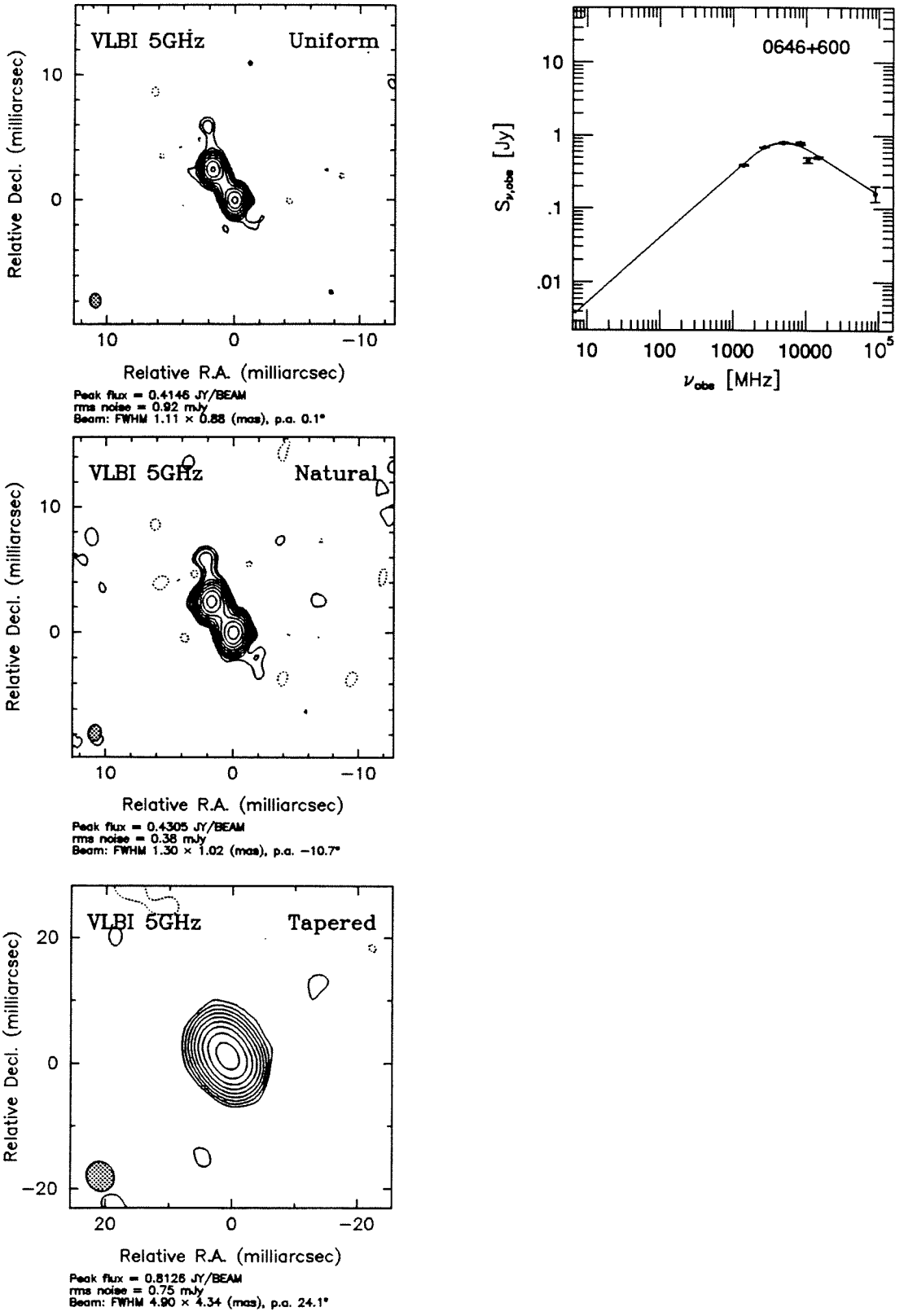

Figure 3.4.10. The maps and spectrum for 0646+600

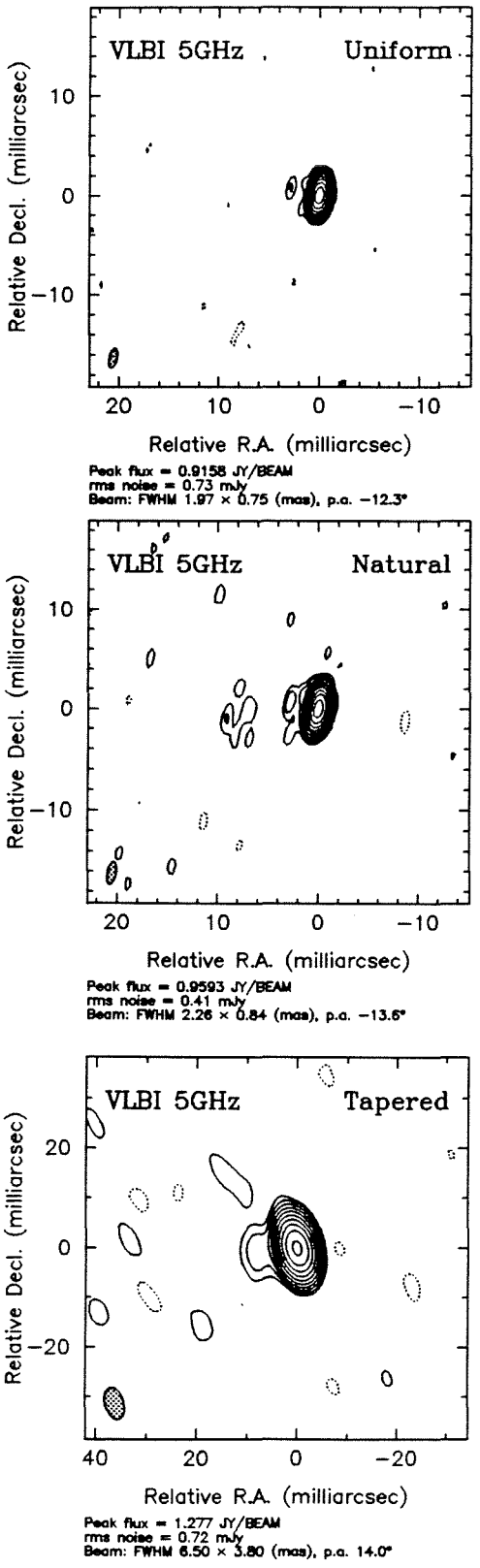

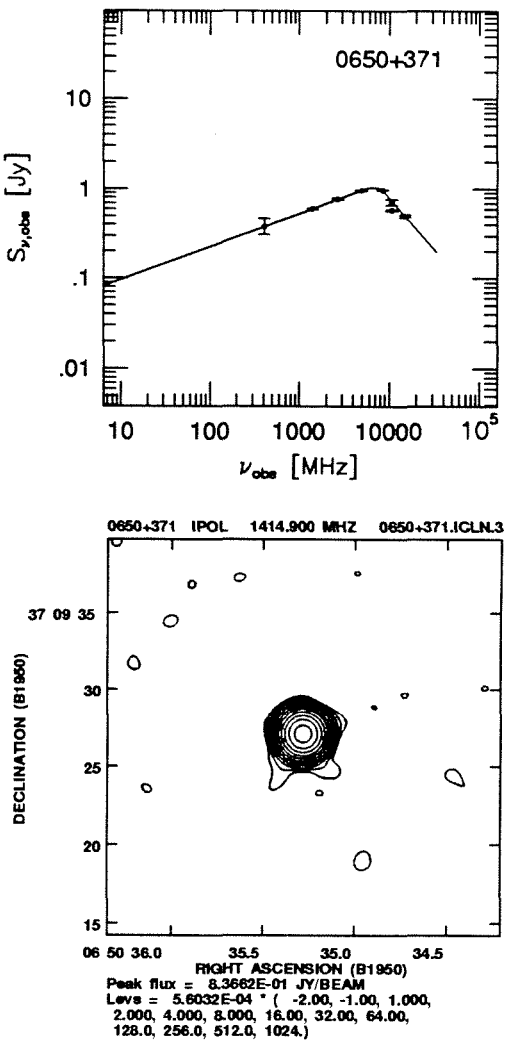

Figure 3.4.11. The maps and spectrum for 0650+371

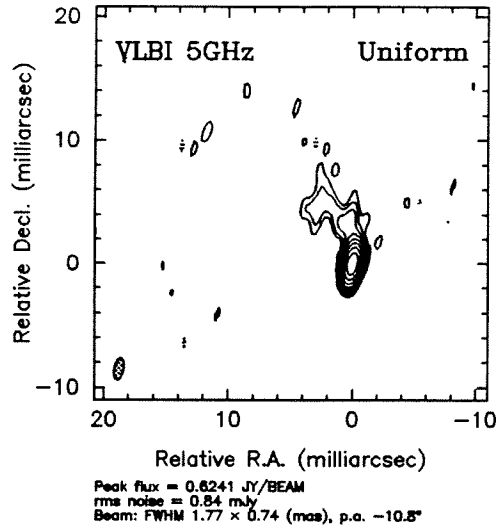

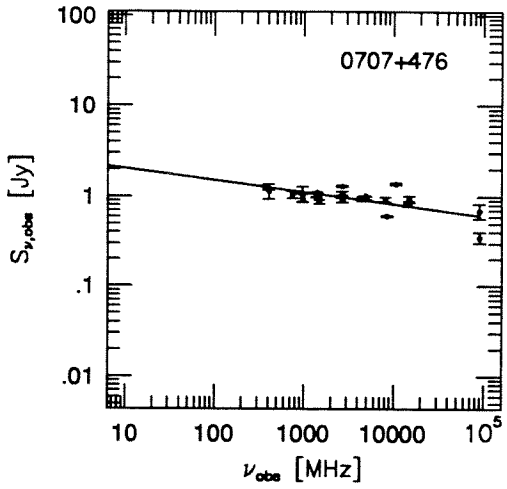

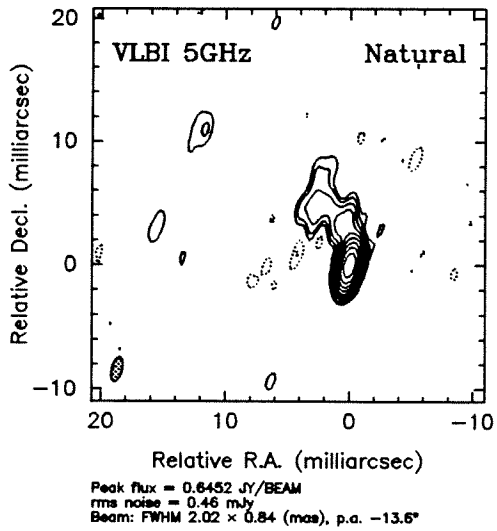

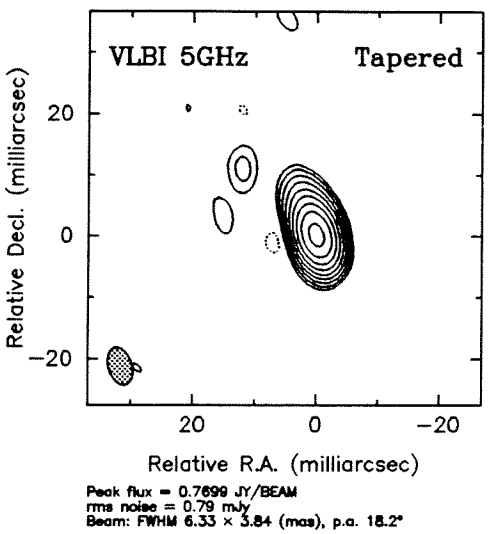

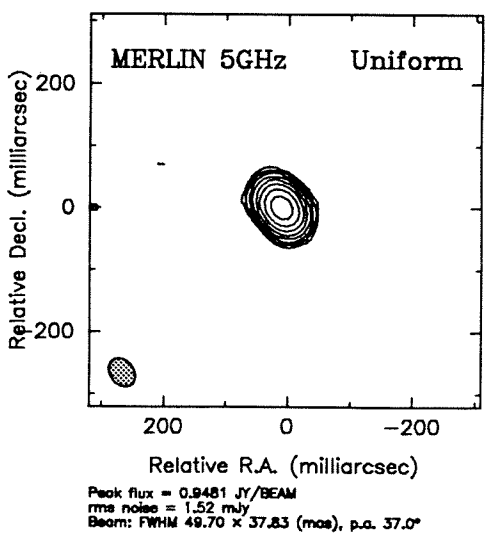

Figure 3.4.12. The maps and spectrum for 0707+476

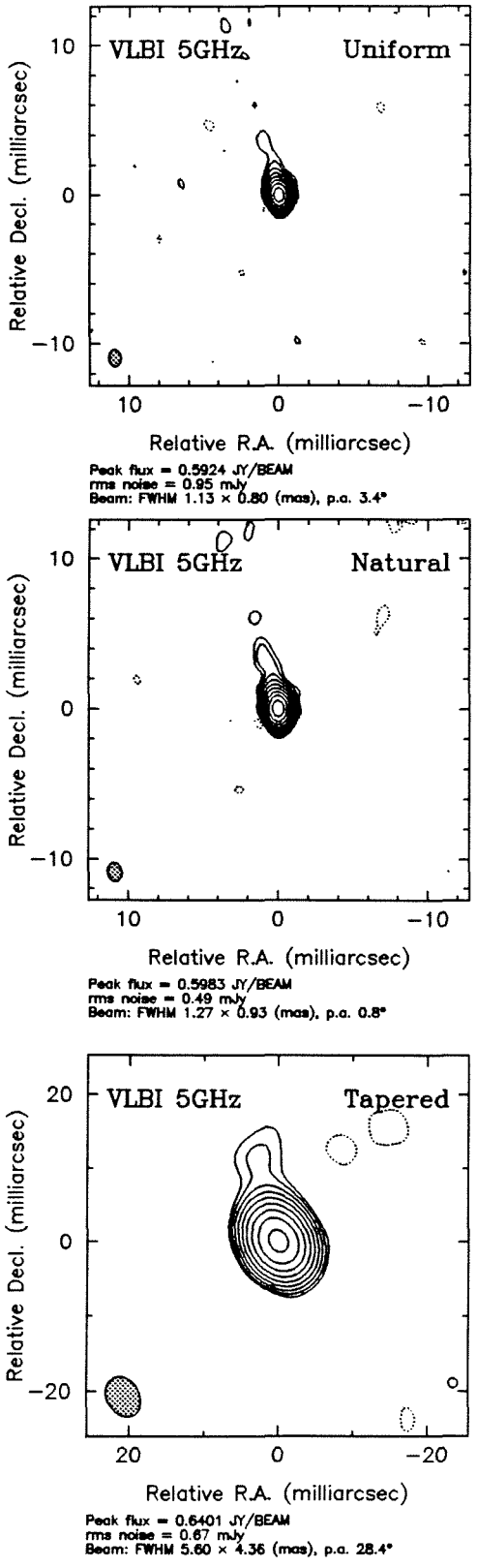

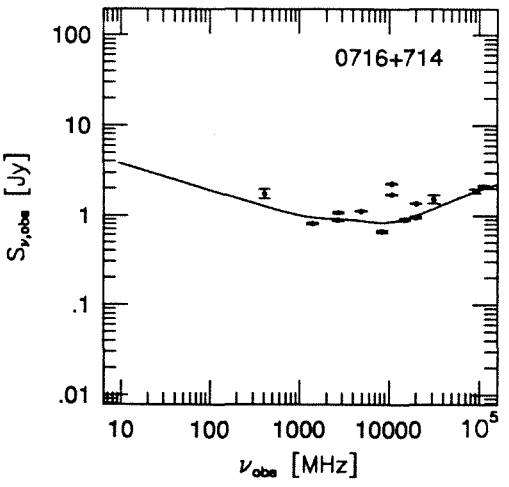

Figure 3.4.13. The maps and spectrum for 0716+714

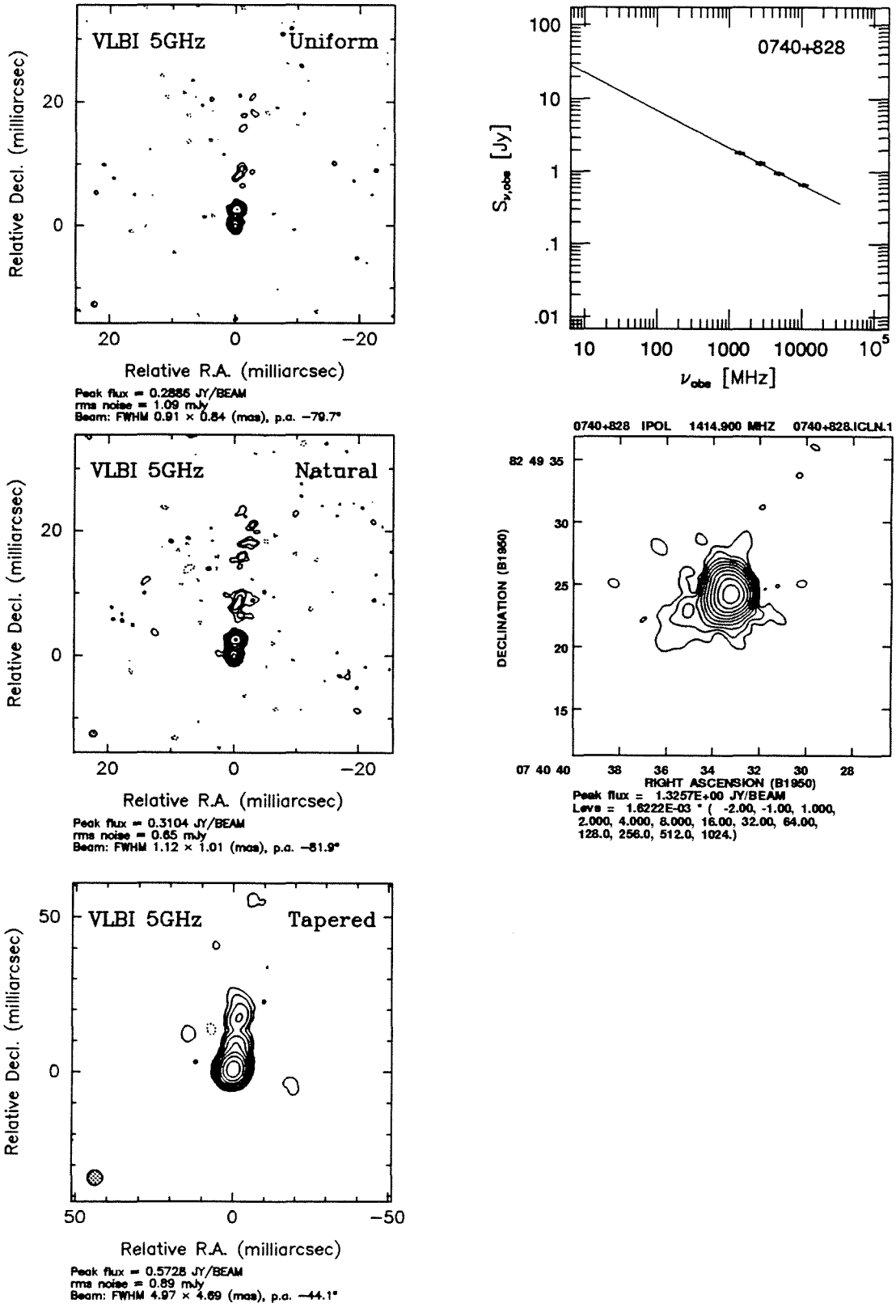

Figure 3.4.14. The maps and spectrum for 0740+828

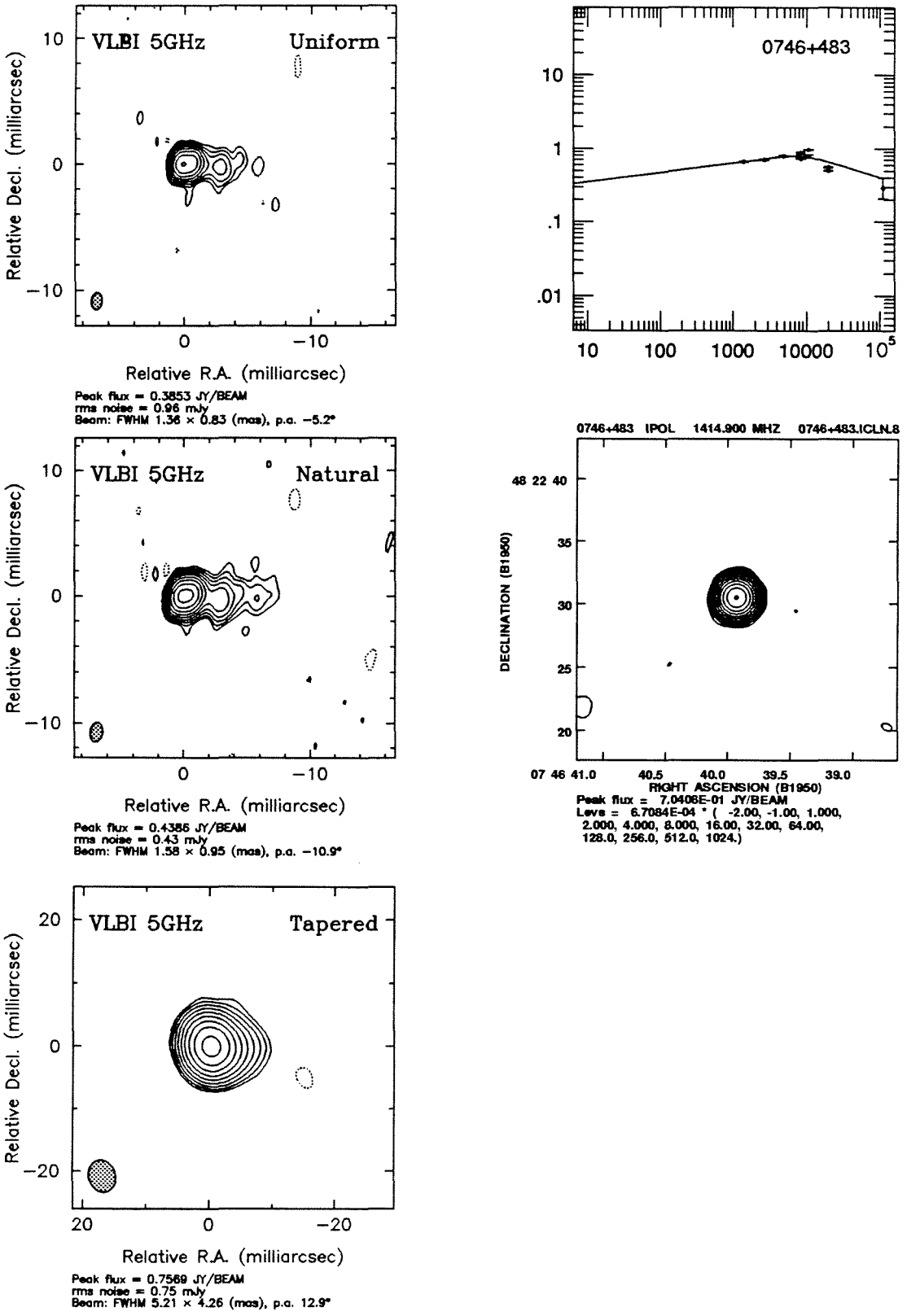

Figure 3.4.15. The maps and spectrum for 0746+483

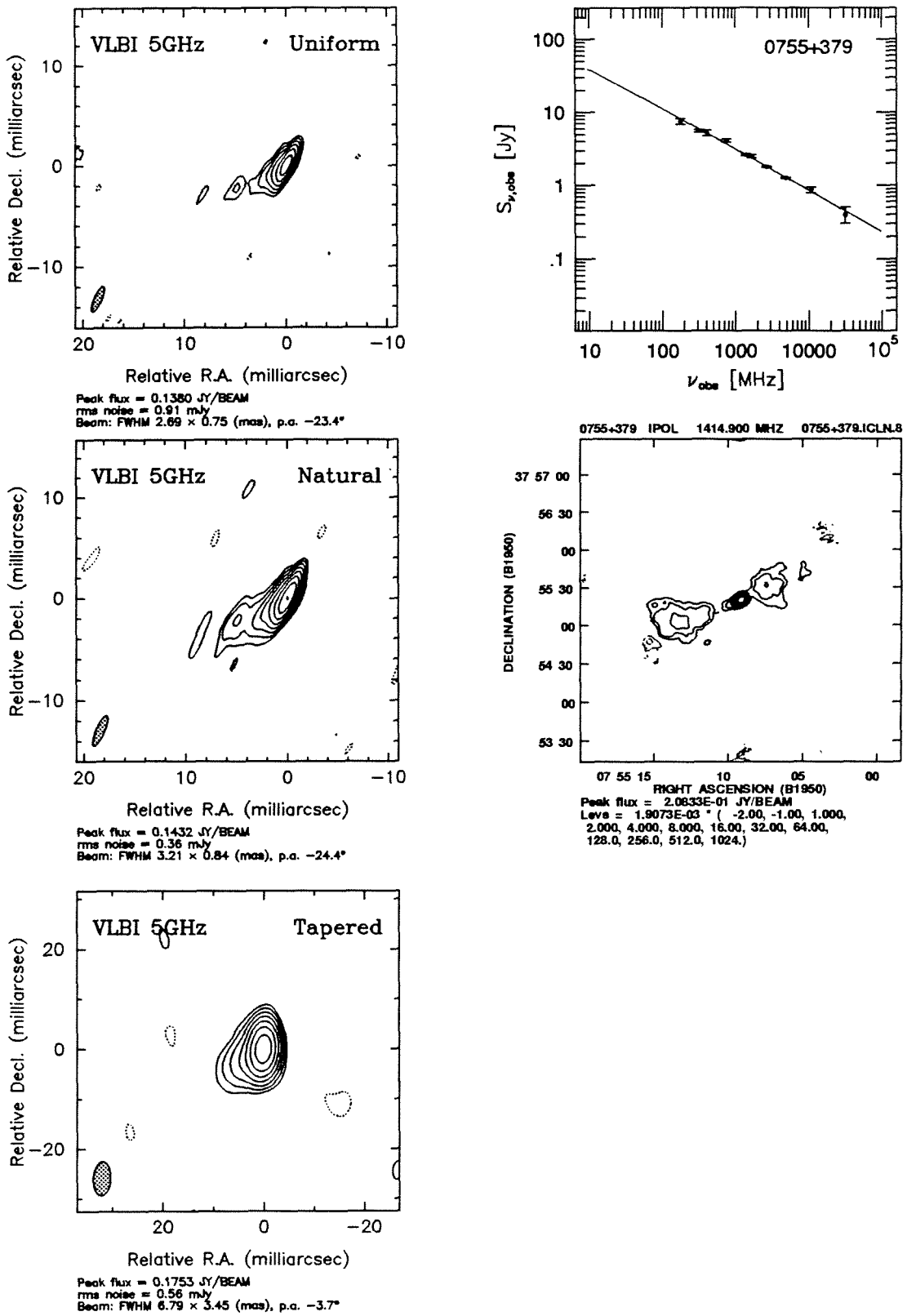

Figure 3.4.16. The maps and spectrum for 0755+379

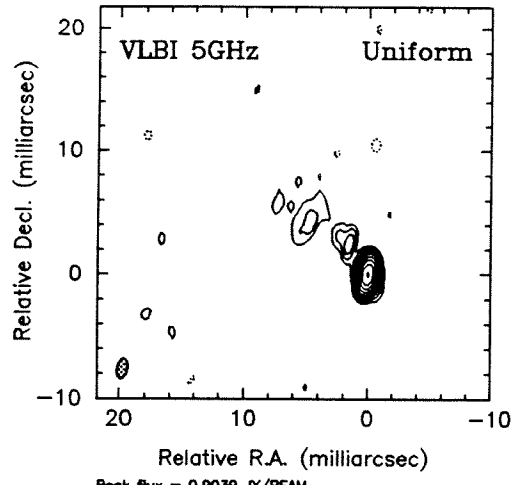

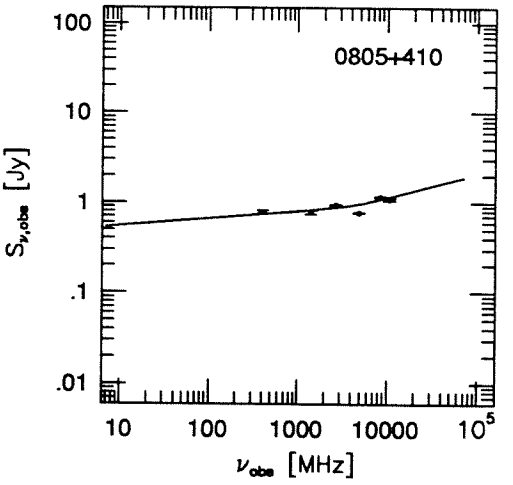

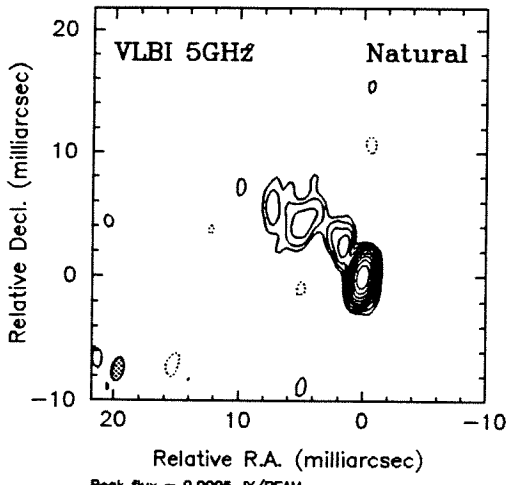

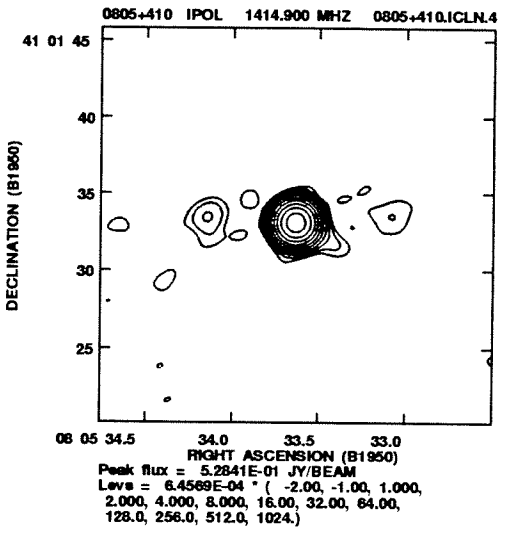

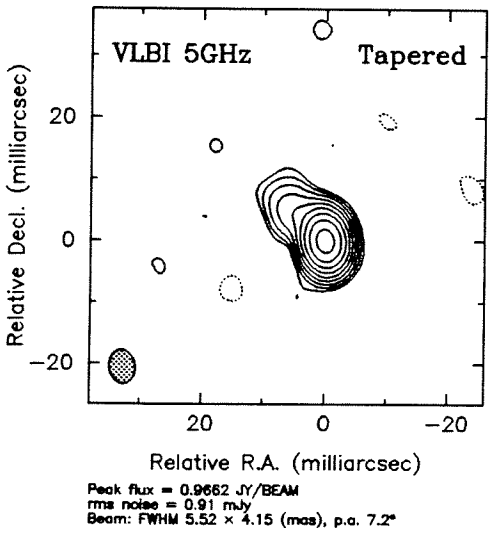

Figure 3.4.17. The maps and spectrum for 0805+410

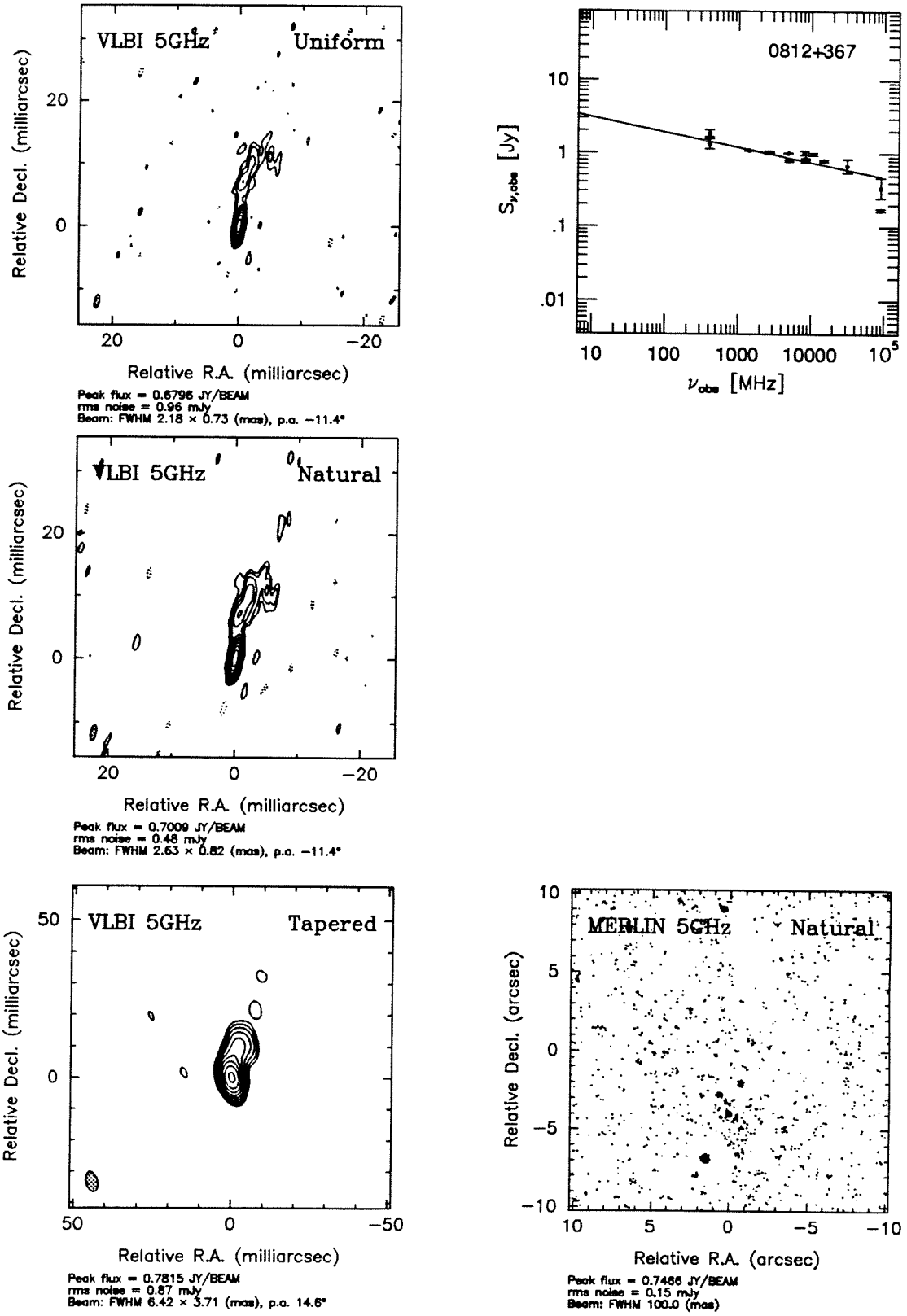

Figure 3.4.18. The maps and spectrum for 0812+367

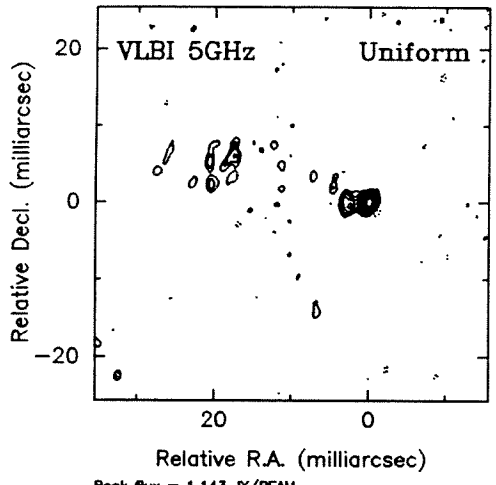

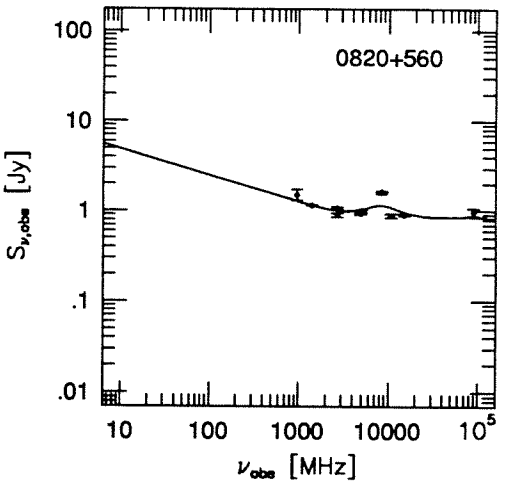

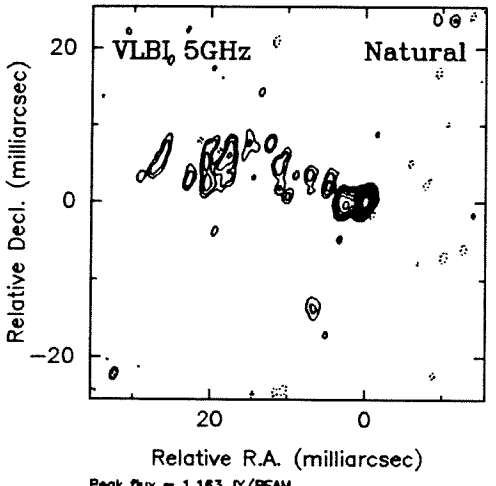

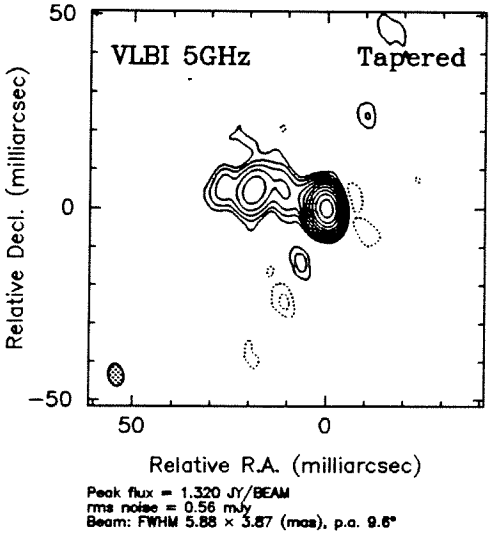

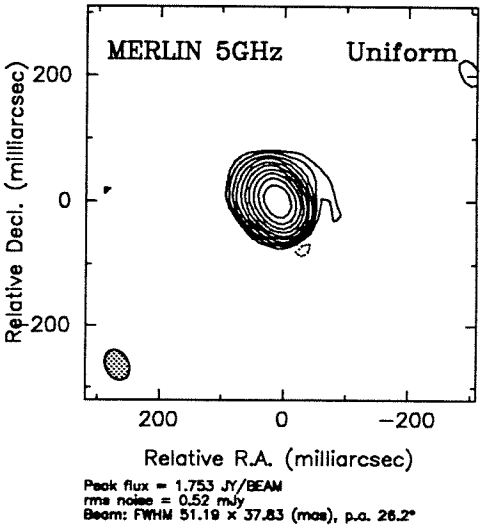

Figure 3.4.19. The maps and spectrum for 0820+560

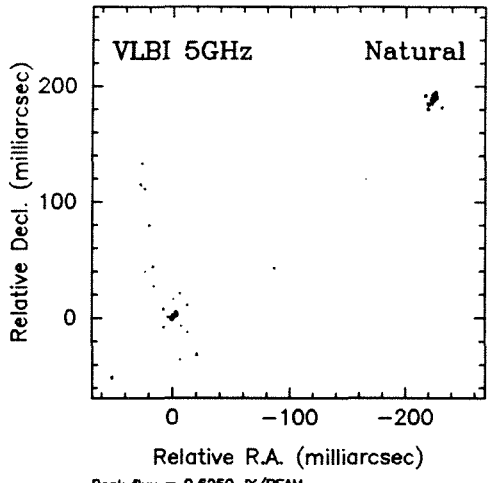

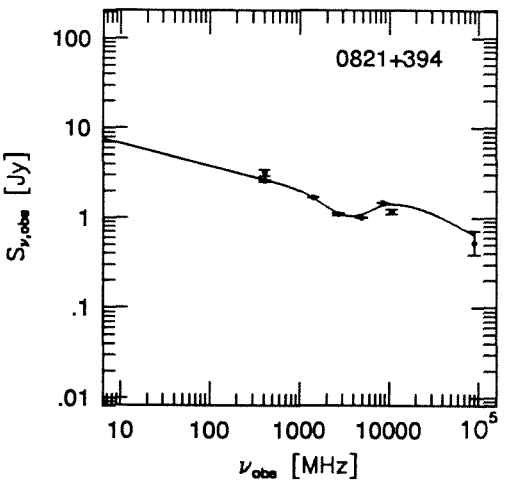

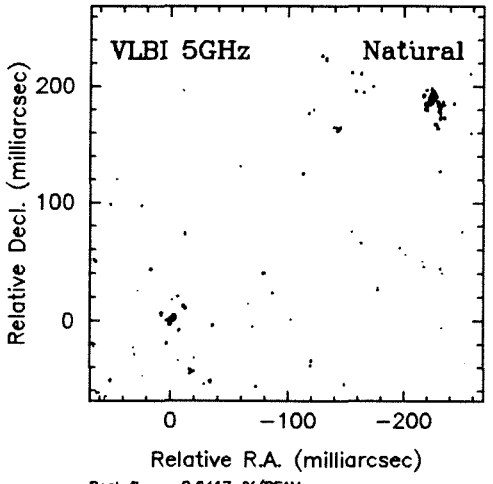

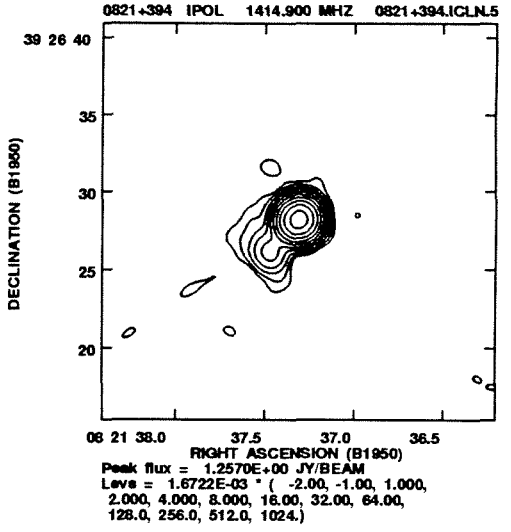

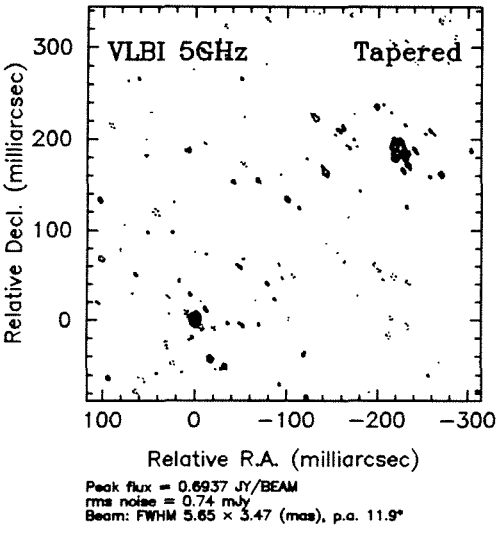

Figure 3.4.20. The maps and spectrum for 0821+394

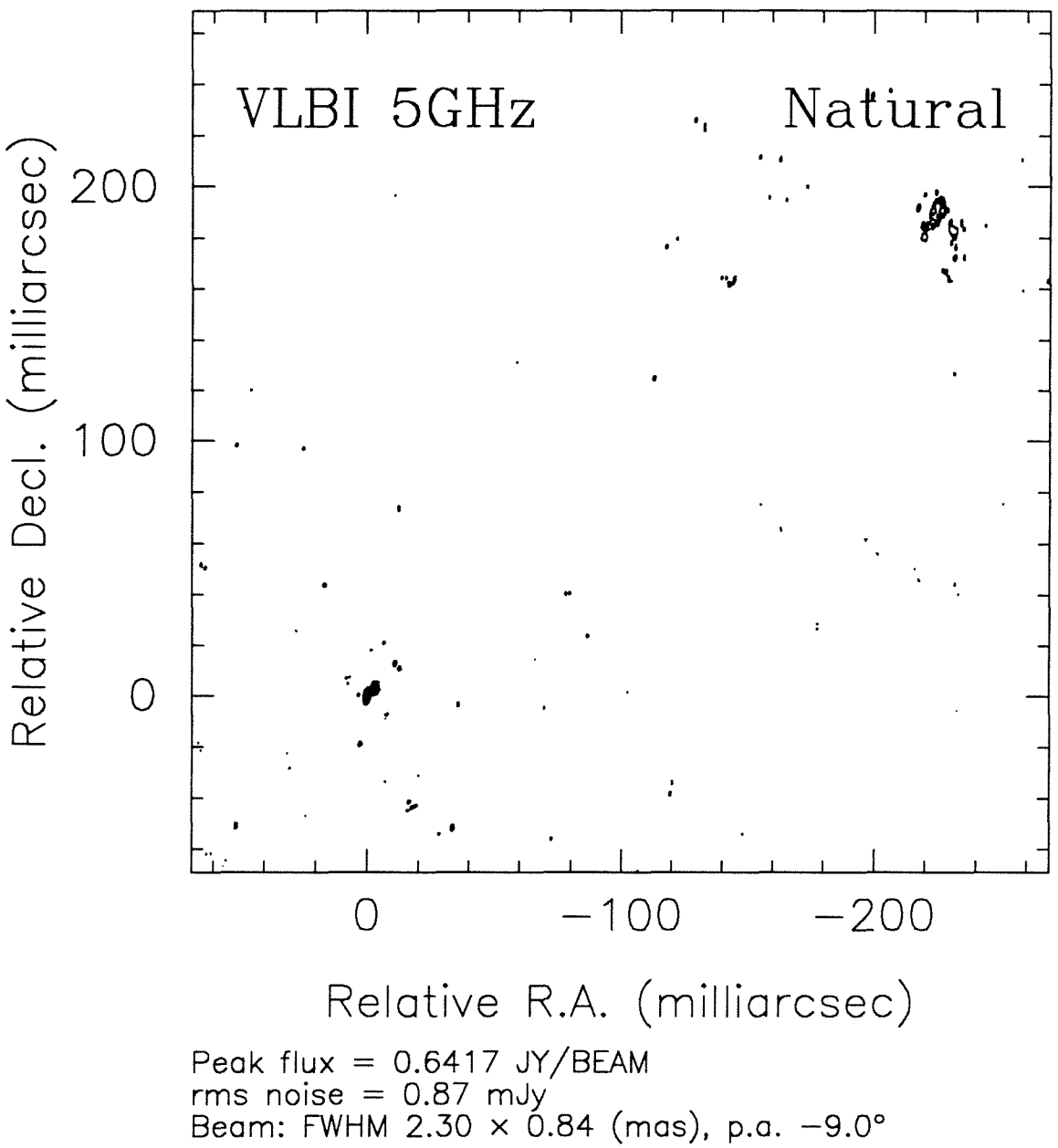

Figure 3.4.20. The VLBI map of 0821+394

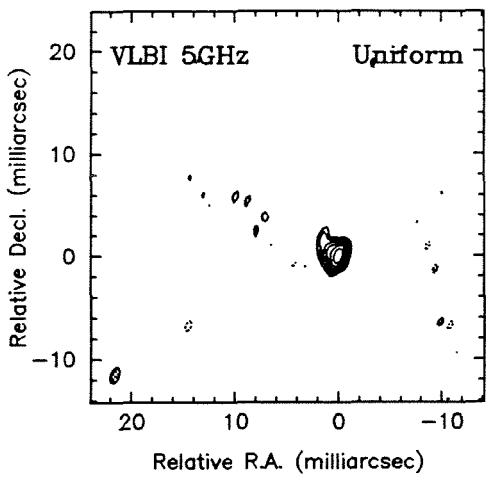

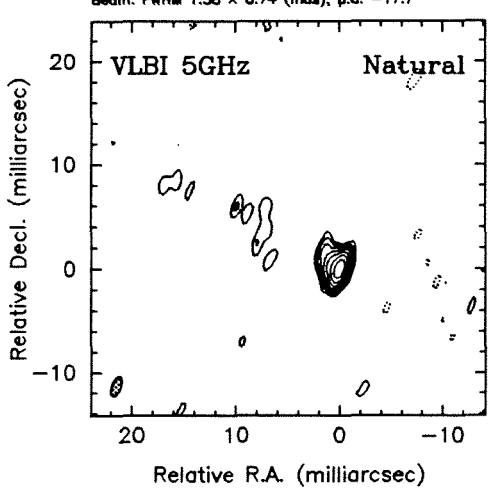

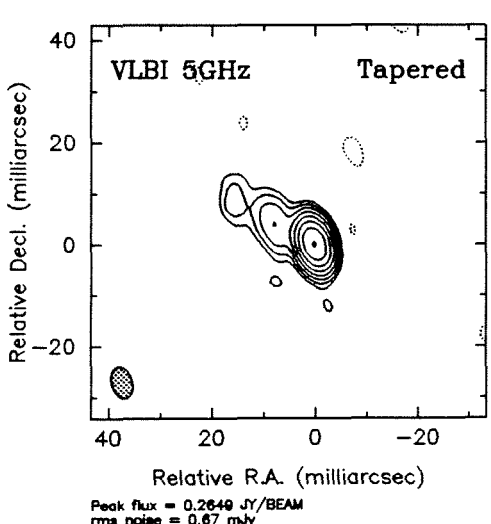

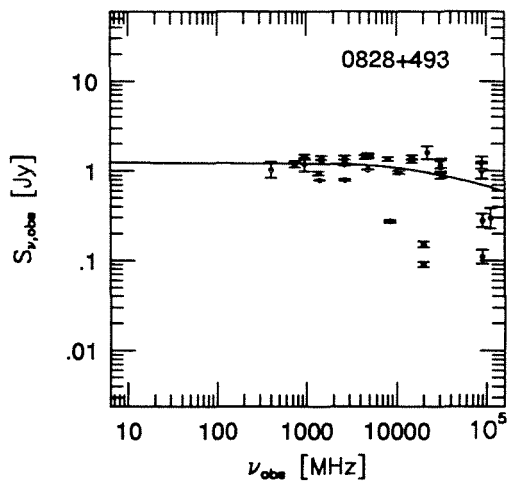

Figure 3.4.20. The maps and spectrum for 0828+493

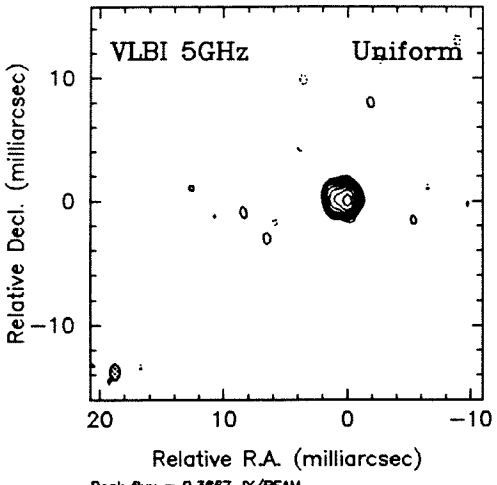

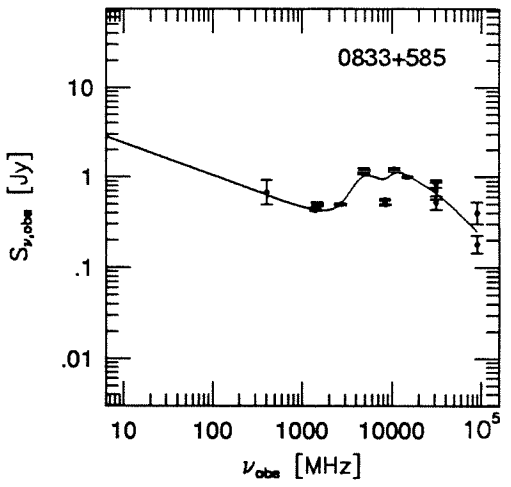

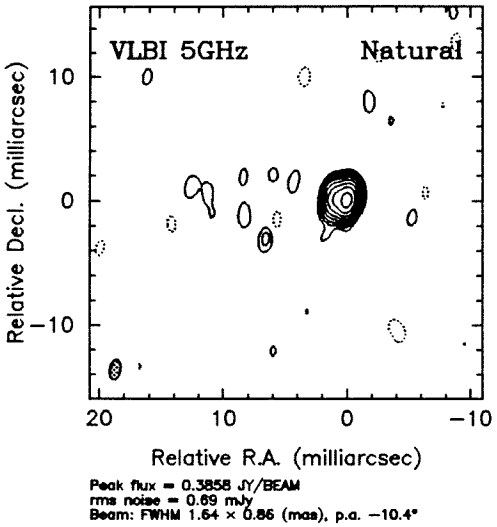

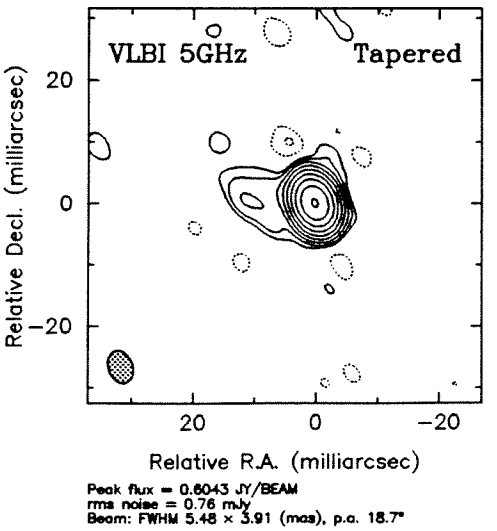

Figure 3.4.21. The maps and spectrum for 0833+585

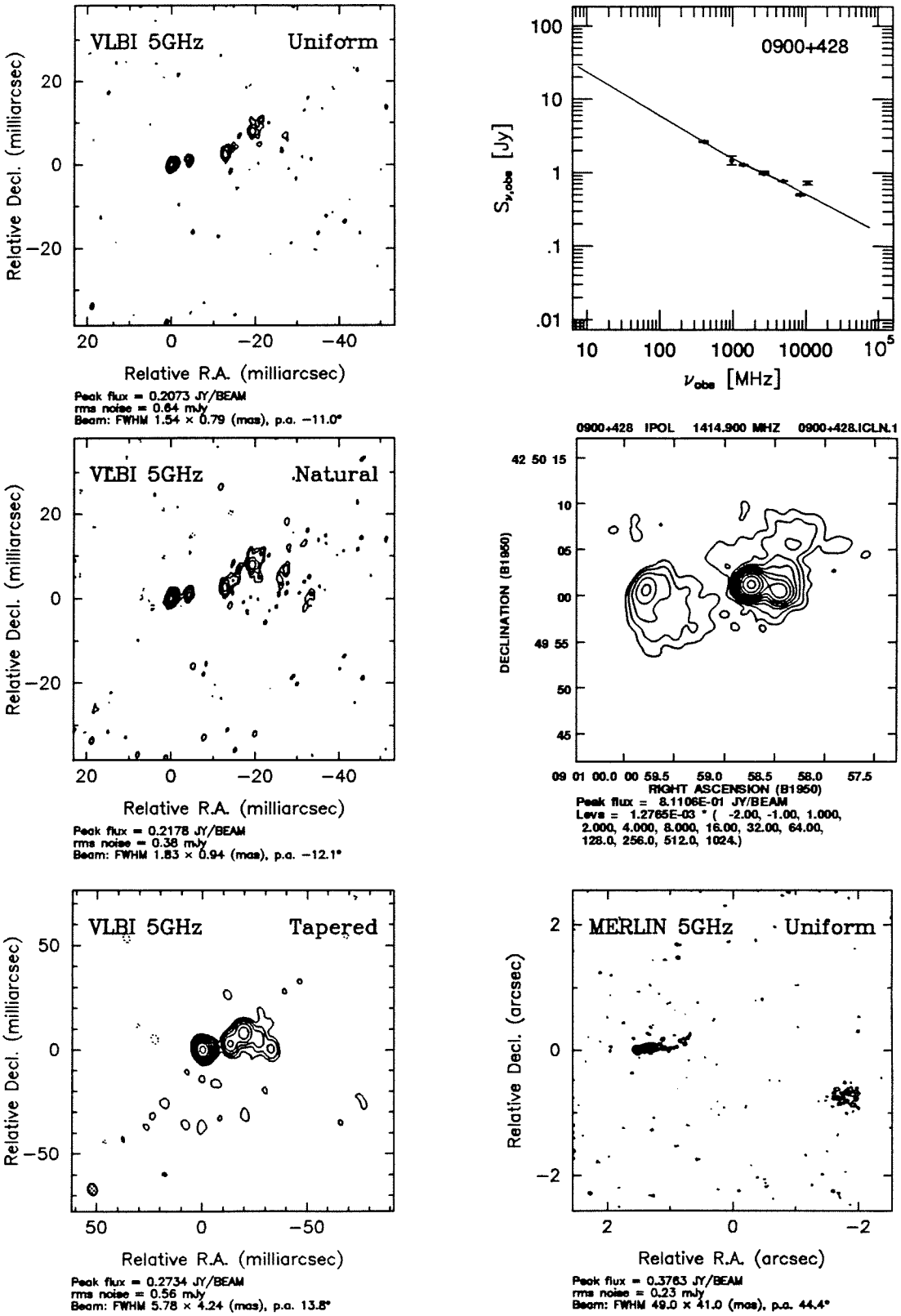

Figure 3.4.22. The maps and spectrum for 0900+428

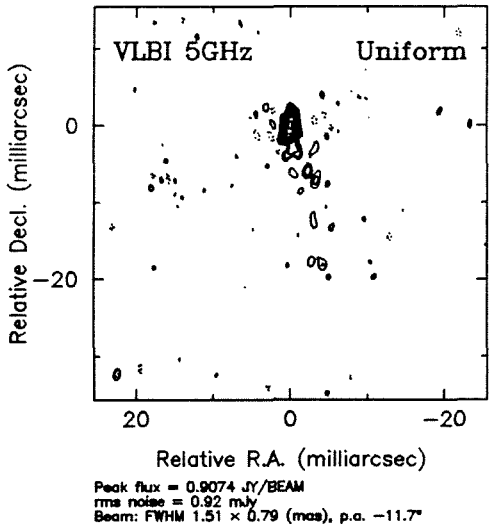

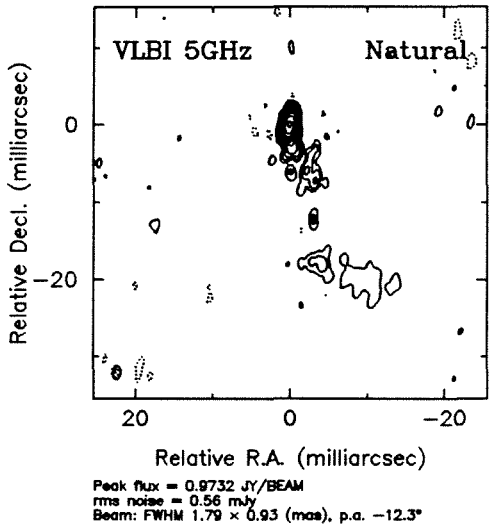

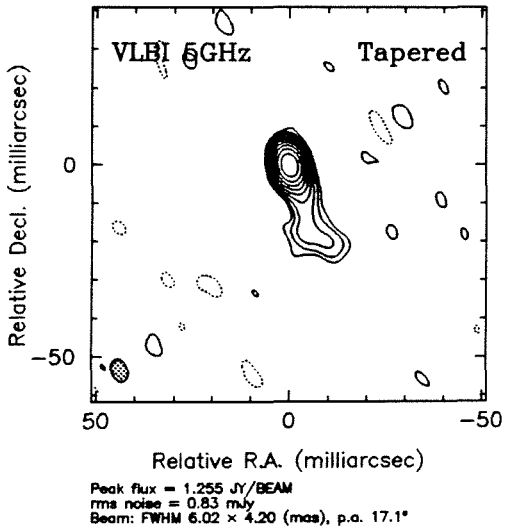

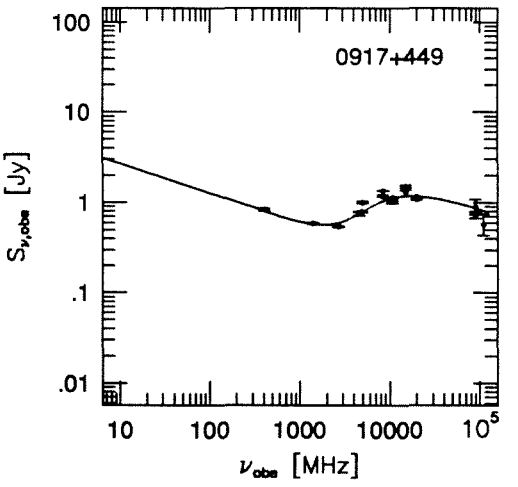

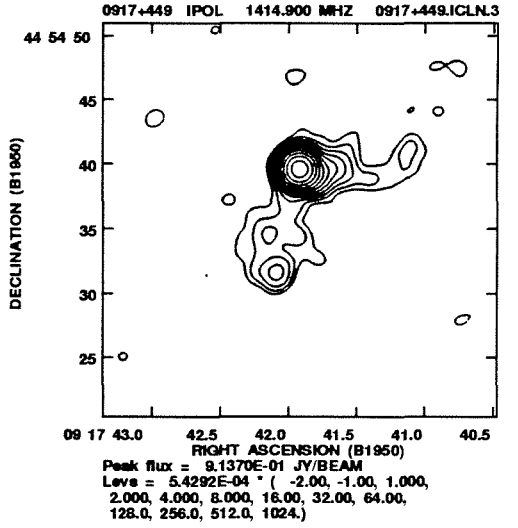

Figure 3.4.23. The maps and spectrum for 0917+449

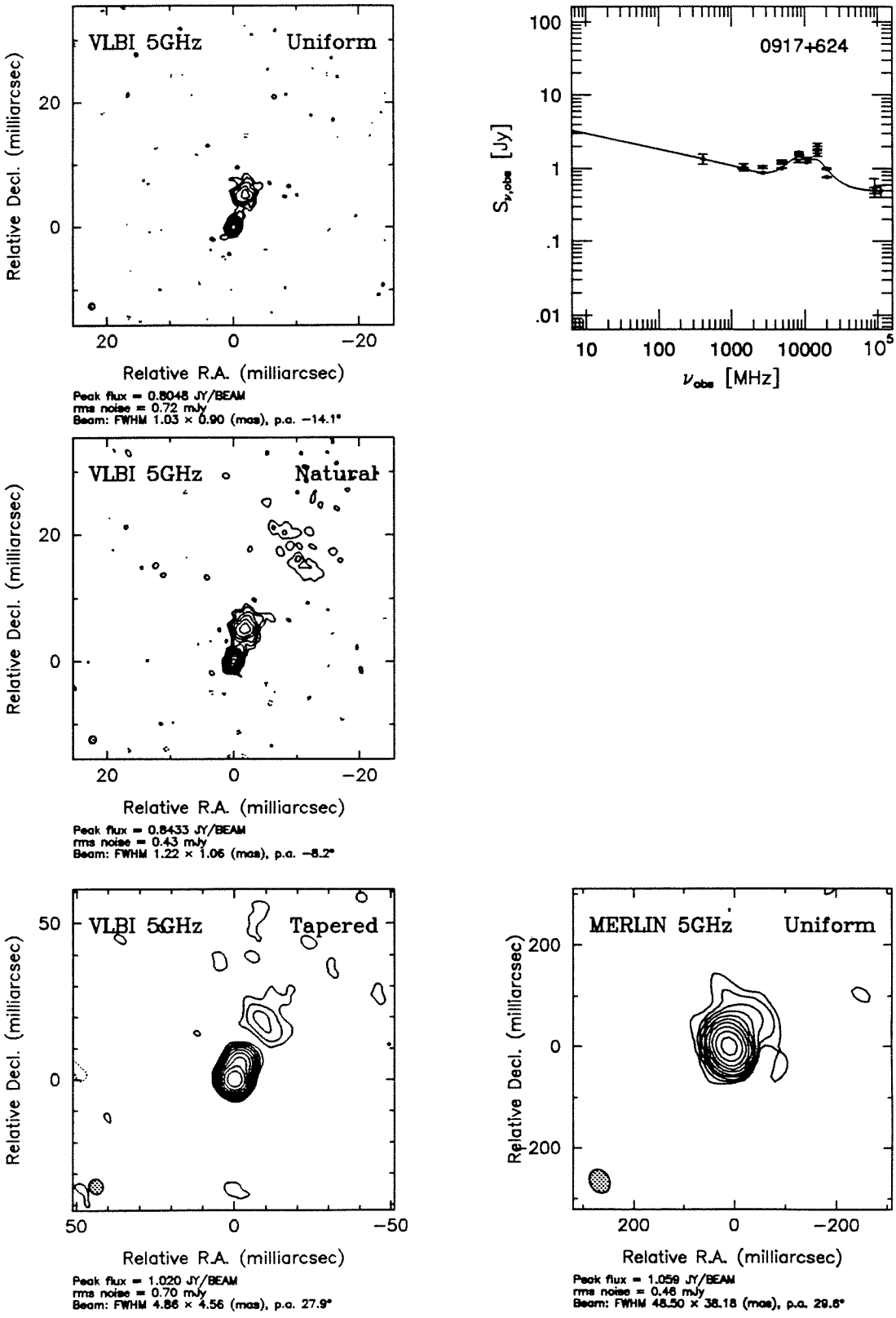

Figure 3.4.24. The maps and spectrum for 0917+624

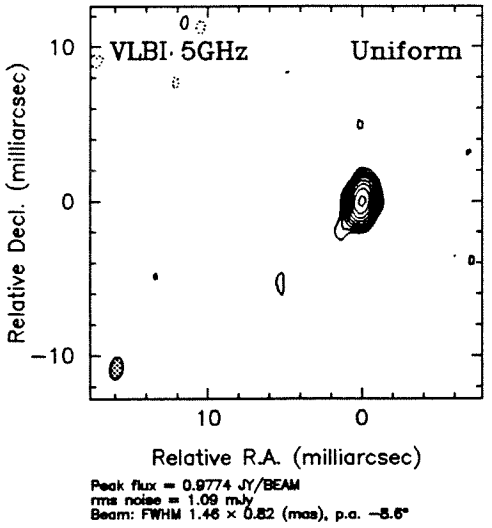

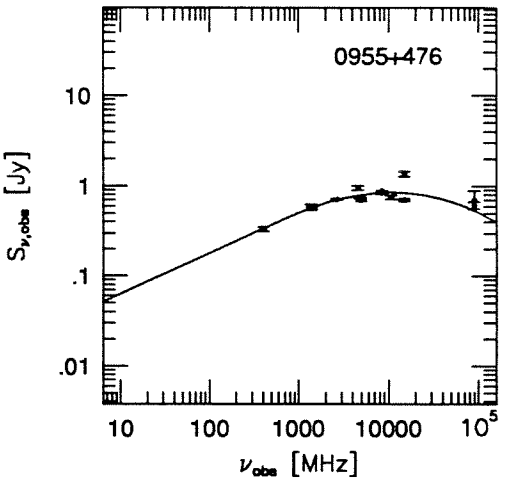

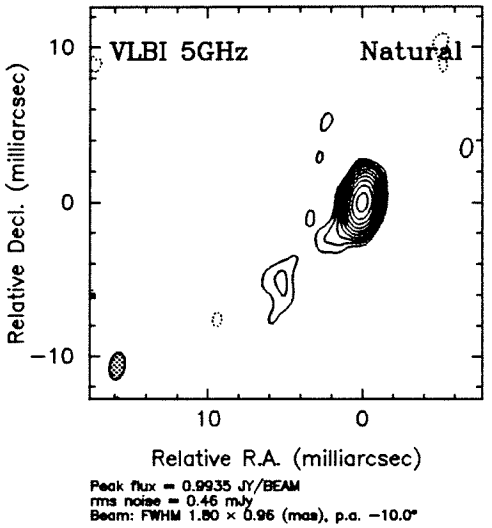

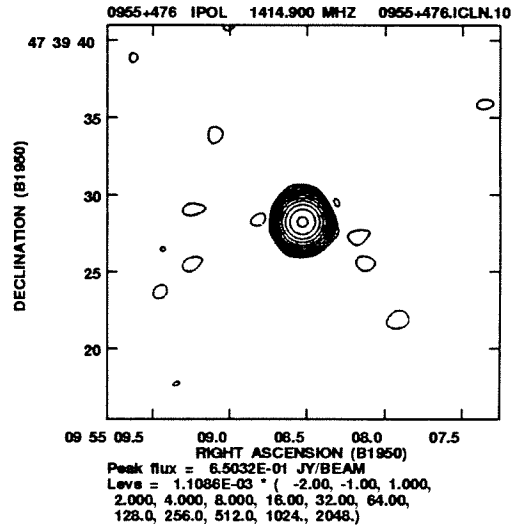

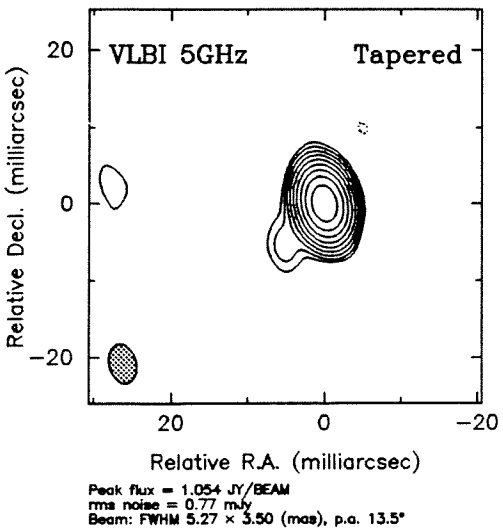

Figure 3.4.25. The maps and spectrum for 0955+476

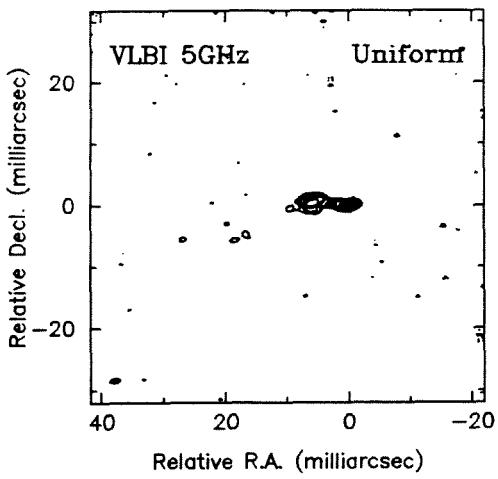

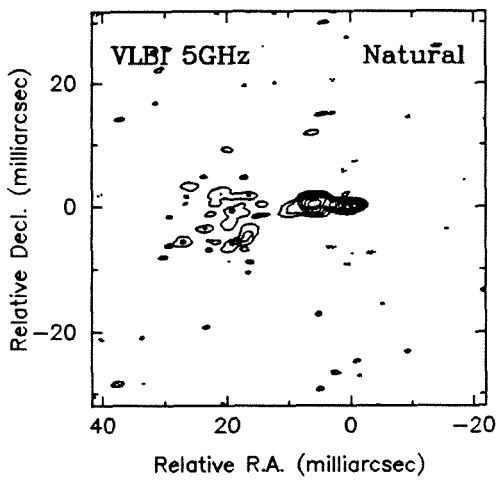

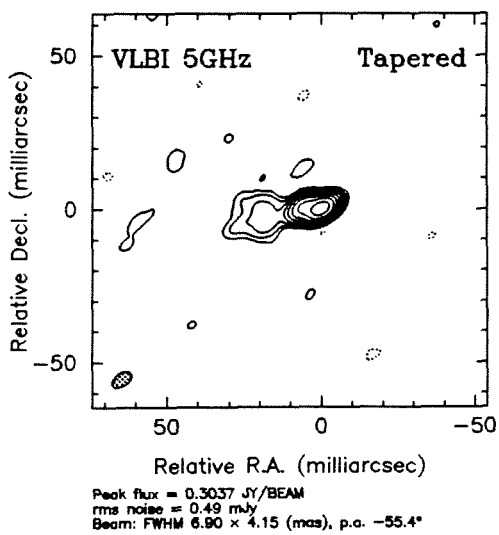

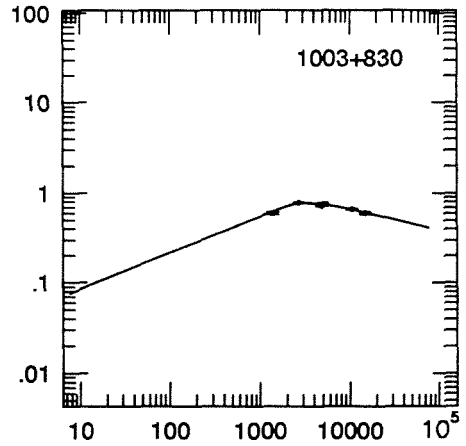

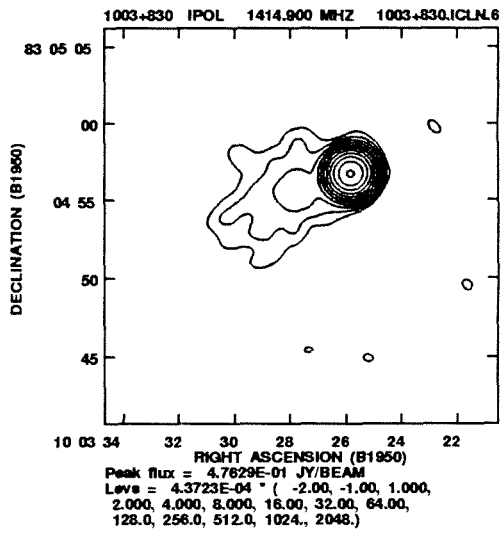

Figure 3.4.26. The maps and spectrum for 1003+830

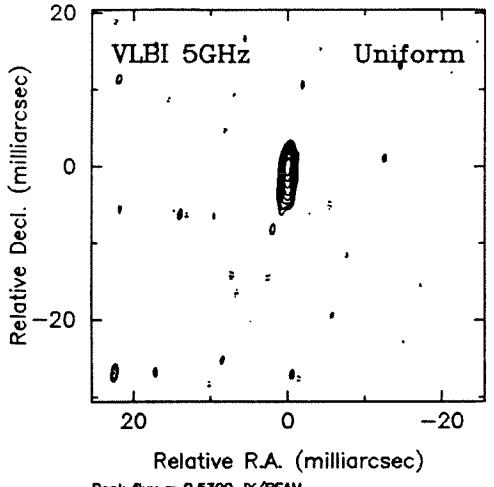

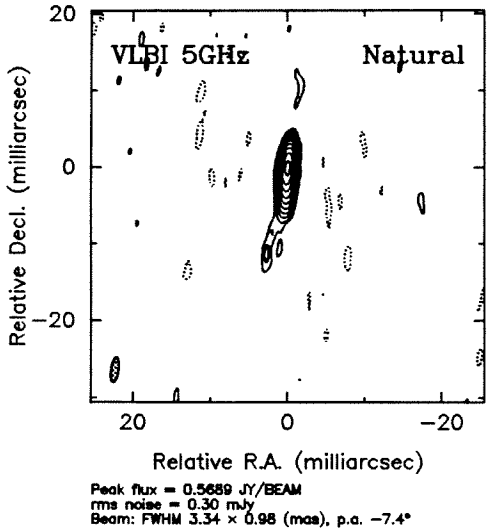

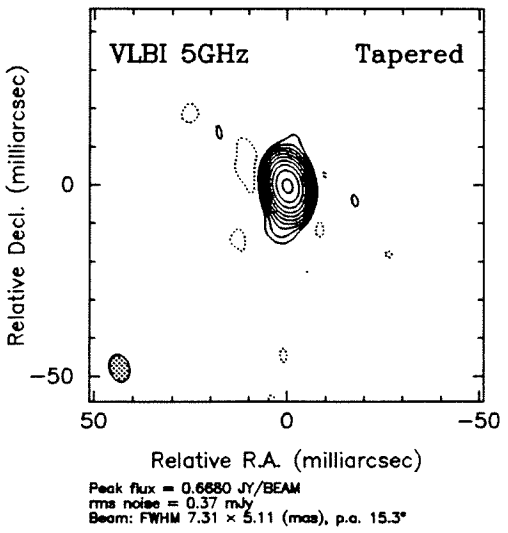

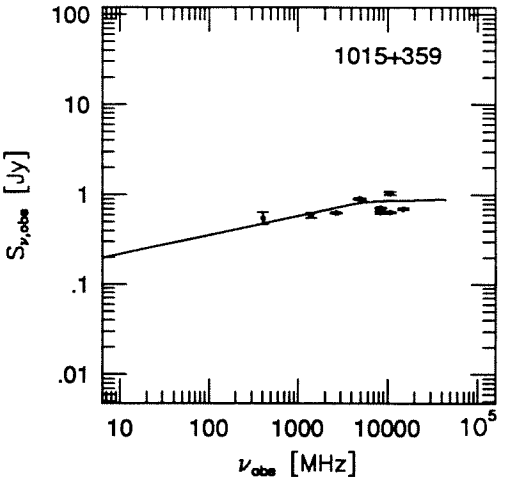

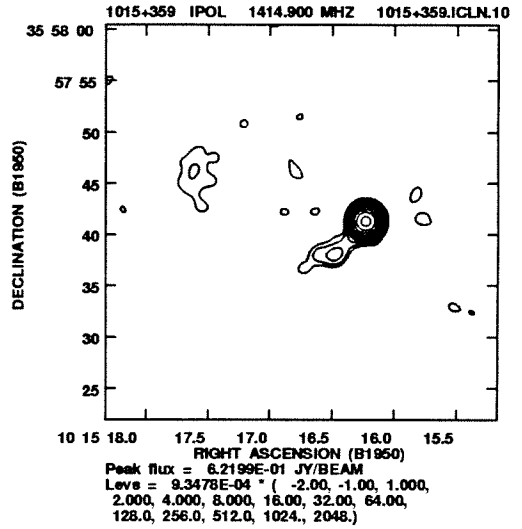

Figure 3.4.27. The maps and spectrum for 1015+359

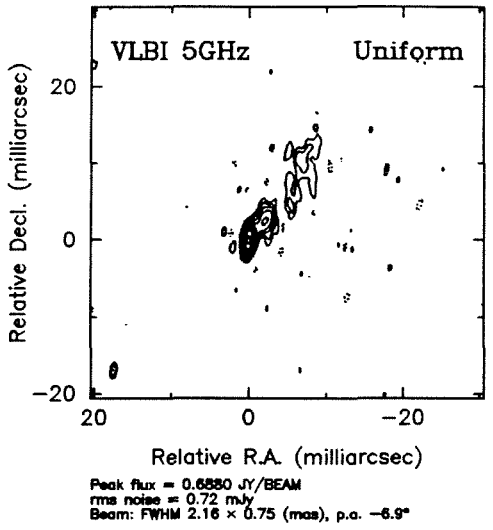

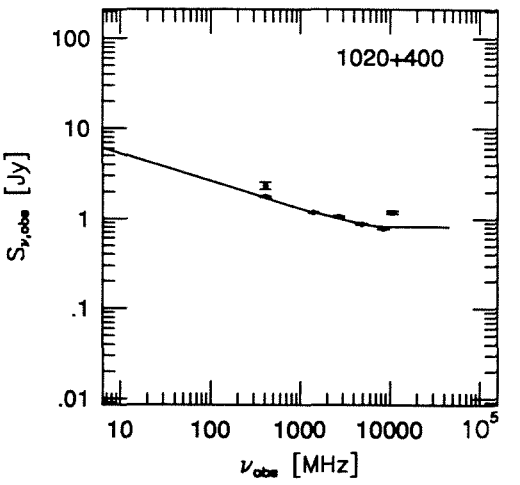

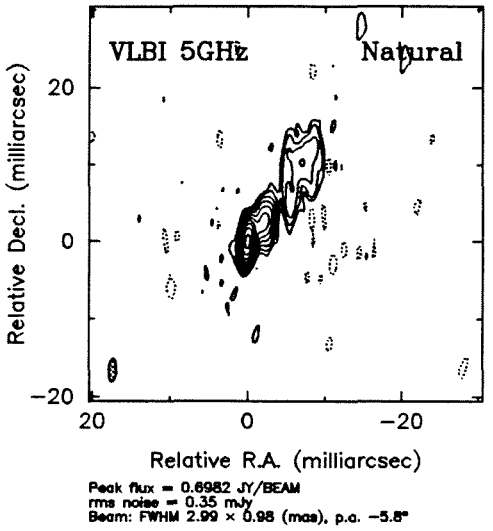

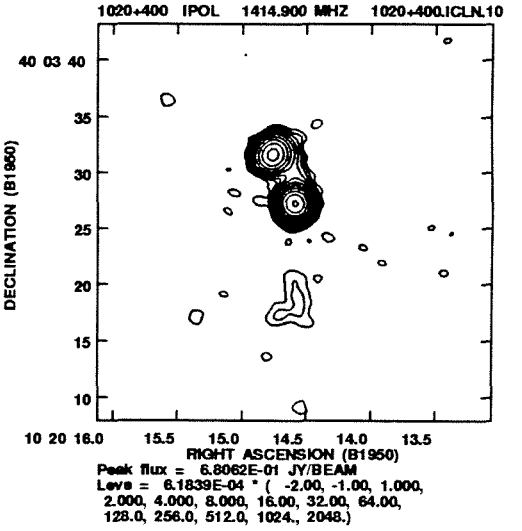

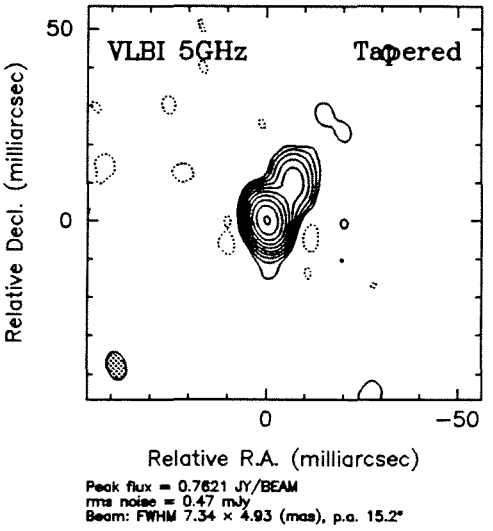

Figure 3.4.28. The maps and spectrum for 1020+400

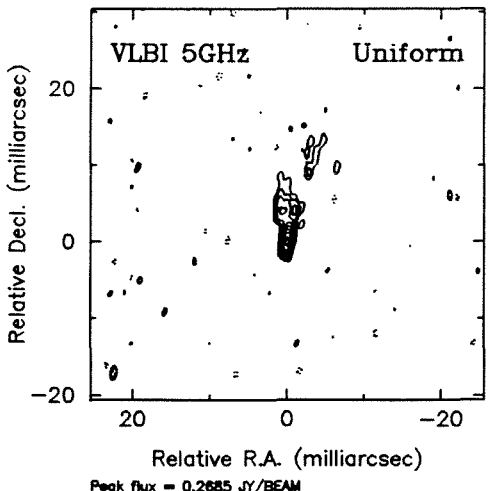

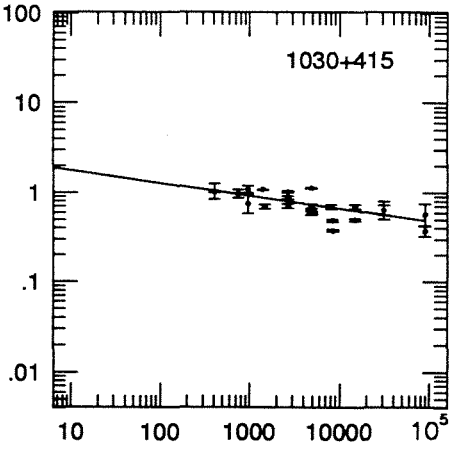

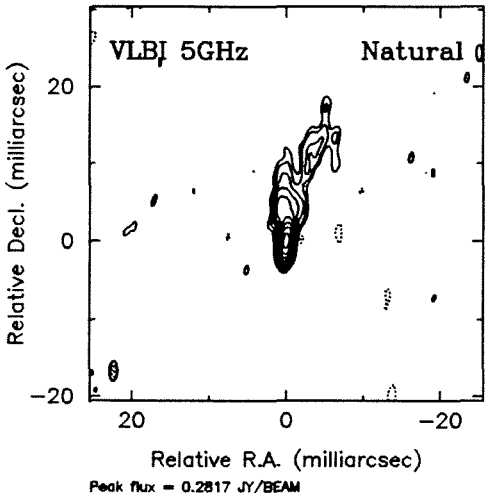

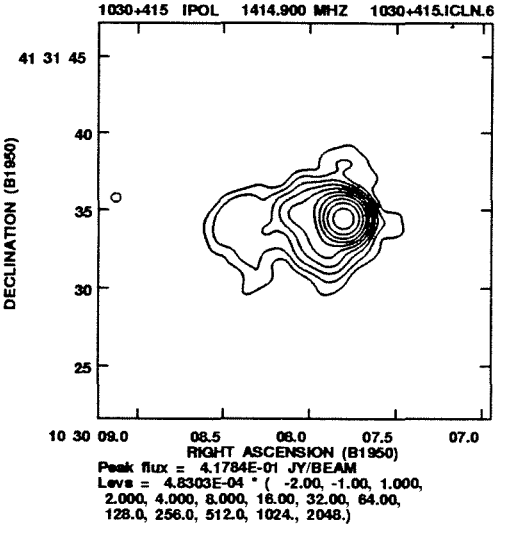

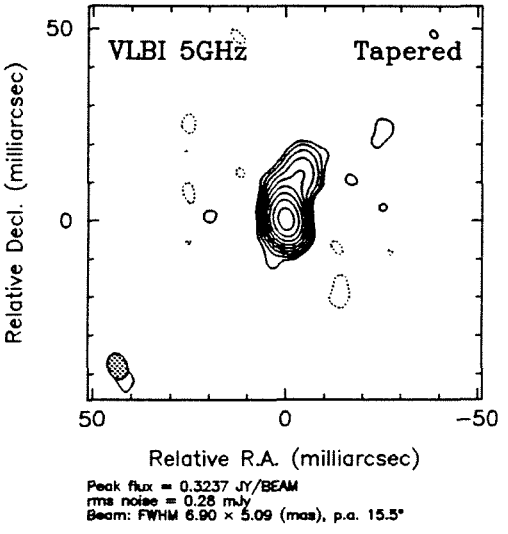

Figure 3.4.29. The maps and spectrum for 1030+415

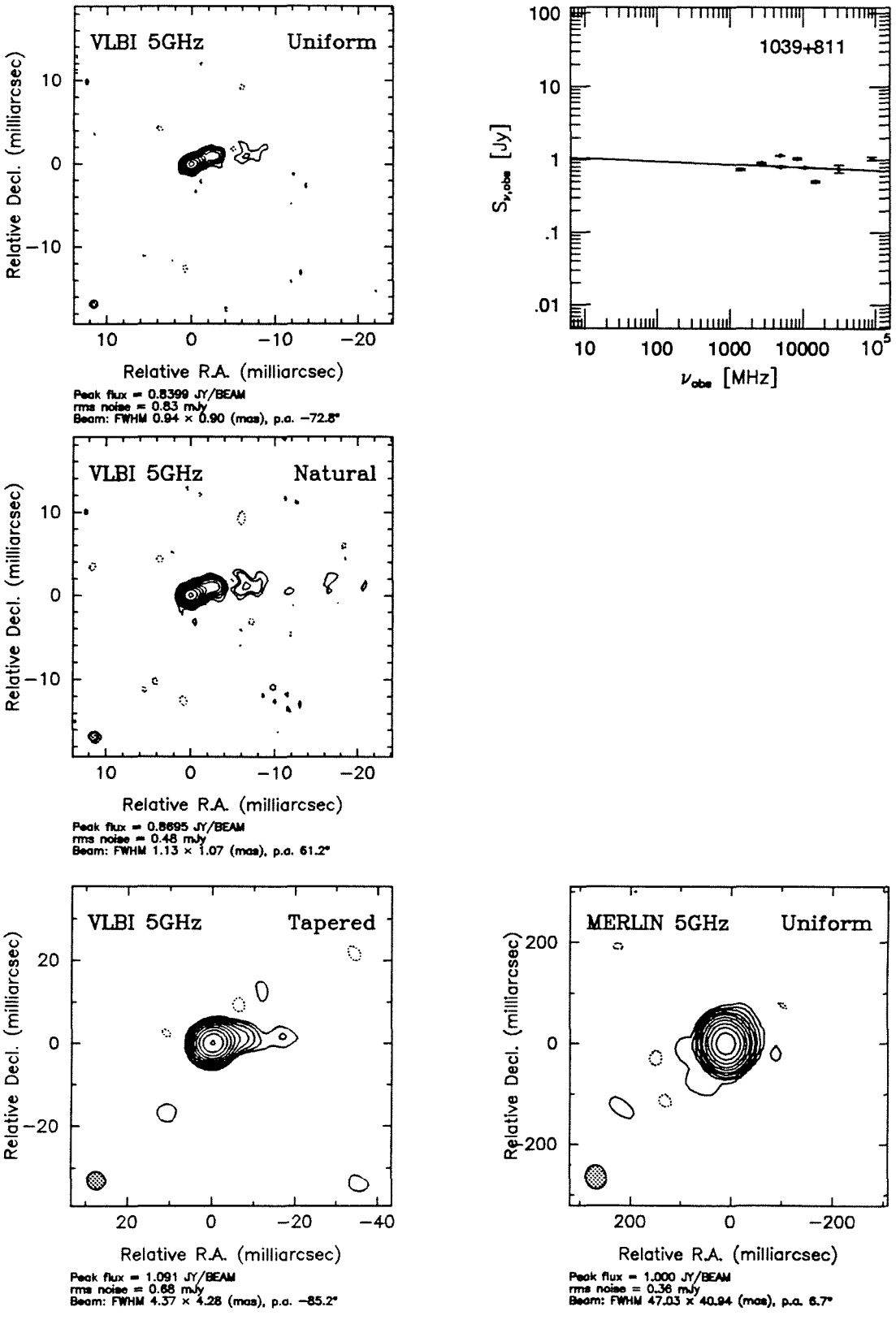

Figure 3.4.30. The maps and spectrum for 1039+811

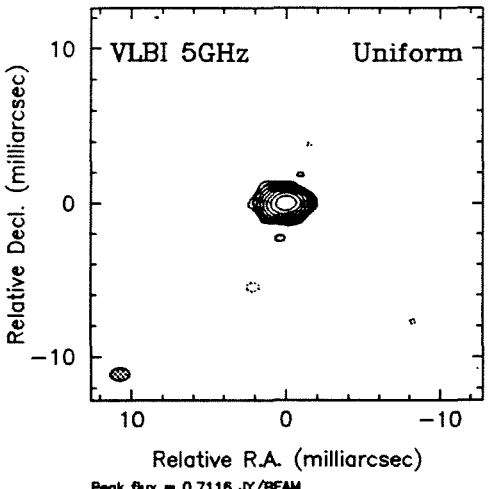

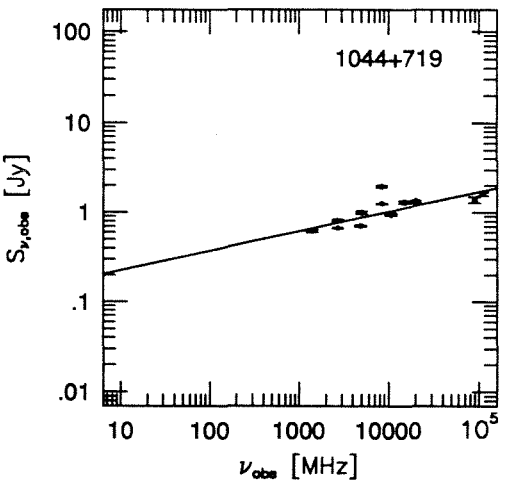

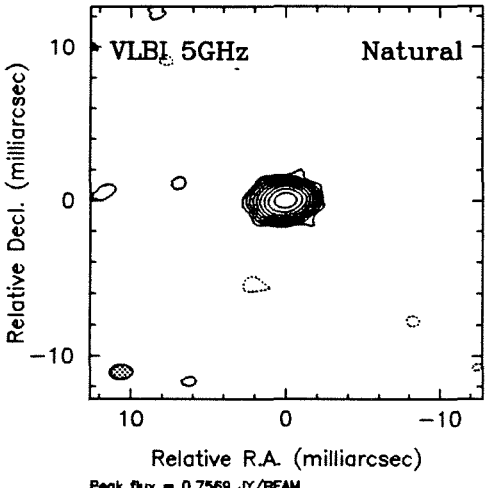

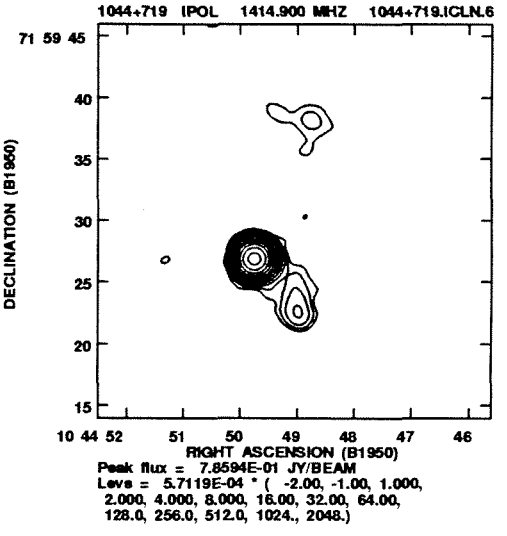

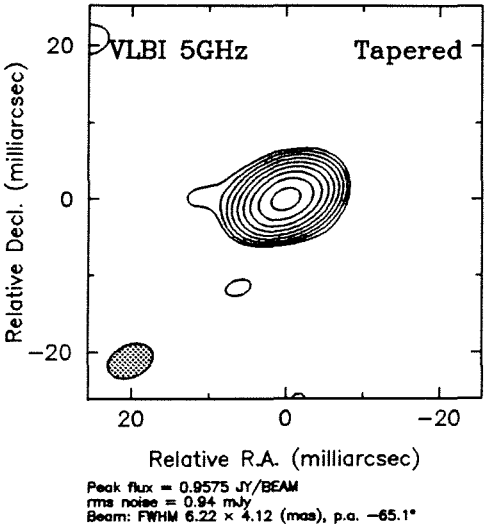

Figure 3.4.31. The maps and spectrum for 1044+719

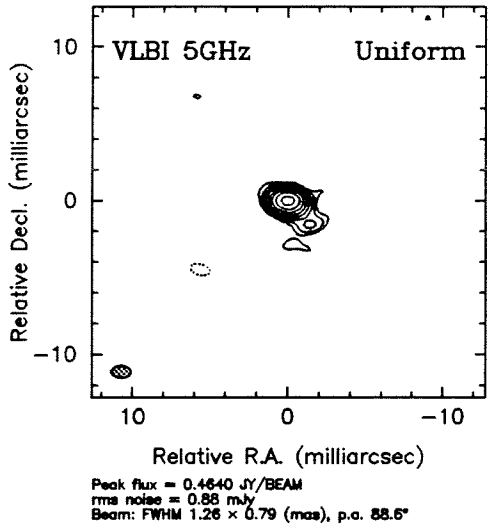

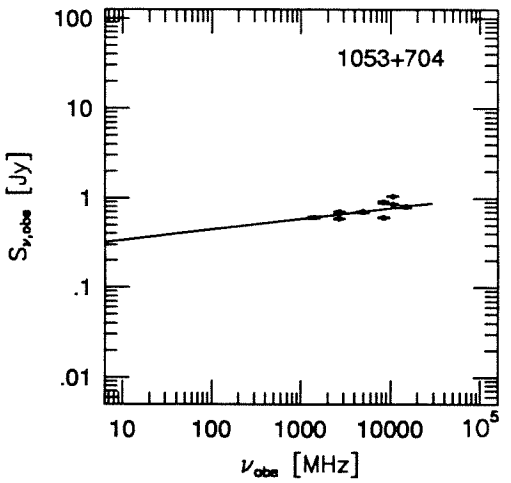

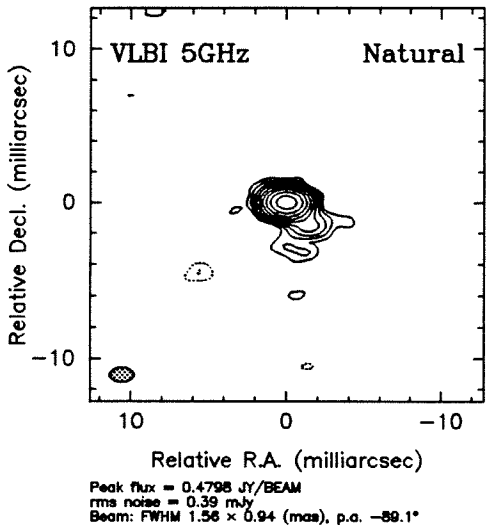

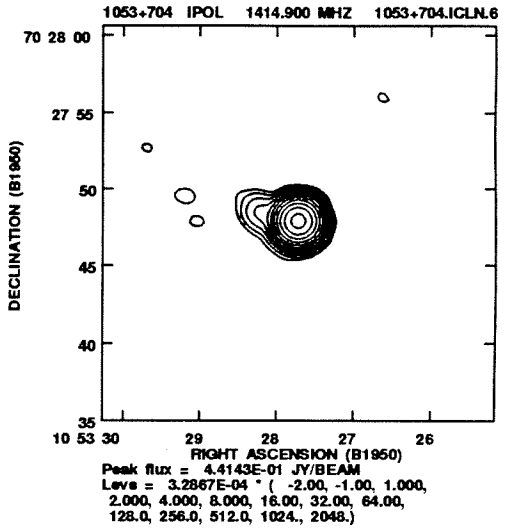

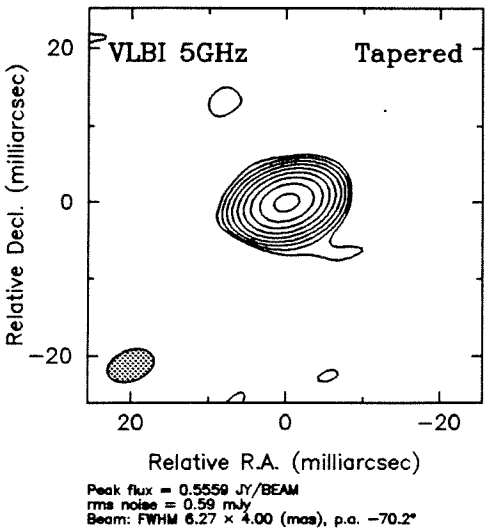

Figure 3.4.32. The maps and spectrum for 1053+704

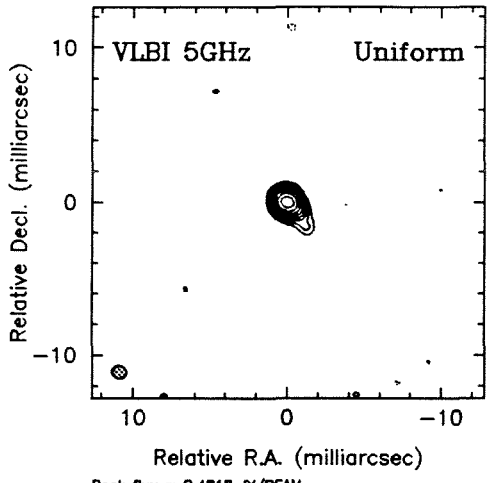

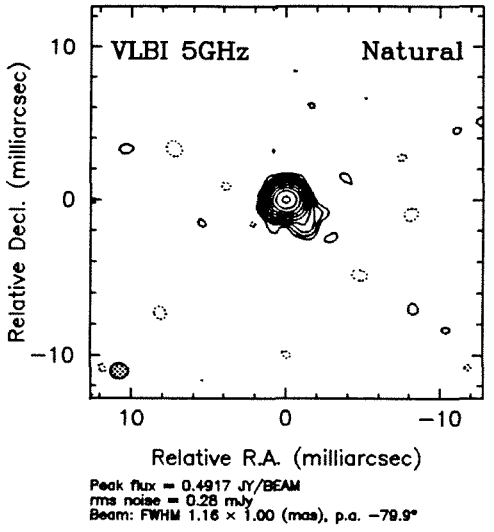

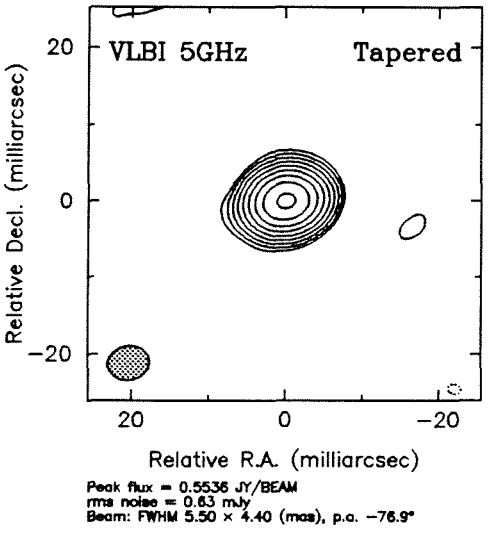

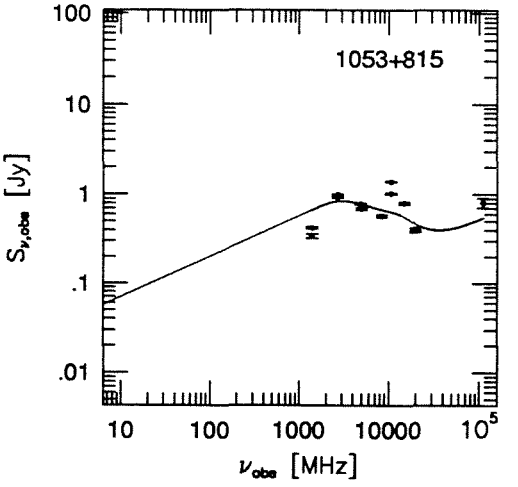

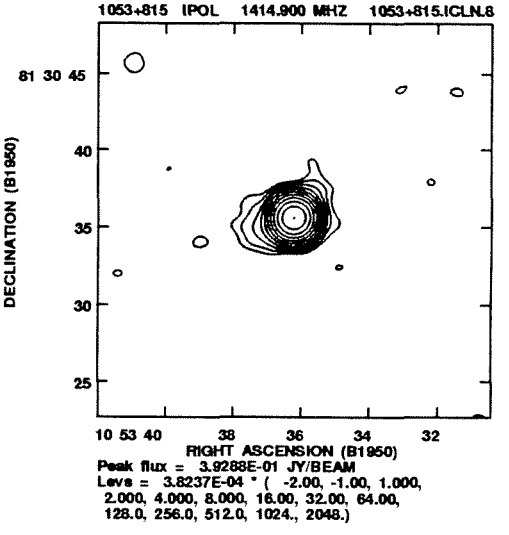

Figure 3.4.33. The maps and spectrum for 1053+815

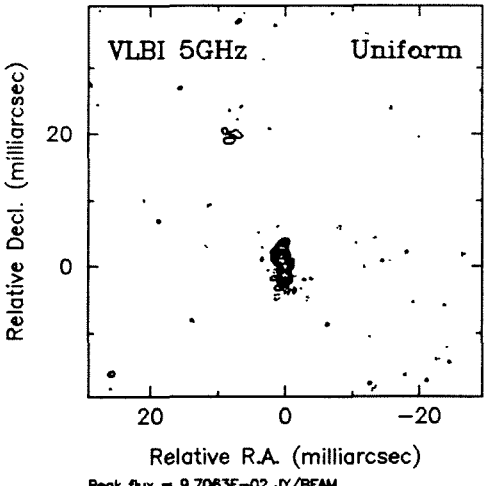

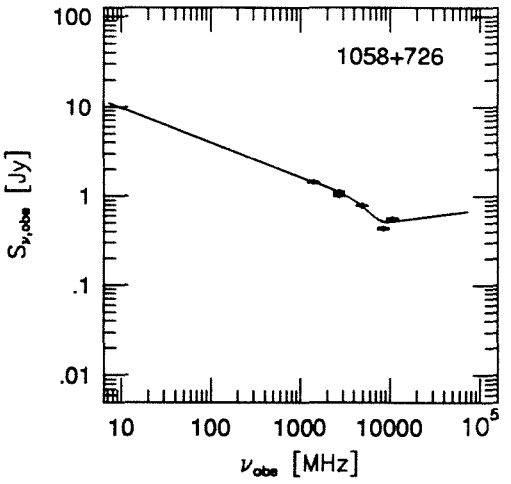

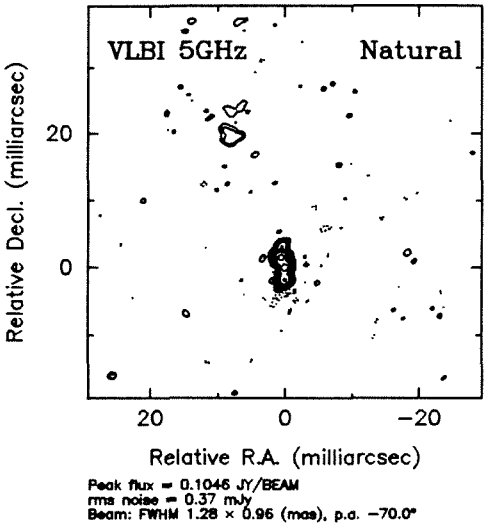

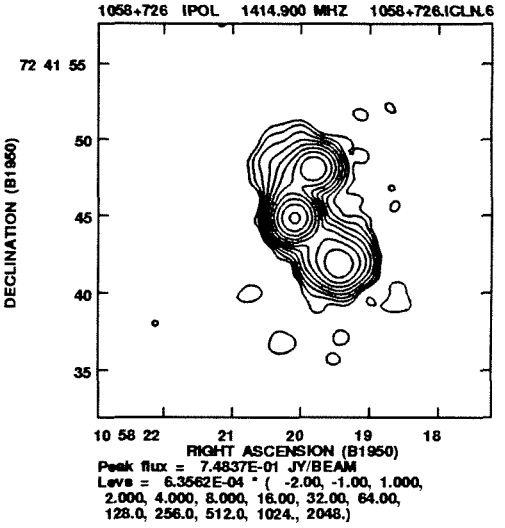

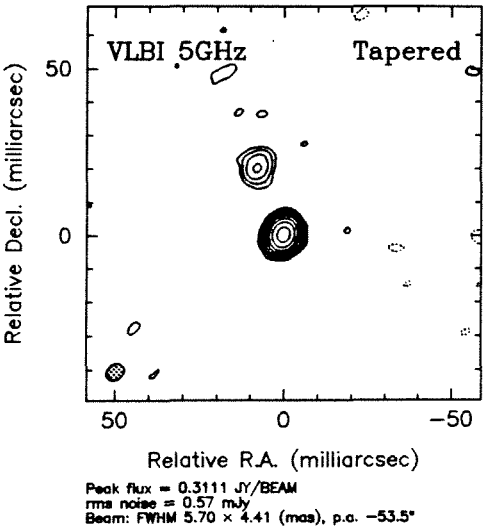

Figure 3.4.34. The maps and spectrum for 1058+726

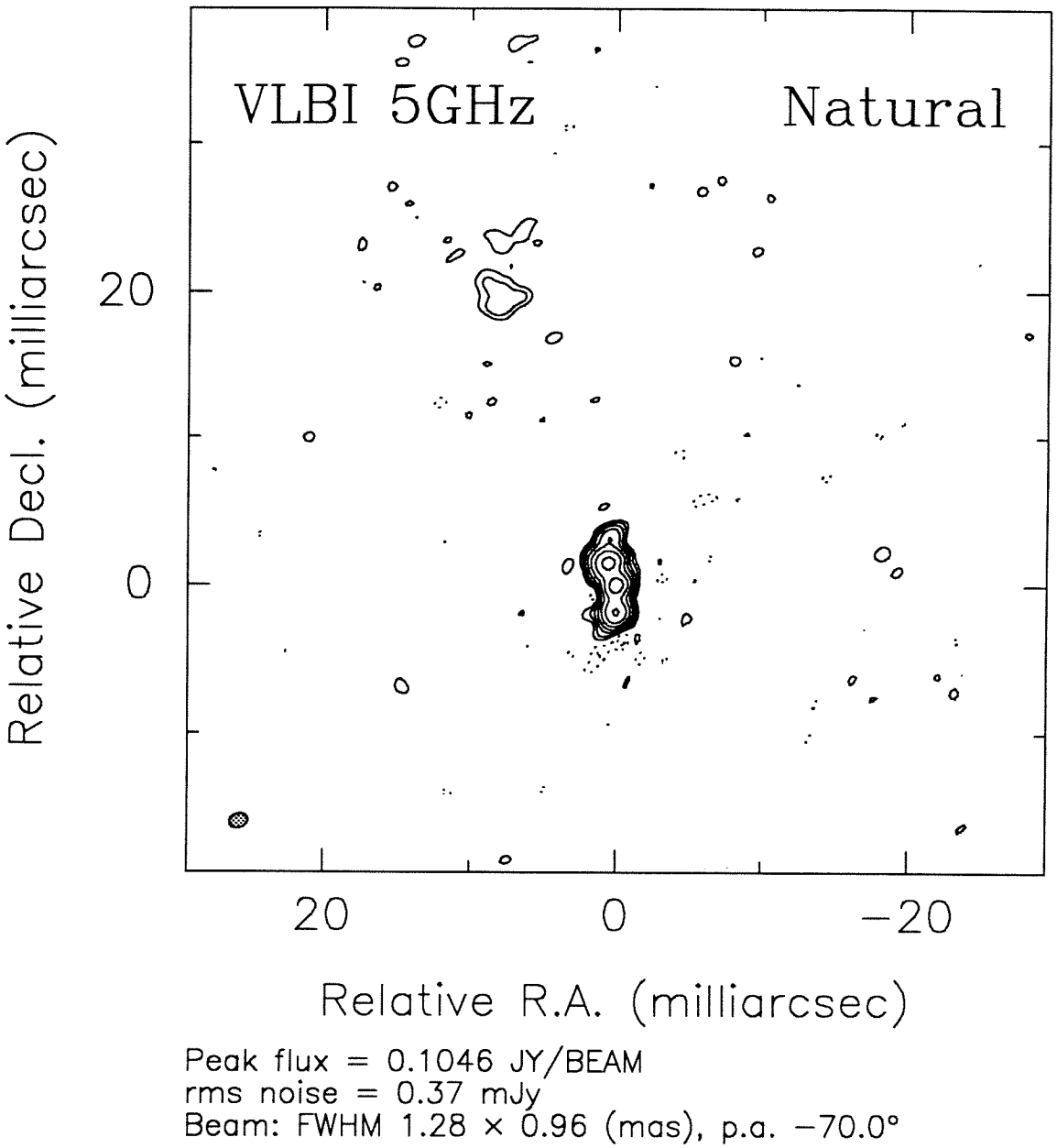

Figure 3.4.34. The VLBI map of 1058+726

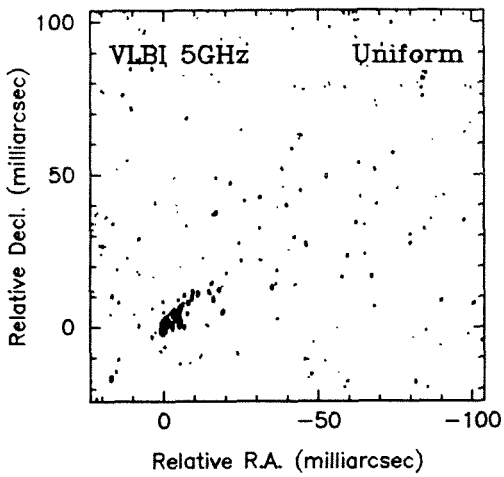

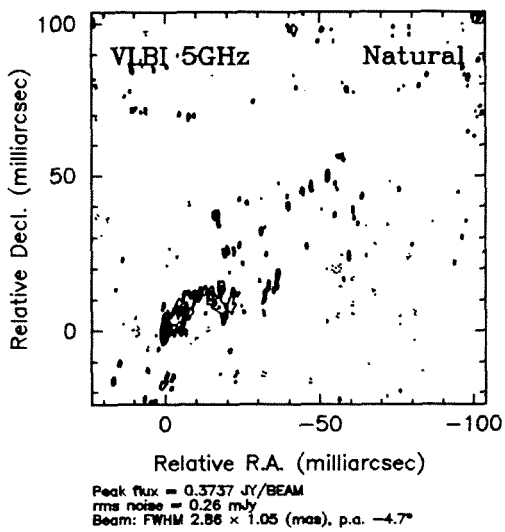

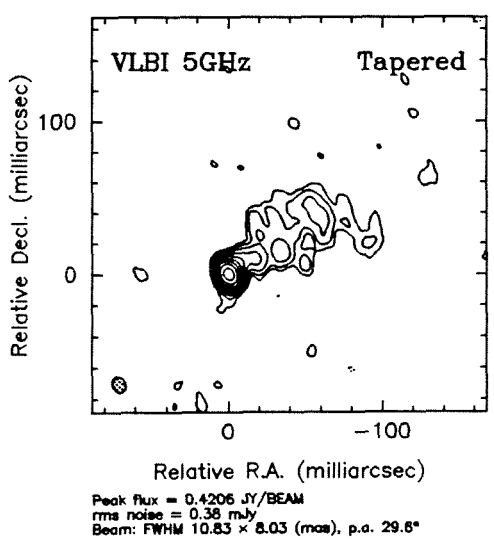

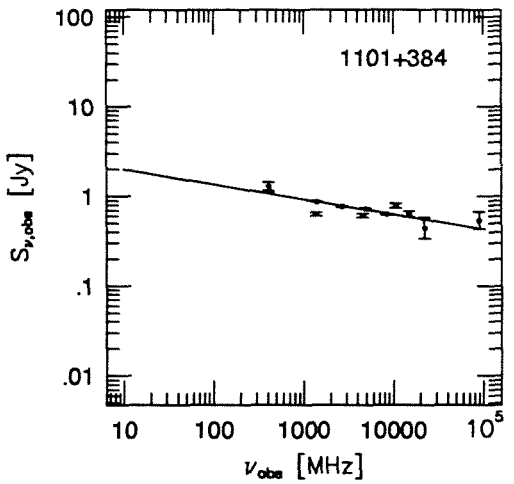

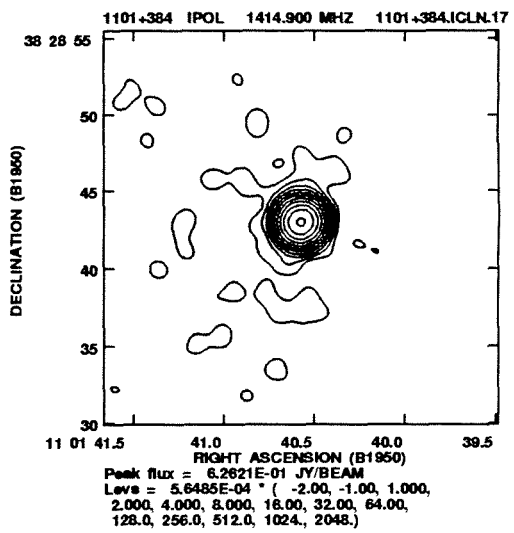

Figure 3.4.34. The maps and spectrum for 1101+384

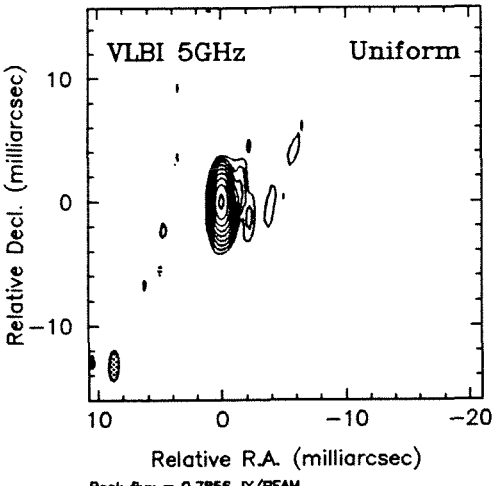

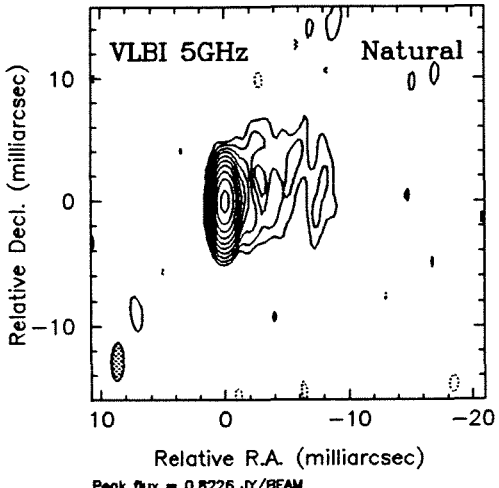

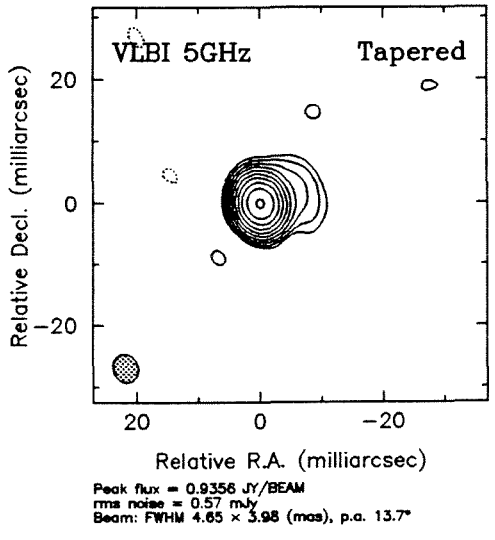

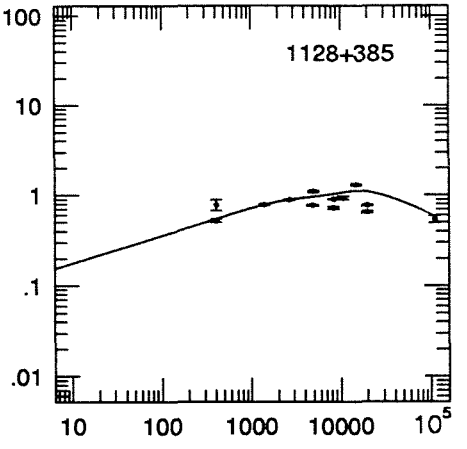

Figure 3.4.35. The maps and spectrum for 1128+385

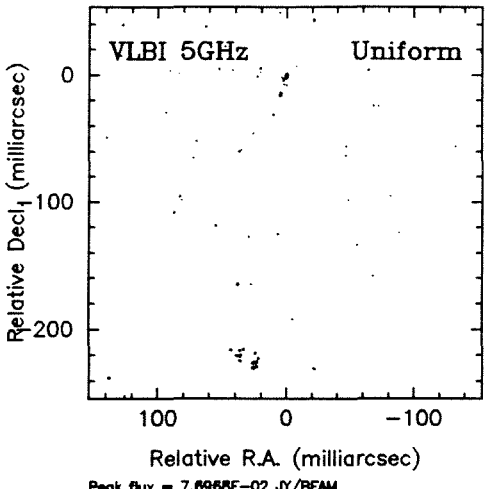

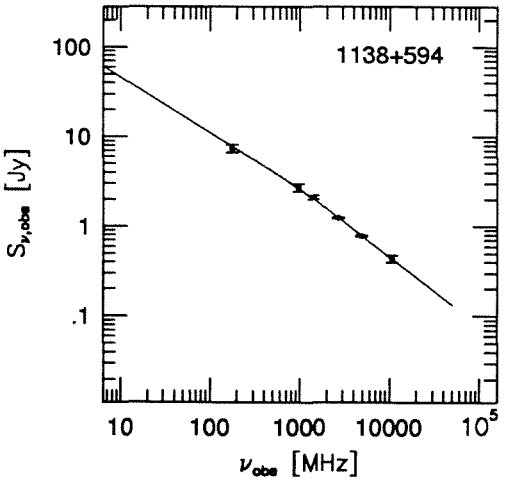

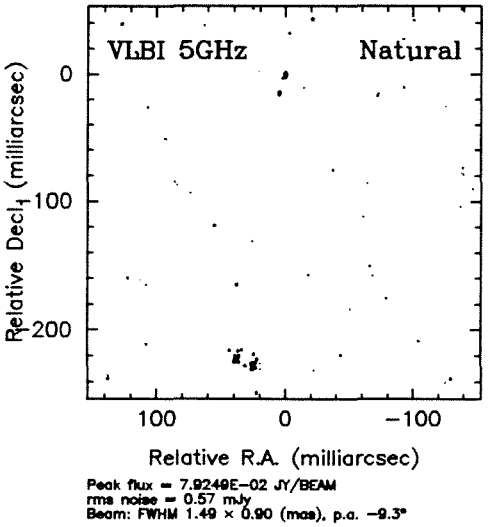

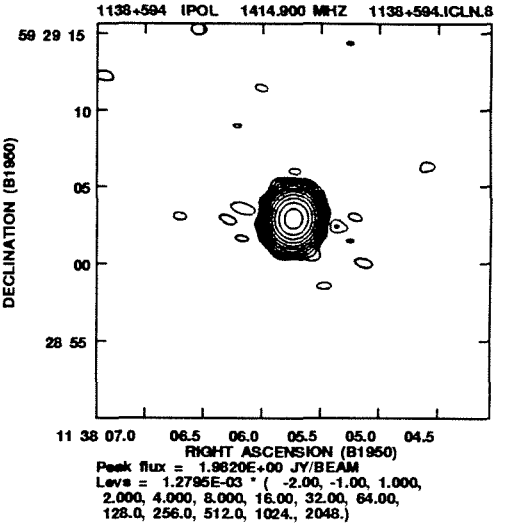

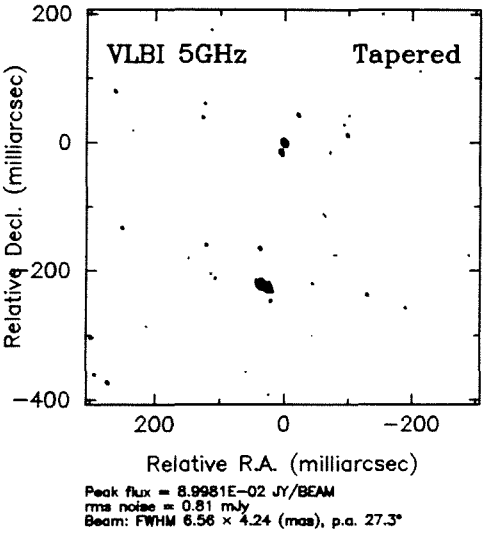

Figure 3.4.36. The maps and spectrum for 1138+594

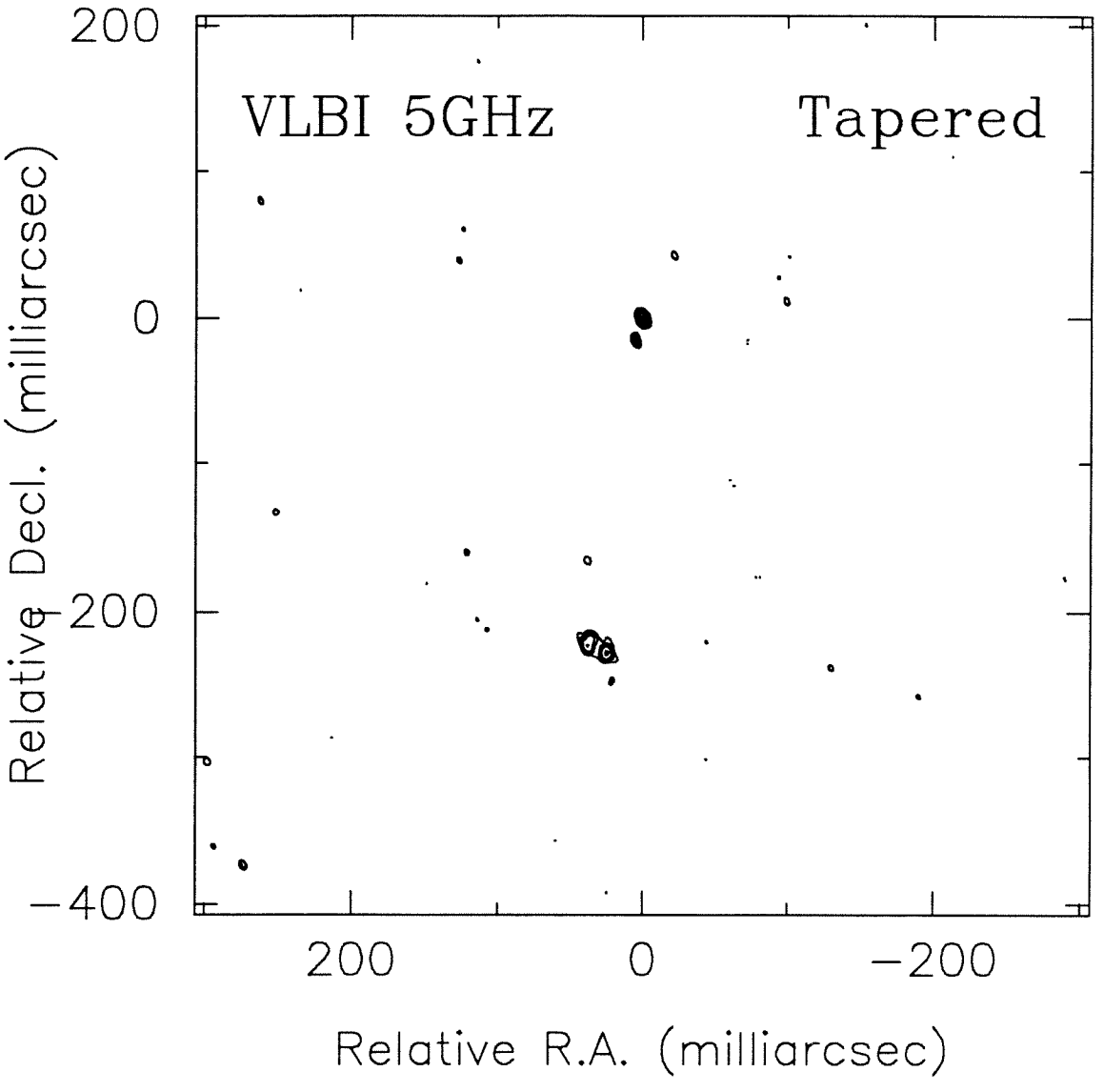

Figure 3.4.36. The VLBI map of 1138+594

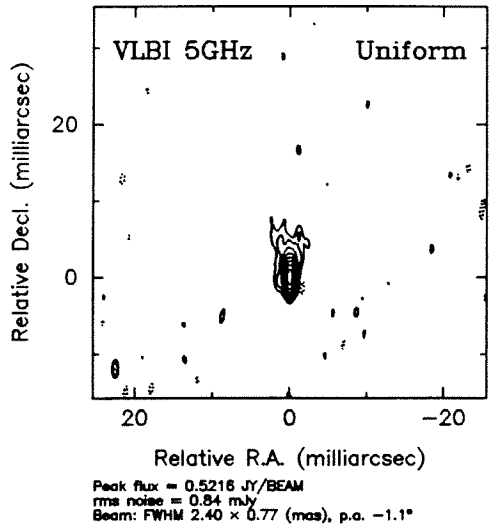

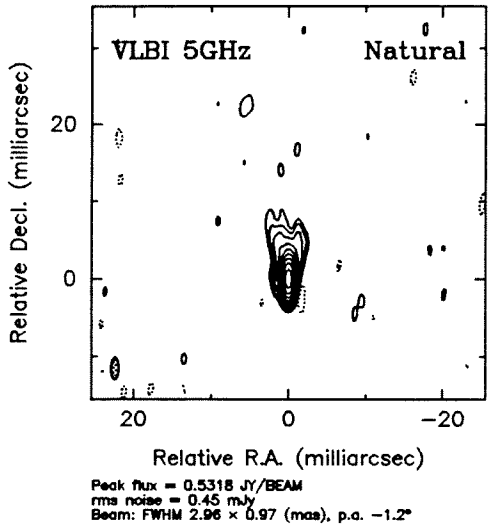

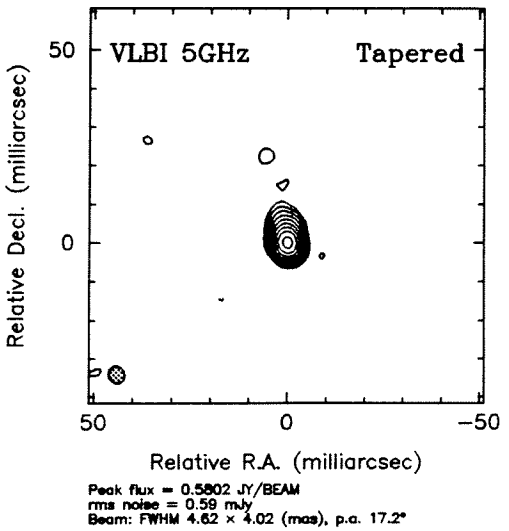

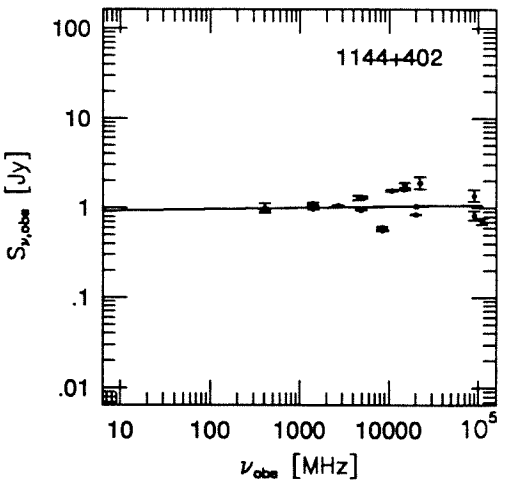

Figure 3.4.36. The maps and spectrum for 1144+402

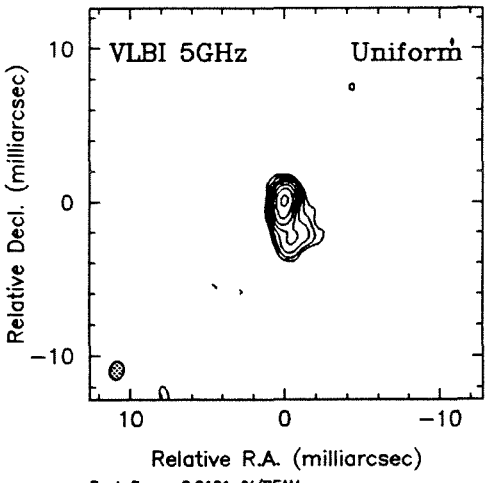

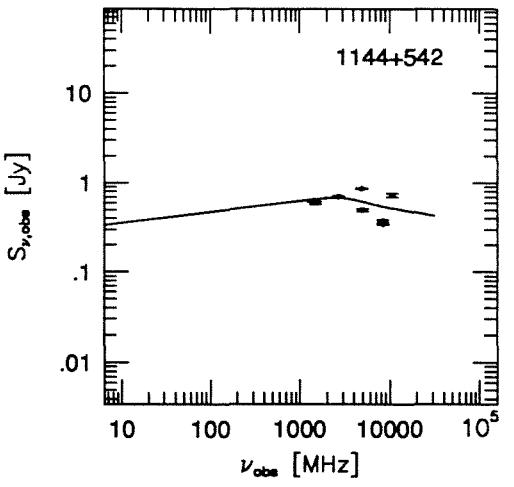

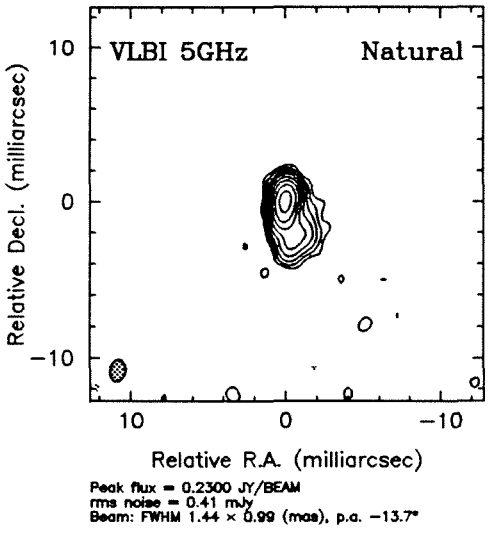

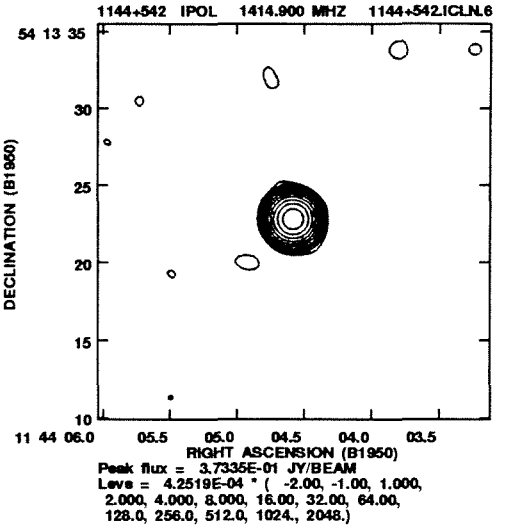

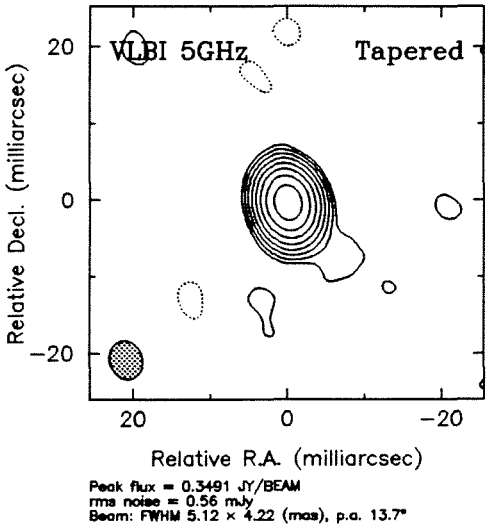

Figure 3.4.37. The maps and spectrum for 1144+542

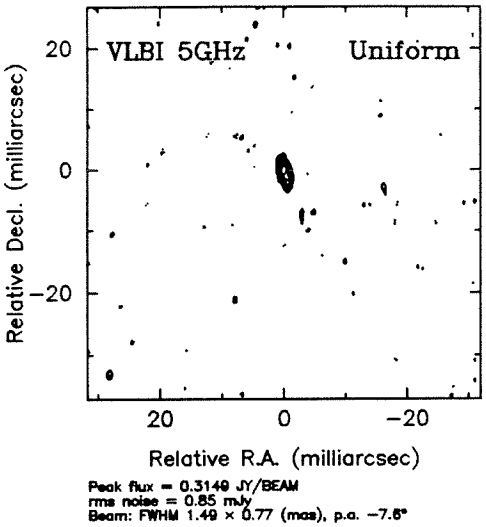

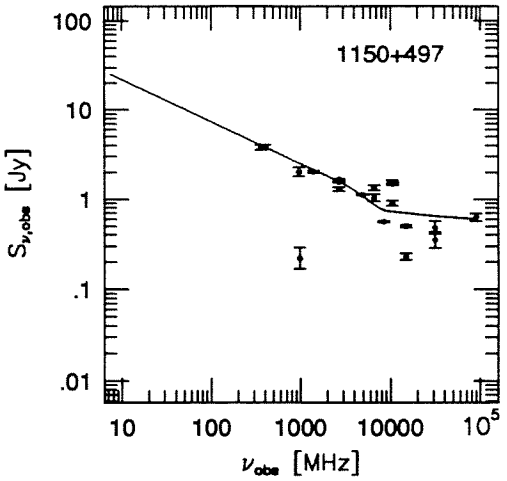

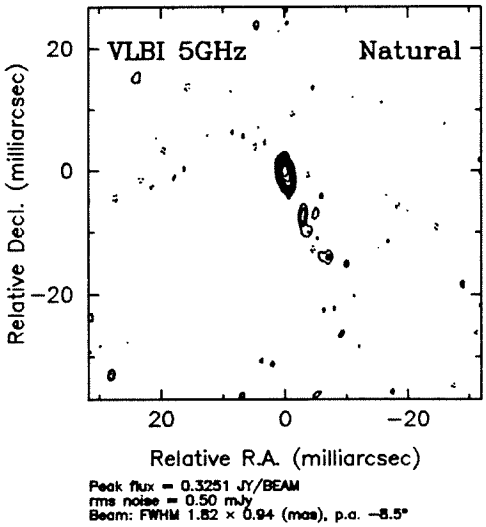

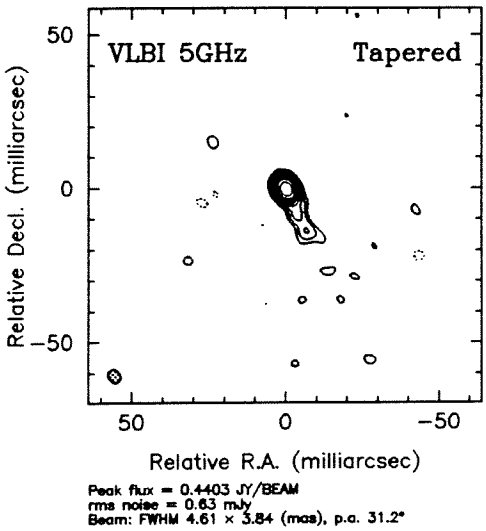

Figure 3.4.38. The maps and spectrum for 1150+497

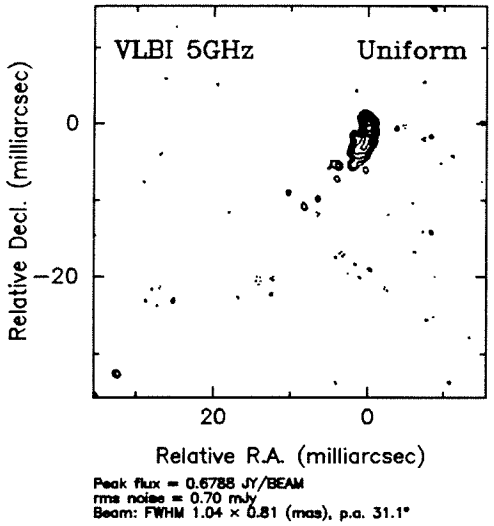

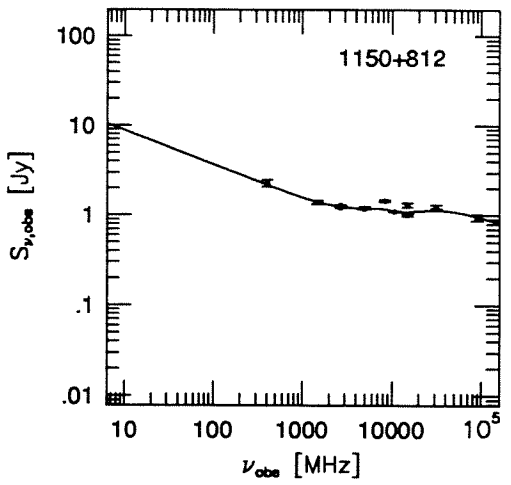

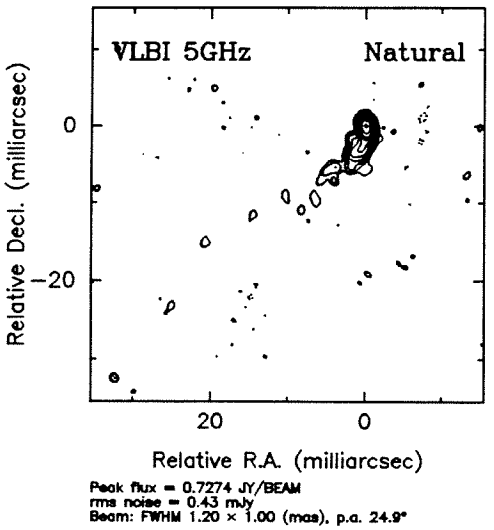

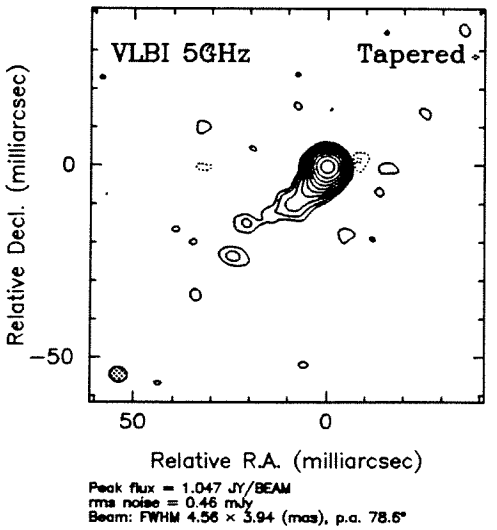

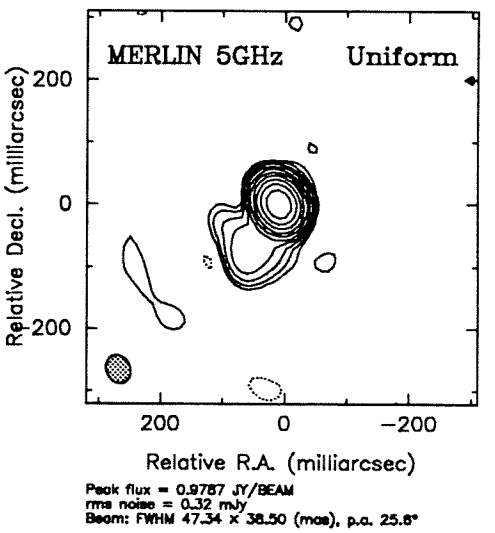

Figure 3.4.39. The maps and spectrum for 1150+812

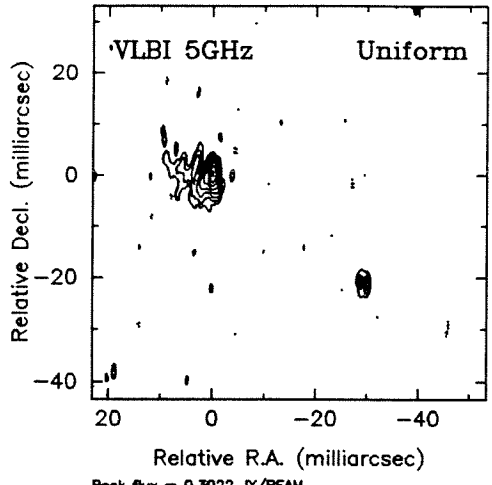

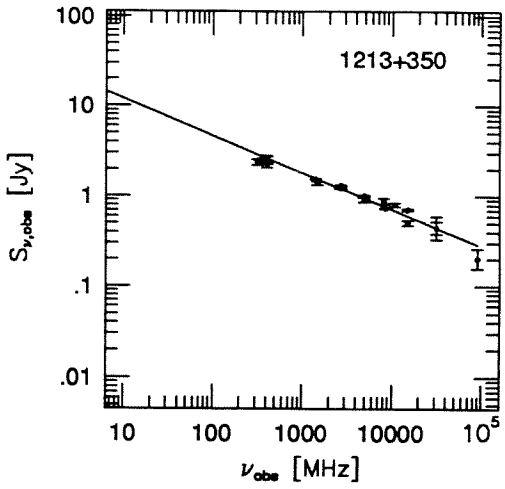

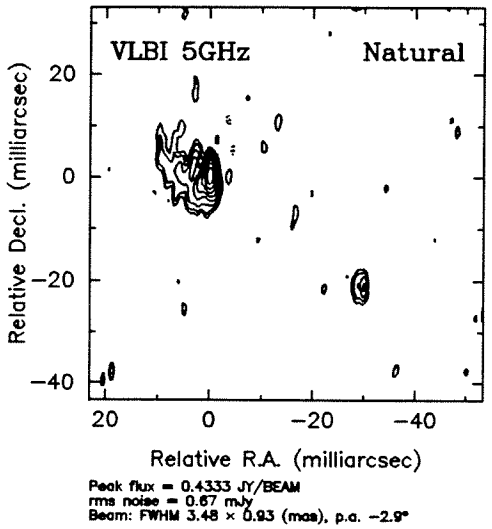

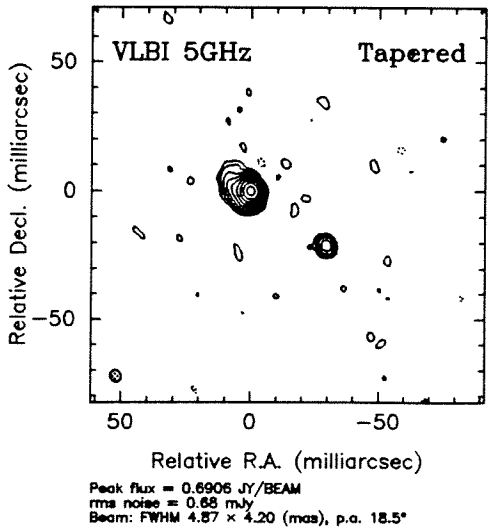

Figure 3.4.40. The maps and spectrum for 1213+350

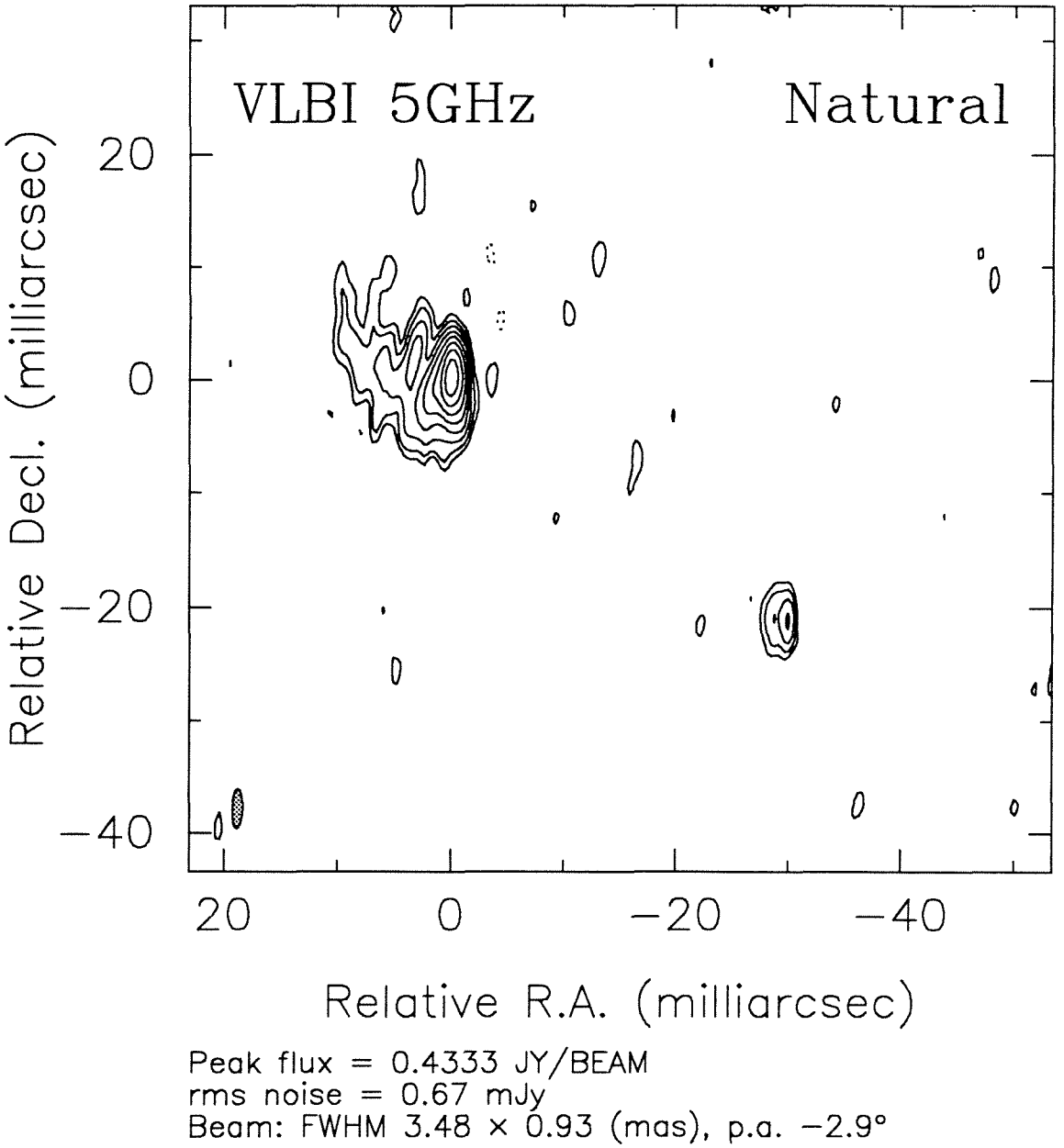

Figure 3.4.40. The VLBI map of 1213+350

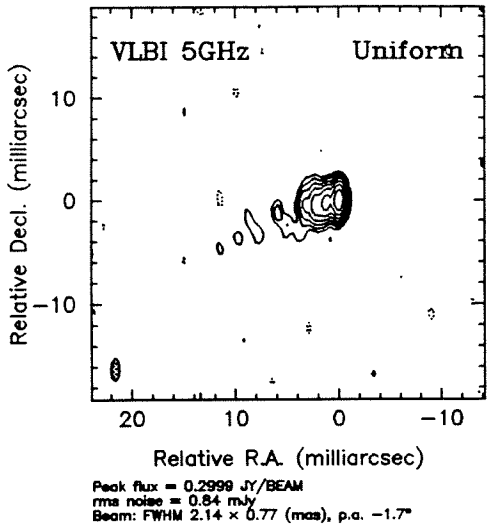

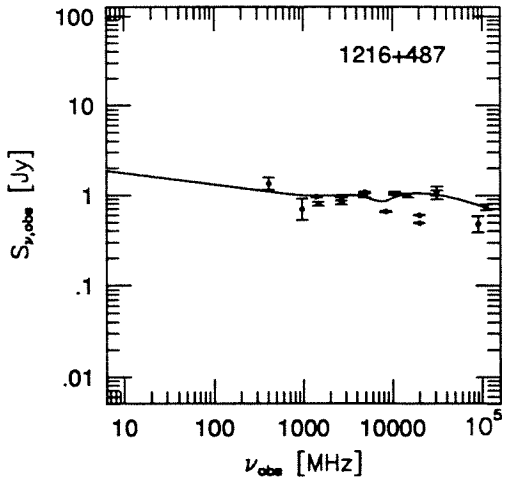

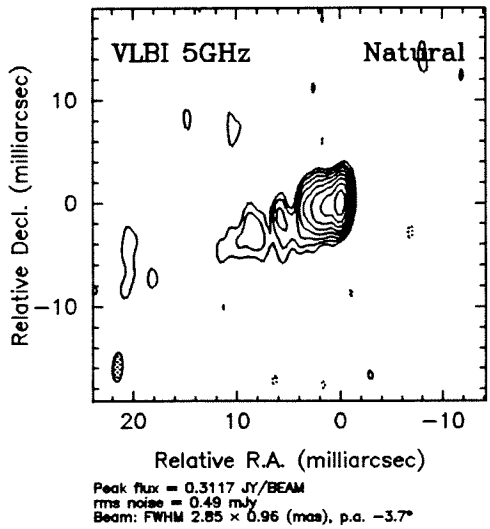

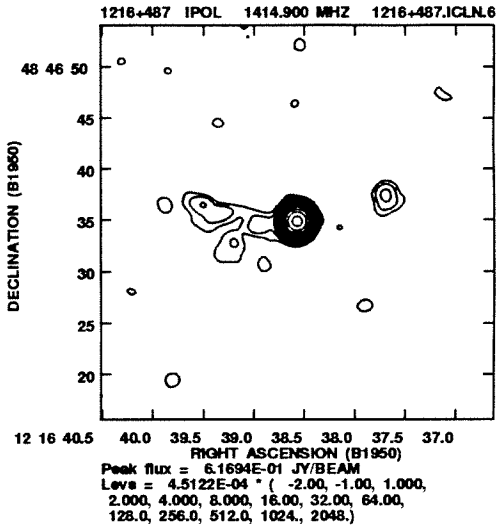

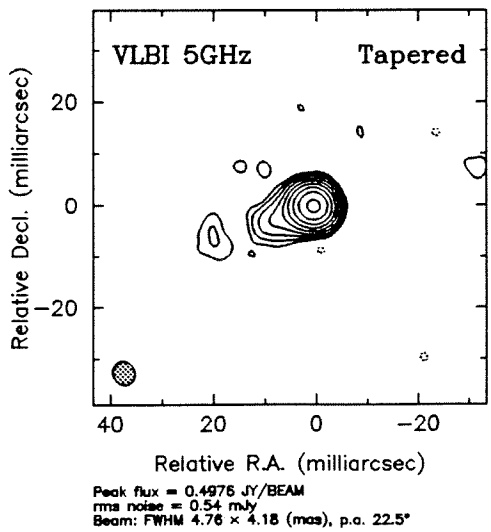

Figure 3.4.40. The maps and spectrum for 1216+487

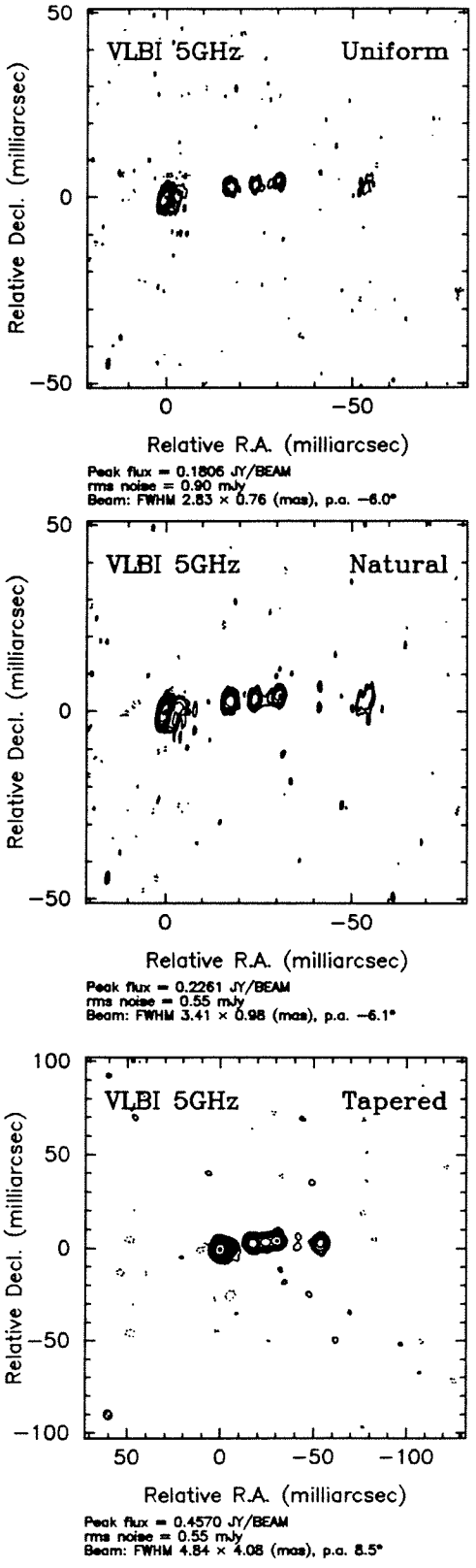

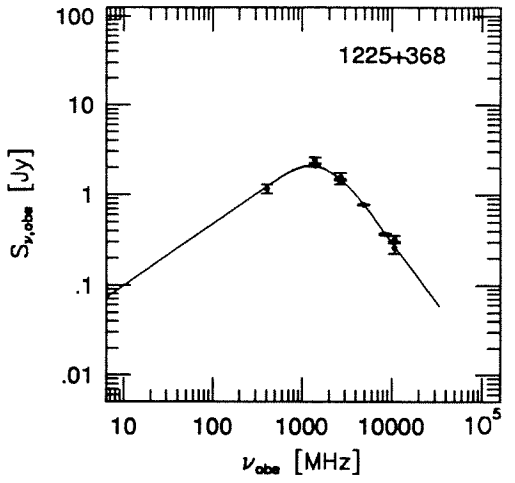

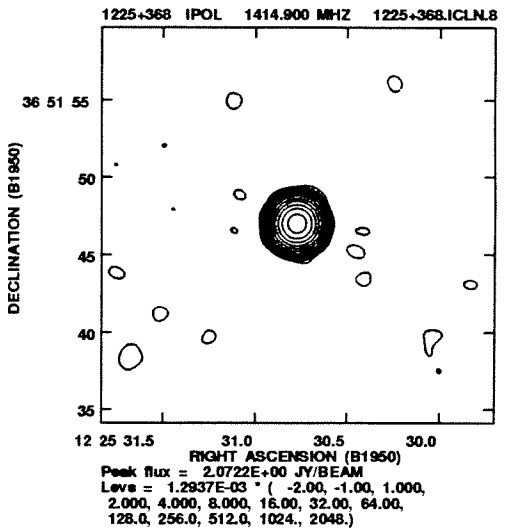

Figure 3.4.41. The maps and spectrum for 1225+368

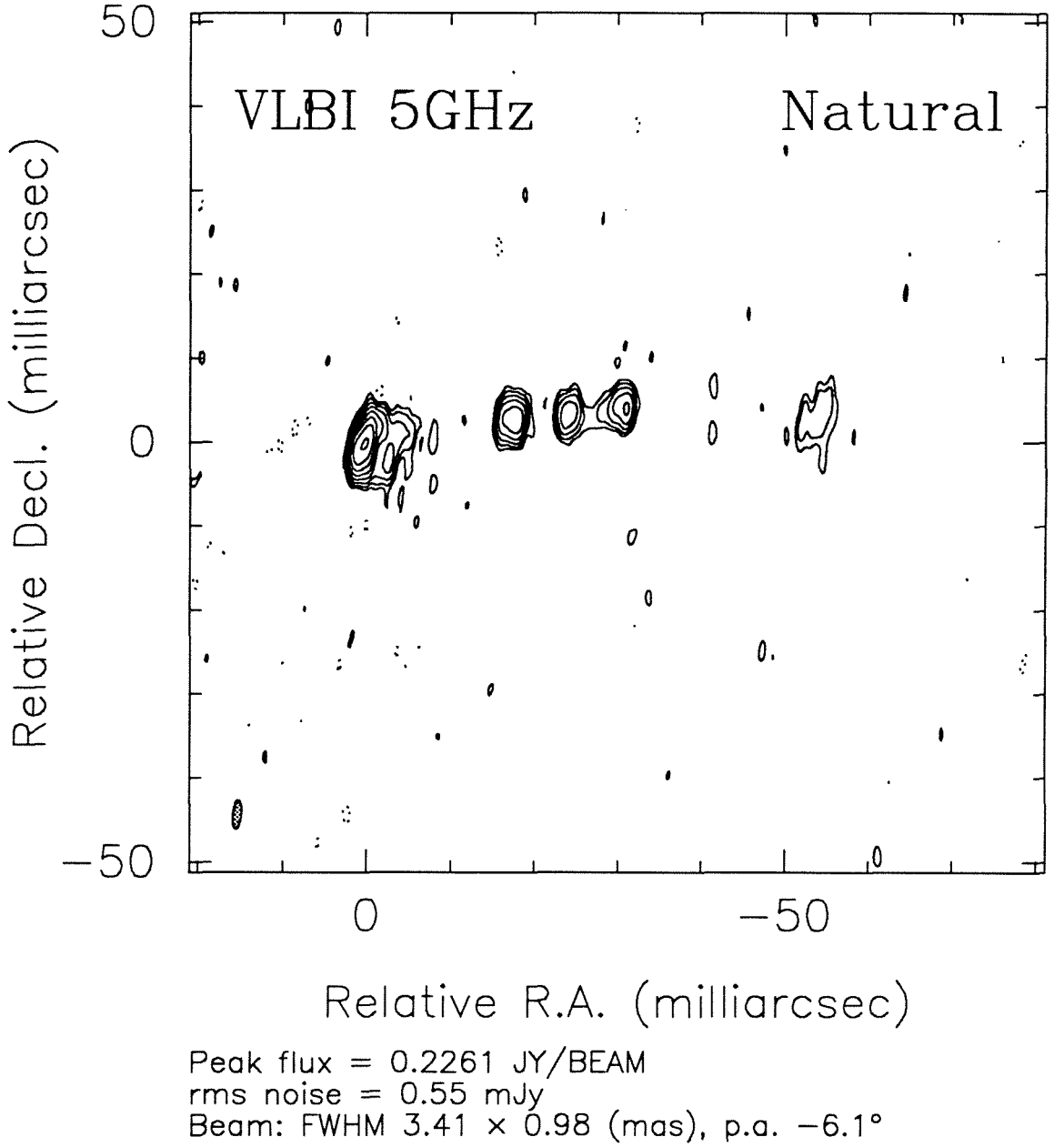

Figure 3.4.41. The VLBI map of 1225+368

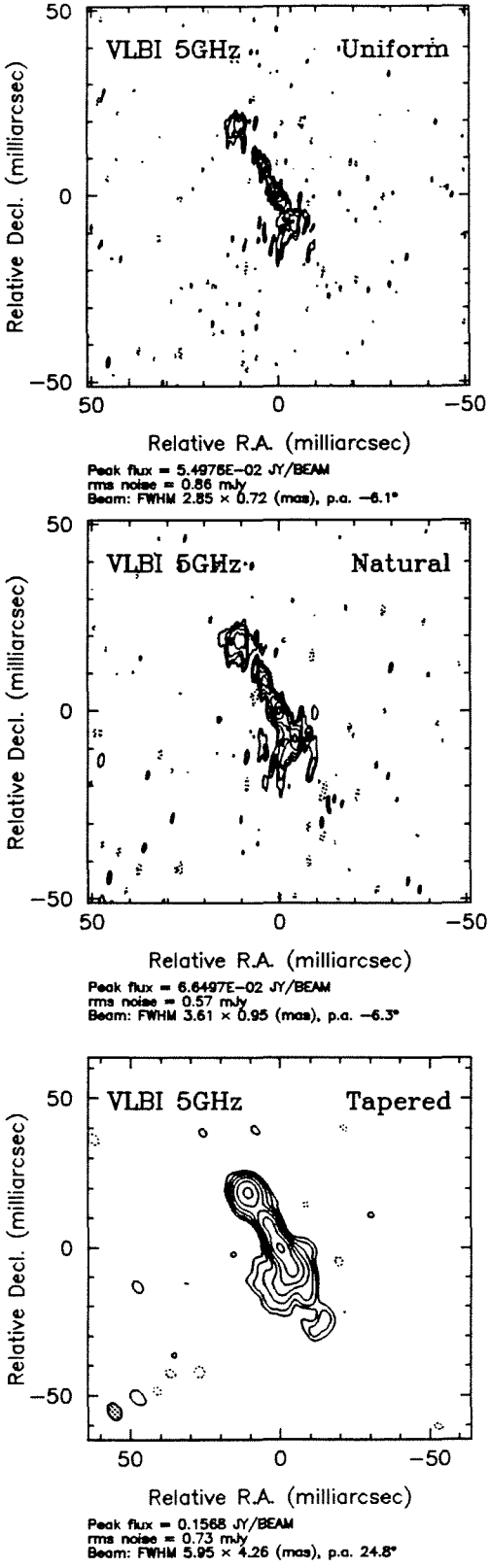

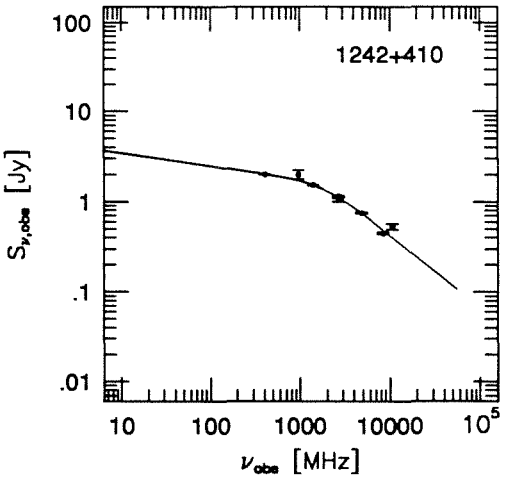

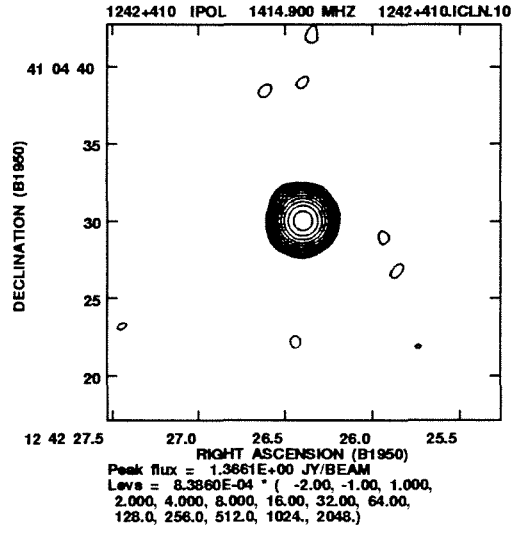

Figure 3.4.41. The maps and spectrum for 1242+410

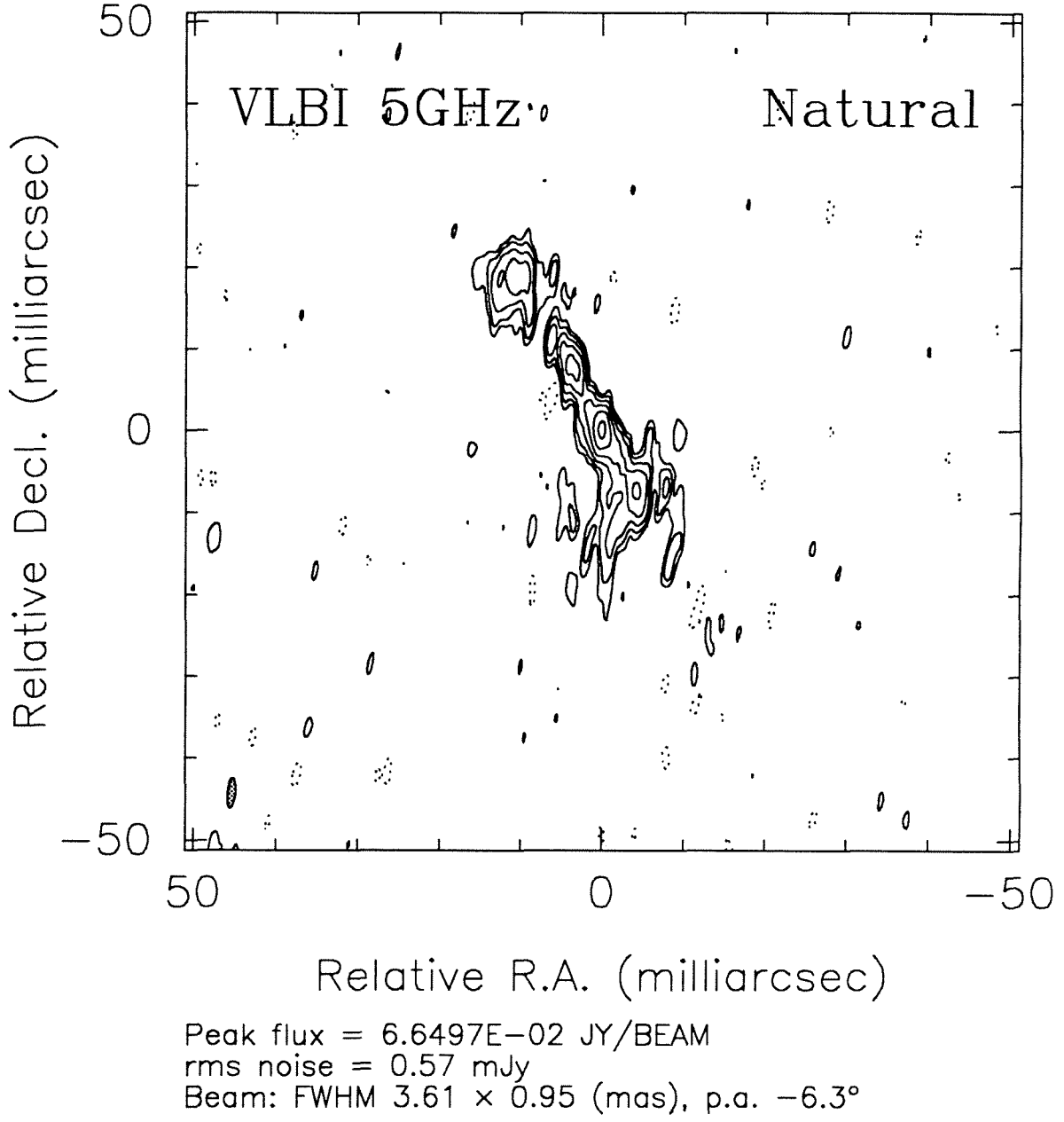

Figure 3.4.41. The VLBI map of 1242+410

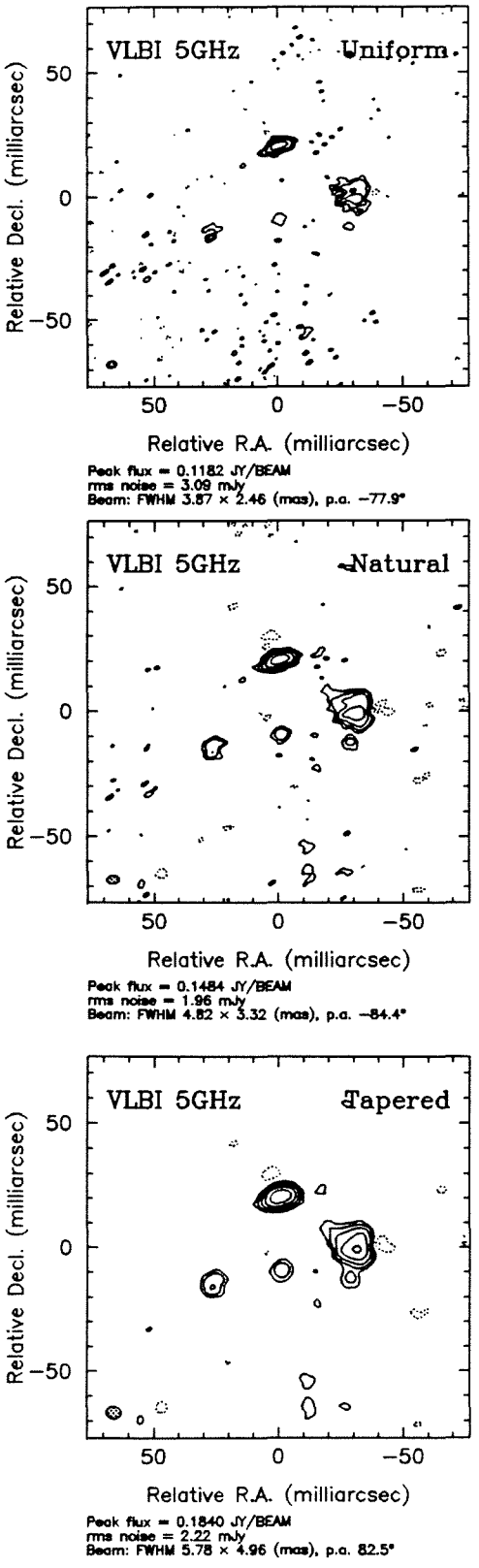

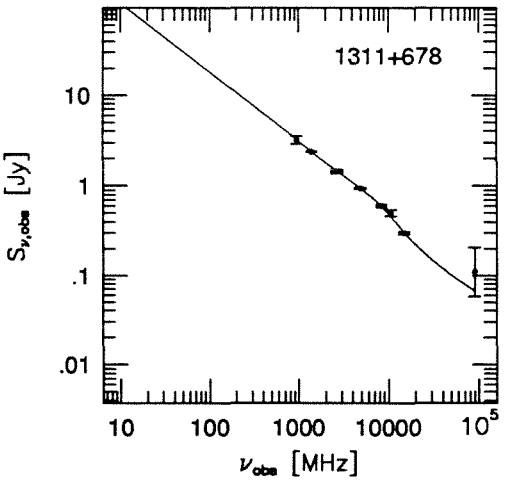

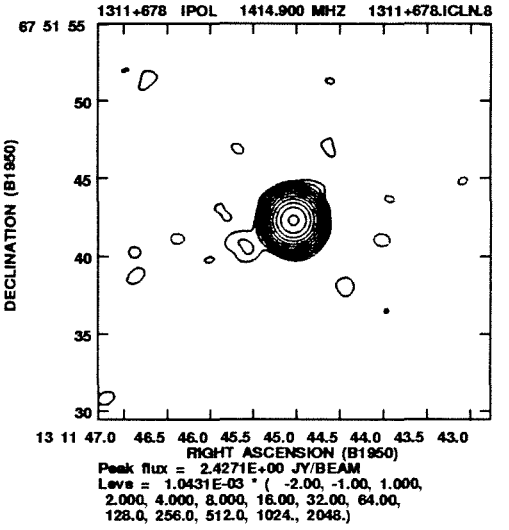

Figure 3.4.41. The maps and spectrum for 1311+678

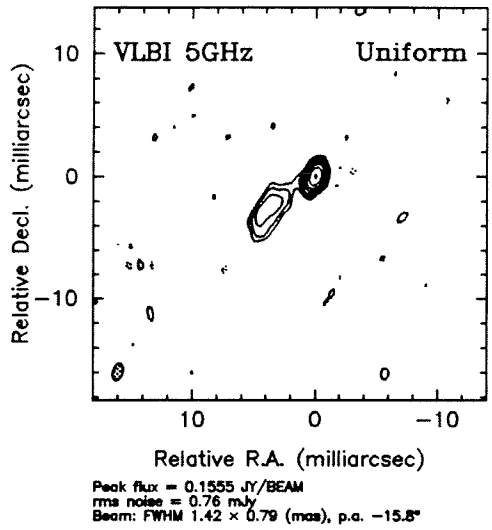

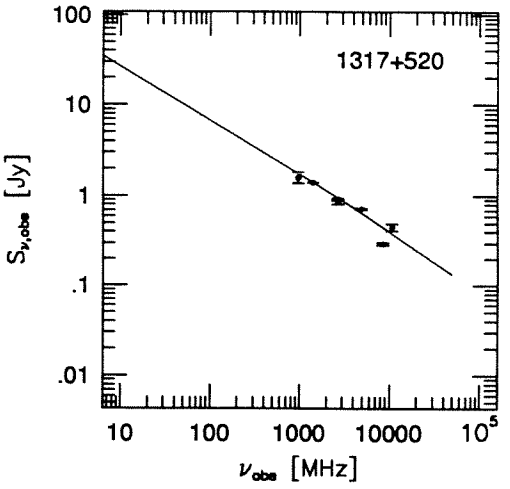

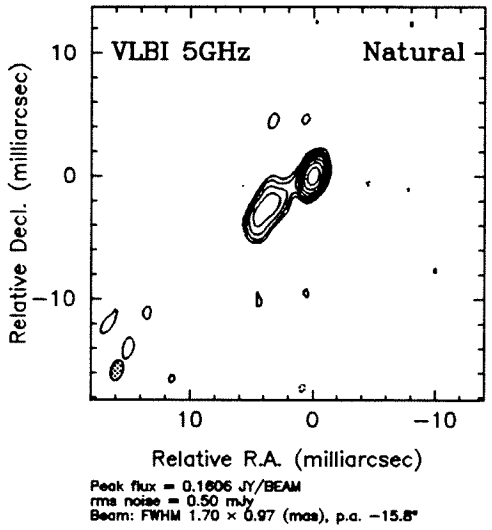

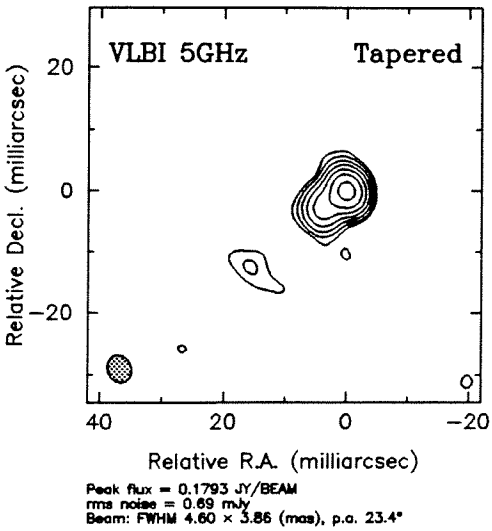

Figure 3.4.42. The maps and spectrum for 1317+520

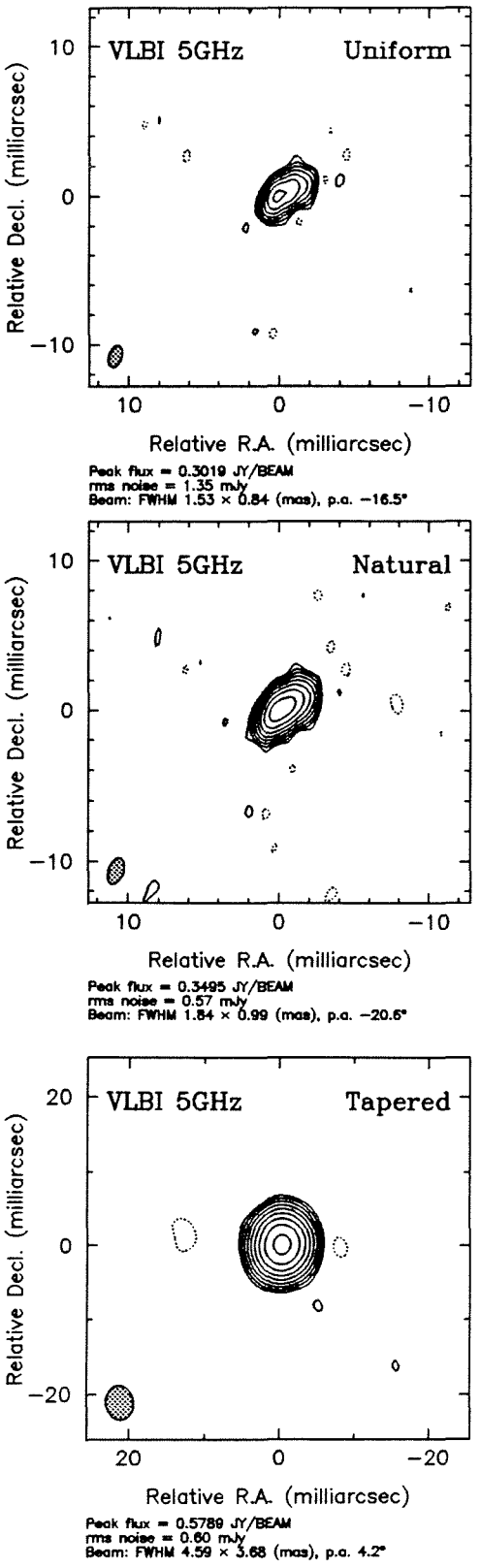

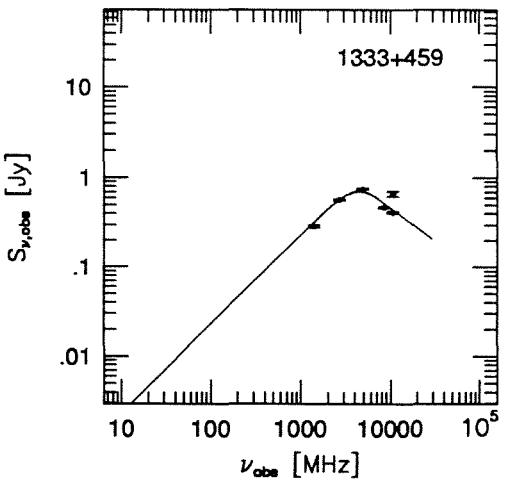

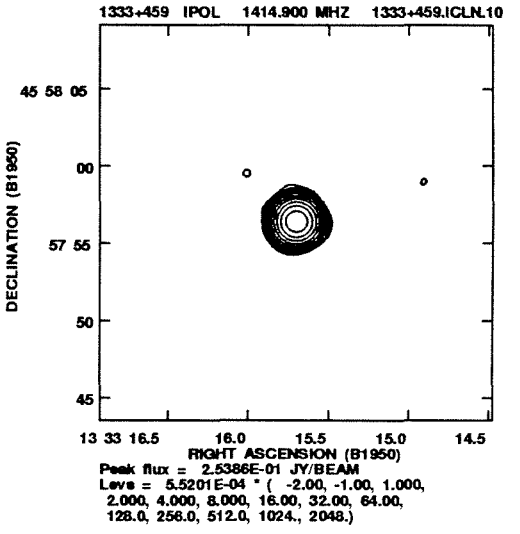

Figure 3.4.43. The maps and spectrum for 1333+459

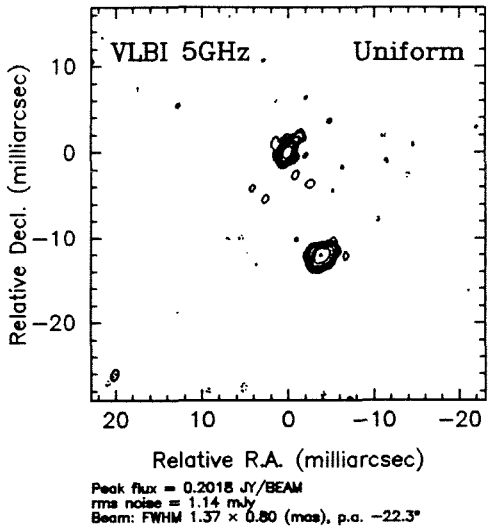

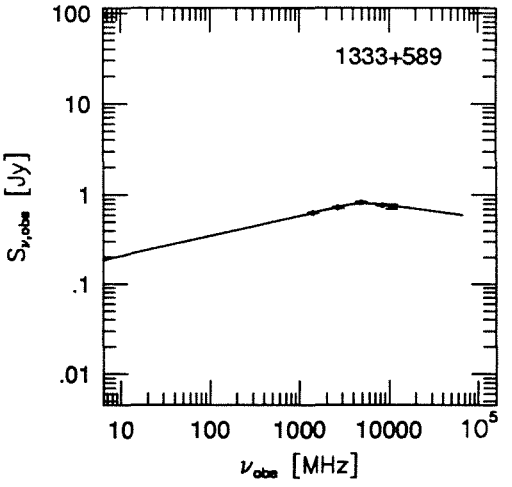

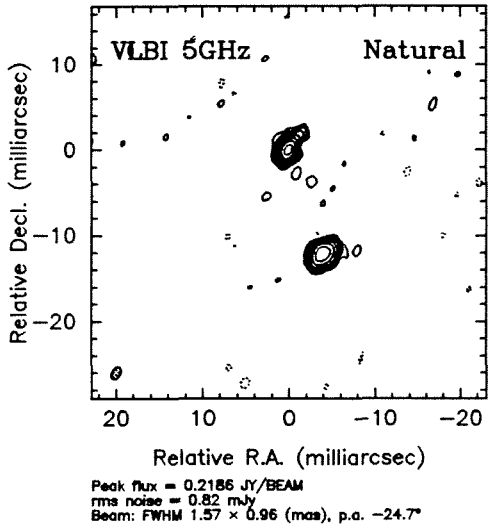

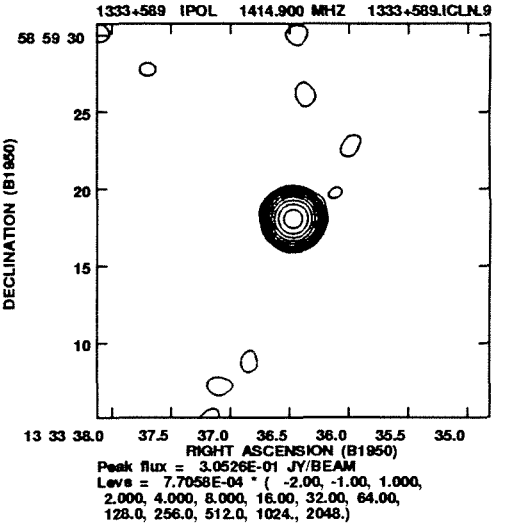

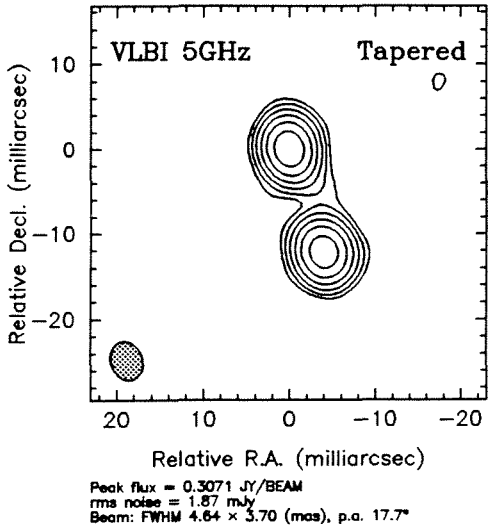

Figure 3.4.44. The maps and spectrum for 1333+589

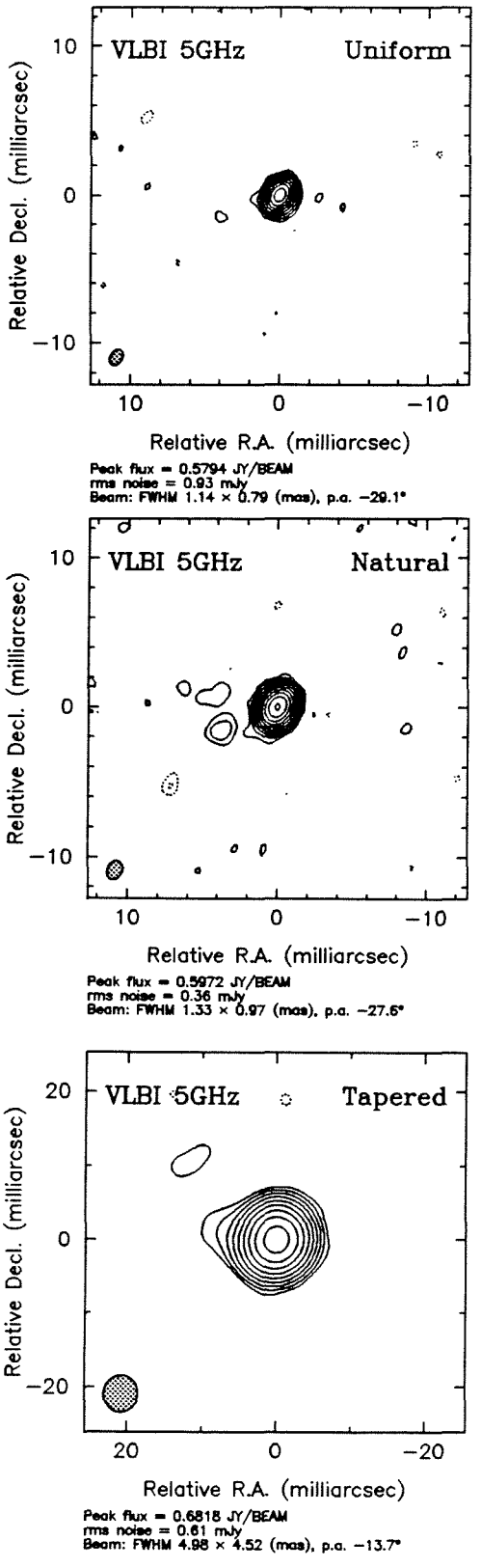

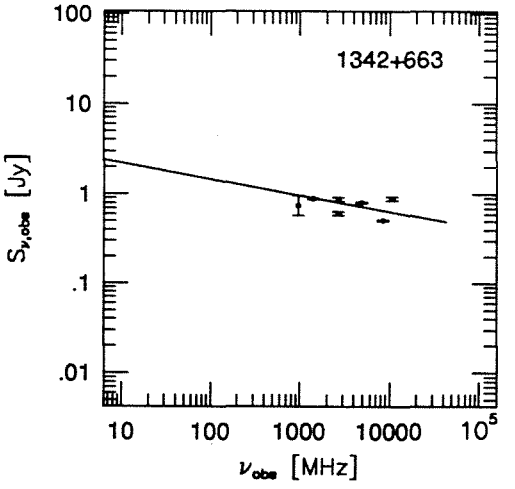

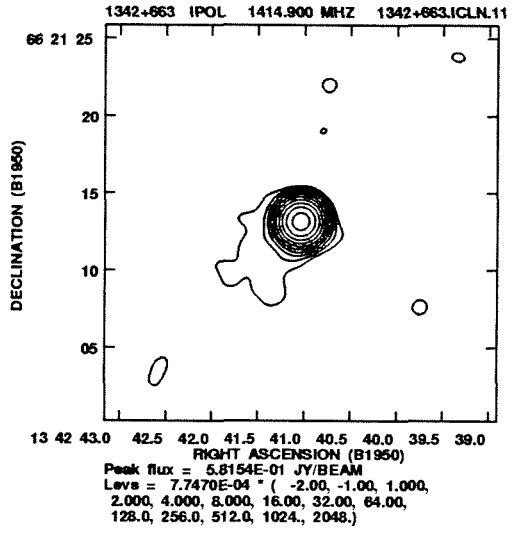

Figure 3.4.45. The maps and spectrum for 1342+663

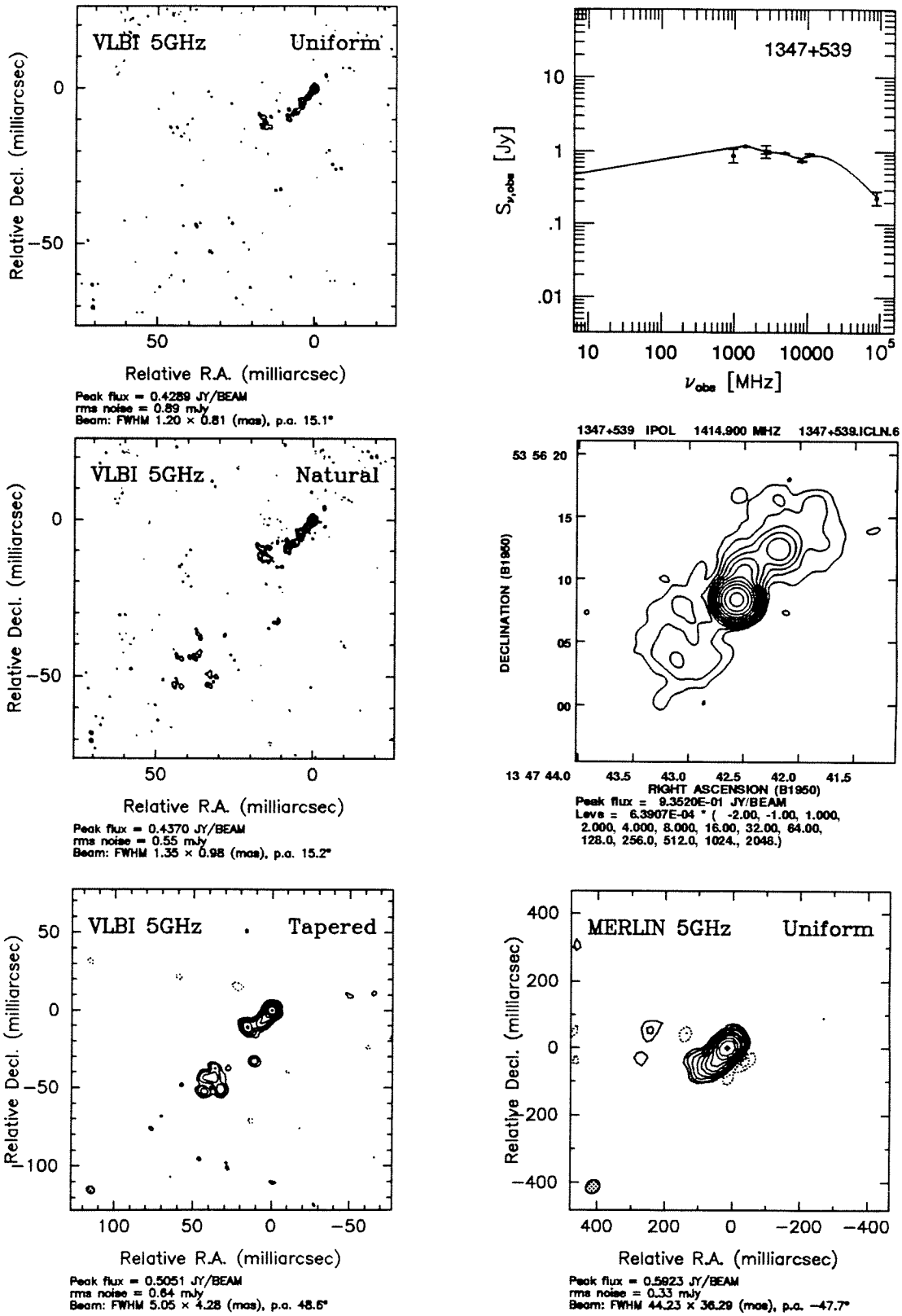

Figure 3.4.46. The maps and spectrum for 1347+539

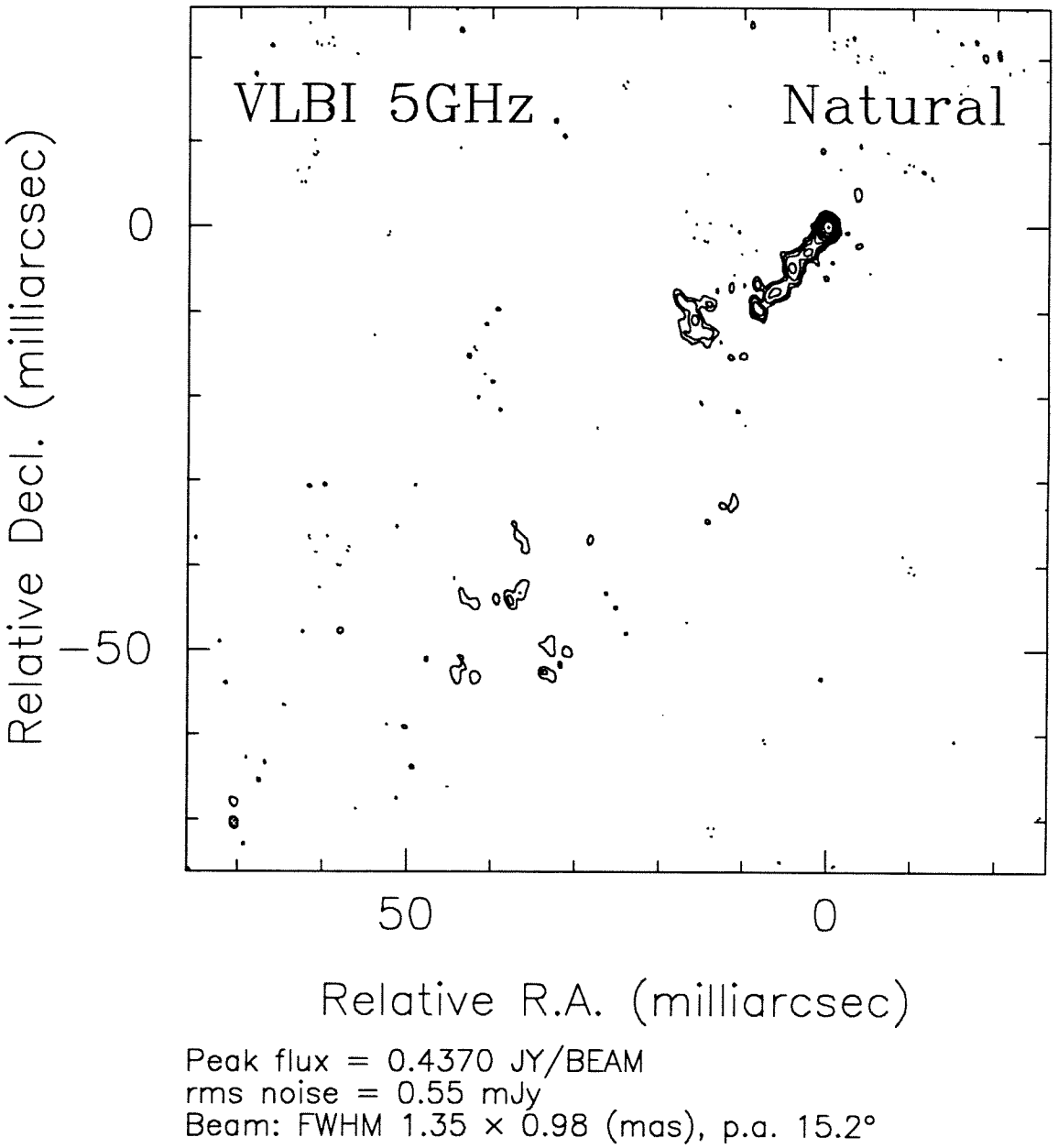

Figure 3.4.46. The VLBI map of 1347+539

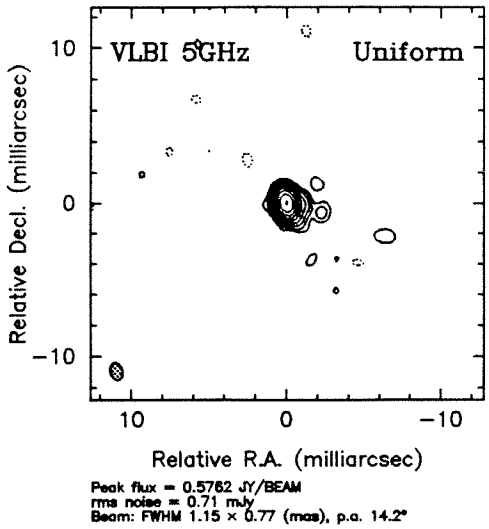

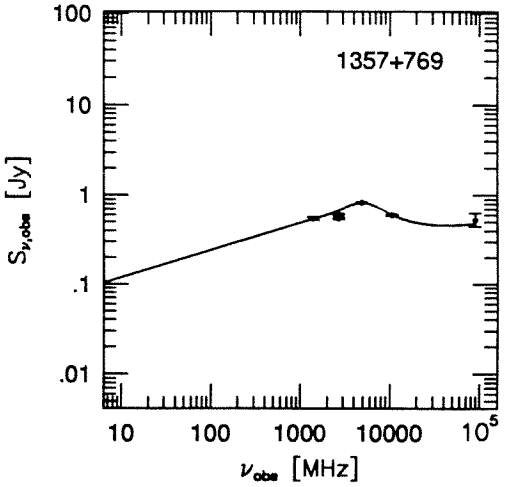

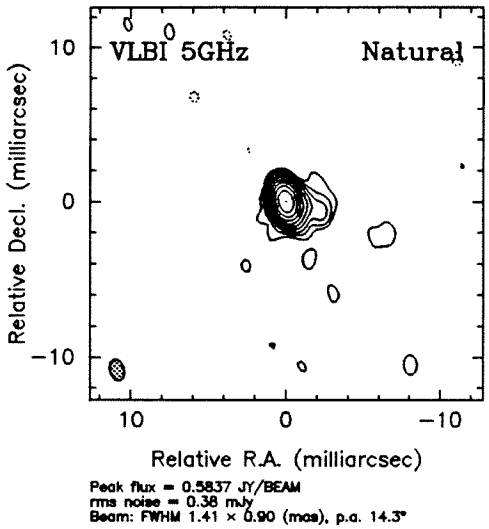

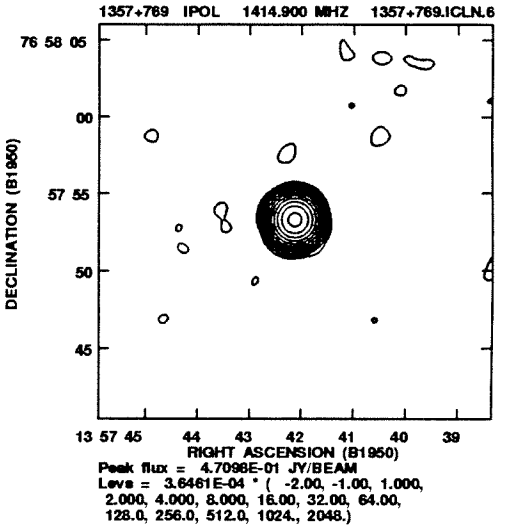

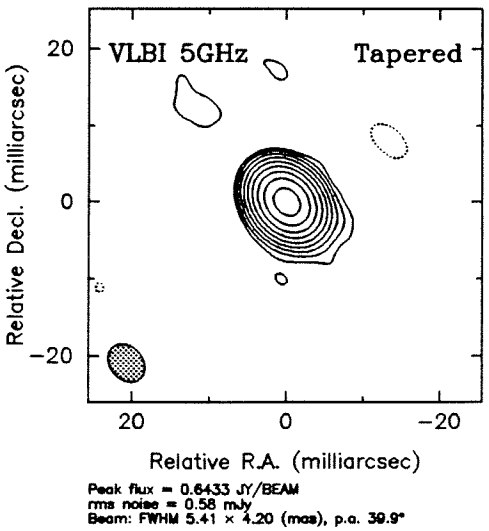

Figure 3.4.47. The maps and spectrum for 1357+769

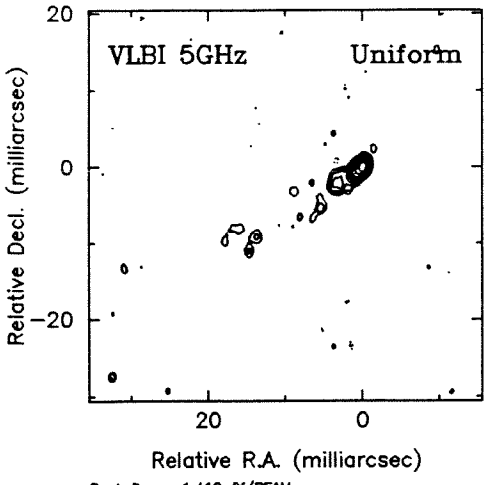

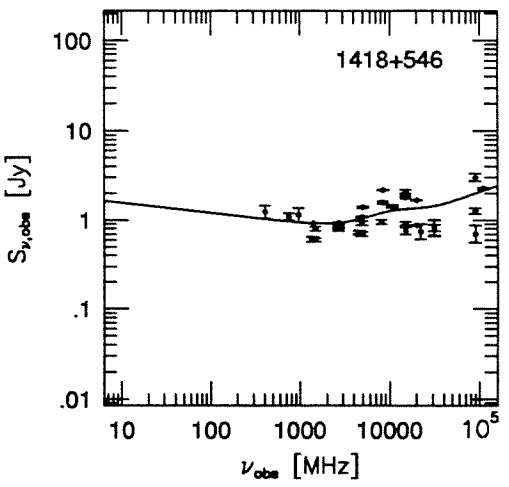

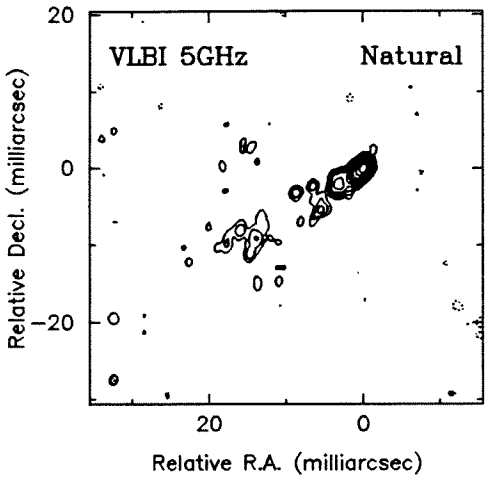

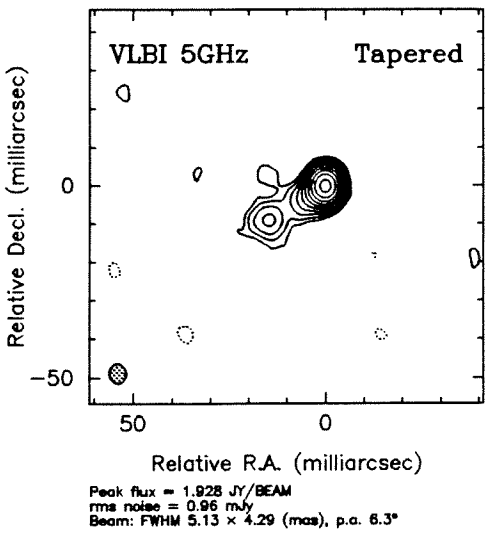

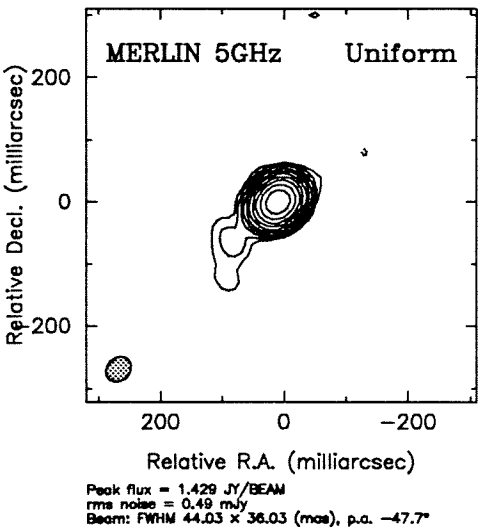

Figure 3.4.48. The maps and spectrum for 1418+546

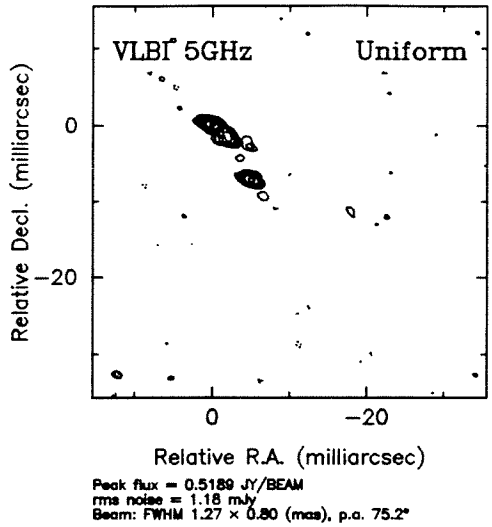

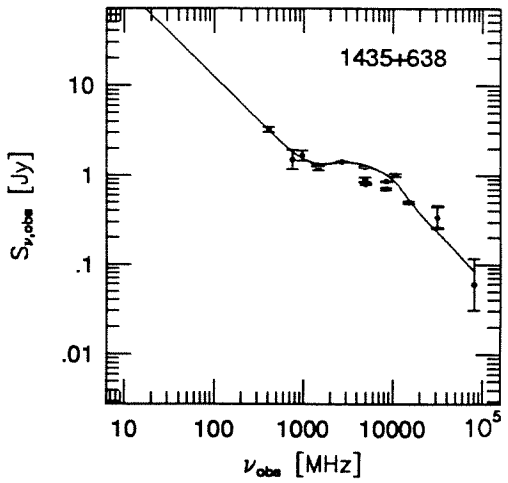

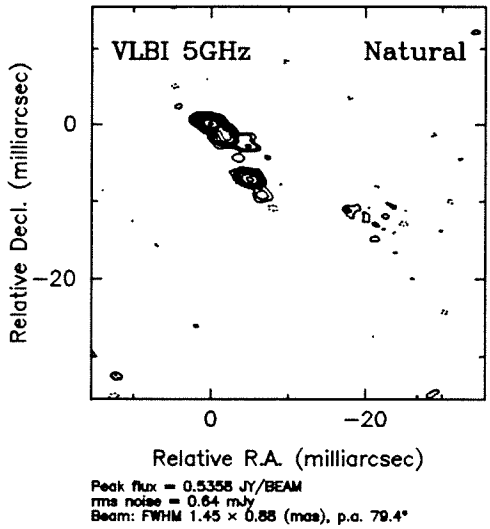

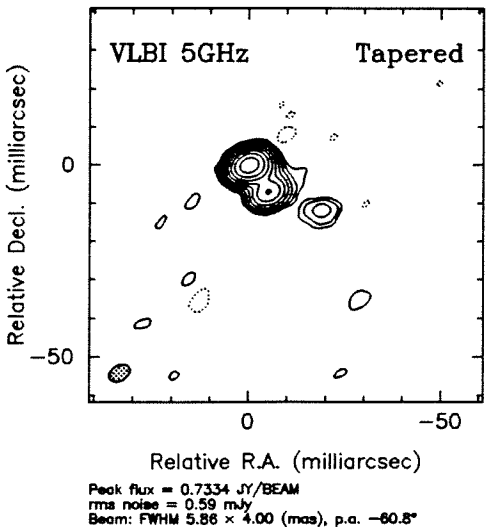

Figure 3.4.49. The maps and spectrum for 1435+638

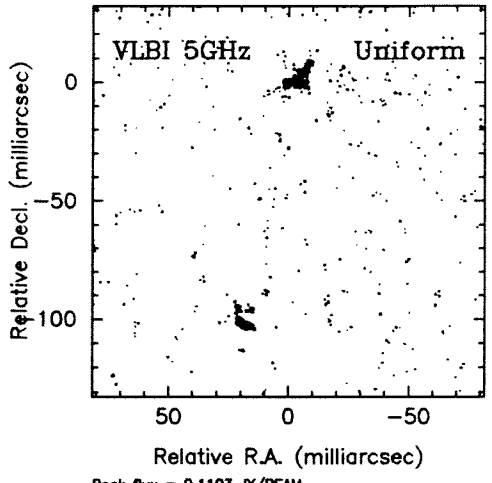

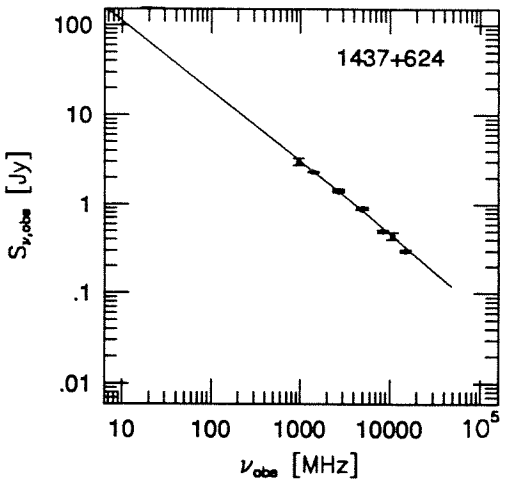

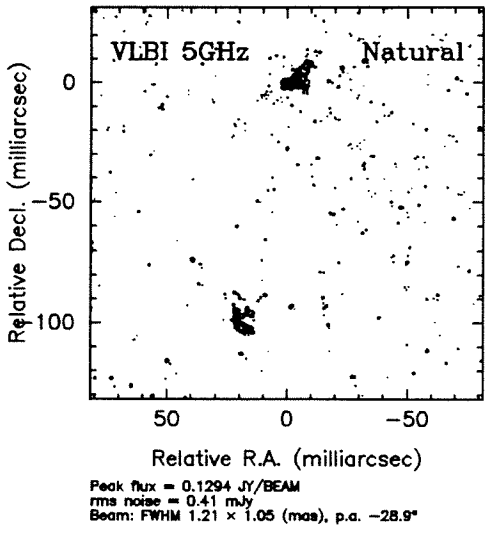

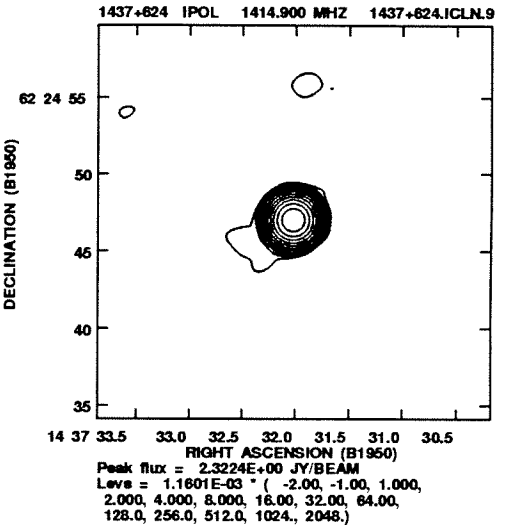

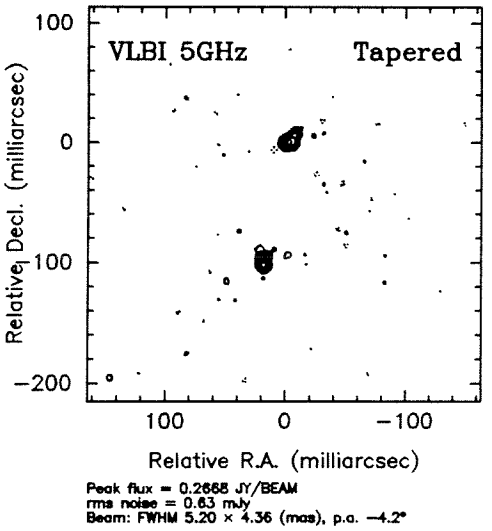

Figure 3.4.50. The maps and spectrum for 1437+624

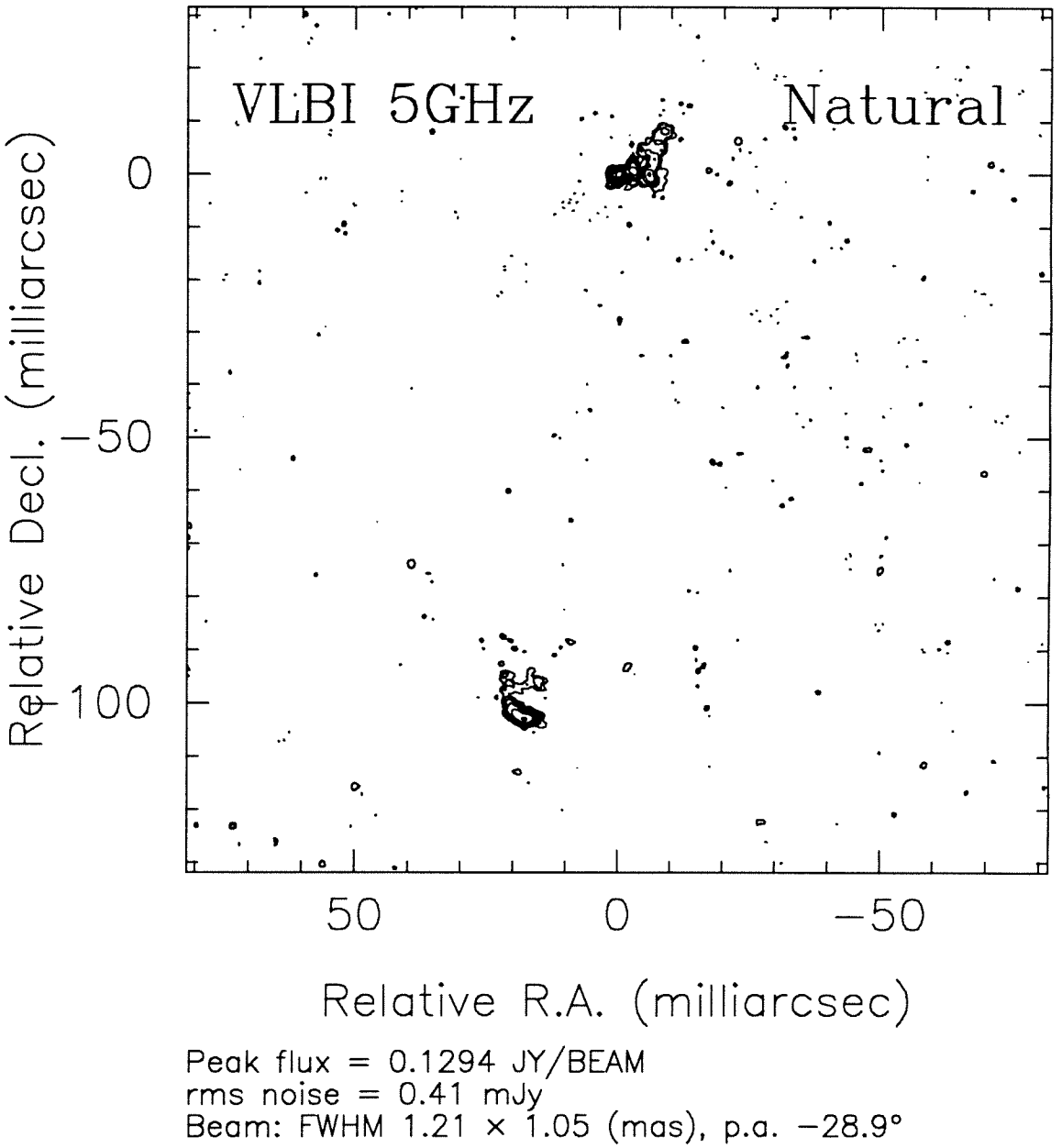

Figure 3.4.50. The VLBI map of 1437+624

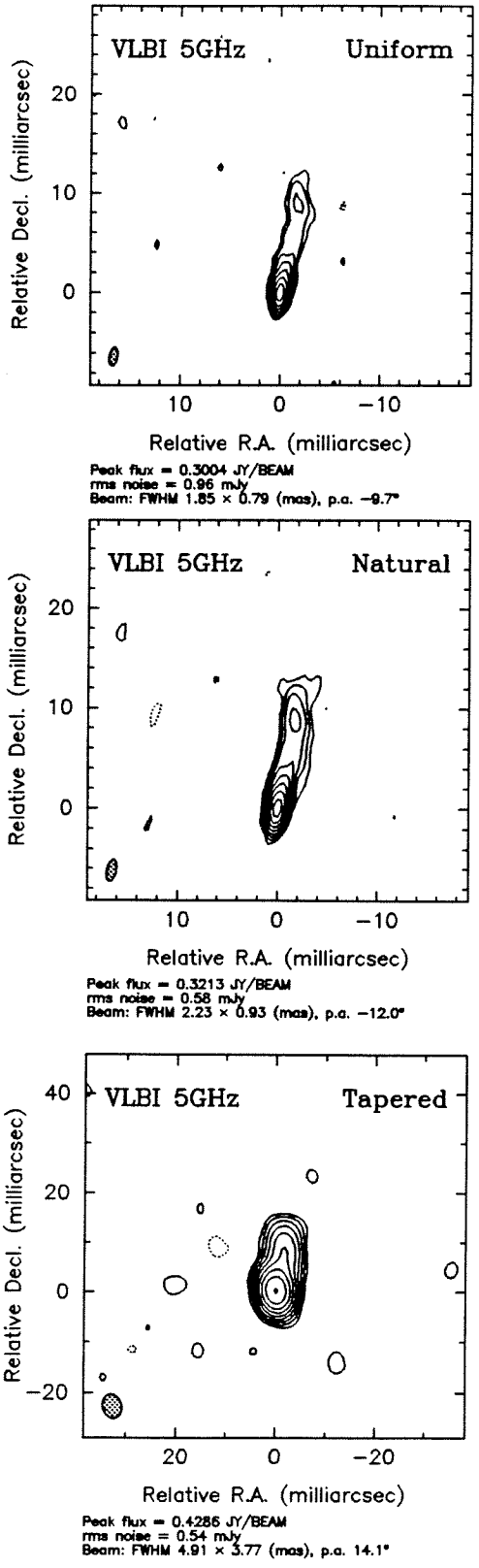

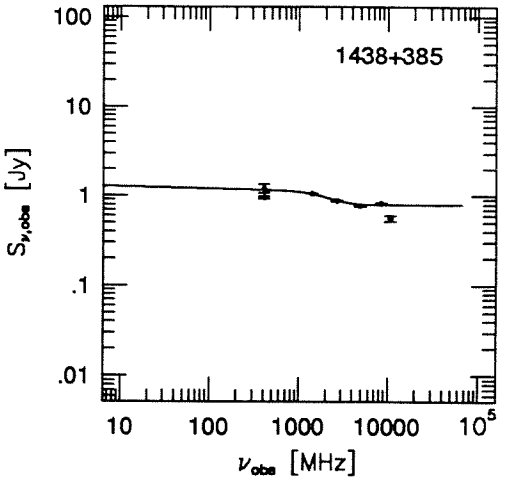

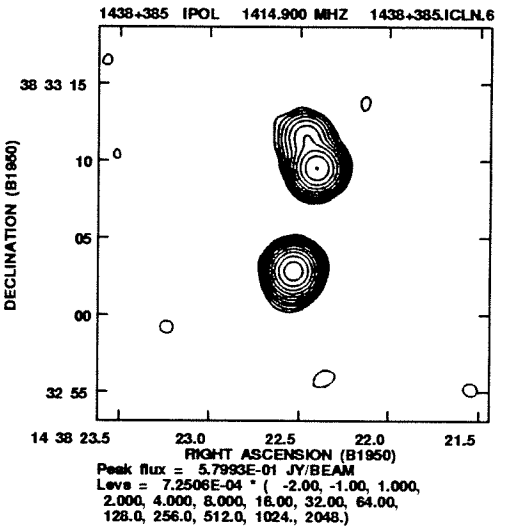

Figure 3.4.51. The maps and spectrum for 1438+385

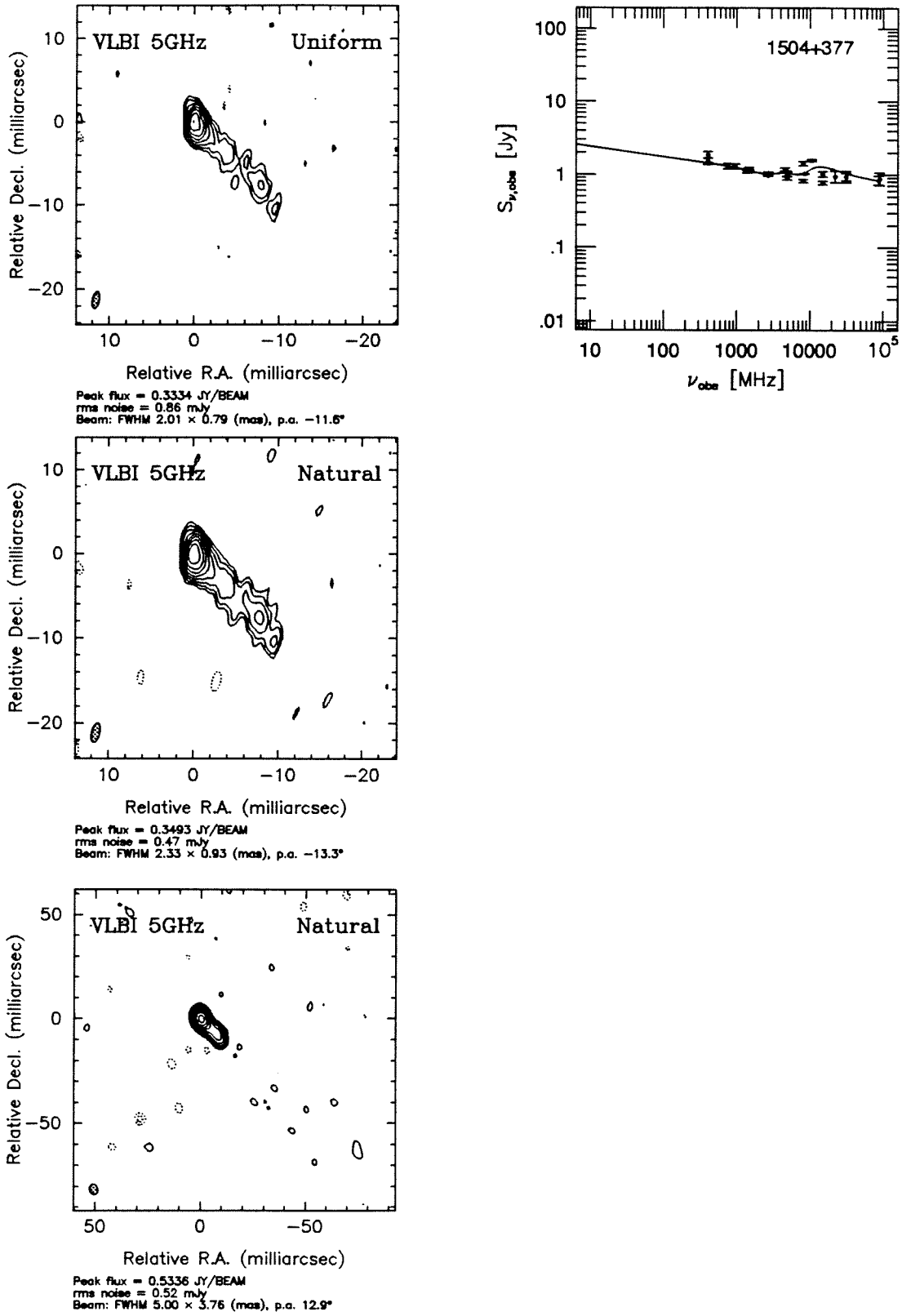

Figure 3.4.52. The maps and spectrum for 1504+377

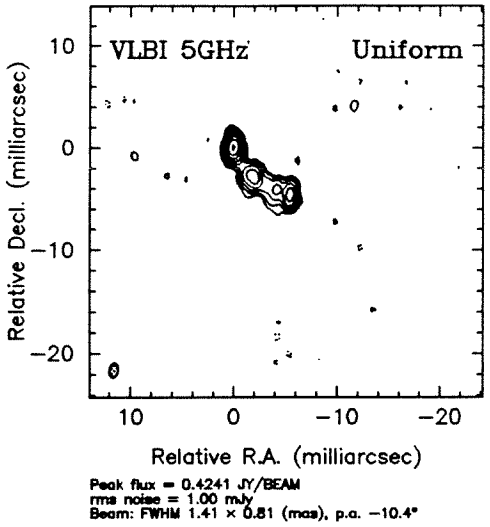

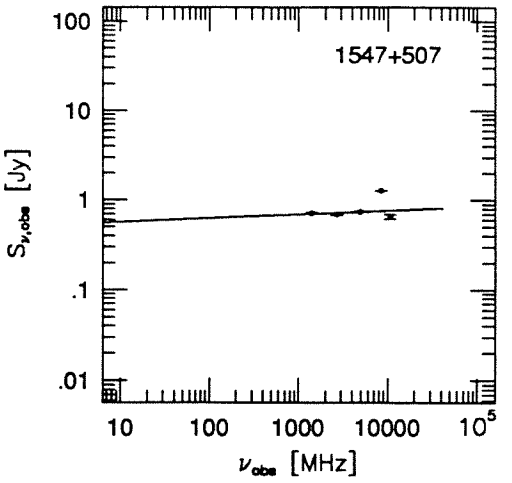

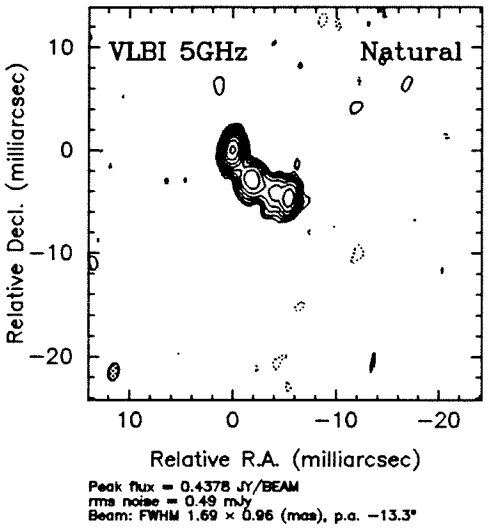

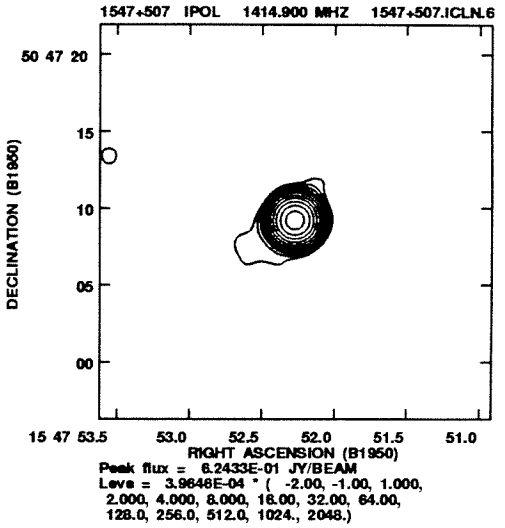

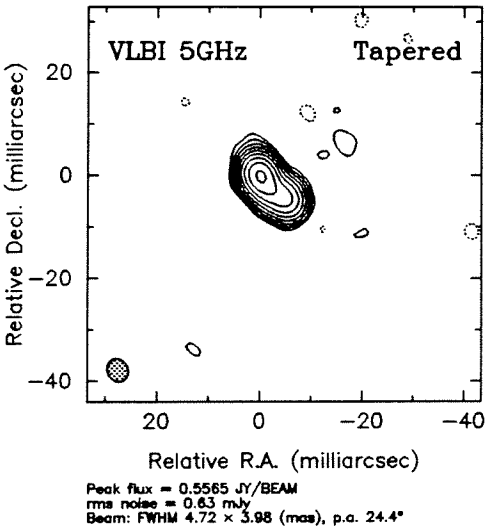

Figure 3.4.53. The maps and spectrum for 1547+507

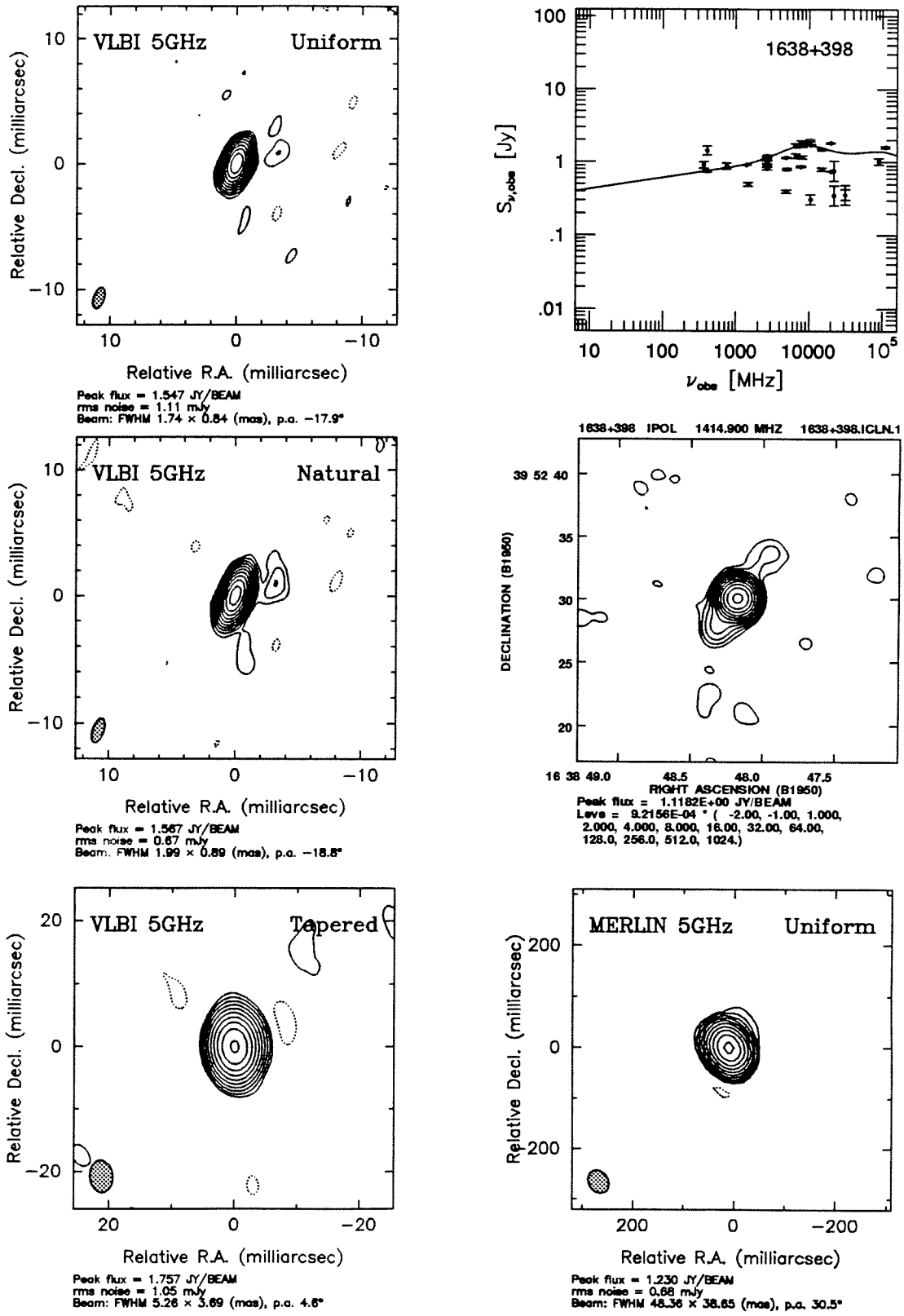

Figure 3.4.54. The maps and spectrum for 1638+398

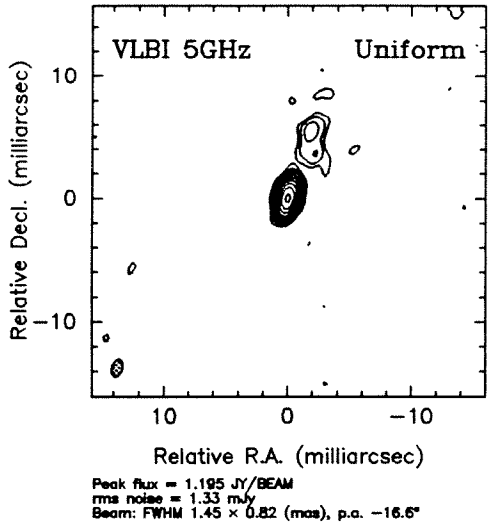

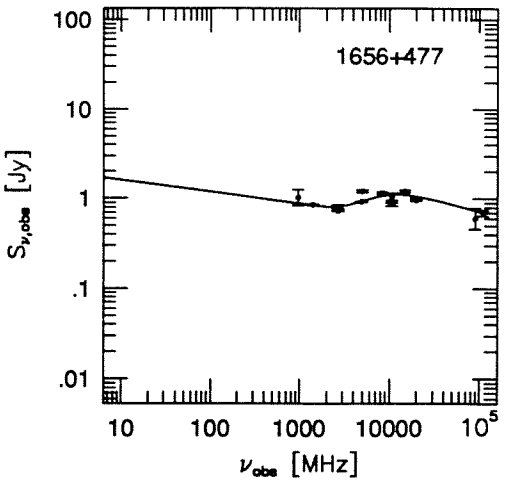

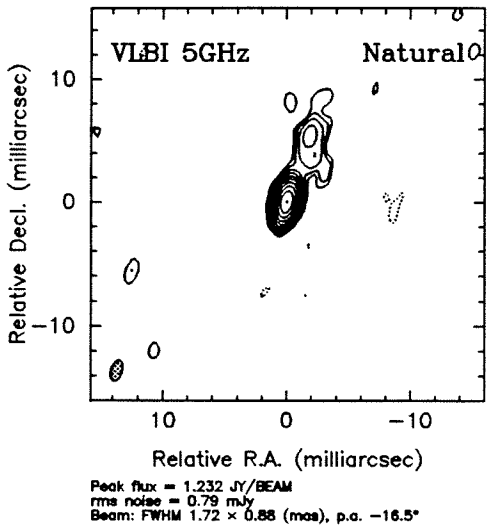

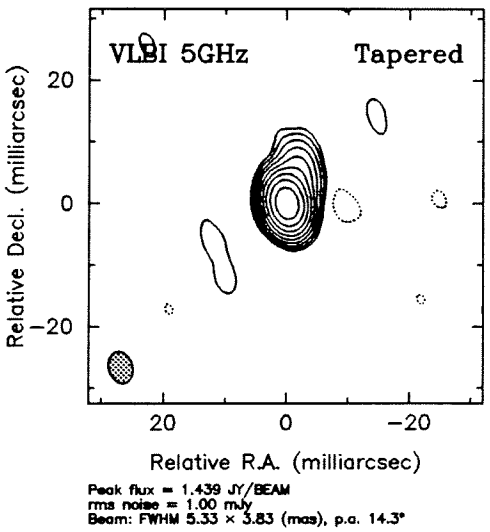

Figure 3.4.55. The maps and spectrum for 1656+477

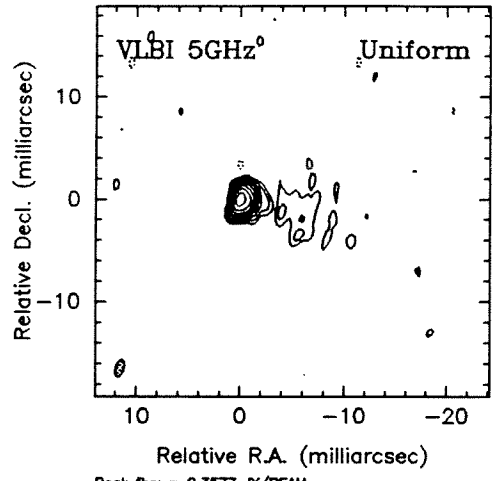

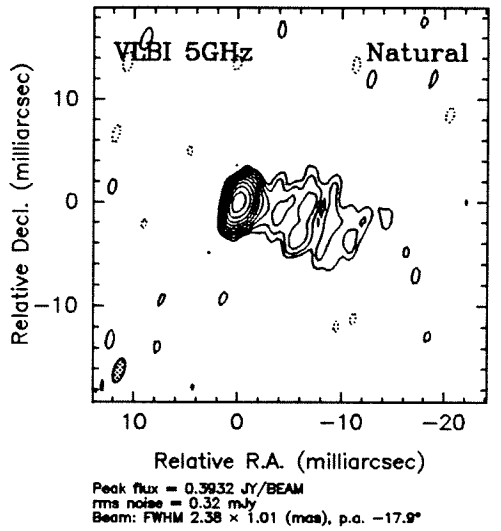

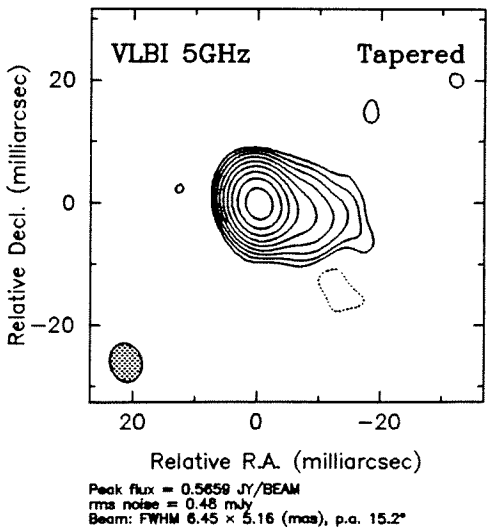

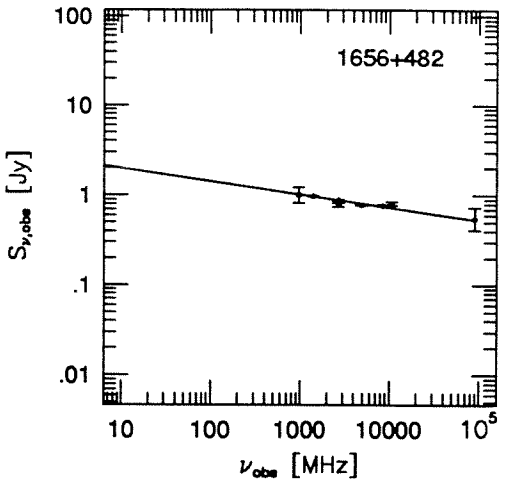

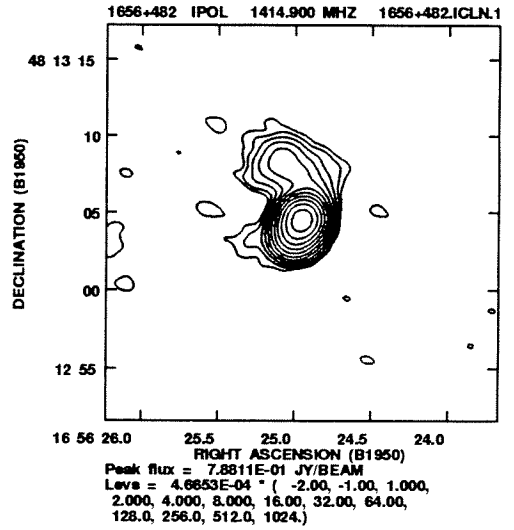

Figure 3.4.56. The maps and spectrum for 1656+482

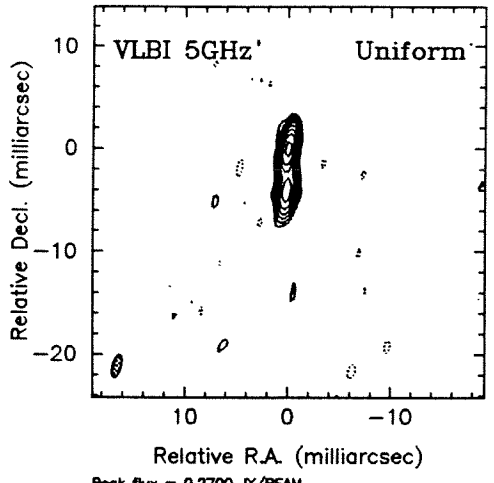

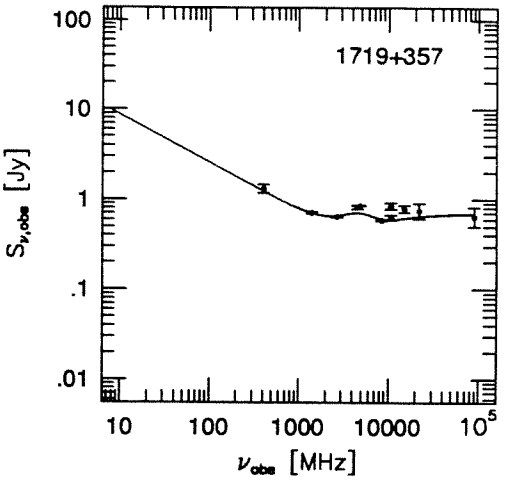

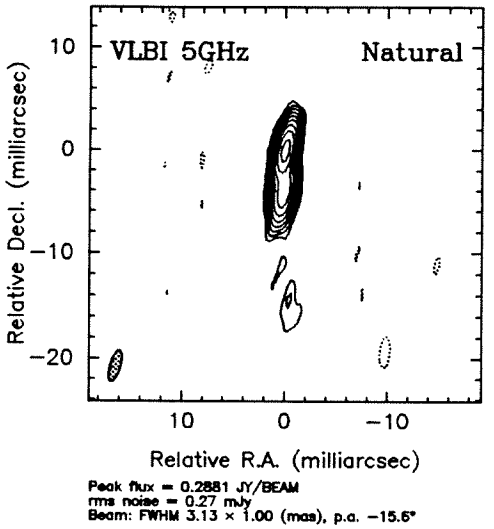

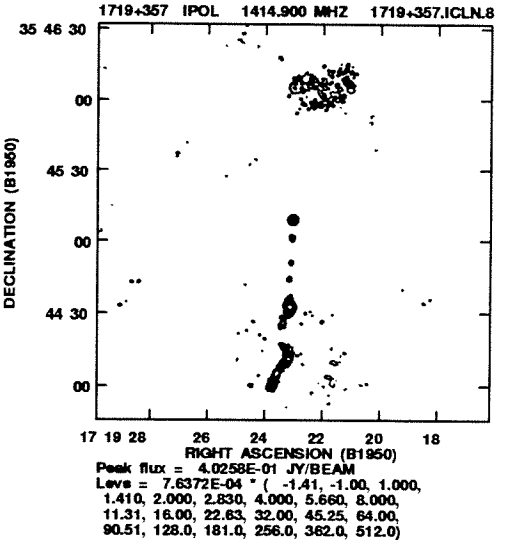

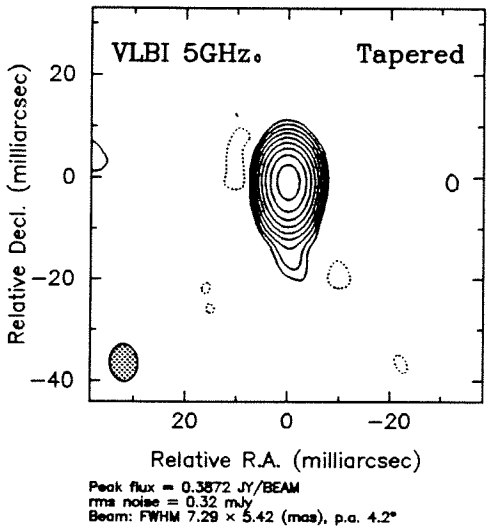

Figure 3.4.57. The maps and spectrum for 1719+357

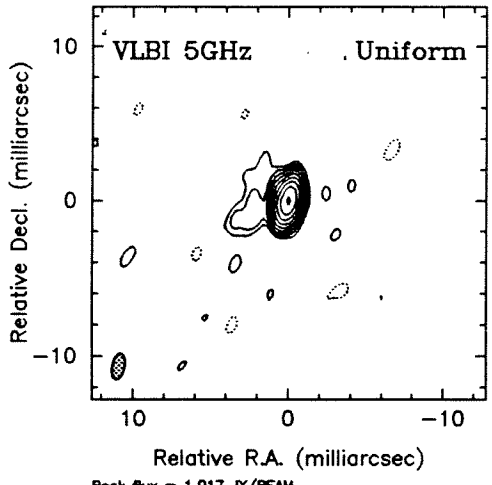

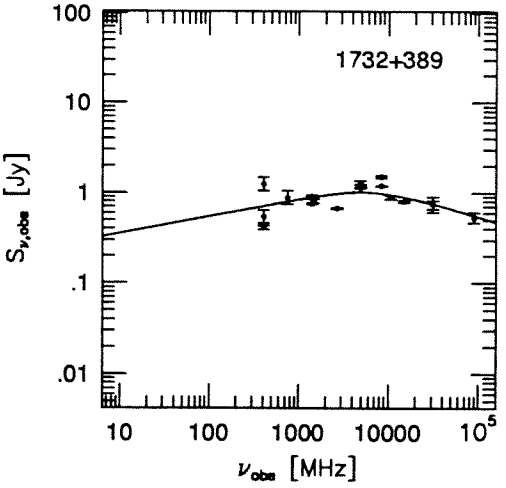

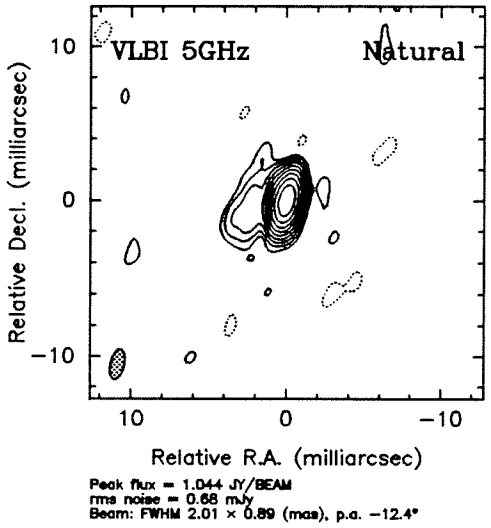

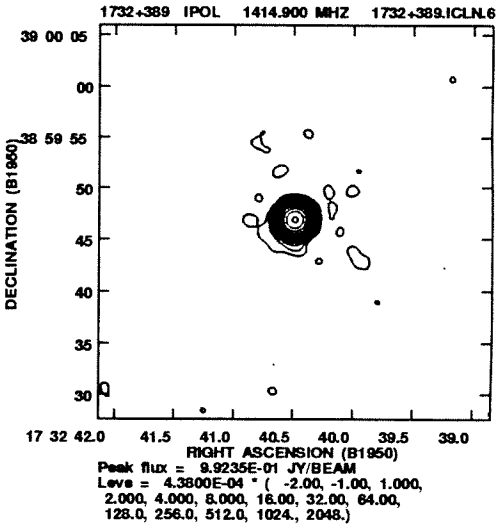

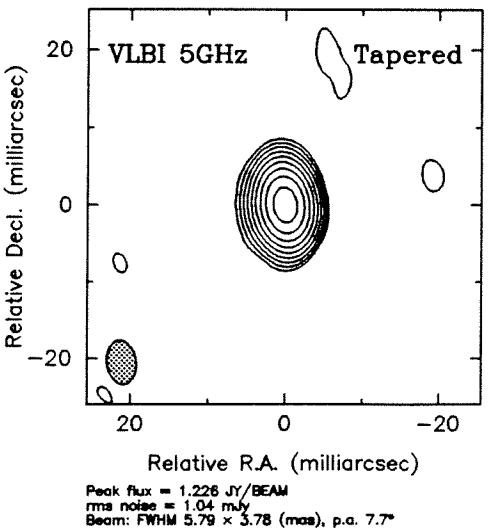

Figure 3.4.58. The maps and spectrum for 1732+389

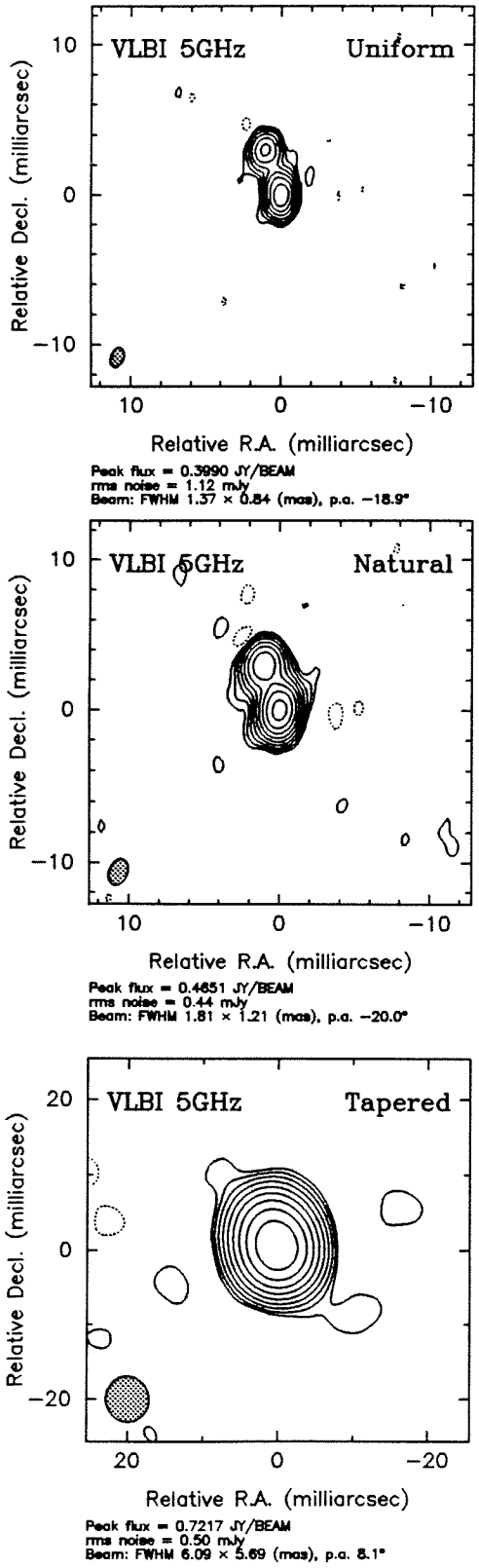

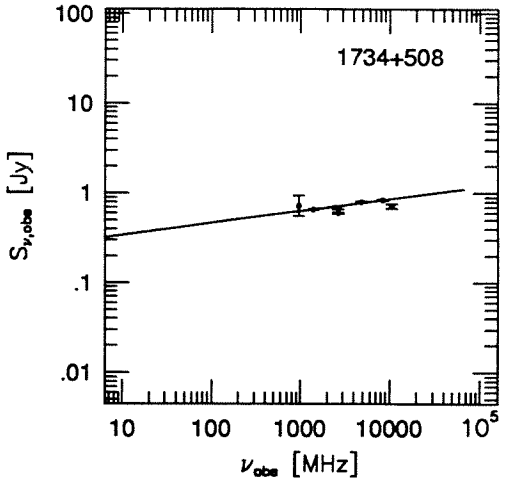

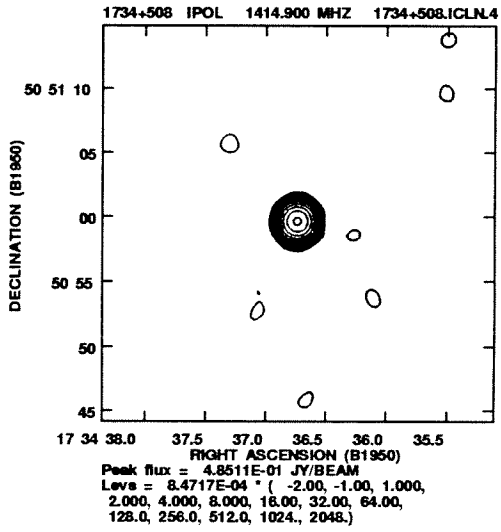

Figure 3.4.59. The maps and spectrum for 1734+508

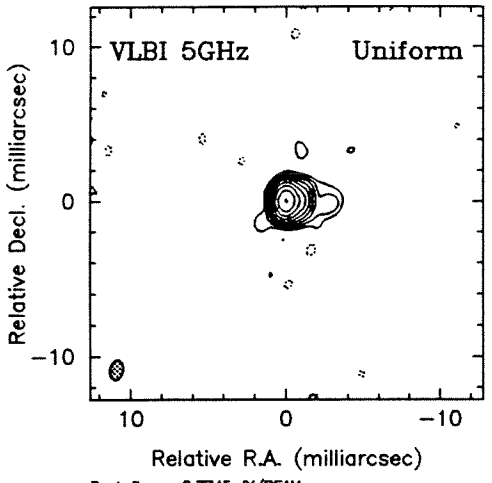

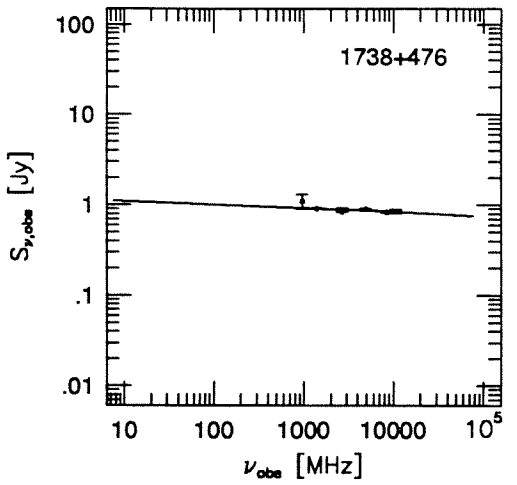

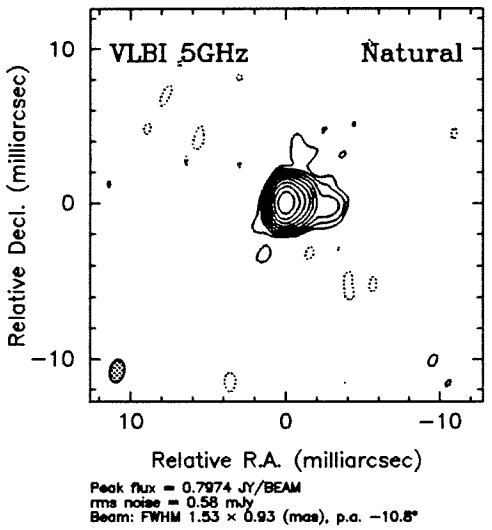

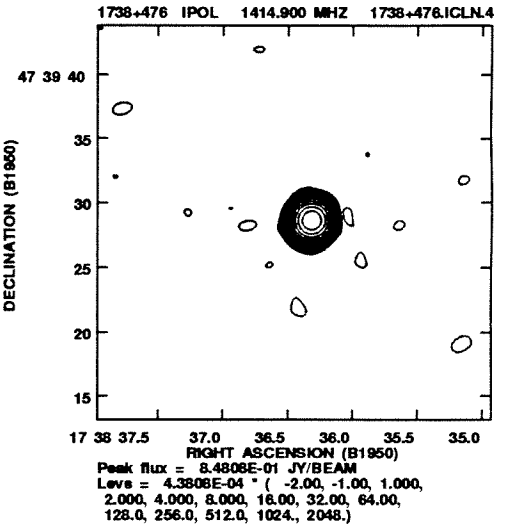

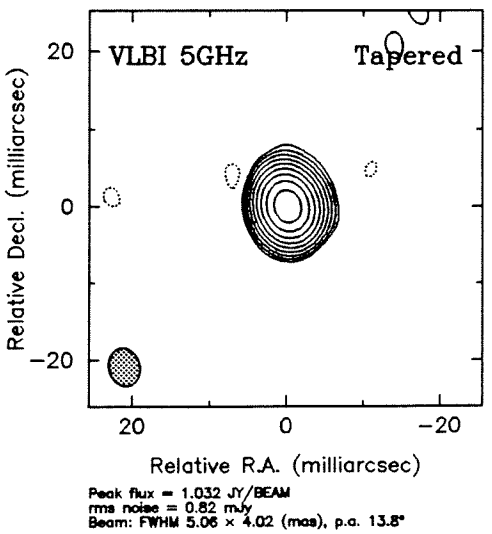

Figure 3.4.60. The maps and spectrum for 1738+476

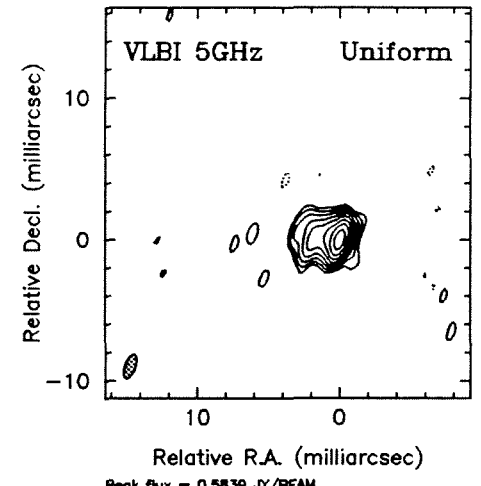

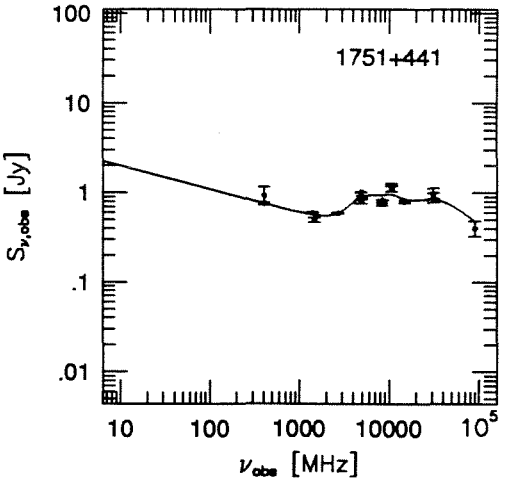

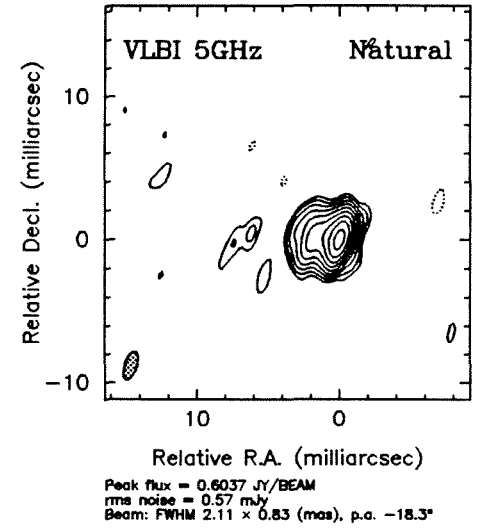

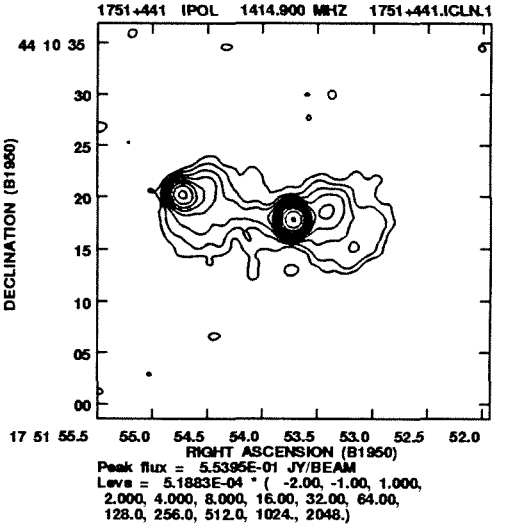

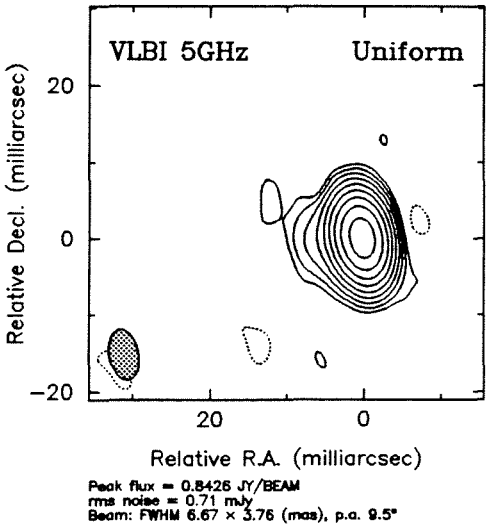

Figure 3.4.61. The maps and spectrum for 1751+441

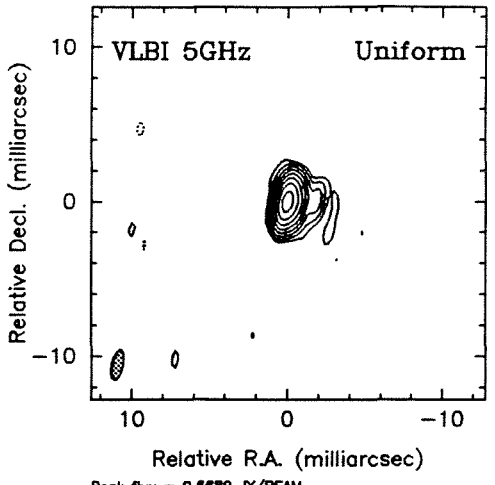

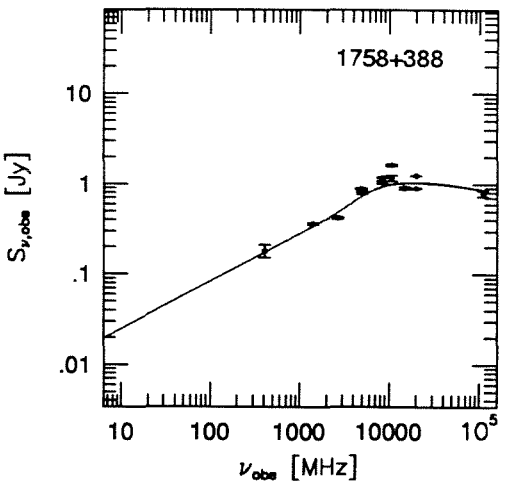

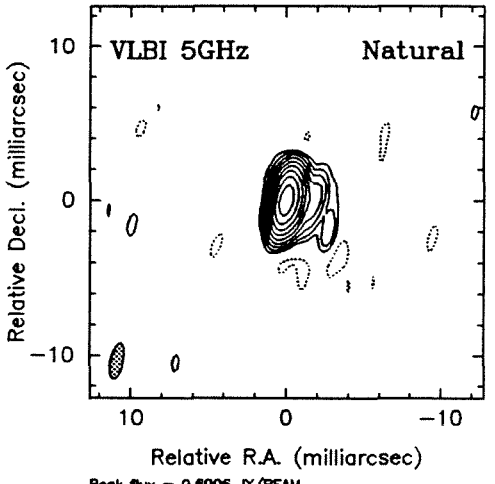

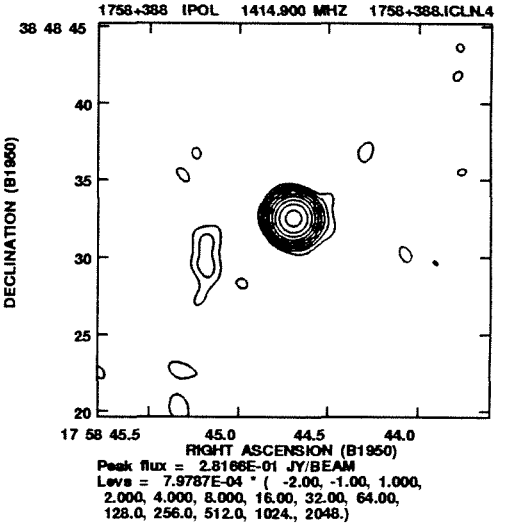

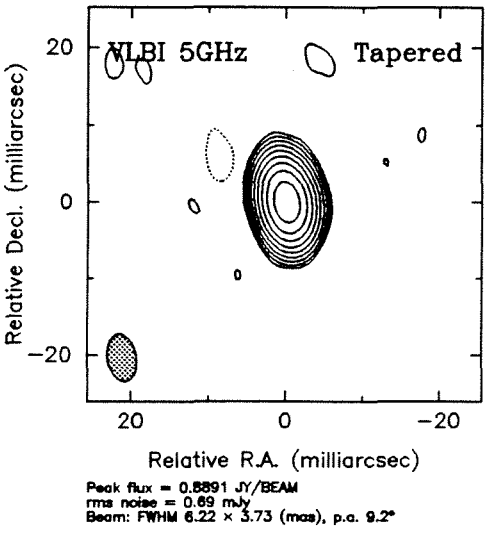

Figure 3.4.62. The maps and spectrum for 1758+388

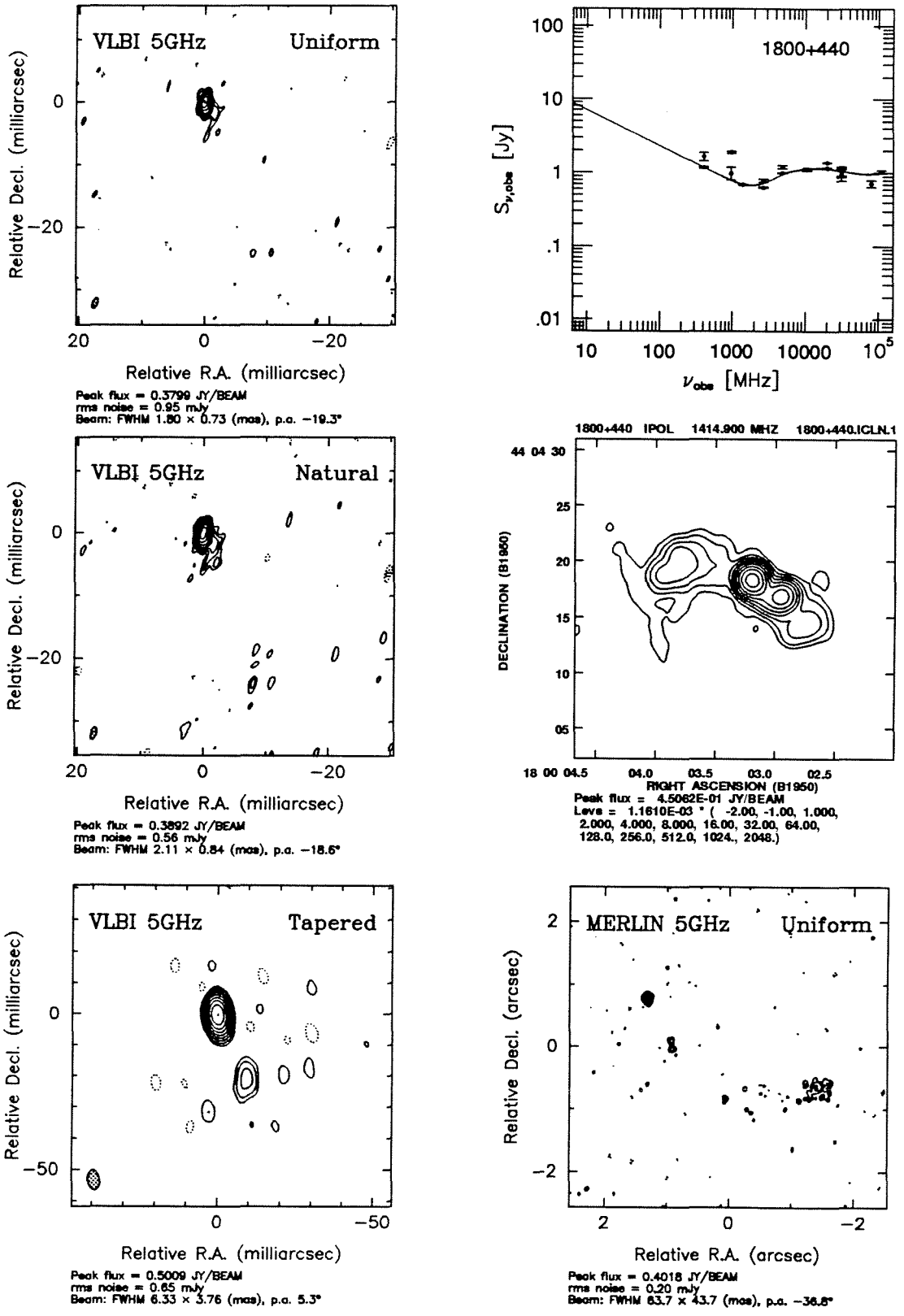

Figure 3.4.63. The maps and spectrum for 1800+440

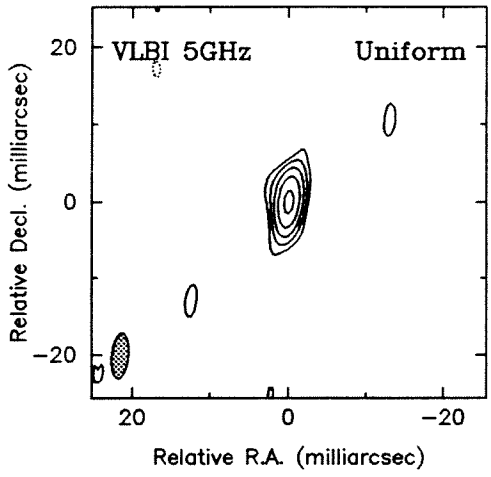

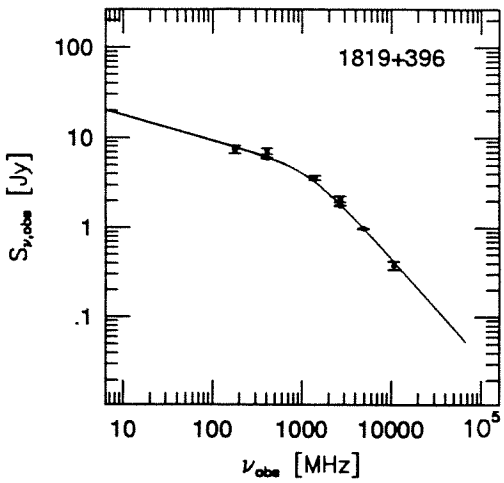

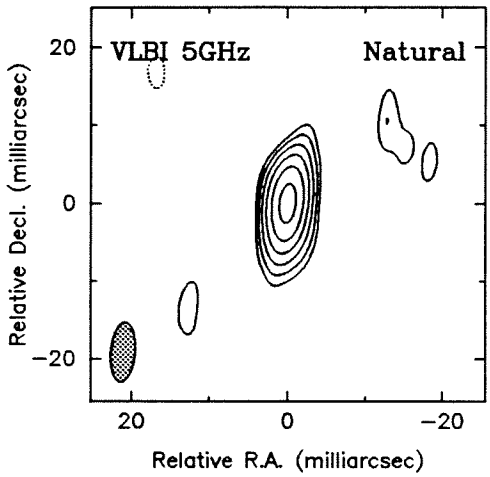

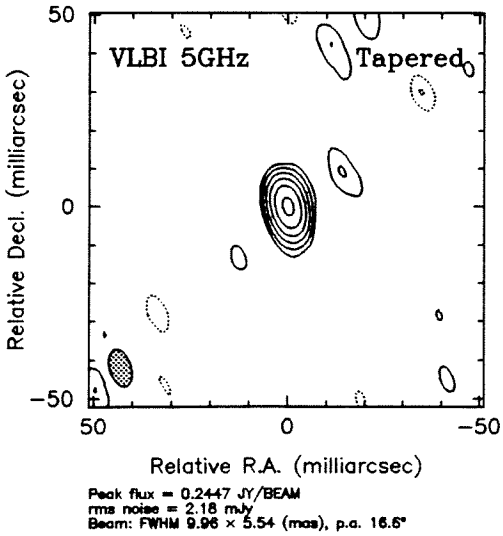

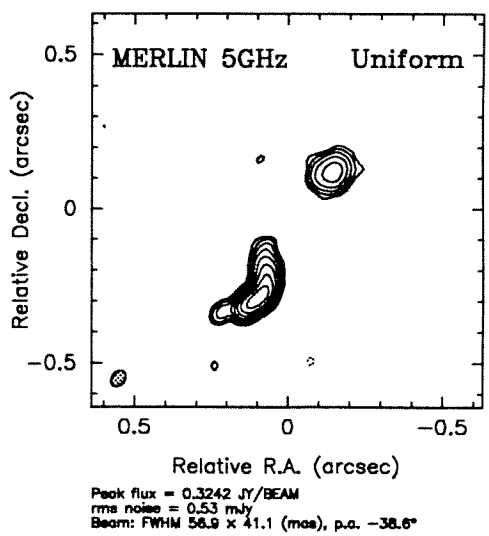

Figure 3.4.64. The maps and spectrum for 1819+396

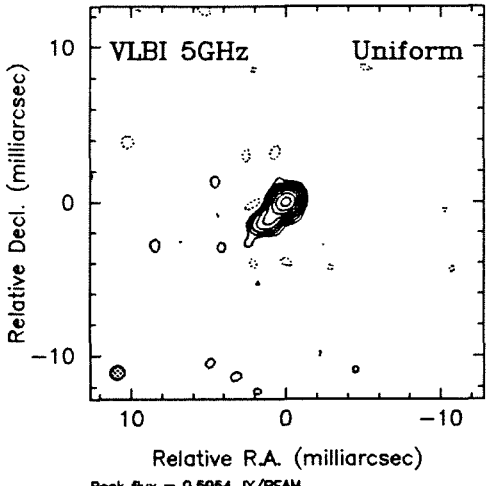

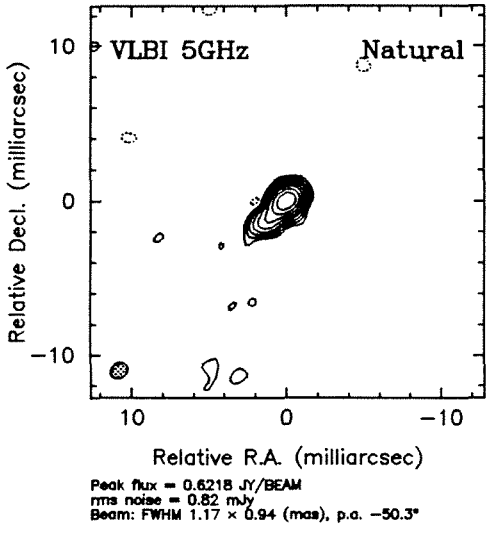

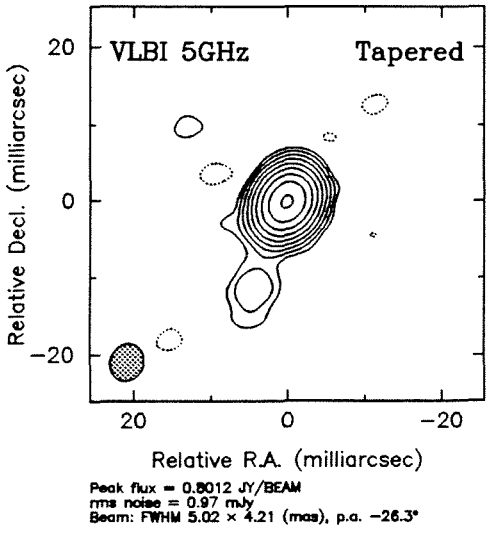

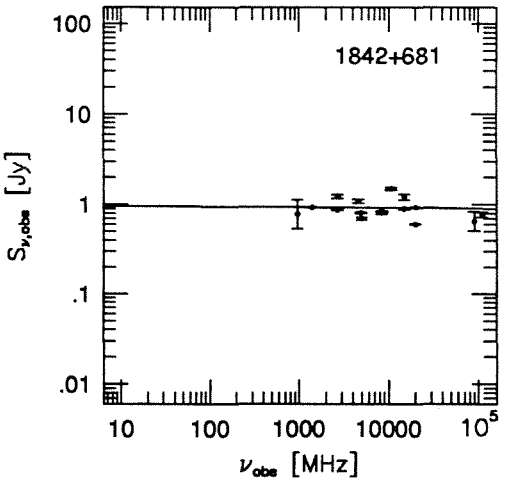

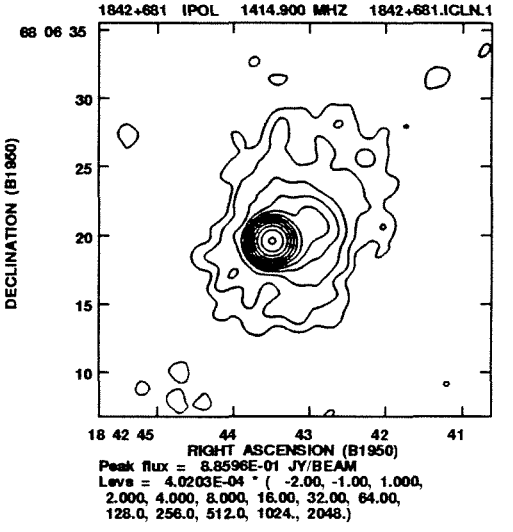

Figure 3.4.65. The maps and spectrum for 1842+681

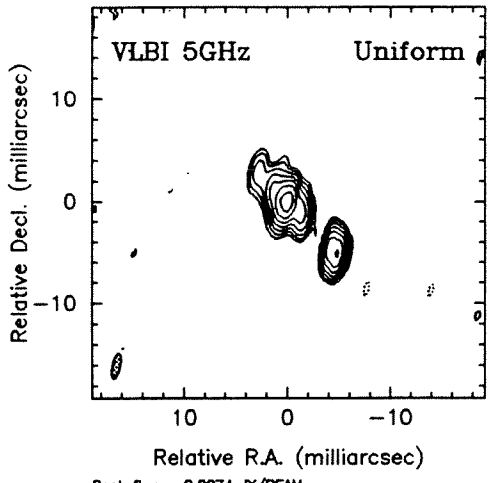

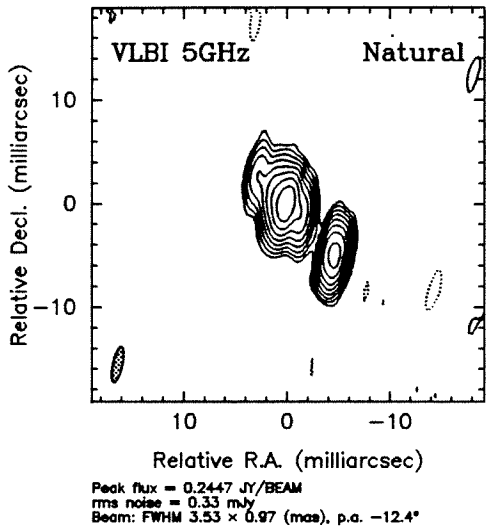

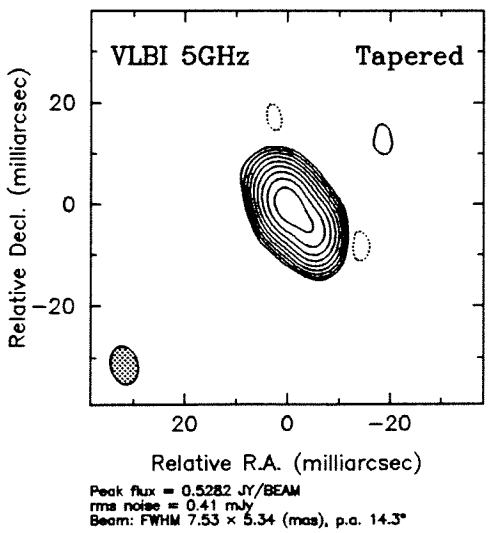

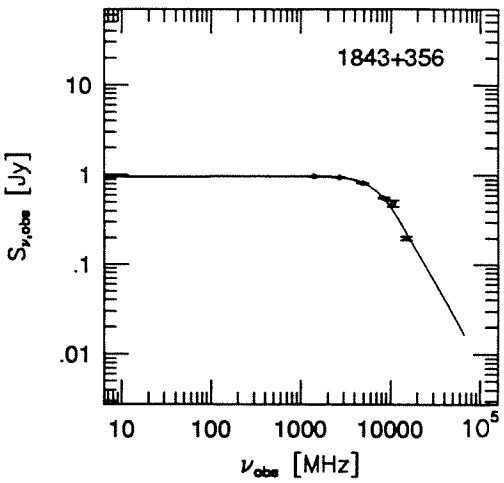

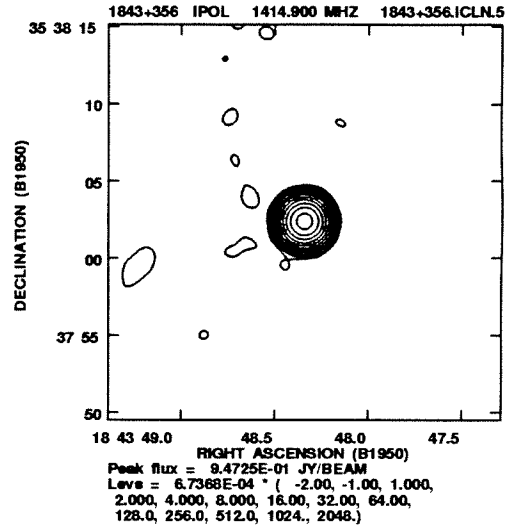

Figure 3.4.66. The maps and spectrum for 1843+356

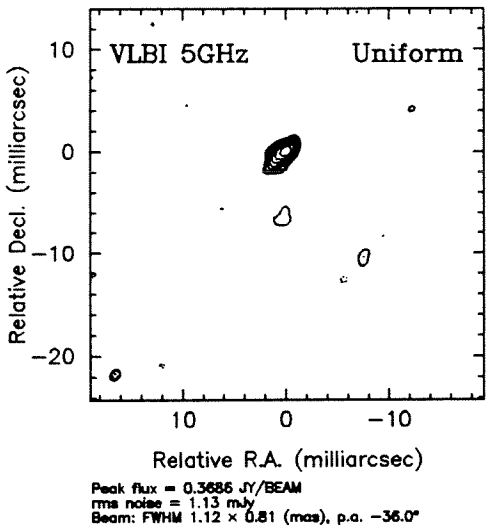

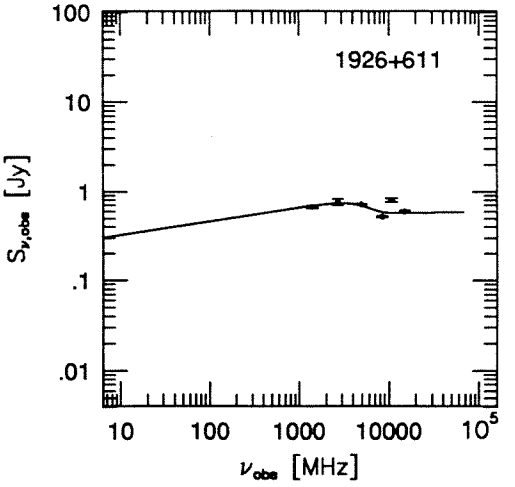

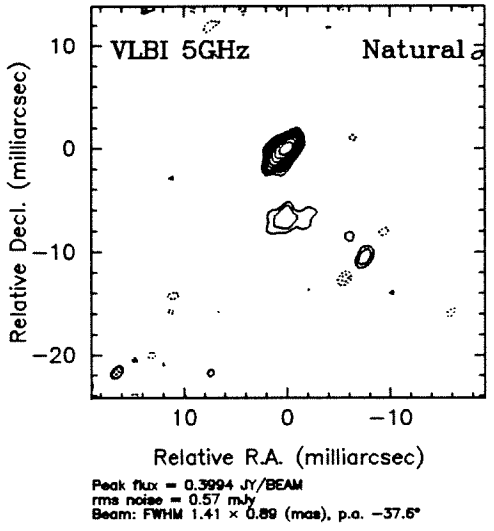

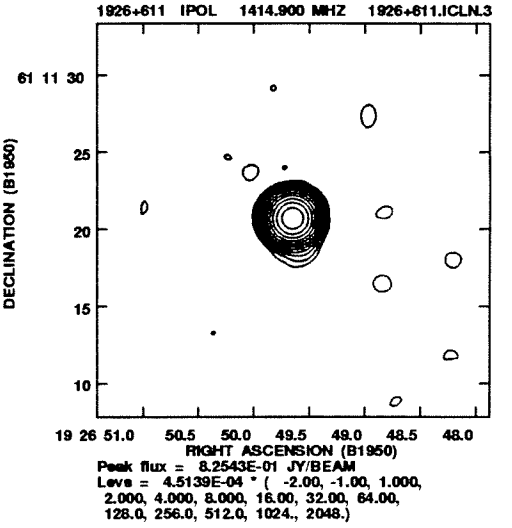

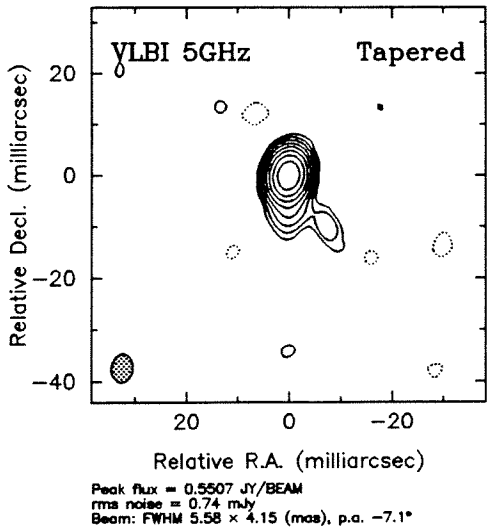

Figure 3.4.67. The maps and spectrum for 1926+611

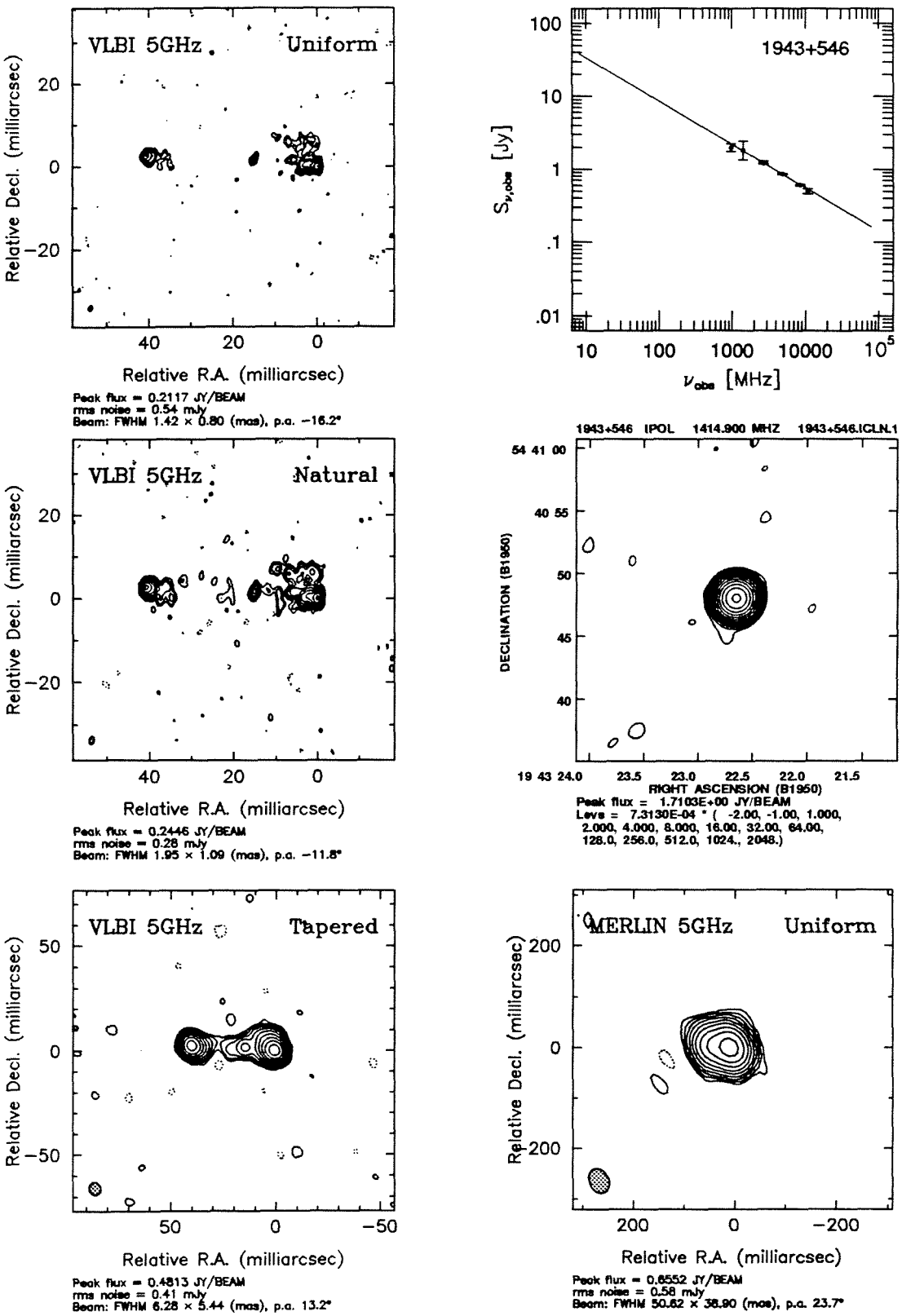

Figure 3.4.68. The maps and spectrum for 1943+546

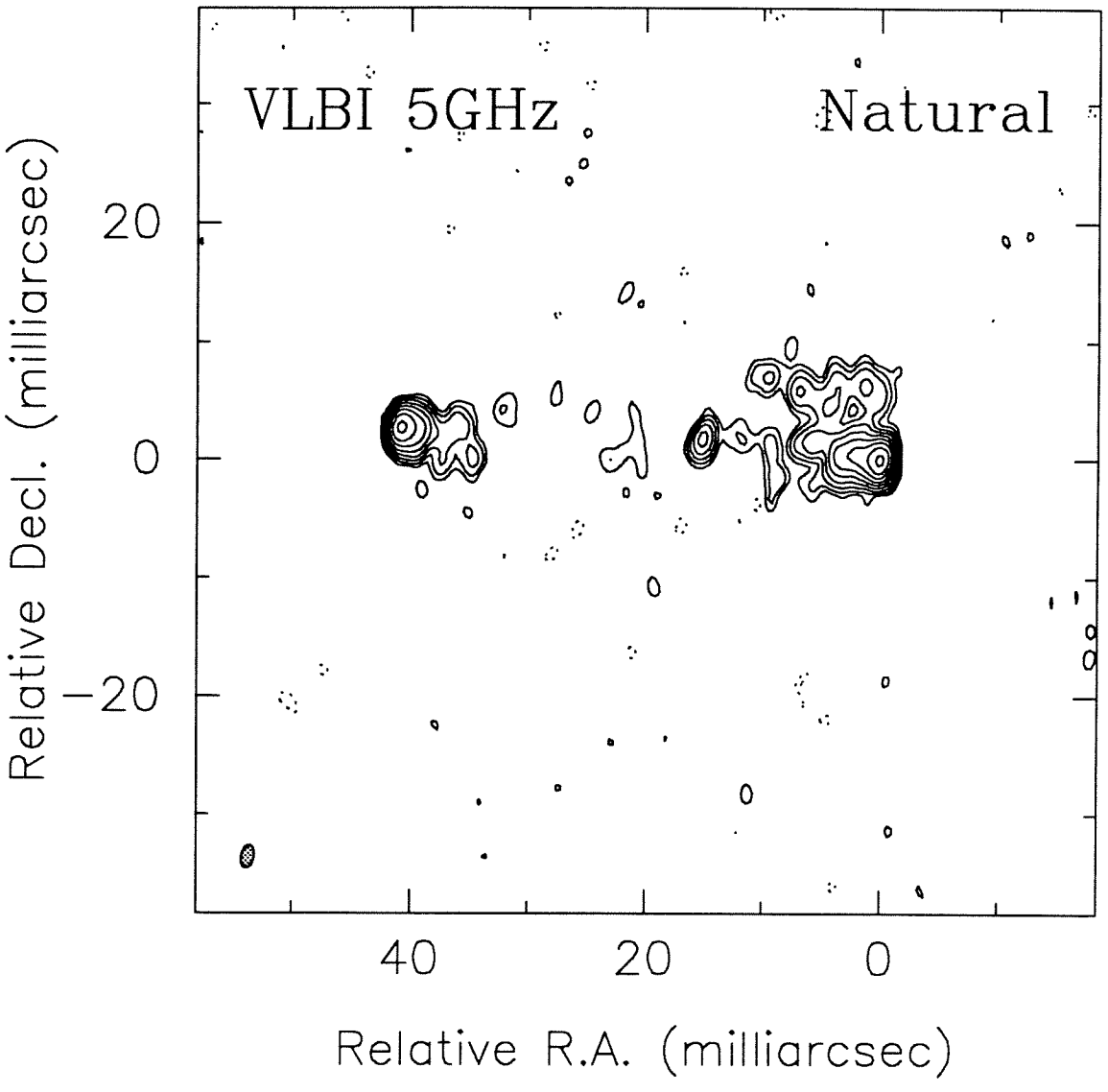

Figure 3.4.68. The VLBI map of 1943+546

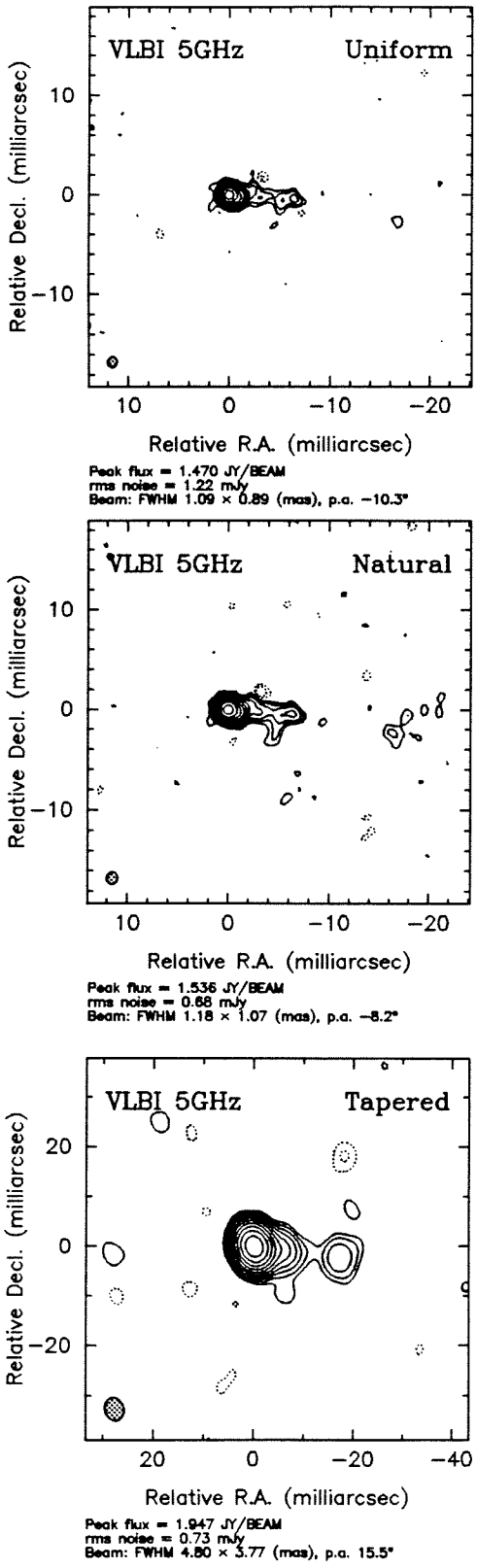

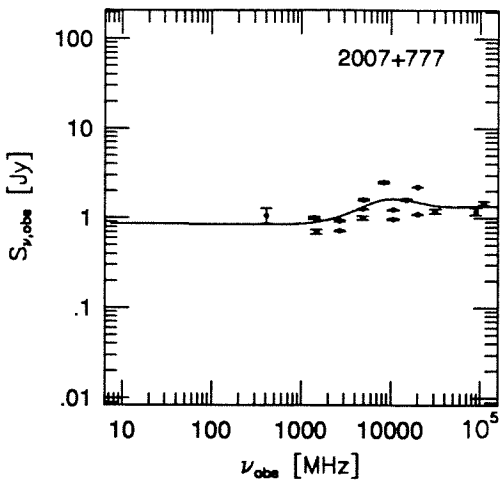

Figure 3.4.69. The maps and spectrum for 2007+777

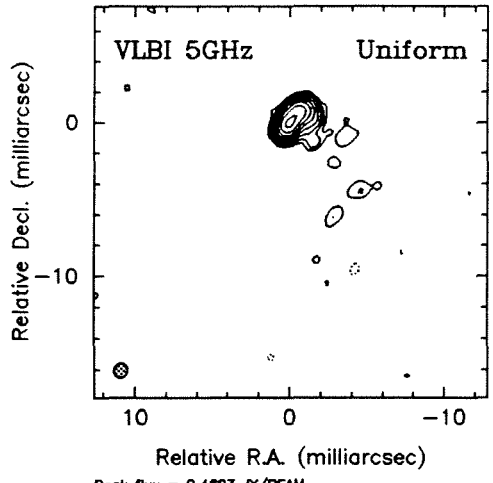

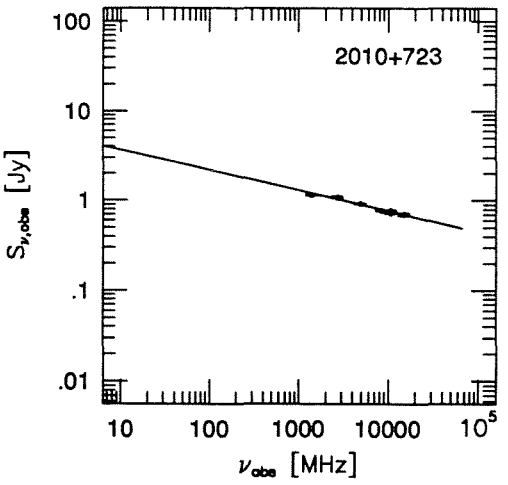

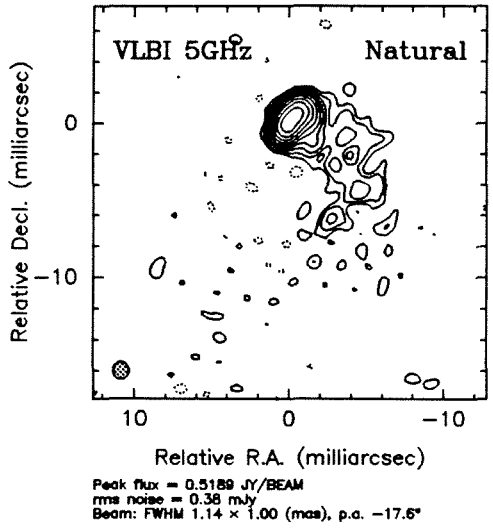

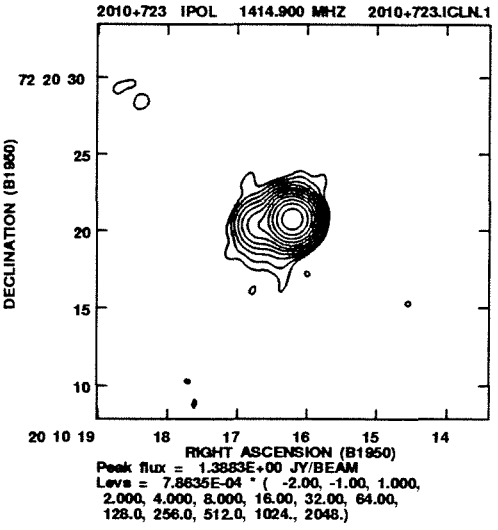

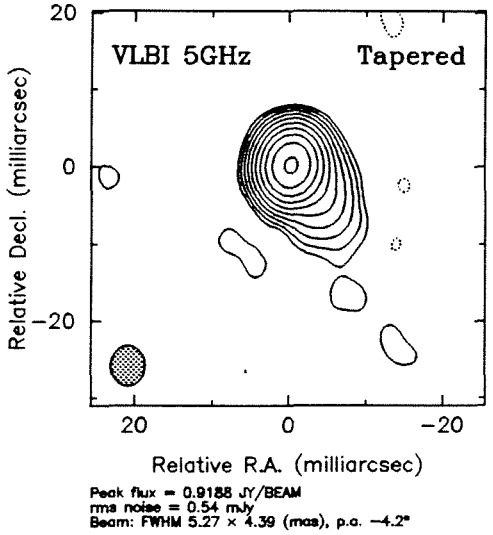

Figure 3.4.70. The maps and spectrum for 2010+723

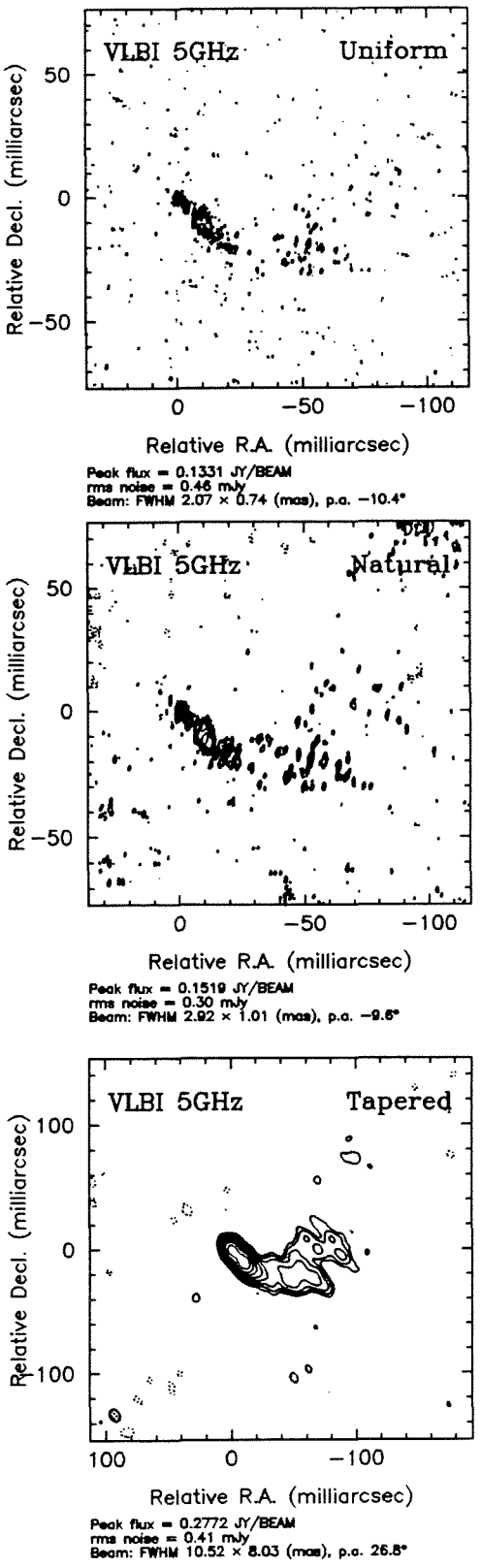

Figure 3.4.71. The maps and spectrum for 2207+374

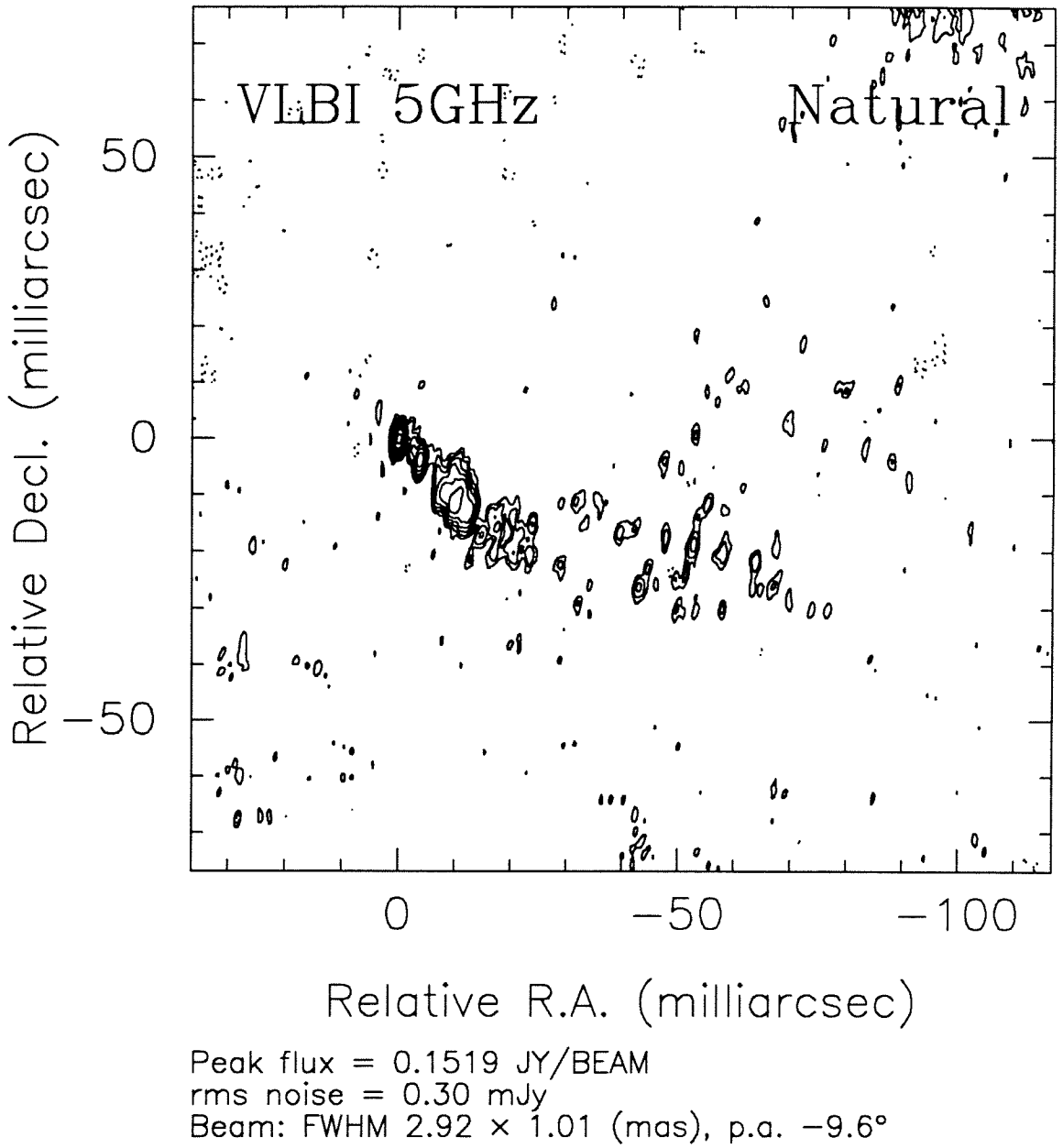

Figure 3.4.71. The VLBI map of 2207+374

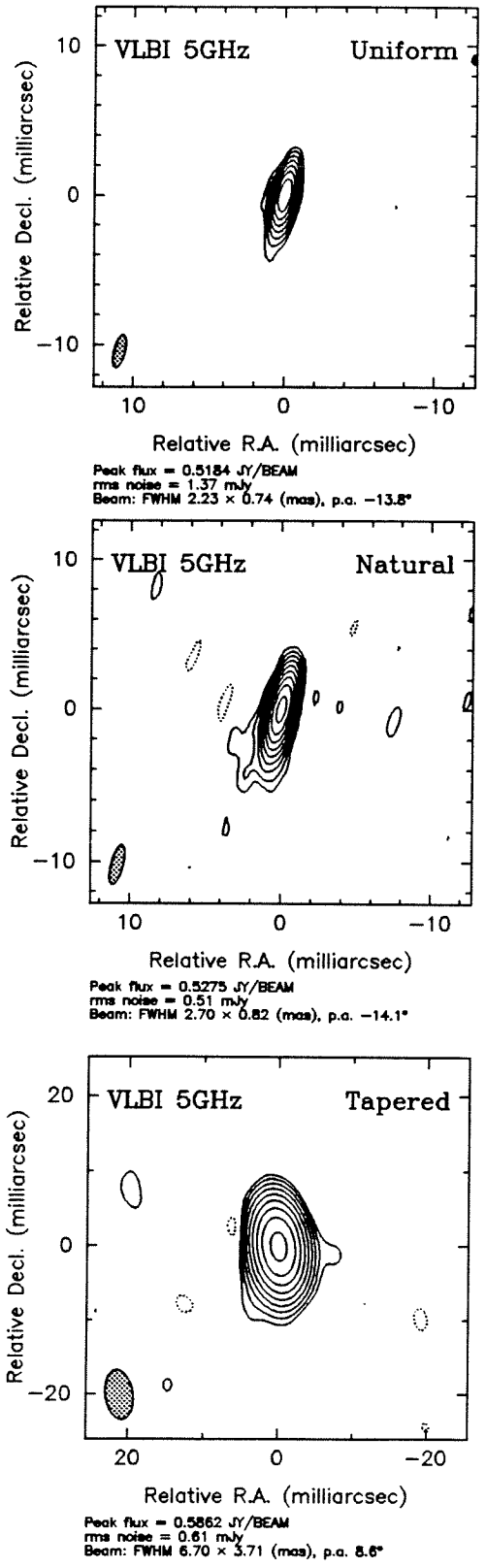

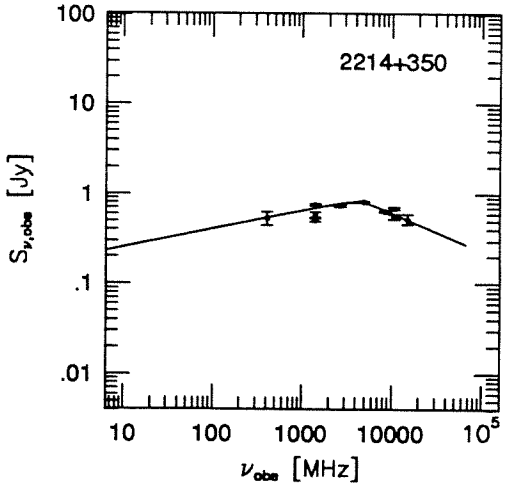

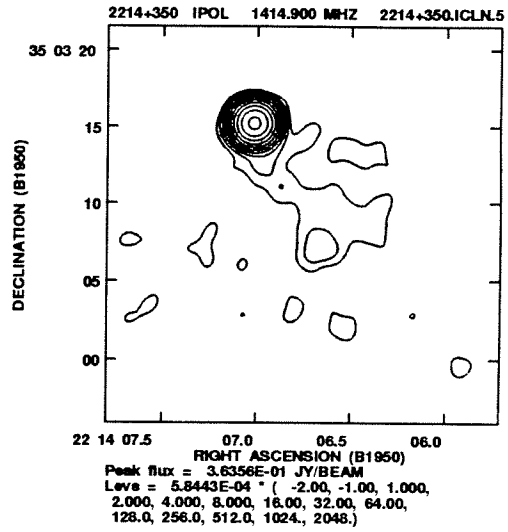

Figure 3.4.72. The maps and spectrum for 2214+350

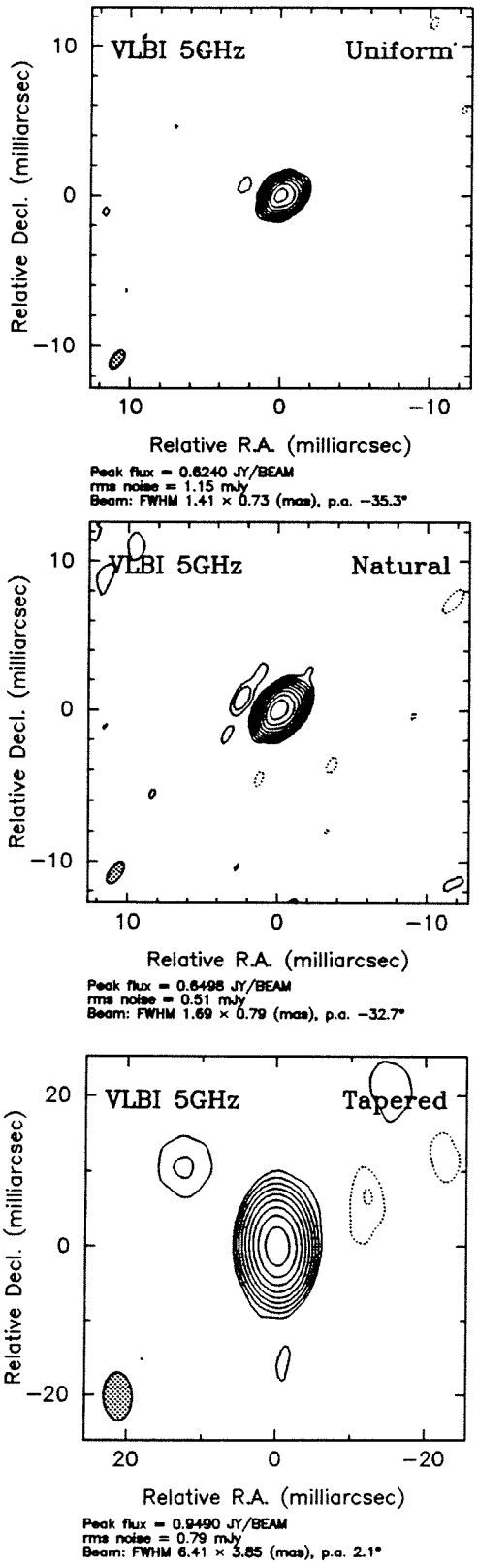

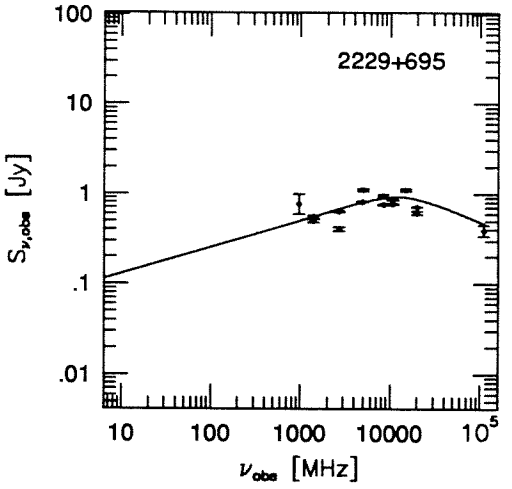

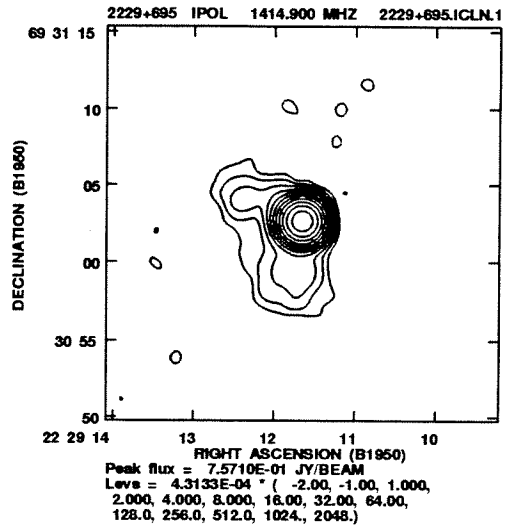

Figure 3.4.73. The maps and spectrum for 2229+695

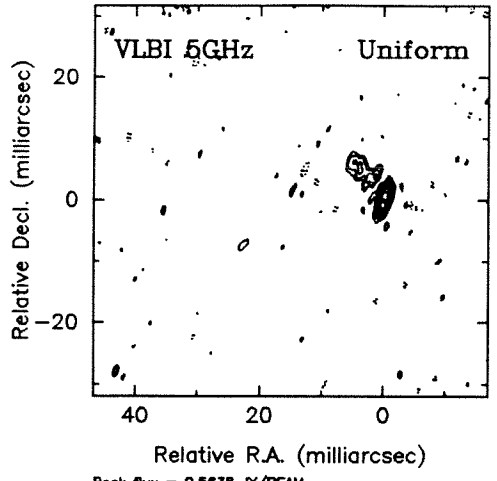

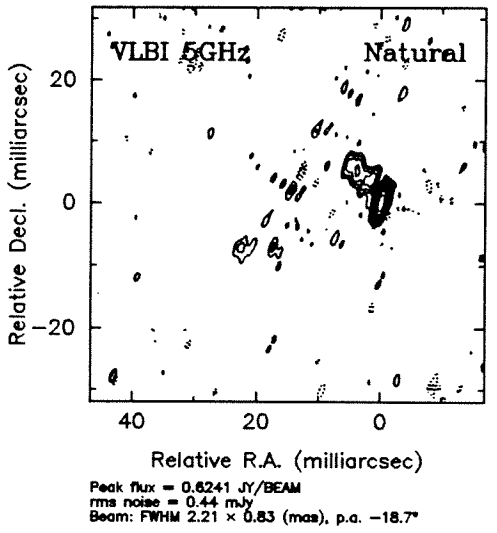

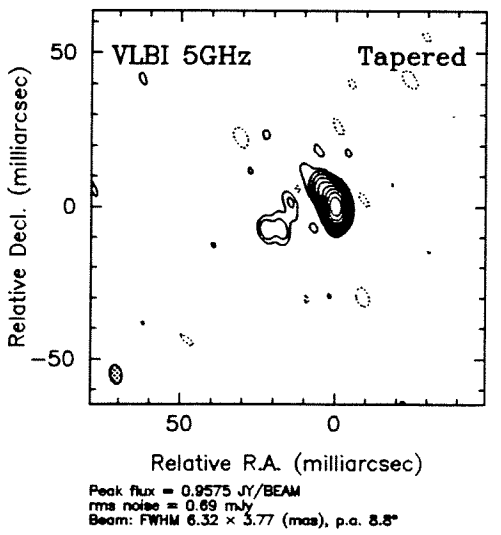

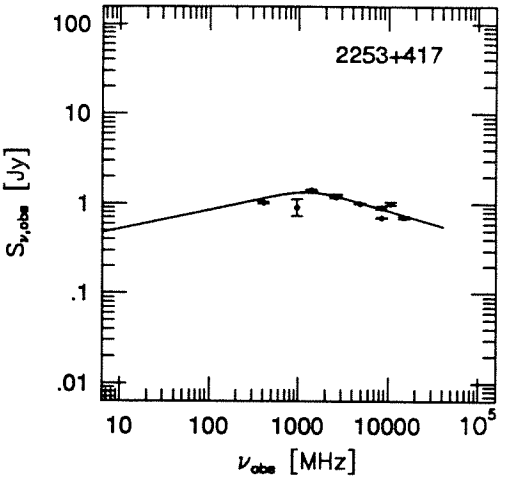

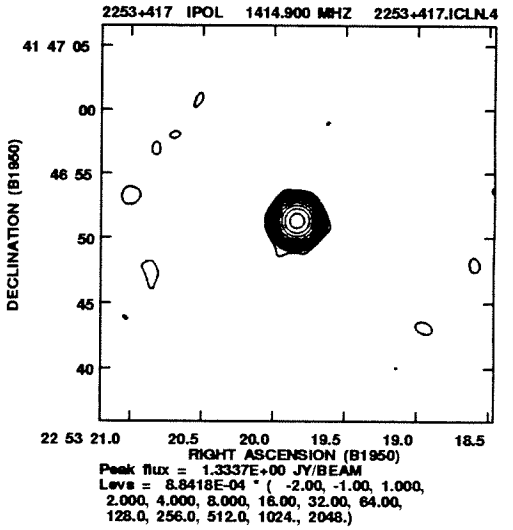

Figure 3.4.74. The maps and spectrum for 2253+417

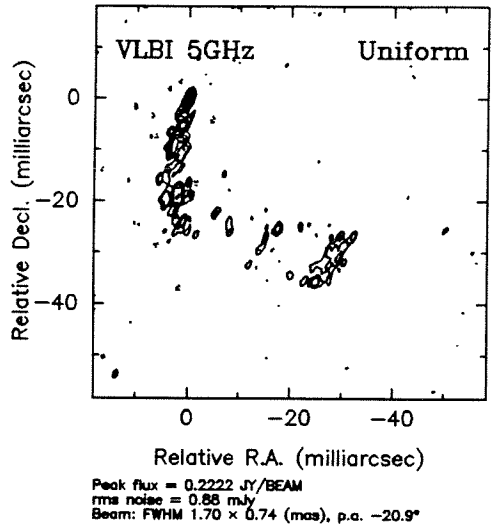

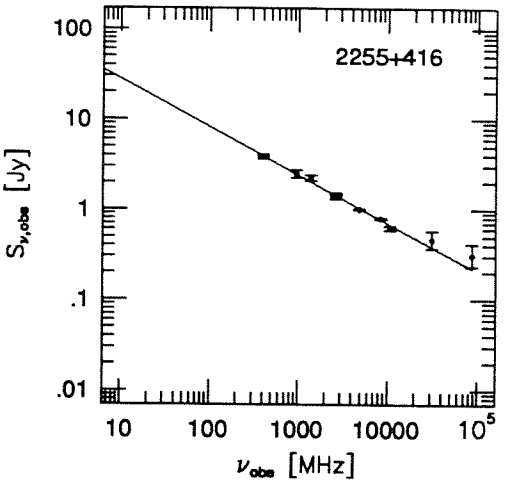

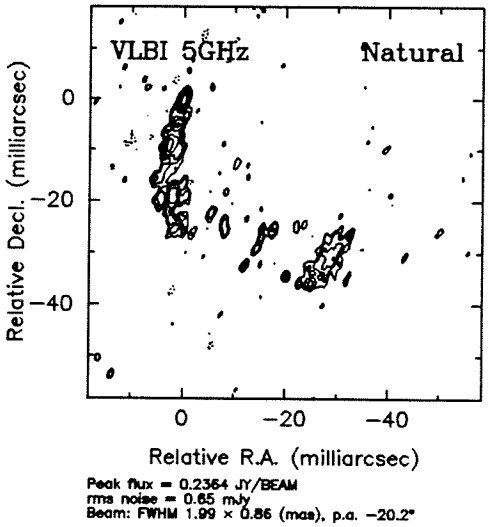

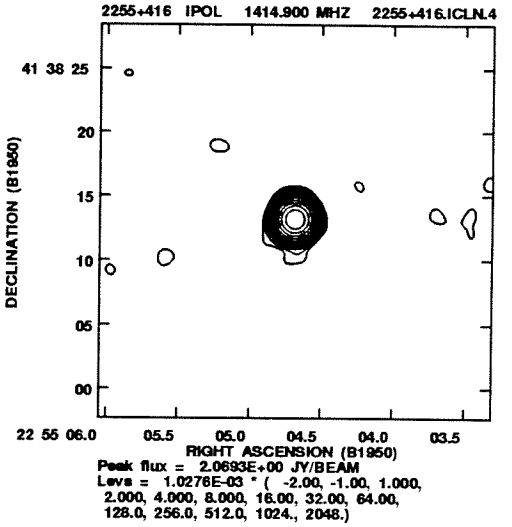

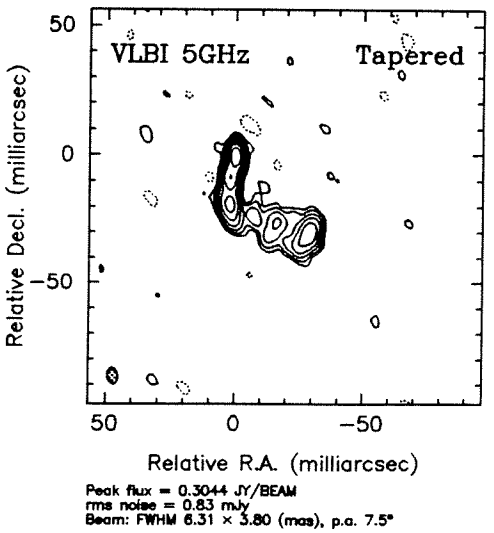

Figure 3.4.75. The maps and spectrum for 2255+416

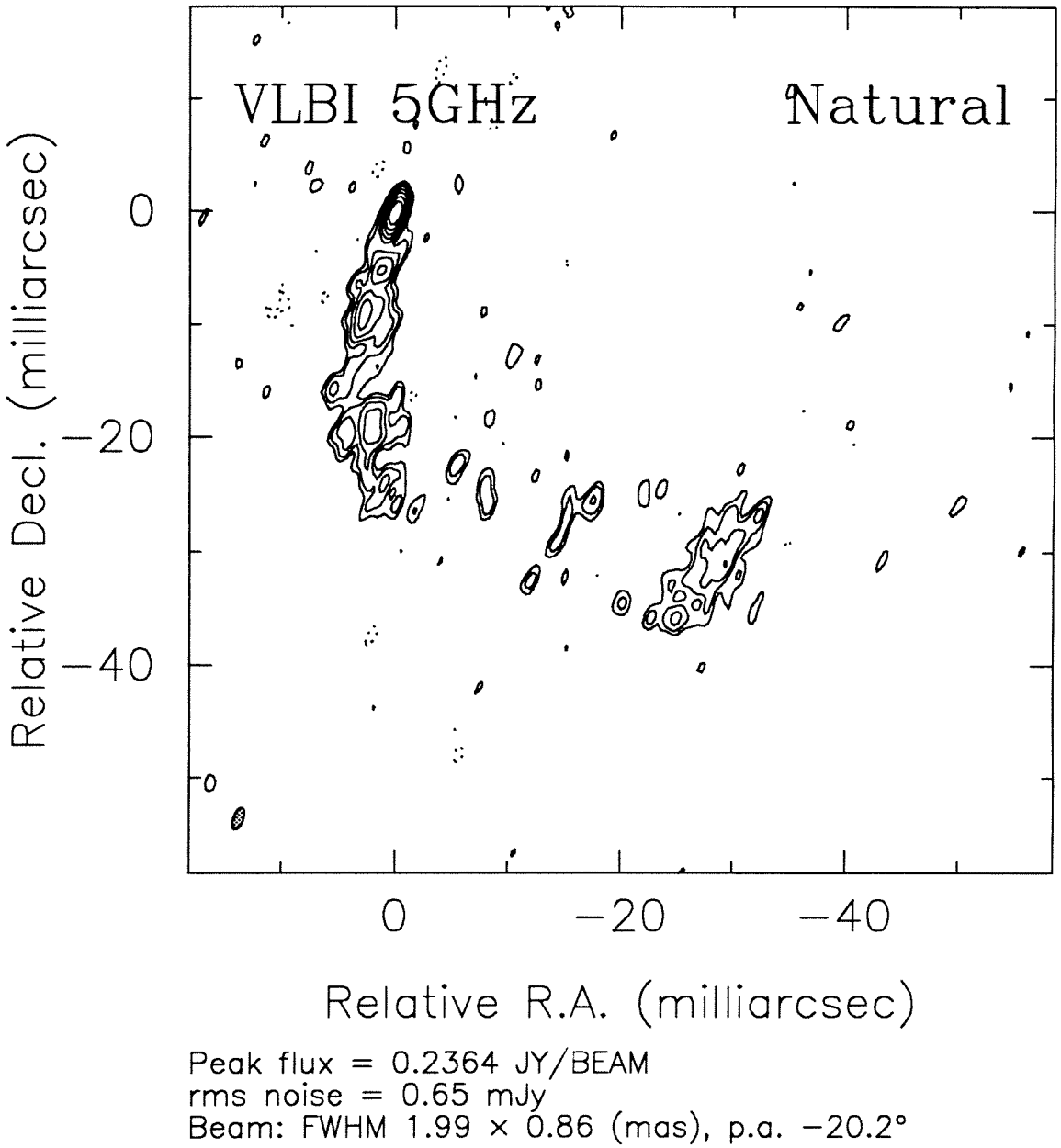

Figure 3.4.75. The VLBI map of 2255+416

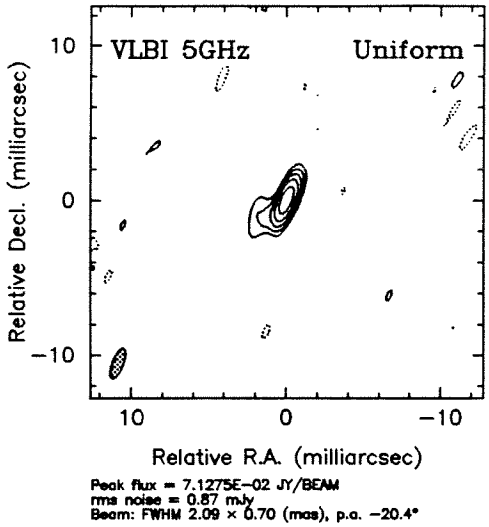

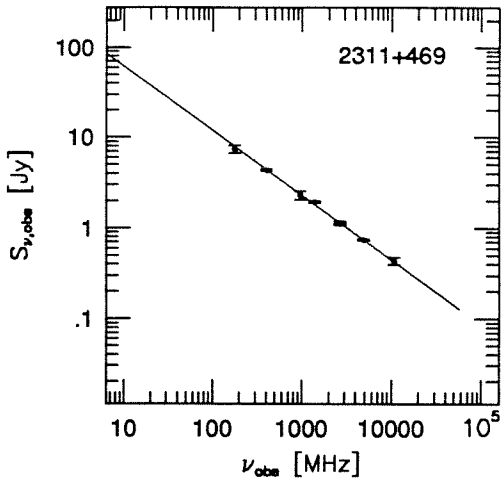

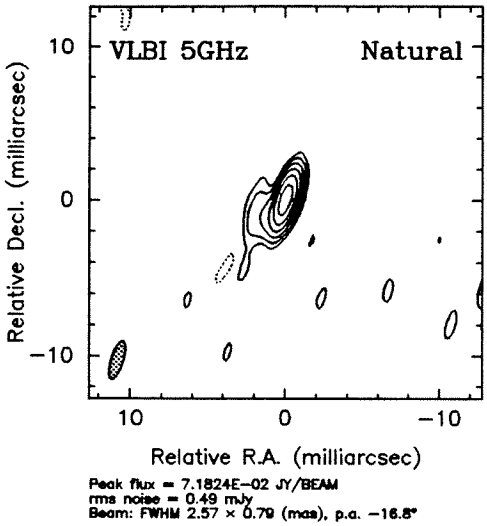

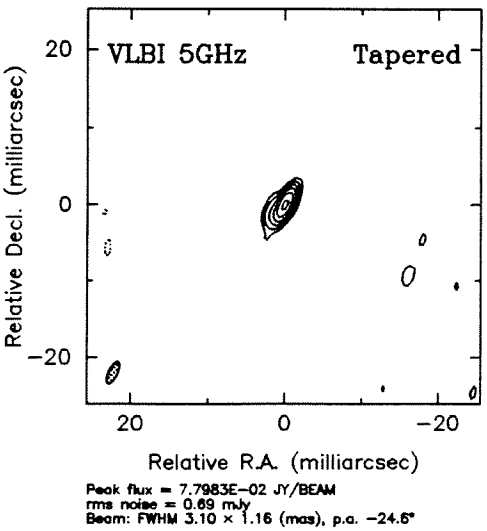

Figure 3.4.76. The maps and spectrum for 2311+469

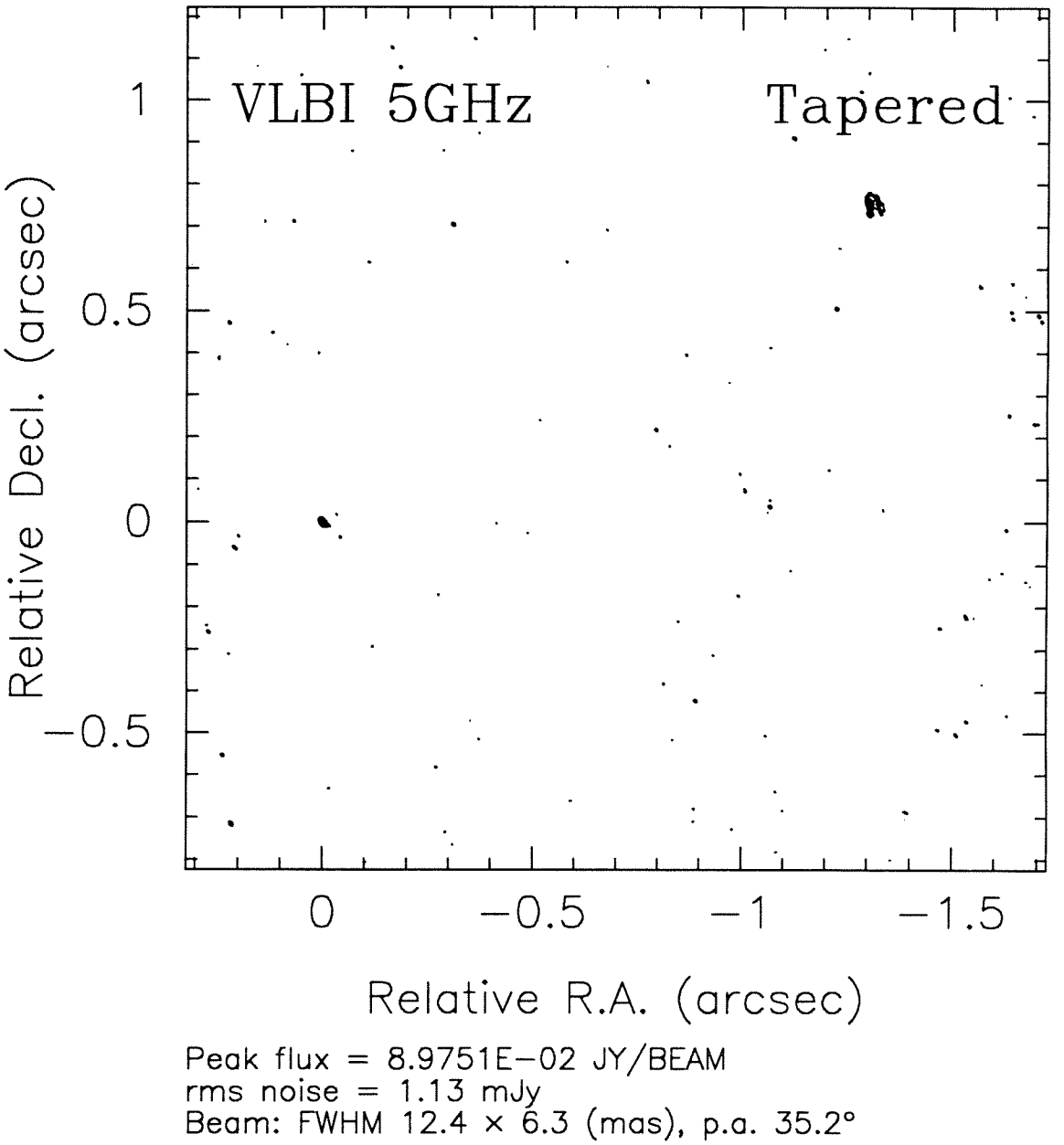

Figure 3.4.76. The VLBI map of 2311+469
showing the hotspot to the North-West of the core

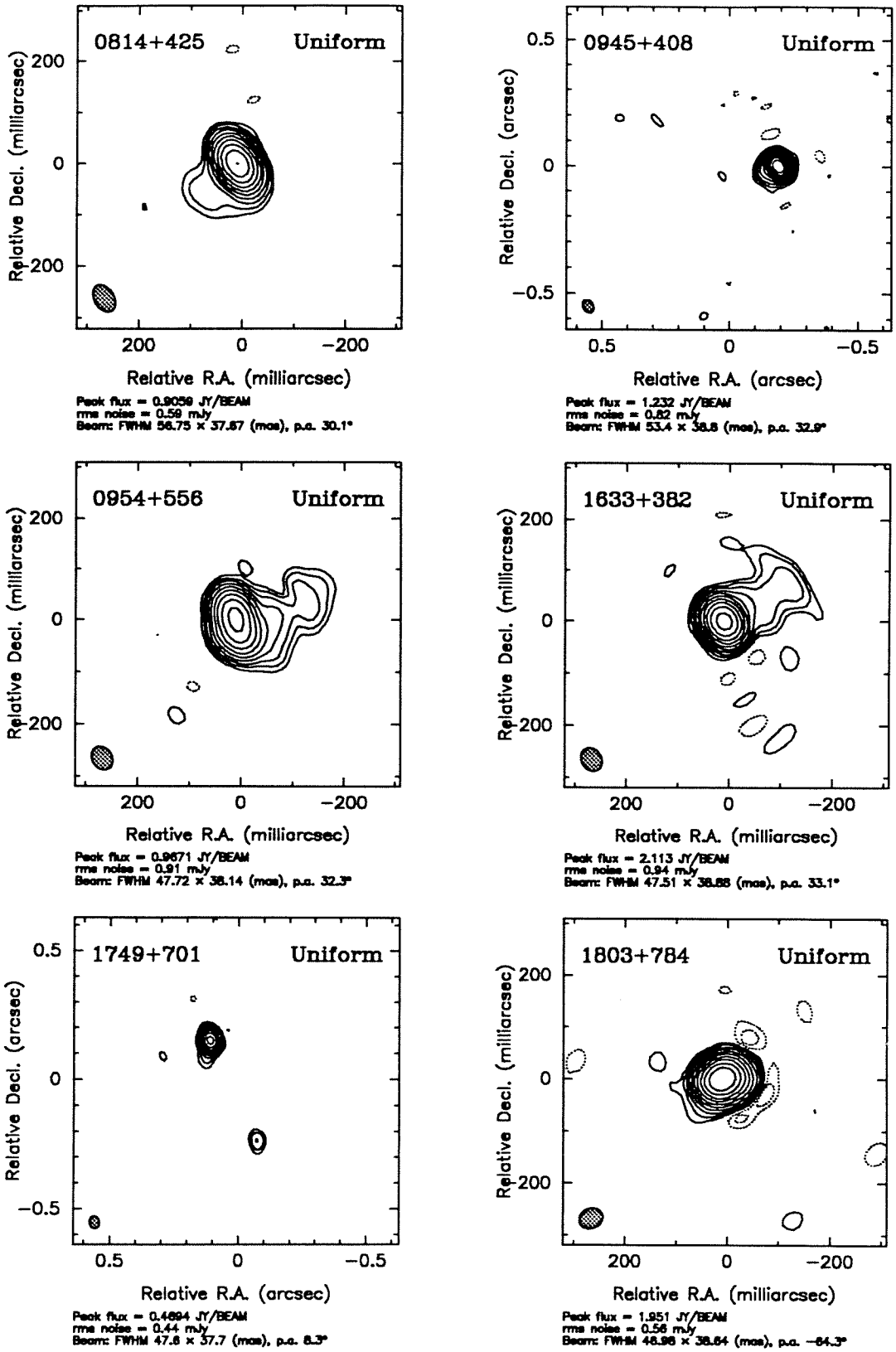

Figure 3.5. MERLIN 5GHz maps for 0814+425, 0945+408, 0954+556, 1633+382, 1749+701, 1803+784

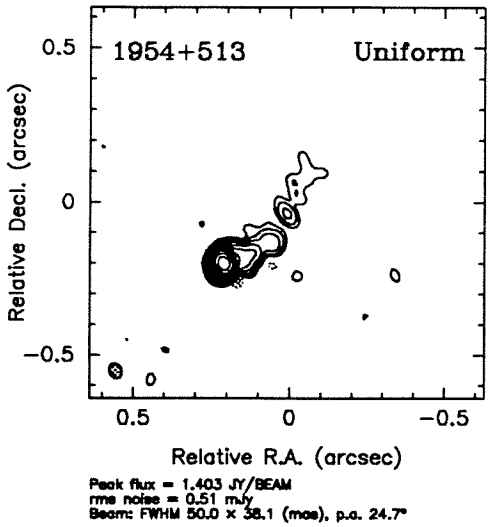

Figure 3.5. (*continued*) MERLIN 5GHz map for 1954+513

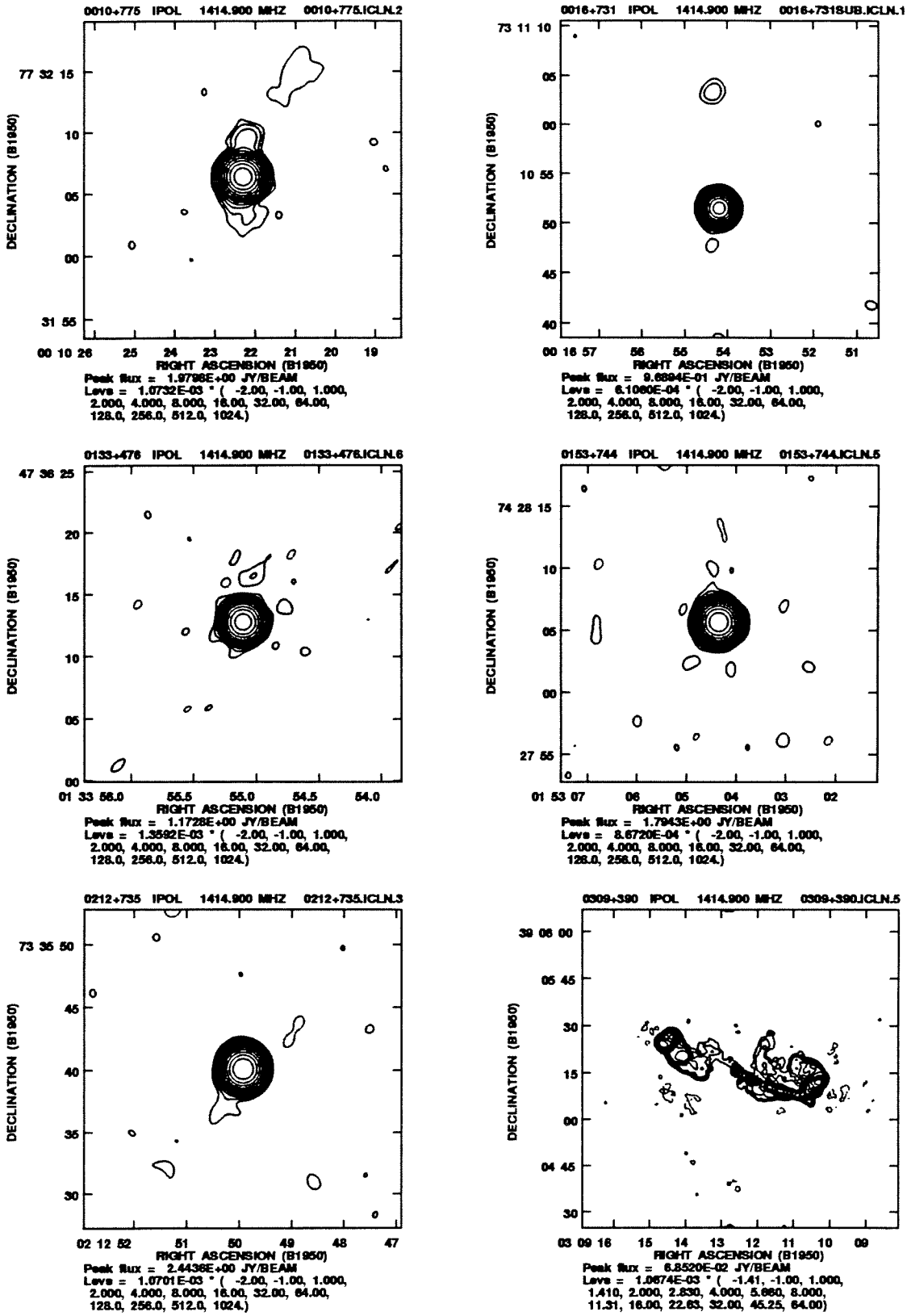

Figure 3.6. (*continued*) VLA maps for 0010+775, 0016+731, 0133+476, 0153+744, 0212+735 and 0309+390

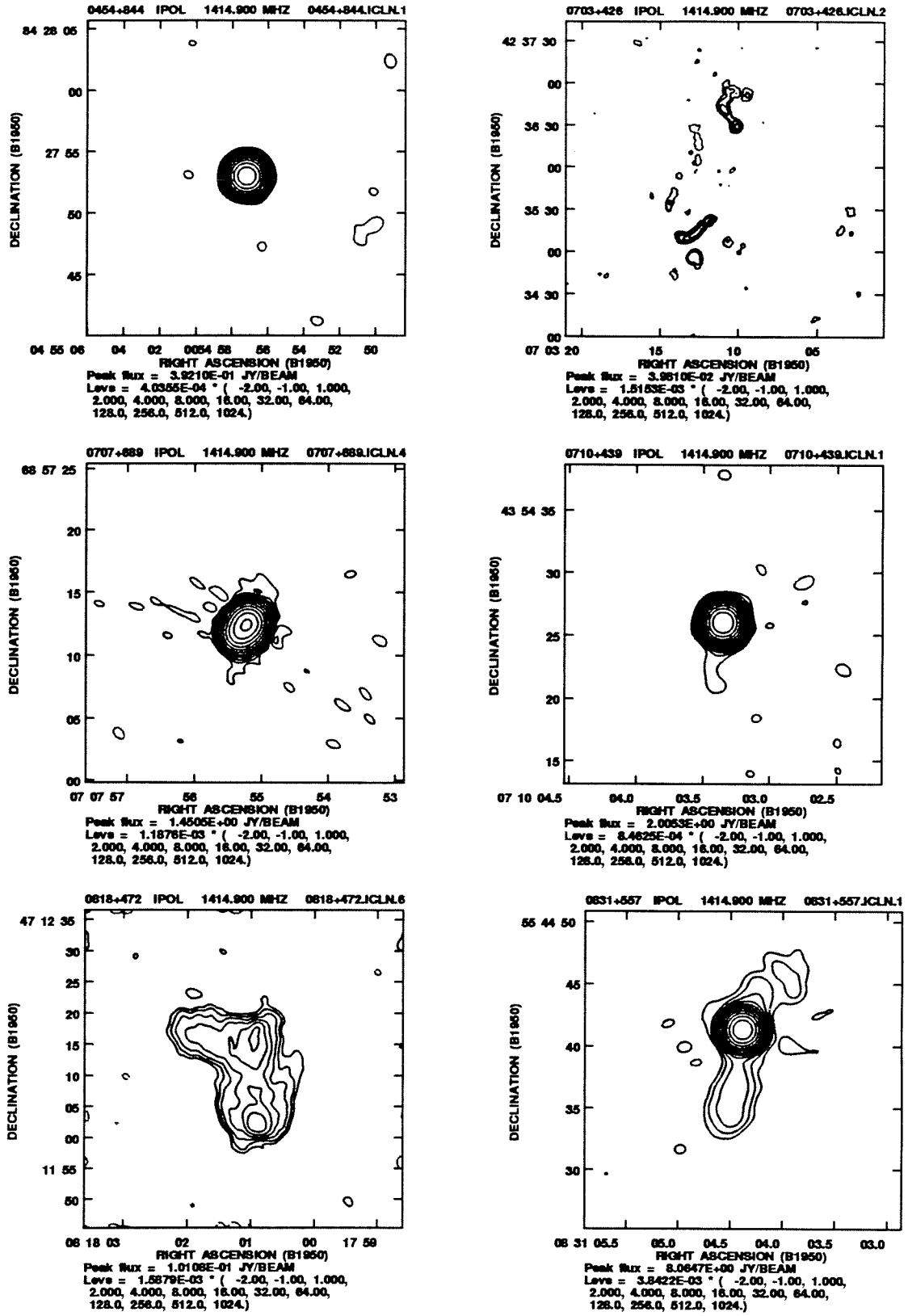

Figure 3.6. (*continued*) VLA maps for 0454+844, 0703+426, 0707+689, 0710+439, 0818+472 and 0831+557

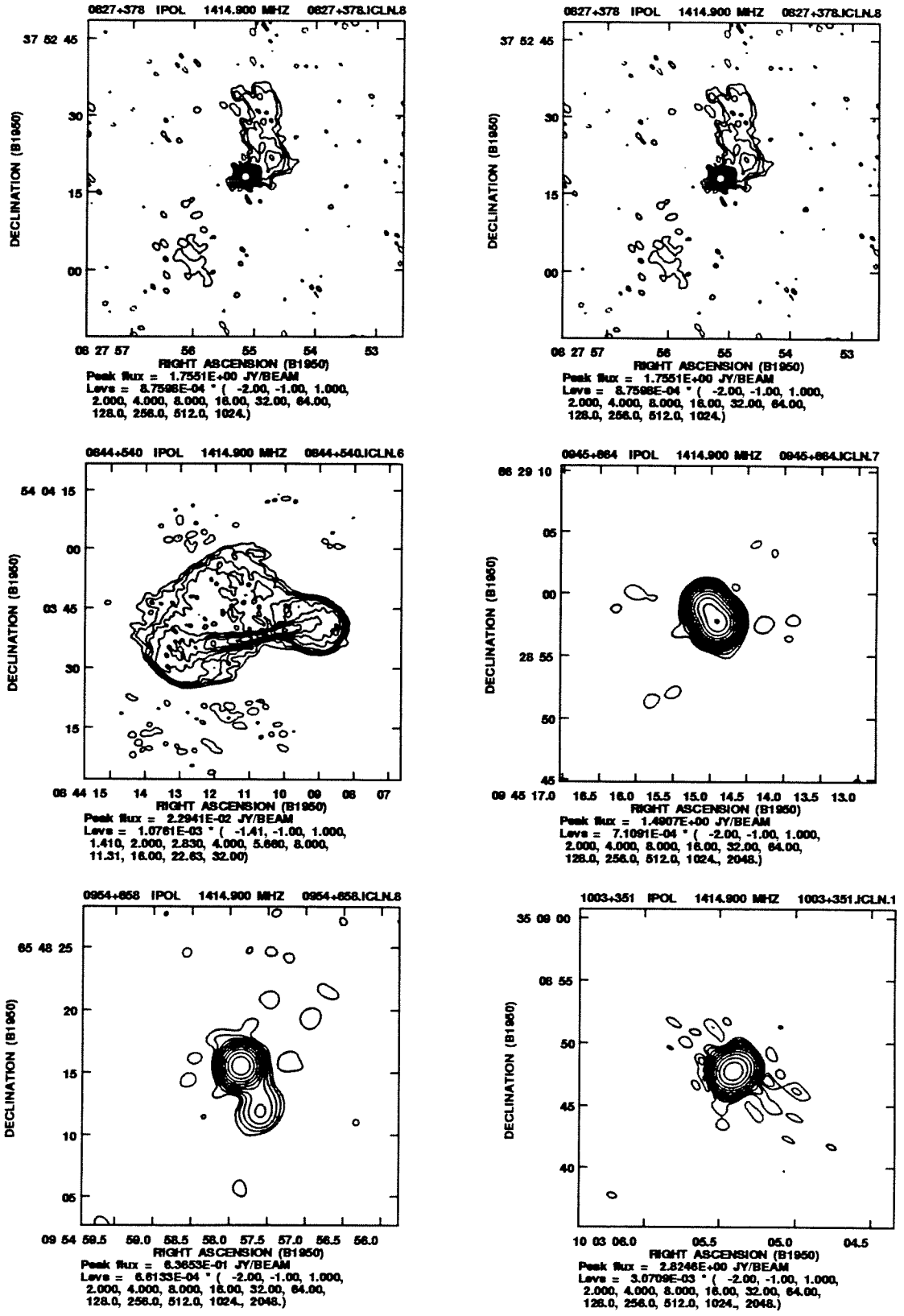

Figure 3.6. (*continued*) VLA maps for 0827+378, 0827+378, 0844+540, 0945+664, 0954+658 and 1003+351

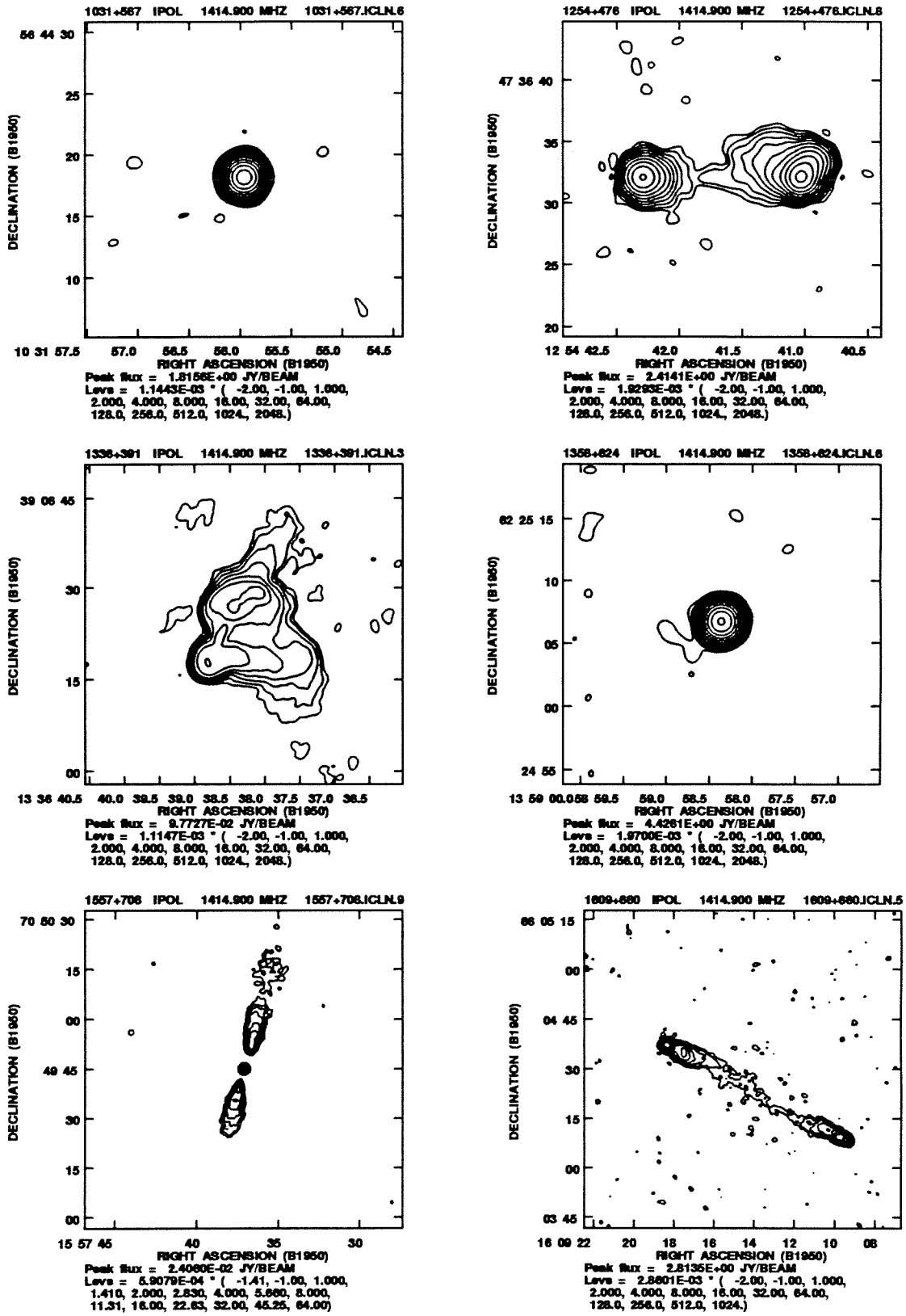

Figure 3.6. (*continued*) VLA maps for 1031+567, 1254+476, 1336+391, 1358+624, 1557+708 and 1609+660

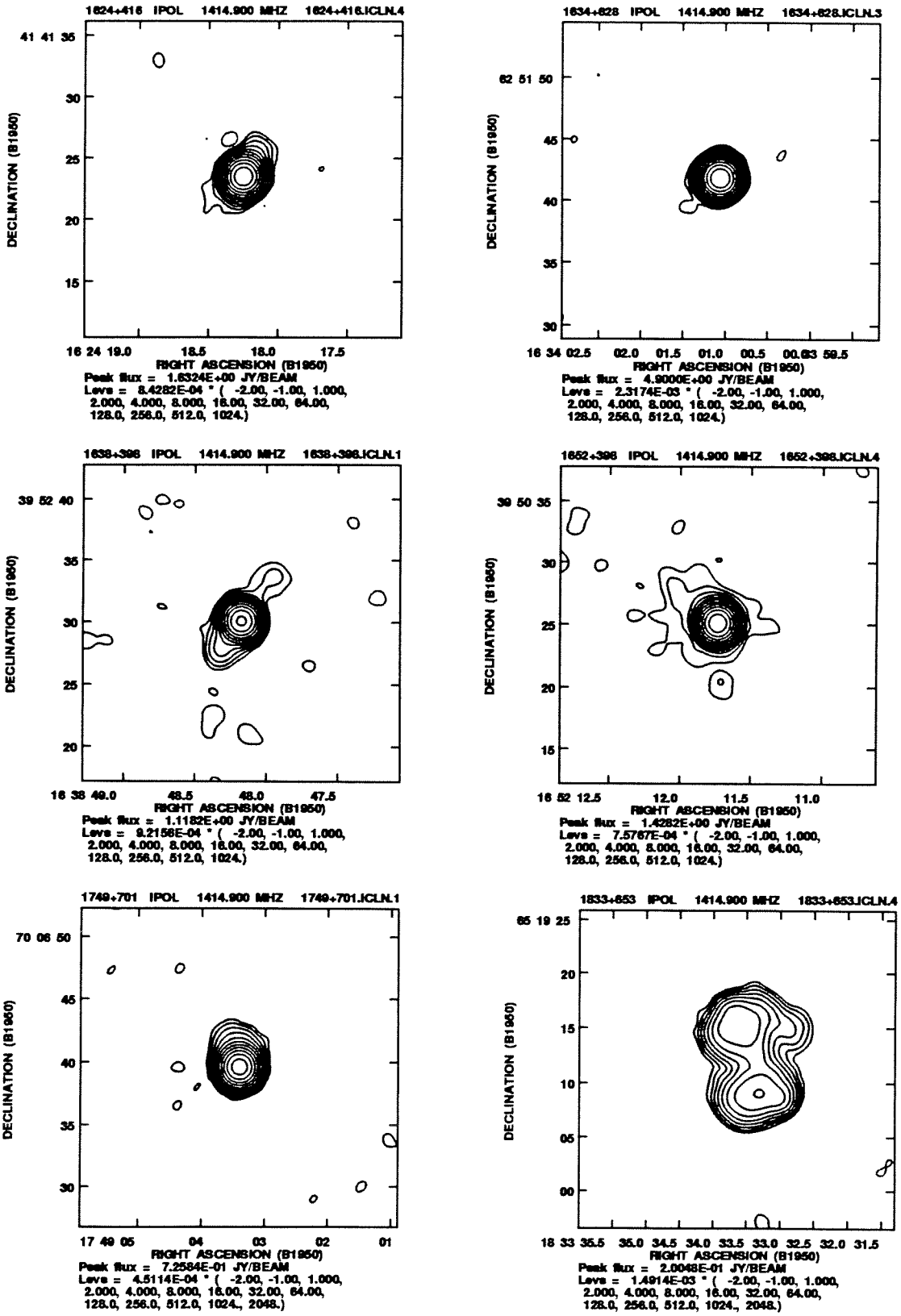

Figure 3.6. (*continued*) VLA maps for 1624+416, 1634+628, 1638+398, 1652+398, 1749+701 and 1833+653

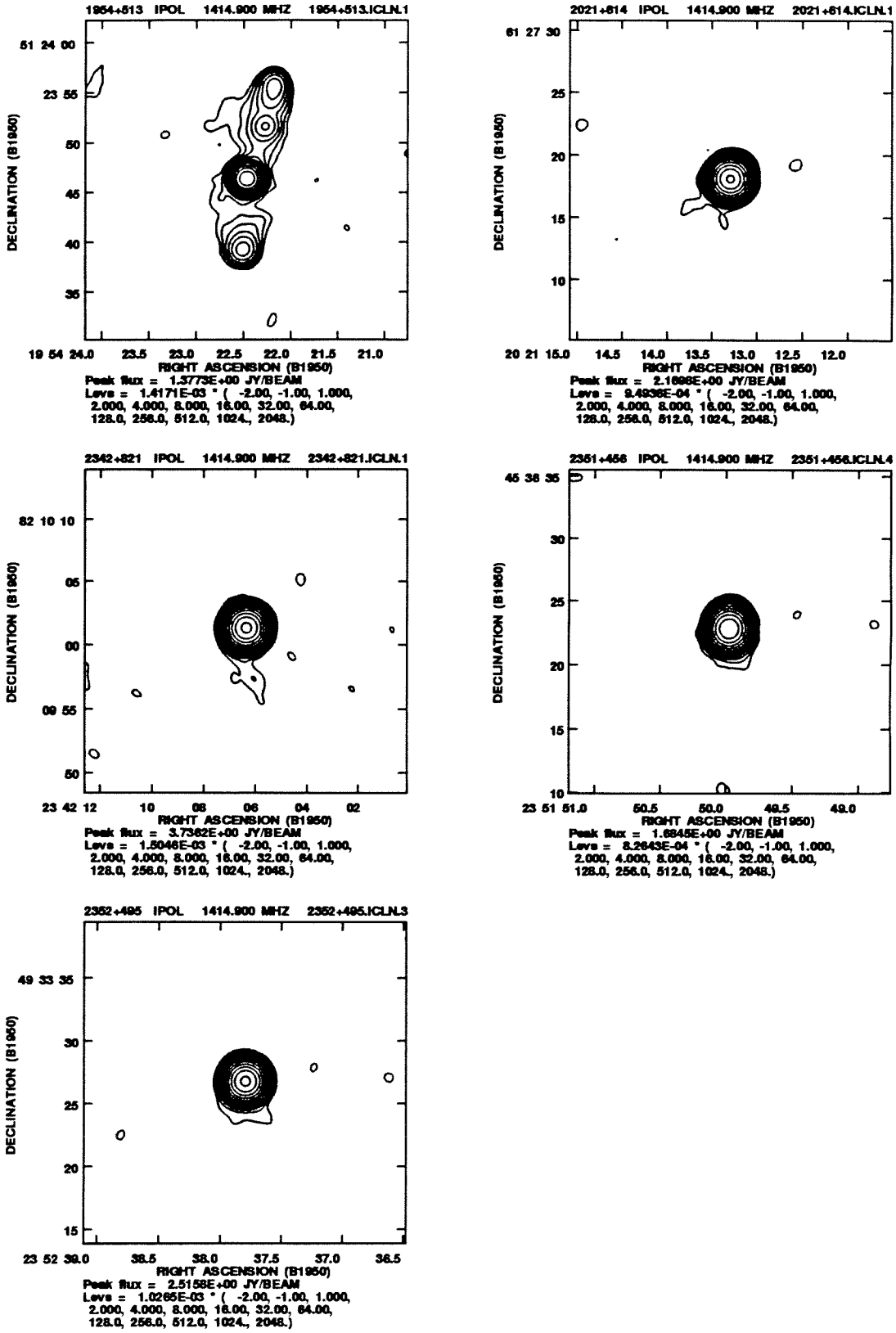

Figure 3.6. (*continued*) VLA maps for 1954+513, 2021+614, 2342+821, 2351+456 and 2352+495

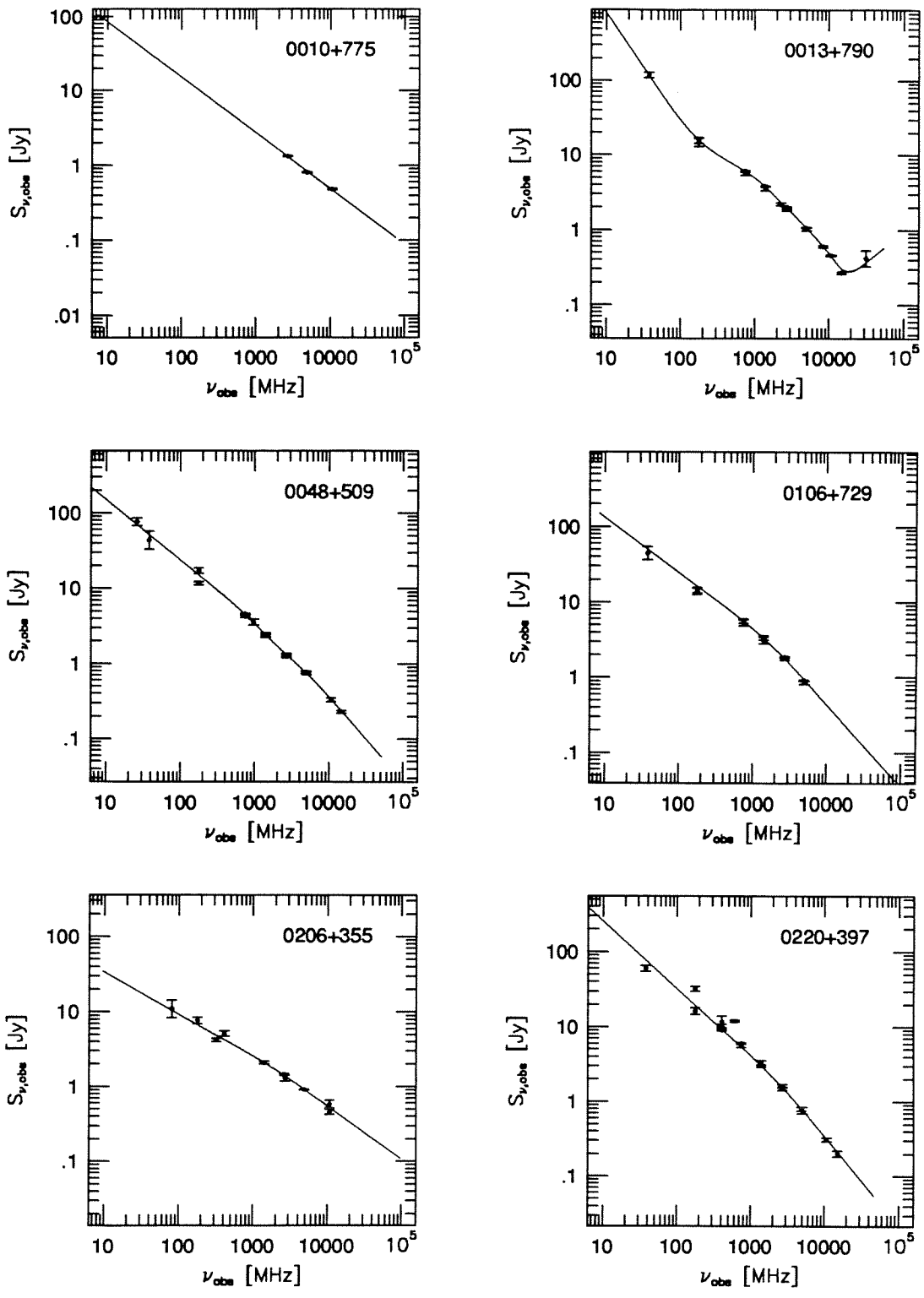

Figure 3.7. Spectra for 0010+775, 0013+790, 0048+509, 0106+729, 0206+355 and 0220+397

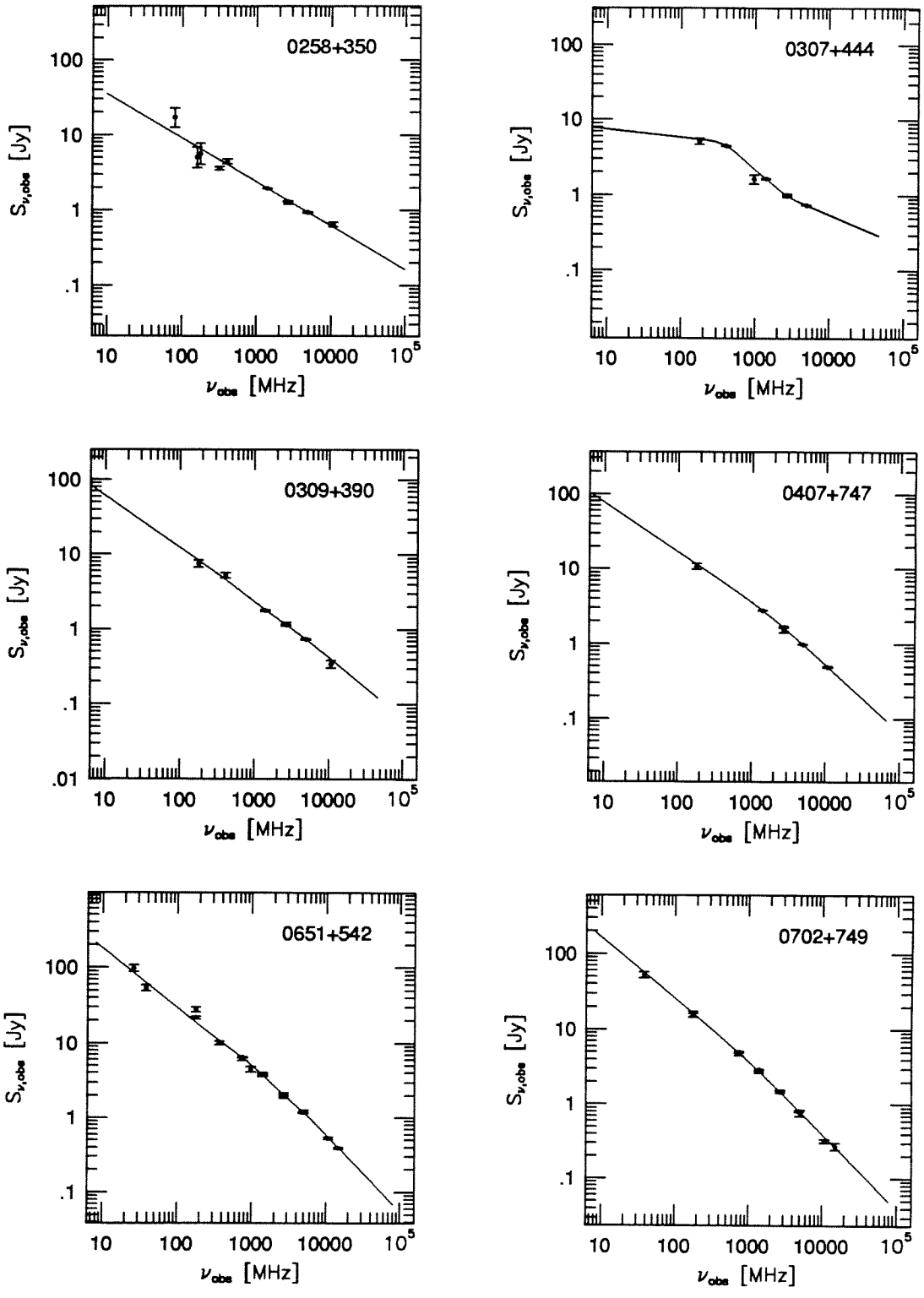

Figure 3.7. (*continued*) Spectra for 0258+350, 0307+444, 0309+390, 0407+747, 0651+542 and 0702+749

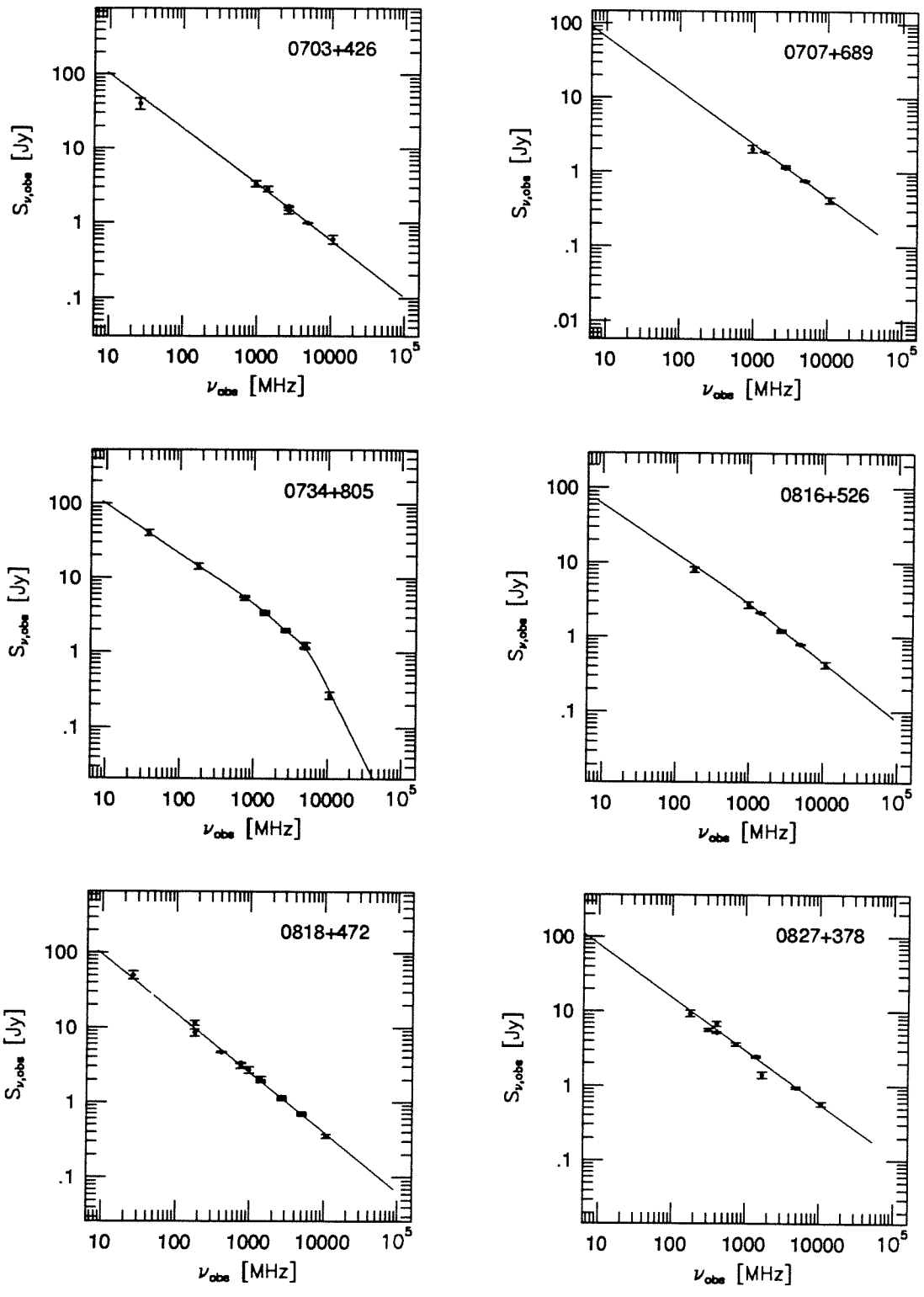

Figure 3.7. (*continued*) Spectra for 0703+426, 0707+689, 0734+805, 0816+526, 0818+472 and 0827+378

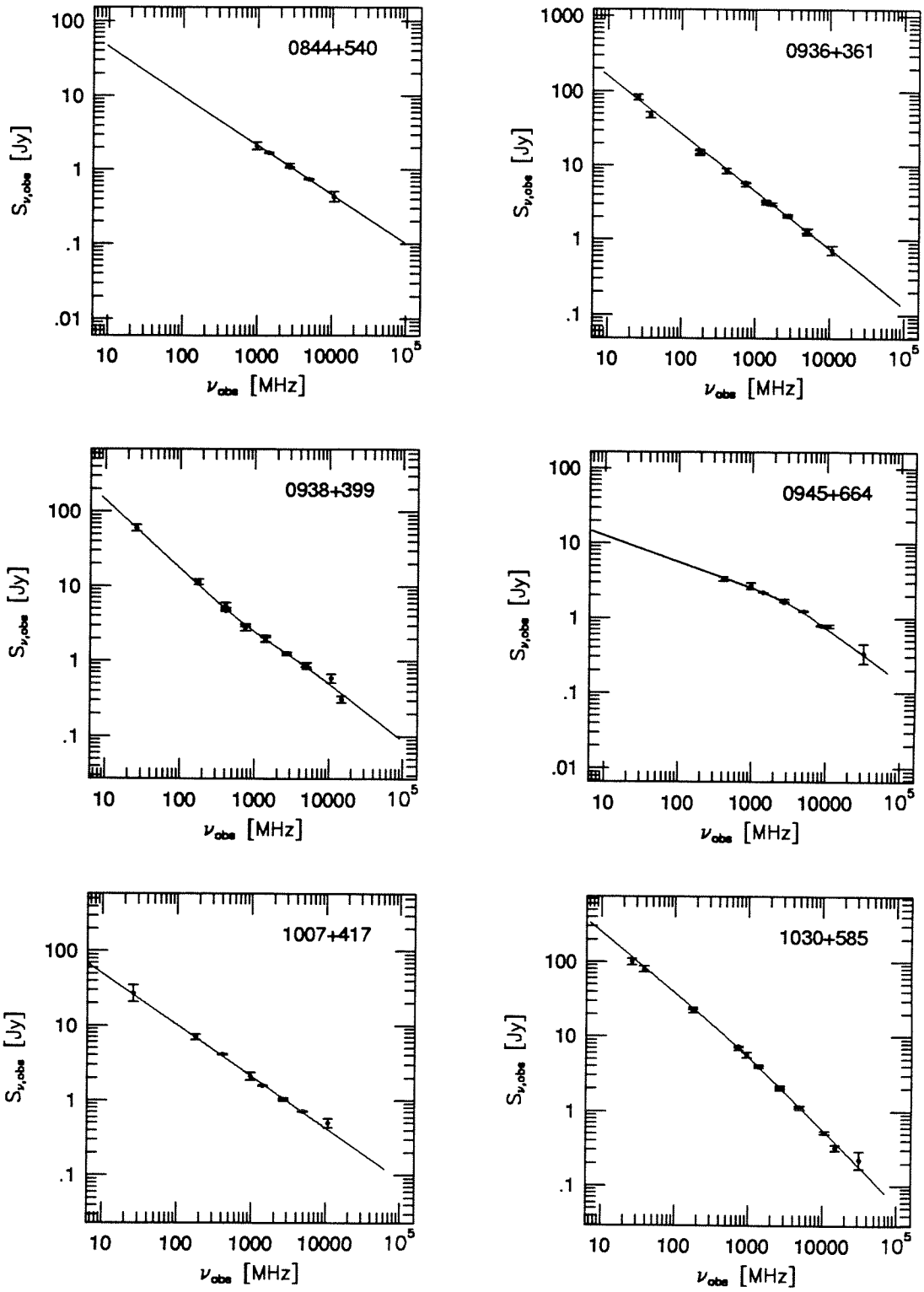

Figure 3.7. (*continued*) Spectra for 0844+540, 0936+361, 0938+399, 0945+664, 1007+417 and 1030+585

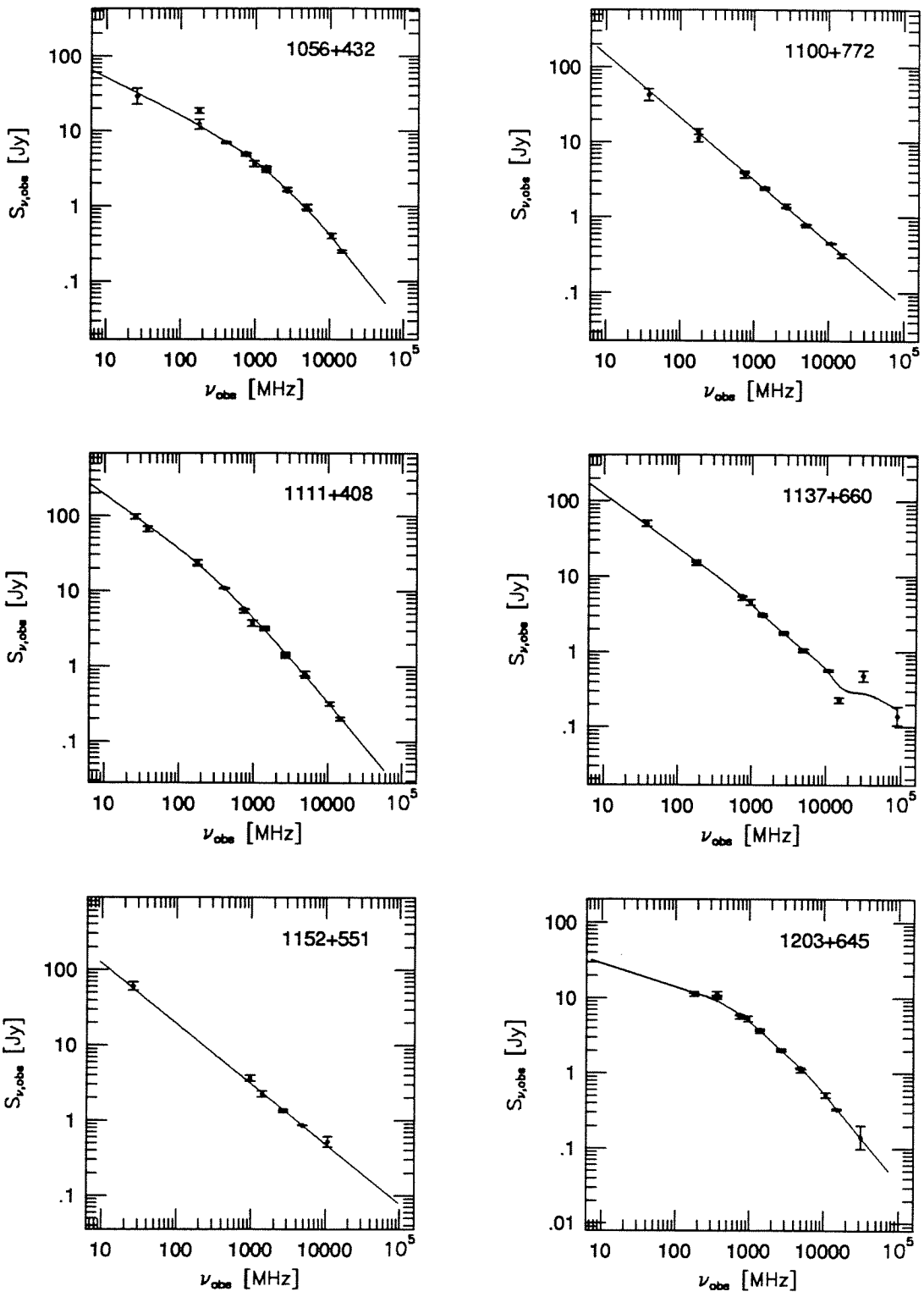

Figure 3.7. (*continued*) Spectra for 1056+432, 1100+772, 1111+408, 1137+660, 1152+551 and 1203+645

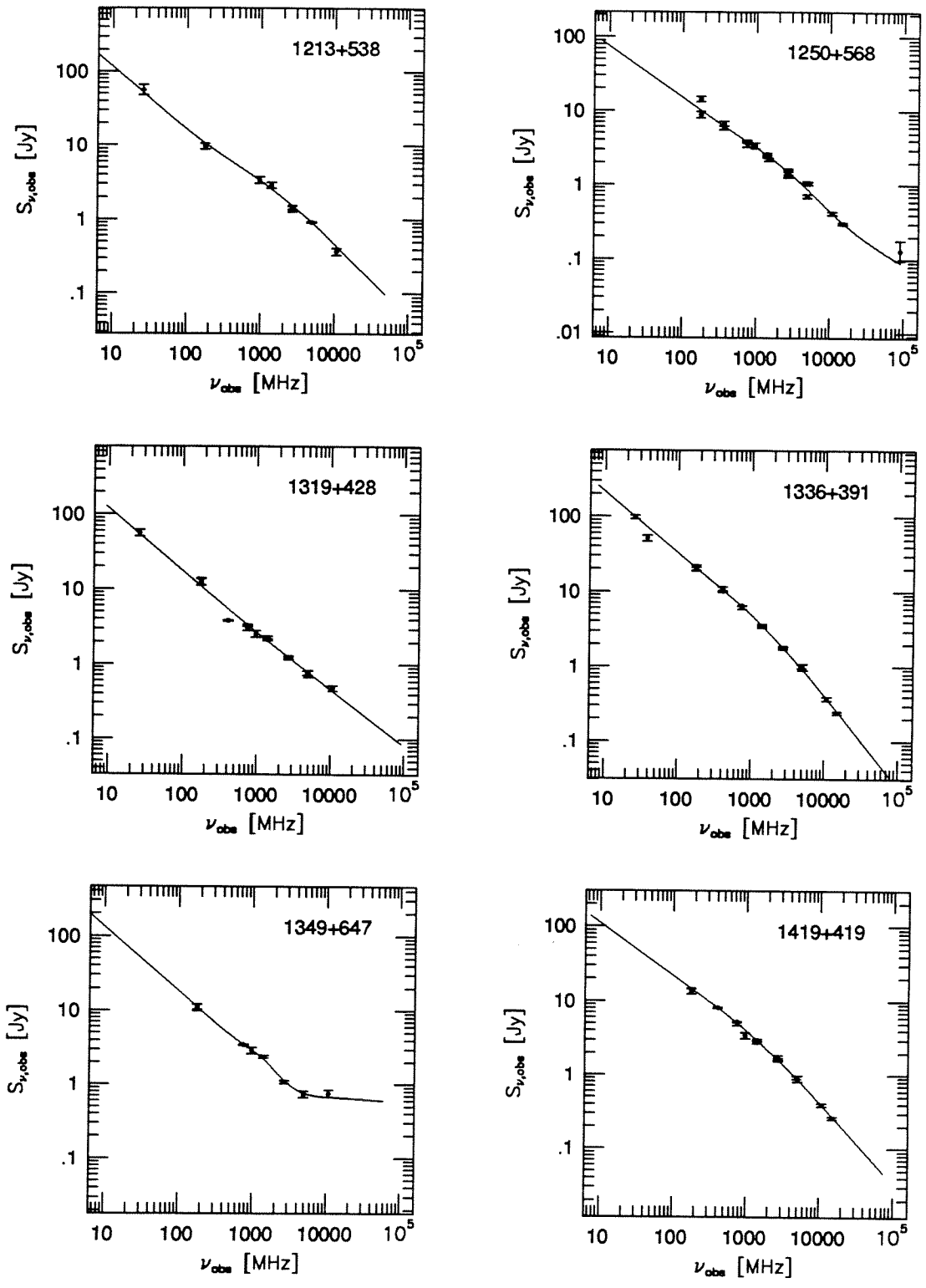

Figure 3.7. (*continued*) Spectra for 1213+538, 1250+568, 1319+428, 1336+391, 1349+647 and 1419+419

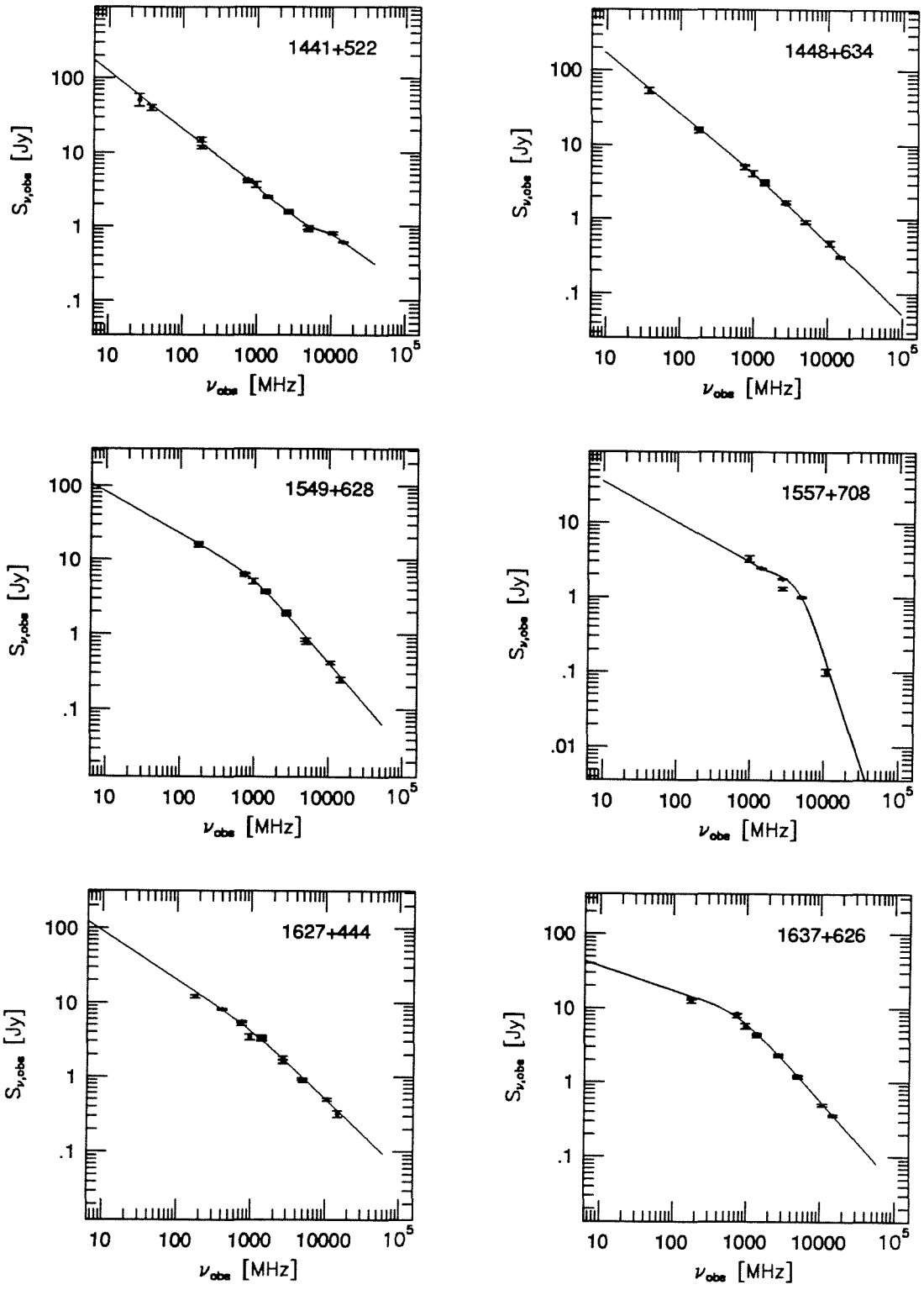

Figure 3.7. (*continued*) Spectra for 1441+522, 1448+634, 1549+628, 1557+708, 1627+444 and 1637+626

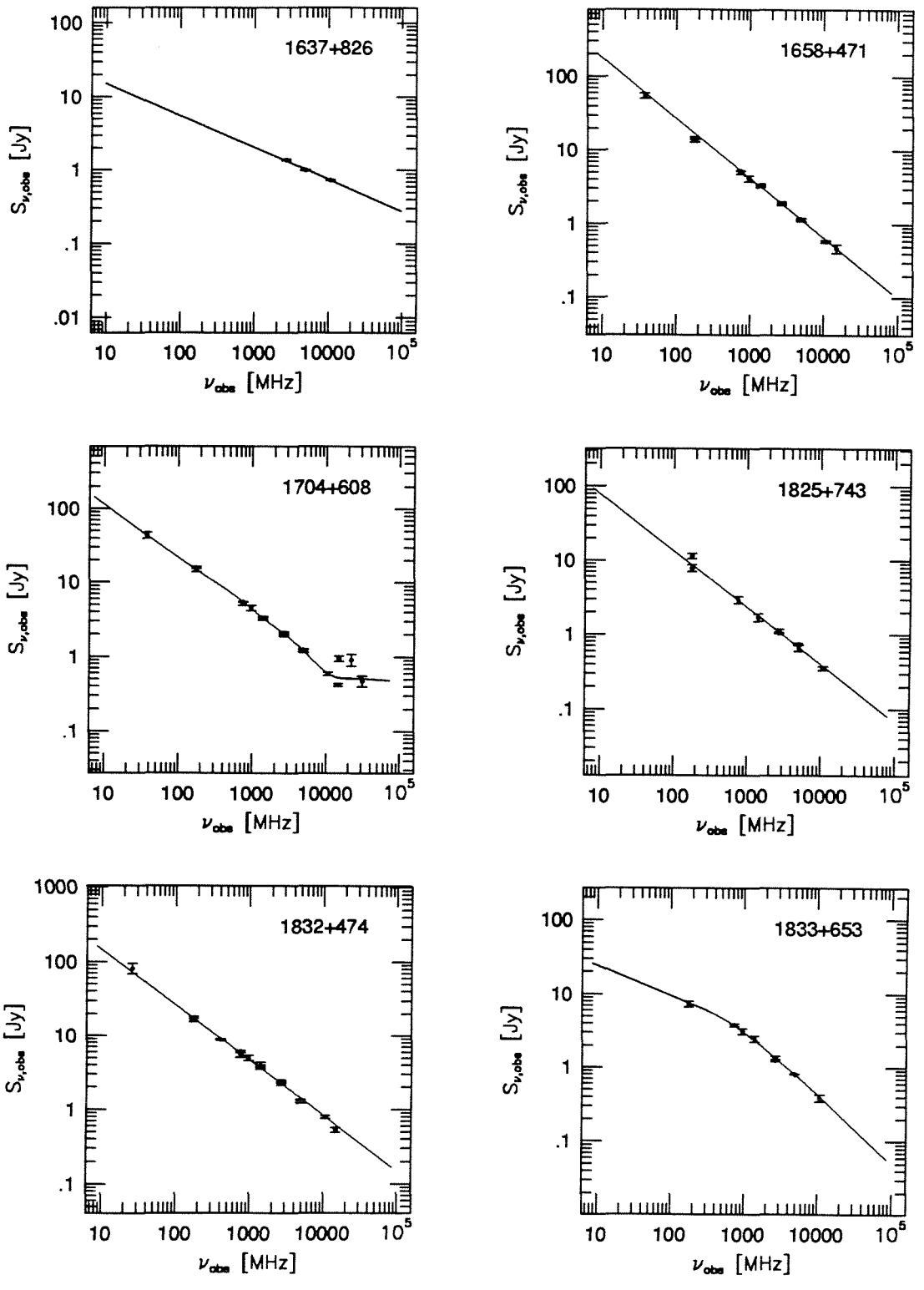

Figure 3.7. (*continued*) Spectra for 1637+826, 1658+471, 1704+608, 1825+743, 1832+474 and 1833+653

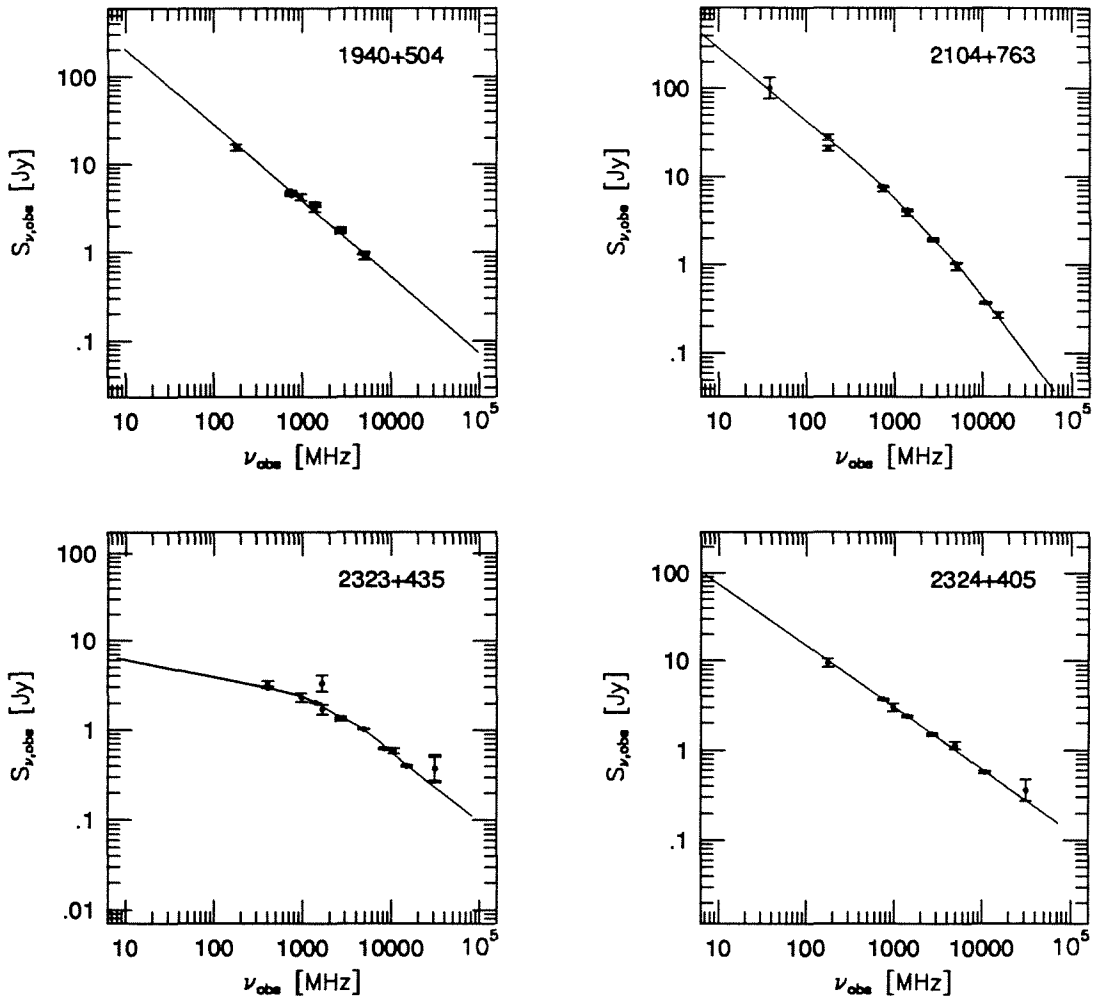

Figure 3.7. (*continued*) Spectra for 1940+504, 2104+763, 2323+435, and 2324+405

Chapter 4

OPTICAL OBSERVATIONS AND DATA REDUCTION

4.1. INTRODUCTION

The optical identification of the radio sources is important since it is not possible generally to determine the distance of a radio source from radio measurement alone. At the beginning of the project there were 38 objects in the CJ1 sample with unknown redshift and 15 objects with at best unreliable optical identifications. We measured redshifts for 23 of the 38 sources in three observing sessions using the Double-Spectrograph on the 200-inch Hale telescope of Palomar Observatory. We observed 14 of the 15 empty fields at Gunn r band with the 60-inch telescope at Palomar. There is an optical counterpart within 3σ of the radio coordinates in all 14 fields. However, the quality of the images is often not good enough to tell whether the objects are galaxies or quasars. Unfortunately, due to bad weather, we could not obtain spectra of any of the newly identified or confirmed objects. During the past three years, redshifts for an additional 6 objects were published. At present 115 objects in the CJ1 sample and 64 objects in the PR sample have known redshifts. Thus redshifts are 90% complete for the combined sample of PR & CJ1.

We have also made optical polarimetry observations for 58 objects brighter than $\sim 19^m.5$ in the CJ1 sample with the 90-inch and 61-inch telescopes of the Steward Observatory, University of Arizona. These data are used to study the distribution of the misalignment angles (*Chapter 6*).

4.2. NEW REDSHIFTS

This section is a reproduction of a paper which we have published in the *Astronomical Journal*, 108, 395 (1994).

NEW REDSHIFTS OF RADIO SOURCES FROM THE S4 AND S5 SURVEYS

W. Xu, C. R. Lawrence, A. C. S. Readhead, and T. J. Pearson

Owens Valley Radio Observatory, 105-24 California Institute of Technology, Pasadena, California 91125

ABSTRACT

Redshifts are reported for 23 objects in the Caltech–Jodrell Bank VLBI survey.

1. INTRODUCTION

We are engaged in VLBI surveys of two complete samples of radio sources. The Pearson–Readhead (PR) survey (Pearson & Readhead 1988) contains 65 sources in the S4 (Pauliny-Toth *et al.* 1978) and S5 (Kühr *et al.* 1981) surveys with $S(5\ \mathrm{GHz}) \geq 1.3$ Jy, $\delta > 35°$ and $|b| \geq 10°$. The Caltech–Jodrell Bank (CJ) survey[1](Xu *et al.* 1993; Wilkinson *et al.* 1993) includes 135 sources in the S4 and S5 surveys with $0.7\ \mathrm{Jy} \leq S(5\ \mathrm{GHz}) < 1.3$ Jy in the same sky region, which can be combined with the PR sample to form a flux-limited complete sample of 200 sources [2]. The CJ survey aims at mapping all objects strong enough for MK II VLBI at both 1.67 GHz and 5 GHz. The combined PR and CJ sample will make

[1] The Caltech–Jodrell Bank VLBI survey is in collaboration with P. N. Wilkinson and A. Polatidis of Nuffield Radio Astronomy Laboratories, Univ. of Manchester, Jodrell Bank, U.K.

[2] Two sources in the S4 survey are not included in the CJ sample. One is a planetary nebula. The other is actually a quasar pair, each of which has a flux density less than 0.7 Jy.

possible a more detailed classification of AGNs and provide a sample which is sufficiently large to make interesting statistical tests by class.

When we began the CJ survey in early 1990, about one-third of the objects had unknown redshifts or optical identifications. We therefore began a project at the Palomar Observatory to determine as many of the missing optical identifications and redshifts as possible. Our observations are not yet complete; however, we have determined about half of the missing redshifts.

2. OBSERVATIONS

All of the spectra were taken with the Double Spectrograph on the Palomar 200-inch telescope. A 300 line/mm grating was used in the blue and a 158 line/mm grating in the red, providing resolution of 9 Å in the blue and 18 Å in the red, respectively. An 800 × 800 Texas Instruments CCD detector was used in both the blue and red. The incoming beam was divided with a dichroic beamsplitter either at 4800 Å, giving an overall wavelength coverage of 3200 – 9300 Å, or at 5200 Å, giving an overall wavelength coverage of 3800 – 10000 Å. The dates of observations and integration times are listed in Table 1.

The rms error in fitting He–Hg–Ar arc lines was typically about 0.3 Å in the blue and 0.5 Å in the red. The wavelength scale was shifted slightly based on the He comparison spectra obtained immediately after each object spectrum to compensate for flexure in the instrument. Correction for atmospheric absorption and absolute flux density calibration were based on observations of Oke & Gunn (1983) standard stars.

3. REDSHIFTS

After continuum subtraction, the emission and absorption features were modeled with Gaussian or Lorentzian functions. No statistical criteria were used to evaluate the quality of the fit; rather the residuals were compared visually to noise in adjacent parts of the spectrum. A weighted-mean redshift was calculated for each source, with the weight of

each line component given by the ratio of height to width. An uncertainty was calculated by a weighted average of the deviations of the line components from the mean redshift and a 0.5 Å wavelength error, added in quadrature. The results are presented in Table 1, along with a list of the line components used in the calculation. Many of the objects have complex spectra as can be seen in the table. Additional features, both in absorption and emission, are seen in some of the objects, but were not useful in determining the redshift and are therefore not listed. The spectra and further analysis will be published when the project is complete.

ACKNOWLEDGEMENTS

The reference search has made use of the NASA/IPAC Extragalactic Database (NED) which is operated by the Jet Propulsion Laboratory, California Institute of Technology, under contract with the National Aeronautics and Space Administration.

This work is supported in part by the National Science Foundation under grants AST–8814554 and AST–9117100 to the Owens Valley Radio Observatory.

REFERENCES

Browne, I. W. A., Patnaik, A. R., Walsh, D., & Wilkinson, P. N. 1993, MNRAS, 263, L32

Carilli, C., Rupen, M., & Yanny., B. 1993, in preparation

Kühr, H., Pauliny-Toth, I.I.K., Witzel, A., & Schmidt, J. 1981, AJ, 86, 854

Lawrence, C.R. et al. 1994, ApJ, in press

O'Dea, C.P., Baum, S.A., Stanghellini, C., Dey, A., van Breugel, W., Deustua, S., & Smith, E.P. 1992, AJ, 104, 1320

Oke, J.B., & Gunn, J.E. 1983, ApJ, 266, 713

Pauliny-Toth, I.I.K., Witzel, A., Preuss, E., Kühr, H., Kellermann, K.I., Fomalont, E.B., & Davis, M. M. 1978, AJ, 83, 451

Pearson, T.J., & Readhead, A.C.S. 1988, ApJ, 328, 114

Stickel, M., Padovani, P., Urry, C.M., Fried, J.W., & Kühr, H. 1991, ApJ, 374, 431

Véron-Cetty, M.-P., & Véron, P. 1991, A Catalog of Quasars and Active Nuclei (5th Edition)

Vigotti, M., Merighi, R., Vettolani, G., Lahulla, J.F., & Lopez-Arroyo, M. 1990, A&AS, 83, 205

Walsh, D., Beckers, J.M., Carswell, R.F., & Weymann, R.J. 1984, MNRAS, 211, 105

Wilkinson, P.N., Polatidis, A.G., Readhead, A.C.S., Xu, W., & Pearson, T.J. 1993, in Sub Arcsecond Radio Astronomy, eds. Davis, R.J., & Booth, R.S., p.213

Xu, W., Readhead, A.C.S., Pearson, T.J., Wilkinson, P.N., & Polatidis, A. 1993, Bull. AAS, 24, 1300

Table 1. Redshifts of Caltech–Jodrell Bank VLBI Survey Sources

Source	RA (1950.0)	Dec (1950.0)	z	Integration Time(s)	Observation Date	Features used in redshift determination
0010+775	00:10:22.31	77:32:06.4	0.326 ± 0.001	3000	22 Jan 1990	Mg II λ 2798, [O II] λ 3727, [O III] λλ 4959, 5007, Hα, [S II] λλ 6717, 6734.
0022+390	00:22:46.67	39:02:59.0	1.946 ± 0.002	3000	31 Dec 1989	Lyα, O I λ 1303, Si IV/O IV λ ∼ 1400, C IV λ 1549, C III] λ 1909, Mg II λ 2798.
0218+357	02:18:04.13	35:42:32.0	———[a]	3000	31 Dec 1989	Featureless spectrum.
0402+379	04:02:29.88	37:55:26.9	0.055 ± 0.001	3000	31 Dec 1989	[O I] [S III] λ 6300, O I] λ 6364, Hα, [N II] λ 6549, [N II] λ 6583, [S II] λλ 6717, 6734.
0407+747	04:07:04.6	74:43:29	———	3000	31 Dec 1989	Featureless spectrum.
0620+389	06:20:51.53	38:58:27.3	3.469 ± 0.004	3000	23 Jan 1990	Lyα, N V λ 1240, Si IV/O IV λ ∼ 1400, C IV λ 1549, C III] λ 1909.
0707+689	07:07:55.24	68:57:12.7	1.141 ± 0.002	3000	23 Jan 1990	C III] λ 1909, Mg II λ 2798, [O II] λ 3727.
0716+714	07:16:13.03	71:26:15.2	———	1500	24 Jan 1990	Featureless spectrum.
0740+828	07:40:33.18	82:49:24.2	1.991 ± 0.001	1180	22 Jan 1990	Lyα, N V λ 1240, Si IV/O IV λ ∼ 1400, C IV λ 1549, C III] λ 1909, Mg II λ 2798.
0805+410	08:05:33.63	41:01:33.1	1.420 ± 0.003[b]	3000	22 Jan 1990	C IV λ 1549, C III] λ 1909, Mg II λ 2798.
1003+830	10:03:25.84	83:04:56.7	0.322 ± 0.001	3000	23 Jan 1990	Mg II λ 2798, [O III] λλ 4959, 5007, Hα, [N II] λ 6549, [N II] λ 6583.
1020+400	10:20:14.59	40:03:27.2	1.254 ± 0.002[b]	1500	23 Jan 1990	Si IV/O IV λ ∼ 1400, C IV λ 1549, C III] λ 1909, Mg II λ 2798.
1053+704	10:53:27.72	70:27:47.9	2.492 ± 0.001	3000	23 Jan 1990	Lyα, N V λ 1240, C IV λ 1549, C III] λ 1909.
1053+815	10:53:36.22	81:30:35.6	0.706 ± 0.006[h]	3000	23 Jan 1990	C III] λ 1909, Mg II λ 2798.
1128+385	11:28:12.52	38:31:51.5	1.733 ± 0.003	3000	23 Jan 1990	Lyα, N V λ 1240, Si IV/O IV λ ∼ 1400, C IV λ 1549, C III] λ 1909, Mg II λ 2798.

Table 1. Redshifts of Caltech–Jodrell Bank VLBI Survey Sources (*continued*)

1144+402	11:44:21.02	40:15:14.1	1.088 ± 0.001[c]	2400	24 Jan 1990	C IV λ 1549, C III] λ 1909, Mg II λ 2798, Hγ.
1144+542	11:44:04.58	54:13:22.8	2.201 ± 0.007	3000	24 Jan 1990	Lyα, N V λ 1240, Si IV/O IV λ ∼ 1400, C IV λ 1549, C III] λ 1909, Mg II λ 2798.
1225+368	12:25:30.77	36:51:47.0	1.973 ± 0.002[h]	3000	24 Jan 1990	Lyα, C IV λ 1549.
1242+410	12:42:26.40	41:04:30.0	0.813 ± 0.002	3000	24 Jan 1990	C III] λ 1909, Mg II λ 2798, Hβ, [O III] λλ 4959, 5007, [O II] λ 3727, Hζ.
1333+459	13:33:15.70	45:57:56.4	2.449 ± 0.001[d]	2000	22 Jan 1990	O VI λ 1035, Lyα, N V λ 1240, Si IV/O IV λ ∼ 1400, C IV λ 1549, He II λ 1640, O III λ 1667, C III] λ 1909.
1342+663	13:42:41.04	66:21:13.1	1.351 ± 0.003	3000	23 Jan 1990	Si IV/O IV λ ∼ 1400, C IV λ 1549, C III] λ 1909, Mg II λ 2798.
1347+539	13:47:42.57	53:56:08.4	0.980 ± 0.003[e]	1500	22 Jan 1990	C III] λ 1909, Mg II λ 2798, [Ne V] λ 3426, [O II] λ 3727, Hδ, Hγ.
1418+546	14:18:06.19	54:36:58.0	———[f]	3000	22 Jan 1990	Featureless spectrum.
1557+708	15:57:37.1	70:49:45	0.026 ± 0.001	900	22 Jan 1990	Cross-correlation with an averaged spectrum of 3C galaxies in the Pearson–Readhead sample (Lawrence *et al.* 1994).
1738+476	17:38:36.32	47:39:28.6	———[i]	1800	9 Aug 1991	Featureless spectrum.
1842+681	18:42:43.49	68:06:19.6	0.472 ± 0.002[e]	1800	9 Aug 1991	Mg II λ 2798, [Ne V] λλ 3341,3426, Hβ, [O III] λλ 4959, 5007, Hα.
1926+611	19:26:49.65	61:11:20.7	———[g]	1800	9 Aug 1991	Featureless spectrum.
2010+723	20:10:16.21	72:20:20.7	———[g]	3000	9 Aug 1991	Featureless spectrum.
2207+374	22:07:11.72	37:27:33.0	1.493 ± 0.004[b]	3000	9 Aug 1991	C IV λ 1549, He II λ 1640, Al III λ 1863, C III] λ 1909, Mg II λ 2798.
2229+695	22:29:11.65	69:31:02.7	———[g]	3600	9 Aug 1991	Featureless spectrum.

Table 1. Redshifts of Caltech–Jodrell Bank VLBI Survey Sources (*continued*)

2255+416	22:55:04.68	41:38:13.2	———[i]	3000	24 Jan 1990	Featureless spectrum.
2311+469	23:11:28.87	46:55:54.4	0.742 ± 0.001	1500	23 Jan 1990	C III] λ 1909, Mg II λ 2798, [Ne V] λ 3426, [O II] λ 3727, [Ne III] λ 3869, [Ne III] Hε λ 3970, Hδ, Hγ, [O III] λ 4363, Hβ, He I λ 4922, [O III] λλ 4959, 5007.

Notes to Table 1

[a] O'Dea *et al.* (1992) reported a tentative redshift of 0.68 for the lens object. Carilli *et al.* (1993) confirmed it via HI absorption, and Browne *et al.* (1993) also confirmed it. However, the redshift of the quasar is still unknown.

[b] Confirms redshifts suggested by Wills, Wills & Douglas (unpublished).

[c] Confirms redshift reported by Vigotti *et al.* (1990).

[d] Confirms redshift published in the Veron-Cetty & Veron catalog (5th edition).

[e] Confirms redshifts reported by Walsh *et al.* (1984).

[f] Stickel *et al.* (1991) reported a redshift of 0.152. Our observation cannot confirm their result.

[g] There were thin clouds scattered on the sky during observation.

[h] Tentative redshift.

[i] A preliminary redshift from our work, referred by M. Stickel & H. Kühr (1994, A&AS, 103, 349), is not correct.

4.3. OPTICAL IDENTIFICATIONS

4.3.1. OBSERVATIONS

Fourteen fields were imaged at the Gunn r band with camera 4 on the Palomar 60-inch telescope in February and May of 1991. The detector in this camera is a CCD manufactured by Texas Instruments with an array size of 800 × 800 and a pixel size of 15 μm. The CCD chip has a gain of approximately 2 electrons per DN and readout noise of 9.5 electrons. The angular scale of the imaging system was $0''.23$ per pixel giving a field of view of $3'$. The weather conditions were not good in both observing sessions since there were cirrus clouds scattered across the sky. The seeing measured during the observations varied from $1''$ to $3''.5$. Exposure times were 3600 seconds, except for one object 1333+589 (1900 seconds). The observation journal is given in Table 4.2.

A series of flat fields was obtained by exposing to the top of the dome uniformly illuminated by an incandescent light source. They were averaged and normalized to yield a standard flat field. The images were flat fielded using the normal procedure of subtracting the bias level and dividing each image by the standard flat field.

4.3.2. IDENTIFICATION PROCEDURE

A transformation from XY positions on the CCD frame to sky coordinates has to be established in order to measure the coordinates of candidates for optical counterparts shown in the CCD images. We measured the XY positions of SAO stars (primary reference stars) within 2° of the radio position and of stars (secondary reference stars) within $3'$ of the radio position on the blue POSS plates using an XY measuring machine at the Observatories of the Carnegie Institute of Washington in Pasadena. The numbers of the primary and secondary reference stars used are listed in Table 4.3. A least-squares fit between the XY positions and sky coordinates of the primary reference stars was used to establish the XY–to–(sky coordinate) transformation system, under which the coordinates of the secondary reference stars were calculated. The *rms* deviation of the coordinates of the SAO stars

ranges from $\sim 0''.4$ to $0''.7$, except in one case 1438+385. Since this object is close to the edge of the Palomar sky survey plate, only 4 SAO stars were used and hence an artificially small error was obtained. The XY positions on the CCD frames and sky coordinates of the secondary reference stars were used in a similar fashion to calculate the coordinates of the candidates for optical counterpart. The *rms* deviations of the first and secondary reference stars were combined to estimate the errors of the optical coordinates (Table 4.3). In the case of 1438+385, we replaced the small value with the average of errors for other sources to reflect the likely accuracy of the method used.

Following de Ruiter et al. (1977) we define the normalized distance R to the radio position

$$R = \left[\frac{\Delta_\alpha^2}{(\sigma_{opt})_\alpha^2+(\sigma_r)_\alpha^2} + \frac{\Delta_\delta^2}{(\sigma_{opt})_\delta^2+(\sigma_r)_\delta^2}\right]^{\frac{1}{2}}$$

where Δ is the difference between the optical and the radio position and σ_{opt} and σ_r are errors of the optical position and the radio position, respectively. The error of the radio position was estimated based on the position code listed in *THE VLA CALIBRATION MANUAL — 1990 EDITION*, with the exception of 1152+551. This object 1152+551 is a double–lobed radio source as revealed by the VLA A array image at 6 cm (Polatidis 1993). The position of this object was measured from the map.

The probability that a true identification has a value of R greater than some value R_0 is given by

$$P(R > R_0) = \exp(-R_0^2/2)$$

Since there is only $\sim 1\%$ chance of correct identification having $R > 3$, we choose $R = 3$ as our cutoff for accepting an object as a correct identification. All 14 sources have an object providing $R < 3$, which we considered as the identification (Table 4.2).

Table 4.2. Optical Identification

Source	Obs. Date	Time		RA	Δ_α	Dec	Δ_δ	R
		(s)		(B1950.0)	(″)	(B1950.0)	(″)	
(1)	(2)	(3)		(4)	(5)	(6)	(7)	(8)
0602+673	2-13-91	3600	optical	$06^h02^m39^s.033\pm0''.72$	0.758	$67°21'19''.70\pm0''.52$	1.30	2.61
			radio	06 02 38.890±0.15		67 21 18.40±0.15		
0646+600	2-13-91	3600	optical	06 46 04.203±0.83	0.718	60 05 13.36±0.71	−0.96	1.57
			radio	06 46 04.107±0.15		60 05 14.20±0.15		
0945+664	2-13-91	3600	optical	09 45 14.930±0.74	0.180	66 28 58.67±0.95	0.96	0.99
			radio	09 45 14.900±0.30		66 28 57.71±0.30		
1044+719	2-13-91	3600	optical	10 44 49.738±0.64	−0.065	71 59 26.64±0.83	−0.41	0.50
			radio	10 44 49.752±0.002		71 59 26.85±0.002		
1138+594	2-13-91	3600	optical	11 38 05.609±1.11	−0.962	59 29 04.08±1.04	1.16	1.39
			radio	11 38 05.735±0.20		59 29 02.92±0.20		
1152+551	2-13-91	3600	optical	11 52 55.566±0.92	0.960	55 10 36.50±0.78	−0.50	1.18
			radio	11 52 55.502±0.25		55 10 37.00±0.25		
1311+678	2-13-91	3600	optical	13 11 44.984±0.80	−0.300	67 51 41.42±0.93	−0.90	1.02
			radio	13 11 45.037±0.15		67 51 42.32±0.15		
1333+589	2-13-91	1900	optical	13 33 36.586±0.54	0.876	58 59 16.73±0.65	−1.32	2.47
			radio	13 33 36.473±0.20		58 59 18.05±0.20		

Table 4.2. Optical Identification (*continued*)

Source	Obs. Date	Time		RA	Δ_α	Dec	Δ_δ	R
		(s)		(B1950.0)	(″)	(B1950.0)	(″)	
(1)	(2)	(3)		(4)	(5)	(6)	(7)	(8)
1357+769	5-12-91	3600	optical	13 57 42.121±0.83	−0.024	76 57 52.84±1.03	−0.46	0.45
			radio	13 57 42.128±0.002		76 57 53.30±0.002		
1438+385	5-12-91	3600	optical	14 38 22.539±0.78	0.057	38 33 04.34±0.60	1.40	2.21
			radio	14 38 22.543±0.20		38 33 02.9± 0.20		
1504+377	5-12-91	3600	optical	15 04 12.988±0.88	0.344	37 42 22.80±0.77	−0.49	0.75
			radio	15 04 12.959±0.002		37 42 23.29±0.002		
1656+482	5-12-91	3600	optical	16 56 24.875±0.91	−0.780	48 13 06.39±1.07	1.88	1.92
			radio	16 56 24.953±0.20		48 13 04.51±0.20		
1734+508	5-12-91	3600	optical	17 34 36.703±0.51	−0.341	50 50 58.51±0.81	−1.13	1.49
			radio	17 34 36.739±0.20		50 50 59.64±0.20		
1843+356	5-12-91	3600	optical	18 43 48.336±0.81	−0.073	35 38 01.16±0.80	−1.24	1.53
			radio	18 43 48.342±0.15		35 38 02.40±0.15		

Table 4.3. Error Estimation for Optical Coordinates

Source	1st Ref.	σ_1 (″)	2nd Ref.	$\sigma_{2\alpha}$ (″)	$\sigma_{2\delta}$ (″)	$(\sigma_{opt})_\alpha$ (″)	$(\sigma_{opt})_\delta$ (″)
0602+673	10	0.47	9	0.55[b]	0.23	0.72	0.52
0646+600	13	0.52	10	0.65	0.49	0.83	0.71
0945+664	9	0.39	5	0.63	0.87	0.74	0.95
1044+719	11	0.60	7	0.22	0.58	0.64	0.83
1138+594	15	0.62	5	0.92	0.83	1.11	1.04
1152+551	12	0.65	12	0.65	0.44	0.92	0.78
1311+678	9	0.47	10	0.65	0.84	0.80	0.93
1333+589	10	0.34	14	0.42	0.55	0.54	0.65
1357+769	12	0.53	10	0.64	0.88	0.83	1.03
1438+385	4	0.54[a]	10	0.57	0.23	0.58	0.25
1504+377	7	0.66	6	0.58	0.39	0.88	0.77
1656+482	15	0.61	6	0.67	0.88	0.91	1.07
1734+508	9	0.46	7	0.21	0.67	0.51	0.81
1843+356	19	0.73	30	0.36	0.34	0.81	0.80

Notes:

[a] The error cannot be adequately estimated because of the small number of stars used, thus we used the average value of the other 13 objects.

[b] A very small error was obtained through the least-squares fitting, which was replaced with the average value of the other 13 objects.

4.4. OPTICAL POLARIMETRY MEASUREMENTS*

4.4.1. INTRODUCTION

There is a significant relationship between polarized optical emission and radio emission from compact radio sources. Impey et al. (1991) made optical polarimetry observations of 50 sources in the Pearson–Readhead sample. They found that high polarization ($p > 3\%$) is strongly correlated with the fraction of the total flux density at 5 GHz contained in a milliarcsecond core (F_c). The fraction of sources with high optical polarization rises from 13% for sources with $F_c < 0.1$ to 45% for sources with $F_c > 0.1$. Almost every radio source with all of its flux in an unresolved milliarcsecond core is highly polarized. They also confirmed in the complete PR sample that there is a striking alignment between the position angle of the VLBI structure axis and the position angle of optical polarization in highly polarized sources (Rusk & Seaquist 1985; Impey 1987; Rusk 1988). Pearson & Readhead (1988) discovered that the distribution of position angle difference between the radio structures on VLBI scale and arcsecond scale $|\theta_{\rm VLBI} - \theta_{\rm arcsec}|$ peaks at both 0° and 90°. Impey et al. found that the distributions of $|\theta_{\rm VLBI} - \theta_{\rm arcsec}|$ are dramatically different for sources with high and low optical polarization. Five out of the eight sources in the PR sample with high optical polarization ($p < 3\%$) have a high degree of misalignment ($|\theta_{\rm VLBI} - \theta_{\rm arcsec}| > 70°$), whereas seven out of the nine objects with low optical polarization have a small misalignment ($|\theta_{\rm VLBI} - \theta_{\rm arcsec}| < 25°$). When combined with a larger but inhomogeneous sample (Rusk 1988), the distribution of $|\theta_{\rm VLBI} - \theta_{\rm arcsec}|$ is broadly peaked around zero for low-polarization objects, while for high-polarization objects the distribution has twin peaks around 0° and 90°.

These results are intriguing. However, they were obtained in a relatively small and inhomogeneous sample, thus it is important to confirm them with the combined PR and

* This project is in collaboration with C. R. Lawrence (Caltech), C. D. Impey and P. S. Smith (Univ. of Arizona).

CJ1 sample, which is three times as large as the PR sample. We therefore decided to make optical polarimetry observations of objects brighter than $\sim 19^m.5$ in the CJ1 sample. Thus far we have observed 58 objects.

4.4.2. OBSERVATIONS

The observations were taken with the 'Two–Holer' polarimeter/photometer (Sitko, Schmidt & Stein 1985). The Two–Holer is patterned after a design described by Serkowski (1974) and optimized to measure linear polarization. It uses a rapidly rotating, semi-achromatic $\lambda/2$ waveplate and a Wollaston prism to modulate and analyze incident linear optical polarization. Two RCA C31034 GaAs photomultiplier tubes (PMT) are used as detectors. The PMT has relatively high quantum efficiency (10% – 20%) in the 2100 – 8600 Å range and gives a thermal background "dark current" of 1 – 3 counts per second when cooled by dry ice. The Wollaston prism splits the incident beam into two orthogonally polarized beams, each of which is detected by a PMT as a sinusoidal variation in the number of photons. The amplitude of the variation gives the degree of the polarization. The phase of the variations with respect to the waveplate position gives information on the plane of polarization and can be converted to a real position angle on the sky by observing standard stars with known polarization.

The observations were made in six sessions in 1991 – 1993 at the Steward Observatory 90-inch telescope located on Kitt Peak, Arizona and the 61-inch telescope located on Mount Bigelow, Arizona. Sky subtraction was done automatically at the telescope by the instrument control computer. The sky-subtracted and unfiltered polarization data were reduced following the procedure described by Sitko et al. (1985). The normalized Stokes parameters Q/I and U/I, the 1σ uncertainty in Q/I (it is assumed that $\sigma_{Q/I} = \sigma_{U/I}$), P, and 1σ uncertainty of P $(= \sigma_{Q/I})$ are presented in Table 4.4. All of these quantities have been scaled by the photometric efficiency of the Two–Holer. In addition to the efficiency correction, P has been corrected for the statistical bias inherent in measurement of the

degree of polarization since

$$P = [(Q/I)^2 + (U/I)^2]^{1/2}$$

and cannot be measured to be negative (Wardle & Kronberg 1974). We use Wardle & Kronberg's method to correct P for this bias. The correction is given by

$$P = \sqrt{P_{\rm obs}^2 - \sigma_{\rm P}^2}$$

where $P_{\rm obs}$ is the efficiency corrected observed degree of polarization. For high SNR observations the bias correction is negligible.

The polarization angle, θ, is given by

$$\theta = \tfrac{1}{2}\tan^{-1}(\tfrac{U}{Q})$$

and is also listed in Table 4.4. together with its uncertainty σ_θ.

These results are used in *Chapter 6*, along with other optical polarization data collected from the literature, in a discussion of the bimodal distribution of the misalignment angles.

Table 4.4. Optical Polarimetry for CJ1 Sources

Source	Tel-Apt[a]	UT Time (yymmdd.hh.mm)	Q/I (%)	U/I (%)	$\sigma_{Q/I}$ (%)	P[b] (%)	P_σ (%)	θ (°)	σ_θ (°)
0010+775	90-0	920926. 4.44	0.555	1.495	1.280	< 2.56			
0010+405	90-0	910912. 8.48	−9.525	−3.399	0.616	10.09	0.62	99.8	1.7
0022+390	90-0	910912. 8.19	−6.507	2.965	1.083	7.07	1.08	77.8	4.3
0248+430	90-0	910912.11.47	−0.156	−0.031	0.575	< 1.15			
0402+379	61-0	911010.10.22	−3.144	−3.235	1.211	4.35	1.21	112.9	7.7
0615+820	90-0	910912.10.41	0.482	0.779	2.158	< 4.32			
0642+449	90-0	910913.11.36	2.229	−0.889	1.083	2.14	1.08	169.1	15.3
0650+371	61-0	911010.11.35	−1.283	0.182	0.938	< 1.88			
0716+714	90-0	910912.11.59	−1.029	4.868	0.134	4.97	0.13	51.0	0.8
0740+828	90-0	920926.10.52	−0.980	0.227	0.597	< 1.19			
0746+483	61-0	911011.11.04	0.652	0.112	1.656	< 3.31			
0755+379	61-0	911010.12.17	−0.426	−1.066	0.474	1.05	0.47	124.1	13.6
0805+410	61-0	911102. 9.55	2.537	0.835	1.172	2.40	1.17	9.1	14.7
0812+367	61-0	911105.10.24	1.774	−0.064	1.029	< 2.06			
0820+560	61-0	911102.10.59	2.298	−0.298	0.797	2.18	0.80	176.3	10.8
0821+394	61-0	911102.11.42	2.425	6.508	0.548	6.92	0.55	34.8	2.3
0828+493	61-0	911101.11.56	0.010	9.499	1.100	9.44	1.10	45.0	3.3
0833+585	61-0	911102.12.13	−1.117	0.131	1.059	< 2.12			
0917+449	61-0	911105.11.22	6.224	20.385	0.792	21.30	0.79	36.5	1.1
0917+624	90-3	930425. 5.29	−0.320	−0.187	1.300	< 2.60			
0955+476	61-0	911106.11.39	−3.984	−0.486	0.884	3.92	0.88	93.5	6.3
1015+359	61-0	930417. 5.38	−0.035	−0.937	1.149	< 2.30			
1020+400	61-0	911107.12.14	−1.608	−1.959	0.780	2.41	0.78	115.3	8.8

Table 4.4. Optical Polarimetry for CJ1 Sources (*continued*)

Source	Tel-Apt[a]	UT Time (yymmdd.hh.mm)	Q/I (%)	U/I (%)	$\sigma_{Q/I}$ (%)	P[b] (%)	P_σ (%)	θ (°)	σ_θ (°)
1030+415	61-0	930419. 4.28	3.705	7.902	2.486	8.37	2.49	32.4	8.2
1030+415	90-3	930426. 4.38	−0.287	2.402	2.054	< 4.11			
1039+811	90-0	920404. 6.07	0.698	0.279	1.085	< 2.17			
1053+704	90-0	920404. 7.30	0.946	−1.837	1.484	< 2.97			
1053+704	90-3	930426. 5.40	1.630	−2.204	1.374	< 2.75			
1053+815	90-3	930425. 6.12	−7.900	−6.853	3.582	9.83	3.58	110.5	10.8
1058+726	90-0	920404. 6.43	−1.027	1.184	0.549	1.47	0.55	65.5	11.1
1101+384	90-1	920404. 8.00	4.473	0.934	0.051	4.57	0.05	5.9	0.3
1128+385	61-0	930418. 7.35	−0.738	0.160	1.747	< 3.49			
1137+660	90-1	920404. 8.21	−0.301	0.443	0.203	0.50	0.20	62.1	12.2
1144+402	90-0	920404. 9.29	3.073	−1.657	1.018	3.34	1.02	165.8	8.4
1150+497	90-1	920405. 7.21	0.508	0.332	0.421	< 0.84			
1150+812	90-3	930425. 6.51	−1.628	−1.201	1.322	1.53	1.32	108.2	25.5
1216+487	90-3	930425. 7.55	−1.266	−2.556	1.984	< 3.96			
1333+459	90-0	920405. 9.47	−0.167	1.700	0.502	1.63	0.50	47.8	8.4
1342+663	90-3	930425. 9.27	1.544	18.706	1.404	18.72	1.40	42.6	2.1
1347+539	90-0	920404. 8.37	0.170	0.298	0.593	< 1.17			
1418+546	90-0	920404.10.40	2.035	−0.504	0.454	2.05	0.45	173.1	6.2
1435+638	90-0	920404. 8.52	0.104	−0.203	0.443	< 0.89			
1547+507	90-0	910913. 3.13	0.351	0.950	0.831	< 1.66			
1637+826	90-0	910913. 3.41	0.289	−0.963	0.276	0.97	0.28	143.4	7.9
1638+398	90-0	910913. 4.58	−2.709	−1.470	1.704	< 3.41			
1656+477	90-0	910912. 3.13	0.298	0.077	0.591	< 1.18			
1738+476	90-0	910912. 3.58	7.114	26.404	2.156	27.26	2.16	37.5	2.3
1751+441	61-0	911011. 4.27	1.866	−2.929	2.375	< 4.75			
1758+388	90-0	910912. 4.39	0.142	0.583	0.800	< 1.60			

Table 4.4. Optical Polarimetry for CJ1 Sources (*continued*)

Source	Tel-Apt[a]	UT Time (yymmdd.hh.mm)	Q/I (%)	U/I (%)	$\sigma_{Q/I}$ (%)	P[b] (%)	P_σ (%)	θ (°)	σ_θ (°)
1800+440	61-0	911010. 4.55	2.160	−1.658	0.586	2.66	0.59	161.2	6.2
1800+440	90-0	920405.12.00	0.284	4.043	0.759	3.98	0.76	43.0	5.4
1842+681	90-0	910912. 5.04	−0.516	−1.987	0.889	1.85	0.89	127.7	14.5
1842+681	90-0	920404.11.38	−3.054	2.381	0.694	3.81	0.69	71.0	5.1
1926+611	90-0	910913. 6.45	−8.853	−11.488	0.689	14.49	0.69	116.2	1.4
1943+546	61-0	911010. 6.29	−1.204	−1.174	2.696	< 5.39			
2007+777	90-0	910913. 6.26	−9.993	5.714	1.095	11.46	1.09	75.1	2.7
2010+723	90-0	910912. 5.54	7.560	−21.832	2.302	22.99	2.30	144.6	2.9
2207+374	90-0	910912. 6.47	0.257	−0.072	1.458	< 2.92			
2214+350	90-0	910912. 7.38	−0.413	1.961	0.853	1.81	0.85	50.9	14.1
2253+417	90-0	910912. 7.15	−0.391	0.287	1.122	< 2.24			
2311+469	90-0	910913. 7.01	−0.483	1.661	0.869	1.50	0.87	53.1	17.7
2323+435	61-0	911010. 8.36	−0.050	−0.900	1.251	< 2.50			

Note to Table 4.4.

[a] Telescope and aperture used — 61-0: the 61-inch telescope with a 5″ aperture; 90-0: the 90-inch telescope with a 3″ aperture; 90-3: the 90-inch tepescope with a 5″ aperture.

[b] Upper limits are 2 σ.

Chapter 5

THE CLASSIFICATION OF POWERFUL EXTRAGALACTIC RADIO SOURCES

5.1. INTRODUCTION

VLBI observations have revealed a variety of morphological types of extragalactic radio sources on milliarcsecond scales. The different morphologies may result from fundamental differences in underlying physical processes, e.g., the central engine, from relativistic beaming effects or from environmental effects. Detailed studies of the characteristics of different morphological types should enable us to gain some insight into their nature. Pearson & Readhead (1988) made the first attempt to classify 65 powerful extragalactic radio sources in a complete flux density limited sample into five main classes and a total of ten subclasses based primarily on their morphologies on either arcsecond or milliarcsecond scales. In their classification scheme, the radio structures on arcsecond scales were not used for most of the objects observed with VLBI, whereas the structures on milliarcsecond scales were not used for some of the lobe-dominated sources. As a result, it is difficult to address the underlying physical processes with this classification scheme.

The main goal of our study is to use the morphological information on both arcsecond and milliarcsecond scales so as **to identify meaningful physically distinct classes of powerful extragalactic radio sources**. Our study has several advantages over the study of Pearson & Readhead (1988). First, the combined CJ1 and PR sample is three times as large as the PR sample; second, we have VLBI maps at both 1.6 and 5 GHz for all objects detectable with VLBI, which enable us to identify the core with confidence in almost all

cases; third, we have fairly complete VLA observations of all objects at 1.4 GHz and of flat-spectrum objects at 8.4 GHz (Patnaik et al. 1992). In this chapter we classify radio sources into physically distinct classes based on morphological attributes of both small-scale (< 5 kpc) and large-scale (≥ 5 kpc) radio structures. At first, the morphological **attributes** on both scales are used to separate the objects into a number of groups with similar characteristics; and the association of types of morphological attributes on both scales are then used to identify physically distinct classes.

5.2. MORPHOLOGICAL ATTRIBUTES

We discuss below the morphological attributes.

5.2.1. MORPHOLOGICAL ATTRIBUTES ON SCALES $\geq$ 5 KPC

Lobe-dominated sources have been classified as FR I or FR II sources (Fanaroff & Riley 1974). We attempted to classify the core-dominated sources in the complete CJ1 and PR sample in a similar fashion. In the classification of morphological attributes on arcsecond scales, we used an overall projected linear size of 5 kpc to distinguish between extended and compact sources. Spectral information was not used as a criterion of classification directly. However, it often indicates whether a compact core exists. The flat- and steep-spectrum criteria and overall projected linear size criteria are defined below.

Morphology

Overall Projected Linear Sizes

The largest angular sizes of the objects in the complete sample are measured from VLA, Cambridge 5-km or MERLIN maps at various frequencies. Sources with a projected linear size less than 5 kpc are classified as **compact (C)** objects. Others are separated into several groups according to their morphology. For objects having structures on both sides of the core, we adopt the original definition of FR I and FR II sources introduced by Fanaroff & Riley (1974). Namely, if the distance between the two brightest features on opposite sides

of the core exceeds half of the overall size, the object belongs to **FR II class**, otherwise it belongs to **FR I class**. For objects having extended structures only on one side of the core, we adopt the **D2 class**, which was introduced by Miley (1971). Some objects have diffuse structure all around the core, which will be referred to as a **Halo**. Thus objects with an unresolved core surrounded by a halo will be grouped as a **Core + Halo (C+H)** class. Likewise, objects with well-defined structure at one side of the core plus a halo will be grouped as a **D2+H** class. The **Unclassified (U)** class is used to accommodate objects which do not fit into the above classes. The classification of objects into D2 or C class depends on the quality of the map used. Many D2 and C objects may have faint extended structure which have not been detected yet. Considering this, we combine the **D2** and **D2+H** classes into simply a **D2** structure, and **C** and **C+H** into a **C** structure. Therefore, there are four types of possibly distinct structure on arcsecond scales: **FR I, FR II, D2** and **C** apart from the unclassified objects.

Spectrum

The objects have various shapes of overall spectrum (see Figures 3.4.1 – 3.4.84 and Figure 3.7). The high-frequency spectra correlate well with the radio morphology. A flat high-frequency spectrum always indicates the existence of a strong compact component, which is associated with the core. A steep high-frequency spectrum indicates the absence of such a strong compact component. Thus we adopt the spectral index α at 15 GHz in the rest frame as our standard. The spectral indices were calculated by the spline fits (Herbig & Readhead 1992). We believe such a calculation is accurate enough to reflect the nature of the spectrum judging from the fit of the spline to the spectral data. We designate a spectrum as flat when $\alpha \geq -0.5$ and steep when $\alpha < -0.5$ ($S_\nu \propto \nu^\alpha$). The spectral indices are listed in column 11 and the types of spectrum are indicated with letter ***S*** or ***F*** in column 12 in Table 5.1 and similarly in columns 13 and 14 in Table 5.2.

Some objects have a spectrum which is steep at high frequency and flattens or falls off

at low frequency ($\sim$ 1 GHz). These are referred to as Gigahertz-Peaked Spectrum (GPS) sources. We use letter ***G*** to indicate these sources.

SUMMARY

As described in Chapter 3, we have observed 92 core-dominated sources in the combined CJ1 and PR sample. Together with observations made by others, we have collected a complete set of VLA images at 1.4 GHz for all core-dominated sources in the sample. These maps have fairly good quality, generally with dynamic range $\geq$ 3000:1. Extended emission has been found in many sources. Maps of extended sources have also been collected through an extensive literature search. Based on structures revealed by these images, the morphologies on arcsecond scales are separated into seven classes, which are listed in Table 5.1, Column 13 and Table 5.2, Column 15. In some cases, the morphology is not well-defined. For example, there are not obvious jets or hotspots. For these objects we list tentative classification with a question mark beside it. In the combined CJ1 and PR sample, there are 7 FR I's, 98 FR II's, 37 D2's, 5 D2+H's, 4 C+H's, 43 C's and 6 U's. However, if observed with greater dynamic range, it is possible that many of the D2 and C sources will show FR I, FR II or other forms of extended structure.

We briefly describe the unclassified sources below.

0218+357: This is a gravitational lens system (*see the discussion in Section 5.2.2*).

0651+542 (3C 171): This object contains two well-defined hotspots. However, it has large extended structure in the direction almost perpendicular to its axis (Leahy & Perley 1991). The overall size is more than twice the distance between the two hotspots. The morphology is very different from that of a typical FR I or FR II sources, thus we did not classify it.

0703+426 (4C 42.23): This object has a short one-sided jet and a large, very distorted lobe-like structure at a relatively large distance on the other side (Burns & Gregory 1982). The morphology does not resemble that of FR I and FR II sources.

1448+634 (3C 305): This object is similar to 0651+542, with large extended structure perpendicular to its axis (Antonucci 1985).

1634+628 (3C 343): The visibility data of our VLA A-array observations indicate that this object contains substructure. A map convolved with a smaller beam shows emission on axes perpendicular to each other. The morphology does not fit any of the classes.

2229+695: This object also has extended structure on axes perpendicular to each other (Fig. 3.4.81).

5.2.2. MORPHOLOGICAL ATTRIBUTES ON SCALES < 5 KPC

Amongst the 200 sources in the combined CJ1 and PR sample, 131 have structure detectable on milliarcsecond scales with Mark II VLBI. The classification of morphological attributes on scales $\leq$ 5 kpc is based primarily on Mark II VLBI observations at both 5 GHz (*see Chapter 3*; Pearson & Readhead 1988) and 1.6 GHz (Polatidis et al. 1995; Thakkar et al. 1995). The objects are grouped into three classes:

(a) **Asymmetric Objects (e.g., Core and Core-jet Objects)**;

(b) **Symmetric Objects**;

(c) **Unclassified**.

The assignment of an object to a certain morphological type is straightforward in most cases. However, the two-frequency observations enable us to clarify ambiguous cases. The 1.6 GHz observations often detect faint steep-spectrum jet-like features which are not present in the 5 GHz map. On the other hand, the 5 GHz observations provide higher resolution. In several cases a compact object at 1.6 GHz is found to have core-jet or symmetric structure at 5 GHz. More important — the two-frequency observations provide spectral information. We are confident that in almost all core-jet sources we have identified the core, which is compact and has a flat or inverted spectrum. In addition, we have 8.4 GHz observations of 8 objects, which help to identify 5 new compact symmetric objects or candidates in the CJ1 sample, and add more information for three known compact

symmetric objects in the PR sample (0108+388, 0710+439, and 2352+495) (*see Chapter 7*). The classification of morphological attributes is listed in Table 5.1, column 14 for the CJ1 sample and Table 5.2, column 16 for the PR sample, and summarized in Table 5.3.

Asymmetric Objects — Core and Core-Jet Objects

The distinguishing feature of these sources is a bright compact component with a flat or inverted spectrum between 1.6 and 5 GHz. This feature seems to be most closely associated with the central engine and therefore will be referred to as the "core" component. The results of model-fitting (see Table 3.6) were used to determine the flux densities of the cores. The fractions F_c of the total flux density in the core were calculated by dividing the core flux density by the total flux density measured in the S4 and S5 surveys. However, flux densities of many objects have changed since these surveys were made, introducing errors in F_c. Several sources have brightened so much that the core flux density alone exceeds the total flux density measured in the S4 and S5 surveys—for these F_c was estimated by dividing the core flux density by the total flux density in the VLBI map. For the objects observed by others, the peak flux densities of the published VLBI maps were adopted as the core flux densities. We did not attempt to make a finer classification according to the parameter F_c because of these uncertainties. The division between core and core-jet objects is entirely based on the morphology.

Core Objects (4)

The core objects are the sources which have all their detected flux density on scales ≤ 5 kpc confined to a region less than the VLBI beam size at the observing frequencies (i.e., $\sim$ 1 mas at 5 GHz, and $\sim$ 3 mas at 1.6 GHz). There are four core sources in the combined PR and CJ1 sample. All of them are quasars with flat radio spectra.

We note that judging from the visibility amplitudes, all these sources are resolved to some degree. **There is not a single case of a completely unresolved object.** This agrees with the similar finding by Pearson & Readhead (1988). We also note that three

sources (0602+673, 0615+820, and 1732+389) in the 1 Jy subsample classified as core based on the 1.6 GHz VLBI maps (Polatidis 1993) show a core-jet-like morphology on the 5 GHz maps. The object 1739+522 is slightly resolved at 1.6 and 5 GHz, but shows a core-jet structure at 8.4 GHz. Eckart et al. (1987) discovered a similar effect. They found that a core source (0454+844) at 5 GHz has a core-jet structure at 22 GHz. It is very likely that all core sources are core-jet sources when viewed at a high enough resolution or dynamic range. This is why core and core-jet sources have been combined into one class.

Core-Jet Objects (105)

The core-jet objects are those which have a bright and unresolved core at one end of a jet-like feature. The appearance of these objects varies—from a strong core with a short jet to a relatively faint core with a well-developed jet. Bending of the jet ranges from a few degrees to more than 90 degrees. Bending of $\sim 180°$ is also seen. Among 105 core-jet objects 8 are galaxies and the rest are quasars or BL Lac objects (besides 1 empty field). All but 19 objects have flat high frequency spectra. The 8 galaxies consist of 5 flat-spectrum objects and 3 steep-spectrum objects.

High dynamic range VLA and MERLIN maps show that many of the core-jet objects have structures on arcsecond scales. In some cases the structures on milliarcsecond and arcsecond scales are well aligned, while in some other cases the position angle of milliarcsecond-scale structure differs from that of arcsecond-scale structure by as much as 180°. However, the milliarcsecond-scale jet almost always connects with or bends toward the arcsecond-scale jet. There is only one counter example – 0820+560, in which the position angles of the milliarcsecond- and arcsecond-scale jet differ by 155° (Fig. 3.4.21). There is no hint of a connection of the two jets in the available VLBI and MERLIN maps, but it is possible that the jet shown in the VLBI map turns sharply within ~50 mas to connect with the jet show in the MERLIN map. Observations with intermediate resolution are needed to test this. We discuss the alignment or misalignment of the milliarcsecond- and

arcsecond-scale structures in detail in Chapter 6.

Compact Symmetric Objects or Candidates (24)

Although the majority of strong radio sources studied with VLBI belong to the asymmetric class, objects consisting of two well separated components with similar brightness, size and spectrum were discovered by Phillips & Mutel (1982), who introduced the term "*compact double*" to describe these sources. Pearson & Readhead (1988) divided this class into flat- and steep-spectrum compact doubles. More detailed studies (Conway et al. 1994; Hummel et al. 1988; Alberdi et al. 1993; Marscher et al. 1991) show that as expected the flat-spectrum compact doubles are actually core-jet sources in disguise. On the other hand, two steep-spectrum compact doubles, 0710+439 and 2352+495, actually have a triple morphology with the middle component being associated with the central engine (Readhead et al. 1984; Pearson & Readhead 1988; Conway et al. 1992, 1994; Wilkinson et al. 1994; Readhead et al. 1994). The object 0108+388 probably has a similar morphology (Conway et al. 1994). It seems clear that the term "compact double" can no longer adequately describe this class of objects. Thus we adopt a new term "Compact Symmetric Object" (CSO) to describe sources with proven symmetric structure on small scales. The CSO's in the CJ1 and PR samples are generally less than 1 kpc in projected linear size. However, these objects are probably closely related to the steep spectrum sources studied by Fanti et al. (1985, 1990), which are typically ten times larger than those in our samples. This remains to be proven. For the present **we define a CSO as a radio source in which the radio morphology on scales less that 5 kpc exhibits high luminosity structure on both sides of the central engine**. The size restriction is so chosen to avoid the confusion between CSO's and small FR II sources. There seem to be two types of symmetric objects, one is edge-dimmed and other edge-brightened, which are indicated with **S1** & **S2**.

Objects with symmetric structure on milliarcsecond scales are relatively rare. Detailed studies of these objects may well provide insights into the central engine. It is possible

that some of the CSO candidates will be found to be core-jet objects when studied in more detail over a range of frequencies.

We have identified 17 CSO's and CSO candidates based on the VLBI observations and another 7 based on the MERLIN and EVN observations. These objects will be discussed in detail in Chapter 7. There are two S1 objects. Others appear to be S2 objects with hotspots at both ends. A core has been found in six cases (0404+768, 0538+498, 0710+439, 1250+568, 1943+546 and 2352+495), and tentatively identified in another four cases (0108+388, 1225+368, 1242+410 and 1843+356). Oppositely directed jets on milliarcsecond scales have been detected in 1242+410 and 2352+495.

Unclassified (5)

This class is adopted to accommodate the objects which do not fit into the above two classes. There are 5 objects in this class:

0218+357 — This is a gravitationally lensed system. Two images are shown in the VLBI map (Fig. 3.4.4). The image to the North-East has a core-jet morphology, and the image to the South-West is elongated along the SE–NW direction. Due to unknown complexity of the gravitationally lensed system, it is difficult to have a clear picture of the unlensed structure without detailed modeling.

1213+350 — This object has two emission regions separated by $\sim$ 30 mas (Fig. 3.4.45). The brighter component shows a "core-jet" morphology at 1.6 and 5 GHz, but observations at 8.4 and 15 GHz show that the "core" is quite resolved. The faint component is compact and has an inverted spectrum between 1.6 and 15 GHz. Among many possible explanations are (1) a faint core with a bright hot spot; (2) twin nuclei and (3) complex gravitational lens system.

1311+678 — This object has a complex structure (Fig. 3.4.49). The 1.6 GHz VLBI observations detected one more component $\sim$ 100 mas to the South-East (Thakkar et al. 1995). High-frequency observations are needed to identify the core.

1419+419 — This object has a bright component and faint component separated by ~12 arcsecond in PA=−150° (Pearson et al. 1985; van Breugel et al. 1984, 1992; Fanti et al. 1990c). Van Breugel et al. (in preparation) detected a weak radio core 2 arcsecond SW of the primary component. Thus the primary component, which has been mapped with EVN (Spencer et al. 1991), is in fact the NE 'hot-spot' of this very asymmetric source.

1634+628 — This object has a very complex radio structure ~200 mas in extent (Schilizzi et al. 1990).

SUMMARY

Thanks to the dual-frequency observations, which complement each other in resolution and sensitivity and help to clarify ambiguous cases, we are able to present a clear picture of the morphologies on milliarcsecond scales. Structures on milliarcsecond scales can be grouped into two main classes: (1) Asymmetric Sources (~ 90%) and (2) Symmetric Sources (~ 10%). Jets are common phenomena. About 90% of the sources observed with VLBI show jet-like structures, some of which are well-developed jets and others are merely a short extension of the core. The vast majority of the milliarcsecond jets are one-sided. However we do detect oppositely directed jets in two compact symmetric sources (1242+410 and 2352+495). We believe that these are the first examples of counterjets on milliarcsecond scales. They are of great importance to understanding the nature of compact symmetric sources.

5.3. PHYSICALLY DISTINCT CLASSES

We have defined four possible distinct structures on arcsecond scales, namely edge-brightened symmetric structure (FR II), edge-dimmed symmetric structure (FR I), one-sided structure (D2), and compact structure (C). And there are two distinct structures on milliarcsecond scales—asymmetric (A) and symmetric (S) (including S1 and S2 sources). Morphological attributes on both arcsecond and milliarcsecond scales are needed for a source to be placed

in a distinct class. Considering structures on both arcsecond and milliarcsecond scales, there might, therefore, be eight distinct classes; however, only six are observed.

(1) FR II A – FR II source with asymmetric nuclear structure;

(2) FR II S – FR II source with symmetric nuclear structure;

(3) D2A – One-sided source with asymmetric nuclear structure;

(4) D2S – One-sided source with symmetric nuclear structure;

(5) CA – Compact source with asymmetric nuclear structure;

(6) CS – Compact source with symmetric structure.

The two other possibilities:

(1) FR I A – FR I source with asymmetric nuclear structure; and

(2) FR I S – FR I source with symmetric nuclear structure

have not thus far been observed in the CJ1 and PR samples. The classification is listed in Table 5.1, column 15 and Table 5.2, column 17.

5.4. DISCUSSION

FR II A & S Objects

There are 42 FR II A objects and 2 FR II S objects identified in the CJ1+PR sample. We note that these FR II objects all have strong cores. Due to the low sensitivity of the MK II VLBI system, we were unable to observe sources with FR II morphology on scales > 5 kpc but weak cores (less than 100 mJy). However, in a study of nuclear regions in lobe-dominated quasars (Hough 1986; Hough & Readhead 1987; Hough, Vermeulen & Readhead 1993), all of the 11 sources observed so far belong to the FR II A class although the cores are weaker by an order of a magnitude than those observed by us. We discuss the two FR II S objects, 0402+379 and 1003+351 (3C 236), in Chapter 7.

FR I A & FR I S Objects

Since all sources with FR I morphology on arcsecond scales have weak cores, we were unable to observe them with VLBI. However, a sample of FR I sources has been studied with VLBI (e.g., Venturi et al. 1993b). Most sources observed thus far show one-sided jets and therefore belong to the FR I A class. However, one object 3C 338 has symmetric structure on scales of a few parsec (Feretti et al. 1993) and thus belongs to the FR I S class.

D2A & D2S Objects

There are 42 D2A objects and 1 D2S object, 0108+388. Many of D2A objects show well-defined jets on both milliarcsecond and arcsecond scales, which indicate they are currently powered by a central engine. However, the extended structure of some D2 objects may be relic emission from past activity as first suggested by Miley (1971). The object 0108+388 is probably such a case (Baum et al. 1990a, b). Since it is dominated by a compact emission region < 5 kpc which shows symmetric structure, we included 0108+388 in the CSO class (*see Chapter 7*).

CA Objects

There are 19 CA objects. Their appearance on milliarcsecond varies from relatively weak cores with well-developed jets to dominant cores with relatively faint and/or short jets. The differences may be caused by a combination of objects' intrinsic property, orientation and relativistic beaming effect, and finite resolution.

CS Objects (CSO)

There are 24 CSO's and CSO candidate. We discuss this class in detail in Chapter 7.

Table 5.1. Physical Classification of the CJ1 Sample

Source	ID	z	LAS ($''$)	LLS (kpc)	Ref	VLB?	S_{total} (Jy)	S_{core} (Jy)	F_c	α_{em}^{15}	Spec	Attr. ($\geq$ 5 kpc)	Attr. ($<$ 5kpc)	Class
(1)	(2)	(3)	(4)	(5)	(6)	(7)	(8)	(9)	(10)	(11)	(12)	(13)	(14)	(15)
0010+405	G	0.255	37.8	94.06	2	Y	1.050	0.400	0.38	+0.10	F	FR II	Core-Jet	FR II A
0010+775	G	0.326	14.7	42.43	1	N	0.781			−0.74	S	FR I	—	—
0013+790	G	0.840	25.9	107.60	3	N	1.044			−1.14	S	FR II	—	—
0022+390	Q	1.946	9.2	37.92	1	Y	0.859	0.371	0.43	−0.10	F	FR II	Core-Jet	FR II A
0048+509	G	0.937	23.9	101.03	4,5	N	0.760			−1.06	S	FR II	—	—
0102+480	EF	—	< 0.2	—	6	Y	0.982	0.667	0.68	−0.48	G	C	Core-Jet	CA
0106+729	G	0.181	243.8	479.29	7	N	0.890			−1.09	S	FR II	—	—
0206+355	G	0.037	90.0	45.45	8	N	0.894			−0.71	S	FR I	—	—
0218+357	BL	>0.686	24.5	97.16	9	Y	1.170	—		−0.19	F	U	U	—
0220+397	G	1.176	18.1	77.93	10	N	0.770			−1.17	S	FR II	—	—
0248+430	Q	1.316	17.1	73.65	1	Y	1.210	0.473	0.39	+0.20	F	D2	Core-Jet	D2A
0258+350	G	0.027	2.8	1.05	8,11	N	0.926			−0.58	S	C	S2	CSO
0307+444	Q	1.165	4.4	18.94	12	N	0.733			−0.41	F	FR II	—	—
0309+390	G	1.161	58.1	250.06	1	N	0.728			−0.79	S	FR II	—	—
0402+379	G	0.055	17.6	12.82	1	Y	1.150	—[a]	—	−0.68	S	FR II	S2 ?	FR II S
0407+747	G	—	12.5	—	13	N	0.962			−0.89	S	FR II	—	—
0602+673	Q	—	10.1	—	14	Y	1.070	0.634	0.59	−0.04	F	D2	Core-Jet	D2A
0615+820	Q	0.710	17.1	68.44	2	Y	0.999	0.491	0.49	−0.20	G	D2	Core-Jet	D2A
0620+389	Q	3.470	1.0	3.43	1,6	Y	0.874	0.420	0.48	−0.20	F	C	Core-Jet	CA
0642+449	Q	3.406	< 0.2	0.69	6	Y	0.778	1.476	0.92*	+0.46	F	C	Core-Jet	CA

Table 5.1. Physical Classification of the CJ1 Sample (*continued*)

Source	ID	z	LAS	LLS	Ref	VLB?	S_{total}	S_{core}	F_c	α_{em}^{15}	Spec	Attr.	Attr.	Class
			($''$)	(kpc)			(Jy)	(Jy)				($\geq$ 5 kpc)	($<$ 5 kpc)	
(1)	(2)	(3)	(4)	(5)	(6)	(7)	(8)	(9)	(10)	(11)	(12)	(13)	(14)	(15)
0646+600	Q	0.455	< 0.2	0.68	6	Y	0.788	—	—	−0.53	G	C	S2	CSO
0650+371	Q	1.982	< 0.2	0.82	6	Y	0.971	1.277	0.98*	+0.37	G	C	Core-Jet	CA
0651+542	G	0.239	33.4	79.68	7	N	1.160			−1.03	S	U	—	—
0702+749	G	0.292	62.8	170.00	7	N	0.789			−1.01	S	FR II	—	—
0703+426	G	0.060	261.8	206.29	15	N	0.985			−0.76	S	U	—	—
0707+476	Q	1.310	11.7	50.39	2,16	Y	0.998	0.425	0.44	−0.13	F	FR II	Core-Jet	FR II A
0707+689	Q	1.141	1.3	5.59	11	N	0.749			−0.72	S	FR II	—	—
0716+714	BL	—	17.4	—	2,17	Y	1.121	0.617	0.55	+0.27	F	FR II	Core-Jet	FR II A
0734+805	G	0.119	193.9	275.55	7	N	1.134			−1.93	S	FR II	—	—
0740+828	Q	1.991	7.4	30.35	1	Y	0.931	0.329	0.35	−0.51	S	FR II	Core-Jet	FR II A
0746+483	Q	1.951	< 0.2	0.82	6	Y	0.796	0.353	0.44	+0.08	F	C	Core-Jet	CA
0755+379	G	0.043	186.9	108.58	41	Y	1.260	0.124	0.10	−0.55	S	FR II ?	Core-Jet	FR II A
0805+410	Q	1.420	12.2	40.19	1	Y	0.766	0.947	0.91*	+0.26	F	FR II	Core-Jet	FR II A
0812+367	Q	1.025	16.4	70.03	18	Y	1.010	0.543	0.54	−0.20	F	FR II	Core-Jet	FR II A
0816+526	G	0.189	37.9	76.88	13,19	N	0.776			−0.78	S	FR II	—	—
0818+472	G	0.130	26.7	40.74	1	N	0.860			−0.79	S	FR II ?	—	—
0820+560	Q	1.417	3.0	12.88	20	Y	0.917	1.149	0.74*	+0.28	F	D2	Core-Jet	D2A
0821+394	Q	1.216	2.8	12.06	1	Y	0.993	0.582	0.59	+0.49	F	D2	Core-Jet	D2A
0827+378	Q	0.914	40.9	172.29	1	Y	0.930			−0.71	S	FR II	(resolved)	—
0828+493	BL	0.548	1.2	4.43	16	Y	1.020	0.176	0.17	−0.09	F	C	Core-Jet	CA

Table 5.1. Physical Classification of the CJ1 Sample (*continued*)

Source	ID	z	LAS	LLS	Ref	VLB?	S_{total}	S_{core}	F_c	α_{em}^{15}	Spec	Attr.	Attr.	Class
			($''$)	(kpc)			(Jy)	(Jy)				($\geq$ 5 kpc)	($<$ 5 kpc)	
(1)	(2)	(3)	(4)	(5)	(6)	(7)	(8)	(9)	(10)	(11)	(12)	(13)	(14)	(15)
0833+585	Q	2.101	11.1	44.99	16	Y	1.110	0.392	0.34	+0.52	F	D2	Core-Jet	D2A
0844+540	G	0.0453	55.0	33.53	1	N	0.732			−0.66	S	FR I	—	—
0900+428	Q	0.328	24.1	69.81	1	Y	0.761	0.179	0.24	−0.51	S	FR II	Core-Jet	FR II A
0917+449	Q	2.180	14.4	57.86	1	Y	0.803	0.692	0.86	+0.57	F	FR II	Core-Jet	FR II A
0917+624	Q	1.446	6.1	26.16	16	Y	0.996	0.813	0.82	+0.83	F	D2	Core-Jet	D2A
0936+361	G	0.137	311.8	496.01	7	N	1.290			−0.78	S	FR II	—	—
0938+399	G	0.108	76.1	99.87	21	N	0.870			−0.75	S	FR II	—	—
0945+664	G	—	1.5	—	6	N	1.220			−0.71	S	FR II ?	—	—
0955+476	Q	1.880	$<$ 0.2	0.83	6	Y	0.739	0.982	0.92*	+0.15	F	C	Core-Jet	CA
1003+830	Q	0.322	9.8	28.09	1	Y	0.716	0.273	0.38	−0.22	F	D2	Core-Jet	D2A
1007+417	Q	0.613	36.0	137.89	22,23	N	0.706			−0.69	S	FR II	—	—
1015+359	Q	1.226	19.2	82.74	1	Y	0.916	0.415	0.45	+0.09	F	D2	Core-Jet	D2A
1020+400	Q	1.254	15.2	65.50	1	Y	0.866	0.689	0.80	−0.12	F	FR II	Core-Jet	FR II A
1030+415	Q	1.120	9.1	39.11	1	Y	1.130	0.218	0.19	−0.14	F	D2	Core-Jet	D2A
1030+585	G	0.428	51.9	172.51	7	N	1.120			−0.99	S	FR II	—	—
1039+811	Q	1.259	2.9	12.50	2	Y	1.144	0.339	0.30	−0.04	F	D2	Core-Jet	D2A
1044+719	Q?	—	15.7	—	1	Y	0.707	0.965	1.00*	+0.22	F	FR II	Core	FR II A
1053+704	Q	2.492	2.6	10.07	1	Y	0.710	0.267	0.38	+0.12	F	D2	Core-Jet	D2A
1053+815	G	0.706	4.1	16.39	1	Y	0.770	0.370	0.48	−0.23	F	D2	Core-Jet	D2A
1056+432	G	0.749	13.2	53.54	13	N	0.949			−1.14	S	FR II	—	—

Table 5.1. Physical Classification of the CJ1 Sample (*continued*)

Source	ID	z	LAS	LLS	Ref	VLB?	S_{total}	S_{core}	F_c	α_{em}^{15}	Spec	Attr.	Attr.	Class
			($''$)	(kpc)			(Jy)	(Jy)				($\geq$ 5 kpc)	($<$ 5kpc)	
(1)	(2)	(3)	(4)	(5)	(6)	(7)	(8)	(9)	(10)	(11)	(12)	(13)	(14)	(15)
1058+726	Q	1.46	6.8	29.14	1,6	Y	0.778	0.117	0.15	+0.13	F	FR II	Core-Jet	FR II A
1100+772	Q	0.311	46.2	129.81	7	N	0.772	0.035[b]	0.05	−0.83	S	FR II	—	—
1101+384	BL	0.030	127.2	52.70	24	Y	0.725	0.363	0.50	−0.17	F	C+H	Core-Jet	CA
1111+408	Q	0.734	15.2	61.35	22	N	0.790			−1.17	S	FR II	—	—
1128+385	Q	1.733	16.1	67.71	16	Y	0.771	0.753	0.77*	+0.13	F	D2	Core-Jet	D2A
1137+660	Q	0.652	48.8	190.74	2	N	1.040	0.097[b]	0.09	−1.02	S	FR II	—	—
1138+594	Q?	—	0.54	—	6	Y	0.767	0.091	0.12	−0.77	S	C	Core-Jet	CA
1144+402	Q	1.088	11.2	48.05	16	Y	0.941	0.455	0.48	+0.01	F	D2	Core-Jet	D2A
1144+542	Q	2.201	< 0.2	0.80	6	Y	0.878	0.164	0.19	−0.24	F	C	Core-Jet	CA
1150+497	Q	0.334	25.1	73.45	2	Y	1.110	0.337	0.30	−0.10	F	FR II	Core-Jet	FR II A
1150+812	Q	1.250	5.2	22.41	16	Y	1.181	0.441	0.37	−0.02	F	D2	Core-Jet	D2A
1152+551	G	0.050	140.0	93.47	13	N	0.843			−0.80	S	FR II	—	—
1203+645	G	0.371	1.9	5.88	25	Y	1.160			−1.19	S	FR II ?	(resolved)	—
1213+350	Q	0.860	15.5	64.67	26	Y	1.010	–	–	−0.41	F	FR II	U	—
1213+538	Q	1.065	35.8	153.36	22	N	0.904			−0.96	S	FR II	—	—
1216+487	Q	1.073	20.0	85.72	1	Y	1.080	0.285	0.26	−0.11	F	FR II	Core-Jet	FR II A
1225+368	Q	1.974	0.055	0.23	1,27	Y	0.767	0.043	0.06	−1.29	G	C	S2	CSO
1242+410	Q	0.813	< 0.2	0.83	6	Y	0.744	0.113	0.15	−0.80	G	C	S1	CSO
1250+568	Q	0.320	1.7	4.86	28	N	1.050			−0.92	S	C	S2	CSO
1311+678	G	—	$<$1.5	—	1	Y	0.923	0.177	0.19	−1.12	S	C	U	—

Table 5.1. Physical Classification of the CJ1 Sample (*continued*)

Source	ID	z	LAS	LLS	Ref	VLB?	S_{total}	S_{core}	F_c	α_{em}^{15}	Spec	Attr.	Attr.	Class
			($''$)	(kpc)			(Jy)	(Jy)				($\geq$ 5 kpc)	($<$ 5kpc)	
(1)	(2)	(3)	(4)	(5)	(6)	(7)	(8)	(9)	(10)	(11)	(12)	(13)	(14)	(15)
1317+520	Q	1.060	35.2	150.74	29	Y	0.716	0.184	0.26	−0.68	S	FR II	Core-Jet	FR II A
1319+428	G	0.079	185.5	186.55	30	N	0.760			−0.75	S	FR II	—	—
1333+459	Q	2.449	< 0.2	0.78	6	Y	0.757	0.353	0.47	+0.06	G	C	S2 ?	CSO
1333+589	Q?	—	< 0.2	—	6	Y	0.826	—	—	−0.12	G	C	S2 ?	CSO
1336+391	G	0.246	35.6	86.55	1	N	0.992			−1.22	S	FR II ?	—	—
1342+663	Q	1.351	5.0	21.52	1	Y	0.817	0.690	0.84	−0.18	F	D2	Core-Jet	D2A
1347+539	Q	0.978	20.0	84.99	1	Y	0.962	0.412	0.43	−0.12	F	FR II	Core-Jet	FR II A
1349+647	G	0.710	133.1	532.71	30	N	0.720			−0.08	F	FR II	—	—
1357+769	Q	—	< 0.2	—	6	Y	0.844	0.638	0.75	−0.47	F	C	Core-Jet	CA
1418+546	BL	0.152	35.1	60.54	16	Y	1.090	1.428	0.67*	+0.19	F	D2	Core-Jet	D2A
1419+419	G	0.367	11.2	34.49	31	N	0.900			−1.09	S	FR II	U	—[a]
1435+638	Q	2.060	15.3	62.29	20	Y	1.240	0.428	0.35	−0.29	F	D2	Core-Jet	D2A
1437+624	Q	1.090	< 0.2	0.86	6	Y	0.862	0.214	0.25	−0.86	S	C	S2	CSO
1438+385	Q?	—	8.8	—	1,6	Y	0.770	0.258	0.34	0.00	F	D2	Core-Jet	D2A
1441+522	G	0.141	45.5	193.75	7	N	0.940			−0.70	S	FR II	—	—
1448+634	G	0.041	13.8	7.84	32	N	0.920			−0.96	S	U	—	—
1504+377	G	0.674	31.2	—	2	Y	1.100	0.362	0.33	−0.32	F	FR II	Core-Jet	FR II A
1547+507	Q	2.169	< 0.2	0.86	6	Y	0.738	0.438	0.59	+0.04	F	C	Core-Jet	CA
1549+628	G	0.860	15.6	65.08	4	N	0.830			−1.11	S	FR II	—	—
1557+708	G	0.026	597.8	216.13	33	N	1.020			−2.95	S	FR I	—	—

Table 5.1. Physical Classification of the CJ1 Sample (*continued*)

Source	ID	z	LAS	LLS	Ref	VLB?	S_{total}	S_{core}	F_c	α_{em}^{15}	Spec	Attr.	Attr.	Class
			($''$)	(kpc)			(Jy)	(Jy)				($\geq$ 5 kpc)	(< 5 kpc)	
(1)	(2)	(3)	(4)	(5)	(6)	(7)	(8)	(9)	(10)	(11)	(12)	(13)	(14)	(15)
1627+444	G	0.635	43.5	168.67	34	N	0.910			−0.92	S	FR II	—	—
1637+626	G	0.750	0.24	0.97	25	Y	1.200			−1.11	S	C	S2 ?	CSO
1637+826	G	0.023	3352.8	1077.81	35	Y	0.978	0.350	0.36	−0.44	F	FR II	Core-Jet†	FR II A
1638+398	Q	1.666	8.9	37.62	36	Y	1.160	1.751	1.00*	+0.34	F	FR II	Core-Jet	FR II A
1656+477	Q	1.622	13.5	57.33	16	Y	0.923	1.116	0.73*	+0.29	F	D2	Core-Jet	D2A
1656+482	Q?	—	4.3	—	1	Y	0.776	0.386	0.50	−0.14	F	FR II	Core-Jet	FR II A
1658+471	G	0.205	86.4	185.68	7	N	1.140			−0.81	S	FR II	—	—
1704+608	Q	0.371	70.9	219.56	7	N	1.210			−0.59	S	FR II	—	—
1719+357	Q	0.263	138.8	352.25	1	Y	0.859	0.204	0.24	+0.08	F	FR II	Core-Jet	FR II A
1732+389	Q	0.976	< 0.2	0.85	6	Y	1.150	0.966	0.84	−0.10	F	C	Core-Jet	CA
1734+508	Q?	—	< 0.2	—	6	Y	0.803	0.480	0.60	+0.13	F	C	S2	CSO
1738+476	BL	—	< 0.2	0.57	6	Y	0.904	0.908	0.85*	−0.05	F	C	Core-Jet	CA
1751+441	Q	0.871	23.3	97.42	1	Y	1.040	0.687	0.66	+0.04	F	FR II	Core-Jet	FR II A
1758+388	Q	2.092	6.5	26.37	1	Y	0.916	0.830	0.91	+0.38	F	D2	Core-Jet	D2A
1800+440	Q	0.663	17.7	69.43	1	Y	1.020	0.320	0.31	+0.13	F	FR II	Core-Jet	FR II A
1819+396	G	(0.4)*	0.85	(2.95)	25	Y	0.971			−1.12	S	C	S2 ?	CSO
1825+743	G	0.256	81.6	203.56	37	N	0.728			−0.77	S	FR II	—	—
1832+474	G	0.161	76.0	136.95	7	N	1.290			−0.75	S	FR II	—	—
1833+653	G	0.161	12.2	21.98	1,13	N	0.799			−0.93	S	FR II ?	—	—
1842+681	Q	0.475	18.1	62.93	1	Y	0.810	0.635	0.78	0.00	F	D2+H	Core-Jet	D2A

Table 5.1. Physical Classification of the CJ1 Sample (*continued*)

Source	ID	z	LAS	LLS	Ref	VLB?	S_{total}	S_{core}	F_c	α_{em}^{15}	Spec	Attr.	Attr.	Class
			($''$)	(kpc)			(Jy)	(Jy)				($\geq$ 5 kpc)	(< 5 kpc)	
(1)	(2)	(3)	(4)	(5)	(6)	(7)	(8)	(9)	(10)	(11)	(12)	(13)	(14)	(15)
1843+356	G?	—	< 0.2	—	2	Y	0.812	0.171	0.21	−1.42	G	C	S2 ?	CSO
1926+611	BL	—	2.0	—	1	Y	0.721	0.367	0.51	−0.05	F	D2	Core-Jet	D2A
1940+504	G	0.0239	481.4	160.56	38	N	0.933			−0.86	S	FR II	—	—
1943+546	G	0.263	0.041	0.11	1,13	Y	0.850	0.016	0.019	−0.59	S	C	S2	CSO
2007+777	BL	0.342	27.0	80.05	17	Y	1.279	0.967	0.76	−0.03	F	FR II	Core-Jet	FR II A
2010+723	BL	—	2.3	—	1,6	Y	0.917	0.358	0.39	−0.23	F	D2	Core-Jet	D2A
2104+763	G	0.572	24.5	91.77	39	N	0.997			−1.31	S	FR II	—	—
2207+374	Q	1.493	1.6	6.85	1,6	Y	0.791	0.140	0.18	−0.52	S	D2	Core-Jet	D2A
2214+350	Q	0.510	10.6	38.02	1	Y	0.824	0.543	0.66	−0.42	F	D2	Core-Jet	D2A
2229+695	G	—	11.3	—	1	Y	0.812	0.460	0.57	+0.09	F	U	Core-Jet	—
2253+417	Q	1.476	< 0.2	0.86	6	Y	0.990	0.519	0.52	−0.27	F	C	Core-Jet	CA
2255+416	Q	1.149	< 0.2	0.84	6	Y	0.993	0.167	0.17	−0.53	S	C	Core-Jet	CA
2311+469	Q	0.742	2.7	10.93	6,13	Y	0.726	0.054	0.07	−0.71	S	FR II	Core-Jet	FR II A
2323+435	G	0.145	1.7	2.83	40	N	1.010			−0.83	S	C	S2	CSO
2324+405	G	0.394	27.9	89.09	2	N	1.120			−0.70	S	FR II	—	—

Notes to Table 5.1.

Column (1) — Source name in IAU convention.

Column (2) — Optical ID - G: galaxy; Q: quasar; BL: BL Lac object; EF: empty field.

Column (3) — Redshift: * estimated by Herbig & Readhead (1992).

Column (4) — Largest angular size.

Column (5) — Largest projected linear size (H_0 = 100 km/s/Mpc and q_0 = 0.5).

Column (6) — References for the largest angular size: 1- this work; 2- Rusk 1988; 3- Pooley & Henbest 1974; 4- Jenkins et al. 1977; 5- Kapahi & Neff 1982; 6- Patnaik et al. 92; 7- Leahy & Perley 1991; 8- Fanti et al. 1986; 9- O'Dea et al. 1993; 10- Longair 1975; 11- Sanghera 1990; 12- Saikia et al. 1989; 13- Polatidis 1993; 14- Rudnick & Jones 1982; 15- Burns & Gregory 1982; 16- Murphy 1988; 17- Antonucci et al. 1986; 18- Perley, private communication; 19- Burns & Christiansen 1980; 20- Jodrell 966 MHz paper; 21- Gregorini et al. 1988; 22- Owen & Puschell 1984; 23- Saikia, Kulkarni & Porcas 1986; 24- Antonucci & Ulvestad 1985; 25- Spencer et al. 1989; 26- Perley, private communication; 27- Dalacassa, private communication; 28- Foulsham 1989; 29- Hintzen et al. 1983; 30- Alexander & Leahy 1987; 31- Liu & Pooley 1991; 32- Antonucci 1985; 33- Kapahi 1981; 34- Pedelty et al. 1989; 35- Jones et al. 1985; 36- Kollgaard et al. 1990; 37- Spangler & Sakurai 1985; 38- Jagers 1987; 39- Laing 1981; 40- Sanghera 1992; 41- Vigotti et al. 1989.

Column (7) — Status of VLBI observation: Y - observed with VLBI at 5 GHz; N - not observed with VLBI.

Column (8) — Total flux density at 5 GHz as measured in the S4 and S5 surveys.

Column (9) — Flux density at 5 GHz in the VLBI core: [a] the core is not well defined; [b] taken from Hough (1986).

Column (10) — Fraction of the total flux density in the core: * ratio of the core flux to the total flux in the VLBI map, see Section 5.5 for explanation.

Column (11) — Spectral Index at 15 GHz in the rest frame.

Column (12) — Spectral types: F – flat high-frequency spectrum; S – steep high-frequency spectrum; G – Gigahertz peaked spectrum.

Column (13) — Morphological attributes on scales $\geq$ 5 kpc.

Column (14) — Morphological attributes on scales $<$ 5 kpc. † Eckart et al. 1987.

Column (15) — Physically Distinct classes.

Table 5.2. Physical Classification of the PR Sample

Source	Alias	ID	V	z	Ref	LAS ($''$)	LLS (kpc)	Ref	VLB	S_{total} (Jy)	Fc	α_{em}^{15}	Spec	Attr. ($\geq$ 5 kpc)	Attr. ($<$ 5 kpc)	Class
(1)	(2)	(3)	(4)	(5)	(6)	(7)	(8)	(9)	(10)	(11)	(12)	(13)	(14)	(15)	(16)	(17)
0016+731	—	Q	18	1.781	1	11.7	48.99	0	Y	1.7	0.95	−0.34	F	D2	Core	D2A
0040+517	3C 20	G	19	0.174	1	51.1	97.59	1	N	4.18		−0.99	S	FR II	—	—
0108+388	OC 314	G	22	0.669	1	18.5	72.85	2	Y	1.6	—	−0.77	G	D2	S2	D2S
0133+476	OC 457	Q	19	0.859	1	<0.2	0.83	3	Y	1.8	0.89	−0.01	F	C	Core-Jet	CA
0153+744	—	Q	17	2.338	1	<0.15	0.59	4	Y	1.5	0.43	−0.35	F	C	Core-Jet	CA
0210+860	3C 61.1	G	19	0.184	1	185.6	369.26	1	N	1.68		−0.61	S	FR II	—	—
0212+735	—	Q	19	2.367	1	<0.2	0.79	3	Y	2.3	0.59	−0.11	F	C	Core-Jet	CA
0220+427	3C66B	G	12.9	0.0215	1	432.6	130.33	5	N	3.75		−1.51	S	FR I	—	—
0314+416	3C83.1B	G	12.5	0.0181	1	76.2	19.44	6	N	3.53		−1.38	S	FR I	—	—
0316+413	3C84	G	11.9	0.0172	1	42.5	10.32	4	Y	57.0	—[a]	+0.32	F	FR II	Core-Jet	FR II A
0404+768	4C 76.03	G	22	0.5985	1	0.195	0.74	0	Y	2.79	—	−0.57	S	C	S2	CSO
0454+844	—	BL	18	—	2	<0.2	0.85	3	Y	1.0	0.51	+0.68	F	C	Core-Jet	CA
0538+498	3C 147	Q	17.8	0.545	1	0.68	2.50	4	Y	8.18	—	−0.99	S	C	Core-Jet	CSO
0605+480	3C 153	G	18.5	0.2769	1	8.0	20.96	7	N	1.35		−1.11	S	FR II	—	—
0710+439	OI 417	G	20.7	0.518	1	0.026	0.09	8	Y	1.6	0.45	−0.78	G	C	S2	CSO
0711+356	OI 318	Q	17	1.62	1	13.1	55.59	9	Y	1.1	0.24	−0.53	G	FR II	Core-Jet	FR II A
0723+679	3C 179	Q	18	0.846	1	15.9	66.14	4	Y	1.31	0.31	−0.41	F	FR II	Core-Jet	FR II A
0804+499	OJ 508	Q	17.5	1.43	1	4.3	18.45	9	Y	1.4	0.99	−0.43	F	D2	Core	D2A
0809+483	3C 196	Q	17.8	0.871	1	5.4	22.58	7	N	4.35		−1.12	S	FR II	—	—
0814+425	OJ 425	BL	17.7	0.258	2	4.1	10.28	4	Y	1.9	0.84	−0.07	F	D2 ?	Core-Jet	D2A

Table 5.2. Physical Classification of the PR Sample (*continued*)

Source	Alias	ID	V	z	Ref	LAS ($''$)	LLS (kpc)	Ref	VLB	S_{total} (Jy)	Fc	α_{em}^{15}	Spec	Attr. ($\geq$ 5 kpc)	Attr. ($<$ 5 kpc)	Class
(1)	(2)	(3)	(4)	(5)	(6)	(7)	(8)	(9)	(10)	(11)	(12)	(13)	(14)	(15)	(16)	(17)
0831+557	4C 55.16	G	17.5	0.242	1	12.5	30.02	0	Y	5.3	—[a]	−1.38	S	FR II	Core-Jet	FR II A
0836+710	4C 71.07	Q	16.5	2.17	1	1.7	6.84	4	Y	2.6	0.40	−0.64	S	D2	Core-Jet	D2A
0850+581	4C 58.17	Q	18	1.322	1	20.7	89.14	4	Y	1.1	0.85	−0.06	F	FR II	Core-Jet	FR II A
0859+470	4C 47.29	Q	18.7	1.462	1	2.8	12.00	10	Y	1.7	0.68	−0.33	F	FR II	Core-Jet	FR II A
0906+430	3C 216	Q	18.5	0.668	1	2.3	9.05	11	Y	1.9	0.45	−0.28	F	FR II	Core-Jet	FR II A
0917+458	3C 219	G	17.2	0.1744	1	188.9	361.35	12	N	2.29		−0.91	S	FR II	—	—
0923+392	4C 39.25	Q	17.9	0.699	1	4.1	16.34	13	Y	7.5	0.63	−0.37	F	FR II	Core-Jet	FR II A
0945+408	4C 40.24	Q	17.5	1.252	1	4.3	18.53	10	Y	1.5	0.48	−0.06	F	D2	Core-Jet	D2A
0951+699	M82	G	8.4	0.0009	1	66.4	0.87	14	N	3.94		−0.71	S	C	—	—
0954+556	4C 55.17	Q	17.7	0.909	1	3.3	13.89	9	Y	2.27		−0.49	F	D2 ?	Core-Jet	D2A
0954+658	—	BL	16.7	0.368	2	4.1	12.64	0	Y	1.46	0.47[b]	−0.59	S	D2	Core-Jet	D2A
1003+351	3C 236	G	16	0.0989	1	2457.3	2995.99	15	Y	1.32	0.06[d]	−0.43	F	FR II	S1	FR II S
1031+567	OL 553	G	21.3	0.45	1	$<$0.2	0.68	3	Y	1.31		−0.77	S	C	S2	CSO
1157+732	3C 268.1	G	21.5	0.9737	1	43.0	182.64	1	N	2.63		−0.96	S	FR II	—	—
1254+476	3C 280	G	20	0.994	1	13.7	58.32	0	N	1.53		−0.92	S	FR II	—	—
1358+624	4C 62.22	G	20.9	0.431	1	$<$0.1	0.33	16	Y	1.77		−0.74	S	C	S2	CSO
1409+524	3C 295	G	20.1	0.4614	1	4.6	15.82	1	N	6.48		−1.33	S	FR II	—	—
1458+718	3C 309.1	Q	16.8	0.905	1	2.3	9.67	4	Y	3.3	0.18	−0.68	S	FR II	Core-Jet	FR II A
1609+660	3C 330	G	20.3	0.549	1	61.9	228.43	0	N	2.35		−1.15	S	FR II	—	—
1624+416	4C 41.32	Q	22	2.55	1	2.7	10.38	0	Y	1.2	0.35	−0.33	F	D2	Core-Jet	D2A

Table 5.2. Physical Classification of the PR Sample (*continued*)

Source	Alias	ID	V	z	Ref	LAS ($''$)	LLS (kpc)	Ref	VLB	S_{total} (Jy)	Fc	α_{em}^{15}	Spec	Attr. ($\geq$ 5 kpc)	Attr. ($<$ 5 kpc)	Class
(1)	(2)	(3)	(4)	(5)	(6)	(7)	(8)	(9)	(10)	(11)	(12)	(13)	(14)	(15)	(16)	(17)
1633+382	4C 38.41	Q	18	1.814	1	10.3	43.00	9	Y	2.3	0.37	−0.04	F	FR II	Core-Jet	FR II A
1634+628	3C 343	Q	20.6	0.988	1	1.3	5.53	0	N	1.50		−1.12	S	U	U	—
1637+574	OS 562	Q	17	0.745	1	13.8	55.90	13	Y	1.9	0.96	+0.51	F	C+H	Core	CA
1641+399	3C 345	Q	16	0.595	1	24.1	91.50	9	Y	7.5	0.35	+0.27	F	D2+H	Core-Jet	D2A
1642+690	4C 69.21	Q	19.2	0.751	1	9.6	38.96	9	Y	1.9	0.86	+0.23	F	FR II	Core-Jet	FR II A
1652+398	4C 39.49	BL	13.8	0.0337	2	80.8	37.37	17	Y	1.3	0.35	−0.29	F	C+H	Core-Jet	CA
1739+522	4C 51.37	Q	18.5	1.375	1	3.4	14.62	4	Y	1.0	0.91	−0.10	F	D2	Core-Jet	D2A
1749+701	—	BL	17	0.77	2	3.4	13.88	0	Y	1.3	0.67	−0.01	F	D2+H	Core-Jet	D2A
1803+784	—	BL	17	0.684	2	45.1	178.42	9	Y	2.9	0.74	−0.20	F	D2	Core-Jet	D2A
1807+698	3C 371	BL	14.2	0.051	2	260.0	173.58	18	Y	2.4	0.40	−0.06	F	FR II	Core-Jet	FR II A
1823+568	4C 56.27	BL	18.4	0.664	2	21.2	83.30	9	Y	1.5	0.74	+1.23	F	D2+H	Core-Jet	D2A
1828+487	3C 380	Q	16.8	0.692	1	16.4	65.19	4	Y	3.0	0.34[c]	−0.72	S	D2+H	Core-Jet	D2A
1842+455	3C 388	G	15.3	0.0908	1	37.9	42.98	1	N	1.77		−1.03	S	FR II	—	—
1845+797	3C 390.3	G	15	0.0569	1	210.7	158.26	4	Y	2.3	0.13	−0.20	F	FR II	Core-Jet	FR II A
1928+738	4C 73.18	Q	16.5	0.302	1	59.1	163.22	4	Y	3.3	0.64	−0.29	F	FR II	Core-Jet	FR II A
1939+605	3C 401	G	18	0.201	1	19.3	40.91	1	N	1.52		−1.12	S	FR II	—	—
1954+513	OV 591	Q	18.5	1.22	1	17.0	73.25	0	Y	1.5	0.57	+0.01	F	FR II	Core-Jet	FR II A
2021+614	OW 637	G	19.5	0.2266	1	$<$0.2	0.46	3	Y	2.2	0.45	−0.71	G	C	Core-Jet	CA
2153+377	3C 438	G	19.2	0.292	1	20.2	54.68	1	N	1.54		−1.50	S	FR II	—	—
2200+420	BL Lac	BL	14.5	0.069	2	34.7	31.38	19	Y	2.3	0.52	+0.06	F	C+H	Core-Jet	CA

Table 5.2. Physical Classification of the PR Sample (*continued*)

Source	Alias	ID	V	z	Ref	LAS	LLS	Ref	VLB	S_{total}	Fc	α_{cm}^{15}	Spec	Attr.	Attr.	Class
						($''$)	(kpc)			(Jy)				($\geq$ 5 kpc)	(< 5 kpc)	
(1)	(2)	(3)	(4)	(5)	(6)	(7)	(8)	(9)	(10)	(11)	(12)	(13)	(14)	(15)	(16)	(17)
2229+391	3C 449	G	13.2	0.0171	1	923.5	222.96	20	N	1.39		−0.77	S	FR I	—	—
2243+394	3C 452	G	16	0.0811	1	337.8	347.55	6	N	3.26		−0.88	S	FR II	—	—
2342+821	—	Q	20.5	0.735	1	<1.0	4.04	0	N	1.30		−0.83	S	C	S2 ?	CSO
2351+456	4C 45.51	Q	20.6	1.992	1	1.5	6.15	4	Y	1.1	0.29	−0.34	F	FR II ?	Core-Jet	FR II A
2352+495	OZ 488	G	19	0.237	1	0.07	0.16	0	Y	1.6	0.45	−0.61	G	C	S2	CSO

Notes to Table 5.2.

Column (1) — Source name in the IAU Convention.

Column (2) — Alternative name.

Column (3) — Optical identification.

Column (4) — Approximate visual magnitude.

Column (5) — Redshift.

Column (6) — Reference for Columns (4) – (6): 1 – Pearson & Readhead (1988) and references therein; 2 – Stickel et al. (1992) and references therein.

Column (7) — Largest angular size.

Column (8) — Largest projected linear size (H_0 = 100 km/s/Mpc and q_0 = 0.5).

Column (9) — Reference for the largest angular size: 0 – this work; 1 – Laing 1981; 2 – Baum et al. 1990; 3 – Patnaik et al. 1992; 4 – Rusk 1988; 5 – Northover 1973; 6 – Riley & Pooley 1975; 7 – Lonsdale & Morison 1983; 8 – Pearson & Readhead 1988; 9 – Murphy 1988; 10 – Foley 1982; 11 – Fejes & Porcas 1990; 12 – Bridle et al. 1986; 13 – Kollgaard et al. 1990; 14 – Unger et al. 1984; 15 – Wills et al. 1974; 16 – Spencer et al. 1989; 17 – van Breuel & Schilizzi 1986; 18 – Ulvestad & Johnston 1984; 19 – Antonucci 1986; 20 – Perley et al. 1979.

Column (10) — Status of VLBI observation: Y – observed with VLBI; N – not observed with VLBI.

Colume (11) — Total flux density at 5 GHz.

Column (12) — Fraction of the total flux density at 5 GHz in the VLBI core: [a] Core is complex and its flux density could not be determined; [b] core flux = peak flux in the VLBI map (Gabuzda et al. 1990); [c] core flux = peak flux in the VLBI map (Pearson & Readhead 1988); [d] core flux = peak flux in the VLBI map (Barthel et al. 1985).

Column (13) — Spectral index at 15 GHz in the rest frame.

Column (14) — Spectral type: F – flat high-frequency spectrum; S – steep high-frequency spectrum;

G – Gigahertz-peaked spectrum.

Column (15) — Morphological attributes on arcsecond scales.

Column (16) — Morphological attributes on milliarcsecond scales.

Column (17) — Distinct classes.

Chapter 6

STATISTICAL STUDIES

6.1. GENERAL STATISTICS

The main objective of the CJ1 survey was to increase the statistics of the PR survey by a factor of 3. However, before proceeding with a discussion on the statistics of the combined PR+CJ1 sample, it is important to demonstrate that these two samples are homogeneous in all important properties. Therefore, we begin our discussion by comparing the general properties of the objects in these two samples.

The redshift distributions of the PR, CJ1, and combined PR+CJ1 samples are shown in Fig. 6.1a. The redshift distributions of galaxies, BL Lac objects, and quasars in these samples are shown in Figs. 6.1b and 6.1c. The optical magnitude distributions of the samples and galaxies, BL Lac objects and quasars in the samples are shown in Fig. 6.2. The spectral index distributions of the samples and galaxies, BL Lac objects and quasars in the samples are shown in Fig. 6.3.

No significant differences are seen between the PR sample and the CJ1 sample in any of these distributions. This is expected since the flux density limits of the two samples differ only by a factor of 2. Therefore, it is justified to combine the PR and CJ1 samples and discuss them together.

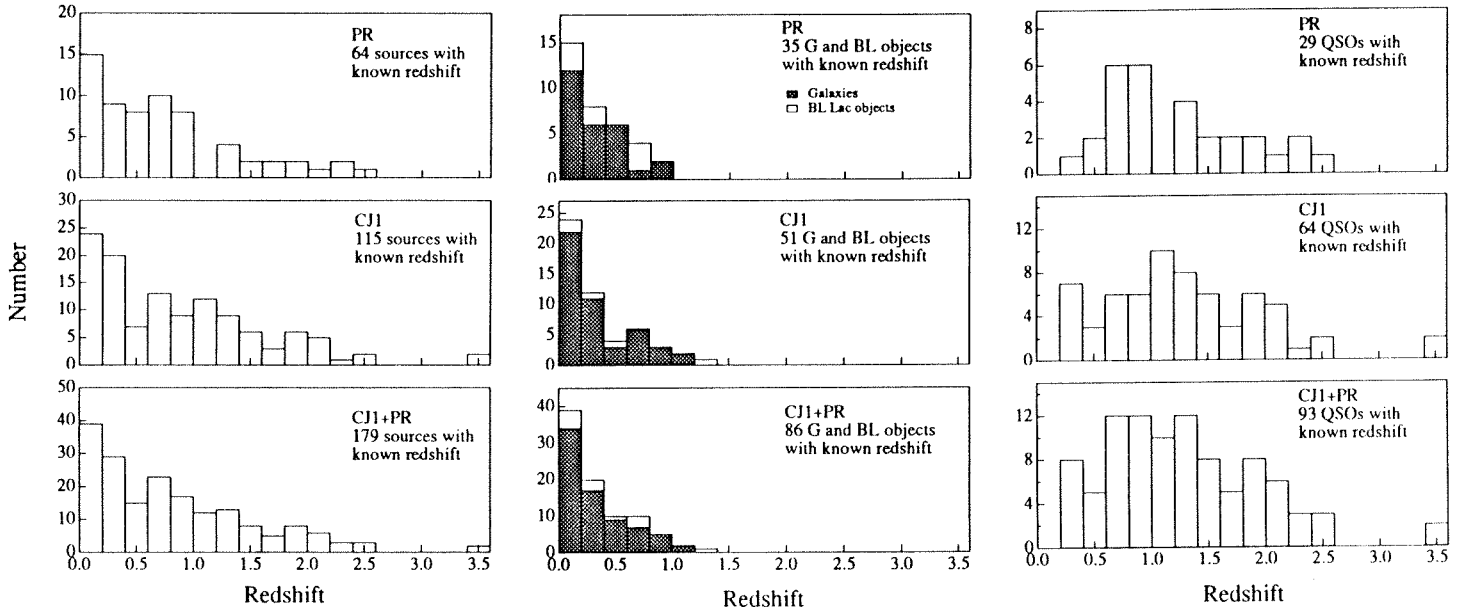

Fig. 6.1. Redshift distributions of the PR, CJ1 and CJ1+PR samples
(a) the whole sample; (b) galaxies and BL Lac objects; (c) quasars.

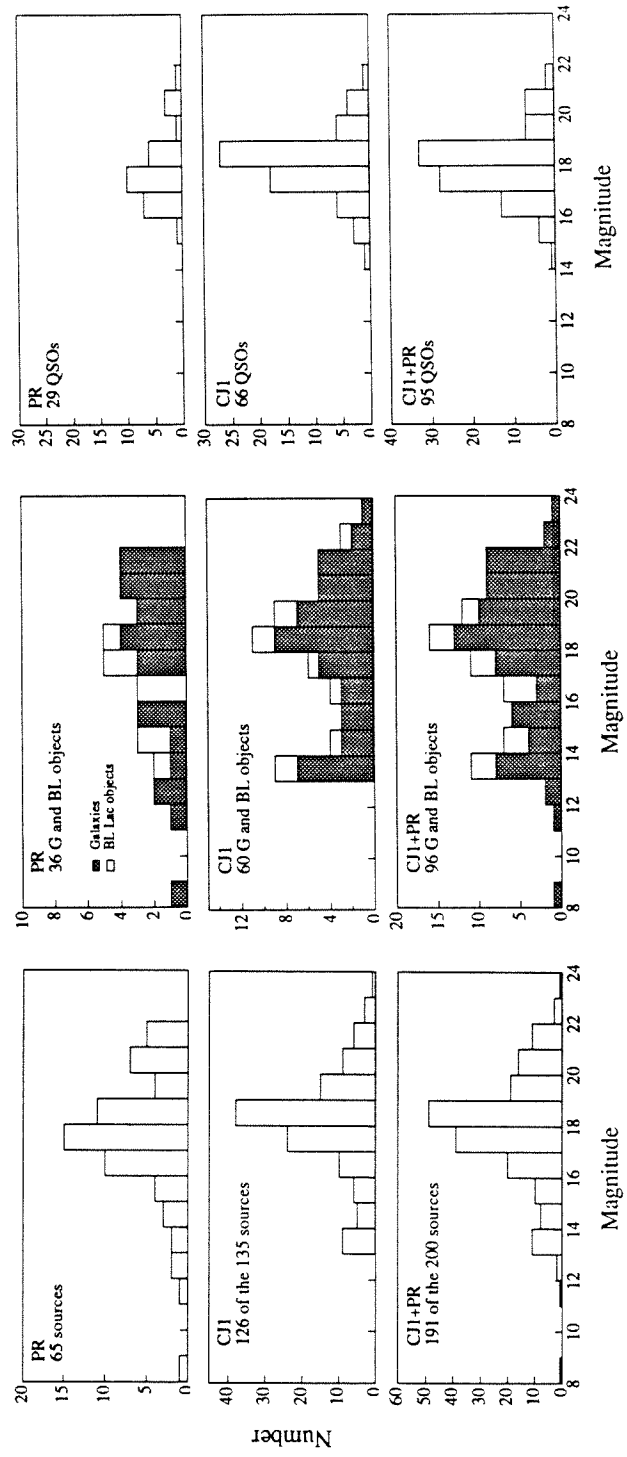

Fig. 6.2. Optical magnitude distributions of the PR, CJ1 and CJ1+PR samples (a) the whole sample; (b) galaxies and BL Lac objects; (c) quasars.

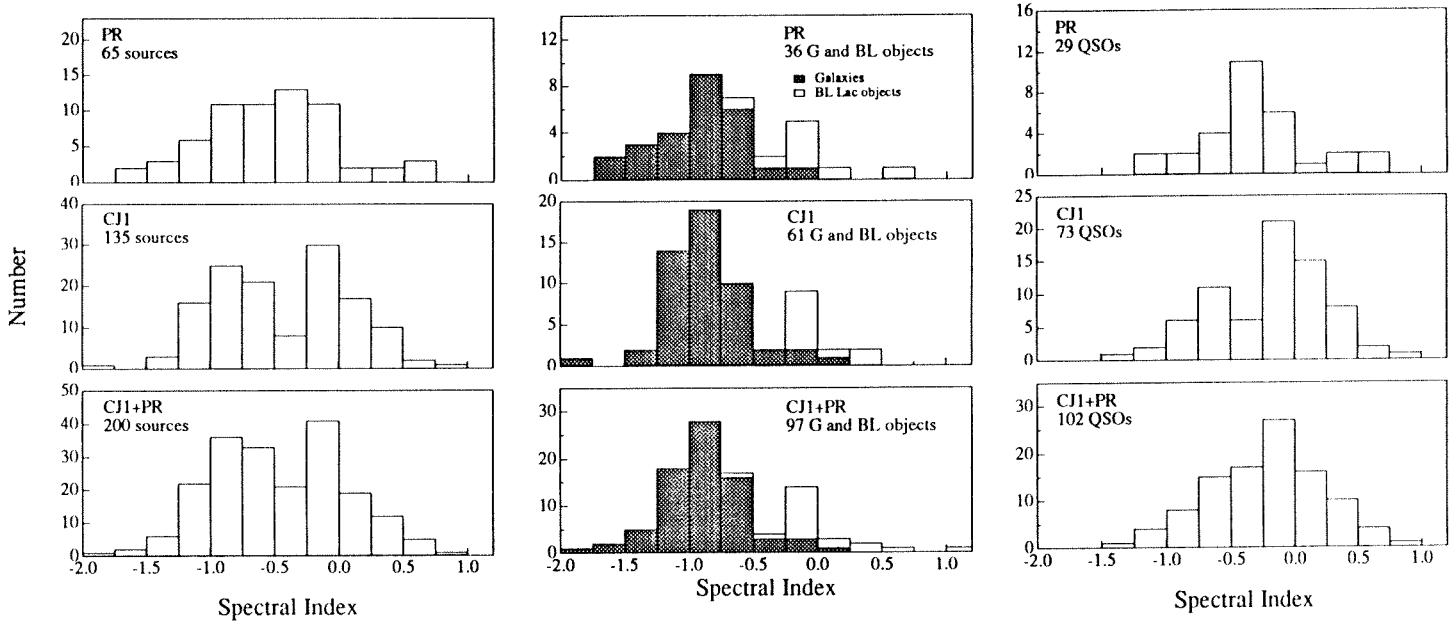

Fig. 6.3. Spectral index distributions of the PR, CJ1 and CJ1+PR samples (a) the whole sample; (b) galaxies and BL Lac objects; (c) quasars.

6.2. LINEAR SIZE DISTRIBUTIONS OF PHYSICAL CLASSES

In Chapter 5, we divided the objects in the PR and CJ1 samples into eight physically distinct classes according to morphological attributes on $\geq$ 5 kpc and $<$ 5 kpc scales. The number of objects of the combined PR+CJ1 sample in each attribute class is given in Tables 6.1 and 6.2, and the number of objects in each physical class is summarized in Table 6.3.

The distributions of linear sizes amongst the physical classes are shown in Fig. 6.4. For the CA class (shown in Fig. 6.4a), the upper limit on linear size is calculated from an upper limit of 0.2 arcsecond in angular size. There are four sources in this class with Log(Linear Size) between 4.4 and 4.8. These are core+halo sources.

The most important new statistical result from the PR+CJ1 sample is the relative population of the compact symmetric objects (CSO) and large-scale radio sources. Apart from candidate compact symmetric objects with overall linear sizes less than 5 kpc, three objects, 0108+388, 0402+379 and 1003+351 (3C 236), have symmetric structure on scales $<$ 1 kpc as well as much larger extended structure. On $\geq$ 5 kpc scales, the object 0108+388 has a faint component on one side of the core, i.e., a D2 structure. The objects 0402+379 and 1003+351 are FR II sources. 1003+351 is the largest source in the combined PR+CJ1 sample.

The CSO's resemble FR II sources morphologically. Comparing the linear size distribution of CSO candidates (Fig. 6.4a) and FR II sources (Fig. 6.4b), it is clear that the CSO candidates are $\sim$ 100–1000 times smaller than FR II's. We discuss the CSO's in more detail in Chapter 7.

Table 6.1.
Distribution of Morphological Attributes on Scales $\geq$ 5 kpc

	FR I	FR II	D2	D2+H	C	C+H	U
QSO	0	42	30	3	25	1	1
GAL	7	52	2	0	14	0	4
BL LAC	0	3	6	2	3	3	1
Unidentified	0	0	0	0	1	0	0
Total	7	97	38	5	43	4	6

Table 6.2.
Distribution of Morphological Attributes on Scales $<$ 5 kpc

	Asymmetric		Symmetric	Unclassified
	Core	Core-Jet		
QSO	4	76	10	2
GAL	0	11	14	2
BL LAC	0	17	0	1
Unidentified	0	1	0	0
Total	4	105	24	5

Table 6.3.
Distribution Amongst Physical Classes

	FR II A	FR II S	D2A	D2S	CA	CS
QSO	32	0	32	0	16	10
GAL	7	2	1	1	1	11
BL LAC	3	0	8	0	6	0
Unidentified	0	0	0	0	1	0
Total	42	2	42	1	24	21

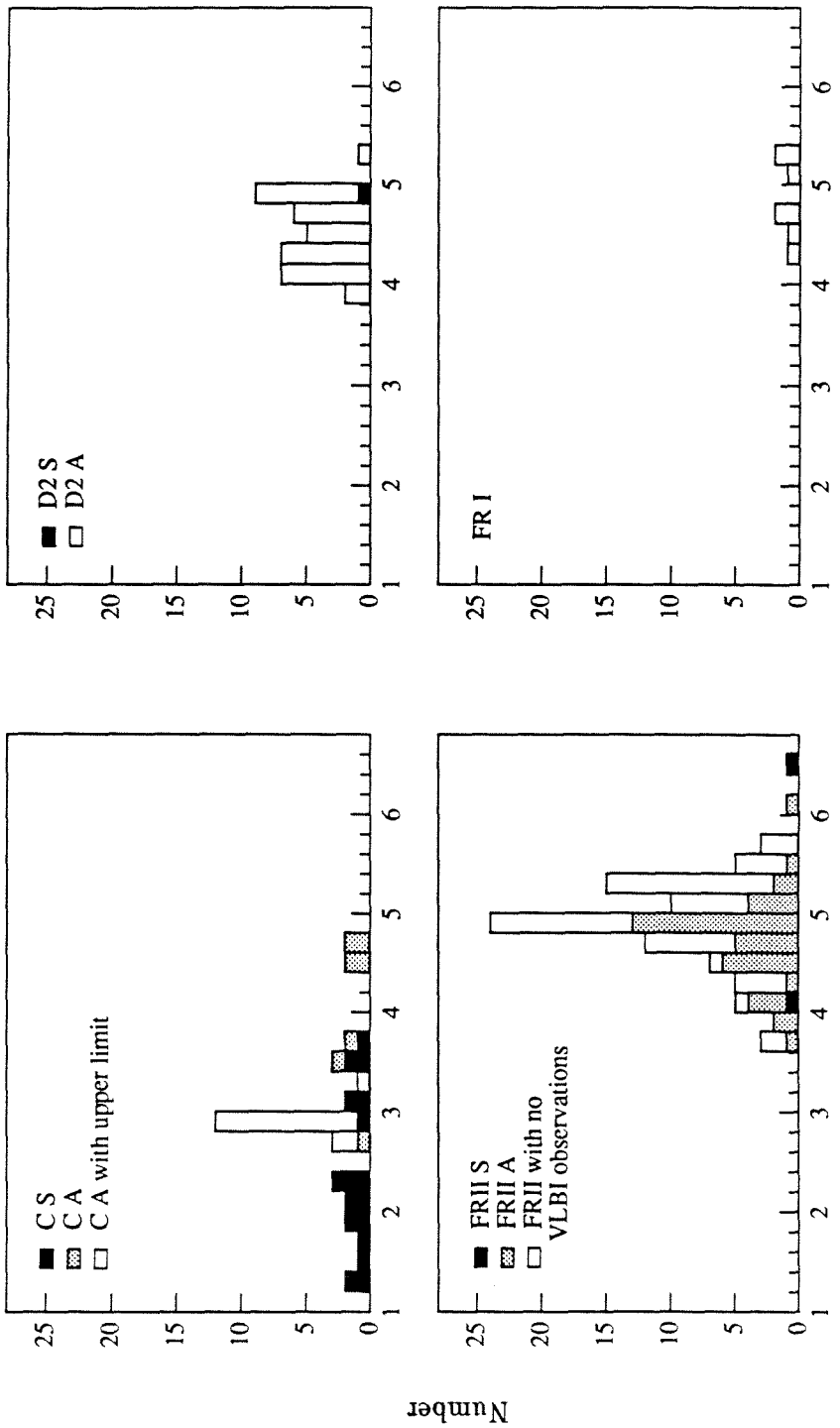

Fig. 6.4. Distributions of the projected linear sizes of the CJ1+PR sample
(a) upper-left: C objects; (b) lower-left: FR II objects;
(c) upper-right: D2 objects; (d) lower-right: FR I objects.

6.3. ALIGNMENT OF STRUCTURES ON MILLIARCSEC AND ARCSEC SCALES

Source orientation in active galaxies is widely recognized as an important factor in their appearance (e.g., Antonucci 1993). A measure of source orientation which has been used in studies of samples of these objects is the distribution of position angle differences between radio structures on the milliarcsecond and arcsecond scales (i.e., $|\theta_{\rm VLBI} - \theta_{\rm arcsec}|$ or ΔPA) (Readhead et al. 1978, 1983). In the relativistic beaming model, small intrinsic bends of the jets can have large ΔPA if sources are oriented close to the line of sight, owing to projection effects. Models can be fitted to the observed misalignment distribution to constrain the distribution of source orientation and hence detect differences between different classes of radio sources.

The most surprising result to emerge from the PR survey was the discovery of the bimodality of the distribution of position angle differences, ΔPA, between the nuclear radio structure and the extended radio structure. The distribution of ΔPA found in the PR survey showed two distinct peaks, one near 0° (aligned sources) and the other near 90° (misaligned sources). Examples of aligned and misaligned sources are shown in Fig. 6.5a and 6.5b.

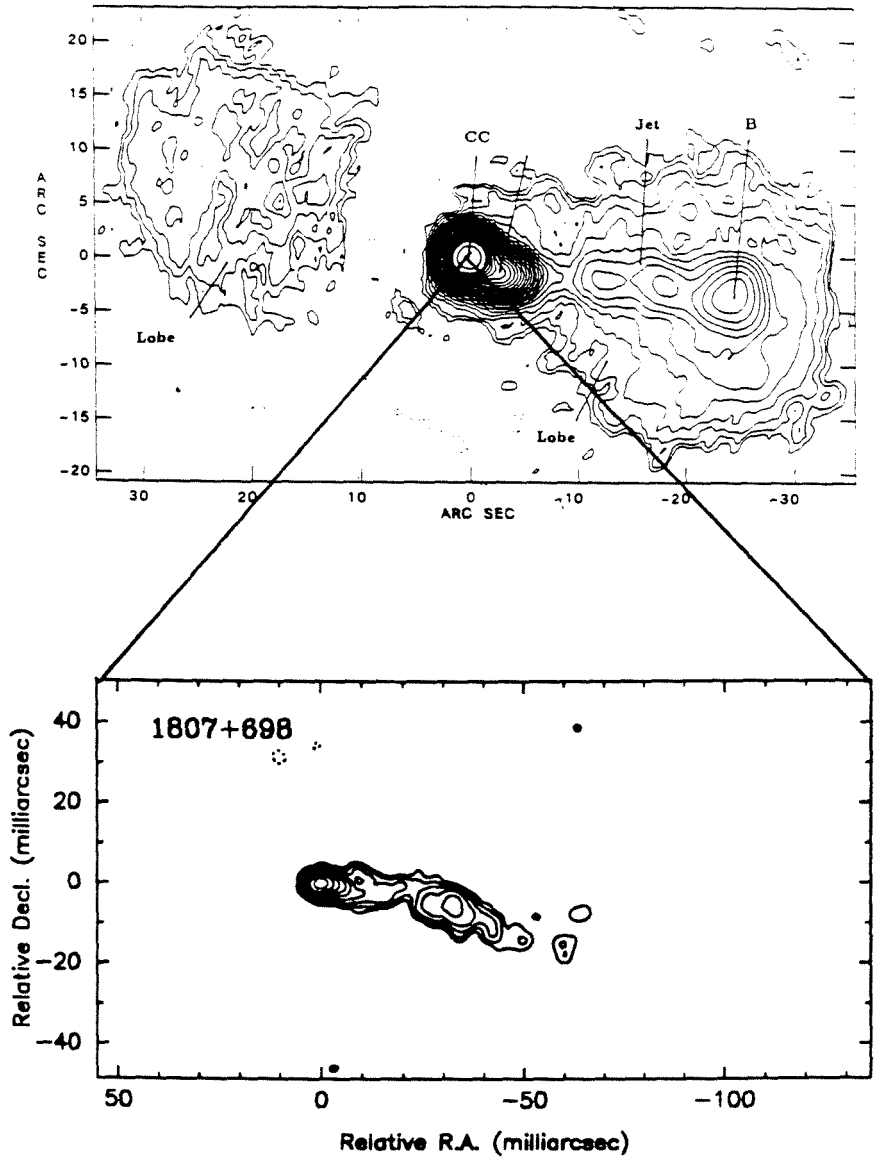

Fig. 6.5a. An example of aligned object—1807+698 (3C 371)

Upper panel: A 5 GHz image made from VLA B-configuration data (taken from Wrobel & Lind 1990);

Lower panel: Our 1.6 GHz VLBI image (Polatidis et al. 1995).

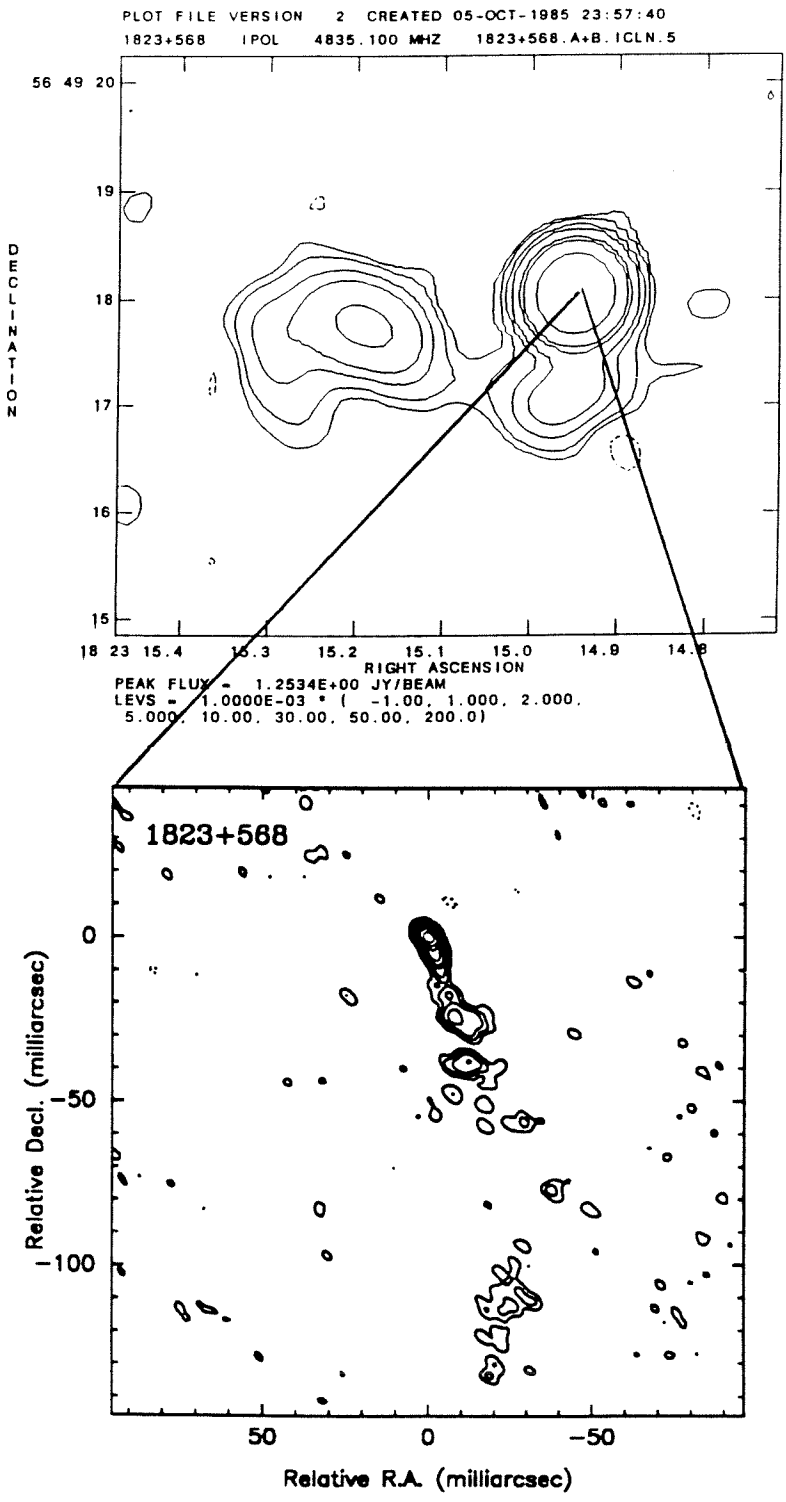

Fig. 6.5b An example of misaligned object—1823+568

Upper panel: A 5 GHz VLA image (taken from O'Dea and Barvainis 1986);

Lower panel: Our 1.6 GHz VLBI image (Polatidis et al. 1995).

Although the result looked convincing (see Fig. 6.6a), the distribution of ΔPA was *not* bimodal in a larger but less well defined sample (Rusk 1988). Impey *et al.* (1991) resolved this discrepancy by showing that the ΔPA distributions are different for sources with high and low optical polarization, and that the distribution for highly polarized sources ($p \geq 3\%$), which dominate the PR sample, is bimodal, while that for weakly polarized sources ($p < 3\%$), which dominate the larger Rusk sample, is not. Although the distributions appeared quite different, the peak near 90° rested only on eight objects in the PR study and it was clear that a larger sample was needed to confirm this result. The next development came from a semi-independent VLBI survey of a sample of 45 highly variable radio sources with $\delta \geq -18°$ and flux densities at 8.4 GHz above 4.5 Jy at some epoch (Wehrle et al. 1992). 21 sources in the sample with measurable ΔPA also showed a bimodal distribution, although the peak near 90° was somewhat less pronounced than that in PR. However, the combination of these two samples strengthened the case for bimodality.

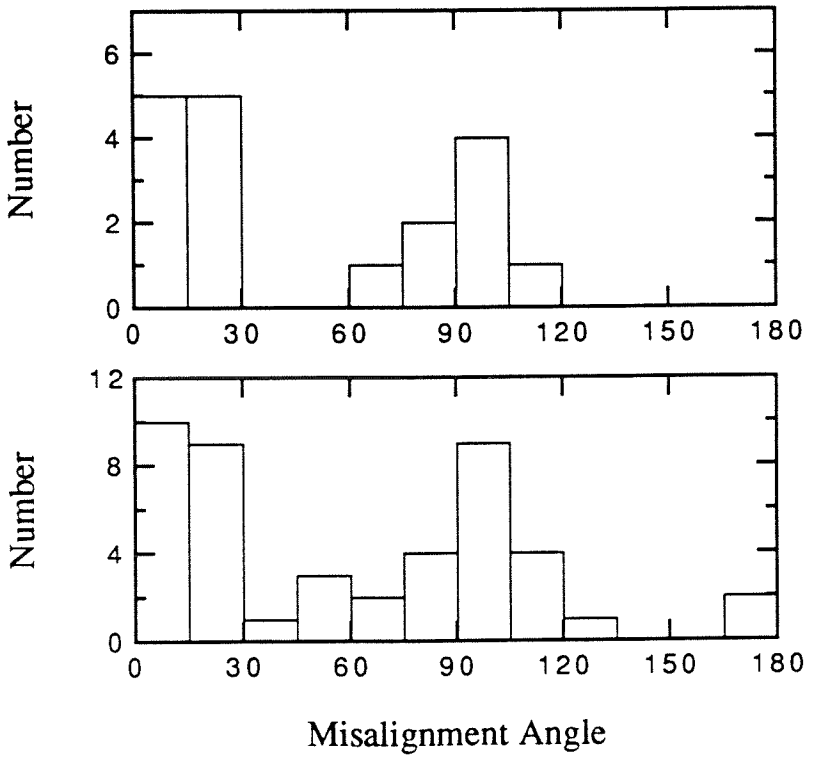

Fig. 6.6. — (a) upper panel: ΔPA distribution of Pearson & Readhead (1988); (b) lower panel: ΔPA distribution of Conway & Murphy (1993)

Conway & Murphy (1993) have proposed an interesting explanation for the bimodal ΔPA distribution. They suggest that helical jets with low pitch angles are responsible for the peak near 90°. In their model, as in most models of the central radio emission regions in active galaxies, the material is moving relativistically along the jets. Objects are therefore preferentially selected in which the angle between the jet axis and the line-of-sight is small, due to Doppler boosting of the radiation within an angle $\sim 1/\gamma$ of the direction of motion. In flux density limited samples, objects will be selected preferentially in which the edge of the helical cone is close to the line-of-sight, and the projection of this edge onto the sky is normal to the cone axis — so that if the large-scale jet is aligned with the axis of the cone, it will be orthogonal to the small-scale jet on the surface of the cone. In order for this model to work, the amplitude of the helical jet must saturate at some point after which the material moves out along the surface of a cylinder.

In this section we present new results on the ΔPA distribution, drawn from the combined PR and CJ1 surveys. This is the first homogeneous complete sample that is large enough to provide a reliable measure of the bimodality of the ΔPA distribution. It is shown that the effect is certainly real, and that the excess of objects in which the nuclear jet is orthogonal to the large-scale jet is due to objects with high optical polarization, high radio variability, and flat radio spectra, and in which the fraction of radio emission from the central component to the total radio emission is high.

6.3.1. DISTRIBUTION OF MISALIGNMENT ANGLES IN PR+CJ1 SAMPLES

6.3.1.1. Position Angle Measurements

We took the innermost position angle of the nuclear jet as the position angle on milliarcsecond scales. For the objects in the CJ1 sample, we used a four-step modelfitting procedure to fit models of Gaussian components to the self-calibrated 5 GHz VLBI data in order to determine this position angle. First, we constructed a model according to the structure

shown in the VLBI map and allowed all parameters to change. The resulting model often contains an elongated core. Second, we changed the ratio of minor to major axis to 1. This almost always significantly worsened the agreement factors between the model and data, which indicated that the elongation of the core was required by the data. Third, we kept the ratio of minor to major axis as 1 and allowed the other parameter to change. This forced the size of the core to decrease, but it reached agreement factors as good as those in the first step by adjusting other components. Fourth, we allowed every parameter to vary again. The resulting model once again had an elongated core, but its other parameters were similar to those in the third step. Since the agreement factors from the third and fourth steps were almost identical, we concluded that the elongation of the core was no longer significant because of its small size. Therefore, the position angle of the component closest to the core represents the innermost position angle which can be derived from the data. The models from the fourth step are presented in Chapter 3. The brightest and most compact Gaussian component is taken to be the core. The position angle of the Gaussian component closest to the core is taken as the position angle on milliarcsecond scales. The position angles on milliarcsecond scales of five objects were measured from published maps (see Table 6.4 for references). For the objects in the PR sample, we used the models in Pearson & Readhead (1988) and took the position angle of the component closest to the core as the position angle on milliarcsecond scales.

The position angle on arcsecond scales was determined between the core and brightest feature on either side of the core. In some cases (for example, 0716+714) for which there are hot-spots at both sides of the core, the hot-spot on the side that the milliarcsecond jet points to was used to measure the position angle. When maps were available at multiple frequencies, the best map, which clearly shows the extended structure, was used for the position angle measurement. Our method to determine the position angle on arcsec scales is slightly different from Pearson & Readhead's. They took the position angle relative to the core of either a portion of the large-scale jet or a compact hot spot, choosing the angle

which maximized ΔPA. The method used here leads to a different ΔPA for only five sources with the largest difference being 22°. Consequently, the ΔPA distribution is not changed significantly. The results are listed in Table 6.4.

6.3.1.2. ΔPA Distribution

There are 86 sources in the combined CJ1 and PR sample which have measurable position angles on both milliarcsecond and arcsecond scales. The ΔPA of these sources have a weak bimodal distribution, as shown in Fig. 6.7a. Contrary to the sharp peak near 90° shown by PR (Fig. 6.6a) and more recently by Conway & Murphy (1993) (Fig. 6.6b) using both the PR sample and the sample of 45 highly variable sources (Wehrle et al. 1992), our combined CJ1 and PR sample shows a broad peak near 90°.

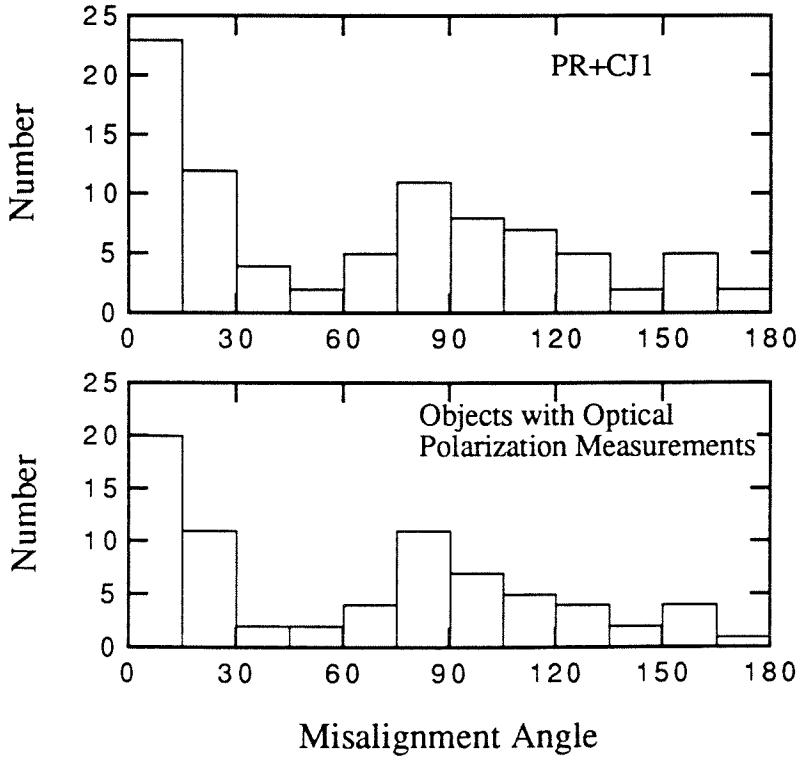

Fig. 6.7. ΔPA Distribtion of PR+CJ1 Sample — (a) upper panel: 86 objects with ΔPA measurements; (b) lower panel: 73 objects with optical polarization measurements.

Table 6.4. ΔPA, F_c, P, α and V

Source	ID	PA (mas)	Ref	PA (arcsec)	Ref	ΔPA	F_c	P (%)	Ref	α_{em}^{5GHz}	V
0010+405	G	330	1	327	2	3	0.38	10.1±0.6	1	−0.42	0.06
0022+390	Q	160	1	250	1	90	0.43	7.1±1.1	1	−0.10	0.19
0402+379	G	246	1	225	2	21	—	4.4±1.2	1	−0.60	0.15
0602+673	Q	160	1	54	3	106	0.59	—	—	−0.04	0.21
0615+820	Q	239	1	320	4	81	0.49	< 4.32	1	0.13	—
0620+389	Q	161	1	358	2	163	0.48	—	—	−0.18	0.02
0707+476	Q	344	1	87	5	103	0.44	—	—	0	0.33
0711+356	Q	338	2	295	5	41	0.24	1.0±1.0	2	0.08	0.22
0716+714	BL	28	1	301	6	87	0.55	28.6±0.3	3	−0.10	0.30
0723+679	Q	272	2	275	4	3	0.31	1.5±1.0	2	−0.44	0.20
0740+828	Q	10	1	30	2	20	0.35	—	—	−0.51	—
0755+379	G	128	1	111	1	17	0.10	1.1±0.5	1	−0.57	0.00
0804+499	Q	86	2	201	5	115	0.99	8.6±0.7	2	0	0.52
0805+410	Q	28	1	85	1	57	0.91	2.4±1.2	1	0.14	0.09
0812+367	Q	348	1	3	7	15	0.54	1.5±1.0	1	0	0.10
0814+425	BL	149	2	231	4	82	0.84	12.0±0.6	4	0	0.52
0820+560	Q	97	1	308	8	149	0.74	2.2±0.8	1	0	0.08
0821+394	Q	338	1	138	1	160	0.59	6.9±0.6	1	−0.05	0.07
0828+493	BL	68	1	65	5	3	0.17	9.4±1.1	1	−0.03	0.32
0833+585	Q	85	1	155	5	70	0.34	< 2.12	1	0	0.11

Table 6.4. ΔPA, F_c, P, α and V (*continued*)

Source	ID	PA (mas)	Ref	PA (arcsec)	Ref	ΔPA	F_c	P (%)	Ref	α_{em}^{5GHz}	V
0836+710	Q	214	2	204	4	10	0.40	1.0±0.5	2	−0.26	0.27
0850+581	Q	156	2	163	4	7	0.85	0.4±0.2	2	−0.05	0.17
0859+470	Q	5	3	335	9	30	0.68	0.7±0.8	2	−0.22	0.18
0900+428	Q	298	1	257	1	41	0.24	—	—	−0.46	0.10
0906+430	Q	155	2	242	10	87	0.45	21.0±2.6	4	−0.56	0.32
0917+449	Q	176	1	279	1	103	0.86	21.3±0.8	1	−0.08	0.11
0917+624	Q	339	1	232	5	107	0.82	2.2±0.7	4	−0.15	0.11
0923+392	Q	83	2	78	11	5	0.63	0.9±0.4	9	1.02	0.50
0945+408	Q	127	2	32	9	95	0.48	0.3±0.5	2	−0.30	0.41
0954+658	BL	306	2	202	1	104	0.47	33.7±0.7	4	−0.15	0.16
1003+351	G	292	4	304	12	12	0.06	0.2±0.3	2	−0.62	0.12
1003+830	Q	83	1	108	1	25	0.38	2.7±1.5	4	0	—
1015+359	Q	187	1	73	1	114	0.45	< 2.30	1	0.22	0.07
1020+400	Q	319	1	24	1	65	0.80	2.4±0.8	1	−0.25	0.20
1030+415	Q	355	1	93	1	98	0.19	8.4±2.5	1	0	0.10
1039+811	Q	295	1	214	4	81	0.30	< 2.17	1	−0.04	—
1053+704	Q	200	1	75	1	125	0.38	< 2.97	1	0.12	—
1053+815	G	217	1	110	1	107	0.48	9.8±3.6	1	0.10	—
1058+726	Q	355	1	337	1	18	0.15	1.5±0.5	1	−0.59	—
1100+772	Q	90	5	92	13	2	0.03	1.0±0.5	5	−0.84	—

Table 6.4. ΔPA, F_c, P, α and V (*continued*)

Source	ID	PA (mas)	Ref	PA (arcsec)	Ref	ΔPA	F_c	P (%)	Ref	α_{em}^{5GHz}	V
1128+385	Q	293	1	186	5	107	0.77	< 3.49	1	0.05	0.22
1137+660	Q	106	5	111	4	5	0.10	0.5±0.2	1	−0.84	0.00
1138+594	Q	162	1	355	2	167	0.12	—	—	−0.76	0.04
1144+402	Q	11	1	34	5	23	0.48	3.3±1.0	1	0.02	0.19
1150+497	Q	202	1	193	14	9	0.30	4.0±0.8	8	−0.10	0.13
1150+812	Q	182	1	260	5	78	0.37	1.5±1.3	1	−0.18	—
1216+487	Q	102	1	80	1	22	0.26	< 3.96	1	0	0.22
1317+520	Q	124	1	112	15	12	0.26	0.5±0.3	5	−0.61	0.07
1342+663	Q	108	1	137	1	29	0.84	18.7±1.4	1	0	0.10
1347+539	Q	145	1	320	1	175	0.43	< 1.17	1	0	0.21
1418+546	BL	129	1	264	5	135	0.67	19	6	0.23	0.33
1435+638	Q	225	1	231	8	6	0.35	< 0.89	1	0	0.08
1438+385	Q	9	1	355	1	14	0.34	—	—	−0.20	0.00
1458+718	Q	164	2	96	4	68	0.18	1.0±0.4	2	−0.77	0.09
1504+377	G	219	1	264	4	45	0.33	—	—	−0.10	0.08
1624+416	Q	239	2	351	4	112	0.35	—	—	−0.32	0.19
1633+382	Q	296	2	10	5	74	0.37	2.6±1.0	9	−0.04	0.51
1637+574	Q	10	2	282	5	92	0.96	2.4±0.8	2	0.10	0.37
1637+826	G	299	1	312	16	13	0.36	1.0±0.3	1	−0.44	—
1638+398	Q	285	1	144	1	141	1.00	9.9±2.0	4	0	—

Table 6.4. ΔPA, F_c, P, α and V (*continued*)

Source	ID	PA (mas)	Ref	PA (arcsec)	Ref	ΔPA	F_c	P (%)	Ref	α_{em}^{5GHz}	V
1641+399	Q	230	2	329	5	99	0.35	36.0±1.0	10	0	0.56
1642+690	Q	195	2	170	5	25	0.86	16.6±1.7	2	0	0.58
1652+398	BL	133	2	50	17	83	0.35	6.8±0.1	11	−0.18	0.13
1656+477	Q	2	1	347	5	15	0.73	< 1.18	1	−0.07	0.07
1656+482	Q	251	1	19	1	128	0.50	—	—	−0.14	0.27
1719+357	Q	184	1	176	1	6	0.24	—	—	0	0.27
1739+522	Q	25	1	258	4	127	0.91	3.7±0.2	2	0	0.47
1749+701	BL	296	2	18	1	82	0.67	11.5±0.3	12	−0.01	0.47
1751+441	Q	87	1	78	1	9	0.66	< 4.75	1	0.47	0.25
1758+388	Q	261	1	111	1	160	0.91	< 1.60	1	0.54	0.07
1800+440	Q	200	1	242	1	42	0.31	4.0±0.8	1	0.44	0.22
1803+784	BL	268	2	192	5	76	0.74	35.2±0.4	3	0.31	0.34
1807+698	BL	263	2	261	18	2	0.40	12.0±0.2	7	−0.05	0.23
1823+568	BL	197	2	95	5	102	0.74	16.8±0.7	2	0	0.29
1828+487	Q	328	2	312	4	16	0.34	0.4±0.4	5	−0.58	0.25
1842+681	Q	134	1	293	1	159	0.78	3.8±0.7	1	−0.01	0.24
1845+797	G	322	2	324	4	2	0.13	3.5	6	−0.88	0.19
1926+611	BL	119	1	198	1	79	0.51	14.5±0.7	1	0	0.20
1928+738	Q	166	2	166	4	0	0.64	1.2±0.1	2	−0.03	0.30
1954+513	Q	294	2	344	1	50	0.57	1.5±0.5	9	−0.23	0.30

Table 6.4. ΔPA, F_c, P, α and V (*continued*)

Source	ID	PA (mas)	Ref	PA (arcsec)	Ref	ΔPA	F_c	P (%)	Ref	α_{em}^{5GHz}	V
2007+777	BL	253	1	255	6	2	0.76	15.1±0.9	3	0.42	0.20
2010+723	BL	335	1	101	1	126	0.39	29.1±5.1	4	−0.23	—
2207+374	Q	210	1	47	1	163	0.18	< 2.92	1	−0.60	0.01
2229+695	G	72	1	71	1	1	0.57	—	—	0.30	—
2311+469	Q	124	1	107	19	17	0.07	1.5±0.9	1	−0.71	0.03
2351+456	Q	287	2	348	4	61	0.29	—	—	−0.50	0.32

Notes to Table 6.4.

Column (1) — Source name in the IAU convention.

Column (2) — Position angle on the milliarcsec scales.

Column (3) — Reference for Column (2). 1 – this work; 2 – Pearson & Readhead 1988; 3 – Pearson et al. 1994b, in preparation; 4 – Barthel et al. 1985; 5 – Hough 1986.

Column (4) — Position angle on arcsec scales.

Column (5) — Reference for Column (4). 1 – this work; 2 – Patnaik et al. 1992; 3 – Rudnick & Jones 1982; 4 – Rusk 1988; 5 – Murphy 1988; 6 – Antonucci et al. 1988; 7 – Perley (private communication); 8 – Perley (private communication); 9 – Foley 1982; 10 – Fejes & Porcas 1990; 11 – Kollgaard et al. 1990; 12 – Willis et al. 1974; 13 – Leahy & Perley 1991; 14 – Owen & Puschell 1984; 15 – Hintzen et al. 1983; 16 – Perley, Bridle & Willis 1984; 17 – van Breugel & Schilizzi 1986; 18 – Wrobel & Lind 1990; 19 – Polatidis 1993;

Column (6) — Difference of the position angles on milliarcsec and arcsec scales.

Column (7) — Optical polarization.

Column (8) — Reference for Column (7): 1 – this work; 2 – Impey et al. 1991 and references therein; 3 – Biermann et al. 1981; 4 – Kühr & Schmidt 1990; 5 – Stockman et al. 1984; 6 – Angel & Stockman 1980. 7 – Kinman 1976; 8 – Stockman 1978; 9 – Moore & Stockman 1984; 10 – Smith et al. 1986; 11 – Takalo 1991; 12 – Wells et al. 1980; 13 – Takalo et al. 1992.

6.3.2. CORRELATIONS OF ΔPA WITH OTHER OBSERVABLE PROPERTIES

Impey et al. (1991) found that sources with high optical polarization showed a bimodal ΔPA distribution while sources with low optical polarization showed only one peak near 0°. We therefore divided our 86 sources into two groups according to (1) optical polarization; (2) spectral indices; (3) radio variability indices; and (4) the fraction of the total flux density in the core, F_c. The results are striking as shown below.

6.3.2.1 ΔPA and Optical Polarization

Amongst the 86 sources with measured ΔPA, 73 have optical polarization measurements. The ΔPA distribution of 25 sources with high polarization ($P > 5\%$ at any epoch) is shown in Fig. 6.8a, and that of 48 sources with low polarization ($P \leq 5\%$) is shown in Fig. 6.8b. We note that there is only an upper limit on optical polarization for some objects. All of the upper limits are less than 5%, these objects are thus treated as low polarization objects and included in Fig. 6.8b.

Figs. 6.8 show that high polarization sources have a bimodal distribution with a prominent peak around 90°, 14 of 25 objects belong to the misaligned population (i.e., $70° < \Delta PA < 110°$), while low polarization sources peak near 0° and have a ΔPA distribution which is not bimodal. Our results thus confirm the findings of Impey et al. (1991).

The Kolmogorov-Smirnov test shows that the ΔPA distributions of objects with high and low optical polarizations differ at the 99.8% confidence level. Determination of ΔPA may be complicated by many factors, but such factors would almost certainly tend to smear out any intrinsically bimodal distribution. Therefore, it is clear that the peak around 90° for the high polarization sources is real.

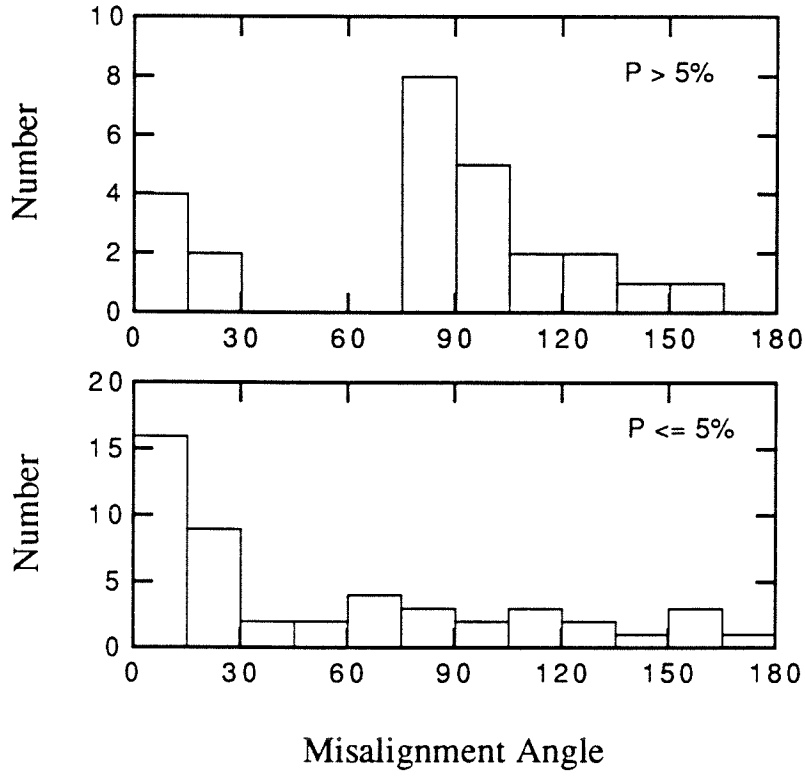

Fig. 6.8. — (a) upper panel: ΔPA distribution of objects with optical polarization > 5%; (b) lower panel: ΔPA distribution of objects with optical polarization ≤ 5%.

6.3.2.2. ΔPA and Spectral Indices

We used the spectral index α at 5 GHz in the rest frame for this study. The spectral indices were calculated using the spline-fit (Herbig & Readhead 1992). Such a calculation is accurate enough for most sources to reflect the nature of the spectra judging from the fit of the spline to spectral data. However, the spline-fits could not fit well sources with high radio variability. Thus we manually estimated the spectral indices of these sources.

In Figs. 6.9a and 6.9b we show the ΔPA distributions of sources with $\alpha > -0.5$ and $\alpha \leq -0.5$, repectively. It is clear that the ΔPA distribution of 70 sources with flatter high-frequency spectra is bimodal, whereas that of 16 sources with steeper high-frequency spectra is not. The Kolmogorov-Smirnov test shows that these two distributions differ at the 97% confidence level.

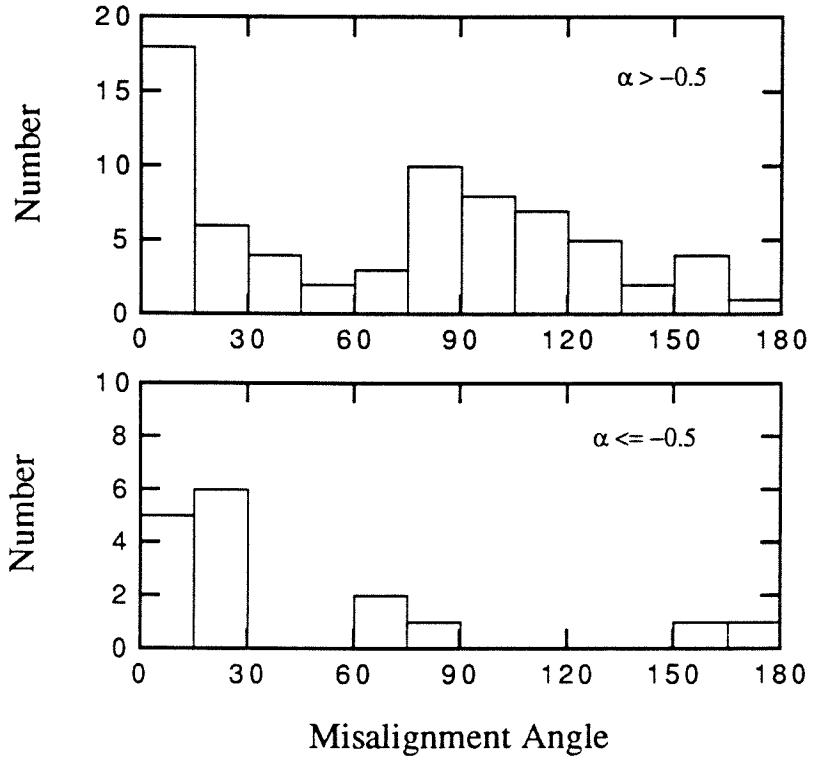

Fig. 6.9. — (a) upper panel: ΔPA distribution of objects with flat spectrum; (b) lower panel: ΔPA distribution of objects with steep spectrum.

6.3.2.3. ΔPA and F_c: the fraction of the total flux density in the core

In Figs. 6.10a and 6.10b we show the ΔPA distributions of sources with $F_c > 0.3$ and $F_c \leq 0.3$, respectively. The ΔPA distribution of 65 sources with fractional core flux densities higher than 0.3 is bimodal, while that of 20 sources with weaker fractional core flux densities peaks near 0°. The Kolmogorov-Smirnov test shows that these two distributions differ at the 97% confidence level.

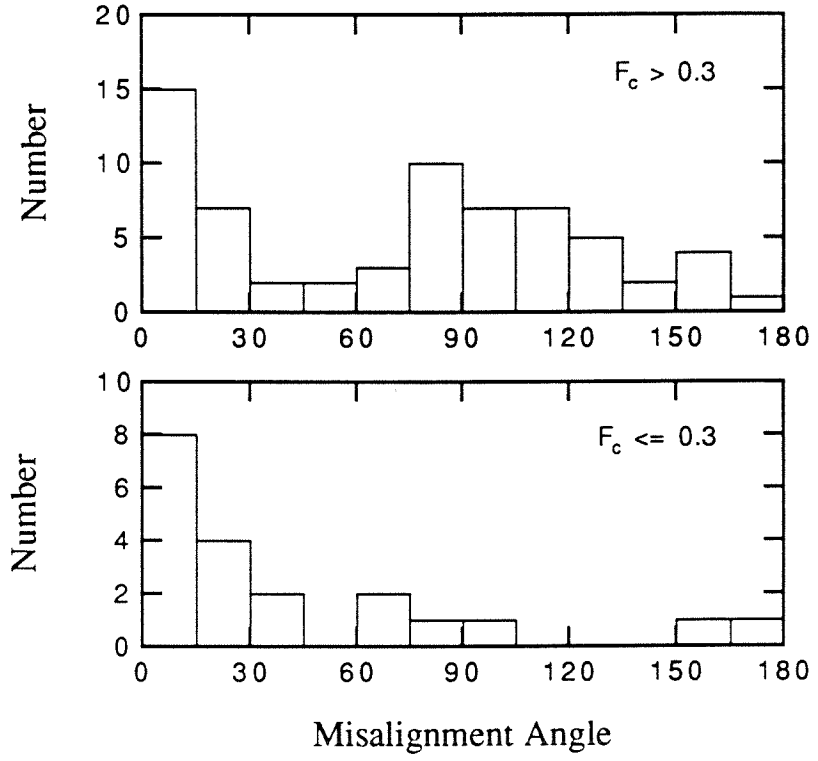

Fig. 6.10. — (a) upper panel: ΔPA distribution of objects with $F_c > 0.3$; (b) lower panel: ΔPA distribution of objects with $F_c \leq 0.3$.

6.3.2.4. ΔPA and Radio Variability

The 62 sources south of 82° in the PR sample have been monitored by Aller et al. (1992) at 15 GHz for a time range between 5 and 10 years. Some well-known sources have been monitored for $\sim$ 25 years. They defined a radio variability index

$$V = \frac{(S_{\max} - \sigma_{S_{\max}}) - (S_{\min} + \sigma_{S_{\min}})}{(S_{\max} - \sigma_{S_{\max}}) + (S_{\min} + \sigma_{S_{\min}})}$$

We found in the PR sample that sources with high radio variability indices show a hint of bimodality in their ΔPA distribution. For sources in the CJ1 sample, we used the monitoring data at 10 GHz obtained by Seielstad et al. (1984) and calculated the radio variability index following the definition by Aller et al. (1992).

The ΔPA distribution of 44 sources with $V > 0.15$ shows a bimodality (Fig. 6.11a) whereas that of 29 sources with $V \leq 0.15$ does not show such an effect (Fig. 6.11b). However, the Kolmogorov-Smirnov test shows that these two distributions differ only at the 29% confidence level.

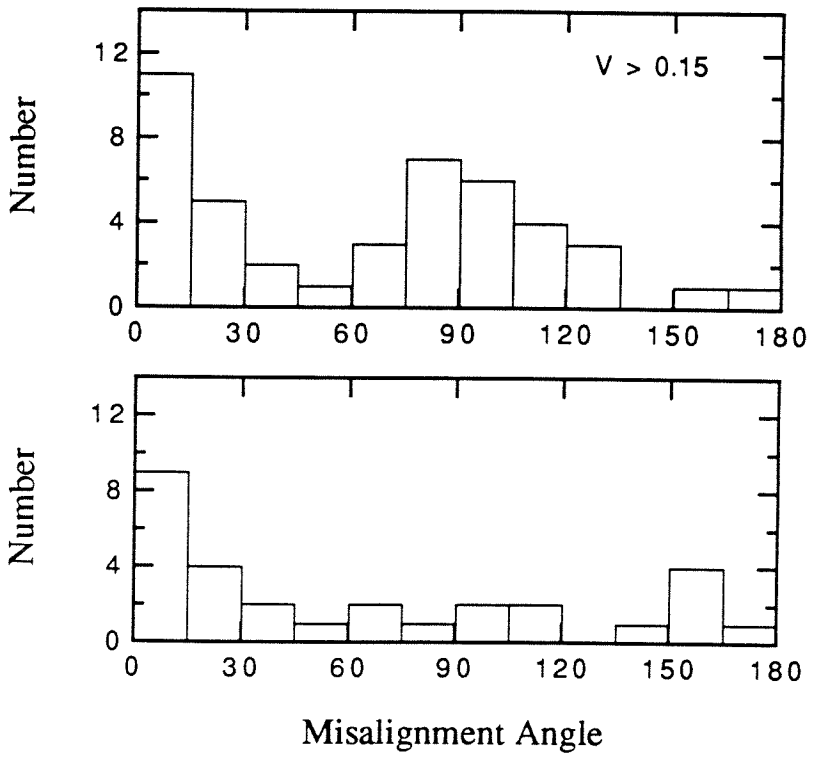

Fig. 6.11. — (a) upper panel: ΔPA distribution of objects with $V > 0.15$; (b) lower panel: ΔPA distribution of objects with $V \leq 0.15$.

6.3.2.5. Summary of Observation Status

The combined PR and CJ1 sample does not show strong bimodality in its ΔPA distribution. However, once we divided sources into subgroups according a certain threshold of P, F_c, α, or V, the subgroup with values larger than the threshold of each chosen property shows a striking bimodal ΔPA distribution while the subgroup with values lower than the threshold shows only one peak near 0°. Thus it is clear that the bimodality of ΔPA distribution is real. There is a peak near 90° in all four subgroups chosen according to P, F_c, α, or V. There is clearly a group of objects which have high optical polarization, high fractional core flux densities, flat radio spectra, high radio variability as well as ΔPA near 90°. In Table 6.5, we summarize the results of the Kolmogorov-Smirnov tests. In Fig. 6.12 we plot the optical polarization P vs. the fractional core flux densities F_c with symbols indicating three other properties: ΔPA, radio spectral indices and radio variability. We see here the group of objects with high optical polarization, high fractional core flux densities, flat radio spectra, and high radio variability, which contribute the peak near 90° in ΔPA.

Table 6.5.
Summary of the KS Tests

Samples	Result of KS Test
$P > 5\%$ vs. $P \leq 5\%$	99.8%
$\alpha > -0.5$ vs. $\alpha \leq -0.5$	97%
$F_c > 0.3$ vs. $F_c \leq 0.3$	97%
$V > 0.15$ vs. $V \leq 0.15$	29%

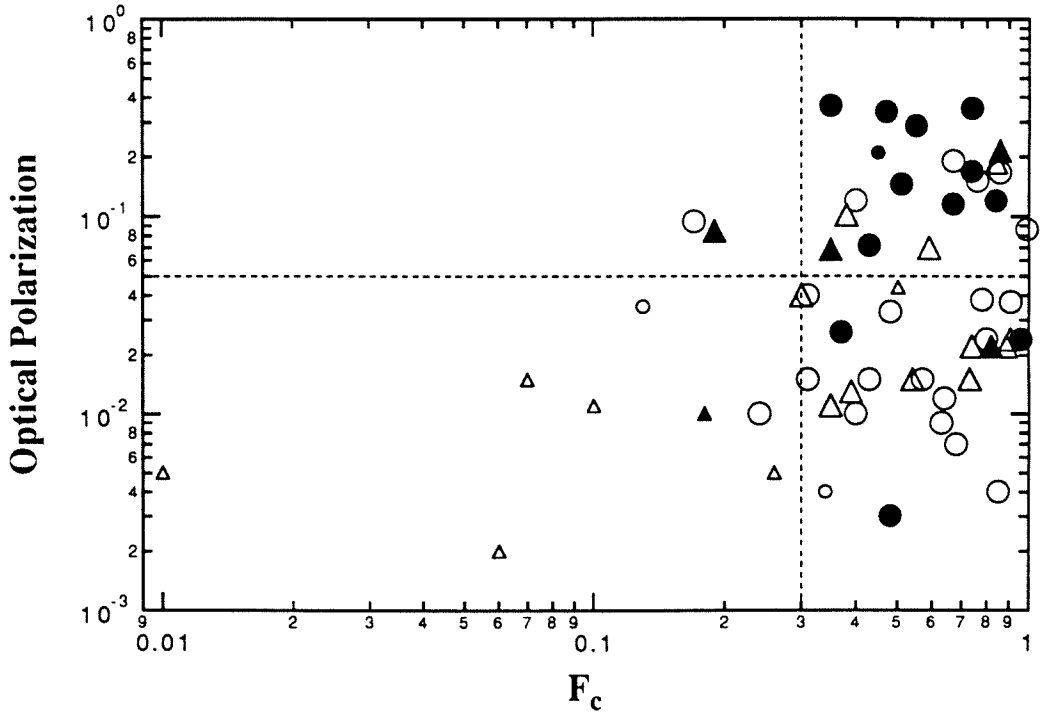

Fig. 6.12. Summary of observation status
Filled symbol — 70° < ΔPA < 110°;
Open symbol — ΔPA < 70° or ΔPA > 110°;
Large symbol — Flat radio spectrum ($\alpha > -0.5$);
Small symbol — Steep radio spectrum ($\alpha \leq -0.5$);
Circle — High radio variability ($V > 0.15$);
Triangle — Low radio variability ($V \leq 0.15$).

6.3.4. POSSIBLE MODELS

The observed bimodal distribution of ΔPA shows that these objects must be drawn from two populations. The aligned sources can easily be explained with a simple model in which the jet bends slightly between milliarcsecond and arcsecond scales (Readhead et al. 1983). However, the misaligned sources must be produced by a different population.

Pearson & Readhead (1988) considered two populations consisting of objects which were reasonably well aligned (with a intrinsic bend of 15°) and objects which were intrinsically orthogonal. They showed that it was possible to fit the observed distribution with this model, although it does not appear very physical. A more physical model has been proposed by Begelman, Blandford & Rees (1980) to account for large misalignments between structures probed by VLBI and the VLA. In their model jets precess around a cone resulting from a massive binary black hole. Any extended radio structure associated with jets, built up over many precession periods, will be aligned with the orbital angular momentum, i.e., the cone axis, while Doppler boosted jet appears orthogonal to the cone axis when observed close to the line of sight. Such a geometry can produce objects with $\sim 90°$ misalignment. Conway & Murphy (1993) used similar geometry and performed detailed numerical simulations. They showed that the peak near 90° could be produced as a result of relativistic beaming with a geometric configuration in which the parsec scale jets occur on conical helices with opening angles of 10°–20° and pitch angles of $\sim 1°$. The predicted distribution of misalignment angles is fairly sensitive to the geometry and Lorentz factor of the jet.

It seems that some sort of helical motion of jets around a cone may be necessary to produce large misalignments. The most interesting mechanism to produce a helical motion is precession induced by a binary black hole. This raises the question of whether objects with large misalignment have binary black holes in their nuclei. The answer to this question could have a profound impact on our understanding of active galaxies. According

to Begelman, Blandford and Rees (1980) the precession period of close binary black holes is

$$P_{\rm prec} = 3 \times 10^4 (M/m)^{3/8} M_8^{3/8} \qquad yr$$

where M is the mass of the primary black hole and m is the mass of the secondary black hole. Precession periods for a range of M and M/m are listed in Table 6.6.

Table 6.6. Precession Periods of Close Binary Black Holes

	M = 10^6 $M_\odot$	10^7 $M_\odot$	10^8 $M_\odot$	10^9 $M_\odot$
M/m = 1	5.3×10^3	12.7×10^3	30.0×10^3	71.1×10^3
5	9.8×10^3	23.1×10^3	54.8×10^3	130.0×10^3
10	12.7×10^3	30.0×10^3	71.1×10^3	168.6×10^3

Another possibility to induce helical motion might be helical Kelvin-Helmholtz instabilities produced by random jitter in the initial jet direction (Hardee et al. 1994).

6.4. ANGULAR SIZE – REDSHIFT TEST

In cosmological models based on the Friedmann-Robertson-Walker geometry, the angular size of a rigid rod varies with redshift in a way that depends on the deceleration parameter q_0. Many efforts have gone into searching for such a 'standard rod' at optical and radio wavelengths. At optical wavelengths, various *metricdiameters* have been considered as the 'standard rod'. Some examples are Petrosian's η index (defined as the radius at which the ratio of surface brightness averaged over the area interior to that radius to the surface brightness at that radius is an adopted fixed number), the effective radius which contains half the light, the Hubble a radius where the surface brightness falls to one fourth of its 'central value', and the King core radius where the surface brightness is one half of the 'central value'. Since it is defined as a ratio, the η index has many advantages, such as being nearly independent of luminosity evolution, of K correction, and of the wavelength of observations (e.g., Sandage 1988). However, it is affected if the light profile and radial gradients of galaxies change. Both of these two effects almost undoubtedly exist at some level (Djorgovski & Spinrad 1981). The chief observational problem is that the angular diameter where $\eta = 2$ is only ~ 2 arcsecond at $z = 1$, comparable with the seeing, which makes it difficult to define a true metric diameter (e.g., Sandage 1988). At radio wavelengths, FR II sources have been used as a standard rod to test the cosmological models (e.g., Miley 1971; Kapahi 1987, 1989; Nilsson et al. 1993). These objects have well defined structure, and thus their sizes can be measured unambiguously. Although FR II sources have a range of angular sizes at a certain redshift, it might be explained by the projection effects and the assumption that the mean size of FR II sources is independent of redshift (i.e., rigid rod). In this case variation of the mean size with redshift would yield the deceleration parameter q_0. However, studies show that the sizes of FR II sources decrease with redshift according to Euclidean geometry (i.e., size $\propto z^{-1}$) rather than varying in the way predicted by the Friedmann-Robertson-Walker cosmological models. If the models are

correct, a straightforward explanation of the observed distribution is that the sizes of FR II sources were systematically smaller at earlier epochs, or that the more luminous sources must be intrinsically smaller than the less luminous sources.

Recently Kellermann (1993a; see also 1993b and 1993c) has investigated the use of structure of compact radio sources on milliarcsecond scales as a standard rod to test the cosmological models. He suggested that these sources may be free from systematic evolutionary effects, and that their sizes should be independent of the intergalactic medium. It is by no means obvious that the parsec-scale jets of active galaxies provide a "rigid rod" suitable for the θ–z test. Nevertheless, this result would be of great importance if it were substantiated. Therefore, we explore here our observations in order to determine the situation for our well-defined PR+CJ1 sample. Simulations of the apparent angular size of the parsec-scale jets are being carried out by many workers including Marscher and Readhead. Independent of the possible though unlikely use of the θ–z diagram to test cosmology, we are interested in any possible variation of properties of our objects with redshift for the light that this may cast on cosmological evolutionary effects in these objects.

Kellermann collected data on 79 compact sources found in the literature, and plotted the mean angular size vs. redshift (see Fig. 6.13b). His results show that the mean angular size decreases with redshift up to $z = 0.5$, and remains constant for $0.5 < z < 3$. More recently, Gurvits et al. (1994) have added some sources with $z > 3$ which show an upturn in the angular size. These results seem to support the Einstein-de Sitter model. Kellermann's result has attracted considerable attention, and was printed on the cover of *Observational Cosmology* (ASP Conference Series 51).

It is clearly important to test this result with a larger and better defined sample of objects. Therefore, we have attempted to reproduce Kellermann's analysis using the CJ1 and PR sample. Since the compact symmetric and GPS objects are probably intrinsically different from the core-jet sources, we use only the core-jet sources. Following the method

used by Kellermann, we selected sources with luminosities $P_{5\mathrm{GHz}} > 10^{24}$ W Hz^{-1} and measured the angular size θ from the the peak of the core (usually the brightest peak) to the peak of the most distant component whose peak brightness exceeds 2% of the peak brightness in our 5 GHz VLBI maps made with natural weighting. In a few cases, we used maps convolved with a smaller beam ($\sim$ 0.7 mas). For two sources, 1342+663 and 1638+398, which are barely resolved, we used modelfitting and took the size from the peak to 2% contour. There are 87 core-jet sources having known redshifts and satisfying the luminosity criteria, among which 45 were used by Kellermann. The angular sizes have been averaged in redshift bins similar to those selected by Kellermann. The redshifts and angular sizes of objects in our sample and those used by Kellermann are given in Table 6.7, together with the averaged values of each redshift bin. The data of individual objects are plotted in Fig. 6.13a (KIK sample) and Fig. 6.13c (PR+CJ1 sample), and the averaged data are plotted in Fig. 6.13b (KIK) and Fig. 6.13d (PR+CJ1). For the PR+CJ1 sample, the mean angular sizes are approximately constant in the redshift range $0.04 < z < 3$ and show only a slight dependence of the mean angular size on redshift, contrary to the findings of Kellermann. Our data disagree most with Kellermann's in the lowest-redshift bin, where only a small number of powerful sources are available. However, it is only this bin that provides the evidence for a dependence of the mean angular size on redshift. Thus, it is important to check the data in the lowest-redshift bin in the PR+CJ1 and Kellermann's samples in order to understand the disagreement between our results and Kellermann's. There are three common objects in this bin, amongst which one object, 1652+398, has large discrepancy in measured angular sizes. We used a 5 GHz VLBI map and found 8.2 mas in angular size, while Kellermann used an EVN map and found 23.3 mas. Moreover, we found that the angular size 210 mas of 1228+12 (M87, 3C 274) used by Kellermann is surprisingly large. We found $\sim$ 65 mas from the best available VLBI map at 1.6 GHz (Reid et al. 1989) and $\sim$ 6 mas from a tapered 15 GHz VLBI map (Junor & Biretta 1994). It is clear that the jet of M87 has a steep spectrum. Thus we expect that its angular size

falls between 6 and 65 mas. The questionably large angular size of this object contributed significantly to the average value of the lowest redshift bin in Kellermann's study and was largely responsible for the agreement between the mean angular sizes and the cosmological model. Without this object, the average angular size would decrease from 44 mas to 20 mas. Therefore, Kellermann's test has been strongly biased by including this questionably large value.

The measured angular size is strongly affected by both the intrinsic structure of the source and the observing technique. VLBI observations have demonstrated that in many objects a jet extends much further from the core with steadily decreasing brightness. Which particular knot in the jet is selected to measure the angular size depends both on the resolution of the observations and the brightness of the core, which may be a function of the angle to the line of sight and varies, sometimes strongly, with time. Due to different resolution and hence different sensitivity to extended structure, different features were used to measure the angular size which resulted in the large discrepancy. The case of 1652+398 clearly demonstrates the problem with resolution and sensitivity. Moreover, the objects used in this study are primarily core dominated and thus are very likely beamed toward the observer. Small changes in angle to the line of sight will cause large changes in apparent angular size so there should be a wide scatter of angular sizes, as is observed.

Our result contradicts the assumption that the nuclear structures of compact radio sources may be used as "rigid rods." It is possible that more careful selection of the objects, for example, by selecting a narrower luminosity range, will produce a more homogeneous sample of objects. It is also important to investigate the effects of finite resolution and dynamic range on the measurement of the angular size. It will be interesting to explore the angular size–redshift relation with images with the same linear size resolution and at the same emission frequency in objects' rest frame.

We note that there is an absence of objects with angular sizes smaller than $\sim$ 5 mas

at $z < 0.1$, as shown in Fig. 6.13c. The Kolmogorov-Smirnov test shows that the angular size distributions of objects with $z < 0.1$ (Fig. 6.14a) and those with $z > 0.1$ (Fig. 6.14b) are different at 99.4% significance level. This result is intriguing. It may indicate that the objects have smaller angular sizes at early epoch. However, the objects in the sample are affected strongly by the relativistic beaming effect. With the second epoch observations of the CJ1 sample and the second and third epochs observations of the PR sample, we may be able to untangle the relativistic beaming effect and select a subsample based on the intrinsic luminosity and use it to study the possible evolution of angular size with redshift.

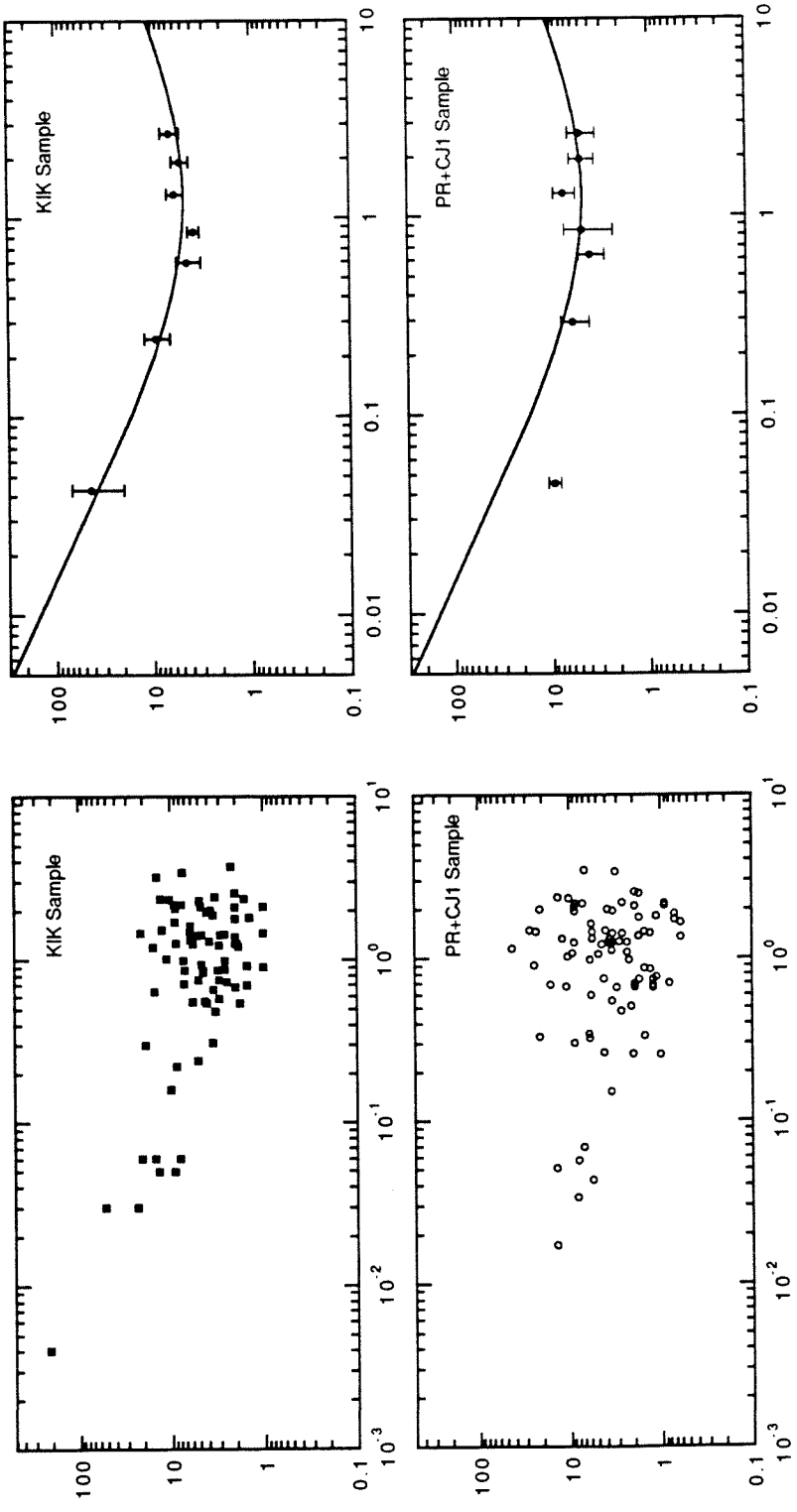

Fig. 6.13. Angular Size—Redshift relation
(a) upper-left: Data of the KIK sample; (b) upper-right: Averaged data of the KIK sample;
(c) lower left: Data of the PR+CJ1 sample; (d) lower-right: Averaged data of the PR+CJ1 sample.
The solid curve in (b) and (d) represents the expected angular size of a standard source with a linear size of 41 parsec on the Friedmann cosmological model with $q_0 = 0.5$.

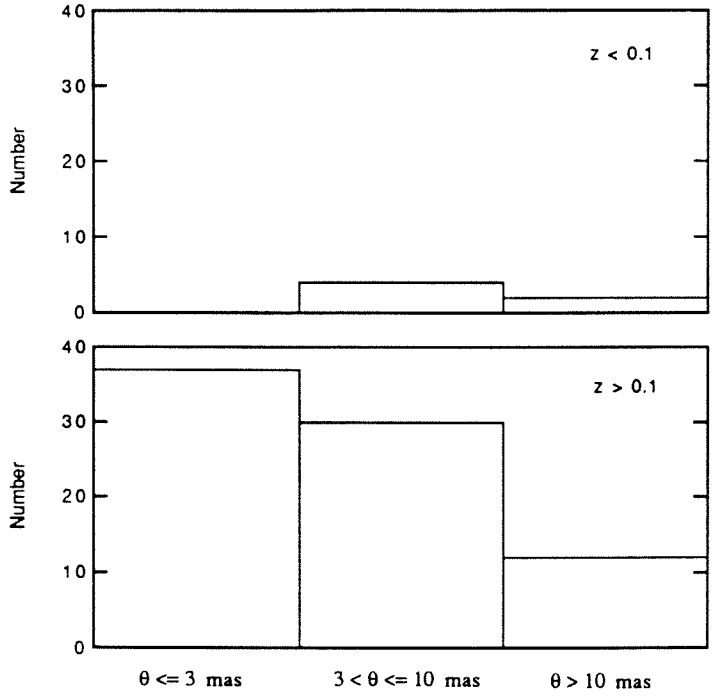

Fig. 6.14. — (a) upper panel: Angular size distribution of objects with $z < 0.1$; (b) lower panel: Angular size distribution of objects with $z > 0.1$.

Table 6.7. Angular Sizes of the PR+CJ1 and Kellermann's Samples

PR+CJ1 Sample					Kellermann's Sample				
Object	z	θ	$\overline{z}$	$\overline{\theta} \pm \delta_\theta$	Object	z	θ	$\overline{z}$	$\overline{\theta} \pm \delta_\theta$
* 1652+398	0.0337	8.2	0.045	9.5±1.4	1652+398	0.03	23.3	0.043	44.0±24.2
* 1807+698	0.051	14.0			1807+698	0.05	13.7		
* 1845+797	0.0569	8.0			1845+797	0.06	8		
0316+413	0.0172	14.0			0415+379	0.05	9.2		
0755+379	0.043	5.6			0430+05	0.03	52		
2200+420	0.069	7.0			1144+35	0.06	20.7		
					1228+12	0.004	210		
					1957+40	0.06	14.8		
* 1928+738	0.302	8.8	0.28	6.0±2.0	1928+738	0.3	19	0.25	9.3±2.7
0010+405	0.255	1.0			0410+110	0.31	3.5		
0814+425	0.258	2.0			0831+557	0.24	5.14		
0900+428	0.328	21.4			1226+023	0.16	10		
1003+830	0.322	6.0			2021+614	0.22	8.6		
1150+497	0.334	1.5							
1418+546	0.152	3.5							
1719+357	0.263	4.2							
2007+777	0.342	6.1							
* 0923+392	0.699	1.9	0.63	4.0±1.2	0923+392	0.7	1.5	0.59	4.4±1.3
* 1641+399	0.595	5.8			1641+399	0.55	5.8		
* 1800+440	0.663	3.0			1800+440	0.66	3.5		
* 1803+784	0.684	1.2			1803+784	0.68	2		
* 1842+681	0.475	2.7			1842+681	0.48	3.3		
0828+493	0.548	3.4			1011+232	0.56	4.3		
0906+430	0.668	1.9			1253-055	0.54	4.1		
1053+815	0.706	0.8			1334-127	0.54	1.8		
1504+377	0.674	10.9			1901+319	0.64	15.1		
1823+568	0.664	1.2			2345-167	0.58	3		
1823+568	0.664	1.2							
1828+487	0.692	16.1							
2214+350	0.51	2.1							

Table 6.7. Angular Sizes of the PR+CJ1 and Kellermann's Samples (*continued*)

PR+CJ1 Sample					Kellermann's Sample				
Object	z	θ	$\overline{z}$	$\overline{\theta} \pm \delta_\theta$	Object	z	θ	$\overline{z}$	$\overline{\theta} \pm \delta_\theta$
* 0133+476	0.859	1.3	0.84	4.8±2.5	0133+476	0.86	3.1	0.84	3.8±0.5
* 1637+574	0.745	1.2			1637+574	0.75	3		
* 1642+690	0.751	4.2			1642+690	0.75	5		
* 1732+389	0.976	2.2			1732+389	0.98	2.6		
* 1751+441	0.871	1.5			1751+441	0.87	2.6		
1347+539	0.978	5.9			0235+164	0.94	4.6		
1458+718	0.905	24.3			0336+019	0.85	4.4		
1749+701	0.77	1.1			0420-014	0.92	1.5		
2311+469	0.742	1.7			0615+820	0.71	7.2		
					1022+194	0.83	4.5		
					1156+295	0.73	2.5		
					1730-130	0.9	1		
					2251+158	0.86	7		
* 0707+476	1.31	3.6	1.29	7.5±1.9	0707+476	1.29	3.8	1.31	5.9±1.1
* 0804+499	1.43	1.3			0804+499	1.43	2.6		
* 0805+410	1.42	2.6			0805+410	1.42	2.9		
* 0812+367	1.025	10.5			0812+367	1.02	11		
* 0820+560	1.417	3.3			0820+560	1.42	4.62		
* 0850+581	1.322	5.6			0850+581	1.32	6.1		
* 0859+470	1.462	1.5			0859+470	1.46	1		
* 0917+624	1.446	5.6			0917+624	1.44	6.1		
* 0945+408	1.252	8.8			0945+408	1.25	5.7		
* 1039+811	1.259	2.3			1039+811	1.26	2		
* 1058+726	1.46	23.3			1058+726	1.46	21		
* 1150+812	1.25	3.7			1150+812	1.25	1.9		
* 1739+522	1.375	1.7			1739+522	1.38	2		
* 1954+513	1.22	3.4			1954+513	1.22	3		
* 2253+417	1.476	4.0			2253+417	1.48	6.2		
0248+430	1.316	12.0			0234+285	1.21	1.85		
0821+394	1.216	4.4			0333+32	1.26	8.6		
1015+359	1.266	2.8			1127-145	1.19	15.4		
1020+400	1.254	3.3			2145+067	0.99	7.3		
1030+415	1.12	3.4			2223-052	1.4	5.1		
1144+402	1.088	2.3							
1216+487	1.073	9.3							

Table 6.7. Angular Sizes of the PR+CJ1 and Kellermann's Samples (*continued*)

PR+CJ1 Sample					Kellermann's Sample				
Object	z	θ	$\overline{z}$	$\overline{\theta} \pm \delta_\theta$	Object	z	θ	$\overline{z}$	$\overline{\theta} \pm \delta_\theta$
1317+520	1.06	4.8							
1342+663	1.351	0.6							
2207+374	1.493	27.1							
2255+416	1.149	42.8							
* 0016+731	1.781	1.7	1.93	5.0±1.4	0016+731	1.78	2	1.91	5.2±1.0
* 0746+483	1.951	3.3			0746+483	1.95	4.08		
* 0833+585	2.101	0.9			0833+585	2.1	2		
* 0836+710	2.17	8.5			0836+710	2.17	9.2		
* 1435+638	2.06	8.8			1435+638	2.06	8.8		
* 1633+382	1.814	1.1			1633+382	1.81	1.4		
* 1656+477	1.622	5.7			1656+477	1.62	6.1		
* 2351+456	1.992	3.8			2351+456	2	3.7		
0022+390	1.946	8.7			0040+258	2.11	4.7		
0740+828	1.991	21.1			0106+013	2.11	1		
0955+476	1.88	0.7			1354+195	1.52	12.4		
1128+385	1.733	0.7			1743+173	1.7	8.9		
1547+507	2.169	7.1			2121+053	1.88	3.5		
1638+398	1.666	0.6							
1758+388	2.092	1.9							
* 0153+744	2.338	10.1	2.63	5.1±1.6	0153+744	2.34	10.2	2.69	6.6±1.4
* 0212+735	2.367	13.3			0212+735	2.37	12.8		
* 0642+449	3.402	3.1			0642+449	3.41	7.4		
* 0917+449	2.18	0.9			0917+449	2.18	7.7		
* 1624+416	2.55	1.9			1624+416	2.55	2		
0620+389	3.47	6.8			0458-02	2.29	4.9		
1053+704	2.492	1.7			0552+398	2.37	1.6		
1144+542	2.201	2.6			0636+68	3.7	2.2		
					1402+044	3.21	14		
					2136+141	2.43	3.3		

Explanation of Columns —

(1) Objects in the CJ1+PR sample; * indicates objects in common with the Kellermann's sample.

(2) Redshift; (3) Angular size; (4) Average redshift; (5) Average angular size;

(6) Objects in the Kellermann's sample; (7) Redshift; (8) Angular size; (9) Average redshift; (10) Average angular size.

Chapter 7

COMPACT SYMMETRIC OBJECTS

7.1. INTRODUCTION

The distinguishing feature of Compact Symmetric Sources (CSO's) is that the nuclear structure is symmetric about the center of activity on scales less than a few hundred parsecs, in contrast to the asymmetric structure found in the majority of radio loud objects. There has been confusion over the nature of these compact symmetric objects and their role in the unification schemes ever since they were discovered by Phillips & Mutel (1980, 1982). A number of interesting questions remain un-answered. Why are they so different from the asymmetric objects? What is the typical lifetime for an active galaxy in this phase? Is this active phase recurrent? Why are they so much smaller in overall extent than the asymmetric objects—are they more strongly confined by the interstellar medium, or do they have shorter lifetimes, or are they simply young? It is clear that CSO's comprise a very interesting class of radio-loud objects. The original discovery of the asymmetric, one-sided nuclear jets in radio loud sources played an important role in the acceptance of the standard relativistic beaming model and stimulated the development of "unified theories" of active galaxies. The discovery of a class of objects with symmetric nuclear structure may prove equally important to our understanding of the activity as well as environments in active galaxies.

In this thesis, we use the following criteria as the working definition of Compact Symmetric Sources:

(1) The radio structure is dominated by compact emission regions (< 5 kpc);

(2) They have radio lobes which straddle the central engine, i.e., they are symmetric about the central engine on scales < 5 kpc;

(3) They have low radio polarization, typically $< 2\%$;

(4) They exhibit weak variability.

Thus, properties (1) and (2) show that the CSO's include FR II S, D2S and CS sources.

As a guide to the reader, we summarize the properties of our CSO's and CSO candidates in Table 7.1. There are 9 CSO's or CSO candidates out of 65 objects in the PR sample. Of these, 7 are identified with galaxies and 2 are identified with quasars. There are 15 CSO's and CSO candidates out of 135 objects in the CJ1 sample. Seven of them are identified with galaxies and 6 are identified with quasars. The other two objects, 1333+589 and 1734+508, are classified as quasars based on our own images (*see Chapter 4*). Thus the CSO class comprises $\sim 10\%$ of complete samples selected at 5 GHz.

Among the 24 CSO's and CSO candidates, 9 objects have GHz-Peaked spectra, 13 objects have have steep spectra, and 2 objects have flat spectra at high frequencies. The total spectra are presented in Section 7.2 and Fig. 3.7.

Our observations have led to the first detailed study of one archetypal CSO, 2352+495, which began to reveal the underlying physics of CSO's and their relationship to other radio loud objects (Readhead et al. 1995; see below also). This chapter presents detailed information on the CSO's and CSO candidates, gathered in our observations and an extensive literature search. The observational details are summarized in Table 7.2. We have measured flux densities for individual components from the maps wherever possible. In a few cases, we used modelfitting to estimate flux densities. Details are presented in Section 7.1. The results are summarized in Table 7.3.

Table 7.1. The CSO's and CSO Candidates in the PR+CJ1 Sample

Source	ID	z	Spec.	Core	Jets	F_j	R_j	Lobes	Hot Spot	Pol. (%)	Var. Index	LLS (kpc)
0108+388...PR	G	0.669	G	Yes	1	0.65	30:1	2	2	0.2±0.1	NV	72.85
0258+350...CJ1	G	0.027	S	?	1	—	—	2?	?		NV	1.05
0402+379...CJ1	G	0.055	S	?	–	—	—	2?	?		0.01	12.82
0404+768...PR	G	0.599	S	Yes	1	0.86	30:1	2	?	< 1	NV	0.55
0538+498...PR	Q	0.545	S	Yes	1	0.55	10:1	2	?	1.1±0.3	0.05	2.50
0646+600...CJ1	Q	0.455	G	No	0	—	—	2	?	< 1	0.08	0.03
0710+439...PR	G	0.528	G	Yes	2	< 0.05	—	2	2	< 1	NV	0.09
1003+351...PR	G	0.0989	F	Yes	1	—	—	2	?	0.0±0.1	NV	2995.99
1031+567...PR	G	0.45	S	No	0	< 0.05	—	2	?	< 1	NV	0.13
1225+368...CJ1	Q	1.974	G	Yes	1	0.20	40:1	2	1	0.0±0.3	0.07	0.06
1242+410...CJ1	Q	0.813	G	Yes	2	0.29	1:1	2	1	< 1	0.04	0.22
1250+568...CJ1	Q	0.320	S	Yes	0	< 0.01	—	2	1		NV	4.86
1333+459...CJ1	Q	2.449	G	No	0	—	—	2?	?	< 1	0.09	0.02
1333+589...CJ1	Q?	—	G	No	0	—	—	2	?	< 1	NV	—
1358+624...PR	G	0.431	S	?	1	—	—	2	?	< 1	0.12	0.22
1437+624...CJ1	Q	1.090	S	No	0	—	—	2?	?	< 1	NV	129
1637+626...CJ1	G	0.850	S	?	1	—	—	2?	?	0.0±0.1	0.01	0.97
1734+508...CJ1	Q?	—	F	No	–	—	—	2?	?	< 1	0.02	—
1819+396...CJ1	G	—	S	?	1	—	0.9	2	?		NV	—
1843+356...CJ1	G	—	G	No	–	—	—	2	?	< 1	NV	—
1943+546...CJ1	G	0.263	S	Yes	0	< 0.05	—	2	2	< 1	NV	0.11
2323+435...CJ1	G	0.145	S	No	0	< 0.05	—	2	?	0.2±0.1	NV	2.83
2342+821...PR	Q	0.735	S	No	0	—	—	2	?	< 1	—	1.21
2352+495...PR	G	0.237	G	Yes	2	< 0.05	—	2	2	< 1	0.13	0.16

Notes to Table 7.1.

Column 1: Source name in the IAU convention.

Column 2: Optical Identification - G: galaxy; Q: quasar; ?: tentative classification.

Column 3: Redshift;

Column 4: Spectrum — S: Steep; F: Flat; G: GHz-peaked spectrum.

Column 5: Core — Yes: Core identified; No: Core not yet identified; ?: Core identified tentatively.

Column 6: Jets — 0: no jet detected; 1: jet on one side; 2: jets on both sides.

Column 7: Fractional flux in the jets;

Column 8: Jet to counterjet radio;

Column 9: Lobes — 2: 2 lobes detected; 2?: 2 lobes tentatively identified.

Column 10: Hotspots — 0: no hotspots; 1: one hotspot; 2: two hotspots detected.

Column 11: Radio Polarizarion at L band ($\sim$ 1.4 GHz);

Column 12: Radio Variability Index (see Section 6.3.3.5);

Column 13: Largest Linear Size (in kpc).

Table 7.2. Journal of VLBI Observations

Source	Frequency (MHz)	Epoch	Int. Time (hour)	Telescopes
0108+388	1667	Sep 1990	1.5	BWJLRGKKpPtLaNlYO
	4992	Nov 1986	4	SJ2BWKGFYO
	8418	Mar 1993	3	BLScHnNlKpPtOvBrY
0404+768	1667	Sep 1990	1.5	BWJ1LRGKKpPtLaNlYO
	4992	Sep 1991	1.5	SBWJ2LNoCKnTDeDaKGNlFdLaPtKpBrYO
	4992	Sep 1991	3	MERLIN
0646+600	1667	Sep 1991	1.5	BWJ1GKKpPtLaNlFdBrYO
	4992	Jun 1991	1.5	SBWJ2LNoKGNlFdLaPtKpYO
	8418	Mar 1993	3.3	BLScHnNlKpPtOvBrY
0710+439	610	Apr 1992	9.5	BWJ1KpLaFdBrNl
	1667	Jun 1992	13	BWJ1LRBlKGKpPtLaFdNlOvBr
	8418	Mar 1993	2.7	BLScHnNlKpPtOvBrY
1225+368	4992	Mar 1992	1.5	SBWJ2LNoCKGNlFdLaPtKpOvBrY
1242+410	1667	Nov 1991	1.5	BWJ1LRGKpPtLaNlYO
	4992	Mar 1992	1.5	SBWJ2LNoCKGNlFdLaPtKpOvBrY
	8418	Mar 1993	3	BLScHnNlKpPtOvBrY
1333+459	1667	Nov 1991	1.5	BWJ1LRGKpPtLaNlYO
	4992	Jun 1992	1	SWLNoKGNlFdLaPtKpOvBrY
1333+589	1667	Sep 1991	1.5	BWJ1GKKpPtLaNlFdBrYO
	4992	Jun 1992	1	WSWLNoKGNlFdLaPtKpOvBrY

Table 7.2. Journal of VLBI Observations (*continued*)

Source	Frequency (MHz)	Epoch	Int. Time (hour)	Telescopes
1437+624	1667	Sep 1991	1.5	BWJ1GKKpPtLaNlFdBrYO
	4992	Jun 1991	1.5	SBWJ2LNoKGNlFdLaPtKpYO
1734+508	1667	Sep 1991	1.5	BWJ1GKKpPtLaNlFdBrYO
	4992	Sep 1991	1.5	SBWJ2LNoCKnTDeDaKGNlFdLaPtKpBrYO
	8418	Mar 1993	1	BLScHnNlKpPtOvBrY
1843+356	1667	Nov 1991	1.5	BWJ1LRGKpPtLaNlYO
	4992	Sep 1991	1.5	SBWJ2LNoCKnTDeDaKGNlFdLaPtKpBrYO
	8418	Mar 1993	1.3	BLScHnNlKpPtOvBrY
1943+546	1667	Jun 1991	1.5	SBWJ1LREvPuBlGKKpPtLaNlYO
	4992	Sep 1991	1.5	SBWJ2LNoCKnTDeDaKGNlFdLaPtKpBrYO
	8418	Mar 1993	7	BLScHnNlKpPtOvBrY
2352+495	610	Apr 1992	8	BWJ1KpLaFdBrNl
	1667	Sep 1992	9	SBWJ1LGKpPtLaNlBrOv
	4992	Nov 1986	4	SJ2BWKGFYO
	8418	Mar 1993	4	BLScHnNlKpPtOvBrY

Explanation of Columns:
Col. 1: Source name in the IAU convention; Col. 2 & 3: Observing frequency and session; Col. 4: Total integration time; Col. 5: Antennas that participated in the observations — J1 (76 m antenna): Nuffield Radio Astronomy Laboratories, Jodrell Bank, UK; R (22 m), Ev (70 m), Pu (22 m), Bl (64 m): IKI Moscow, USSR; see Table 3.1 for other antennas.

Table 7.3. Spectral Indices of Individual Emission Regions

Source	Comp.	$S_{1.6GHz}$	S_{5GHz}	$S_{8.4GHz}$	$\alpha_{1.6}^{5}$	$\alpha_{5}^{8.4}$
0108+388	A	0.311	0.865	0.467	0.93	−1.18
	B	–	0.021	0.063	—	+2.1
	C	0.293	0.465	0.274	0.42	−1.01
0404+768	A	0.557	0.295	—	−0.58	—
	B	0.086	0.153	—	+0.52	—
	C	3.857	2.603	—	−0.36	—
0646+600[a]	A	0.325	0.494	0.583	+0.38	+0.32
	B	0.325	0.522	0.334	+0.43	−0.86
0710+439[b]	A	1.652	0.846	0.507	−0.61	−0.98
	B	0.591	0.552	0.558	−0.06	+0.02
	B1	—	0.426	0.270	—	−0.87
	B2	—	0.129	0.249	—	+1.26
	C	0.311	0.275	0.127	−0.11	−1.48
1225+368[c]	A	0.720	0.428	—	−0.47	—
	B	0.173	0.081	—	−0.69	—
	C	0.086	0.040	—	−0.70	—
	D	0.043	0.040	—	−0.07	—
	E	0.058	0.020	—	−0.97	—
1242+410	A	0.513	0.281	0.188	−0.55	−0.77
	B	0.253	0.183	0.114	−0.30	−0.91
	C	0.446	0.281	0.146	−0.42	−1.25
1333+459	A	0.164	0.353	—	+0.70	—
	B	0.166	0.298	—	+0.53	—
1333+589	A	0.129	0.334	—	+0.87	—
	B	0.307	0.310	—	+0.02	—
1437+624	A	1.641	0.596	—	−0.92	—
	B	0.785	0.367	—	−0.69	—
1734+508[d]	A	0.215	0.204	0.153	−0.05	−0.55
	B	0.413	0.610	0.727	+0.36	+0.34
1843+356	A	0.808	0.561	0.288	−0.33	−1.28
	B	0.054	0.280	0.247	+1.50	−0.24
	B1	—	0.116	0.120	—	+0.06
	B2	—	0.173	0.107	—	−0.92
1943+546	A	0.580	0.294	0.162	−0.62	−1.14
	B	0.051	0.023	0.012	−0.73	−1.25
	C	1.408	0.669	0.429	−0.68	−0.85

Notes to Table 7.3.

[a] $S_{1.6GHz}$ is taken as half of the total flux density.

[b] S_{5GHz} is taken from Conway et al. (1992).

[c] Flux densities shown are the peak flux density of each region. See text for details.

[d] $S_{1.6GHz}$ is estimated with modelfitting.

7.2. DETAILED DISCUSSION OF CSO'S IN PR+CJ1 SAMPLE

0108+388

In the course of this thesis work we made 4 maps of 0108+388 – at 1.6, 5, 8.4 and 10.7 GHz. The first three images are shown in Fig. 7.1.

The object 0108+388 has been monitored at 5 GHz as part of the continuing Pearson-Readhead(PR) survey. The first-epoch observations at 5 GHz with the US VLBI network revealed that this object consisted of two components of almost equal flux densities separated by $\sim$ 5 mas and thus the object was classified as a compact double (Pearson & Readhead 1988). Subsequent observations showed that each component has sub-structure (Conway et al. 1994). We compared the second- and third-epoch observations in detail and found that the separation velocity of the two main components is less than $0.18h^{-1}c$. The 10.7 GHz observations made with four stations, i.e., Bonn, HSTK, NRAO, and OVRO showed a component between the two main components (Conway et al. 1994). We also found that all physical parameters derived from the 5 GHz and 10 GHz observations are consistent with the terminating jet model, i.e., the main components observed are hot spots and lobes formed by interaction between jets and interstellar medium. We noted that, except for its smaller size, this object is morphologically similar to the two archetypal compact symmetric objects in the PR sample—0710+439 and 2352+495 (Conway et al. 1992).

Our 1.67 GHz observations (Fig. 7.1(a)) show the two main components and reveal no other components at a dynamic range (peak:rms) of $\sim$ 500:1. I have re-mapped the third-epoch observations at 5 GHz with the DIFMAP package. The new and better map (Fig. 7.1(b)) reveals that there is a faint bridge connecting the two main components. The earlier map published by Conway et al. was made with clean windows just in the two main components, which may account for the lack of the bridge emission in that map. The 8.4 GHz observations (Fig. 7.1(c)) resolved both main components substantially. The

eastern and western lobes consist of several subcomponents lying along the main axis of the object, with the brightest component at the extreme end. The middle component in the 8.4 GHz map is coincident with the middle component detected in our 10.7 GHz observations, and we identify this with the core. The total flux densities in the 1.6, 5 and 8.4 GHz maps are about equal to the single-dish flux densities. However, the flux density in the 10.7 GHz map is only 496 mJy out of a total of 860 mJy. The missing flux is due to the lack of short baselines. We attempted to measure the flux densities of distinguishable components using the 1.67, 5 and 8.4 GHz maps. We designate the east component (without the core region) as component A, the possible core as component B, and the west component as component C. Both component A and C have gigahertz peaked spectra, as listed in Table 7.3 and shown in Fig. 7.1(d). Due to lower resolution, the core is not distinguishable in the 1.67 and 5 GHz maps. Nevertheless, we measured the flux density in the core region in the 5 GHz map. The result of 20.8 mJy indicates a spectral index of +2.1, comparable to the theoretical spectral index of 2.5 expected for a simple homogeneous synchrotron self-absorbed component. In view of the above evidence, we are confident that 0108+388 is a CSO.

0108+388 exhibits radio emission on scales larger than 5 kilo-parsecs (Baum et al. 1990). In a 1.4 GHz VLA map and a 0.6 GHz map from the Westerbork Synthesis Radio Telescope (WSRT), a weak feature is detected $\sim 20''$ to the east of the parsec-scale structure. A bridge connects this feature with the parsec-scale structure. Baum et al. (1990) suggested that this could be a jet which has recently been "smothered" by the infall of dense gas onto the nucleus, or by recurrent activity. This is consistent with our hypothesis that the CSO's are short-lived and may re-activate many times in a Hubble time.

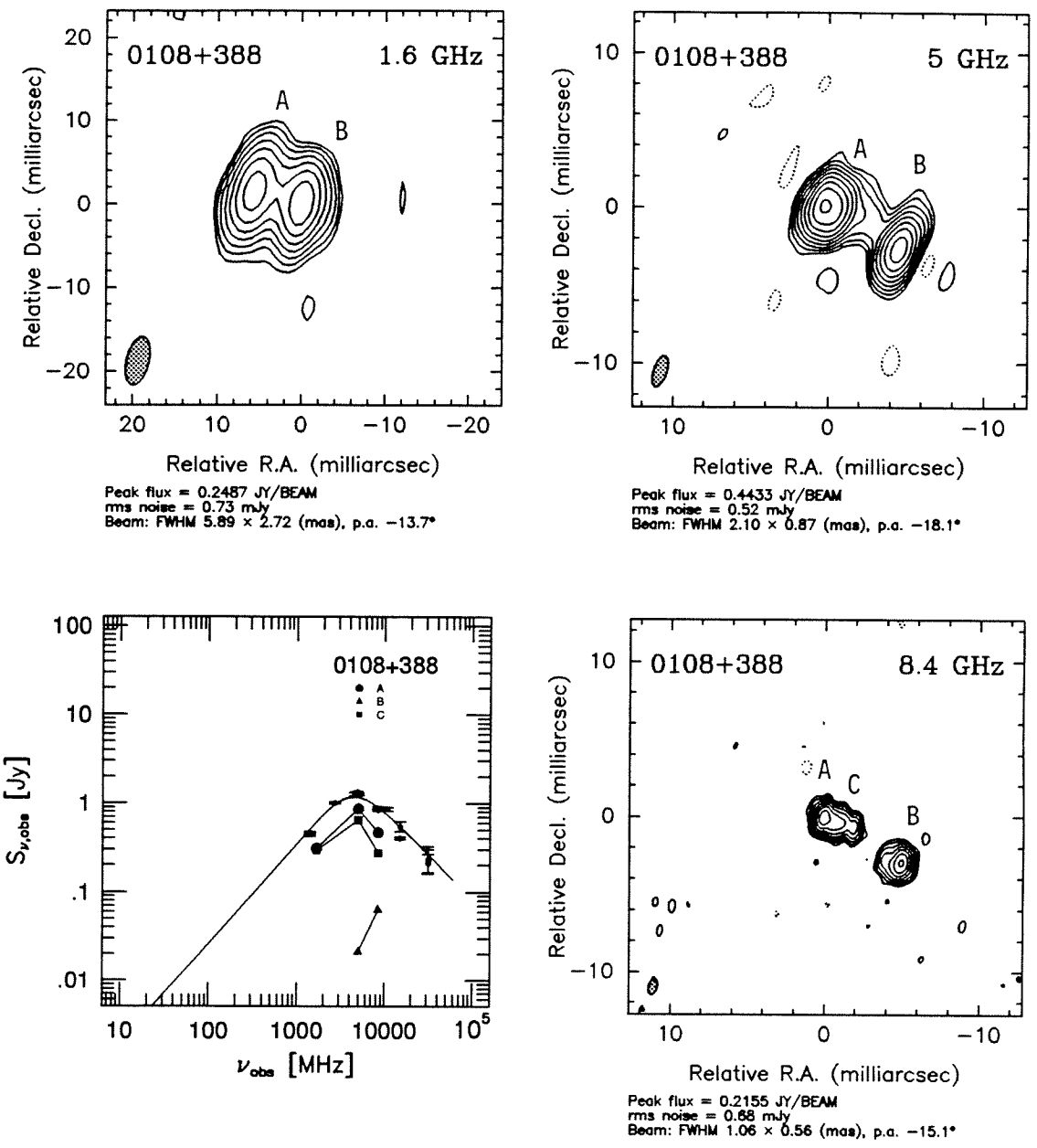

Figure 7.1. VLBI observations and spectra of 0108+388.
(a) top left; (b) top right; (c) bottom right; (d) bottom left.

0258+350 (NGC 1167)

A VLA map at 5 GHz (Fanti et al. 1986) and a MERLIN map at 1.4 GHz (Sanghera 1990) show that the S0 Seyfert galaxy 0258+350 has a bright feature straddled by extended emission. This is very much like 3C 147 seen by the MERLIN or VLA (Preuss & Kellermann 1990), or 0404+678 seen at low resolution (see below). Its flux density at 5 GHz is 0.93 Jy, corresponding to a luminosity $P_{5\mathrm{GHz}} \simeq 3 \times 10^{23}$ W Hz^{-1}. Assuming a spectral index of -0.7, the boundary between FR I and FR II sources is $\sim 5 \times 10^{25}$ W Hz^{-1}. Thus 0258+350 is a low luminosity object compared with other CSO's and CSO candidates. It will be interesting to compare the properties of this object with other CSO's to investigate possible differences in the nuclei of elliptical and spiral galaxies.

0404+768

This object was not observed in the PR survey because it was too heavily resolved. Our full resolution map at 5 GHz (Fig. 7.2(c)) shows that this object consists of a compact feature (B), a jet to its southwest (C) and a lobe to its northeast. The 1.67 GHz map (Fig. 7.2(a)) and tapered 5 GHz map (Fig. 7.2(b)) clearly show the northeast lobe. And the map made with the MERLIN data alone (Fig. 7.2(e)) shows the full extent of its structure on parsec-scales. We have measured the flux densities of individual components on the 1.67 and 5 GHz maps. The spectral index between 1.67 and 5 GHz of the northeast lobe (A) is -0.58 while that of the southwest jet (C) is -0.36. However, the compact feature (B) has an inverted-spectrum with a spectral index of $+0.52$. We believe that the compact feature is associated with the center of activity and therefore 0404+768 is a "true" compact symmetric object.

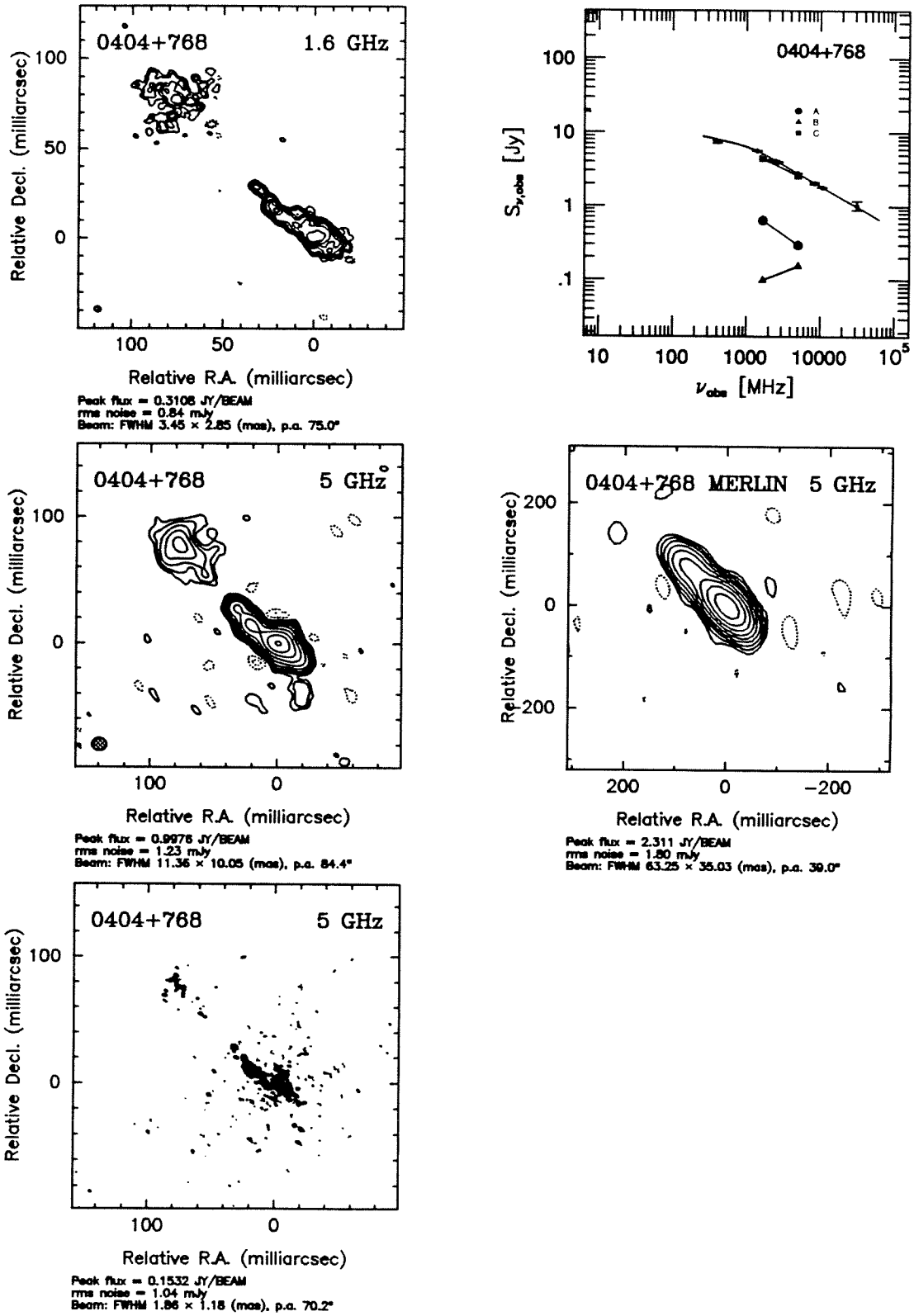

Figure 7.2. (a) top-left: 1.6 GHz VLBI image; (b) mid-left: 5 GHz VLBI image (tapered); (c) bottom-left: 5 GHz VLBI image (full resolution); (d) top-right: Spectra; (e) mid-right: 5 GHz MERLIN image.

0646+600

Our 5 GHz observations (Fig. 7.3(b)) revealed two distinct components with almost equal brightness. The two components are separated by $\sim$ 3 mas, corresponding to a projected linear separation of $\sim$ 10 pc. Our observations at 8.4 GHz (Fig. 7.3(c)) show a bridge connecting the two components. Interestingly, there is clearly a narrow feature to the north of component A, which is also present in the 5 GHz map. The nature of this feature and its relation with component A are not clear. We measured flux densities of components A and B from the 5 and 8.4 GHz maps. Due to lack of resolution, it is impossible to measure accurately the flux densities from the 1.67 GHz map (Fig. 7.3(a)). It is clear from the near equality of flux densities of the two components at both 5 and 8.4 GHz and from the turnover in the total spectrum that both components have gigahertz peaked spectra. Component C has a spectral index close to 0 between 5 and 8.4 GHz.

This object is almost certainly a CSO although we have not detected the core. It is most likely that the components A and B are jet-lobe structures expanding in opposite directions and the core is located between them. If component A is associated with the core, the existence of component C will also make it a CSO. Only if B or C is associated with the core, will it be a core-jet source. This seems unlikely in the case of B because of the steep high frequency total spectrum, and in the case of C because of morphology.

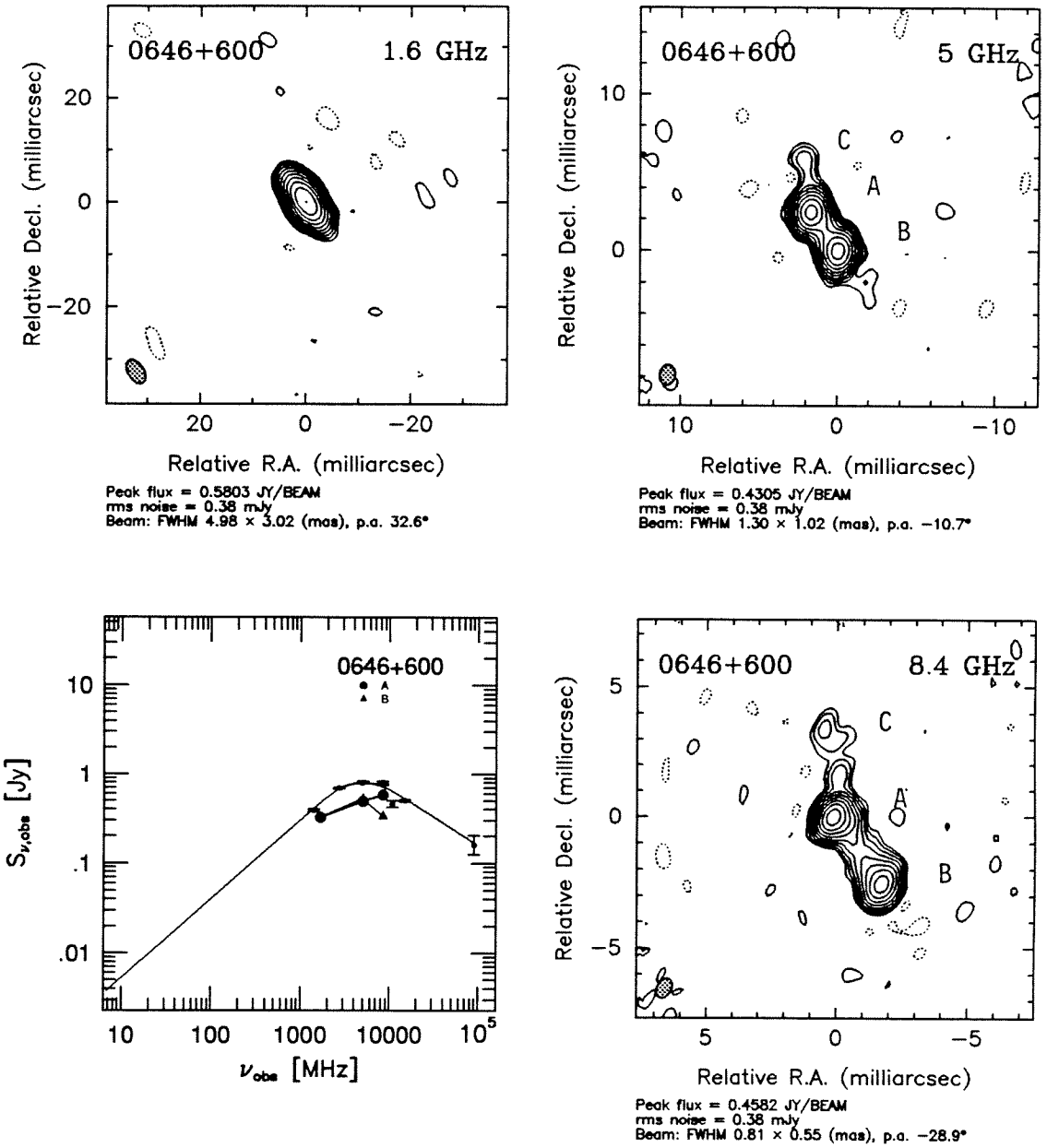

Figure 7.3. VLBI observations and spectra of 0646+600.
(a) top left; (b) top right; (c) bottom right; (d) bottom left.

0710+439

0710+439 was the first compact object ever discovered which consists of a central component straddled by two other components (Readhead et al. 1984). These authors reported this as the most interesting compact structure that had been observed in the PR survey. Based on spectral index information, they correctly identified the central component with the center of the activity and concluded that the two outer components were regions of enhanced emission in two oppositely directed jets. It was clear from the start that this compact triple object had much in common with some members of the class of compact double objects. Pearson & Readhead (1988) placed this object in the compact double class because of its similarity with the Phillips & Mutel doubles.

Previous VLBI observations of this object at 1.67, 5 and 10.7 GHz have been reported by Readhead et al. (1984), Pearson & Readhead (1988) and Conway et al. (1992). Here we present our recent observations at 610 MHz, 1.67 GHz and 8.4 GHz. The 610 MHz map (Fig. 7.4(a)) shows the full extent of the compact structure. The 1.67 GHz observations yielded maps (Fig. 7.4(b) and (c)) with dynamic range of $\sim$ 3600:1 (rms = 0.26 mJy). These maps show, for the first time, that there is a faint jet-like feature connecting the central component B with the southern component C. They also show evidence that there is faint extended emission surrounding component A. The 8.4 GHz (Fig. 7.4(e)) map has a flux density of 1.12 Jy which is $\sim$ 94% of the total flux. Since this object is not variable (Aller et al. 1991; Seielstad et al. 1984), the missing flux density could be due to a calibration error, but it is more likely due to extended emission. It is possible that both factors contribute to some extent. Nevertheless, the flux densities of the three components can be measured from this map with small error. In contrast, the total cleaned flux density of our previous 10 GHz map (Conway et al. 1992) is 0.664 Jy, which only accounts for $\sim$ 68% of the total flux density of 0.97 Jy. Thus we re-calculated the spectral indices of individual components with these more accurate measurements. The flux densities at 1.6

and 8.4 GHz were measured from Fig. 7.4(b) and (e) while those at 5 GHz were taken from Conway et al. (1992). The flux in the 5 GHz map is 1.25 Jy out of the total flux density of 1.67 Jy at this frequency. We assume that the missing flux density is due to the extended emission around components A and C and add the missing flux density to the measured flux densities of A and C according to their ratio. Similarly, we add the missing flux density at 8.4 GHz to the measured flux densities. As listed in Table 7.3 and shown in Fig. 7.4(d), component B has a flat spectrum with spectral index near 0 while both components A and C have steep spectra. The spectral index between 5 and 8.4 GHz of component B is +0.02, which differs significantly from the result of −0.68 found by Conway et al. (1992). The difference is due to our new flux density measurement at 8.4 GHz. We found a flux density for component B at 8.4 GHz of 0.56 Jy whereas Conway et al. got 0.33 Jy at 10.7 GHz, but the 10.7 GHz map only gave 68% of the total flux density. If simply adjusted with a factor of 100/68, the flux density of B would be 0.49 Jy, which would yield a spectral index of −0.17. We were unable to measure the flux densities from the 610 MHz map due to its low resolution. However, since 0710+439 has a gigahertz peaked spectrum, the spectrum of each component has to turn over at some point near 1 GHz. As indicated in Fig. 7.4(d), component B probably turns over at frequency near 2 GHz while component C does so at a frequency near or below 1 GHz.

1031+567

The radio galaxy 1031+567 is shown by VLBI observations at both 1.67 and 5 GHz to be a double separated by $\sim$ 30 mas, i.e., 100 pc (Pearson 1994, private communication). Both components are resolved. High frequency observations are needed to search for the compact component which may be associated with the center of activity.

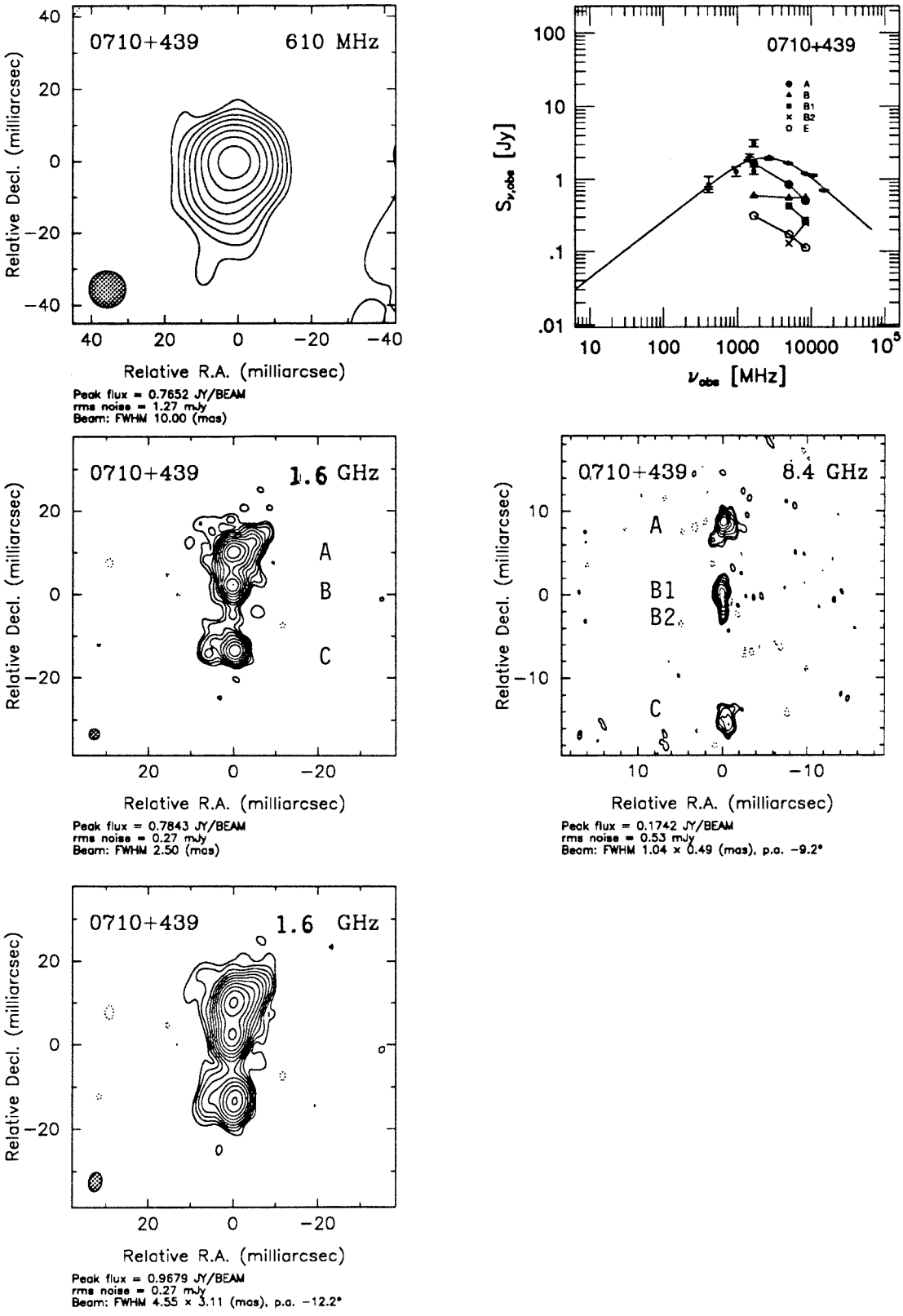

Figure 7.4. VLBI observations and spectra — (a) top-left: 0.6 GHz VLBI image; (b) mid-left: 1.6 GHz VLBI image (super resolved); (c) bottom-left: 1.6 GHz VLBI image (full resolution); (d) top-right: Spectra; (e) mid-right: 8.4 GHz VLBI image.

1225+368

The quasar 1225+368 was found to have double structure on parsec scales by Hodges (1984). Our VLBI observations at 5 GHz (Fig. 7.5(a) and (b)) reveal a string of emission region (A to E from east to west). A contains the brightest feature in the map, but it is resolved and surrounded by extended emission. E is clearly extended. B, C and D all contain substructure. The naturally weighted map (Fig. 7.5(b)) shows that there is a faint bridge connecting C and D. The VLBI observations at 1.6 GHz made by D. Dallacasa (private communication) show that emission regions A through D are linked together with faint bridge emission and that there is a clear gap between D and E. Due to the lack of multi-frequency data, we cannot determine the spectral indices for each individual emission region. However, the morphology suggests that emission region D coincides with the center of activity. Assuming that the core is located at the west end of D, we estimated from the map that it contains $\sim$ 43 mJy at 1.6 GHz. Convolving the 5 GHz data with the same beam, we estimated that it contains $\sim$ 40 mJy. Thus the west end of region D has a flat spectrum ($\alpha \simeq -0.07$). Similarly, we found that the other regions have steep spectra. This supports the hypothesis that D contains the center of activity. Therefore, this object is a CSO.

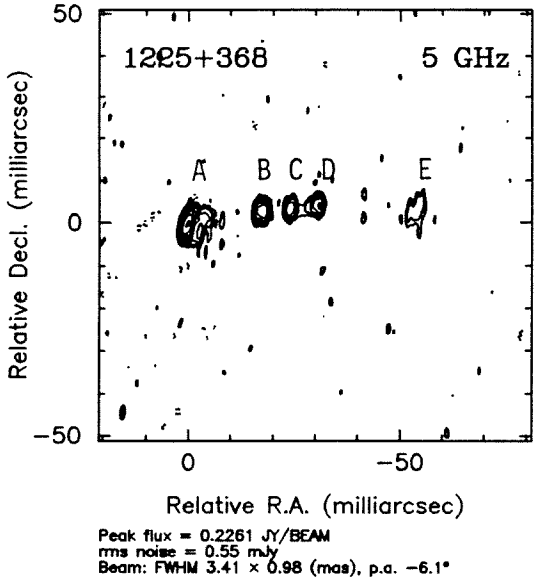

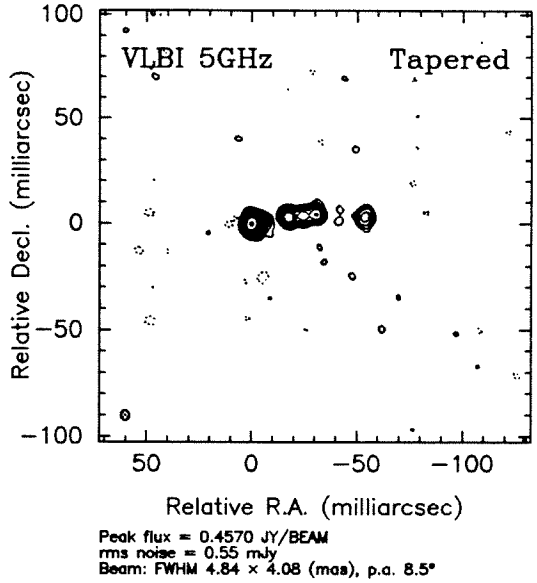

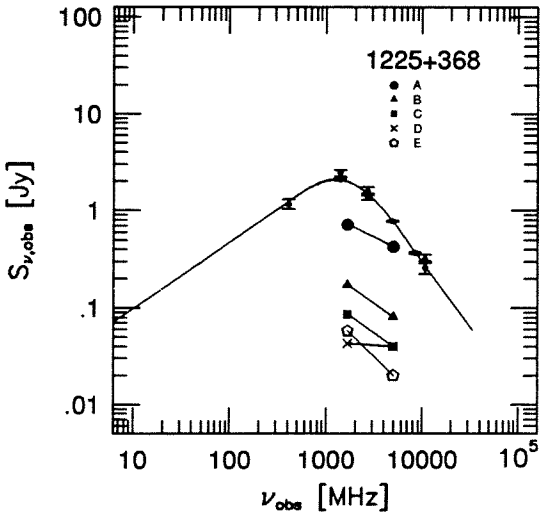

Figure 7.5. VLBI observations and spectra of 1225+368.
(a) top left; (b) top right; (c) bottom left.

1242+410

The 5 GHz map (Fig. 7.6(c)) shows that this object consists of a central component and jet-like structure on both sides. The 1.6 GHz map (Fig. 7.6(a)) and tapered 5 GHz map (Fig. 7.6(b)) show a lobe to the south. The 8.4 GHz maps (Fig. 7.6(e) and (f)) show clearly that the central component contains the most compact feature. It also shows the enhanced emission along the jets on both side, which is also visible on the 1.67 and 5 GHz maps. We have measured the flux densities of the north region (A), the central region (B) and the south region (C) from maps at these three frequencies. The spectra of all three regions are flatter at frequencies below 5 GHz, while B has the flattest spectrum between 1.67 and 5 GHz. It is difficult to determine which region is associated with the center of activity from these spectra. However, the compact feature in region B is almost certainly associated with the center of activity.

The structure of 1242+410 is somewhat different from other CSO's and CSO candidates. The difference is similar to that between the extended FR I and FR II objects. The object 1242+410 is similar to a miniature FR I object whereas other CSO's are similar to miniature FR II objects. The identification with a quasar makes this object even more interesting. According to the unification between radio galaxies and quasars, the jet axis in quasars lies close to the line of sight and thus is subject to relativistic beaming effect, which causes the one-sided appearance in the vicinity of core as observed in almost all quasars. This is the first quasar discovered with symmetric structure on scales down to $\sim$ 5 mas, i.e., 20 pc.

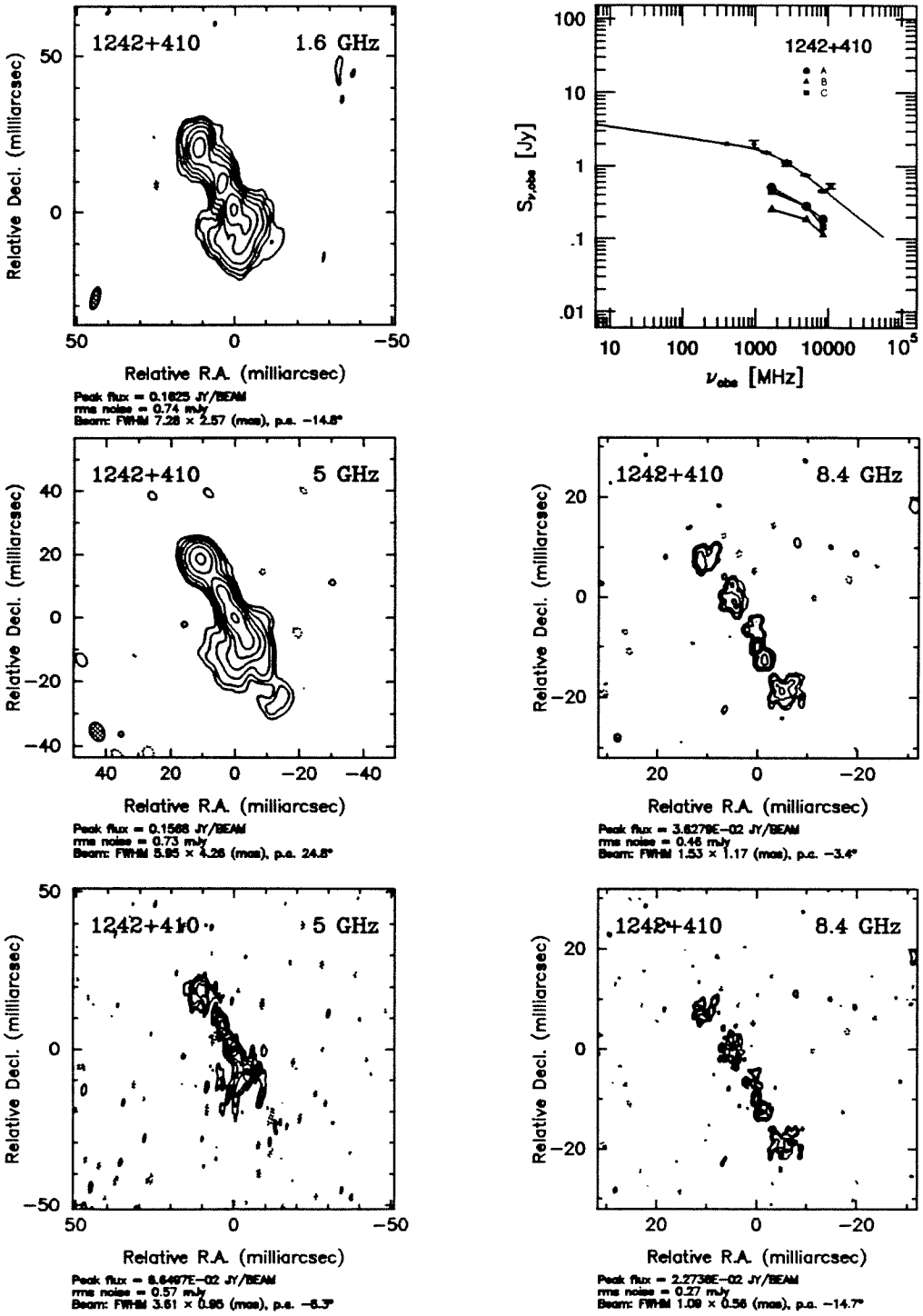

Figure 7.6. VLBI observations and spectra of 1242+410 — (a) top-left: 1.6 GHz VLBI image; (b) mid-left: 5 GHz VLBI image (tapered); (c) bottom-left: 5 GHz VLBI image (full resolution); (d) top-right: Spectra; (e) mid-right: 8.4 GHz VLBI image (tapered); (f) bottom-right: 8.4 GHz VLBI image (full resolution).

1250+568

A 1.6 GHz map made with combined data from MERLIN and EVN (Sanghera 1992) revealed that this object consists of a compact component straddled by two extended lobes, which resembles the morphology of FR II objects. Our MERLIN observations at 5 GHz (Polatidis 1993) confirmed the structure. This object is clearly a CSO based on its morphology. VLBI observations are needed to study the structure of the central component.

1333+459

Our VLBI observations at 5 GHz (Fig. 7.7(b)) show that this object has two components of almost equal brightness. Modelfitting shows that at 5 GHz the two components have flux densities of 0.35 Jy and 0.30 Jy, respectively. It appears unresolved in the 1.67 GHz map (Fig. 7.7(a)). However, the UV data indicate that it is resolved on long baselines. Starting with the two-component Gaussian model established from the 5 GHz data, modelfitting yields a two-component model which fits the 1.67 GHz data very well. We used the Gaussian models to estimate the spectral indices of the two components between 1.67 GHz and 5 GHz. As listed in Table 7.3 and shown in Fig. 7.6(c), both components have inverted spectra. High resolution observations are needed to explore whether it has symmetric structure and to detect the core.

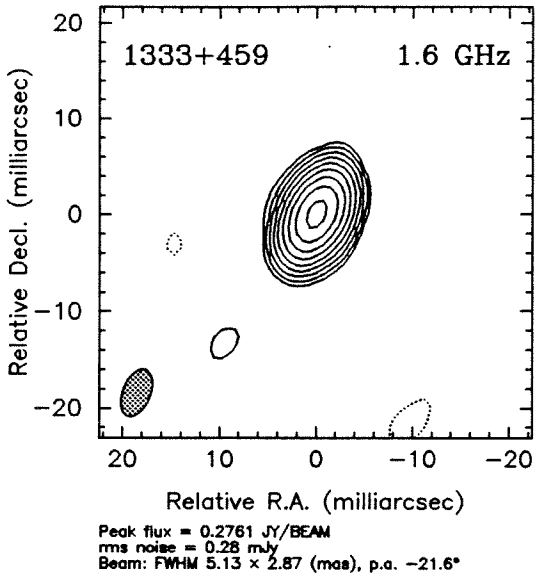

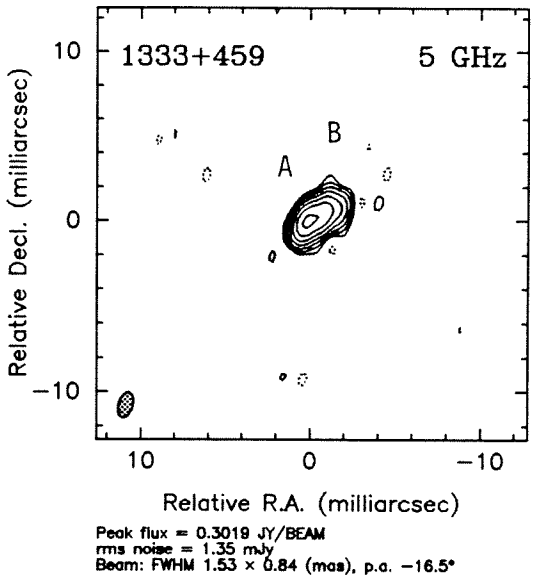

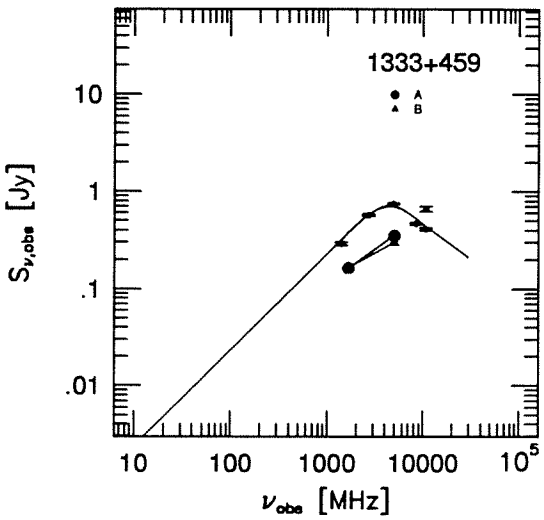

Figure 7.7. VLBI observations and spectra of 1333+459.
(a) top left; (b) top right; (c) bottom left.

1333+589

It has been reported that this object is associated with 4C 58.26 (Kühr et al. 1981, S4) and that its flux density at 1.4 GHz is 893 mJy (White & Becker 1992). Our VLA observations with the A-array at 1.4 GHz show that there is an extended double-lobed object $\sim 200''$ to the west and another faint object $\sim 350''$ to the east. The 1.4 GHz survey had a resolution of $\sim 700''$ (White & Becker 1992), and hence measured the total flux densities of all three objects. Our maps show that 1333+589 itself has a flux density of 325 mJy at 1.4 GHz. The extended object must contribute most of the rest 568 mJy detected in the 1.4 GHz survey. Assuming that the extended object has a spectral index of -1, it should have a flux density of ~ 4.5 Jy at 178 MHz, which is consistent with the flux density of 4.0 ± 0.05 Jy reported for 4C 58.26 by Caswell & Crowther (1969). Therefore, we conclude that the extended object is 4C 58.26 and that 1333+589 is a separate object. Patnaik et al. (1992) measured a flux density of 766 mJy at 8.4 GHz with the VLA. Kapahi (1981) reported that the flux density at 5 GHz was 865 mJy measured with the Westerbork Synthesis Radio Telescope. Its flux densities at 1.4, 5 and 8.4 GHz show that it has a gigahertz peaked spectrum, rather than a flat spectrum reported by Kühr (1979) (Fig. 7.8(d)).

Our VLBI observations at both 1.67 and 5 GHz (Fig. 7.8(a), (b) and (c)) reveal a well separated double. The northern component A contains the brightest feature in the 5 GHz map, but both components are clearly resolved. Using flux densities measured from the maps, we calculate that the northern component (A) has a spectral index of +0.87 between 1.67 and 5 GHz while the southern component B has a spectral index of +0.01 (*see* Table 7.3 and Fig. 7.8(d)). We note that the flux density in the 5 GHz map is 0.65 Jy, i.e., $\sim$ 0.2 Jy less than the 0.865 Jy reported by Kapahi (1981). Seielstad et al. (1984) reported that this object did not exhibit variability, thus the discrepancy is probably not due to variability. It is very likely that 1333+589 has more extended structure around the two components which is too faint to be detected by our snapshot observations. Comparing

the 1.67 GHz map (Fig. 7.8(a)) with the tapered 5 GHz map (Fig. 7.8(c)), there is some emission to the south-east of component A which is not visible at 5 GHz, which supports this interpretation.

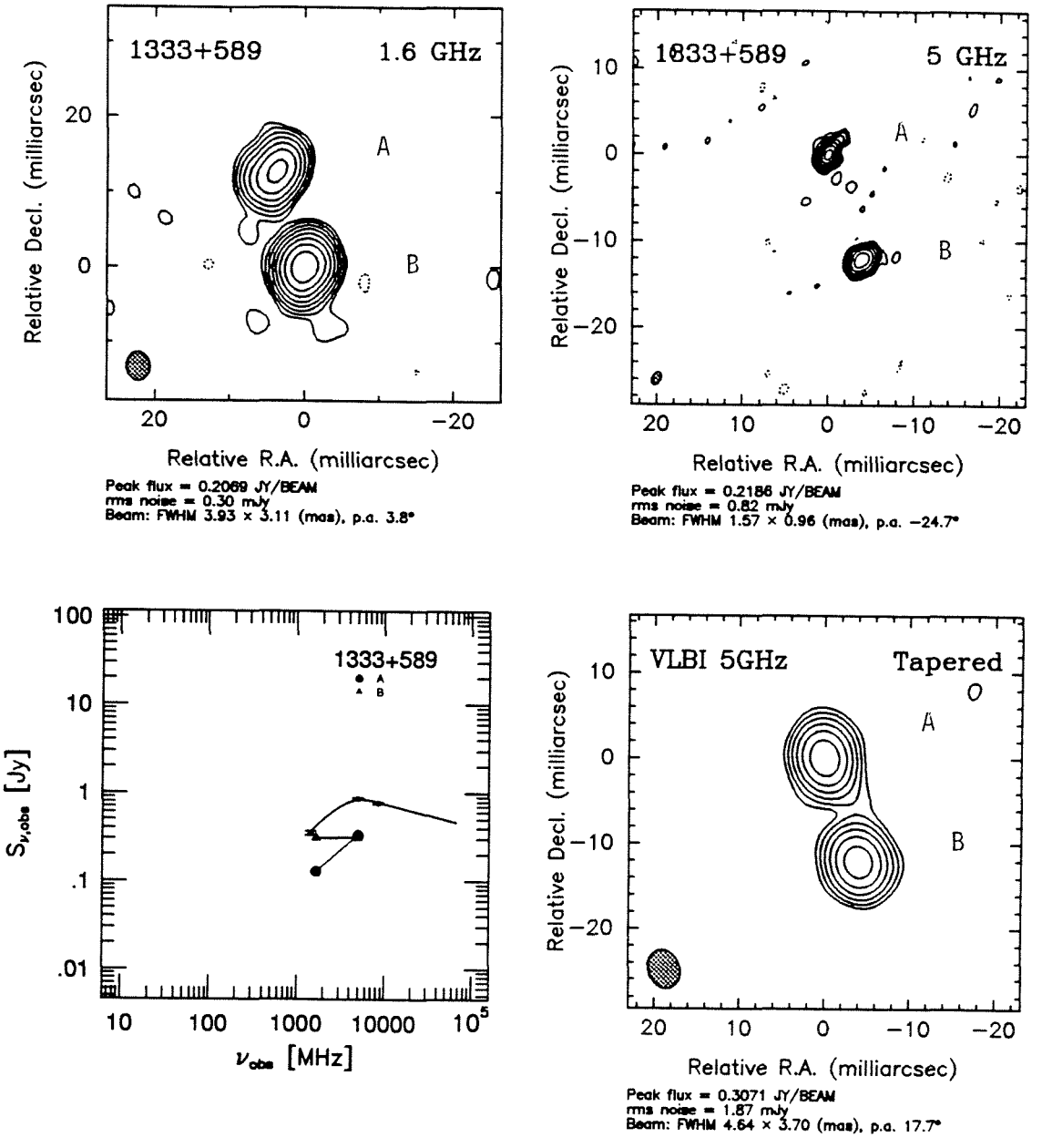

Figure 7.8. VLBI observations and spectra of 1333+589.
(a) top left; (b) top right; (c) bottom right; (d) bottom left.

1358+624

VLBI observations at 608 MHz reveal a double and a possible bridge in between with the largest angular size of 46 mas at P.A. 125° (Padrielli et al. 1991). VLBI observations at 1.67 GHz (Pearson 1994, private communication) confirmed that there are indeed two lobe-like components and another elongated component in between. VLBI observations at 5 GHz (Pearson et al. 1994) show that the elongated middle component contains a compact feature and jet-like structure which connects with the lobe-like component to the south-east. It is very likely that the compact component is associated with the center of activity.

High frequency VLBI observations are needed to make sure that the compact component is indeed associated with the center of activity.

1437+624

Our VLBI observations at both 1.67 and 5 GHz (Fig. 7.9(a) and (b)) reveal a double with a largest angular size of $\sim$ 130 mas. Both components have steep spectra between these two frequencies (Table 7.3 and Fig. 7.9(d)). The southern component (B) has lobe-like structure while the northern component (A) has complicated structure. Component A contains a bright feature at its east end, a couple of knots to the west and a tail pointing to the north-west, as shown in Fig. 7.9(a). Additional emission is visible to the south-east of component A, as shown in Fig. 7.9(b). These two components could be the outer lobes where jets interact with the interstellar medium.

To confirm that it is truly a member of the CSO class, it is necessary to identify the center of activity or find more compelling evidence of symmetry, e.g., more extended tails leading to its center. Thus observations at high and low frequencies are needed.

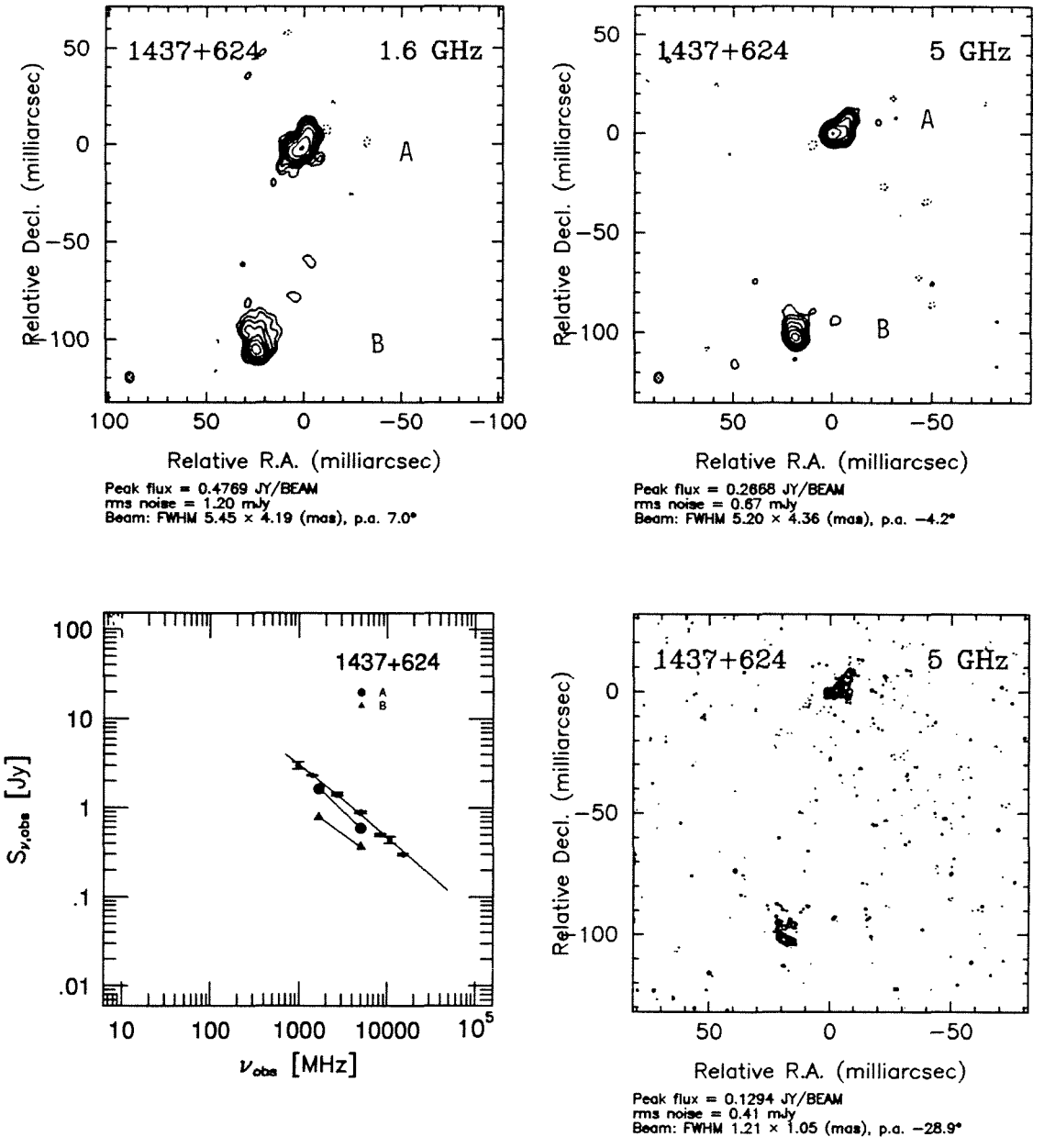

Figure 7.9. VLBI observations and spectra of 1437+624.
(a) top left; (b) top right; (c) bottom right; (d) bottom left.

1637+626

A 15 GHz VLA map showed that it has a double structure (Spencer et al. 1989), and an EVN map at 1.6 GHz revealed a bright feature straddled by extended emission (Fanti et al. 1985).

1734+508

Our VLBI observations at 5 GHz (Fig. 7.10(b)) reveal a double with a separation $\sim$ 3.4 mas and flux density ratio $\sim$ 1:3. The visibility data indicate that both components are resolved. Our VLBI observations at 8.4 GHz (Fig. 7.10(c)) show that both components have a bright feature at their far end and a 'tail' towards each other, while the southern emission region contains the brightest feature in the map. It seems unresolved in the 1.67 GHz map (Fig. 7.10(a)). However, the visibility data indicate that it is resolved at long baselines. It can be modeled with two Gaussian components. We calculated the spectral indices of the two emission regions using the flux densities estimated from modelfitting with the 1.67 GHz data and measured from the 5 and 8.4 GHz maps (Table 7.3 and Fig. 7.10(d)). The northern emission region A has a gigahertz peaked spectrum while the southern emission region B has an inverted spectrum ($\alpha = +0.31$).

It is possible that the brightest feature in the southern emission region is associated with the center of activity and therefore that 1734+508 belongs to the class of asymmetric objects. However, we cannot rule out the possibility that it is a CSO in which both emission regions represent mini-lobes and the bright features are hot-spots. High frequency observations are needed to determine the correct interpretation.

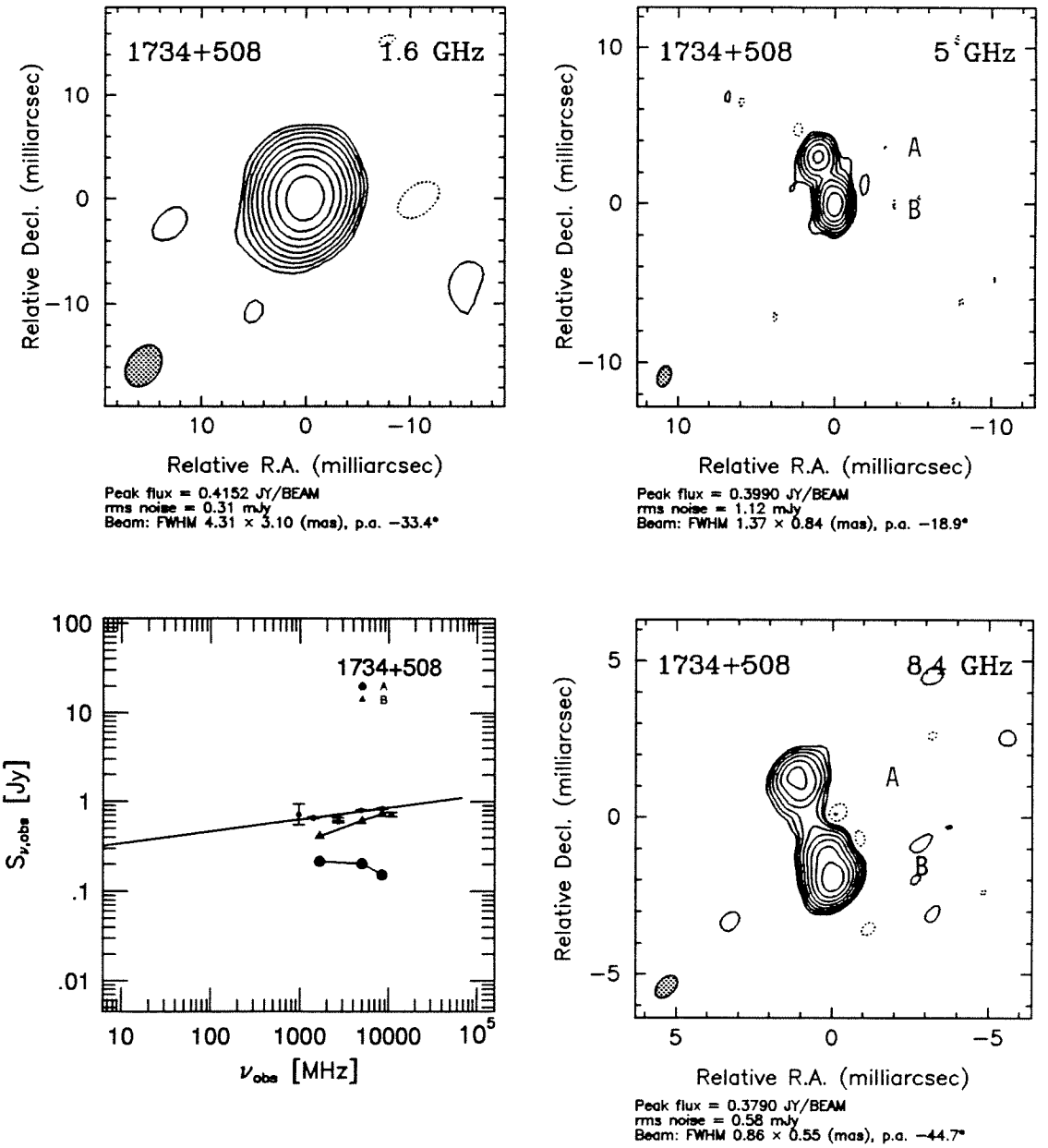

Figure 7.10. VLBI observations and spectra of 1734+508.
(a) top left; (b) top right; (c) bottom right; (d) bottom left.

1819+396

Our MERLIN map reveals that this object consists of two components (Fig. 7.11a). The northern component is extended and the southern component is a narrow curved feature. VLA maps by Spencer et al. (1989b) detected no large scale structure other than these two components. VLBI observations at 1.6 GHz showed that the southern component is a curved jet with a compact component at its northern end and a hot spot at its southern end, and that the north component is completely resolved (Dallacasa et al. 1990). However, our VLBI observations at 5 GHz only detect this object at short baselines. The resulting map only shows a bright spot with a total flux density $\sim$ 270 mJy (Fig. 7.11b). It is probably the hot spot at the southern end of the jet shown at the 1.6 GHz map. If this is true, the hot spot has a rather flat spectrum with a spectral index ~ -0.1. It is possible that this component contains the core, which will make this object a one-sided jet leading to an extended lobe. However, we cannot rule out the possibility that the compact component at the northern end of the jet is the core. High quality observations at high frequency are needed to locate the core.

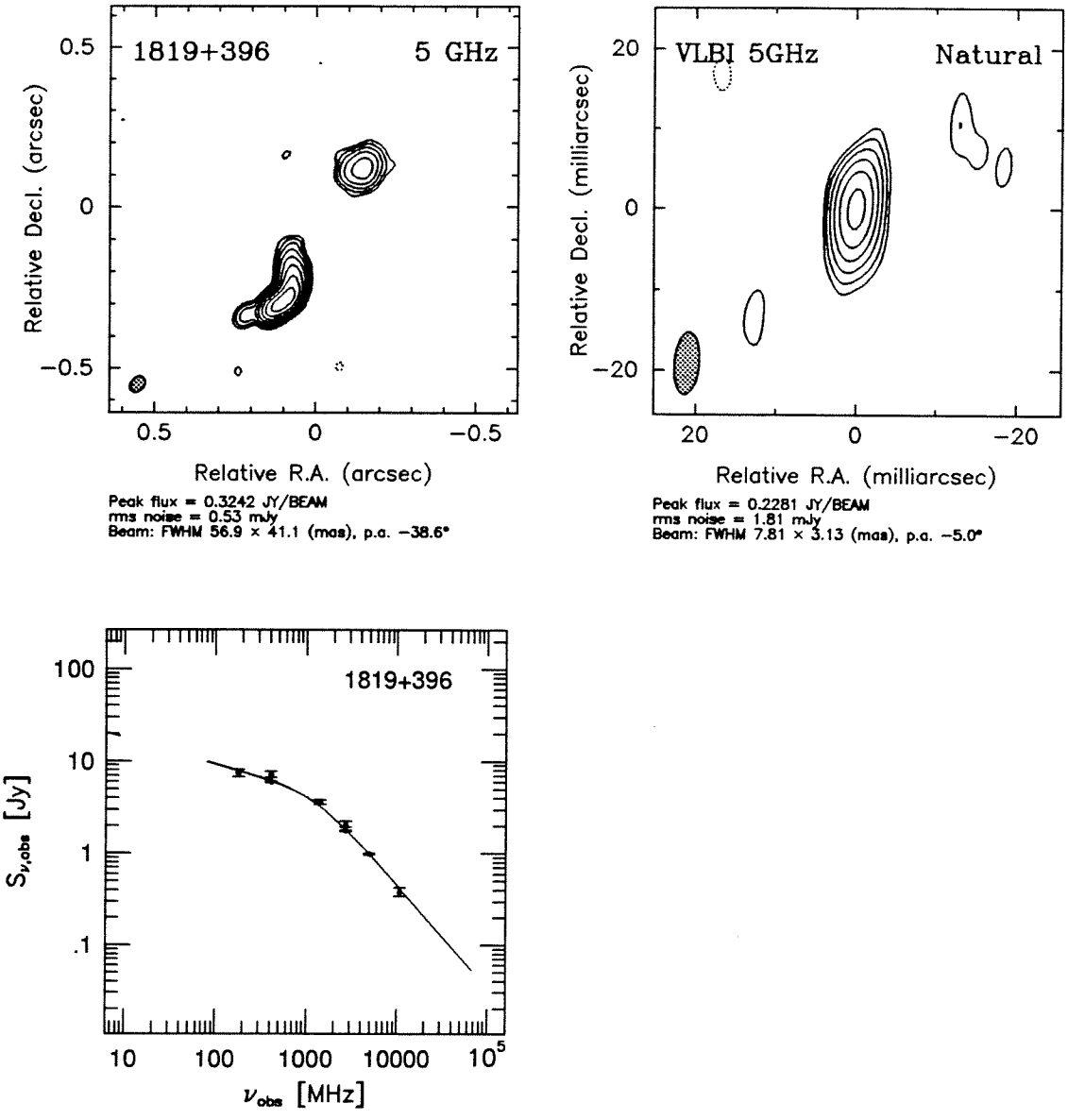

Figure 7.11. VLBI observations and spectra of 1819+396.
(a) top left; (b) top right; (c) bottom left.

1843+356

Our 5 GHz observations (Fig. 7.12(b)) reveal two major emission regions. The emission region to the north-east (A) is clearly extended while the other emission region to the south-west (B) can be modeled with two Gaussian components (B1 and B2) (Table 7.3). The 8.4 GHz observations (Fig. 7.12(c)) show that B indeed consists of two components and that there is some faint emission connecting A and B. The 1.67 GHz map is dominated by the emission region A (Fig. 7.12(a)). We noticed that the total cleaned flux density in the 1.67 GHz map is $\sim$ 10% less than the interpolated flux density between 1.4 and 2.7 GHz. This could be due to a calibration error. It could also be due to a faint extended halo which is beyond the sensitivity of our data. We calculated the spectral indices for the two emission regions using flux densities measured from the maps and estimated the spectral indices between 5 and 8.4 GHz for components B1 and B2 using flux densities obtained from modelfitting (Table 7.3 and Fig. 7.12(d)). The spectrum of A is steep between 5 and 8.4 GHz and flatter between 1.6 and 5 GHz, which suggests that A might have a gigahertz peaked spectrum. B clearly has a gigahertz peaked spectrum as a whole, and B1 has a flat spectrum between 5 and 8.4 GHz and B2 has a steep spectrum.

Component B1 is the most compact and the brightest feature in the 8.4 GHz map, which is likely to be associated with the center of activity. If this is the case, B2 could be explained as the approaching jet while the faint bridge and A could be explained as the counter jet and lobe. This would mean that this object has an arm ratio of $\sim$ 1:10, which is rather unusual. It is possible that we have not detected the center of activity yet. Nevertheless the symmetric structure qualifies 1834+356 as a CSO candidate.

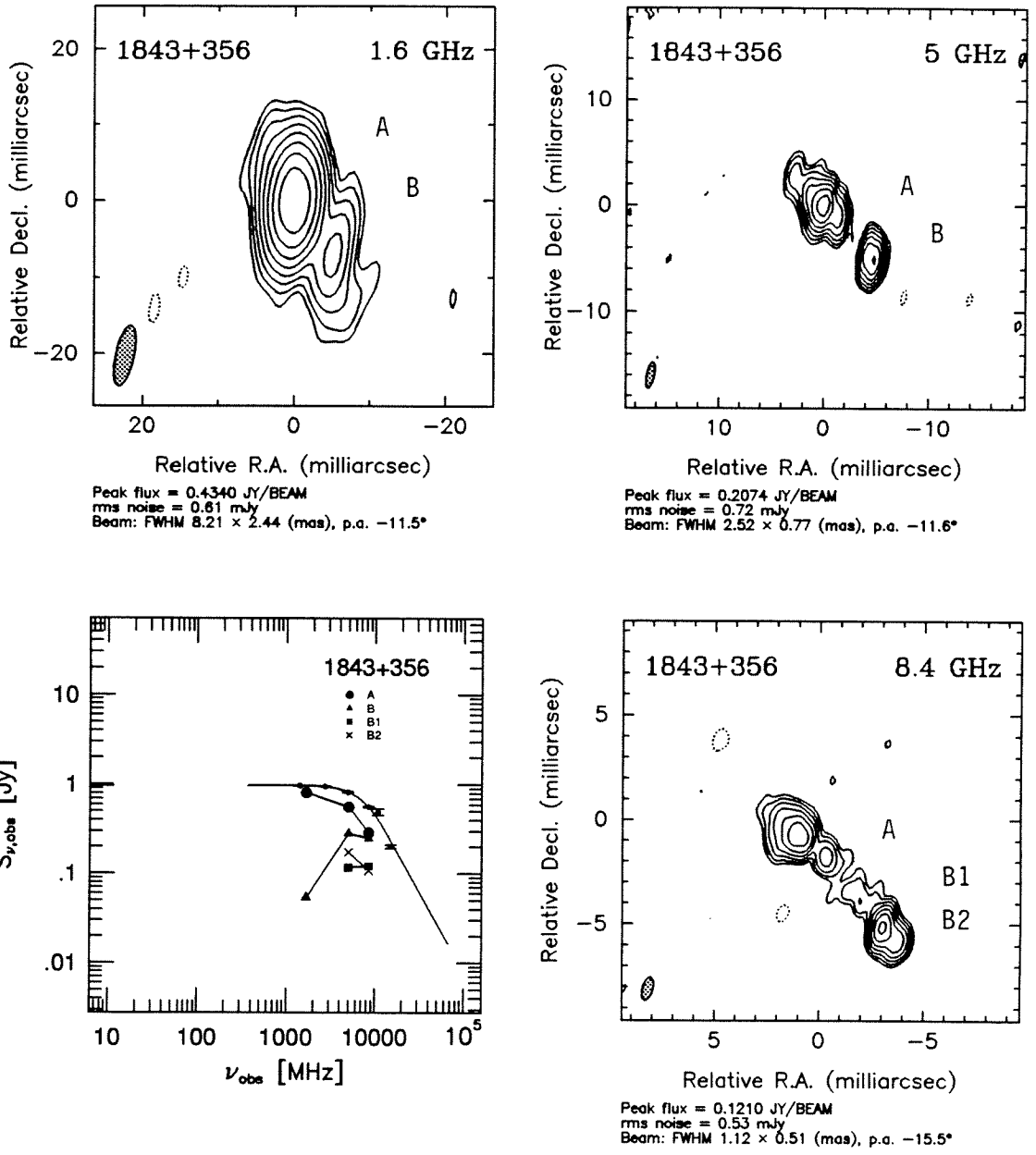

Figure 7.12. VLBI observations and spectra of 1843+356.
(a) top left; (b) top right; (c) bottom right; (d) bottom left.

1943+546

Our MERLIN observations at 5 GHz reveal a double (Fig. 7.13(a)). This object has been observed with the global VLBI network at 1.6, 5 and 8.4 GHz. These observations (Fig. 7.13(b)-(d)) reveal that this object consists of a compact central component straddled by two outer lobes, which is morphologically identical with the typical FR II radio sources, but $\sim$ 1000 times smaller. The 8.4 GHz map (Fig. 7.13(d)) clearly shows the compact central component and the hot-spots in both outer lobes. The 1.6 GHz and 5 GHz maps show that there is a faint extended halo surrounding the west lobe. 1943+546 is clearly a CSO based on its structural symmetry. We calculated spectral indices for these three emission regions (A to C from east to west) using flux densities measured from the maps. As shown in Table 7.3 and Fig. 7.13(e), all three regions have steep spectra from 1.6 to 8.4 GHz. The compactness of the central component B and structural symmetry suggest that B is associated with the center of activity.

2323+435

Maps at 1.6 GHz made with MERLIN data alone and combined MERLIN and EVN data (Sanghera 1990) revealed that it consists of two lobes with faint extended emission tailing toward each other, which resembles FR II sources in which the cores are too weak be seen.

2342+821

Our MERLIN map at 5 GHz revealed that this object consists of three emission regions in a line with the brightest component at one end (Polatidis 1993). And our VLBI observations at 1.6 GHz showed that all three emission regions are resolved (Polatidis et al. 1995). Since it is very different from the core-jet morphology and we cannot rule out the possibility that the central component contains a faint core, we consider it as a CSO candidate. High quality images at high and low frequencies are needed to search for the core and possible faint extended lobes to establish structural symmetry.

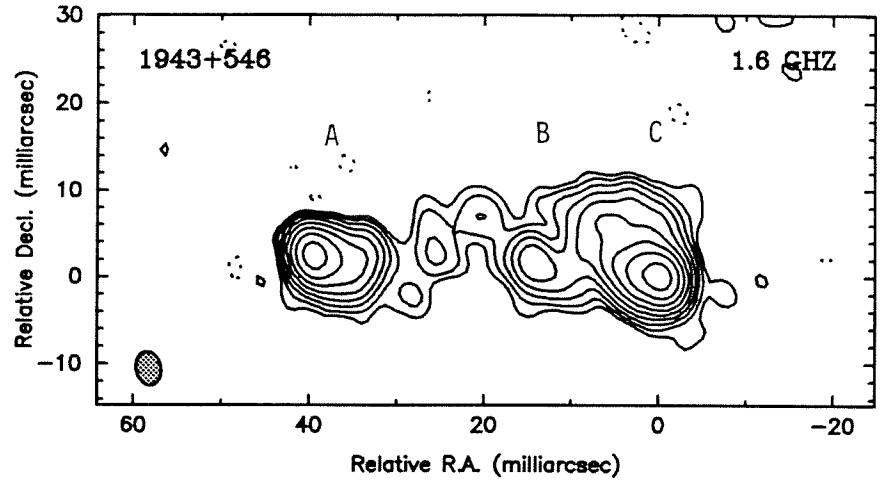

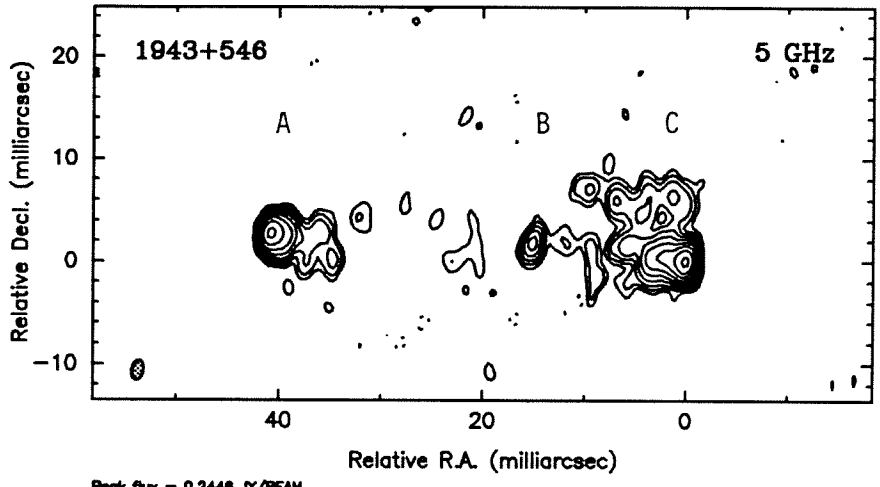

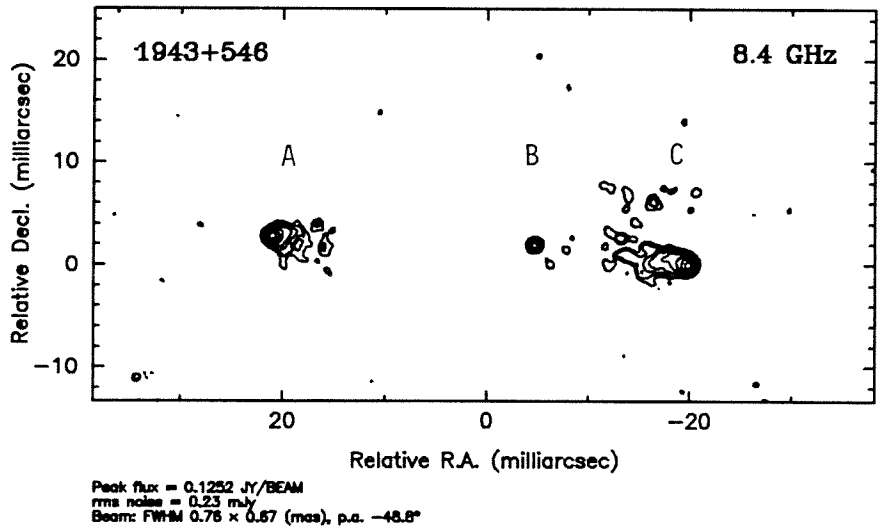

Figure 7.13. VLBI observations of 1943+546.
(a) top: 1.6 MHz; (b) middle: 5 GHz; (c) bottom: 8.4 GHz

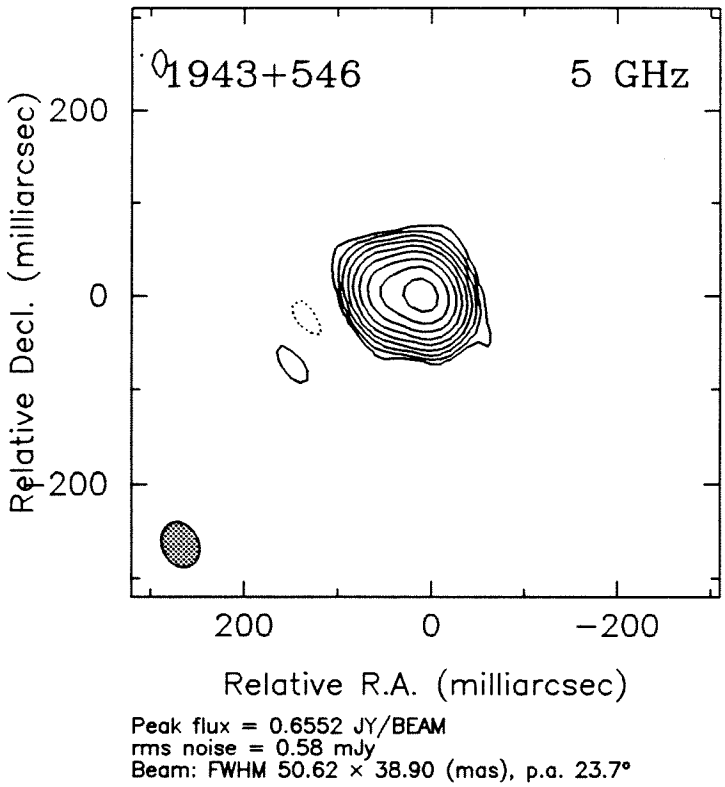

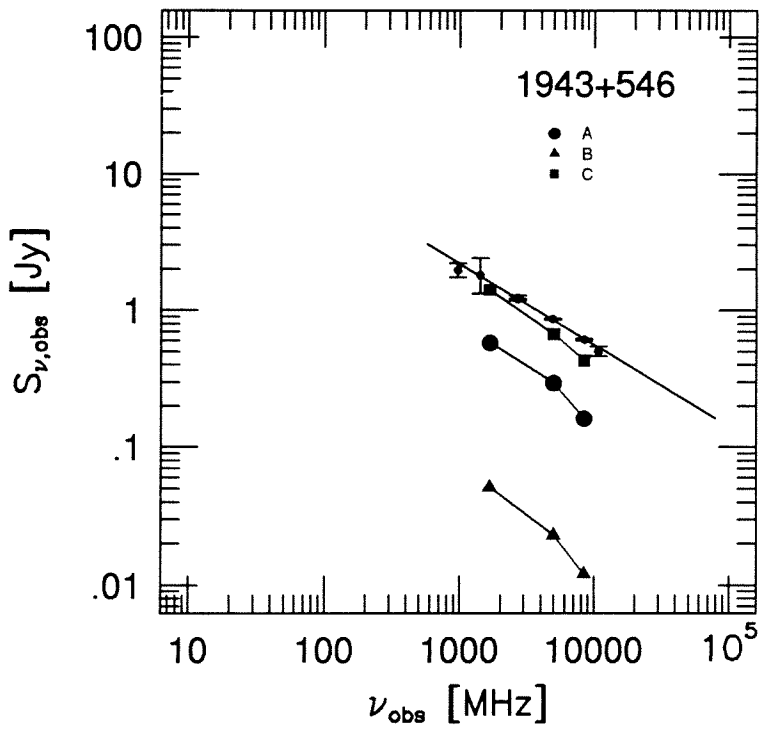

Figure 7.13(d) top: VLBI observations of 1943+546 at 5 GHz.
(e) bottom: spectra

2352+495 — An Archetypal CSO

$2352+495$ is identified with an elliptical galaxy at $z = 0.237$. O'Dea et al. (1990) detected distortions in its elliptical isophotes and some nearby sources, so this object may have undergone recent interaction. This object was first observed with VLBI at 5 GHz as part of the Pearson-Readhead survey and classified as a Compact Double (Pearson & Readhead 1988). Later observations revealed a third component, and analysis of multi-epoch data showed that the central component was varying with time and thus coincided with the center of activity (Conway et al. 1992). Our first observations at 1.67 GHz (not shown), made as part of the CJ1 survey, detected outer lobes surrounding the hot spots visible at higher frequencies (Polatidis 1993; Wilkinson et al. 1994). It was the first convincing example showing a hotspot-outer lobe structure on milliarcsecond scales. Follow-up observations at 610 MHz (Fig. 7.14(a)) and at 1.67 GHz (Fig. 7.14(b)) enabled us to determine the spectra of the substructure.

Our new 1.67 GHz observations revealed clearly for the first time a twin-jet on the mas scales connecting the central component with hot spots and lobes on both sides, while the 610 MHz observations showed the full extent of the lobes. These observations contribute crucial information to our detailed analysis (Readhead et al. 1995). The 8.4 GHz observations (Fig. 7.14(c)) show the southern component with higher fidelity than the previous 10.7 GHz map. The combination of these observations shows that we are seeing symmetric structures including jets, hot spots and outer lobes, which are morphologically identical to large-scale symmetric radio-loud objects except that its size is $\sim$ 1000 times smaller.

Based on both the symmetry of their structures and statistics of the parent population, we argue (Wilkinson et al. 1994) that CSO's are not subject to strong relativistic beaming, as is the case for the asymmetric objects. Therefore, we can apply a number of physical arguments to parsec-scale emission regions for the first time.

We considered two scenarios. First, $2352 + 459$ is young with an age of $\sim 10^3$ years,

but certainly no more than 3×10^4 years. Two independent age estimates support this scenario. The lifetime for energy supply to the lobes is $\sim$ 3000 years and the synchrotron loss timescale is $\sim$ 1500 years. The total energy in this object is $\sim 4 \times 10^{54}$ erg, i.e., $\sim 2M_\odot c^2$, which could be produced by the capture of a small interstellar cloud by a supermassive black hole residing in its nucleus. Alternatively, this object might occur in a "starburst" galaxy in which the jets are "frustrated," with an advance speed $\ll 0.01c$ due to ram pressure confinement in an unusually dense interstellar medium—a possible explanation for gigahertz peaked spectrum (GPS) objects and and compact steep spectrum (CSS) objects suggested by O'Dea et al. (1991) and de Young (1993). In the case of CSO's, a cloud of mass $\sim 6 \times 10^{10} M_\odot$ and a radius $\sim$ 200 pc is required. If this explanation is correct, it would constitute an important link between active galaxies and starburst galaxies, as suggested by Norman & Scoville (1988). However, strong infrared emission is expected under this scenario, and it is not observed. The morphology of CSO's is very different from the morphology of frustrated jet objects as obtained in simulations (De Young 1990, 1993). Furthermore, the optical spectra of CSO's are typical of elliptical galaxy hosts of an active galaxy. In view of this evidence, we favor the hypothesis that CSO's are young objects. Once we accept that CSO's are young, the statistics of these objects in the PR sample indicate that they are short-lived as high luminosity objects and that the luminosity must drop by a factor of 20 after the CSO phase. If this explanation is true, the CSO's are not part of an early evolutionary stage in the development of high luminosity FR II objects, as has been suggested for the compact double objects by Phillips & Mutel (1982) and Carvalho (1985). But they might develop into low luminosity FR II objects and FR I objects, or simply die out after the CSO phase. We conclude that CSO's most likely comprise a class of powerful short-lived active galaxies with an active phase lasting less than $\sim 10^4$ years. Moreover, we suggested, based on space density, that either many elliptical galaxies with luminosity $> 0.3\ L^*$ must pass through one or a few such active phases in a Hubble time, or a smaller subset of such galaxies must pass through many, but fewer than 10^4, such

phases in a Hubble time.

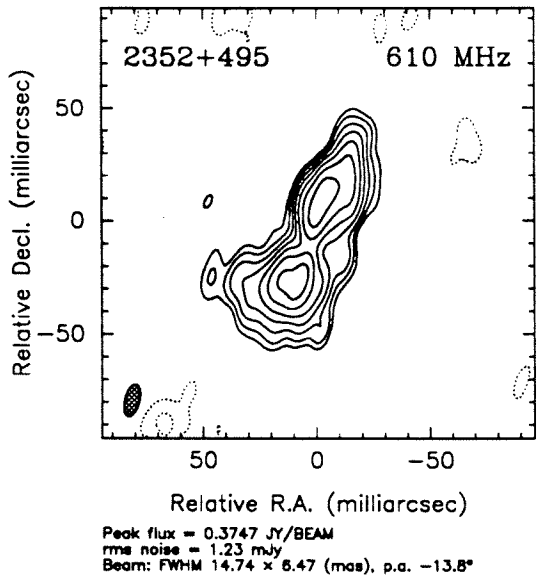

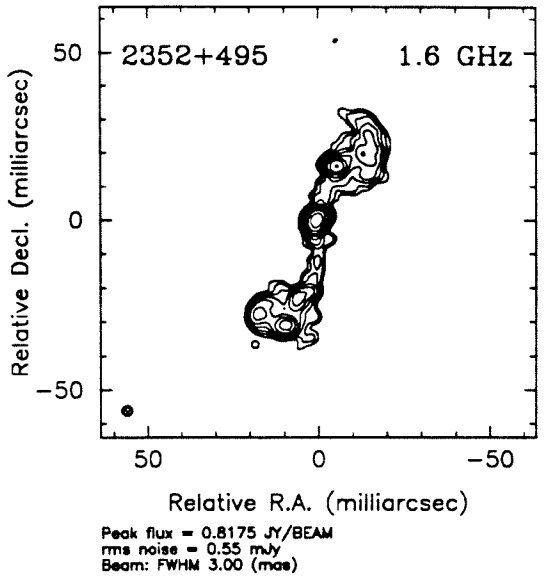

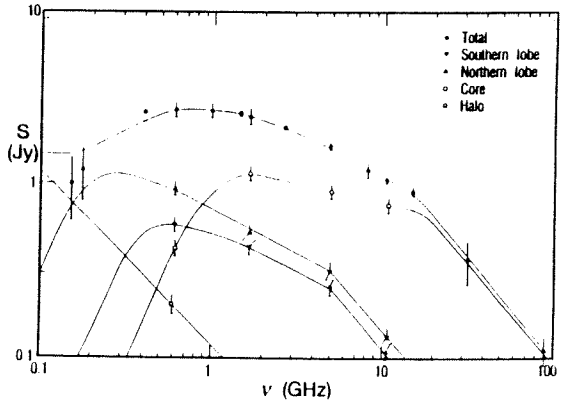

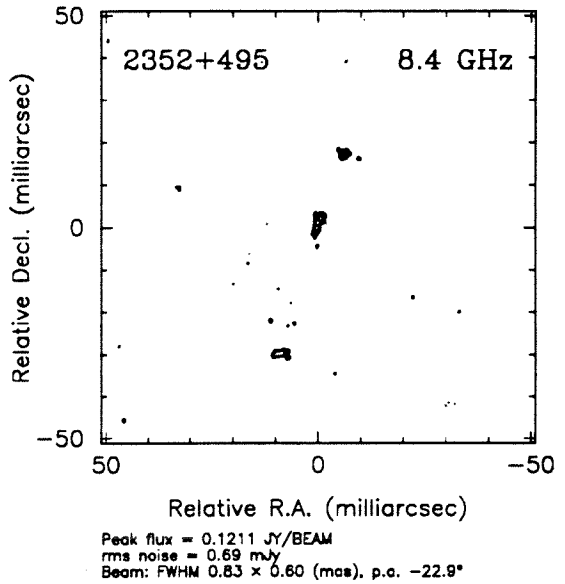

Figure 7.14. VLBI observations and spectra of 2352+495.
(a) top left; (b) top right; (c) bottom right; (d) bottom left.

7.3. SUMMARY

We have shown the CSO's comprise an important class ($\sim$ 10%) of AGN. With the detailed study of 2352+495, we have begun to understand some aspects of the CSO's. However, in order to determine whether the CSO's are young and short-lived, or an early stage of FR I or FR II sources, multi-waveband observations are needed. For example, we can derive the gas density in CSO's from HI absorption and CO emission, hence the advance speed of the nuclear jets and the age of CSO's. CCD imaging of some CSO galaxies suggests that they probably are interacting or merging (O'Dea et al. 1990a; Stanghellini et al. 1993). HST observations are needed to confirm this, which in turn will shed light on whether the CSO's are fuelled by interaction with other galaxies. Some CSO's galaxies have $(r-i)$ color 1 mag. redder than typical elliptical galaxies. IR observations are needed to determine whether this is common to the CSO galaxies. It is also interesting to study the CSO quasars in these aspects to explore whether there are differences between their environment and that of the CSO galaxies.

Chapter 8

CONCLUSIONS

8.1 THE SNAPSHOT TECHNIQUE

We have developed and demonstrated the viability of the snapshot observation technique. Compared to conventional VLBI observations, the snapshot technique improves the observing efficiency by nearly a factor of 10. Our success has led to the second Caltech-Jodrell Bank VLBI survey and the second epoch observations of the CJ1 survey.

8.2. IDENTIFICATION OF PHYSICALLY DISTINCT CLASSES OF POWERFUL EXTRAGALACTIC SOURCES

The combined CJ1+PR sample forms a flux density limited complete sample of 200 objects, which treble the number of objects in the PR sample. Our main objectives were to identify physically distinct classes of AGN and to provide a sample which is large enough to make interesting statistical tests both as a whole and with and between different classes.

We made 5 GHz VLBI observations of all objects in the CJ1 sample which are accessible to the Mark II VLBI system, except one which has been mapped by others. Companion VLBI observations at 1.6 GHz have been presented by Polatidis et al. (1995) and Thakkar et al. (1995). Thus far we have complete information at both 1.6 GHz and 5 GHz on the milliarcsecond scale structure of all objects with a nuclear region brighter than $\sim$ 100 mJy. In addition, we mapped 8 CSO's or CSO candidates at 8.4 GHz. In the CJ1+PR sample 92 objects were mapped with the VLA A-array at 1.4 GHz. These observations, combined with

the VLA surveys of core-dominated sources by Murphy (1988, 1993) and Rusk (1988) and other published works, provided a complete set of images on arcsecond scales. The maps of core-dominated sources generally have dynamic range $> 3000 : 1$. Many of them show extended structure. With MERLIN at 5 GHz, 28 objects were observed, amongst which 20 were processed by the author and are presented in the thesis. Furthermore, complementary optical observations were also made to measure redshifts, search for optical counterparts and obtain optical polarimetry data. Currently the combined sample is 90% complete on redshifts and 95% complete on optical identification. We confirmed five questionable identifications and found possible optical counterparts for nine objects.

The dual-frequency VLBI observations provided valuable spectral information and enabled us to identify unambiguously the real core in core-jet sources and distinguish between the compact symmetric objects and core-jet sources. Based on morphological attributes on scales ≤ 5 kpc and > 5 kpc, we identified six physically distinct classes in the CJ1+PR sample. They are:

FR II A — FR II sources with asymmetric nuclear structure;

FR II S — FR II sources with symmetric nuclear structure;

D2A — One-sided structure on kilo-parsec scales with asymmetric nuclear structure;

D2S — One-sided structure on kilo-parsec scales with symmetric nuclear structure;

CA — Compact sources with asymmetric nuclear structure;

CS — Compact sources with symmetric structure.

Due to our flux density limit, we have no examples of the other two classes in our sample, namely,

FR I A — FR I sources with asymmetric nuclear structure;

FR I S — FR I source with symmetric nuclear structure.

We identified 24 CSO's and CSO candidates. Thus CSO's constitute $\sim$ 10% of samples selected at high frequency. Identification of the class of compact symmetric objects may have a profound impact on our understanding of AGN. Detailed study of one archetypal

CSO, 2352+495, has demonstrated that the CSO's are likely a class of short-lived powerful galaxies.

8.3. CONFIRMATION OF THE BIMODAL DISTRIBUTION OF THE MISALIGNMENT ANGLE

With the wealth of data we have collected, not only did we confirm the bimodal distribution of the misalignment angle, which was first discovered by Pearson & Readhead (1988), but we were also able to identify that the peak near 90° is contributed by a group of objects with high optical polarization, high fractional core flux, high radio variability and flat radio spectrum, all of which are symptoms of relativistic beaming. Thus these objects are very likely to have fast superluminal motion and strong X-ray emission. To explain the observed bimodal distribution of the misalignment angle, two populations of objects are required. The peak near 0° can be easily explained with objects having small intrinsic bends. However, to explain the peak near 90°, some sort of helical motion seems to be necessary. A binary black hole is the most interesting mechanism which can introduce helical motion. The group of objects which we have identified may have binary black holes.

8.4. ANGULAR-SIZE — REDSHIFT RELATION

We were unable to confirm the finding by Kellermann (1993a) that the angular size of radio sources on parsec scales can be used as a standard rod to test cosmological models. The mean angular sizes of the CJ1+PR objects show only slight dependence on redshift. However, there is an absence of objects with small angular size at $z < 0.1$. The Kolmogorov-Smirnov test shows that the angular size distributions of objects with $z < 0.1$ and those with $z > 0.1$ are significantly different. This may indicate an evolutionary effect.

8.5. IDENTIFICATION OF INTERESTING OBJECTS

We have identified a number of interesting objects for follow-up studies. Most of them are CSO's and CSO candidates. The object 1213+350 has a unique morphology, which consists

of two well-separated emission regions. Among many possible explanations are (1) a faint core with a bright hot spot; (2) twin nuclei and (3) complex gravitational lens system.

After a decade of slow progress in VLBI, this thesis, demonstrating the viability of snapshot imaging, has helped to spark a dramatic increase in the information available on parsec-scale structures in active galaxies. The many new avenues of enquiry that this opens up will no doubt be pursued rigorously by a number of works over the next decade.

REFERENCES

Abraham, R. G., McHardy, I. M., & Crawford, C. S. 1991, MNRAS, 252, 482

Alberdi, A., Marcaide, J. M., Marscher, A. P., Zhang, Y. F., Elósegui, P., Gómez, J. L., & Shaffer, D. B. , 1993, ApJ, 402, 160

Alef, W. 1988, in IAU Symposium 129, *The Impact of VLBI on Astrophysics and Geophysics*, eds. M.J. Reid & M.J. Moran, 523

Alexander, P., & Leahy, J. P. 1987, MNRAS, 225, 1

Aller, M. F., Aller, H. D., & Hughes, P. A. 1992, ApJ, 399, 16

Ananthakrishnan, S., Kulkarni, V. K., Ponsonby, J. E. B., Spencer, R. E., Graham, D. A., Porcas, R. W., Van Ardenne, A., Schilizzi, R. T., et al. 1989, MNRAS, 237, 341

Angel, J. P. R., & Stockman, H. S. 1980, ARAA, 18, 321

Antonucci, R. R. J. 1985, ApJS, 59, 499

Antonucci, R. R. J., & Ulvestad, J. S. 1985, ApJ, 294, 158

Antonucci, R. R. J. 1986, ApJ, 304, 634

Antonucci, R. R. S. 1993, ARAA, 31, 473

Antonucci, R. R. J., Hickson, P., Olszewski, E. W., & Miller, J. S. 1986, AJ, 92, 1

Argyle, R. W., & Eldridge, P. 1990, MNRAS, 243, 504

Barthel, P. D., Schilizzi, R. T., Miley, G. K., Jägers, W. J., & Strom, R. G. 1985, A&A, 148, 243

Barthel, P. D. 1989, ApJ, 336, 606

Baum, S. A., O'Dea, C. P., de Bruyn, A. G., & Murphy, D. W. 1990a, *Compact Steep-Spectrum and GHz-Peaked Spectrum Radio Sources*, eds. C. Fanti, R. Fanti, C. P. O'Dea & R. T. Schilizzi (Bologna: Consiglio Nazionale delle Ricerche), 53

Baum, S. A., O'Dea, C. P., Murphy, D. W., & de Bruyn, A. G. 1990b, A&A, 232, 19

Begelman, M. C., Blandford, R. D. & Rees, M. J. 1980, Nature, 287, 307

Begelman, M. C., Blandford, R. D. & Rees, M. J. 1984, Rev. Mod. Phys., 56, 255

Bicknell, G. V. 1994, AJ, 422, 542

Biermann, P. L., Duerbeck, H., Eckart, A., Fricke, K., Johnston, K. J., Kühr, H., Liebert, J., Pauliny-Toth, I. I. K., Schleicher, H., Stockman, H., Strittmatter, P. A., & Witzel, A. 1981, ApJ, 247, L53

Blandford, R. D. 1990, Saas–Fee Advanced Course 20, *Active Galactic Nuclei*, eds. T. J.-L. Courvoisier & M. Mayor (Berlin: Springer–Verlag), 161

Blandford, R. D., & Königl, A. 1979, ApJ, 232, 34

Blandford, R. D. & Rees, M. J. 1978, Pittsburgh conference in BL Lac objects, ed. A. M. Wolfe (University of Pittsburgh Press), 328

Bridle, A. H., Hough, D. H., Lonsdale, C. J., Burns, J. O., & Laing, R. A. 1994, AJ, submitted

Bridle, A. H., & Perley, R. A., 1984, ARAA, 22, 319

Bridle, A. H., Perley, R. A., & Henriksen, R. N., 1986, AJ, 92, 534

Browne, I. W. A., Clark, R. R., Moore, P. K., Muxlow, T. W. B., Wilkinson, P. N., et al. 1982, Nature, 299, 788

Burns, J. O., & Christiansen, W. A. 1980, Nature, 287, 208

Burns, J. O., & Gregory, S. A. 1982, AJ, 87, 1245

Cawthorne, T. V., Wardle, J. F. C., Roberts, D. H., & Gabuzda, D. C. 1993b, ApJS, 416, 519

Cawthorne, T. V., Wardle, J. F. C., Roberts, D. H., Gabuzda, D. G., & Brown, L. F. 1993a, ApJS, 416, 496

Chiu, H.-Y. 1964, Physics Today, 17, 21

Clark, B. G. 1973, Proc. IEEE, 61, 1242

Clark, B. G. 1980, A&A, 89, 377

Cohen, M. H., Moffet, A. T., Romney, J. D., Schilizzi, R. T., Shaffer, D. B., Kelermann, K. I., Purcell, G. H., Grove, G., Swenson, G. W., Yen, J. L., Pauliny-Toth, I. I. K., Preuss, E., Witzel, A., & Graham, D. 1975, ApJ, 201, 249

Condon, J. J., 1992, ARAA, 30, 575

Conway, J. E., & Murphy, D. W. 1993, ApJ, 411, 89

Conway, J. E., Myers, S. T., Pearson, T. J., Readhead, A. C. S., Unwin, S. C., & Xu W. 1994, ApJ, 425, 568

Conway, J. E., Pearson, T. J., Readhead, A. C. S., Unwin, S. C., Xu, W., & Mutel, R. M. 1992, ApJ, 396, 62

Conway, J. E., Unwin, S. C., Pearson, T. J., Readhead, A. C. S., & Xu W. 1990, *Compact Steep-Spectrum and GHz-Peaked Spectrum Radio Source*, eds. C. Fanti, R. Fanti, C. P. O'Dea & R. T. Schilizzi, 157

Cornwell, T. J., & Wilkinson, P. N. 1981, MNRAS, 196, 1067

De Ruiter, H. R., Willis, A. G., & Arp, H. C. 1977, A&AS, 28, 211

Djorgovski, S., & Spinrad, H. 1981, ApJ, 251, 417

Eckart, A., Witzel, A., Biermann, P., Johnston, K. J., Simon, R., Schalinski, C., & Kühr, H. 1987, AAS, 67, 121

Fanaroff, B. L., & Riley, J. M. 1974, MNRAS, 167, 31p

Fanti, C., Fanti, R., de Ruiter, H. R., & Parma, P. 1986, A&AS, 65, 145

Fanti, C., Fanti, R., Parma, P., Schilizzi, R. T., & van Breugel, W. J. M. 1985, AA, 143, 292

Fanti, R., Fanti, C., Schilizzi, R. T., & Spencer, R. E. 1990a, AA, 231, 333

Fanti, R., Fanti, C., Schilizzi, R. T., Spencer, R. E., van Breugel, W. J. M., Parma, P., Venturi, T., Nan, R. D., & Muxlow, T., 1990b, *Compact Steep-Spectrum and GHz-Peaked Spectrum Radio Sources*, eds. C. Fanti, R. Fanti, C. P. O'Dea & R. T. Schilizzi (Bologna: Consiglio Nazionale delle Ricerche), 64

Fanti R., Fanti C., Stanghellini C., Schilizzi R. T., Spencer R. E., & van Breugel W. J. M.

1990c, *Compact Steep-Spectrum and GHz-Peaked Spectrum Radio Source*, eds. C. Fanti, R. Fanti, C. P. O'Dea & R. T. Schilizzi (Consiglio Nazionale delle Ricerche - Instituto di Radioastronomia), 48

Fejes, I., & Porcas, R. 1990, *Compact Steep-Spectrum and GHz-Peaked Spectrum Radio Sources*, eds. C. Fanti, R. Fanti, C. P. O'Dea & R. T. Schilizzi (Bologna: Consiglio Nazionale delle Ricerche), 128

Feretti, L., Comoretto, G., Giovannini, G., Venturi, T., & Wehrle, A. E. 1993, ApJ, 408, 446

Fernini, I., Burns, J. O., Bridle, A. H., & Perley, R. A. 1993, AJ, 105, 1690

Foley, A. R. 1982, Ph.D. thesis, University of Manchester

Foulsham, P. A. 1989, Ph.D. thesis, University of Manchester

Garrington, S. T., Leahy, J. P., Conway, R. G., & Laing, R. A. 1988, Nature, 331, 147

Giovannini, G., Comoretto, G., Feretti, L., Marcaide, J., Venturi, T., Vermeulen, R., & Wehrle, A. E. 1992, *Physics of Active Galactic Nuclei*, eds. W. J. Duschl & S. J. Wagner (Berlin: Springer-Verlag), 561

Greenstein, J. L., & Matthews, T. A. 1963, Nature, 197, 1041

Gregorini, L., Padrielli, L., Parma, P., & Gilmore, G. 1988, A&AS, 74, 107

Gurvits, L. I. 1993, *Sub-arcsecond Radio Astronomy*, eds. R. J. Davis & R. S. Booth (Cambridge: Cambridge University Press), 380

Gurvits, L. I., Kardashev, N. S., Popov, M. P., Schilizzi, R. T., Barthel, P. D., Pauliny-Toth, I. I. K., & Kellermann, K. I., 1992, A&A, 260, 82

Gurvits, L. I., Lobanov, A. P., Schilizzi, R. T., Kellermann, K. I., Barthel, P. D., Pauliny-Toth, I. I. K., Kardashev, N. S., & Popov, M. V. 1994, BAAS, 25, 1410

Hardee, P. E., Cooper, M. A., & Clarke, D. A. 1994, ApJ, 424, 126

Heckman, T. M., Smith, E. P., Baum, S. A., van Breugel, W. J. M., Miley, G. K., Illingworth, G. D., Bothun, G. D., & Balick, B., 1986, ApJ, 311, 526

Herbig, T., Readhead, A. C. S., & Xu, W. 1995, in preparation

Hes, R., Barthel, P. D., & Fosbury, R. A. E., 1993, Nature, 362, 326

Hewitt, A., & Burbidge, G. 1987, ApJS, 63, 1

Hewitt, A., & Burbidge, G. 1989, ApJS, 69, 1

Hewitt, A., & Burbidge, G. 1993, ApJS, 87, 451

Hey, J. S., Parsons, S. J., & Phillips, J. W., 1946, Nature, 158, 234

Hintzen, P., Ulvestad, J., & Owen, F. N. 1983, AJ, 88, 709

Hodges, M. W., & Mutel, R. L. 1987, *Superluminal Radio Sources*, eds. J. A. Zensus & T. J. Pearson (Cambridge: Cambridge University Press), 168

Hodges, M. W., Mutel, R. L., & Phillips, R. B. 1984, AJ, 89, 1325

Högbom, J. A. 1974, A&AS, 15, 417

Hooimeyer, J. R. A., Barthel, P. D., Schilizi, R. T., & Miley, G. K. 1992 A&A, 261, 61

Hough, D. H. 1986, Ph.D. thesis, California Institute of Technology

Hough, D. H., & Readhead, A. C. S. 1987, *Superluminal Radio Sources*, eds. J. A. Zensus & T. J. Pearson (Cambridge: Cambridge University Press), 114

Hough, D. H., & Readhead, A. C. S. 1989, AJ, 98, 1208

Hough, D. H., Vermeulen, R. C., & Readhead, A. C. S. 1993, *Sub-arcsecond Radio Astronomy*, eds. R. J. Davis & R. S. Booth (Cambridge: Cambridge University Press), 193

Impey, C. D., 1987, *Superluminal Radio Sources*, eds. J. A. Zensus & T. J. Pearson (Cambridge: Cambridge University Press), 23

Impey, C. D., Lawrence, C. R., & Tapia, S. 1991, ApJ, 375, 46

Jägers, W. J. 1987, 71, 603

Jenkins, C. J., Pooley, G. G., & Riley, J. M. 1977, MNRAS, 84, 61

Jones, D. L., Unwin, S. C., Readhead, A. C. S., Sargent, W. L. W., Seielstad, G. A., Simon, R. S., Walker, R. C., Benson, J. M., Perley, R. A., Bridle, A. H., Pauliny-Toth, I. I. K., Romney, J., Witzel, A., Wilkinson, P. N., Bääth, L. B., Booth, R. S., Fort, D. N., Galt, J. A., & Linfield, R. P., 1986, ApJ, 305, 684

Junor, W., & Biretta, J. A. 1994, *Compact Extragalactic Radio Sources*, eds. J.A. Zensus & K.I. Kellermann, p97

Kapahi, V. K. 1981, A&AS, 43, 381

Kapahi, V. K. 1987, *IAU Symposium 124, Observational Cosmology*, eds. Hewitt, A, Burbidge, G., & Fang, L. Z., 251

Kapahi, V. K. 1989, AJ, 97, 1

Kapahi, V. K. 1990, *Parsec-scale Radio Jets*, eds. J. A. Zensus & T. J. Pearson (Cambridge: Cambridge University Press), 304

Kapahi, V. K., & Neff, S. G. 1982, Journal of Astrophy. and Astro., 3, 173

Kellerman, K. I. 1993a, Nature, 361, 134

Kellerman, K. I. 1993b, *Sub-arcsecond Radio Astronomy*, eds. R. J. Davis & R. S. Booth (Cambridge: Cambridge University Press), 386

Kellerman, K. I. 1993c, *Observational Cosmology* (ASP Conference Series 51), eds. G. Chincarini, A. Iovino, T. Maccacaro, & D. Maccagni (San Francisco: ASP), 50

Kellerman, K. I. & Owen, F. N., 1988, *Galactic and Extragalactic Radio Astronomy*, ed. Verschuur, G. L. & Kellerman, K. I., 563

Kellerman, K. I., & Pauliny-Toth, I. I. K., 1981, ARAA, 373

Kellermann, K. I., Sramek, R., Schmidt, M., Shaffer, D. B., Green, R., 1989, AJ, 98, 1195

Kinman, T. D. 1976, ApJ, 205, 1

Kollgaard, R. I., Wardle, J. F. C., & Roberts, D. H. 1990, AJ, 100, 1057

Krolik, J. H., 1992, *The Astronomy and Astrophysics Encyclopedia*, ed. Maran, S. P., 7

Kühr, H., Johnston, K. J., Odenwald, S., & Adlhoch, J. 1987, A&AS, 71, 493

Kühr, H., Nauber, U., Pauliny-Toth, I. I. K., & Witzel, A. 1979, MPIfR Preprint 55

Kühr, H., Pauliny-Toth, I. I. K., Witzel, A., & Schmidt, J. 1981a, AJ, 86, 854

Kühr, H., & Schmidt, G. D. 1990, AJ, 99, 1

Kühr, H., Witzel, A., Pauliny-Toth, I. I. K., & Nauber, U. 1981b, A&AS, 45, 367

Laing, R. A. 1981, MNRAS, 195, 261

Laing, R. A. 1988, Nature, 331, 149

Laing, R. A., Riley, J. M., & Longair, M. S. 1983, MNRAS, 204, 151

Lawrence, C. R., 1990, *Parsec-scale Radio Jets*, ed. J. A. Zensus & T. J. Pearson (Cambridge: Cambridge University Press), 280

Leahy, J. P., Muxlow, T. W. B., & Stephens, P. W. 1989, MNRAS, 239, 401

Leahy, J. P., & Perley, R. A. 1991, AJ, 102, 1627

Liu, R., & Pooley, G. 1991, MNRAS, 253, 669

Longair, M. S. 1975, MNRAS, 173, 309

Lonsdale, C. J., & Morison, I. 1983, MNRAS, 203, 833

Marscher, A. P., Zhang, Y. F., Shaffer, D. B., Aller, H. D. & Aller, M. F. 1991, ApJ, 371, 491

McCarthy, P. J. 1993, ARAA, 31, 639

Miley, G. 1971, MNRAS, 152, 477

Miley, G. 1980, ARAA, 18, 165

Moore, R. L., & Stockman, H. S. 1984, ApJ, 279, 465

Morabito, D. D., Preston, R. A., Slade, M. A., & Jauncey, D. L. 1982, AJ, 87, 417

Murphy, D. W., 1988 Ph.D. thesis, University of Manchester

Murphy, D. W., Browne, I. W. A., & Perley, R. A. 1993, MNRAS, 264, 298

Mutel R. L., & Hodges, M. W. 1986, ApJ, 307, 472

Mutel R. L., Hodges, M. W., & Phillips, R. B. 1985, ApJ, 209, 86

Mutel, R. L. & Phillips, R. B. 1988, in IAU Symposium 129, *The Impact of VLBI on Astrophysics and Geophysics*, eds. M. J. Reid & J. M. Moran (Dordrecht: Kluwer), 73

Muxlow, T. W. B., & Garrington, S. T. 1991, *Beams and Jets in Astrophysics*, ed. P. A. Hughes (Cambridge: Cambridge University Press), 52

Nilsson, K., Valtonen, M. J., Kotilainen, J., & Jaakola, T. 1993, ApJ, 413, 453

Northover, K. J. E. 1973, MNRAS, 165, 370

O'Dea, C. P., & Barvainis, R. 1986, in IAU Symposium 119, *Quasars*, ed. Swarup, G., & Kapahi, V. K., 217

O'Dea, C. P., Baum, S. A., & Morris, G. B., 1990a, A&AS, 82, 261

O'Dea, C. P., Baum, S. A., & Stanghellini, C. 1991, ApJ, 380, 66

O'Dea, C. P., Baum, S. A., Stanghellini, C., Dey, A., van Breugel, W. J. M., Deustua, S. & Smith, S. P. 1992, AJ, 104, 1320

Orr, M. J. L., & Browne, I. W. A. 1982, MNRAS, 200, 1067

Owen, F. N., & Puschell, J. J. 1984, AJ, 89, 932

Owen, F. N., & Rudnick, L. 1976, ApJ, 205, L1

Owen, F. N., Wills, B. J., & Wills, D. 1980, ApJ, 235, L57

Padovani, P., & Urry, C. M., 1992a, ApJ, 387, 449

Patnaik, A. R., Browne, I. W. A., King, L. J., Muxlow, T. W. B., Walsh, D. & Wilkinson, P. N. 1993, MNRAS, 261, 435

Patnaik, A. R., Browne, I. W. A., Wilkinson, P. N., & Wrobel, J. M. 1992, MNRAS, 254, 655

Peacock, J. A., & Wall, J. V. 1982, MNRAS, 198, 843

Pauliny-Toth, I. I. K., Witzel, A., Preuss, E., Kühr, H., Kellermann, K. I., Fomalont, E. B. & Davis, M. M. 1978, AJ, 83, 451

Pearson, T. J. 1991, BAAS, 23, 991

Pearson, T. J. 1995, in preparation

Pearson, T. J., Perley, R. A., & Readhead, A. C. S. 1985, AJ, 90, 738

Pearson, T. J., & Readhead, A. C. S. 1981, ApJ, 248, 61

Pearson, T. J., & Readhead, A. C. S. 1984, in IAU Symposium 110, *VLBI & Compact Radio Sources*, eds. R. Fanti, K. Kellermann & G. Setti (Dordrecht: Reidel), 15

Pearson, T. J., & Readhead, A. C. S. 1988, ApJ, 328, 114

Pearson, T. J., Readhead, A. C. S., & Barthel, P. D. 1987a, *Superluminal Radio Sources*, eds. J. A. Zensus & T. J. Pearson (Cambridge: Cambridge University Press), 94

Pedelty, J. A., Rudnick, L., McCarthy, P. J., & Spinrad, H. 1989, AJ, 98, 1232

Perley, R. A., 1982, AJ, 87, 859

Perley, R. A., Bridle, A. H., & Willis, A. G. 1984, ApJS, 54, 291

Perley, R. A., Fomalont, E. B., & Johnston, K. J. 1982, ApJ, 255, 93

Perley, R. A., Willis, A. G., & Scott, J. S. 1979, Nature, 281, 437

Phillips, R. B., & Mutel, R. L. 1980, ApJ, 236, 89

Phillips, R. B., & Mutel, R. L. 1981, ApJ, 244, 19

Phillips, R. B., & Mutel, R. L. 1982, A&A, 106, 21

Polatidis, A. G. 1993, Ph.D. thesis, University of Manchester

Polatidis, A. G., Wilkinson, P. N., Xu, W., Readhead, A. C. S., & Pearson, T. J. 1995, ApJS, in press

Pooley, G. G., & Henbest, S. N. 1974, MNRAS, 169, 477

Porcas, R. W. 1987, *Superluminal Radio Sources*, eds. J. A. Zensus & T. J. Pearson (Cambridge: Cambridge University Press), 12

Preston, R. A., Morabito, D. D., Williams, J. G., Faukner, J., Jaunsey, D., & Nicholson, G. D. 1985, AJ, 90, 1599

Quirrenbach, A., Witzel, A., Krichbaum, T. P., Hummel, C. A., Werner R., Schalinski, C. J., Ott, M., Alberdi, A., & Rioja, M. 1992, A&A, 258, 279

Readhead, A. C. S. 1994a, *Frontiers of Space and Ground-based Astronomy*, eds. W. Wamsteker, M. S. Longair & Y. Knodo (Dordrecht: Kluwer Academic Publishers), 145

Readhead, A. C. S. 1980, *Objects of High Redshifts*, eds Abell & Peebles (Dordrecht: Reidel), 165

Readhead, A. C. S., Cohen, M. H., & Blandford, R. D. 1978a, Nature, 272, 131

Readhead, A. C. S., Cohen, M. H., Pearson, T. J., & Wilkinson, P. N. 1978b, Nature, 276, 768

Readhead, A. C. S., Hough, D. H., Ewing, M. S., Walker, R. C., & Romney, J. D. 1983,

ApJ, 265, 107

Readhead, A. C. S., Pearson, T. J., & Unwin, S. C. 1984, IAU Symposium 110, *VLBI and Compact Radio Sources*, Reidel, 1984, eds. R. Fanti, K. I. Kellermann, & G. Setti (Dordrecht: Reidel), 131

Readhead, A. C. S., Xu, W., Pearson, T. J., Wilkinson, P. N., & Polatidis, A. G. 1995, submitted to ApJ

Rees, M. J. 1984, ARAA, 22, 471

Reid, M. J., Biretta, J. A., Junor, W., Muxlow, T. W. B., & Spencer, R. E. 1989, ApJ, 336, 112

Riley, J. M., & Pooley, G. G. 1975, Mem. RAS, 80, 105

Rudnick, L., & Edgar, B. K., 1984, ApJ, 279, 74

Rudnick, L., & Jones, T. W. 1982 AJ, 88, 518

Rusk, R. E. & Seaquist, E. R. 1985, AJ, 90, 30

Rusk, R. E. 1988, Ph.D. thesis, Univerity of Toronto

Saikia, D. J., Kulkarni, V. K., & Porcas, R. W. 1986, MNRAS, 219, 719

Saikia, D. J., Muxlow, T. W. B., & Junor, W. 1990, MNRAS, 245, 503

Saikia, D. J., & Salter, C. J. 1988, ARAA, 26, 93

Saikia, D. J., Shastri, P., Cornwell, T. J., Junor, W., & Muxlow, T. W. B. 1989, Journal of Astrophy. and Astro., 10, 203

Sandage, A. R. 1965, ApJ, 141, 1560

Sandage, A. R. 1988, ARAA, 26, 561

Sanghera, H. S. 1990, *Compact Steep-Spectrum and GHz-Peaked Spectrum Radio Sources*, eds. C. Fanti, R. Fanti, C. P. O'Dea & R. T. Schilizzi (Bologna: Consiglio Nazionale delle Ricerche), 74

Sanghera, H. S. 1992, Ph.D. thesis, University of Manchester

Saripalli, L., Subrahmanyan, R., & Hunstead, R. W. 1994, MNRAS, 269, 37

Scheuer, P. A. G., & Readhead, A. C. S. 1979, Nature, 277, 182

Schilizzi, R. T., Fanti, C., Fanti, R., Spencer, R. E., Shanghera, H., Venturi, T., Nan, R., & van Breugel, W. J. M. 1990, *Compact Steep-Spectrum and GHz-Peaked Spectrum Radio Source*, eds. C. Fanti, R. Fanti, C. P. O'Dea & R. T. Schilizzi (Consiglio Nazionale delle Ricerche - Instituto di Radioastronomia), 125

Schmidt, M. 1963, Nature, 197, 1040

Schwab, F. R. 1984, AJ, 1076

Schwab, F. R., & Cotton, W. D. 1983, AJ, 88, 688

Seielstad, G. A., Pearsons, T. J., & Readhead, A. C. S. 1983, PASP, 95, 842

Shepherd, M. C., Pearson, T. J., & Taylor, G. B. 1994, BAAS, in press

Sitko, M. L., Schmidt, G. D., & Stein, W. A. 1985, ApJS, 59, 323

Smith, P. S., Balonek, T. J., Heckert, P. A., & Elston, R. 1986, ApJ, 305, 484

Spangler, S. P., & Sakurai, T. 1985, ApJ, 97, 84

Spencer, R. E., McDowell, J. C., Charlesworth, M., Fanti, C., Parma, P., & Peacock, J. A. 1989, MNRAS, 240, 657

Spencer, R. E., Schilizzi, R. T., Fanti, C., Fanti, R., Parma, P., van Breugel, W. J. M., Venturi, T., Muxlow, T. W. B., & Nan, R. 1991, MNRAS, 250, 225

Spinrad, H., Djorgovski, S., Marr, J., & Aguilar, L. 1985, PASP, 97, 932

Stanghellini, C., O'Dea, C. P., Baum, S. A., & Laurikainen, E. 1993, ApJS, 88, 1

Stickel, M., Fried, J. W., & Kühr, H. 1993, A&AS, 98, 393

Stickel, M., & Kühr, H. 1993, A&AS, 100, 395

Stickel, M., & Kühr, H. 1993, A&AS, 101, 521

Stickel, M., & Kühr, H. 1994a, A&AS, 103, 349

Stickel, M., & Kühr, H. 1994b, A&AS, 105, 67

Stickel, M., & Kühr, H. 1994c, A&AS, 105, 221

Stickel, M., Kühr, H., & Fried, J. W. 1993, A&AS, 97, 483

Stockman, H. S. 1978, *Pittsburgh Conference on BL Lac Objects*, ed. A. W. Wolfe, 149

Stockman, H. S., Moore, R. L., & Angel, J. R. P. 1984, ApJ, 279, 485

Takalo, L. O. 1991, A&AS, 90, 161

Takalo, L. O., Sillanpää, A., Nilsson, K., Kidger, M., de Diego, J. A., & Piirola, V. 1992, A&AS, 94, 37

Taylor, G. B., Vermeulen, R. C., Pearson, T. J., Readhead, A. C. S., Henstock, D. R., Browne, I. W. A., & Wilkinson, P. N. 1994, ApJS, in press

Ulvestad, J. S., & Johnston, K. J. 1984, AJ, 82, 189

Unger, S. W., Pedlar, A., Axon, D. J., Wilkinson, P. N., Appleton, P. J. 1984, MNRAS, 211, 783

Urry, C. M. 1993, *Sub-arcsecond Radio Astronomy*, eds. R. J. Davis & R. S. Booth (Cambridge: Cambridge University Press), 333

Urry, C. M., Padovani, P., & Stickel, M. 1991, ApJ, 382, 501

Van Breugel, W. J. M., Fanti, C., Fanti, R., Stanghellini, C., Schilizzi, R. T., & Spencer, R. E. 1992, A&A, 256, 56

Van Breugel, W. J. M., Miley, G., & Heckman, T. 1984, AJ, 89, 5

Van Breugel, W. J. M., & Schilizzi, R. 1986, ApJ, 301, 384

Venturi, T., Feretti, L., Giovannini, G., & Wehrle, A. E., 1993a, *Sub-arcsecond Radio Astronomy*, eds. R. J. Davis & R. S. Booth (Cambridge: Cambridge University Press), 204

Venturi, T., Giovannini, G., Feretti, L., Comoretto, G., & Wehrle, A. E., 1993b, ApJ, 408, 81

Venturi, T., Readhead, A. C. S., Marr, J. M., & Backer, D. C. 1993c, ApJ, 411, 552

Vermeulen, R. C., & Cohen, M. H. 1994, ApJ, in press

Véron, M.-P., & Véron, P. 1991, *E.S.O. Scientific Report No. 10*

Véron-Cetty, M. P., & Woltjer, L. 1990, AA, 236, 69

Vigotti, M., Grueff, G., Perley, R., Clark, B. G. & Bridle, A. H. 1989, AJ, 98, 419

Walker, C. R. 1988, in *Synthesis Imaging in Radio Astronomy*, eds. R. A. Perley, F. R. Schwab, & A. H. Bridle, 355

Wardle, J. F. C., & Kronberg, P. P. 1974, ApJ, 194, 249

Wehrle, A. E., Cohen, M. H., & Unwin, S. C. 1990, *Parsec-scale Radio Jets*, ed. J. A. Zensus & T. J. Pearson (Cambridge: Cambridge University Press), 49

Wehrle, A. E., Cohen, M. H., Unwin, S. C., Aller, H. D., Aller, M. F., & Nicolson, G. 1992, ApJ, 391, 589

Wells, D., Wells, B. J., Breger, M., Hsu, J.-C. 1980, AJ, 85, 1555

White, R. L., & Becker, R. H. 1992, ApJS, 79, 331

Wilkinson, P. N., Polatidis, A. G., Readhead, A. C. S., Xu, W., & Pearson, T. J., 1994, ApJ, 432, L87

Wilkinson, P. N., Tzioumis, A. K., Akujor, C. E., Benson, J. M., Walker, R. C., & Simon, R. S. 1990, *Parsec-Scale Radio Jets*, eds. J. A. Zensus & T. J. Pearson (Cambridge: Cambridge University Press), 152

Willis, A. G., Strom R. G., Perley R. A., & Bridle, A. H. 1982, IAU Symposium 97, *Extragalactic Radio Sources*, eds. D. S. Heeschen & C. M. Wade (Dordrecht: Reidel), 141

Willis, A. G., Strom, R. G., & Wilson, A. S. 1974, Nature, 250, 625

Witzel, A., Schalinski, C. J., Johnston, K. J., Biermann, P. L., Krichbaum, T. P., Hummel, C. A., & Eckart, A. 1988, A&A, 206, 245

Witzel, A., Wagner, S., Wegner, R., Steffen, W., & Krichbaum, T. 1993, *Sub-arcsecond Radio Astronomy*, eds. R. J. Davis & R. S. Booth (Cambridge: Cambridge University Press), 159

Woltjer, L. 1990, Saas–Fee Advanced Course 20, *Active Galactic Nuclei*, eds. T. J.-L. Courvoisier & M. Mayor (Springer–Verlag), 1

Wrobel, J. M., & Lind, K. R. 1990, ApJ, 348, 135

Xu, W., Lawrence, C. R., Readhead, A. C. S., & Pearson, T. J. 1994, AJ, 108, 395

Xu, W., Polatidis, A. G. Readhead, A. C. S., Wilkinson, P. N., & Pearson, T. J. 1993, *Sub-arcsecond Radio Astronomy*, eds. R. J. Davis & R. S. Booth (Cambridge:

Cambridge University Press), 216

Zensus, J. A., & Pearson, T. J. 1987, *Superluminal Radio Sources* (Cambridge: Cambridge University Press)

Zensus, J. A., & Pearson, T. J. 1990, *Parsec-scale Radio Jets* (Cambridge: Cambridge University Press)

Zensus, J. A., & Porcas, R. W. 1985, *Active Galactic Nuclei*, ed. J. Dyson, 54

Zensus, J. A., & Porcas, R. W. 1986, in IAU Symposium 119, *Quasars*, ed. Swarup, G., & Kapahi, V. K., 167